RUHR-UNIVERSITÄT BOCHUM

Antonia Therese Nitsch

A novel framework for the numerical modelling of the hydro-mechanical behaviour of expansive soils

Bochum 2026

Heft 90

Schriftenreihe des Lehrstuhls für
Bodenmechanik, Grundbau und Umweltgeotechnik

Herausgeber: Torsten Wichtmann

ISSN 2699-1020

Antonia Nitsch A novel framework for numerical modelling of expansive soils

90

ISSN 2699-1020

Ruhr-Universität Bochum
Schriftenreihe Bodenmechanik, Grundbau und Umweltgeotechnik
Heft 90

Herausgeber:
Prof. Dr.-Ing. habil. Torsten Wichtmann
Ruhr-Universität Bochum
Fakultät für Bau- und Umweltingenieurwissenschaften
Lehrstuhl für Bodenmechanik, Grundbau und Umweltgeotechnik
44801 Bochum
Telefon: 0234/ 3226135
Internet: www.bgu.ruhr-uni-bochum.de

ISSN 2699-1020

© 2026 der Herausgeber

A novel framework for the numerical modelling of the hydro-mechanical behaviour of expansive soils

Dissertation

as a requirement for the degree of

Doktor-Ingenieur (Dr.-Ing.)

at the Faculty of

Civil and Environmental Engineering

Ruhr-Universität Bochum

submitted by

Antonia Therese Nitsch

from Düsseldorf, Germany

Reviewers:

Prof. Dr.-Ing. habil. Torsten Wichtmann

Prof. Dr.-Ing. Carlos Eduardo Grandas Tavera

Prof. Dr.-Ing. Jan Machaček

Univ.-Prof. Dr. techn. Barbara Schneider-Muntau

Date of the doctoral defence: 6 May 2026

Preface of the editor

Due to their mineralogical composition, expansive soils and rocks tend to increase in volume - a process known as swelling - when exposed to water, or to generate swelling pressures when deformation is restricted. When excavating tunnels or constructing other underground structures in such soils or rocks, high swelling pressures or heave resulting from swelling processes can cause damage to the structures. However, the properties of swellable soils are also exploited technically in artificial sealing systems. One example of this is planned nuclear waste repositories that may be excavated in swellable clay shale or crystalline host rocks, where the tunnels and shafts are to be backfilled with compacted expansive material. Water infiltrating from the surrounding rock will induce swelling of the compacted backfill, which significantly reduces its permeability and thus creates a technical barrier with excellent sealing properties.

In order to perform numerical calculations of such systems with the finite element method, suitable hydro-mechanically coupled models are required. The realistic prediction of the magnitude and the time evolution of swelling require an adequate representation of the underlying coupled hydro-mechanical processes. Various approaches already exist for describing the behaviour of swelling soils or rocks on a constitutive level. However, these are either very simple, mostly one-dimensional, empirical swelling laws or very complex material models, some of which are based on a microstructure with dual porosity. Not all swellable soils exhibit such a microstructure with micro- and macro-pores, however, meaning that these material models cannot be applied universally. Furthermore, calibrating the parameters of these models requires highly complex laboratory tests that can only be conducted in specialized laboratories. Higher-quality material models that do not account for dual porosity (e.g., the Barcelona Basic Model, BBM) are easier to calibrate; however, with a single set of parameters, they can generally only satisfactorily represent one of the two swelling phenomena - i.e., the increase in volume during unimpeded expansion or the development of swelling pressures at constant volume. On the finite element level, the attachment of swelling water to the solid phase has not been considered so far, although it may allow a simpler constitutive description without explicitly considering the microstructure.

The limitations of the existing approaches served as motivation for the doctoral research of Antonia Nitsch. In her dissertation, she developed a novel numerical framework for simulating the complex behaviour of swellable soils under generalized hydro-mechanical loading conditions. Based on her own experiments conducted on reconstituted samples of Opalinus clay, she proposed a hypoplastic constitutive model for swellable soils, as well as an approach for the relative permeability considering its reduction due to the attachment of swelling water to the solid phase. The initially one-dimensional formulations were subsequently generalized to three dimensions. In addition, based on the theory of porous media, Ms. Nitsch extended a finite element to include a fourth phase that accounts for the adsorption of swelling water onto the solid phase, which allows to describe the resulting reduction in permeability. Ms. Nitsch documents the complex implementation of both the mechanical model and the extended finite element into the FE program numgeo and validates them by comparing the simulation results with analytical solutions and commercial FE software. Another step in the validation process involves the successful back-analysis of her own laboratory tests as well as further experiments on bentonite-based materials from the literature. The laboratory experiments were simulated both as single element tests and boundary value problems, the latter allowing to inspect the spatial distribution and time evolution of swelling. The transient behaviour emerges from the adequate representation

of the water attachment in the modelling framework. For the various materials with different contents of swelling minerals very good agreement between the numerical prediction and the experimental measurements was achieved. Finally, Ms. Nitsch demonstrates the applicability of her novel numerical approach to large-scale problems by simulating a tunnel in a nuclear waste repository backfilled with swellable clay and subjected to infiltration from the host rock.

Using the novel numerical approach developed in this dissertation, it is possible to simulate the relevant swelling processes under various boundary conditions (including volume expansion at constant load and swelling pressure development at constant volume) with a single set of material parameters, which can be determined based on relatively simple laboratory experiments. The simulation as a boundary value problem allows the prediction of the temporal evolution of the swelling phenomena. This represents a significant improvement over the approaches implemented in commercial software, which typically capture only selected swelling mechanisms. The model is also more widely applicable than the double-porosity approaches, which are cumbersome to calibrate and whose assumptions do not hold for all soils capable of swelling. Finally, the numerical approach developed in the doctoral research of Ms. Nitsch is of great practical relevance and can be applied to simulate various geotechnical problems involving swellable soils in the future, e.g. in the framework of optimizing sealing systems for nuclear waste repositories.

Bochum, May 2026 Torsten Wichtmann

Acknowledgment

This work was inspired, supervised, and encouraged by many people, to whom I would like to express my heartfelt thanks for their continuous support throughout this journey.

I conducted my PhD work mainly at Ruhr-Universität Bochum under the supervision of Prof. Torsten Wichtmann. I sincerely thank him for giving me the opportunity to pursue my research in Bochum. Exactly ten years ago, he first sparked my interest in soil mechanics when I started my Bachelor's thesis under his supervision at Karlsruher Institut für Technologie (KIT). Since then, he has placed trust in my abilities and encouraged me to follow an academic path.

My PhD project itself has its roots in my Master's thesis at KIT. I would like to thank Dr.-Ing. Julia Leuthold, who introduced me to the experimental investigation of expansive soils and supported the early stages of my research through valuable discussions and guidance. Alongside her, Prof. Carlos Grandas Tavera and Prof. Jan Machaček accompanied this work from its beginnings and continued to supervise my research throughout my PhD. I am deeply grateful to Carlos Grandas Tavera for his endless curiosity and constitutive expertise, and for explaining complex concepts with clarity and enthusiasm. I appreciated the welcoming atmosphere he created during my visits to Brandenburgische Technische Universität Cottbus-Senftenberg, which partly funded my research. I am equally grateful to Jan Machaček for encouraging me to pursue my PhD, for sharing his numerical expertise, and trusting me to contribute to numgeo. I particularly valued his kind and steady guidance through the highs and lows that inevitably come with such a long project. I sincerely thank Prof. Barbara Schneider-Muntau for her time and effort in acting as the external reviewer of my thesis. I appreciated her genuine interest in my work and the encouraging exchange during my research visit at Universität Innsbruck. In a field that is still largely male-dominated, I found this experience particularly valuable.

I would also like to thank all my colleagues and the staff in Bochum and Cottbus for creating a constructive and enjoyable working environment. Special thanks go to Wiebke Baille, from whose deep knowledge of clay mineralogy and laboratory experience I greatly benefited; to Diethard König for his continuous organisational support; to Florian Christ and Wolfgang Lieske for stimulating discussions on clays and many topics beyond; to Maximilian Schoen and Christoph Schmüdderich for guidance through the jungle of numerical methods; to Patrick Staubach and Merita Tafili for bringing KIT spirit to RUB; to Frederik Koch for emergency coffee; to Natascha Kallerhoff for her cheerful spirit; to Felipe Prada, Germán Matos, and Viktor Krause for creating the best office atmosphere and to many others. Beyond the professional exchange and discussions, I truly enjoyed my time in Bochum and the many shared experiences.

Lastly, I am thankful for all the support I received from my friends and my family throughout this journey. I especially thank my partner Marius, my siblings Christina and Max, and my sister-in-law Hanna, for their friendship, patience and encouragement, which I value deeply. Above all, I am grateful for my parents, Bettina and Christian, and for their love and understanding at all times. Thank you for teaching me to stay curious and determined, to believe in myself, to embrace new opportunities, and, most importantly, to keep my joy along the way.

Bochum, May 2026 Antonia Nitsch

Abstract

Some geomaterials tend to expand upon contact with water due to their clay mineralogical composition. They are known as expansive geomaterials and include both soils and clay shales. The tendency, referred to as swelling, manifests either as an increase in volume, if deformation is allowed, or as a stress increase (swelling pressure), if deformation is constrained. Conversely, swelling influences the mechanical and hydraulic properties, leading to increased compressibility and decreases in preconsolidation state, shear strength, and permeability. The hydro-mechanical behaviour of expansive soils is relevant for the design of underground structures in contact with them. For piles, tunnels or retaining structures built in expansive ground, swelling may cause uplift or induce additional loads. In sealing elements of landfills or deep geological repositories, swelling of expansive buffer material can be exploited beneficially to limit water flow and prevent pollutant migration, e.g., in nuclear waste disposal.

Reliable simulation of expansive soils using Finite Element (FE) analysis requires the accurate representation of the acting hydro-mechanical processes. During swelling, a fraction of pore water is attached to clay minerals, reducing the effective porosity. So far, numerical modelling of expansive soils mostly concerns constitutive relationships for the stress-strain behaviour, the water retention behaviour and the permeability reduction of the soil upon swelling. They range from simple moisture swelling models to sophisticated models from unsaturated soil mechanics, in which expansive soil behaviour is commonly represented by differentiation of micro- and macro-structural responses within the double porosity concept. They show promising results, however, necessitate a bi-modal pore size distribution, which is not present in all expansive soils, and the determination of model parameters is challenging due to advanced laboratory testing. While the transition of water from a mobile state to a state attached to the clay minerals is acknowledged as a driving force in the constitutive description, the associated changes in volume fractions and their effect on overall material behaviour are generally neglected in the underlying governing equations of the theory of porous media (TPM) in existing numerical approaches. In various other applications of continuum mechanics, extensions of the TPM for expansive porous media have been successfully employed, e.g. for swelling gels and paperboard, however, they lack in soil mechanics.

In this dissertation, a numerical modelling approach for expansive soils is proposed, which combines an extended TPM with a novel hydro-mechanically coupled constitutive model. The extended TPM includes an independent phase of swelling water alongside the free pore water. This extension does not rely on the concept of double porosity and can be applied to any expansive material. Transition between free and swelling water is achieved by a bidirectional mass transfer. The associated reduction of effective porosity and consistent mass balancing enable the prediction of the swelling-induced decrease in permeability. The novel constitutive model „*Hypoplasticity for expansive soils*“ omits the double porosity concept as well, and instead incorporates a distinct saturation-driven swelling feature. The model relies on internal variables that track the preloading state and evolve with deformation and changes in saturation. It is formulated in terms of net stress and effective degree of saturation, as swelling is perceived as a consequence to changes in saturation. Decoupling the constitutive model from the commonly used suction and avoiding a micro- and macrostructural distinction facilitates the material parameter calibration. Swelling pressure, expansion and swelling-induced changes in mechanical properties are consistently reproduced with a single parameter set. The framework

is developed based on an experimental campaign on reconstituted Opalinus clay shale performed by the author and complementary literature data. The modelling approach was implemented into the FE software package numgeo, which enabled simulation of discretised boundary value problems (BVP). Consequently, the time evolution of swelling in simulations of laboratory tests can be predicted. The applicability within a large-scale BVP is presented in simulations of an emplacement tunnel of a deep geological storage facility backfilled with an expansive material.

Overall, the explicit representation of swelling-induced water attachment at the continuum scale and the consideration of the material-specific mechanical and hydraulic responses at the constitutive level provide an accurate representation of the hydro-mechanical processes involved. The combination of the extended TPM with novel constitutive models can effectively replicate expansive soil behaviour in boundary value problems. Alongside swelling-induced changes in mechanical properties and permeability, both the magnitude and temporal evolution of swelling can be predicted with a single set of parameters.

Zusammenfassung

Einige Geomaterialien neigen aufgrund ihrer tonmineralogischen Zusammensetzung dazu, bei Kontakt mit Wasser zu expandieren. Diese expansiven Geomaterialien umfassen sowohl Böden als auch Tonsteine. Diese Tendenz, die als Quellen bezeichnet wird, äußert sich entweder in einer Volumenzunahme, wenn Verformungen möglich sind, oder in einer Zunahme der Spannung beziehungsweise des Quelldrucks, wenn Verformungen behindert werden. Umgekehrt beeinflusst das Quellen die mechanischen und hydraulischen Eigenschaften und führt zu einer erhöhten Kompressibilität sowie zu einer Abnahme des Vorbelastungszustands, der Scherfestigkeit und der Permeabilität. Das hydromechanische Verhalten expansiver Böden ist für die Bemessung unterirdischer Bauwerke relevant, die mit diesen in Kontakt stehen. Bei Pfählen, Tunneln oder Stützkonstruktionen, die in expansivem Baugrund errichtet werden, kann Quellen Hebungen verursachen oder zusätzliche Lasten induzieren. In Abdichtungselementen von Deponien oder geologischen Tiefenlagern kann das Quellen expansiver Puffermaterialien gezielt genutzt werden, um den Wasserfluss zu begrenzen und die Schadstoffmigration zu verhindern, beispielsweise bei der Endlagerung radioaktiver Abfälle.

Die zuverlässige Simulation expansiver Böden mittels Finite-Elemente-Analysen (FE-Analysen) erfordert eine genaue Abbildung der wirkenden hydromechanischen Prozesse. Während des Quellens wird ein Anteil des Porenwassers an Tonminerale gebunden, wodurch die effektive Porosität reduziert wird. Bisher betrifft die numerische Modellierung expansiver Böden überwiegend konstitutive Beziehungen für das Spannungs-Dehnungs-Verhalten, das Wasserretentionsverhalten und die quellinduzierte Verringerung der Permeabilität des Bodens. Diese reichen von einfachen Feuchtequellmodellen bis hin zu anspruchsvollen Modellen der teilgesättigten Bodenmechanik, in denen das Verhalten expansiver Böden üblicherweise durch die Unterscheidung mikro- und makrostruktureller Reaktionen im Rahmen des Doppelporositätskonzepts beschrieben wird. Diese Modelle liefern vielversprechende Ergebnisse, setzen jedoch eine bimodale Porengrößenverteilung voraus, die nicht in allen expansiven Böden vorhanden ist. Zudem ist die Bestimmung der Modellparameter aufgrund aufwendiger Laborversuche anspruchsvoll. Während der Übergang von Wasser aus einem mobilen Zustand in einen an Tonminerale gebundenen Zustand in der konstitutiven Beschreibung als treibender Mechanismus anerkannt wird, werden die damit verbundenen Änderungen der Volumenanteile und deren Einfluss auf das gesamte Materialverhalten in den zugrunde liegenden Bilanzgleichungen der Theorie poröser Medien (TPM) in bestehenden numerischen Ansätzen im Allgemeinen vernachlässigt. In verschiedenen anderen Anwendungen der Kontinuumsmechanik wurden Erweiterungen der TPM für expansive poröse Medien bereits erfolgreich eingesetzt, beispielsweise für quellende Gele und Kartonwerkstoffe. In der Bodenmechanik fehlen entsprechende Ansätze jedoch bislang.

In dieser Dissertation wird ein numerischer Modellierungsansatz für expansive Böden vorgeschlagen, der eine erweiterte TPM mit einem neuartigen hydromechanisch gekoppelten konstitutiven Modell kombiniert. Die erweiterte TPM umfasst neben dem freien Porenwasser eine unabhängige Phase aus Quellwasser. Diese Erweiterung beruht nicht auf dem Konzept der Doppelporosität und kann auf jedes expansive Material angewendet werden. Der Übergang zwischen freiem Wasser und Quellwasser wird durch einen bidirektionalen Massentransfer beschrieben. Die damit verbundene Verringerung der effektiven Porosität sowie eine konsistente Massenbilanzierung ermöglichen die Vorhersage der quellinduzierten Abnahme der Permeabilität. Das neuartige konstitutive Modell „*Hypoplastizität für expansive Böden*“, verzichtet ebenfalls auf das Konzept

der Doppelporosität und berücksichtigt stattdessen einen eigenständigen sättigungsgetriebenen Quellmechanismus. Das Modell basiert auf internen Variablen, die den Vorbelastungszustand erfassen und sich mit Verformungen sowie Änderungen der Sättigung entwickeln. Es ist in Bezug auf die Nettospannung und den effektiven Sättigungsgrad formuliert, da Quellen als Folge von Änderungen der Sättigung verstanden wird. Die Entkopplung des konstitutiven Modells von der häufig verwendeten Saugspannung sowie der Verzicht auf eine Unterscheidung zwischen Mikro- und Makrostruktur erleichtern die Kalibrierung der Materialparameter. Quelldruck, Expansion und quellinduzierte Änderungen der mechanischen Eigenschaften werden konsistent mit einem einzigen Parametersatz wiedergegeben. Das Rahmenwerk wurde auf Grundlage einer vom Autor durchgeführten experimentellen Untersuchung an rekonstituiertem Opalinuston sowie ergänzender Literaturdaten entwickelt. Der Modellierungsansatz wurde in das FE-Programmpaket numgeo implementiert, wodurch die Simulation diskretisierter Randwertprobleme (RWP) ermöglicht wurde. Dadurch kann die zeitliche Entwicklung des Quellens in Simulationen von Laborversuchen vorhergesagt werden. Die Anwendbarkeit innerhalb eines großskaligen RWP wird anhand von Simulationen eines Einlagerungstunnels eines geologischen Tiefenlagers gezeigt, der mit einem expansiven Material verfüllt ist.

Insgesamt ermöglichen die explizite Darstellung der quellinduzierten Wasserbindung auf der Kontinuumsskala und die Berücksichtigung der materialspezifischen mechanischen und hydraulischen Reaktionen auf konstitutiver Ebene eine genaue Abbildung der beteiligten hydromechanischen Prozesse. Die Kombination der erweiterten TPM mit neuartigen konstitutiven Modellen kann das Verhalten expansiver Böden in Randwertproblemen wirksam reproduzieren. Neben quellinduzierten Änderungen der mechanischen Eigenschaften und der Permeabilität können sowohl das Ausmaß als auch die zeitliche Entwicklung des Quellens mit einem einzigen Parametersatz vorhergesagt werden.

Table of contents

Preface of the editor i

Acknowledgement iii

Abstract v

Zusammenfassung vii

Table of contents ix

1. Introduction 1
- 1.1. Layout of this thesis . . . 4
- 1.2. Notation . . . 5

2. Material behaviour of expansive soils and modelling approaches 7
- 2.1. Expansive soils: unsaturated swelling clays . . . 7
  - 2.1.1. Swellable clay minerals: Structure and hydration . . . 7
  - 2.1.2. Phenomena upon swelling . . . 10
  - 2.1.3. Particularities of compacted clays . . . 12
  - 2.1.4. Disambiguation - Terminology . . . 13
- 2.2. Hydraulic characteristics of expansive soils . . . 14
  - 2.2.1. Soil water retention behaviour . . . 15
  - 2.2.2. Permeability . . . 20
  - 2.2.3. Compatibility of hydraulic models within Finite Element simulations . . . 26
- 2.3. Stress variables in unsaturated soils . . . 27
  - 2.3.1. Effective stress principle . . . 27
  - 2.3.2. Choice of stress variables . . . 28
- 2.4. Hydro-mechanical behaviour of expansive soils . . . 29
  - 2.4.1. Oedometric compression and rebound behaviour at constant water content 29
  - 2.4.2. Wetting at constant load: Expansion . . . 32
  - 2.4.3. Wetting at constant volume: Swelling pressure . . . 36
  - 2.4.4. Shear strength at constant water content . . . 39
- 2.5. Modelling of the hydro-mechanical behaviour of expansive soils . . . 42
  - 2.5.1. Swelling rock models . . . 42
  - 2.5.2. Sophisticated constitutive models for unsaturated soils . . . 44
- 2.6. Implications for the novel modelling framework and concluding remarks . . . 49

3. Extended theory of porous media for expansive soils 53
- 3.1. Theory of porous media for unsaturated soils . . . 53
  - 3.1.1. Kinematics . . . 54
  - 3.1.2. Governing equations . . . 56

3.2. Extension for expansive soils . . . 59
3.2.1. Composition of the mixture . . . 59
3.2.2. Governing equations . . . 63
3.2.3. Mass transfer model . . . 65
3.2.4. Relative permeability due to swelling . . . 66
3.2.5. Material parameters . . . 67
3.2.6. Performance of the mass transfer mechanism . . . 72
3.2.7. Parameter calibration . . . 77
3.3. Concluding remarks . . . 77

4. Hypoplasticity for expansive soils: one-dimensional formulation 81
4.1. One-dimensional formulation and equations . . . 81
4.1.1. Oedometric compression and rebound behaviour . . . 81
4.1.2. Vertically unconfined swelling . . . 84
4.1.3. Constant volume swelling . . . 86
4.1.4. Characteristic curves . . . 87
4.1.5. Evolution equations and material parameters . . . 89
4.2. Discussion and capabilities of the one-dimensional formulation . . . 90
4.2.1. Oedometric compression: influence of saturation . . . 91
4.2.2. Vertically unconfined swelling: swelling strain . . . 91
4.2.3. Constant volume swelling: swelling pressure . . . 92
4.2.4. Collapse upon wetting . . . 93
4.3. Determination of material parameters . . . 93
4.3.1. Parameters h_s, e_N and n of the normal compression curve . . . 95
4.3.2. Elastic indices κ_{ref} and κ_w . . . 95
4.3.3. Parameter b for the evolution of the saturation driven strain . . . 96
4.3.4. Parameter c for the evolution of preloading net stress . . . 97
4.4. Comparison with experimental results . . . 98
4.4.1. Reconstituted Opalinus clay . . . 99
4.4.2. Bentonite-silt mixture . . . 100
4.4.3. Bentonite-sand mixture . . . 101
4.5. Simplified parameter calibration . . . 104
4.5.1. Procedure . . . 104
4.5.2. Application . . . 106
4.6. Concluding remarks . . . 107

5. Hypoplasticity for expansive soils: full formulation 109
5.1. Full formulation and equations . . . 109
5.1.1. Preconsolidation surface ($F = 0$) and overconsolidation ratio . . . 110
5.1.2. Flow rule . . . 112
5.1.3. Direction of saturation-driven strain rate . . . 113
5.1.4. Characteristic curves . . . 113
5.1.5. Evolution equations . . . 114
5.1.6. Parameters of the model . . . 115
5.2. Challenges of the generalisation to the full formulation . . . 115
5.3. Discussion and capabilities of the full formulation . . . 117
5.3.1. Triaxial response . . . 118

5.3.2. Simple shear response . . . 124
5.3.3. Oedometric compression and rebound behaviour . . . 126
5.3.4. Oedometric swelling behaviour . . . 130
5.4. Determination of material parameters . . . 135
5.4.1. Angles of internal friction φ_{ref} and φ_w . . . 135
5.4.2. Shape parameter β . . . 137
5.4.3. Parameters h_s, e_N and n of the normal compression curve . . . 138
5.4.4. Elastic indices κ_{ref} and κ_w . . . 138
5.4.5. Parameters b for the evolution of the saturation-driven strain rate and c for the evolution of preloading net stress . . . 138
5.4.6. Overview of parameter calibration . . . 140
5.5. Comparison with experimental results . . . 141
5.5.1. Reconstituted Opalinus clay . . . 142
5.5.2. Bentonite-silt mixture . . . 143
5.5.3. Bentonite-sand mixture . . . 145
5.6. Concluding remarks . . . 148

6. Finite element implementation of the numerical framework 151
6.1. Constitutive relations and material models . . . 151
6.1.1. Mechanical model . . . 151
6.1.2. Hydraulic model: Saturation-suction relation . . . 157
6.1.3. Relative permeability model . . . 159
6.1.4. Mass transfer model . . . 160
6.1.5. Constitutive stress approach . . . 161
6.1.6. Pore fluid flow . . . 161
6.1.7. Pore fluid compressibility . . . 161
6.2. Finite element library based on the extended theory of porous media . . . 161
6.3. Variational and weak form of governing equations . . . 163
6.4. Spatial discretisation . . . 165
6.5. Solution procedure and time integration . . . 166
6.5.1. Newton-Raphson Method . . . 167
6.5.2. System of equations . . . 167
6.5.3. Element contributions . . . 168
6.5.4. Stabilisation . . . 176
6.5.5. Hourglass stiffness . . . 177
6.5.6. Time stepping algorithm . . . 178
6.6. Discussion and performance of the implementation . . . 182
6.6.1. Performance of the mass transport model and relative permeability model due to swelling . . . 183
6.6.2. Numerical validation of element performance and time-stepping in infiltration problems . . . 185
6.6.3. Numerical integration of the mechanical constitutive model . . . 199
6.7. Concluding remarks . . . 207

7. Application of the numerical framework to boundary value problems 209
7.1. Simulation of laboratory tests as boundary value problems . . . 209
7.1.1. Reconstituted Opalinus clay . . . 210

7.1.2. Bentonite-silt mixture . . . 235
7.1.3. Bentonite-sand mixture . . . 240
7.2. Large-scale example . . . 246
7.2.1. Simulations with uniform, radially symmetric infiltration . . . 249
7.2.2. Simulation with localized water ingress . . . 256
7.2.3. Overview of the simulations . . . 258
7.3. Concluding remarks . . . 259

8. Summary, conclusions and outlook **261**
8.1. Conclusions . . . 262
8.2. Recommendations for further investigations . . . 263

A. Appendix: Experimental campaign on reconstituted Opalinus clay **267**
A.1. Swelling tests, oedometric compression tests and permeability measurement . . . 267
A.2. Additional experiments: Direct shear tests . . . 286
A.3. Additional experiments: Soft oedometer testing . . . 290

Bibliography **295**

1. Introduction

Soils and sedimentary rocks consisting of unsaturated swelling clays exhibit the tendency to expand upon contact with water. This tendency, referred to as swelling, may manifest itself either as an increase in volume, if deformation is allowed, or as the build-up of swelling pressure, if deformation is constrained. Swelling is a consequence of wetting and is accompanied by an alteration of the material properties: compressibility increases, shear strength decreases and the intrinsic permeability decreases, as part of the as mobile water is attached to negatively charged surfaces of the clay minerals, reducing the pore space available for flow. Although swelling is the result of the clay-mineralogical composition of the material, it largely depends on the mechanical and hydraulic boundary conditions. In the design of geotechnical engineering applications, the coupled material behaviour poses a challenge. On the one hand, swelling is critical for structures built in natural expansive ground, as volume increase may cause uplift of structures, whereas swelling pressure may act as an additional, unfavourable load. This affects tunnelling and gallery construction (Grob, 1972; Kovári et al., 1987; Anagnostou, 1993; Steiner, 1993; Amstad and Kovári, 2001), pile foundations (Burke et al., 2022; Gaspar et al., 2022) and other retaining structures in expansive ground or with expansive backfill (Papagiannakis et al., 2014; Liu and Vanapalli, 2019). The interaction between ground and structures can damage the latter through stress redistributions and large deformations, while at the same time alters the state of the ground itself. On the other hand, the same swelling phenomena can have a beneficial function and be utilized within the construction of barrier elements in landfill construction and deep storage facilities. Expansive geomaterials are characterized by low permeability, high plasticity, and a pronounced capacity for water adsorption, and are therefore used to safely seal landfills, whether within geosynthetic or conventional clay liners, or to close cavities to prevent pollutant or radionuclide migration. In nuclear waste disposal, unsaturated swelling clays are implemented in the multi barrier system of deep geological repositories, both in the host rock and in engineered barrier systems (EBS) as buffer around the radioactive waste and as backfill in tunnels and shafts (Pusch, 1977; Nagra, 2005; BGR, 2020). Their sealing functionality is crucial to isolate the waste from the biosphere. For repositories built in swelling clay shale, the favourable self sealing capacity of the rock outweighs the challenges associated with tunnelling in swelling underground (BGR, 2014). Motivated by circular economy considerations, the reuse of excavated clay shale alongside highly expansive materials such as bentonite (mixtures) is increasingly being investigated therein (Zhang and Kröhn, 2019; GRS, 2020).

To predict the behaviour of expansive underground subjected to hydro-mechanical loading when designing the aforementioned structures or dimensioning expansive sealing elements, numerical approaches within the Finite Element (FE) method are commonly applied. Modelling the behaviour of unsaturated swelling clays is highly complex due to hydraulic and mechanical interactions and the reciprocal influence of material properties and state variables involved. The numerical solution of the coupled systems necessitates the formulation of suitable constitutive relationships for the hydro-mechanical behaviour, element formulations and high computational efforts, and reliable simulation of expansive soils using FE analysis requires the accurate repre-

sentation of the acting hydro-mechanical processes. Commercial FE software as Plaxis (Bentley Systems, 2025), Sofistik (SOFiSTiK AG, 2025) and Talpa (IfG, 2025) rely on simple, empirical swelling models for the mechanical behaviour based on the established one-dimensional model by Grob (1972) and its generalization to the three-dimensional space (Anagnostou, 1992; Wittke-Gattermann and Wittke, 2004; Heidkamp and Katz, 2004). Therein swelling is not simulated as a result of water flow through the pore space, but as a specific case of mechanical unloading, and a detailed investigation of the hydro-mechanically coupled swelling process is only possible to a limited extent. Alternatively, simple linear moisture swelling models exist, e.g. in the FE software Abaqus (Dassault Systèmes, 2024), OpenGeoSys (Bilke et al., 2025) and Tough-Flac (Rutqvist et al., 2011), which couple the volumetric swelling behaviour to changes in the degree of saturation. However they lack in further hydro-mechanical coupling of deformation, stress and material properties, which exists in unsaturated swelling clays. Furthermore, numerical investigation of expansive soils concentrates on the formulation of new sophisticated constitutive relationships for the stress-strain response, the soil-water-retention behaviour, or the permeability reduction upon swelling. Numerous mechanical constitutive models have been proposed, mostly in the framework of elasto-plasticity, whereof the Barcelona Basic Model (BBM) by Alonso et al. (1990) created the foundation for many succeeding formulations (Gens et al., 2006; Sheng et al., 2008). The BBM extends the well established Modified Cam Clay model (Burland, 1990) to unsaturated states by considering suction as a second stress variable in addition to net stress (excess of total stress over pore air pressure) and can simulate the most prominent features of unsaturated soils such as the dependency of the preconsolidation pressure on partial saturation as well as the soil expansion or soil collapse upon changes in the degree of saturation. However important aspects of the behaviour of expansive soils cannot be captured. To overcome the deficits, its own successor, the Barcelona Expansive Model (BExM, Gens and Alonso (1992)) introduced microstructure into the BBM. Based on the concept of double-porosity (Lloret et al., 2003; Seiphoori et al., 2014), the macrostructural deformation of an expansive soil was assumed as a mechanical response to swelling on the microstructural level, which manifests itself in the evolution of the pore structure from a bi- to a mono-modal distribution. Based on the double-porosity concept, mechanical constitutive models beyond elasto-plasticity have been applied in the frameworks of generalized plasticity (Sánchez et al., 2005), bounding surface plasticity (Yang et al., 2008), and hypoplasticity (Mašín, 2013). Moreover, novel constitutive relationships for the water retention behaviour based on the double-porosity concept have been proposed, e.g. by Della Vecchia et al. (2015) and Dieudonne et al. (2017) amongst others.

Although the coupling of macro- and microporosity in constitutive relations shows promising results, see e.g. Dieudonne et al. (2017) or Ghiadistri et al. (2019), its application necessitates both the existence and determination of a bi-modal pore size distribution, which does not apply to all expansive soils (Mohajerani et al., 2011; Seiphoori et al., 2016). Furthermore, determination of the model parameters is challenging due to lacking physical meaning and advanced laboratory testing protocols. In the constitutive description, changes of different structural levels induced by a transition of water from a mobile state to a state attached to the clay minerals are acknowledged, however, mass transfer mechanisms are not considered in the formulation of the governing equations (conservation of mass and linear momentum) of the expansive porous medium itself. The governing equations based on the Theory of Porous Media (TPM) consider the simultaneous composition of the soil by different continuous phases and are required to solve boundary value problems within FE analysis. In geotechnics they comprise solid, (pore-)water and (pore-)air, see Schrefler et al. (1990), de Boer (2000) or Ehlers and Bluhm (2002) among others. The ap-

plicability of the TPM for the simulation of a wide range of geotechnical problems dealing with unsaturated and saturated soils was shown by Khoei and Mohammadnejad (2011), Machaček (2020), Staubach et al. (2021) and Machaček et al. (2023) amongst others. For unsaturated swelling clays, the attachment of water to clay minerals upon swelling cannot be considered in a classical three phase TPM in which only one water phase exists. It requires an additional water phase, which does not participate in flow, and a mass transfer mechanism between both water phases. Extensions of the TPM for swelling porous media including mass transfer mechanisms have already been employed in various applications of continuum mechanics, e.g. for swelling gels (Sauerwein and Steeb, 2018) and paperboard (Alexandersson and Ristinmaa, 2019), however, not in the context of soil mechanics.

This dissertation presents a novel numerical framework for modelling of expansive soils. It builds on an experimental campaign on reconstituted Opalinus clay shale, which was conducted by the author of this work (Nitsch et al., 2023a). Therein, the hydro-mechanical response of the material subjected to different loading paths was studied including oedometric swelling tests with varying boundary conditions, oedometric compression and rebound tests under dry and saturated conditions, and permeability tests. The novel modelling approach is realized through the introduction of an extended TPM for expansive soils and the formulation of novel constitutive relationships. The extended TPM accounts for the attachment of water to clay minerals during the swelling process through mass transport between the free pore water and a separate swelling water phase. This extension does not rely on the concept of double porosity. The resulting reduction in pore space is used to derive a simple relationship for the associated reduction in hydraulic conductivity to be considered directly at the element level of the FE formulation. A novel hydro-mechanical constitutive model omits the concept of double-porosity and is developed in the framework of hypoplasticity. It describes the swelling behaviour using internal variables that track the preloading state and evolve with deformation and changes in saturation. It is formulated in terms of net stress and effective degree of saturation instead of suction, as swelling is perceived as a direct consequence to changes in saturation. The model aims to predict the magnitude of both, swelling strain and swelling pressure with a single set of parameters. The numerical framework focusses on the prediction of oedometric swelling behaviour, which is commonly studied in the laboratory. The combination of the extended TPM and the novel constitutive models allows to simulate the magnitude and time evolution of swelling and the associated phenomena. Unsaturated states are considered for the evolution of the material from a nearly dry state towards full saturation. Cyclic drying and wetting and the prediction of strength is not within the scope of this work. Rate dependency, creep, anhydritic swelling, and cementation are not considered. The framework is backwards compatible and applicable to unsaturated soils without explicit consideration of swelling. The swelling mechanism and mass transfer can be eliminated without losing the functionality of the constitutive equations.

The development of the extended TPM and constitutive relationships was first carried out at the single integration point level. The novel framework was subsequently implemented in the FE code `numgeo`, developed by Machaček (2020) and Staubach (2022), which allowed for implementation of all required tools on material, element and solver level. Although commercial FE software packages (e.g., Abaqus, Ansys, Plaxis) enable the consideration of user-defined material routines for mechanical behaviour (stress-strain) and user-defined elements, they do not offer the flexibility required for the implementation of further constitutive relationships or numerical tools that are essential for the strongly hydro-mechanically coupled material behaviour of expansive soils.

1.1. Layout of this thesis

Following the introductory chapter, which outlines the motivation, layout and notation of the thesis, Chapter 2 provides an overview of the hydro-mechanical behaviour of expansive soils and relevant modelling approaches. It introduces key material characteristics and parameters required for their description. After a brief summary of clay mineralogy and swelling mechanisms, the hydraulic behaviour is outlined based on fundamentals of unsaturated soil mechanics. The mechanical response of expansive soils under selected loading paths is discussed, supported by experimental results on reconstituted Opalinus clay shale. In addition, data from the literature on further materials with different, more expansive mineralogical compositions and unsaturated loading paths, is considered. The chapter continues with a review of modelling frameworks, ranging from analytical swelling models to advanced constitutive approaches. It concludes with a summary of the phenomena relevant for the modelling approach developed in this thesis and their constitutive implications.

Chapter 3 presents the governing equations for simulating boundary value problems based on the TPM. For expansive soils, an additional swelling water phase is introduced, which is kinematically attached to the solid phase. The mass transfer between the free pore water and the swelling water represents the uptake of water into the solid structure and the associated reduction in pore space available for flow. As a consequence, a swelling-induced relative permeability model is proposed to capture the resulting decrease in hydraulic conductivity upon swelling. The performance of both models is evaluated through comparison with experimental data and idealised loading scenarios. The chapter concludes by outlining all required constitutive relations.

Chapter 4 introduces the one-dimensional formulation of the novel hydro-mechanical, hypoplastic constitutive model for expansive soils. It is formulated in terms of net stress and degree of saturation and uses the preloading state for the description of the current state, which evolves with deformation and changes in saturation. The strain rate is decomposed into a saturation-driven strain rate and a portion for the evolution of net stress, which allows to predict both swelling strains and swelling stresses, depending on the mechanical and hydraulic boundary conditions. Recommendations for calibration of the material parameters based on standard laboratory tests are given and the model performance is demonstrated for different materials.

Chapter 5 extends the proposed hydro-mechanical model to a three-dimensional tensorial formulation. A dry reference state surface based on the Modified Cam Clay model (Burland, 1990) defines the threshold between a nearly elastic material response and irreversible behaviour. The direction of strain in full space is described with an associated flow rule. Beyond oedometric loading, the model's critical state behaviour is assessed in triaxial and simple shear simulations, as the ability to reach the critical state is essential to ensure consistency in the prediction of material behaviour within a three-dimensional constitutive framework. Similar to the one-dimensional case, a calibration procedure is outlined, and model performance is evaluated against experimental results using single element simulations.

Chapter 6 focusses on the implementation of the modelling framework in the FE code `numgeo`. It includes the numerical treatment of constitutive relations and governing equations, as well as the spatial discretisation and solution strategy. The element library based on the extended TPM is presented. Important aspects of the implementation are discussed to ensure its robustness and applicability for simulation of swelling. They include the performance of the mass transfer

and swelling-induced relative permeability, infiltration behaviour and the integration of the rate formulation of the novel hydro-mechanical constitutive model.

Chapter 7 applies the numerical framework to simulations of boundary value problems, which allows prediction of the temporal evolution of swelling. Experimental tests are revisited as boundary value problems. Finally, a large-scale application is presented in the form of an emplacement tunnel in a high-level radioactive waste repository, wherein the material response of the expansive buffer material subjected to infiltration from the host rock is investigated.

The thesis concludes in Chapter 8. Key findings are presented and suggestions for future extension and application of the modelling framework are provided.

1.2. Notation

Scalar variables are denoted in italic font, e.g. a, σ, vectors and second order tensors in bold font, e.g. $\boldsymbol{f}, \boldsymbol{r}$ and $\mathbf{A}$, $\boldsymbol{\sigma}$, whereas fourth rank tensors are written in sans serif, e.g. L, E. Alternatively, components of a vector, a second and a fourth rank tensor are given in index notation as e.g. f_i, σ_{ij} and B_{ijkl} and $(\boldsymbol{\sigma})_{ij}$ denotes the extraction of the component (i, j) of the tensor $\boldsymbol{\sigma}$. A cartesian coordinate system with the orthogonal unit vectors e_i for $i = 1, 2, 3$ applies. In the two-dimensional setting Latin indices $i, j \in \{1, 2\}$ denote spatial components of vectors and tensors, with index 1 referring to the radial direction and index 2 to the vertical direction. For example, σ_{22} denotes the vertical normal stress, while $\tau_{12} = \sigma_{12}$ represents the shear stress in radial direction on a vertical plane. Single contraction of two vectors is written as $\mathbf{a} \cdot \mathbf{b} = a_i b_i$. Double contraction of two tensors is denoted $\mathbf{A} : \mathbf{B} = A_{ij} B_{ij}$ whereas $\mathbf{AB} = A_{ij} B_{kl}$ is the dyadic product of the tensors, written without $\otimes$. For the trace of a tensor, $\mathrm{tr}(\mathbf{A}) = A_{ii}$ holds. The deviatoric part of a tensor is defined as $\mathbf{A}^* = \mathbf{A} - \mathbf{1}\,\mathrm{tr}(\mathbf{A})/3$. Normalisation of a tensor is written as $(\mathbf{A})^{\rightarrow} = \mathbf{A}/\left\|\mathbf{A}\right\|$, wherein $\left\|\mathbf{A}\right\| = \sqrt{\mathbf{A} : \mathbf{A}} = \sqrt{A_{ij} A_{ij}}$ is the Euclidian norm of the tensor. The norm of a vector is denoted as $|\boldsymbol{f}| = \sqrt{\boldsymbol{f} \cdot \boldsymbol{f}} = \sqrt{f_i f_i} = (f_i f_i)^{1/2}$. $\mathrm{div}\,(\mathbf{A}) = A_{ij,j}$ is the divergence of a tensor and $\mathrm{grad}\,(a) = a_{,i}$ the gradient of a scalar. $\delta_{ij} = 1$ for $i = j$ and $\delta_{ij} = 0$ for $i \neq j$ denotes the Kronecker delta, $(\mathbf{1})_{ij} = \delta_{ij}$ the second order identity tensor, $(\mathsf{J})_{ijkl} = \delta_{ik}\delta_{jl}$ the fourth order identity tensor and $(\mathsf{I})_{ijkl} = \frac{1}{2}\left(\delta_{ik}\delta_{jl} + \delta_{il}\delta_{jk}\right)$ the symmetric part of J. $\langle a \rangle = (a + |a|)/2$ is the definition of the Föppl or Macaulay brackets, extracting only positive values of the scalar a.

2. Material behaviour of expansive soils and modelling approaches

This chapter introduces the fundamentals and existing modelling frameworks for the hydro-mechanically coupled material behaviour of expansive soils and concludes with derived implications for the numerical models developed in this work. It introduces the clay mineralogy of expansive soils and its role for swelling processes and phenomena. Hydraulic characteristics and suitable stress variables for the description of unsaturated soil behaviour are presented and the mechanical material behaviour of expansive soils subjected to monotonic oedometric loading, oedometric swelling and shearing is examined. Moreover, the chapter provides an overview of existing modelling approaches for predicting the mechanical behaviour described above, covering simple empirical formulations and advanced models from unsaturated soil mechanics with particular emphasis placed on the BBM as the most widely used model, whose limitations motivate the development of the novel modelling approach of this work.

Throughout this chapter, emphasis is on the highly non-linear behaviour of expansive soils, which poses significant challenges for both experimental investigations and numerical modelling:

- Strong hydro-mechanical coupling due to reciprocal influence affecting material parameters and state variables with partly opposing tendencies,
- Relatively large deformations and large stresses as a result of changing saturation at small or even absent mechanical loading, and
- Hydraulic regimes with almost impermeable conditions and large hydraulic gradients.

2.1. Expansive soils: unsaturated swelling clays

2.1.1. Swellable clay minerals: Structure and hydration

Clay minerals are characterised by a layered structure of two basic units, the tetrahedral sheet (T) consisting of silicon tetrahedra and the octahedral sheet (O) consisting of aluminium or magnesium octahedra, see Figure 2.1a (Grim, 1968; Mitchell and Soga, 2005; Bergaya et al., 2006). These sheets are connected by sharing outer oxygen or hydroxyl groups, forming so-called layers. Different clay minerals result depending on the stacking sequence of the layers and the nature of its inter-layer space. As the outer surfaces of the sheets expose oxygen-containing groups, the resulting layer structures carry a net negative charge. This charge is balanced by the attachment of water molecules or exchangeable cations in the interlayer region (Okrusch and Matthes, 2013).

Two groups of layers exist, the semibasic units of the TO-layer (1:1) and the TOT-layer (2:1), see Figure 2.1b. In TO-minerals, each octahedral sheet is opposite of a tetrahedral sheet and

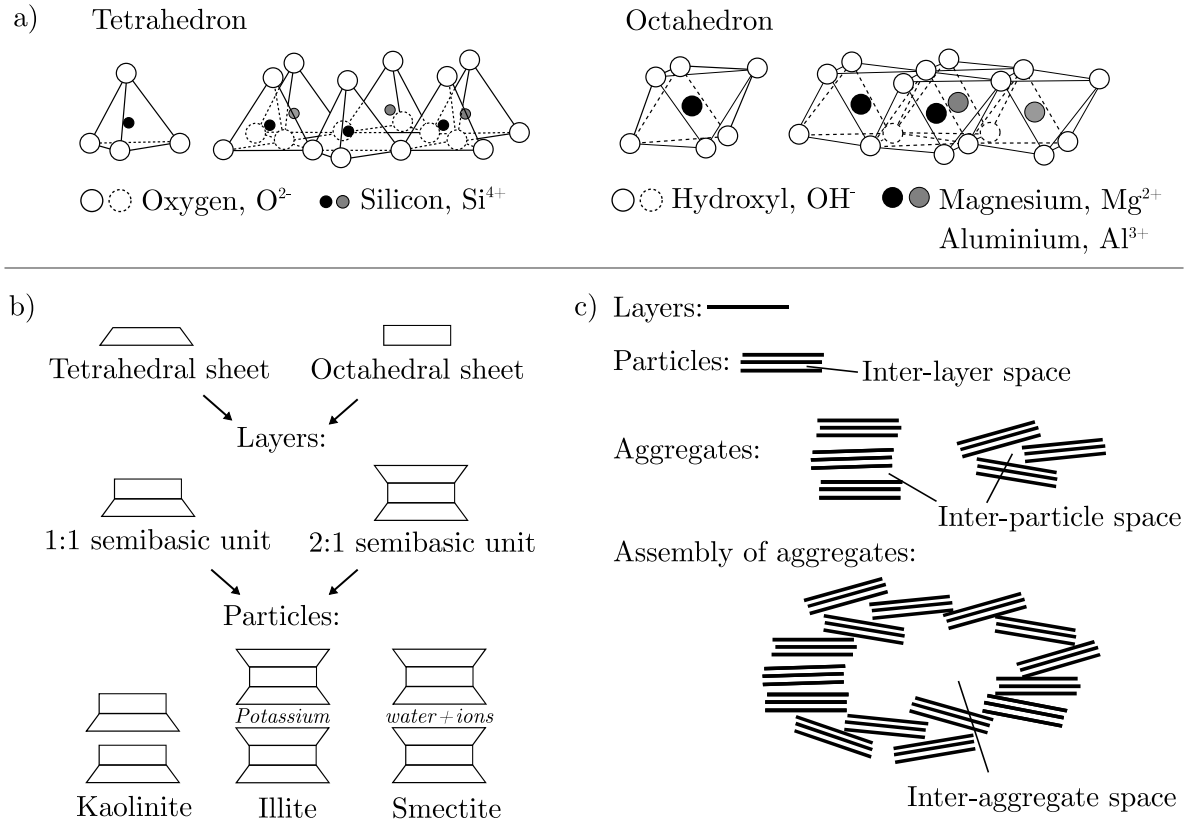

Figure 2.1.: Clay mineralogy: a) Diagrammatic sketch of basic units (tetrahedron and octahedron) Grim (1968), b) classification of clay minerals (Mitchell and Soga, 2005) and c) structural and fabric elements of clays (Bergaya et al., 2006).

hydrogen bonds form between two layers. Thus, the inter-layer space is closed and swelling is prevented. The most common TO-mineral is kaolinite. In TOT-minerals, the inter-layer space can be penetrated by water molecules or ions and the negative excess charge of the opposing tetrahedral layers is equalised. In the case of illite, the layers are strongly connected to each other via ionic bonds of potassium inter-layer cations and the inter-layer space is thus not accessible for water molecules. Attachment of water and thus swelling can, however, take place on the outer surfaces of the layers. In the case of smectite, only a very weak bond between the tetrahedral sheets exists and water molecules can penetrate the inter-layer space and the mineral expands upon wetting. Thus smectites are particularly prone to swelling and their most common mineral is montmorillonite (Mitchell and Soga, 2005). The introduced clay layers stack together in a parallel manner to form particles. Several particles form an aggregate including inter-particle (or intra-aggregate) space, see Figure 2.1c. Furthermore, several aggregates may assemble creating inter-aggregate space (Bergaya et al., 2006).

Swelling phenomena develop due to the attachment of water, which occurs on multiple levels of porosity and interspaces due to the aforementioned complex structure of an expansive clay. In general, two mechanisms or regimes of swelling are identified, which are shown in Figure 2.2:

- **(Inter) Crystalline swelling**, which means hydration of exchangeable cations in the interlayer. Starting from a very close layering at low water contents, the cations on the tetrahedral sheets hydrate when being in contact with water and reduce the ionic bonds

between the layers due to reorientation of the polar water molecules. As a result the inter-layer distance increases, the mineral expands and several layers of water molecules can be attached, see left-hand side of Figure 2.2 (Kraehenbuehl et al., 1987). This mechanism is predominant for smectites, in which the inter-layer space is highly accessible for water. The attached water is referred to as *(inter) crystalline swelling water* (Madsen and Müller-Vonmoos, 1989). It includes both, structural water inside the layers and adsorbed water in between the layers (inter-layer water).

- **Osmotic / Diffuse swelling**, which results from free diffusion processes (osmosis) between neighbouring clay minerals due to differences in the concentration of cations in the vicinity of the clay minerals compared to the pore fluids (Taylor and Smith, 1986; Madsen and Müller-Vonmoos, 1989). At higher water contents, the cations near the clay particle surface tend to diffuse away and form the electrical diffuse-double layer together with the negatively charged clay surface. As the cations are electrostatically bound by the negative electric field, water penetrates between clay particles to achieve an equilibrium of the cation concentration. The water is adsorbed on the external surfaces of the particles. Overlapping diffuse double layers repulse each other and the accumulation of water results in an increase of volume, see right-hand side of Figure 2.2. Consequently, osmotic swelling also occurs in clay minerals whose inter-layer space is not accessible to water (e.g. illite). The attached water is referred to as *diffuse or osmotic swelling water*.

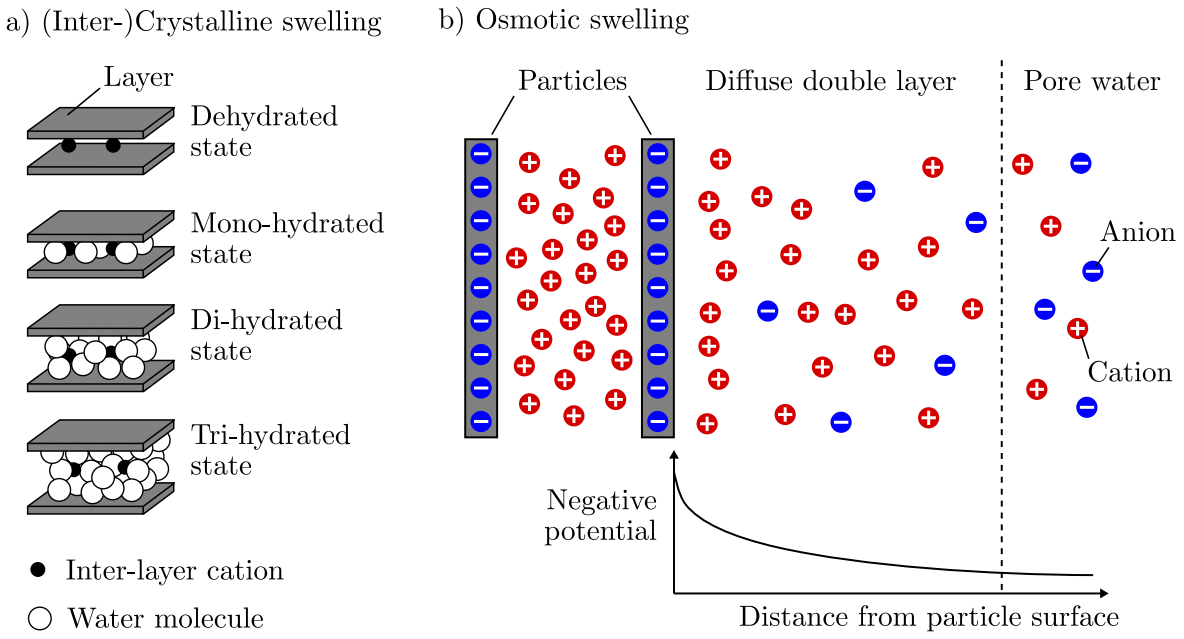

Figure 2.2.: Swelling mechanisms: a) Stepwise hydration of inter-layer cations during (inter) crystalline swelling and b) cation concentration differences between negatively charged clay particles and pore fluid resulting in osmotic swelling (Madsen and Müller-Vonmoos, 1989).

Depending on the mineral composition, the hydration state (water content / degree of saturation) and the level of compaction of the clay, the different swelling processes dominate. A separation of the different water phases is difficult, as the processes overlap and interact with each other. In both cases, the water attached on the clay minerals is no longer available for flow through its pore space and is thus kinematically different from the free (capillary) pore

water. Quantification of the total amount of adsorbed water is challenging and can only be indirectly accomplished through e.g. microstructural analyses (see Section 2.1.3) or pore-space modelling with back-calculation of permeability (see Section 2.2.2). Investigations of the latter have estimated the proportion of free water volume to total water volume as only a few percent in compacted, saturated expansive soils (Pusch et al., 1990; Bradbury and Baeyens, 2001), resulting in adsorbed water contents in the range of $85 - 98\%$. In a recent study, Babiy et al. (2025) proposed a novel methodology to quantify capillary and adsorbed water in bentonite by thermogravimetric analysis and reported comparably smaller adsorbed water contents between 33 and 68%. Therein, the amount of evaporating water at different temperatures of bentonite was quantified in comparison to that of non-active counterparts, prepared by dehydroxylation of the same bentonite (loss of hydroxyl groups at temperatures up to 950°C, which neutralises the ability of the clay minerals to adsorb water, Emmerich et al. (1999)). The findings are limited to the specific conditions of a poured, granular bentonite, and further investigations are required to confirm the broader applicability of the methodology, especially for compacted clays (see Section 2.1.3). Nonetheless, it may offer a useful basis for the quantitative assessment of water adsorption during swelling.

2.1.2. Phenomena upon swelling

The expansion of clay minerals upon hydration manifests as various observable phenomena in the laboratory and field, depending on the mechanical and hydraulic boundary conditions to which the material is subjected. Swelling behaviour exhibits partial reversibility and clay minerals contract upon dehydration (shrinkage), however, this work concentrates on the wetting path mainly. Primary swelling phenomena characterize the macroscopic alterations in the material state, specifically in terms of the engineering quantities of stress and strain, and are the following:

- **Expansion**, if deformation is allowed (under constant or very small load, thus total stress). Expansion and swelling of the clay minerals manifests itself in a global volume change, which is often recalled as *swelling strain* or *swelling heave*.
- **Swelling pressure**, if deformation is not allowed. As the control volume is constant, the hydration of clay minerals manifests itself in the build-up of total stress.

Both phenomena exhibit direction-dependent deformation and stress responses, i.e., they are anisotropic, which is mainly attributed to the preloading history of the material, where a preferred direction of prior stress leads to the development of a layered anisotropic structure. In natural soils, such anisotropy is typically inherent, reflecting geological deposition and diagenesis, whereas in compacted soils it is predominantly induced by the compaction process. As a result, swelling is more pronounced in normal direction to the particle orientation (see Section 2.1.1). Under mixed boundary conditions, comprising both load and deformation constraints, the swelling phenomena develop in an attenuated form. This is characterized by reduced expansion when subjected to higher loads and reduced swelling pressure when partial deformation is permitted.

The experimental investigation of the stress-strain-behaviour of expansive soils is usually performed under oedometric conditions, i.e. only in vertical direction at rigid radial confinement. Oedometer tests do not provide information regarding radial net stress and strain during the experiment, hence the true three-dimensional state of the material during testing is unknown.

Despite this limitation, they are preferred over triaxial experiments due to their simplicity (Gens and Alonso, 1992). From an engineering point of view, the expansion may be described as a vertical strain $\epsilon_{22} = -\Delta h/h_0$, wherein Δh is the deformation with respect to the initial height h_0 (compressive strains are positive, thus swelling strain has a negative sign). Its increment is denoted as $\Delta\epsilon_{22}$. Alternatively, the void ratio e or the specific volume $\nu = (1+e)$ are used as volumetric measures. The void ratio relates the pore volume V_p to the solid volume V_s in a specific control volume, i.e. here inside the soil sample. Further information is given in Chapter 3. For small deformations, the void ratio is approximated as $e = e_0 - \epsilon_{22}(1 + e_0)$, where e_0 is the initial void ratio corresponding to h_0. For a more accurate evaluation, the void ratio is updated incrementally from the change in specimen height. The initial height is decomposed into the initial pore height $h_{p,0}$ and the constant solid height h_s, with $h_0 = h_{p,0} + h_s$ and $e_0 = h_{p,0}/h_s$. In increment i, the height change is defined as $\Delta h_i = h_{i-1} - h_i$ and the corresponding compressive strain increment is $\Delta\epsilon_{22,i} = \epsilon_{22,i} - \epsilon_{22,i-1} = \Delta h_i/h_{i-1}$. Since the solid height remains constant, changes in total specimen height correspond to changes in pore height. Hence, $h_{p,i} = h_{p,i-1} - \Delta h_i$, and the void ratio in increment i is updated as $e_i = h_{p,i}/h_s = e_{i-1} - \Delta h_i/h_s$.

The laboratory test, where a sample can swell in vertical direction under a small load is referred to as *swelling under vertically unconfined conditions* in this work. Swelling pressure refers to the total stress that develops if no deformation of the material is allowed. It can also be understood as the counter pressure that has to be applied to prevent any deformation of an expansive soil sample, maintaining its (initial) volume. In an oedometric test device it is measured (in vertical direction) as a reaction force outside of the sample, referred to the sample cross section and assumed to act homogeneously in the sample. For further discussion and detailed distinction of the term, the interested reader is referred to Sridharan et al. (1986). In this work, the respective laboratory test is referred to as *swelling under constant volume conditions*.

In addition to the manifestation of expansion and swelling pressure, the engineering properties of expansive materials change upon swelling. Some of these changes are directly associated with the swelling process itself, while others are primarily governed by increasing saturation, though swelling can further contribute to their development. They comprise:

- **Reduction of hydraulic conductivity**, as water molecules become immobile through attachment at multiple structural levels within the expansive clay mineral matrix, thereby reducing the volume of water available for unimpeded capillary flow.
- **Softening**, which manifests as the saturation-dependent reduction of material stiffness and corresponding increase in the tendency to deform under applied mechanical loading, whereby unsaturated expansive soils exhibit greater stiffness than their saturated counterparts.
- **Strength reduction**, which is the progressive decrease in shear strength parameters of the material as the degree of saturation increases, with fully saturated expansive soils typically exhibiting significantly lower resistance to shear failure compared to their unsaturated state.

While the volumetric expansion and swelling pressure of expansive soils have been extensively documented, the accompanying changes in material properties remain comparatively underinvestigated in state-of-the-art geotechnical literature. This is mainly due to the complex interactions between hydraulic and mechanical boundary conditions and material response, which complicate the measurement and identification of individual processes in the laboratory.

2.1.3. Particularities of compacted clays

In both engineering practice and research, the magnitude of the primary swelling phenomena is often quantified using the soil's dry density ρ_d, which serves as a proxy indicator for the amount of swellable clay minerals within a given sample. However, the material behaviour is rather governed by the compaction state of the soil matrix, as the swelling characteristics of loose materials differ markedly from those of compacted clays. The primary swelling phenomena are alternatively related to the evolving microstructure of expansive soils during hydration, which builds the basis for double-structure approaches within modelling of expansive soils. Microstructure is usually assessed by the evolution of the pore size density (PSD) determined by using a mercury intrusion porosimeter (MIP). Therein, mercury, which acts as a non-wetting fluid, is injected into the pore space of a soil sample under controlled pressure increments. By measuring the volume of mercury and the intrusion pressure, an intrusion radius or pore entrance radius can be calculated. For a detailed description of MIP in geotechnical application, Sridharan (1968) gives a comprehensive overview. The results of MIP are usually visualized by means of (1) intruded pore volume versus pore entrance radius or (2) the PSD as the derivative of cumulative volume vs. the pore entrance radius. The latter offers the possibility to identify characteristic pore domains within a soil sample by correlating distinct peaks in the PSD with dominant pore dimensions. Threshold pore entrance radii must be defined for different porosity regimes of the clay, e.g. for inter-particle and inter-aggregate pore space. However, the method has some limitations: (a) Isolated pores cannot be detected, (b) variable pore radii of a single pore cannot be measured as only the pore entrance radius can be determined and most importantly, (c) a minimum level of measurable pore diameter always exists due to the maximum applicable intrusion pressure. Therefore, the total porosity of the soil is never completely captured by MIP. Furthermore, samples for MIP have to be carefully prepared. Wet samples are subjected to rapid freezing in liquid nitrogen followed by freeze-drying to preserve the original microstructural fabric as far as possible. However, despite its advantages over conventional drying methods, freeze-drying has also been shown to induce microstructural alterations (Norrish and Rausell-Colom, 1962; Keller et al., 2014).

In the as-compacted state, many studies report a double-structure porosity for expansive soils, separated into micro- and macroporosity and manifests itself in bi-modal PSDs. However, the existence of bi-modal PSDs does not apply to all expansive soils. Remoulded (prepared from slurry), poured or low compacted materials rarely show a bi-modal PSD (Seiphoori et al., 2016). In intact clay shales it also cannot be observed, as was reported for Callovo-Oxfordian clay shale (Mohajerani et al., 2011) or Opalinus clay shale (Seiphoori et al., 2014; Christ, 2025). In compacted clays, hydro-mechanical loading paths significantly alter the PSD. (Oedometric) compression selectively reduces the magnitude of peaks associated with macroporosity, while the microstructural features at smaller pore dimensions remain largely unaffected by the applied stress. Exposure to wetting processes can induce substantial modifications to the pore structure, manifested either as a translational shift of characteristic peaks of the PSD, which is evidenced by a single dominant peak in the PSD. Figure 2.3 shows an exemplary evaluation of MIP measurements on three different samples of London Clay (Monroy et al., 2010). They correspond to the as-compacted state and the saturated state after vertically unconfined swelling (at very low stress) and constant volume swelling. As can be seen on the right-hand side of Figure 2.3, the as-compacted sample shows a bi-modal PSD, while both saturated samples exhibit a mono-modal PSD. The left-hand side of Figure 2.3 reveals the short-coming of MIP: 29 % of the

pores of the as-compacted sample and 16 and 18 % of the pores of the saturated samples were undetected, visualized by the offset Δe between the intruded void ratio measured by MIP (e_{MIP}, black lines) and the known (global) void ratio of the sample (e, coloured markers). Theoretically, the global void ratio corresponds to the smallest pore entrance radius present in the sample. For the sake of simplicity, it is illustrated at a pore entrance radius of approximately 1 nm on the left-hand plot of Figure 2.3.

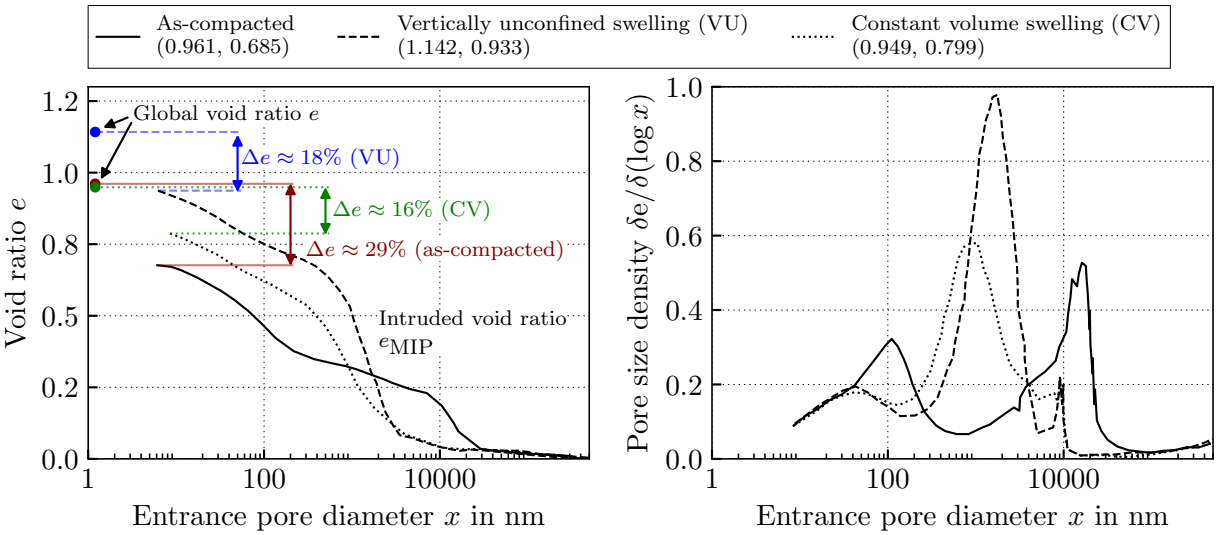

Figure 2.3.: Pore size distribution (left) and density function (right) for three samples of London Clay from Monroy et al. (2010): in the as-compacted state (solid line), after unconfined swelling (dashed line) and constant volume swelling (dotted line). The values in the brackets correspond to (e, e_{MIP}).

The results highlight another difficulty of MIP, as the size of undetected pores differs for different states or loading paths. The quantitative development of PSD due to hydro-mechanical loading derived from MIP must therefore be considered with care. Therefore, despite the clear bimodal nature of the PSD in compacted clays, identifying porosity regimes remains ambiguous due to the inherent methodological uncertainties of the measurement techniques. In this work, the behaviour of compacted clays is evaluated primarily through their preloading state as a more robust indicator of their hydro-mechanical response.

2.1.4. Disambiguation - Terminology

In this work the term *expansive soil* is used for any soil that swells due to its clay mineralogical composition, i.e. exhibits an increase either in volume (expansion) or stress (swelling pressure), when wetted. The flow of water through expansive soils is therefore a prerequisite for their description. Expansive soils are also referred to as *unsaturated swelling clays*. Because all clays swell to some extent upon contact with water, care should be taken when using the term *swelling*, which generally refers to the significantly greater expansion of expansive clays. The change in volume of any soil due to mechanical unloading is also referred to as swelling. However, from a hydro-mechanical point of view, this corresponds to a different loading path and phenomenon, as it is related to changes in stress and occurs even at constant water content for all soils. This deformation is investigated by the Huder-Amberg method (Huder and Amberg, 1970), a specific test protocol for oedometric swelling tests on expansive soils including unloading in the

saturated state. However, to distinguish it from the primary phenomenon of swelling strain, which occurs at constant load, it should rather be referred to as *strain due to unloading*. A further distinction is made with regard to soils that expand due to the presence of anhydrite, as here the chemical process of converting anhydrite into gypsum is accompanied by an increase in volume. English-language literature lacks a distinct terminology and differentiation is generally made by referring to gypsum swelling and clay swelling. Clay shale or argillaceous rock are also unsaturated swelling clays. The degree of expansion might be less pronounced than in highly expansive clays such as bentonite, however, the fundamental behaviour remains the same.

2.2. Hydraulic characteristics of expansive soils

Any unsaturated soil constitutes a multi-phase system consisting of at least three phases: the solid skeleton, the wetting porous fluid (e.g. pore water) and the non-wetting porous fluid (e.g. pore air). For a quantification of the extent of partial saturation, the (water) *degree of saturation* S^w is introduced. It is the ratio of water volume V^w and total pore volume V^p in a soil sample or control volume:

$$S^w = \frac{V^w}{V^p}. \tag{2.1}$$

It is equivalent to:

$$S^w = \frac{w\,\rho_s}{e\,\rho_w}, \tag{2.2}$$

wherein ρ_s and ρ_w are the specific densities of the solid and water phase, e is the void ratio defined as the ratio of the pore volume V^p and the volume of the solid phase V^s and w is the gravimetric water content. The latter is the ratio of the mass of water m_w and the dry mass m_d of a soil sample:

$$w = \frac{m_w}{m_d}. \tag{2.3}$$

It must be distinguished from the volumetric water content θ, which relates the water volume V^w to the total volume of the soil V:

$$\theta = \frac{V_w}{V}. \tag{2.4}$$

The quantities can be converted to one another:

$$\theta = w\,\rho_s \quad \text{and} \quad S^w = \theta\,n, \tag{2.5}$$

wherein the porosity $n = V_p/V$ is a measure for the proportion of pore volume in the total volume of a soil sample and can also be expressed as $n = e/(1+e)$. At ambient conditions without deliberate drying, soils are not completely dry, as they contain a residual water content w^r, which is accounted for by introducing the *effective degree of saturation* S^e:

$$S^e = \frac{S^w - S^{wr}}{1 - S^{wr}} \quad \Leftrightarrow \quad S^w = S^{wr} + (1 - S^{wr}), \tag{2.6}$$

wherein S^{wr} is the residual degree of saturation. Water in the soil is held within the pore space, and the negative pressure required to extract or retain this water is known as suction. The total suction ψ may be divided in two parts $\psi = \pi + s$, wherein π is the osmotic suction due to salinity

effects in the pore water and s is the matrix or capillary suction, which arises at the interface between solid particles and pore water in the soil matrix. As was shown by Fredlund et al. (2012) amongst others, for most geotechnical problems the change in matrix suction is equivalent to the change in total suction and the contribution of osmotic suction can be neglected. In the laboratory, osmotic suction is irrelevant for experiments which are carried out with deionized water. As no salinity effects in the pore water are considered in this work, only the term *suction* is used in the following. Suction is defined as the difference in pore air pressure p^a and pore water pressure p^w:

$$s = p^a - p^w, \tag{2.7}$$

and is also referred to as capillary pressure p^c, as the pores in the soil are assumed to act as capillary tubes (Likos and Lu, 2004). In capillary tubes, the liquid height of the wetting fluid and corresponding surface tension increases with decreasing radius of the tube. Therefore, soil suction can be of different magnitudes for different soils: The finer the soil, the smaller the (idealized) pore radius and the higher the suction values that can develop in the soil.

2.2.1. Soil water retention behaviour

The stored quantity of water in the soil and suction, which is an indicator of the energy state of the water phase in an unsaturated soil, are interrelated by the soil water retention curve (SWRC). For a comprehensive summary of the water retention behaviour including experimental methods required for its determination, the interested reader is referred to Fredlund et al. (2012). The degree of saturation S^w is expressed as a function of soil suction s and other state variables sv, e.g. the void ratio e or porosity n:

$$S^w = S^w(s, sv). \tag{2.8}$$

Alternatively, Equation (2.8) can be expressed in terms of the gravimetric or volumetric water content, which are related to the degree of saturation via Equations (2.2) and (2.5). The SWRC is characterised by three different zones, which are schematically shown in Figure 2.4 for a typical SWRC in terms of degree of saturation vs. suction. These zones were originally defined for drying paths starting from full saturation; however they are also essential to the wetting path and contribute to a general understanding of the processes occurring in the soil. A saturated soil is drained by exceeding the suction corresponding to the air entry value s_{aev}. Smaller suction values correspond to the boundary effect zone. First, large pores are drained and the SWRC exhibits a steep slope, whereas the smaller pore regimes are affected with continuing drying and the change in the degree of saturation decreases with increasing suction (transition or two-phase zone). The residual zone represents the limit at which the pore water becomes discontinuous and no further changes in the degree of saturation are observed with increasing suction. Idealisation of these zones implies that flow, and consequently swelling, occur only in the transition zone and that the boundary and residual zone are assumed to be ideally saturated and dry, respectively.

The SWRC differs between wetting and drying paths, with larger degrees of saturation observed during drying than during wetting for a given suction. This effect is referred to as hysteresis (Haines, 1930). It arises from air entrapment in the pore network (snap-out and by-passing effect (Chatzis and Dullien, 1983)) and different capillary heights and contact angles of spreading and retreating water during wetting and drying (ink-bottle and rain drop effect (Haines, 1930; Bear, 2018)). For changing from wetting to drying paths or vice versa, an infinite number of so-called

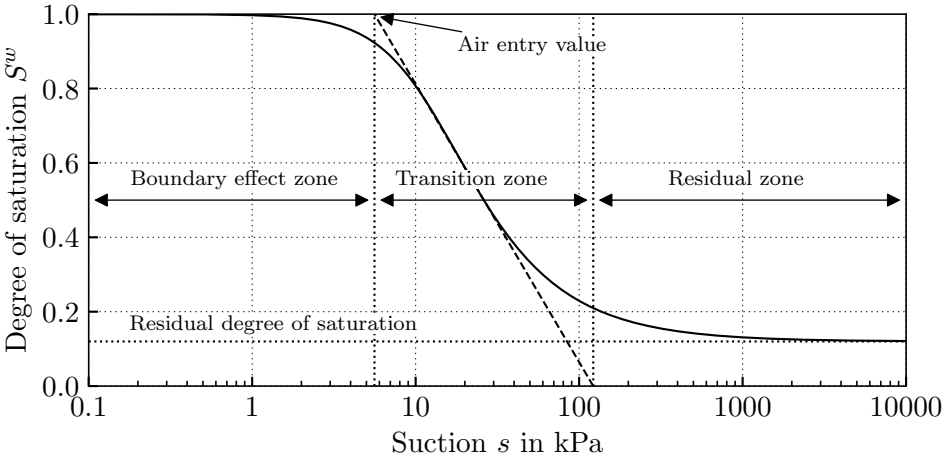

Figure 2.4.: Schematic representation of the soil water retention curve, modified from Fredlund et al. (2012).

scanning curves exist. For wetting-only applications, as considered in this work, the effect of the hysteresis can be neglected and a unidirectional SWRC can be employed to estimate suction for a given degree of saturation (Fredlund et al., 2012).

The water retention behaviour of expansive soils is characterised by several features, some of which are clearly attributed to swelling, while others are generally valid for unsaturated soils and more pronounced in expansive soils. Irrespective of their swelling behaviour, expansive soils feature the smallest pore sizes within the soil mechanical scale leading to suction values up to hundreds of Megapascals in the residual state, see e.g. Romero et al. (1999) or Seiphoori et al. (2014) amongst others. The left-hand side of Figure 2.5 shows the wetting path of the SWRC for reconstituted Opalinus clay (Nitsch et al., 2023a; Machaček et al., 2024). Starting from the initial state (at $w \approx 2\%$), the raw material was directly mixed with water to different water contents, compacted to a target void ratio of $e = 0.387$ and the suction of the compacted samples was determined with the chilled-mirror hygrometer (Leong et al., 2003). At the initial degree of saturation $S_0^w = 0.126$ the measured suction was $s \approx 100$ MPa. Even larger values were measured for smaller degrees of saturation, which were obtained by gentle oven-drying and are thus greyed out on the left-hand side of Figure 2.5.

On the right-hand side of Figure 2.5, the wetting paths of highly expansive bentonite at three different void ratios are shown (Seiphoori et al., 2014). The samples were first compacted in their residual saturation state and then wetted at constant volume conditions using the vapour equilibrium technique (VET), in which specific relative humidities above salt solutions imposed particular suctions (Delage et al., 1998) on the soil samples in closed desiccators. With increasing density, the SWRC is shifted translatory to the right into the area of higher suctions. Higher compacted samples have less overall pore volume that can be potentially filled by water and smaller pores exist compared to less compacted samples. The dependency of the SWRC on the compaction state of the soil is valid for any unsaturated soil, however more pronounced for expansive soils as the pore structure evolves upon swelling.

Moreover, the shape of the SWRC for an expansive soil may differ for wetting paths at different mechanical boundary conditions, which is presented for tests on a sand-bentonite mixture (Lang, 2019) in Figure 2.6. The tests were carried out in a suction-controlled oedometer test device at vertically unconfined conditions, constant volume conditions and under vertical loads

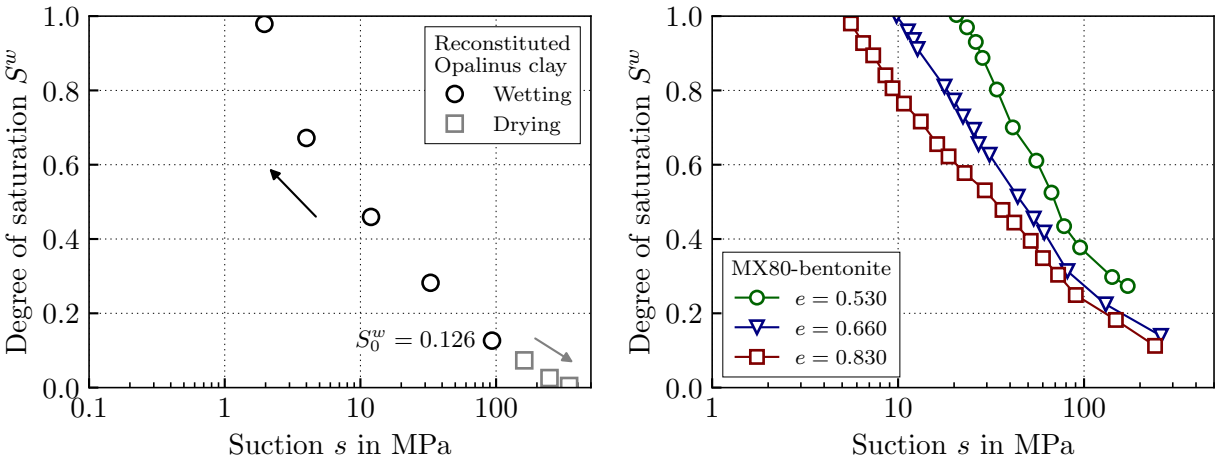

Figure 2.5.: Wetting paths of the SWRC for reconstituted Opalinus clay, modified from Machaček et al. (2024), and for MX80 bentonite at three different void ratios, modified from Seiphoori et al. (2014).

corresponding to 2.5, 50 and 200 kPa. The results are shown in terms of the degree of saturation (left-hand side of Figure 2.6) and water content versus suction (right-hand side of Figure 2.6). For high suctions, regardless of the boundary condition similar water contents are apparent, whereas a higher water content is reached for vertically unconfined conditions than for constant volume conditions at lower suctions. In terms of the degree of saturation, full saturation ($S^w = 1.0$) is reached at larger suctions under constant volume conditions than for vertically unconfined conditions. Constant volume and vertically unconfined conditions represent the two limiting cases, with mixed conditions (swell under load) lying between them in terms of graphical representation. With increasing expansion upon wetting, the total amount of pore space becomes larger and the absolute quantity of attached water is greater. As a result, the less confined the samples were, the flatter the SWRC was found to be.

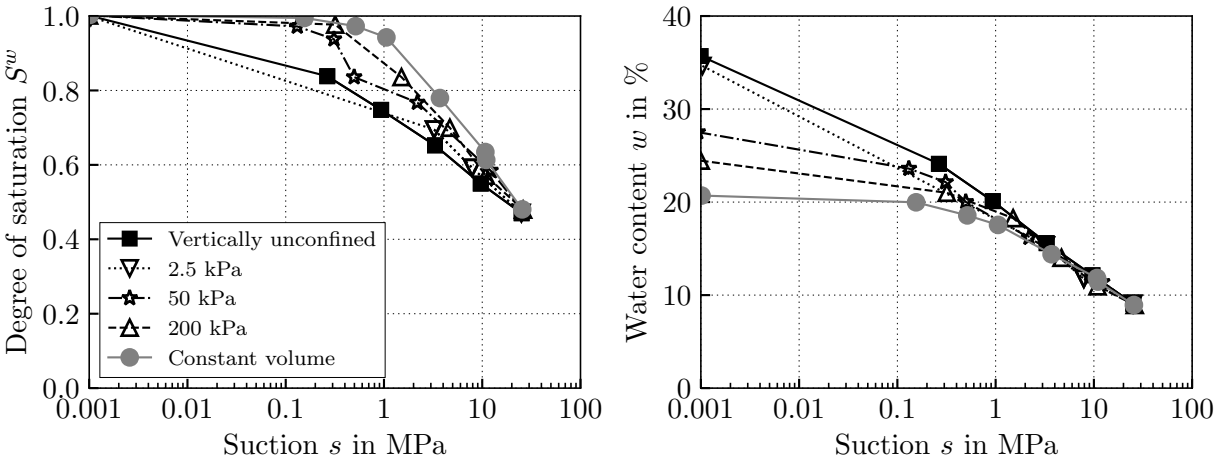

Figure 2.6.: Influence of the boundary conditions on the SWRC (wetting paths) of sand-bentonite mixtures, modified from Lang (2019).

The exemplary results show the complex interactions between suction, porosity and mechanical boundary conditions with regard to the water retention behaviour of expansive soils. In practice, their determination requires complex test set-ups and time-consuming test protocols. The identification and delimitation of individual influences and phenomena is difficult to realise, as

the processes overlap and occur simultaneously. Their mathematical or constitutive description requires selecting a suitable level of complexity that reflects both the objectives and the practical context of the application.

2.2.1.1. Mathematical models

Based on laboratory data, numerous empirical models for the water retention behaviour have been developed in the past. Ideally, they are formulated continuously and offer sufficient flexibility to represent the laboratory data by parameter optimisation. Amongst others, the most commonly used models are those of van Genuchten (1980) and Brooks and Corey (1964), although they exhibit limitations in adequately capturing the experimental data across the full suction range. The model by Fredlund and Xing (1994) offers greater flexibility and improved adaptability due to additional parameters, while remaining sufficiently simple for practical application.

1. **Van Genuchten**
   The following equation was proposed for the effective degree of saturation by van Genuchten (1980):
   $$S^e = \left(\frac{1}{1 + (\alpha\, h_w)^n} \right)^m , \tag{2.9}$$
   where α, n and m are material parameters. For the parameter m the dependency $m = 1 - 1/n$ is often assumed. $h_w = s/\gamma^w$ is the pressure head in mH_2O with suction s and unit weight of water γ^w. If the suction is used in Equation (2.9) instead of h_w, the parameter α (in mH_2O^{-1}) must be modified as α/γ^w (in kPa^{-1}). Considering the degree of saturation, Equation (2.9) reads:
   $$S^w = S^{wr} + (1 - S^{wr}) \left(\frac{1}{1 + (\alpha\, h_w)^n} \right)^m . \tag{2.10}$$
   With increasing α, the air entry value s_{aev} decreases and with increasing n the SWRC exhibits a steeper slope. Design standards often specify value ranges for parameters of Equation (2.9) for certain soil types, see e.g. the German standard DIN 4220:2020-11 (2020).

2. **Brooks & Corey**
   Brooks and Corey (1964) divided the SWRC into two parts, assuming no change in the degree of saturation for suction values below the air entry value s_{aev} and a power function for larger suctions. In terms of the effective degree of saturation the Brooks & Corey model reads:
   $$S^e = \begin{cases} \left(\frac{s_{\text{aev}}}{s}\right)^\lambda & \text{for} \quad s \geq s_{\text{aev}} \\ 1 & \text{for} \quad s < s_{\text{aev}} \end{cases} , \tag{2.11}$$
   or for the degree of saturation:
   $$S^w = S^{wr} + (1 - S^{wr}) \begin{cases} \left(\frac{s_{\text{aev}}}{s}\right)^\lambda & \text{for} \quad s \geq s_{\text{aev}} \\ 1 & \text{for} \quad s < s_{\text{aev}} \end{cases} , \tag{2.12}$$
   wherein λ is a material parameter. Similar as for the parameter n of the van Genuchten model, the SWRC exhibits a steeper slope with increasing λ. An obvious disadvantage of the formulation of Brooks and Corey (1964) is the loss of differentiability due to the piecewise formulation.

3. **Fredlund & Xing**
   The approach of Fredlund and Xing (1994) interrelates the degree of saturation S^w and the suction s:

$$S^w = \left[1 - \frac{\ln\left(1 + \frac{s}{h_r}\right)}{\ln\left(1 + \frac{1\times10^6}{h_r}\right)}\right] \frac{1}{\ln\left(\exp + \left(\frac{s}{a_f}\right)^{n_f}\right)^{m_f}}. \tag{2.13}$$

   The four model parameters h_r (in kPa), a_f (in kPa), n_f and m_f are linked to the suction at residual water content, the air entry value, the slope and the residual water content (or degree of saturation), respectively. The multiplier in square brackets of Equation (2.13) is often defined as a correction function for the residual suction and denoted as $C = C(s, h_r)$. The model of Fredlund and Xing (1994) considers the residual zone directly in its formulation and thus no version using the effective degree of saturation S^e exists.

More advanced models exist, which include void ratio dependency, as e.g. the model by Gallipoli et al. (2003b), which extends the model of van Genuchten (1980) by the specific volume ν. Other approaches incorporate hysteresis, for example those of Tarantino (2009) or Fuentes Lacouture (2014), which require the definition of separate drying, wetting, and scanning curves as functions of void ratio e and suction s. Alternatively, the model by Gao et al. (2021) integrates the contact-angle-dependent hysteresis proposed by Azizi et al. (2017) into the SWRC model of Fredlund and Xing (1994), allowing all drying, wetting and scanning curves to be predicted from a unique SWRC based on the relation between advancing and receding water contact angles upon wetting and drying.

2.2.1.2. Double-structure approaches for expansive soils

Advanced water retention models account for void ratio dependency and hysteresis and, when applied to expansive soils, exhibit a more pronounced dependency of the retention behaviour on porosity than for non-expansive unsaturated soils. Alternatively, models considering the bi-modal pore structure of compacted expansive soils (see Section 2.1.3) were developed. These models explicitly take the pore structure evolution upon wetting (and drying) into account. Therefore, the water retention behaviour is defined on two different levels of porosity, the microstructural level of intra-aggregate pores (index: m) and the macrostructural level of inter-aggregate pores (index: M). Double-structure models are based on the assumption, that different swelling mechanisms dominate at distinct pore scales (see Section 2.1.2). They assume that the volume of micropores increases upon wetting and is unaffected by mechanical loading, whereas the macropore volume changes due to mechanical loading and intrusion by the micropores. Equilibrium exists between both structural levels and thus suction applies to both. Incorporation of double-structure to the SWRC was done e.g. by Romero et al. (2011), Hu et al. (2013), Della Vecchia et al. (2015) and Dieudonne et al. (2017) amongst others. The approach of Dieudonne et al. (2017) is briefly presented as an example. Therein, the degree of saturation S^w is expressed as a weighted average of the micro- and macrostructural void ratios $e_{m/M}$, degrees of saturation $S^w_{m/M}$ or water void ratios $e_{wm/M}$ as:

$$\begin{aligned} S^w &= \frac{e_m}{e} S^w_m + \frac{e_M}{e} S^w_M, \\ \Leftrightarrow S^w &= \frac{e_{wm}}{e} + \frac{e_{wM}}{e}. \end{aligned} \tag{2.14}$$

The water ratio is an alternative volumetric variable to the degree of saturation and is defined as $e_w = e\,S^w$. On the macroscopic level, which is assumed decisive for the coupled hydro-mechanical behaviour, only the macroscopic degree of saturation and void ratio are considered and the water retention domain reads as:

$$e_{wM}(s, e, e_m) = (e - e_m)\ \sqcup, \tag{2.15}$$

wherein $\sqcup$ can be any aforementioned hydraulic model, e.g. the model of van Genuchten (1980). For computation of the macroscopic properties, two evolution equations are required: (1) for the microstructural void ratio e_m and (2) for the microstructural water ratio e_{wm}. For the first, MIP results are considered (including the uncertainties introduced in Section 2.1.3). For the latter, adsorption isotherms (relationships between the adsorbed adsorbate on the surface of a material and the acting pressure) are utilized (Dubinin, 1947). According to Dieudonne (2016), a sophisticated SWRC should be employed in numerical modelling, when an insufficient coupling between mechanical and hydraulic behaviour is incorporated in the mechanical constitutive model.

2.2.2. Permeability

The extent of water movement in the pore space of the soil matrix, i.e. the flow of water, is governed by the hydraulic conductivity tensor $\boldsymbol{k}^w$. Hydraulic conductivity can be isotropic, i.e. $k^w_{ij} = k^w \delta_{ij}$, wherein k^w is the coefficient of hydraulic conductivity (in m/s), or anisotropic. In general, in saturated soils, the hydraulic conductivity mainly depends on the overall pore space, represented by the void ratio e or porosity n, and the tortuosity (connectivity and morphological property of the pore network). A common approach for estimating the hydraulic conductivity of a saturated soil $k^{w,\mathrm{sat}}$ was proposed by Kozeny (1927) and Carman (1939) based on the grain size distribution:

$$k^{w,\mathrm{sat}} = \underbrace{\frac{\gamma^w}{\mu^w}\,\frac{d_{50}^2}{C}}_{\text{const.}}\,\frac{n^3}{(1-n)^2}, \tag{2.16}$$

wherein γ^w is the specific weight of water (10 kN/m^3), μ^w is the dynamic viscosity of water (10^6 kPa/s at 20°C), d_{50} is the mean grain size (in m) and C is a dimensionless material parameter. Although Equation (2.16) was introduced for granular materials, it effectively establishes a general proportionality between the coefficient of saturated hydraulic conductivity $k^{w,\mathrm{sat}}$ and a function of the porosity n:

$$k^{w,\mathrm{sat}} \propto \frac{n^3}{(1-n)^2}. \tag{2.17}$$

In unsaturated soils, the presence of pore air in the pore space reduces the available space for pore water flow (and vice versa, Leong and Rahardjo (1997)). The smaller the pore space occupied by pore air, the less pronounced this phenomenon is. Hence, the coefficient of unsaturated hydraulic conductivity can be associated with the water content w or more commonly the effective degree of saturation S^e, as residual water is usually assumed not to contribute to flow, see Section 2.2.1. It is expressed as:

$$k^w\left(n, S^e\right) = k^{w,\mathrm{sat}}\left(n\right)\, k^{r,w}\left(S^e\right), \tag{2.18}$$

wherein the coefficient of hydraulic conductivity at a specific porosity n and effective degree of saturation S^e is the product of the fully saturated hydraulic conductivity at porosity n

and the relative permeability $k^{r,w}$ (Leong and Rahardjo, 1997). The relative permeability is a dimensionless scalar in the range $0 \leq k^{r,w} \leq 1$. Permeability K^s (in m^2) is defined as an intrinsic property of the solid matrix of the porous medium (superscript s) and relates to the coefficient of hydraulic conductivity k^w (in m/s) as:

$$K^s(n) = \frac{k^{w,\mathrm{sat}}(n)\,\mu^w}{\gamma^w}. \tag{2.19}$$

Permeability is independent of the wetting fluid, whereas the coefficient of hydraulic conductivity depends on the viscosity and specific weight of the fluid. With Equation (2.19), the general relation for hydraulic conductivity under unsaturated conditions of Equation (2.18) reads as:

$$k^w(n, S^e) = \frac{K^s(n)\,\gamma^w}{\mu^w}\,k^{r,w}(S^e). \tag{2.20}$$

When the index w is omitted, Equation (2.19) is applicable to all fluids, not exclusively to water. Analogously to the relative permeability for the water phase, a relative permeability can be formulated for the air phase $k^{r,a}$, see e.g. Burdine (1953). It is not discussed in detail here, as a passive air phase is assumed in the FE implementation in this work (see Chapter 6).

The saturated hydraulic conductivity of expansive soils exhibits the same dependency on porosity and decreases with decreasing porosity as any soil (Gatabin et al., 2016; Lloret et al., 2003; Villar and Lloret, 2004; Ferrari et al., 2016). In unsaturated conditions, the trend of hydraulic conductivity of expansive soils is ambiguous with changes in the degree of saturation. In general, hydraulic conductivity increases with increasing saturation. However, the hydraulic conductivity of expansive soils is simultaneously influenced by the swelling mechanisms that occur upon wetting (or shrinkage during drying). The attachment of water during swelling results in a reduction in pore space available for flow. Thus, independently of the mechanical boundary conditions, a decrease in hydraulic conductivity is expected upon saturation, cf. Villar (2004) amongst others. However, it is challenging to decouple the swelling process from the effects of partial saturation and to unambiguously distinguish the competing processes. Very limited experimental data on the swelling-induced reduction in hydraulic conductivity is available in the contemporary literature.

Investigations on unsaturated permeabilities of expansive soils were carried out by Cui et al. (2008), Ye et al. (2009) and Wang et al. (2013a) using the instantaneous profile method (Daniel, 1982) to compute water permeability depending on suction during infiltration tests. They suggested that the apparent permeability, accounting for the effects of partial saturation and swelling, initially decreases during wetting and subsequently increases as full saturation is approached. However, Dieudonne (2016) offered a comprehensive critique of the interpretation of infiltration data obtained via the instantaneous profile method, highlighting that the evaluation relies on geometric assumptions which can significantly affect the results. Haque Mondol et al. (2008) studied the influence of smectite in six artificial smectite-kaolinite mixtures mimicking a mudstone to evaluate the extent of swelling-induced permeability reduction. They discovered that the saturated permeability of the mixtures logarithmically decreased with increasing smectite content by four orders of magnitude between the limiting states of pure smectite and pure kaolinite. This decrease was attributed to the smectite content and therefore at least partly interpreted as a reduction induced by swelling.

Although it is very difficult to assess if the increase in hydraulic conductivity due to the increase of the degree of saturation prevails over the swelling-induced reduction of hydraulic conductivity

during wetting or vice versa, the states before and after wetting can be evaluated in terms of intrinsic permeability K^s (in m^2) to enhance understanding of the processes in the expansive soil. To determine the intrinsic permeability in the dry reference state, the flow of a non-wetting fluid must be measured in order to prevent swelling. This approach was demonstrated by Nitsch et al. (2023a) for reconstituted Opalinus clay shale under oedometric conditions. Steady-state air permeability measurements with Nitrogen flow at different pressure gradients were carried out on dry, compacted samples. In the water-saturated state, the permeability was measured with steady-state water flow at different volumetric boundary conditions. One sample was wetted at constant volume conditions (swelling pressure test) prior to flow through the sample during the permeability test, and consequently, the global void ratio was equivalent to that in the air permeability tests. The same sample was then mechanically unloaded, inducing an increase in porosity, and again subjected to water flow. A second sample was wetted under vertically unconfined conditions (swelling strain test) prior to flow. Upon saturation the sample expanded and the global void ratio significantly increased. Further details on these permeability tests are given in Appendix A. The results are presented in Table 2.1 and Figure 2.7 in terms of apparent, saturated permeability versus void ratio. Note that the permeability is denoted as a scalar K^s due to the one-dimensional measurement. After constant volume swelling a reduction by approximately three orders of magnitude was observed in comparison to the dry reference sample without change in global porosity. Compared to the influence of wetting, volume changes had a rather small impact on the permeability. However it was measurable and a trend was identified: with increasing porosity, the permeability increased.

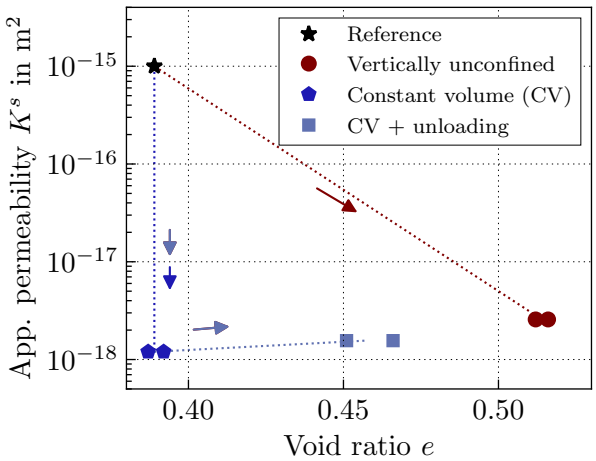

Figure 2.7.: Apparent, saturated permeability vs. void ratio from permeability testing for dry (reference) conditions and after swelling on reconstituted Opalinus clay shale (Nitsch et al., 2023a). The trend of permeability development is indicated by arrows and dotted lines for the saturated tests.

Two distinct intrinsic permeabilities were identified in the idealised dry, hence fully air-saturated, and fully water-saturated state as a result of the differing pore structures of unswollen and swollen soil. Intermediate, unsaturated states could not be quantified. At constant volume conditions, the permeability can be decoupled from changes in global porosity, as the volume of the sample is constant. Consequently, the reduction is entirely attributed to the attachment of water resulting in a reduced effective porosity. Under different volumetric boundary conditions, the change in total porosity relative to the initial porosity (corresponding to constant volume in the saturated state) is the decisive factor for the reduced magnitude of permeability. Therefore,

Table 2.1.: Results of permeability tests on reconstituted saturated Opalinus clay shale (Nitsch et al., 2023a).

Condition	Initial void ratio	Final void ratio	Permeability in m^2
Reference / dry*	0.389	0.389	1.0×10^{-15}
Vertically unconfined swelling	0.387 / 0.392	0.516 / 0.512 [1]	2.6×10^{-18}
Constant volume swelling (CV)	0.387 / 0.392	0.387 / 0.392	1.2×10^{-18}
CV + unloading	0.388 / 0.387	0.466 / 0.451 [2]	1.6×10^{-18}

* Fluid: Nitrogen. All other tests were flushed with water.
[1] Void ratio after unloading from swelling pressure
[2] Void ratio after vertically unconfined swelling

the overall permeability of an unsaturated swelling clay requires an extension of the relative permeability approach expressed by Equation (2.18).

2.2.2.1. Mathematical models for relative permeability

Similar to the SWRC, several equations exist for the relative water permeability, interrelating $k^{r,w}$ with the (effective) degree of saturation or suction. Regardless of the variable chosen, the concept of relative permeability is only applicable outside the residual zone, where flow is assumed to take place. Relationships for relative permeability were derived either empirically, as in the models proposed by Nguyen et al. (2006) and Brooks and Corey (1964), or through statistical approaches. The latter method estimates the relative permeability using the characteristics of the SWRC through integration (Leong and Rahardjo, 1997; Mualem, 1986). Various approaches exist (Childs et al., 1950; Burdine, 1953; Mualem, 1976), all of which follow the same principle: the integral over the degree of saturation from a residual (dry) state (S^{wr}) to the current state (S^w) is compared with the integral to the fully saturated state ($S^w = S^{w,sat}$) and may be expressed as:

$$k^{r,w}(S^w, s) = \frac{k^w(S^w)}{k^{w,\mathrm{sat}}} = \frac{\int_{S^{wr}}^{S^w} \frac{\mathrm{d}S^w}{s^2(S^w)}}{\int_{S^{wr}}^{S^{w,\mathrm{sat}}} \frac{\mathrm{d}S^w}{s^2(S^w)}}. \tag{2.21}$$

The integrals are visualised in Figure 2.8, wherein the reference integral in the denominator of Equation (2.21), is shown on the left-hand side and the integral corresponding to an arbitrary unsaturated state, thus the numerator of Equation (2.21), is shown on the right-hand side. In Equation (2.21) and Figure 2.8, the degree of saturation is applied. The conversion to the effective degree of saturation S^e for the general application of Equation (2.18) is possible at any time using the relation in Equation (2.6). As an alternative to the integration over the degree of saturation, it can be carried out logarithmically over suction. The integral between an upper integration limit $s(S^{wr})$ and the current suction $s(S^w)$ is compared to the total integral between the upper limit and the lower integration limit $s_i = s(S^{w,\mathrm{sat}})$, which corresponds to the saturated state. Equation (2.21) transforms to:

$$k^{r,w}(S^w, s) = \frac{\int_{\ln(s)}^{\ln(s(S^{wr}))} \frac{S^w(e^y) - S^w(s)}{e^y} \left(S^w\right)'(e^y)\,\mathrm{d}y}{\int_{\ln(s_i)}^{\ln(s(S^{wr}))} \frac{S^w(e^y) - S^w(s_i)}{e^y} \left(S^w\right)'(e^y)\,\mathrm{d}y}, \tag{2.22}$$

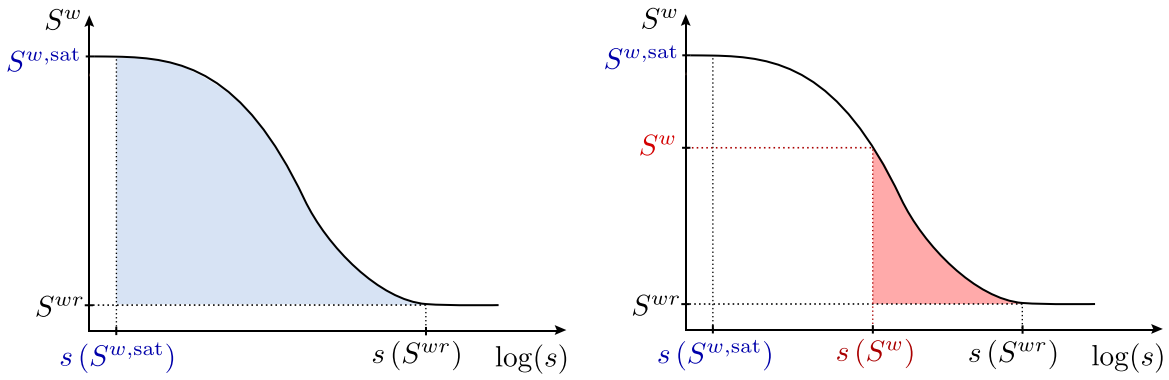

Figure 2.8.: Visualization of statistical approaches for computation of the relative water permeability according to Equation (2.21): integral of the SWRC from the residual to the fully saturated state (left) and to an arbitrary unsaturated state (right).

wherein $(S^w)'$ is the derivative of the specific SWRC with respect to suction. Fredlund et al. (1994) and Fredlund et al. (1998) proposed a constant value of $s(S^{wr}) = 1{\times}10^6$ kPa for the upper integration limit. However, it may violate the assumption that no flow takes place beyond the suction corresponding to the residual degree of saturation and would result in an overestimation of the relative permeability, especially for high suctions near the residual state. To exclude this non-contributing portion of the integral for $s(S^{wr}) < s < 1 \times 10^6$ kPa, the residual degree of saturation is accounted for by usage of the effective degree of saturation and the integral is capped at a horizontal line representing S^{wr} (Figure 2.8). For relatively simple models of the SWRC, e.g. for the model of van Genuchten (1980), a closed analytical equation is achieved in the integration. The relative permeability can be directly computed without evaluation of the integrals. For more complicated models as the approach of Fredlund and Xing (1994) the integral form remains. These two models and the empirical approach of Nguyen et al. (2006) and Brooks and Corey (1964) are presented in the following:

1. **Van Genuchten-Mualem**
   Mualem (1976) evaluated the SWRC of van Genuchten (1980) on the basis of Equation (2.21) and derived the following closed-form analytical equations for the relative permeability of pore water and pore air:

$$k^{r,w} = \sqrt{S^e}\left(1 - \left(1 - (S^e)^{\frac{n}{n-1}}\right)^{\frac{n-1}{n}}\right)^2 \quad \text{and} \quad k^{r,a} = \sqrt{1-S^e}\left(1 - \left(1 - (S^e)^{\frac{n}{n-1}}\right)^{\frac{n-1}{n}}\right)^2. \tag{2.23}$$

2. **Fredlund & Xing**
   For the SWRC of Fredlund et al. (1994, 2012) an analytical solution cannot be derived. Therefore, Equation (2.22) must be evaluated using Equation (2.13) as the integral solution for the permeability equation. The lower limit s_i must be defined for each material individually with the air entry value of the SWRC serving as an appropriate choice. However, this results in an overestimation of $k^{r,w} = 1.0$ for $S^w \leq 1.0$, which might be unfavourable for certain applications. Conversely, the relative permeability might be underestimated if lower values are chosen as the air entry value (Zhang and Fredlund, 2015). Therefore, the selection of the lower limit s_i requires careful consideration.

3. **Brooks & Corey**
   Brooks and Corey (1964) proposed an exponential approach utilizing the parameter λ known from the Brooks & Corey SWRC model (see Equation (2.11)) and the effective degree of saturation. For the pore water and pore air it reads:

$$k^{r,w} = (S^e)^{\frac{2+3\lambda}{\lambda}} \quad \text{and} \quad k^{r,a} = (1 - S^e)^2 \left(1 - (S^e)\frac{2+\lambda}{\lambda}\right). \tag{2.24}$$

4. **Nguyen**
   A similar, more general, exponential expression was empirically derived by Nguyen et al. (2006) based on experimental observations. They proposed:

$$k^{r,w} = (S^e)^3 \quad \text{and} \quad k^{r,a} = (1 - S^e)^3. \tag{2.25}$$

   Note that the approach of Nguyen et al. (2006) can also be generalized by using any other exponent.

2.2.2.2. Approaches for permeability reduction in expansive soils

Most commonly the previously introduced Kozeny-Carman dependency between hydraulic conductivity and porosity is applied to expansive soils combined with any relative permeability model to consider deformation and saturation effects, respectively (see Åkesson et al. (2009), Chen et al. (2009) or Abed and Sołowski (2017) amongst others). Equations (2.16) and (2.17) are rewritten in terms of permeability as:

$$K(n) = K_0 \frac{(1 - n_0)^2}{n_0^3} \frac{n^3}{(1 - n)^2}, \tag{2.26}$$

wherein K_0 is the intrinsic permeability corresponding to a known porosity n_0. The reduction of permeability due to swelling is not explicitly considered. Villar (2004), among others, found that the original Kozeny-Carman dependency does not provide an accurate prediction. As a result, Equation (2.17) is often modified with arbitrary exponents to account for a more pronounced dependency of the permeability on porosity:

$$K(n) = K_0 \frac{(1 - n_0)^{MKC}}{n_0^{NKC}} \frac{n^{NKC}}{(1 - n)^{MKC}}, \tag{2.27}$$

wherein MKC and NKC are material parameters, see e.g. Bosch et al. (2021). Alternatively to the Kozeny-Carman dependency, an exponential approach was utilized as well, see e.g. Sánchez et al. (2012):

$$K(n) = K_0 \exp\left[b\,(n - n_0))\right], \tag{2.28}$$

wherein b is a model fitting parameter. In Equations (2.26) - (2.28) the reference permeability K_0 is most commonly determined after swelling at constant volume conditions in the saturated state. Consequently, the permeability evolution upon wetting results from application of an arbitrary relative permeability model for unsaturated soils, as described in Section 2.2.2. The reduction due to swelling is blended into the porosity dependency by parameter fitting. This approach may be sufficient for certain applications or soils, but it contradicts the acknowledged understanding that permeability is influenced by swelling due to changes in the pore structure.

Similar to the description of the soil water retention (or mechanical) behaviour, double-structure models were incorporated in the hydraulic functions as well. Various approaches have been proposed, which relate permeability with a macroscopic porosity n_M, which evolves during swelling processes. Water flow is assumed in macropores only. Gens et al. (2011) and Sánchez et al. (2012) introduced macroporosity ($n_{M(0)}$) in the exponential approach from Equation (2.28):

$$K(n_M) = K_0 \exp\left[b\left(n_M - n_{M,0}\right)\right], \tag{2.29}$$

and Romero (2013), Dieudonné and Charlier (2017) or Dieudonne (2016) in an extended Kozeny-Carman type model based on Equation (2.27) using the macrostructural void ratio $e_{M(0)}$:

$$K(e_M) = K_0 \frac{(1-e_{M0})^{MKC}}{e_{M0}^{NKC}} \frac{e_M^{NKC}}{(1-e_M)^{MKC}}. \tag{2.30}$$

Therein, the macrostructural porosity or void ratio evolution due to swelling must be provided by a suitable mechanical model, e.g. the Barcelona Expansive Model (see Section 2.5.2.2) and the approach cannot be coupled with a non double-structure mechanical model. The evolution of macroporosity or macroscopic void ratio is governed by the evolution of microstructure, as was discussed in Section 2.2.1.2. The consideration of macroporosity development, which represents an effective porosity during flow, enhances the prediction in both approaches. However, the reference value, K_0, pertains to fully saturated conditions, and accurate prediction of permeability depends on parameter adjustment. The phenomenological limitation remains, as the reference state is not in dry, unswollen conditions. Furthermore, the changes in volume fractions within the soil and the associated storage properties in the underlying balancing equations of the numerical framework are not accounted for.

A different approach was followed in continuum mechanical descriptions of swelling polymer gels. Sauerwein and Steeb (2018) and Sauerwein (2021) proposed a so-called *permeability damage* model. Therein, a mass transfer resulted in capture of polymer in the solid skeleton which caused a permeability damage (equivalent to a permeability reduction) on the macroscopic level, where flow took place. The permeability in the damaged state was calculated as:

$$K^s = K_0^s \frac{(1-n_0)^2}{n_0^3} \frac{n^3}{(1-n)^2} \quad \text{with} \quad K_0^s \propto \frac{n^3}{(1-n)^2}, \tag{2.31}$$

wherein K_0^s was the intrinsic permeability of the solid skeleton without any captured particles. For an expansive soil, this state corresponds to the unsaturated state before swelling and matches the phenomena observed from the permeability measurements on reconstituted Opalinus clay shale.

2.2.3. Compatibility of hydraulic models within Finite Element simulations

The choice of the constitutive models for the SWRC and relative permeability in FE simulations are often independent of each other. In theory, arbitrary combinations of mathematical models can be chosen, and the model of relative permeability can technically even be disregarded as long as the reduced prediction quality of the material behaviour is accepted as a consequence. However, it is recommended to choose the models for the SWRC and relative permeability consistently. To highlight the differences of the presented models, Figure 2.9 shows the evaluation of the SWRCs (left) and the relative permeability models (right) for a very low permeability

expansive soil. The parameters of the respective models were selected with the objective, that the resulting SWRCs were as close to each other as possible in the S^w–log(s) space, considering the limitations of each model.

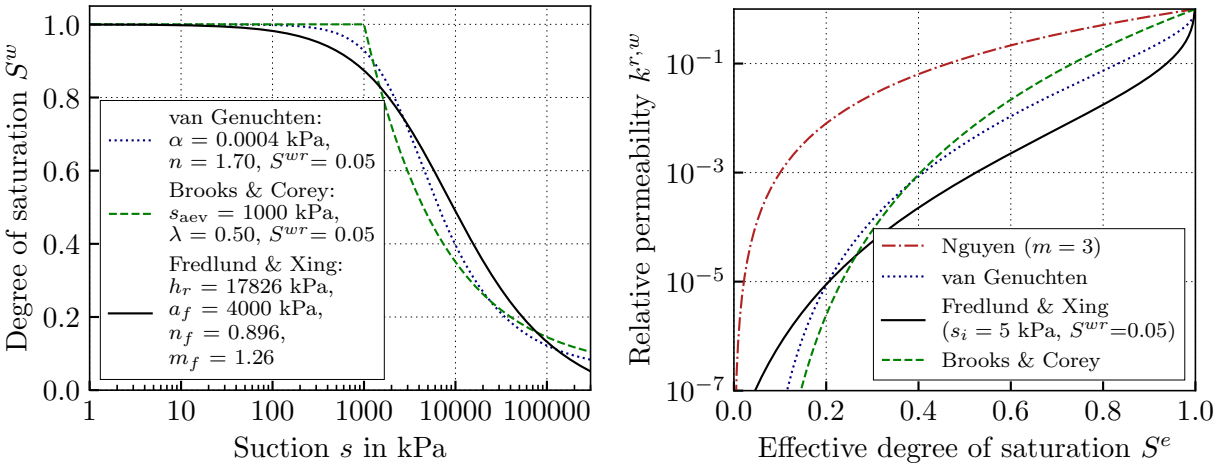

Figure 2.9.: Hydraulic functions: SWRC (left) and relative permeability (right) evaluated for different models.

The differences of the SWRCs on the left-hand side of Figure 2.9 are reflected in the relative permeability on the right-hand side of Figure 2.9, as the evolution of relative permeability varies for the models of van Genuchten (1980), Brooks and Corey (1964), and Fredlund et al. (1994). The purely empirical formulation of Nguyen et al. (2006) shows a more pronounced deviation from the other models, as the relative permeability increases more strongly at low saturation and less pronounced close to full saturation. A combination of different approaches for the SWRC and relative permeability is not recommended, as the storage and flow terms in the underlying governing equations diverge. It may be the case that the degree of saturation should change while the hydraulic conductivity is too low to allow sufficient redistribution of water, or vice versa. A consistent choice of both models therefore reduces numerical difficulties and generally leads to more stable convergence behaviour.

2.3. Stress variables in unsaturated soils

The description of mechanical behaviour and properties and the formulation of constitutive stress-strain relationships requires an accurate definition of stress. In general, the mechanical behaviour of soil as a porous medium does not depend solely on the total stress. Instead, it is influenced by the pore fluids that partially or fully occupy the pore space.

2.3.1. Effective stress principle

Terzaghi (1936) proposed the concept of effective stress for a saturated porous medium, which consists of two incompressible phases, solid and water. If the soil is subjected to mechanical loading, stresses occur both in the grain matrix of the solid as well as in the pore fluid phase, the water. The stresses of both phases are considered in the effective stress $\boldsymbol{\sigma}'$:

$$\boldsymbol{\sigma}' = \boldsymbol{\sigma}^{tot} - p^w \mathbf{1}, \tag{2.32}$$

wherein $\boldsymbol{\sigma}^{tot}$ and p^w are the total stress and pore water pressure, respectively. Geotechnical sign convention is applied, i.e. compressive stress is positive. In this way, a first fundamental hydro-mechanical coupling is achieved. For unsaturated states of the porous medium, Bishop (1959) proposed the modified effective stress principle to account for the presence of pore air in the pore space and the interaction between both fluid phases:

$$\begin{aligned} \boldsymbol{\sigma}' &= \boldsymbol{\sigma}^{tot} - p^a\mathbf{1} + \chi(p^a - p^w)\mathbf{1}, \\ \boldsymbol{\sigma}' &= \boldsymbol{\sigma}^{tot} - p^a\mathbf{1} + \chi s\mathbf{1}, \end{aligned} \tag{2.33}$$

wherein p^a is the pore air pressure, $s = (p^a - p^w)$ is the suction and χ is the so-called Bishop parameter. Equation (2.33) ensures a clear transition from unsaturated to saturated states and corresponds to Equation (2.32) for fully saturated conditions. The product χs considers the contribution of suction in the unsaturated state. The effective degree of saturation serves as the common choice for the Bishop parameter, i.e. $\chi = S^e$ (Pereira et al., 2010). In recent years, many advanced formulations for χ have been proposed, whereby the simplest further development is a power approach to the effective degree of saturation, see Likos and Lu (2004) or Vaunat and Casini (2017) amongst others, requiring a material parameter κ:

$$\chi = \begin{cases} 0 & \text{for } S^w \leq S^{wr} \\ (S^e)^\kappa & \text{for } S^{wr} < S^w < 1 \\ 1 & \text{for } S^w = 1 \end{cases}. \tag{2.34}$$

2.3.2. Choice of stress variables

Fredlund and Morgenstern (1977) and Nuth and Laloui (2008) amongst others stated that in a saturated soil the effective stress is sufficient to describe soil behaviour. However, in an unsaturated soil two independent variables shall be chosen. Any pair of the following is feasible:

- Terzaghi's saturated effective stress: $\boldsymbol{\sigma}' = \boldsymbol{\sigma}^{tot} - p^w\mathbf{1}$,
- Excess of total stress over pore air pressure, referred to as net stress: $\boldsymbol{\sigma} = \boldsymbol{\sigma}^{tot} - p^a\mathbf{1}$,
- Suction: $s = p^a - p^w$.

Note that the suction is related with the degree of saturation at any time. Most commonly, net stress and suction $\{\boldsymbol{\sigma}, s\}$ are chosen together, as both can be determined and controlled in experiments. These stress variables were also adopted in the BBM proposed by Alonso et al. (1990). This is sometimes referred to as *implicit coupling*, as the main constitutive stress (net stress) is independent of the hydraulic variable. In contrast, applying suction and Terzaghi's saturated effective stress is referred to as *double-way coupling* (Ferrari et al., 2021). Models using different combinations were furthermore proposed: Effective stress and suction $\{\boldsymbol{\sigma}', s\}$ (François and Laloui, 2008) or effective stress and a further *modified* hydraulic variable as the modified suction $s^* = s^*(n, s)$ (Wheeler et al., 2003) or the bonding parameter $\zeta = \zeta(s, S_r)$ (Gallipoli et al., 2003a). The latter approaches aimed to modify both, the stress carried by the solid due to the contribution of the pore water and vice versa. However, analogously to the Bishop effective stress, they cannot be measured in the laboratory. Note that under laboratory ambient conditions, where the pore air pressure corresponds to atmospheric pressure, the net stress equals the total stress.

2.4. Hydro-mechanical behaviour of expansive soils

This section is devoted to the description of the hydro-mechanical material response of expansive soils, more specifically the experimental characterisation of the development of swelling pressure, swelling strain, compressibility and shear strength of expansive soils. The bidirectional coupling of mechanical properties with the hydraulic characteristics is shown. This work focuses on the engineering quantities of stress and strain without a description of microstructural processes. For the latter, reference is made for example to the works of Gens and Alonso (1992) or Dieudonne (2016). Results from the author's own experimental work on reconstituted Opalinus clay shale (Nitsch et al., 2023a) are presented. Opalinus clay is a moderately expansive material with 5 weight percent (wt-%) highly expansive clay minerals (pure smectite) and 35 wt-% overall expansive minerals (including illite). The results are complemented by experimental evidence from literature on materials with higher contents of expansive clay minerals and the results of studies from literature including mechanical loading paths at partially saturated conditions. Appendix A includes extensive information regarding the experimental campaign on reconstituted Opalinus clay performed by the author including test devices, experimental protocols, specimen preparation and additional test results, which will not be presented in this section.

2.4.1. Oedometric compression and rebound behaviour at constant water content

The oedometric compression and rebound behaviour of expansive soils is important in two respects: for the mechanical behaviour following wetting in the saturated state, i.e. for the stiffness or volumetric response, and for the dry, mechanical behaviour upon sample preparation. For swelling tests the material is most commonly uniaxially compacted under oedometric conditions. Depending on the target void ratio, a certain pressure is required for compaction. After sample compaction, which corresponds to a loading of the material along a virgin compression line, the sample is unloaded. In oedometric compression and rebound tests on expansive soils, most commonly the vertical net stress σ_{22} is controlled and the vertical deformation is measured. Due to the radial confinement under oedometric conditions, vertical deformation corresponds to volumetric deformation. The material response is characterised by the elastic swelling index κ, the first loading or virgin compression index λ and the vertical net vertical preloading net stress $\sigma_{22,d}$. A compacted sample follows a quasi bi-linear curve in the $e - \log(\sigma_{22})$ space, on which first small elastic volumetric deformation takes place for overconsolidated states ($\sigma_{22} < \sigma_{22,d}$), followed by larger irreversible strains for normally consolidated states ($\sigma_{22} = \sigma_{22,d}$). The transition from overconsolidated to normally consolidated states is correlated with a change in the slope at the (apparent) vertical preloading net stress. The volumetric material response in terms of the increment of the void ratio $\mathrm{d}e$ due to a change in the vertical net stress is described in terms of the logarithmic stress increment $\mathrm{d}\,(\ln \sigma_{22})$:

$$\mathrm{d}e = \begin{cases} -\kappa\, \mathrm{d}\,(\ln \sigma_{22}) & \text{for un-/reloading, } \sigma_{22} < \sigma_{22,d}, \\ -\lambda\, \mathrm{d}\,(\ln \sigma_{22}) & \text{for virgin loading, } \sigma_{22} = \sigma_{22,d}. \end{cases} \tag{2.35}$$

2.4.1.1. Influence of water content

Suction-controlled oedometric compression tests at different water contents allow to evaluate the influence of saturation on the material behaviour. While such oedometric tests require

advanced laboratory equipment, the influence of water content can also be shown by testing a nearly dry and a fully saturated sample. The left-hand side of Figure 2.10 shows the results of oedometric compression and rebound tests on reconstituted Opalinus clay on nearly dry reference material (OPA-0-33) and following different swelling tests: (a) vertically unconfined (OPA-0-24), (b) constant volume (OPA-0-34) and (c) after unloading from constant volume swelling (OPA-0-07). All samples were compacted to a similar initial void ratio of $e_0 \approx 0.387$ following the virgin loading line, which is also depicted in Figure 2.10 based on stress and displacement measurements from sample preparation (see Figure A.4 in the appendix). For swelling tests, the material was directly saturated with water at a vertical net stress of $\sigma_{22} = 35$ kPa. On the right-hand side of Figure 2.10, the results of suction-controlled oedometric compression and rebound tests on a bentonite-silt mixture by Nowamooz and Masrouri (2008) and Nowamooz (2007) are shown. Herein, the samples were also compacted to initial void ratios of $e_0 \approx 1.120$ and subjected to different suctions at a vertical net stress of $\sigma_{22} = 10$ kPa using VET. When equilibrium of deformation upon wetting was reached, oedometric loading and unloading was applied. One sample was loaded and unloaded in the reference state.

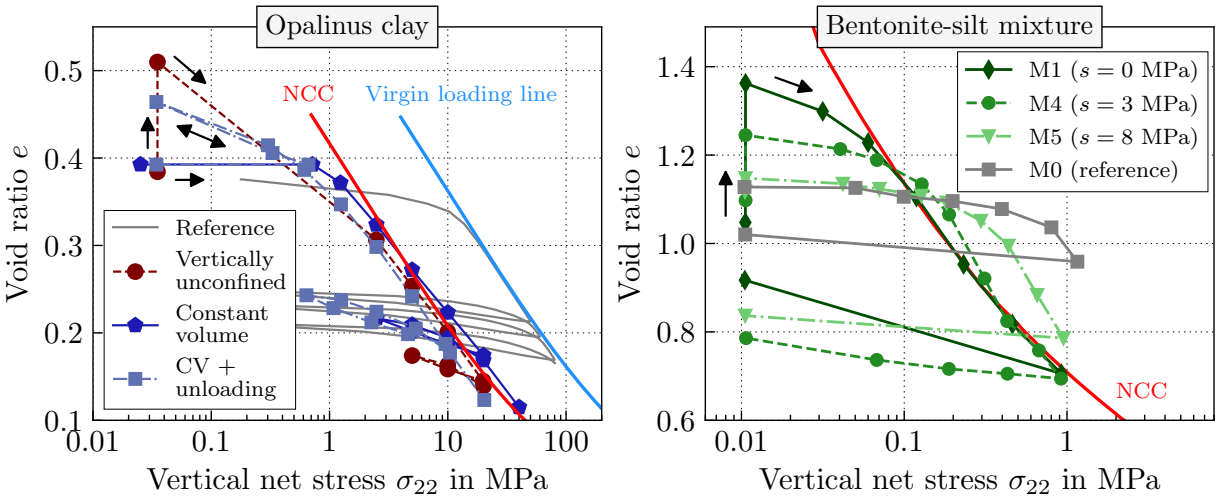

Figure 2.10.: Results of oedometric compression tests on reconstituted Opalinus clay (left, Nitsch et al. (2023a)) and suction-controlled oedometric compression tests on a bentonite-silt mixture (right, Nowamooz and Masrouri (2008)) at different suctions.

The results in Figure 2.10 are consistent with the expected condition $\kappa < \lambda$, indicating that the unloading stiffness is greater than the virgin loading stiffness. In the saturated state, the slope of the un- and reloading paths was significantly higher than in tests on unsaturated specimens, hence $\kappa = \kappa(w)$. Contrary, the virgin loading lines were parallel for unsaturated and saturated samples and independent of the water content ($\lambda = \text{const.}$). In the saturated state, however, the virgin loading lines were shifted to an area of a notably smaller stress level, which indicated a reduction of vertical preloading net stress with increasing water content, hence $\sigma_{22,d} = \sigma_{22,d}(w)$. The compression curves for different water contents / suctions approached a Normal Compression Curve (NCC) regardless of the initial state before loading. The unsaturated loading paths showed a kind of *hook*, which means the overshooting and subsequent re-approaching of the NCC e.g. in test M4 on the right-hand side of Figure 2.10. This behaviour is commonly interpreted as an apparent dependency of λ on the hydraulic state, however, it is rather a transitional area from an overconsolidated state (nearly on a reloading path) to a normally consolidated state (on a unique virgin loading line). With increasing saturation, the loading path converged *faster*

to the NCC. To summarize, the oedometric compression and rebound behaviour in terms of elastic stiffness, preloading state and virgin loading, depends on the water content w. The experiments on reconstituted Opalinus clay shale further highlighted, that the unloading strains after constant volume swelling were less than under vertically unconfined swelling conditions and should thus not be referred to as swelling strain (see Section 2.1.2).

2.4.1.2. Radial net stresses

Standard oedometric tests provide no information about radial net stress σ_{11}. As a result, the latter is often estimated based on vertical net stress σ_{22} using empirical formulas for the stress ratio $K_0 = \sigma_{11}/\sigma_{22}$, most commonly with Jaky's formula $K_0 = 1 - \sin\varphi$ (Jaky, 1944), wherein φ is the friction angle. Extensions such as $K_0 = (1 - \sin\varphi)\mathrm{OCR}^{\sin\varphi}$ (Mayne and Kulhawy, 1982) allow consideration of overconsolidation, with $\mathrm{OCR} = \sigma_{22,d}/\sigma_{22}$ denoting the overconsolidation ratio with vertical preloading net stress $\sigma_{22,d}$. For accurate prediction and understanding of the material's three-dimensional behaviour, knowledge on the radial net stress is essential, even during preparation of compacted samples. Uniaxially compacted specimens remain stable within the oedometer ring after complete removal of the vertical confinement. Moreover, extrusion from the ring requires significant force and does not lead to specimen disintegration. The sample remains mechanically stable. Tripathy et al. (2014) observed larger magnitudes of swelling pressure for laterally released samples than for laterally constrained samples of MX80 bentonite compacted with the same vertical net stress. In their study, laterally released samples were first extruded from the oedometer rings and subsequently reinserted before wetting, whereas laterally constrained samples were wetted without intermediate release. Consequently, compacted specimens must inhibit a significant residual radial net stress after compaction, which influences the subsequent material behaviour.

For a quantitative assessment of radial net stress under oedometric conditions, a so-called soft-oedometer apparatus can be used, see e.g. Kolymbas and Bauer (1993). Unlike conventional oedometric compression and rebound test devices, this device uses a special, soft oedometer ring with radial strain measurements in or on the ring (quasi-rigid confinement). The radial net stress can be computed from the radial strain assuming a linear elastic material behaviour of the soft oedometer ring. Alternatively, radial load cells can be installed inside the oedometer ring for stress measurement. Limited evidence exists on radial net stress development during loading and wetting, particularly during specimen preparation of nearly dry, unsaturated swelling clays. Caicedo et al. (2014) performed oedometric compression and rebound tests with multiple loading- and unloading cycles on a kaolin clay at different water contents in a modified oedometric ring with a radial load cell. Although kaolin clay is not an expansive soil, its mechanical behaviour during loading and unloading at constant water content is expected to be similar. Selected results from Caicedo et al. (2014) are shown on the left-hand side of Figure 2.11 for the driest ($w = 5\%$) and wettest investigated material ($w = 25\%$) in terms of radial net stress versus vertical net stress. Upon vertical loading, radial net stress developed as well, reaching stress ratios of $K_0 = 0.25 - 0.4$. With increasing water content, the ratio between radial and vertical net stress increased, i.e. the material's response became less deviatoric (in terms of deviatoric stress $q = \sigma_{22} - \sigma_{11}$). During unloading, however, the radial net stress did not reduce as fast as the vertical net stress resulting in larger K_0. After unloading to a very small vertical net stress, a relatively larger residual radial net stress remained, shown by the marker on the left-hand side of Figure 2.11. The final stress ratios were $K_0 = 7$ and $K_0 = 9$ for the tests with $w = 5\%$ and

$w = 25\%$, respectively. On the right-hand side of Figure 2.11 the results of three tests performed by the author on nearly dry samples of reconstituted Opalinus clay in a soft-oedometer device are shown. The samples had a similar void ratio of $e_0 \approx 1.1$ and were vertically loaded, un- and reloaded. The experimental procedure is described in Appendix A.3. The results show similar behaviour to that of kaolin clay. Upon loading, radial net stress increased to approximately 20 % of vertical net stress, hence $K_0 \approx 0.2$, and after unloading to small vertical net stress, a significant radial net stress remained, corresponding to a final stress ratio between 1.7 and 2.6 for the three tests.

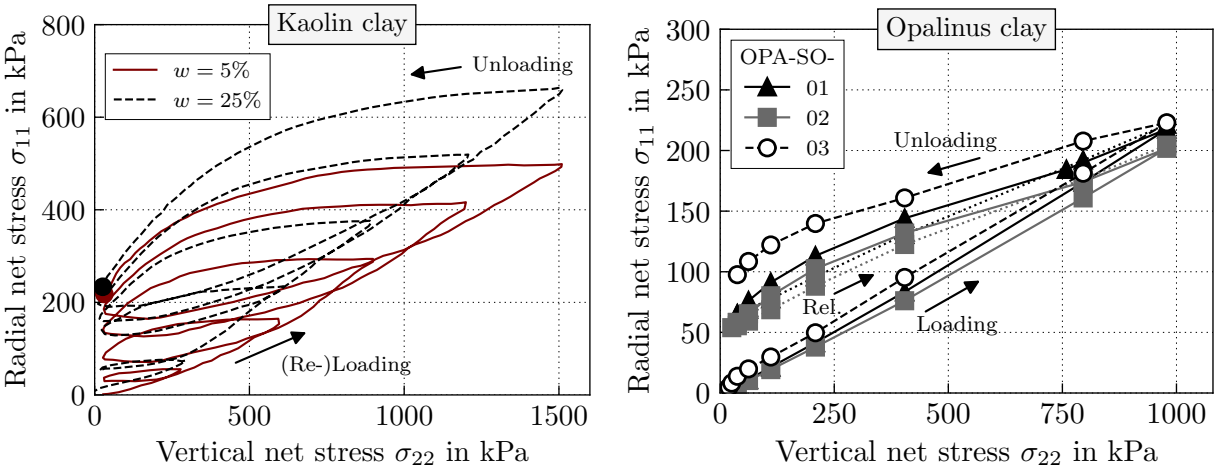

Figure 2.11.: Results of oedometric compression and rebound tests with radial net stress measurement for a kaolin clay (left, modified from Caicedo et al. (2014)) and for reconstituted Opalinus clay (right).

The results show that the stress state after compaction is neither isotropic nor characterised by a constant stress ratio $K_0 = \sigma_{11}/\sigma_{22}$. Consequently, due to negative deviatoric stress ($q = \sigma_{22} - \sigma_{11} < 0$), the stress state of the specimen after compaction and prior to swelling tests is known as triaxial extension, contrary to the usually assumed triaxial compression ($q = \sigma_{22} - \sigma_{11} > 0$) following empirical equations. Moreover the results indicate, that the radial preloading stress is smaller than the vertical preloading net stress.

2.4.2. Wetting at constant load: Expansion

The primary swelling phenomenon of volumetric deformation, i.e. expansion upon wetting under constant stress and unconstrained deformation, was introduced in Section 2.1.2. Under oedometric conditions, however, only vertical deformation is possible and the stress state in a compacted specimen is not isotropic (see Section 2.4.1.2), likely inducing a preferred orientation of clay particles and resulting in an anisotropic tendency to expand. The evolution of swelling strain is a time-dependent process. Depending on the material, sample height and wetting conditions, reaching steady-state conditions (i.e. no further change in deformation or stress) can take between some days up to several weeks. In general, a sigmoid-shaped evolution of deformation over time in a semi-logarithmic space is observed for unsaturated swelling clays (Sridharan and Gurtug, 2004). After a short initialisation phase, a pronounced increase in deformation is observed, followed by a gradual decrease in the deformation rate, see e.g. Figure 2.12 for vertically unconfined swelling tests on reconstituted Opalinus clay (Nitsch et al., 2023a).

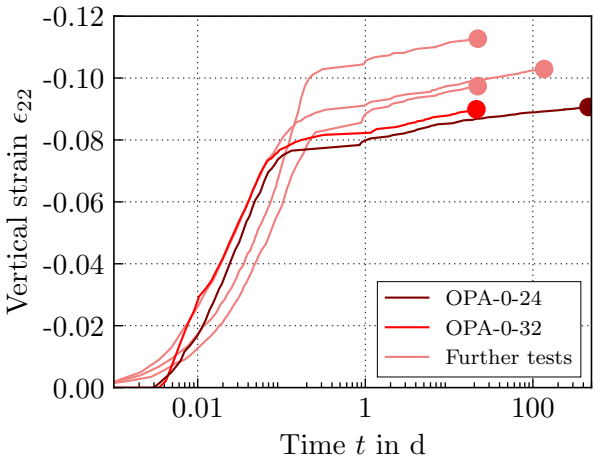

Figure 2.12.: Evolution of vertical strain for reconstituted Opalinus clay (Nitsch et al., 2023a). All samples had a similar initial void ratio $e_0 \approx 0.387$.

The initial increase can be directly attributed to the propagation of the saturation front in the material. The results of a vertically unconfined swelling test in a perspex oedometric ring with wetting from the bottom is shown on the left-hand side of Figure 2.13. Simultaneously with the measurement of the vertical deformation, the height of the *visible* saturation front was evaluated, as displayed on the right-hand side of Figure 2.13. The test was stopped when the saturation front reached the upper end of the sample. The results where normalized to the final values of vertical strain $\epsilon_{22} = -0.066$ and degree of saturation $S^w = 0.98$, which was determined by oven-drying. The disappearance of the visible saturation front, even at a degree of saturation close to $S^w = 1.0$, did not mark the steady state of the swelling process, as further deformation could still occur. The evolution of the vertical strain and the saturation front proceeded parallel to each other, as is evident on the left-hand side of Figure 2.13. A direct coupling between saturation and expansion during infiltration existed.

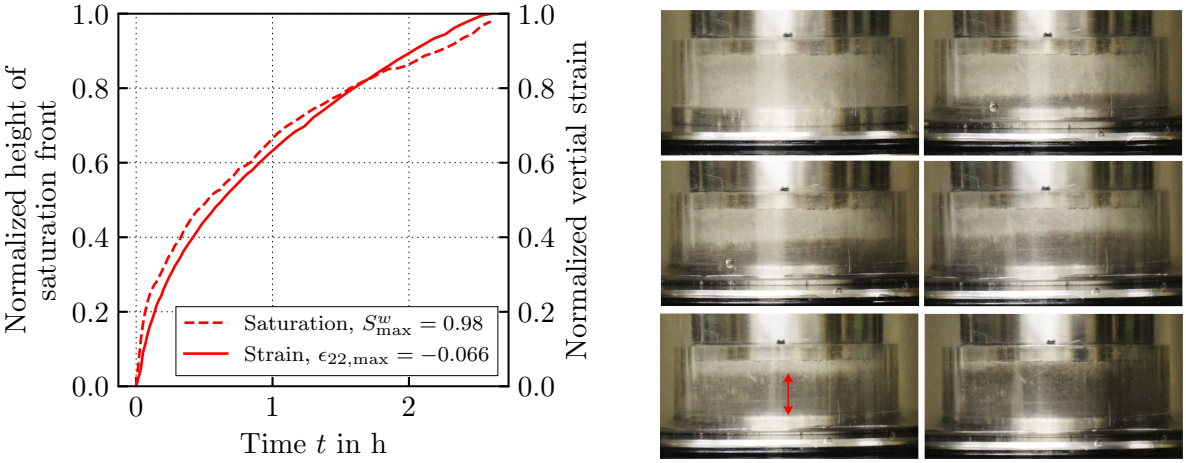

Figure 2.13.: Vertically unconfined swelling of reconstituted Opalinus clay in a perspex oedometer ring. Evolution of normalized strain and height of saturation front vs. time (left) and view of sample during the test (right).

2.4.2.1. Influence of vertical net stress and compaction pressure

The magnitude of vertical deformation due to wetting measured under oedometric conditions depends on the acting vertical net stress and the compaction pressure. If the vertical load corresponds to the preloading load, no deformation occurs, as the load and swelling are in equilibrium. For larger loads, wetting at constant stress results in a further compaction (rather than expansion) of the material, often referred to as „collapse“. The term collapse may be misleading, as the material does not deform suddenly, but gradually with increasing water content, similar to swelling expansion. Amongst others, Villar and Lloret (2008) studied the influence of the vertical net stress level upon wetting and of the compaction pressure (dry density) on the magnitude of vertically unconfined swelling. A very comprehensive experimental campaign on highly expansive Febex bentonite including several initial conditions and vertical net stress levels was conducted. The results of relevant tests are shown in terms of final vertical strain and final void ratio vs. vertical net stress during saturation in Figure 2.14. Samples were prepared by compaction to three different initial dry densities $\rho_d = \{1.5, 1.6, 1.7\}$ g/cm^3, corresponding to initial void ratios of $e_0 = \{0.800, 0.688, 0.588\}$. Vertical net stresses of $\sigma_{22,d} = \{12, 18.5, 33.5\}$ MPa were required for compaction. Before wetting, constant vertical net stresses of 0.1, 0.5, 1.0, and 3.0 MPa respectively, were applied.

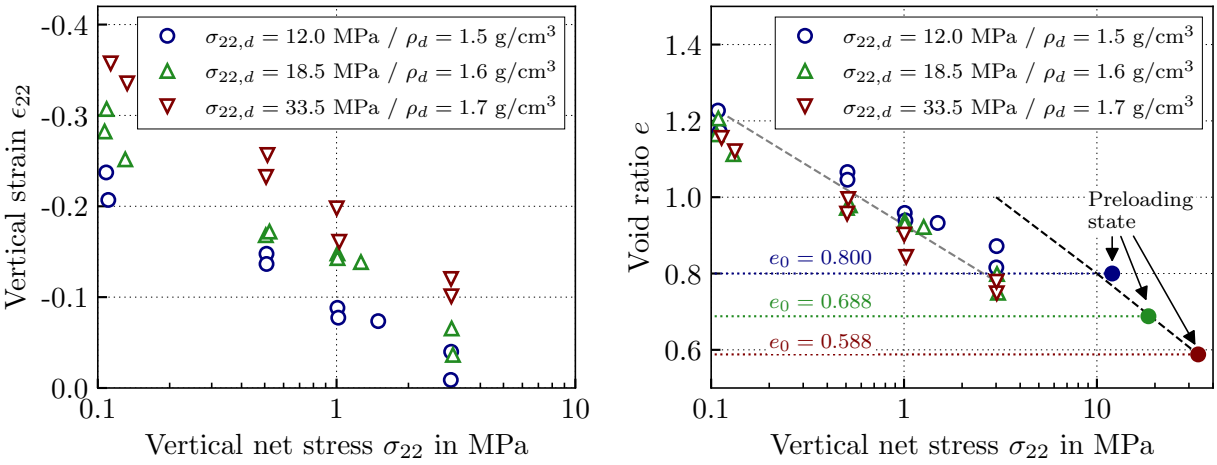

Figure 2.14.: Vertically unconfined swelling in three test series on Febex bentonite compacted with different net stress: Vertical strain vs. vertical net stress (left) and void ratio vs. vertical net stress (right) (Villar and Lloret, 2008).

As can be observed in Figure 2.14, vertical strain (in extension) and the increase in void ratio increased with decreasing constant vertical net stress upon wetting. This trend is linear in the semi-logarithmic stress space. Therein, the magnitude of vertical strain was the largest for the highest vertical preloading net stress. The relation between the magnitude of expansion and the vertical preloading net stress is often described as a dependency of expansion on the initial dry density of the expansive soil. Denser samples experience larger expansion, which is attributed to the higher total amount of swellable clay minerals, see e.g. Sridharan and Gurtug (2004) or Middelhoff et al. (2021). However, in constitutive modelling the dry density is not an adequate controlling variable for describing the hydro-mechanical behaviour of materials in terms of stress and strain. It merely reflects the outcome of a particular compaction process. The corresponding compaction pressure, i.e. the preloading stress, provides a meaningful variable for the material state, that can be consistently incorporated into hydro-mechanical frameworks, cf.

Alonso et al. (1990). The right-hand side of Figure 2.14 highlights that regardless of the initial void ratio (horizontal dotted lines), the final void ratios of the three test series converged within a certain bandwidth. The preloading stresses corresponding to the initial void ratios are shown as coloured markers connected by a theoretical virgin loading line (dashed). An affinity between the bandwidth of final, saturated void ratios, indicated by a grey dashed line on the right-hand side of Figure 2.14, and the virgin loading line becomes apparent.

2.4.2.2. Swelling anisotropy

Test set-ups exist that allow unconstrained deformation in all directions in space and some efforts have been made to measure deformation of compacted expansive soil samples in all directions in space to assess the three-dimensional distribution of the volumetric phenomenon of expansion upon wetting. However, experimental evidence is very limited. Gatabin et al. (2016) investigated free swelling in all directions in space for compacted samples of an MX80 bentonite-sand mixture. The samples were compacted vertically in an oedometric ring and afterwards exposed to various suction by VET without any constraints (no stress acting on the sample). The vertical and radial deformations were measured with a caliper assuming a cylindrical geometry at all times. The results are shown on the left-hand side of Figure 2.15 in terms of vertical and radial strain versus suction. An approximately constant ratio between radial strain and vertical strain $\epsilon_{11}/\epsilon_{22} \approx 50\%$ could be determined over the whole range of suction. Similar tests were conducted by Tang et al. (2008), however on isotropically compacted monolithic MX80 bentonite samples. Compaction took place in a closed neoprene tube under static pressure inside an isochoric cell. Afterwards the samples were subjected to wetting by VET. The results are shown in terms of vertical and radial strain versus suction on the right-hand side of Figure 2.15. No significant difference between the strains in different directions existed due to the isotropic compaction.

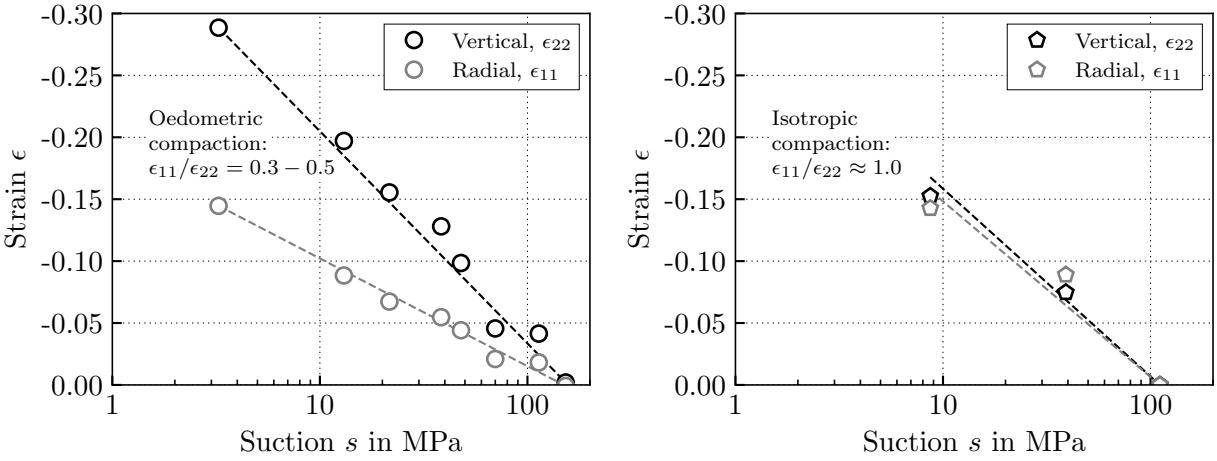

Figure 2.15.: Vertical and radial strain vs. suction for an MX80 bentonite-sand mixture compacted under oedometric conditions modified from Gatabin et al. (2016) (left) and for pure MX80 bentonite compacted under isotropic conditions modified from Tang et al. (2008) (right).

Estabragh et al. (2015) performed cyclic drying-wetting swelling tests on vertically compacted samples of a bentonite-kaolin mixture and measured vertical and radial deformation. After each wetting or drying step, one of the samples was used for volume determination, while the cycles continued on the other samples. However, the radial deformation was only measured starting from the first drying cycle, as initial wetting took place under oedometric conditions. After

several cycles, both the vertical and radial deformation reached equilibrium, with a ratio of $\epsilon_{11}/\epsilon_{22} \approx 30 - 55\%$ depending on the vertical net stress during the tests (between 1 and 10 kPa).

These studies emphasize that a quantification of the volumetric swelling phenomenon across directions in space is difficult, as deformation depends on both, the boundary conditions during compaction and during wetting. However, a compaction-induced anisotropy was clearly evident for wetting-induced deformation of expansive soils and also affects the results of swelling tests under oedometric conditions.

2.4.3. Wetting at constant volume: Swelling pressure

For confined boundary conditions, where deformation is not allowed, the swelling phenomenon upon wetting manifests itself in the build-up of swelling pressure. Under oedometric conditions, a vertically confined boundary condition at the top of the sample corresponds to constant volume conditions. Net stress changes in vertical direction are measured via a load cell at the top of the sample. The tests can also be carried out in an oedometer device in which the top cap is fixed or manually/automatically readjusted to assure constant volume, see e.g. Pimentel (2015) for a discussion on suitable devices. Due to the simple test setup and the precise boundary condition, the measurement of swelling pressure, i.e. of vertical net swelling stress, is much more widespread than that of swelling strain. Analogously to expansion, the development of swelling pressure is a time-dependent process, however, steady-state conditions are attained faster and the shape of the stress-time curve in the semi-logarithmic space has a different form. Figure 2.16 shows the evolution of the swelling pressure in constant volume swelling tests on reconstituted Opalinus clay in the range of initial void ratios $e_0 = 0.351 - 0.576$. In the first phase of the tests, the evolution of net swelling stress showed a pronounced increase, similar to the one of swelling strain shown in Figure 2.12. In the second phase, however, the stress decreased before reaching an equilibrium value. Tests with $e_0 \approx 0.387$ serve as reference, as this initial void ratio was also used in permeability tests (see Table 2.1 and Figure 2.7) and oedometric compression tests (see Figure 2.10) for constant volume conditions.

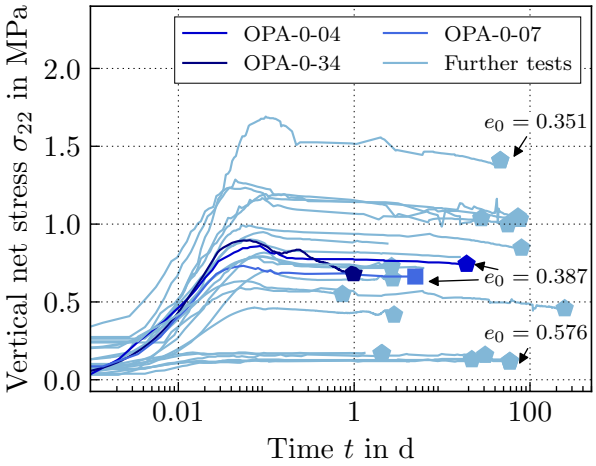

Figure 2.16.: Evolution of vertical swelling pressure for reconstituted Opalinus clay (Nitsch et al., 2023a). The initial void ratios are in the range $e_0 = 0.351 - 0.576$.

The results of a constant volume swelling test in a perspex oedometric ring with wetting from the bottom give further insights into the evolution of swelling pressure. They are presented in Figure 2.17 in a similar manner as for vertically unconfined swelling in Figure 2.13. The test was stopped when the peak in the vertical swelling pressure was reached at $\sigma_{22} = 0.862$ MPa, shortly before the saturation front had fully propagated through the entire specimen and the final degree of saturation was determined to $S^w = 0.94$. Although steady state of the swelling process had not yet been reached, a faster development of swelling pressure than of swelling strain during infiltration is evident. Moreover, it precedes the progression of the saturation front. This indicates that the response of the unsaturated swelling clay to the deformation constraint manifested itself as a more rapid onset of the measurable mechanical swelling phenomenon.

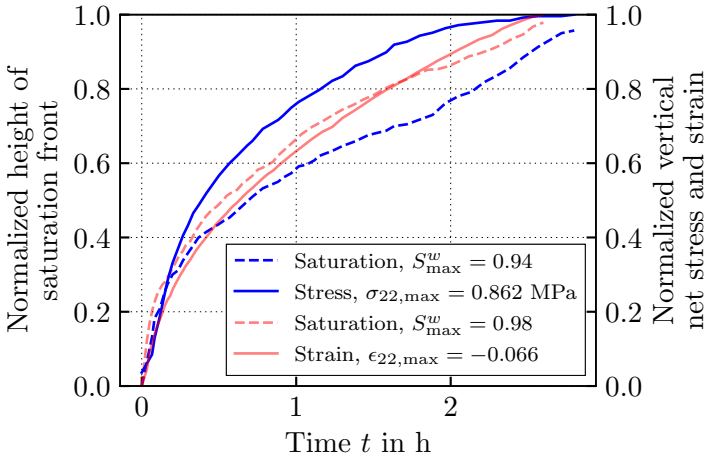

Figure 2.17.: Constant volume swelling of reconstituted Opalinus clay in a perspex oedometer ring. Evolution of normalized stress and height of saturation front vs. time. For comparison, results from Figure 2.13 are shown as well.

2.4.3.1. Influence of compaction pressure

Figure 2.16 shows an increase in vertical swelling pressure with decreasing initial void ratio, hence higher preloading stress. Similar to swelling strain, swelling pressure depends on the initial state and the dependency is often described using the initial dry density of the expansive soil. Numerous studies on swelling pressure at different dry densities or void ratios have been carried out, cf. Mollins et al. (1996), Komine and Ogata (1999), Sridharan and Gurtug (2004), Villar and Lloret (2008), Schanz and Tripathy (2009), Baille et al. (2010), Zou et al. (2020), Jadda and Bag (2020), Middelhoff et al. (2021) and Christ (2025) amongst many others. The compaction pressure or virgin loading line is, however, seldomly reported. The left-hand side of Figure 2.18 shows the equilibrium values of swelling pressure for reconstituted Opalinus clay from Figure 2.16 at the corresponding void ratios in comparison to the virgin loading line measured upon compaction of the samples. An affinity between the virgin loading line and the trend line for the final swelling pressure becomes evident. On the right-hand side of Figure 2.18 the vertical preloading net stress $\sigma_{22,d}$ and equilibrium swelling pressures are presented for three different bentonites (Baille et al., 2010; Jadda and Bag, 2020; Villar and Lloret, 2008). The affinity between preloading and final saturated state after constant volume swelling is evident based on the shown bandwidths.

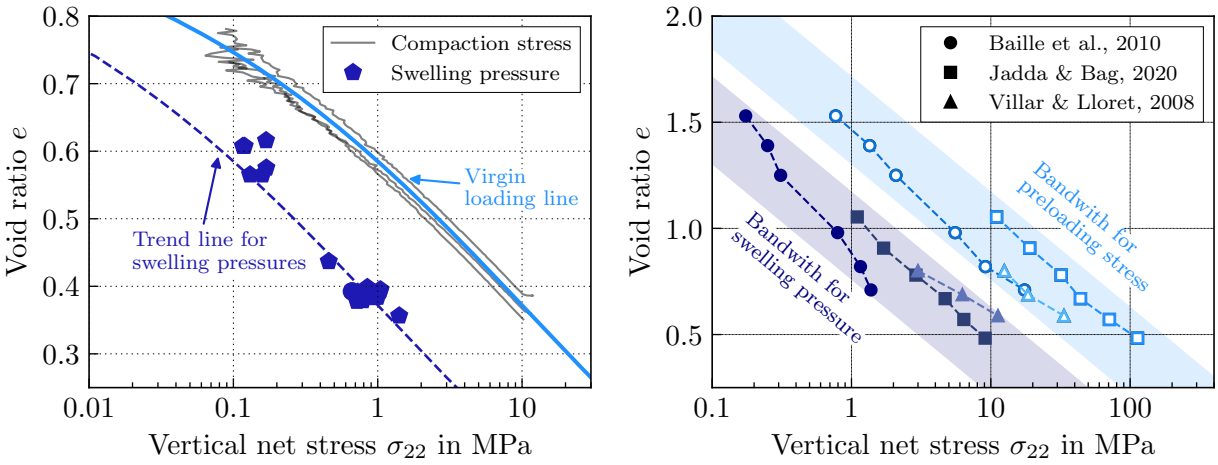

Figure 2.18.: Affinity of preloading stress and swelling pressure for reconstituted Opalinus clay (left, Nitsch et al. (2023a)) and different bentonites (right, Baille et al. (2010); Jadda and Bag (2020); Villar and Lloret (2008)).

2.4.3.2. Anisotropy of net stress upon swelling

Similar to swelling strain, net stress develops not only in the vertical but also in the radial direction during swelling. As swelling pressure is commonly understood as the reaction force of the expansive material against confined expansion, the compaction-induced anisotropy of swelling strain (see Section 2.4.2.2) presumably results in different magnitudes of vertical and radial net stress. The determination of radial net stress during swelling is, however, less straightforward than that of vertical net stress. First, the initial radial net stress prior to wetting is already non-zero (see Section 2.4.1.2), and radial swelling does not necessarily translate into a build-up of additional radial net stress. Second, averaging radial net stress along the sample height during vertical infiltration, analogous to the procedure for vertical net stress, is not meaningful due to the heterogeneous infiltration profile, but may be applicable once steady state is reached. The determination of radial net swelling stress under constant volume conditions can be carried out in soft-oedometer devices or in test set-ups with radial load cells embedded in the oedometer ring. Depending on the measurement method, the radial net stress refers to the whole sample height or to a distinct measurement height.

Experimental evidence is still rare on unsaturated swelling clays. Saba et al. (2014) performed constant volume swelling tests in a test set-up with a radial load cell on an MX80-sand mixture. Therein, vertical and radial net stresses were measured during wetting of samples with different dry densities ranging from 1.22 g/cm^3 to 1.45 g/cm^3. Synthetic groundwater was used, which may have affected the magnitude of swelling due to its different composition compared to deionised water, but it is not expected to have influenced the stress ratio. Most samples were prepared outside of the test set-up, while some were compacted directly inside the test set-up to evaluate the effect of post-compaction residual radial net stress, see Section 2.4.1.2. Test results revealed ratios between radial and vertical swelling stresses in the range of $\sigma_{11}/\sigma_{22} = 0.7 - 1.0$, whereby higher densities, obtained by compaction with larger vertical net stress, led to more isotropic swelling stresses. An influence of the residual radial net stress after compaction on the final swelling stresses, i.e. on the superposition of initial stress and stress build-up during wetting, was not identified. This indicates that the post-compaction residual radial stress was retained inside the samples that were compacted directly inside the test set-up. This residual stress was

then superimposed by the swelling-induced stress increase, which was smaller in absolute value than the stress increase observed in the samples prepared outside the test set-up. Contrary results are reported, however, by Cho et al. (2000) and Lee et al. (2012), who investigated a monolithic Korean bentonite in a similar test set-up and found a slight increase of anisotropy with increasing compaction stress with overall ratios in the range $\sigma_{11}/\sigma_{22} = 0.8 - 0.95$.

A different approach to evaluate compaction-induced anisotropy was followed by Christ (2025). A large block of reconstituted Opalinus clay was compacted and two samples were drilled out afterwards, one in compaction direction (parallel) and one perpendicular to it. The samples were tested in a conventional constant volume cell and vertical net swelling stress was measured. The evolution of net swelling stress is shown in Figure 2.19 for both tests. Note that the *parallel* labelled test corresponds to a standard constant volume swelling test and can thus be considered as exhibiting vertical net swelling stress, where as the *perpendicular* labelled test exhibits radial net swelling stress. A very similar time evolution becomes evident, though different in magnitude. The ratio of the final net swelling stress was $\sigma_\perp/\sigma_\parallel \mathrel{\widehat{=}} \sigma_{11}/\sigma_{22} \approx 0.61$.

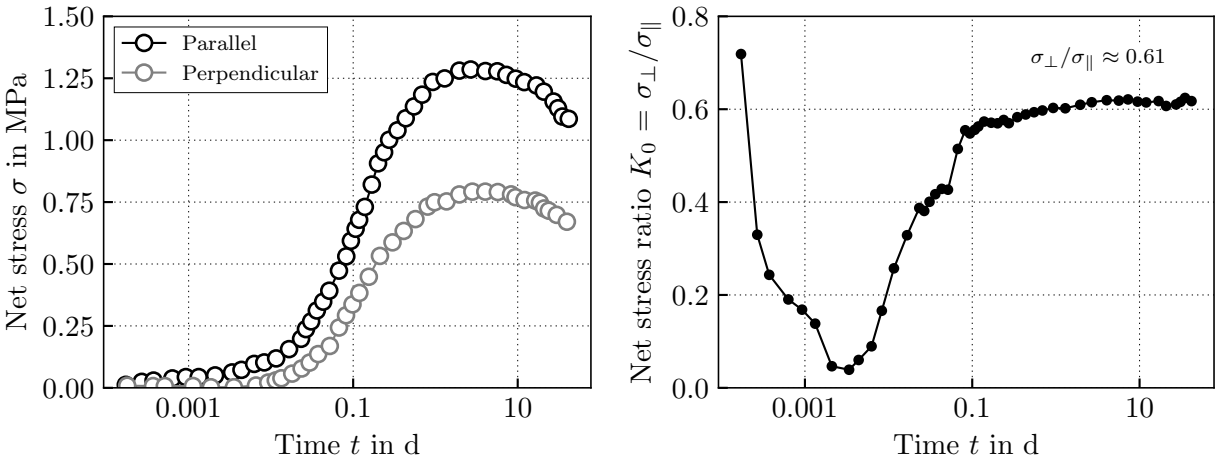

Figure 2.19.: Constant volume swelling tests on reconstituted Opalinus clay using samples wetted perpendicular and parallel to the compaction direction: evolution of net stress (left) and stress ratio (right). Modified from Christ (2025).

The results on anisotropy upon constant volume swelling are more ambiguous than for deformation (Section 2.4.2.2). As swelling pressure is a response of the deformation to the boundary condition, effects can overlap or even compensate each other. Overall, a compaction-induced anisotropy existed for wetting-induced swelling pressure of expansive soils.

2.4.4. Shear strength at constant water content

The shear strength characterises the behaviour of a material at or near failure and is essential for a comprehensive formulation of the mechanical behaviour. While shear strength is commonly formulated in terms of effective stresses for saturated soils, net stresses are adopted here as stress variables for unsaturated conditions. With this assumption, the shear strength envelope (Terzaghi, 1936) is expressed using the shear stress τ and normal net stress σ_n:

$$\tau = c + \sigma_n \tan(\varphi). \tag{2.36}$$

Therein, φ is the angle of internal friction, and c is the cohesion, i.e. the shear stress at zero normal net stress. For unsaturated conditions, a reduction in shear strength with increasing saturation or decreasing suction has been reported (Escario and Sáez, 1986; Fredlund et al., 1978; Gan et al., 2011). Several adaptations of Equation (2.36) have been proposed to capture this effect, most commonly by introducing a suction-dependent term (Bishop and Blight, 1963; Fredlund et al., 1978). Within such formulations, the friction angle is usually treated as unique and independent of saturation, based on the assumption that the structure of the solid phase remains unaffected by changes in suction. This assumption, however, does not hold for unsaturated swelling clays (Romero et al., 2014). The influence of saturation on the shear strength of expansive soils can be assessed through suction-controlled triaxial or direct shear tests. Where advanced laboratory equipment is unavailable, it may be approximated by comparing the behaviour of nearly dry and fully saturated specimens in simple shear tests.

Figure 2.20 shows the results of simple shear tests on reconstituted Opalinus clay in the nearly dry and saturated state in terms of failure envelopes and angle of internal friction in the residual state versus effective degree of saturation. The material was first consolidated and then sheared, either at the consolidation stress (normally consolidated, NC) or at a lower stress level (overconsolidated, OC). The saturated samples were wetted prior to shearing. The experimental procedure is described in detail in Appendix A.2. The results in Figure 2.20 show linear shear strength envelopes in the τ–σ_n space. In the nearly dry reference state, no cohesion component was evident and the internal friction angle was $\varphi_{\text{ref}} \approx 37°$. The latter was averaged between the normally and overconsolidated samples as only small differences were evident. In the saturated state, the linear shear strength envelope exhibited a significantly reduced slope, corresponding to a reduced friction angle φ_w. The results, however, did not clearly indicate whether cohesion was absent or present. Accordingly, two possible shear strength envelopes were established, corresponding either to $c = 0$ kPa with $\varphi_w = 21.1°$ or to $c = 25$ kPa with $\varphi_w = 20.1°$.

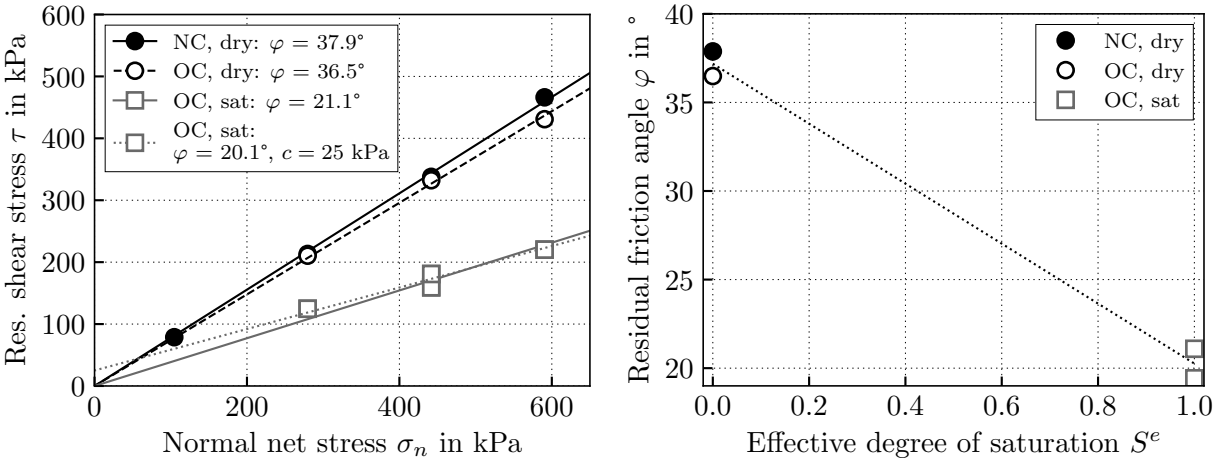

Figure 2.20.: Residual shear strength vs. normal stress (left) and evaluated residual friction angle vs. effective degree of saturation (right) for three test series on Opalinus clay.

Experimental evidence on the influence of suction or saturation on the shear strength properties of expansive soils in the literature is limited. One comprehensive experimental campaign reported in Merchán et al. (2008), Merchan et al. (2011) and Romero et al. (2014) investigated the shear strength of soils with different contents of expansive clay minerals and plasticity indices: Barcelona (clayey) silt, Boom clay and Febex bentonite. They performed ring shear tests on reconstituted specimens prepared at different water contents. After specimen preparation,

the material was first consolidated, then equilibrated at a specified suction (with VET) and finally sheared in a multi-step test under different net normal stresses. Similar to the results on reconstituted Opalinus clay, linear shear strength envelopes with increasing residual friction angle for increasing suction were reported for all materials. In all cases the cohesion was zero and thus the increase of shear strength due to increasing suction could be directly attributed to changes in the friction angle. However, there was no further increase when reaching the suction corresponding to the residual water content or degree of saturation of the material. The systematic increase in the residual friction angle with increasing suction was attributed to the aggregate structure of unsaturated swelling clays. In the saturated state, Merchán et al. (2008) identified large soft aggregates, where in-between water acts like a lubricating film. Upon increasing suction, the aggregates desaturated and shrank, resulting in both, a more granular and brittle behaviour. It was also shown that the initial water content and the direction of the hydraulic loading path (drying or wetting) had no influence on the shear strength in the unsaturated state. The results of the experimental campaign of Romero et al. (2014) and Merchán et al. (2008) are presented in Figure 2.21 in terms of the residual friction angle versus suction and effective degree of saturation together with the data of reconstituted Opalinus clay (without consideration of cohesion in the saturated state). For evaluation of the effective degree of saturation, the SWRCs were used. For Boom clay, the SWRC is reported by Romero et al. (2014) and Romero et al. (2011), for Barcelona silt by Barrera (2002) and for Febex bentonite by Lloret et al. (2003).

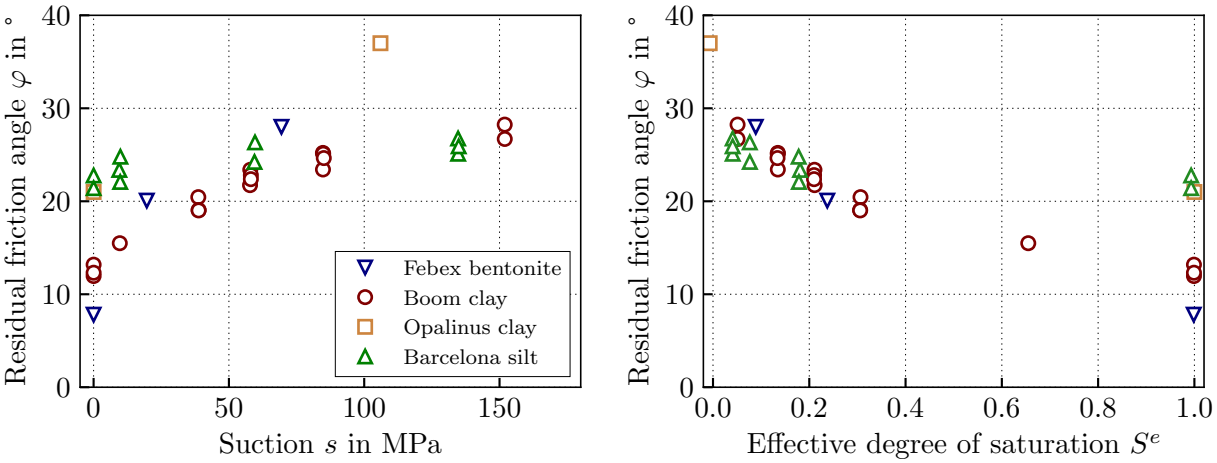

Figure 2.21.: Residual friction angle of Febex bentonite, Boom clay, Opalinus clay and Barcelona silt vs. suction (left) and effective degree of saturation (right). Data from Merchán et al. (2008), Merchan et al. (2011) and Romero et al. (2014).

The results show a very pronounced difference between the saturated and nearly dry reference friction angle φ_{ref} for the highly expansive Febex bentonite ($\varphi_w = 7.8°, \varphi_{\text{ref}} = 28.0°$ with $S^{wr} = 0.316$), a moderate dependency for the moderately expansive Boom Clay ($\varphi_w = 12.0°, \varphi_{\text{ref}} = 28.3°$ with $S^{wr} = 0.042$) and Opalinus clay ($S^{wr} = 0.126$) and only a very little difference for the weakly expansive clayey silt ($\varphi_w = 21.1°, \varphi_{\text{ref}} = 26.8°$ with $S^{wr} = 0.170$). The extremely small friction angle of saturated, highly plastic and expansive clays was also reported for MX80 bentonite as $\varphi_w = 11°$ (Bosch et al., 2021; Dieudonne, 2016) and for Volclay bentonite as $\varphi_w = 7-9°$ (Domitrovic, 2013). Romero et al. (2014) showed furthermore, that an increase in plasticity of the fine-grained soil led to a more pronounced increase in friction angle with decreasing suction. The plasticity is a consequence of the mineralogical composition of the soils: higher contents of expansive clay minerals yield higher plasticity indices and thus a stronger dependency of the

friction angle on saturation or suction. For expansive soils, the shear strength envelope from Equation (2.36) can be expressed without cohesion and with a saturation-dependent friction angle as:

$$\tau = \sigma_n \tan(\varphi\,(S^e)). \tag{2.37}$$

2.5. Modelling of the hydro-mechanical behaviour of expansive soils

This section presents existing modelling approaches for the prediction of the stress-strain behaviour of expansive soils. Depending on the application, approaches at several levels of sophistication exist. Therefore, a brief overview of primarily empirical models used in the scope of tunnelling in swelling rock and very simple saturation-linked approaches is first given. Subsequently more sophisticated models from unsaturated soil mechanics are presented.

2.5.1. Swelling rock models

Empirical approaches describing the stress-strain behaviour were first introduced in tunnelling research on clay rocks, its most prominent representative being the one-dimensional swelling model by Grob (1972). It focused on the estimation of the expected deformation during unloading processes upon tunnel excavation in the fully saturated state and was based on experiments under oedometric conditions following the methods by Huder and Amberg (1970), ISRM (1979) or Vergara Quezada (2019). Lateral stress was deliberately neglected due to insufficient information on the stress state, and the deformation of the tunnel's middle axis was treated as an uniaxial process, thereby transferring the oedometric conditions to the tunnel. The model reads:

$$\epsilon_{22} = -C_s \log\left(\frac{\sigma_{22}}{\sigma_{22,\max}}\right), \tag{2.38}$$

wherein ϵ_{22} is the vertical strain, σ_{22} is the current, vertical total stress, $\sigma_{22,\max}$ is the maximal vertical swelling pressure and C_s is a parameter describing the slope of a semi-logarithmic relationship between σ_{22} and ϵ_{22}. Equation (2.38) does not consider any time effects. Time-dependency was added by Kiehl (1990) with a time parameter η, which exponentially slows down the strain evolution depending on the time t. It is calibrated by fitting the time evolution of the strain to laboratory results. Deformation is not a consequence of flow and independent of the saturation process. The extension of Equation (2.38) results in:

$$\epsilon_{22}(t) = -C_s \log\left(\frac{\sigma_{22}}{\sigma_{22,\max}}\right)\left(1 - \exp\left(\frac{-t}{\eta}\right)\right). \tag{2.39}$$

2.5.1.1. Plaxis, Sofistik and Talpa

Grob's swelling law was generalized for the full stress state, extended and implemented in several FE software packages, including Plaxis, Sofistik and Talpa to investigate problems related to tunnelling and swelling rocks (Wittke-Gattermann and Wittke, 2004; Heidkamp and Katz, 2004; Anagnostou, 1992). These approaches considered a separate, additional strain component for swelling in elasto-(visco-)plastic frameworks where the total strain was decomposed in an elastic, plastic and swelling component. The latter was described similarly to Equation (2.38). For

the design of tunnel structures, application of the models yielded acceptable results regarding swelling uplifts and stress changes (Heidkamp and Katz, 2002; Wittke-Gattermann and Wittke, 2004) as they aimed to add a swelling component to the rock-mechanical behaviour. However, they are not suitable for representing the swelling process as a physical reaction to the flow of water and to describe the general, hydro-mechanically coupled behaviour of expansive soils.

2.5.1.2. Moisture Swelling in Abaqus

Th Moisture Swelling Model of Abaqus is a simple way to incorporate a saturation-dependent swelling strain independently of the applied constitutive model for the mechanical behaviour. The volumetric swelling strain $\epsilon^{sw,v}$ of the porous medium's solid skeleton is computed as a function of the degree of saturation of the wetting liquid. It is decoupled from the volumetric strain ϵ^{v}. The relationship between volumetric swelling strain and degree of saturation is specified by the user in tabular form as pairs of values. The swelling strain $\epsilon^{sw,v} = \epsilon^{sw,v}(S^w) - \epsilon^{sw,v}(S_i^w)$ is computed as the difference between the current volumetric swelling strain $\epsilon^{sw,v}(S^w)$ and an initial value $\epsilon^{sw,v}(S_i^w)$ with corresponding degrees of satuaration S^w and S_i^w. Anisotropy can be considered by defining a ratio between the directions in space. Since the swelling strain of the Moisture Swelling Model is decoupled from the mechanical behaviour, a computation of swelling pressure is not possible. Further, the secondary swelling phenomena, hence dependency of material properties on swelling, are not accounted for. For different initial conditions (e.g. void ratio, stress state), different tabular functions have to be defined.

2.5.1.3. Rockflow, OpenGeoSys and Tough-Flac

A similar approach as in Abaqus was implemented in the research software RockFlow. The swelling strain tensor $\boldsymbol{\epsilon}^{sw}$ is linearly depending on the degree of saturation. A linear (slope) parameter β^{sw} has to be defined, which determines the increment of the swelling strain tensor $\mathrm{d}\boldsymbol{\epsilon}^{sw}$ for an increment in the degree of saturation $\mathrm{d}S^w$:

$$\mathrm{d}\boldsymbol{\epsilon}^{sw} = \mathbf{1}\beta^{sw}\mathrm{d}S^w. \tag{2.40}$$

Contrary to Abaqus, the main evolution equation for the effective stress tensor $\boldsymbol{\sigma'}$ considers a decomposition of the total strain tensor in an elastic strain tensor and swelling strain tensor, $\boldsymbol{\epsilon}^{el} = \boldsymbol{\epsilon} - \boldsymbol{\epsilon}^{sw}$, which also allows the computation of a swelling pressure tensor $\boldsymbol{\sigma'}^{,sw}$ as an effective stress for constrained conditions:

$$\boldsymbol{\sigma'} = \mathsf{C} : \boldsymbol{\epsilon}^{el} \quad \text{and} \quad \boldsymbol{\sigma'}^{,sw} = -\left(\mathsf{C} : \boldsymbol{\epsilon}^{sw}\right), \tag{2.41}$$

wherein $\boldsymbol{\epsilon}^{el}$ is the elastic strain tensor and C is the fourth-order elastic stiffness tensor. However, the overall formulation is not fully hydro-mechanically coupled and considers elastic behaviour only. More details regarding the approach in RockFlow can be found in the works of Ziefle (2008) and Maßmann (2008). In OpenGeoSys (Bilke et al., 2025) and Tough-Flac (Rutqvist et al., 2011), a similar linear saturation-dependent approach is implemented as well, however, for the increment of the swelling pressure $\mathrm{d}\boldsymbol{\sigma'}^{,sw}$ as an effective stress:

$$\mathrm{d}\boldsymbol{\sigma'}^{,sw} = \mathbf{1}\alpha^{sw}\mathrm{d}S^w, \tag{2.42}$$

wherein α^{sw} is a material parameter controlling the slope of the linear increase of swelling pressure with the degree of saturation. Assuming linear elasticity, the swelling strain can be computed analogously to Equation (2.41).

2.5.2. Sophisticated constitutive models for unsaturated soils

Emerging from the research related to nuclear waste disposal, sophisticated constitutive models for unsaturated and expansive soils were introduced, led by the Barcelona Basic Model (BBM) of Alonso et al. (1990). The BBM can simulate the most prominent features of unsaturated soils, such as the apparent increase in preconsolidation net stress due to partial saturation, as well as wetting-induced expansion or soil collapse to some extent. The material behaviour of expansive soils could not be comprehensively captured by the BBM as it was not the objective of the original formulation. For specific loading paths, however, the formulation of the BBM was reinterpreted and extended to allow the prediction of expansive soil behaviour (Dieudonne, 2016). To incorporate expansive soil behaviour, extensions based on the assumption of a double-porosity structure of the swelling material were proposed, as first in the Barcelona Expansive Model (BExM) (Gens and Alonso, 1992; Alonso et al., 1999). Numerous successor models were proposed in the following years; important contributions can be found in Cui and Delage (1996), Sheng et al. (2008), Blatz and Graham (2003), Chiu and Ng (2003) or Georgiadis et al. (2005). Comprehensive overviews of succeeding models are provided by Gens et al. (2006) or Sheng et al. (2008).

The BBM and its successors are formulated as elasto-plastic frameworks. Elasto-plasticity has been originally adopted in soil mechanics evolving from research on continuous materials even though soils do not have a well-defined yield point but rather exhibit a gradual transition from reversible to irreversible deformation. To better represent the non-linear soil behaviour, Sánchez et al. (2005) and Yang et al. (2008) amongst others exchanged the MCC formulation of the BBM with generalized plasticity and bounding surface plasticity, respectively. Another approach to represent soil non-linearity more adequately is offered by the concept of hypoplasticity (Kolymbas, 1977, 1991; Gudehus, 1996; von Wolffersdorff, 1996; Niemunis, 2003; Herle and Kolymbas, 2004). Hypoplasticity describes a continuous deformation process without distinguishing between elastic and plastic strains and the need of a sharp yield point or yield surface. Instead, hypoplastic models are formulated in rate form and the transition from reversible to irreversible behaviour emerges naturally from the continuous constitutive equation and the material's current state relative to its preloading state. A hypoplastic model for non-swelling unsaturated soils including suction was introduced by Mašín and Khalili (2008) and extended with a double-porosity approach for expansive soils in Mašín (2013). Another hypoplastic model for unsaturated soils was proposed by Fuentes and Triantafyllidis (2013) and extended by Tafili and Machaček (2023). A hypoplastic model for expansive soils not relying on double-porosity has not yet been proposed.

2.5.2.1. Barcelona Basic Model

Owing to its conceptual simplicity compared to double-porosity-based extensions and the associated complexity of parameter calibration, the BBM (Alonso et al., 1990) remains the de facto standard for modelling of expansive soils. It is formulated in terms of net stress and suction and can be categorized as an elasto-plastic strain hardening model. In general, the increment of total volumetric strain $\mathrm{d}\epsilon_v$ is the sum of the elastic volumetric strain increment $\mathrm{d}\epsilon_v^e$ and the plastic

volumetric strain increment $\mathrm{d}\epsilon_v^p$. The elastic part consists of two summands, one depending on the mean net stress $p = \mathrm{tr}\,(\boldsymbol{\sigma})$ and one on the suction s. For isotropic conditions it reads as:

$$\mathrm{d}\epsilon_v^e = \frac{\mathrm{d}e}{1+e} = \frac{\kappa}{1+e}\frac{\mathrm{d}p}{p} + \frac{\kappa_s}{1+e}\frac{\mathrm{d}s}{s+p_{\mathrm{atm}}}, \tag{2.43}$$

wherein e is the void ratio, κ and κ_s are the elastic indices for changes in net stress and suction, respectively, and p_{atm} is the atmospheric pressure (usually assumed as 10 kPa). In the original formulation, κ and κ_s were assumed constant, however, more recent formulations consider both as a function of suction (Delahaye and Alonso, 2002; Vaunat and Gens, 2005). κ decreases with increasing suction according to:

$$\kappa(s) = \kappa_0 \left[1 - \alpha_1 s - \alpha_2 \ln\left(\frac{s+p_{\mathrm{atm}}}{p_{\mathrm{atm}}}\right)\right], \tag{2.44}$$

wherein κ_0 is the elastic index in the saturated state and α_1 and α_2 are model parameters. For κ_s the extensions reads:

$$\kappa_s(p,s) = \kappa_{s0}\left[1 + \alpha_p \ln\left(\frac{p}{p_{\mathrm{ref}}}\right)\right]\exp(\alpha_s, s), \tag{2.45}$$

wherein the reference net stress p_{ref} and α_p and α_s are material parameters in addition to the index κ_{s0} in the saturated state. The compression index λ was introduced as dependent on the suction already in the original formulation, decreasing with increasing suction from its value λ_0 in the saturated state:

$$\lambda(s) = \lambda_0\left[(1-r)\exp(-\omega s) + r\right]. \tag{2.46}$$

Therein r and ω are model parameters controlling the compression index for large suctions and the rate of decrease. The suction further influences the preconsolidation net stress p_0, as the elastic domain increases with increasing suction:

$$p_0(s) = p_c\left(\frac{p_0^*}{p_c}\right)^{\frac{\lambda_0-\kappa}{\lambda(s)-\kappa}}, \tag{2.47}$$

wherein p_c is a reference net stress and p_0^* the preconsolidation net stress in the saturated state. Equation (2.47) is referred to as the *Loading-Collapse*-curve (LC) and is one of two yield curves of the BBM. For a net stress exceeding the preconsolidation net stress p_0, hence the yield limit, a plastic strain increment $\mathrm{d}\epsilon_{vp}^p$ for net stress is generated by the first hardening law:

$$\mathrm{d}\epsilon_{vp}^p = \frac{\lambda_0-\kappa}{1+e}\frac{\mathrm{d}p_0}{p_0}, \tag{2.48}$$

Analogously, a yield curve exists for the domain of suction. A volumetric plastic strain increment $d\epsilon_{vs}^p$ is produced for suctions exceeding a threshold suction s_0 by the second hardening law as:

$$\mathrm{d}\epsilon_{vs}^p = \frac{\lambda_s-\kappa_s}{1+e}\frac{\mathrm{d}s_0}{s_0+p_{\mathrm{atm}}}. \tag{2.49}$$

The yield curve, referred to as the *Suction-Increase*-curve (SI), is defined at a constant suction. It has limited relevance, when wetting paths are studied. The yield curves are displayed on the right-hand side of Figure 2.22 and the compression curves for the fully saturated and an arbitrary unsaturated state are shown on the left-hand side of Figure 2.22.

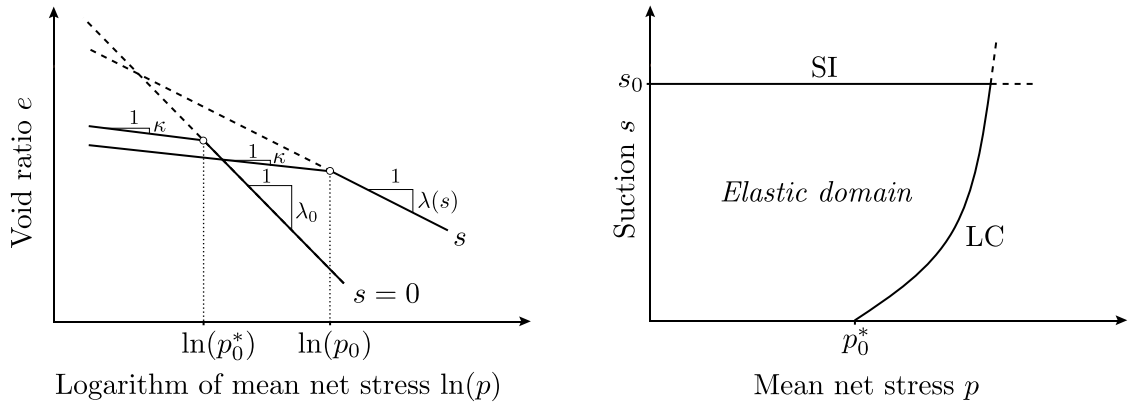

Figure 2.22.: Barcelona Basic Model: Compression curves for saturated and unsaturated states in the $e-\ln(p)$ space (left) and yield curves in the $s-p$ space (right).

In the three-dimensional version, the model is extended by the deviatoric stress $q = \sigma_{22} - \sigma_{11}$, wherein σ_{22} and σ_{11} denote the major and minor principal stresses, respectively. The elliptic yield surface f of the MCC is adopted:

$$f \equiv q^2 - M^2(p + p_s)(p_0 - p) = 0, \tag{2.50}$$

wherein p_s is responsible for the increase of shear strength with increasing suction. For a certain suction s, the yield surface is limited by $p_0(s)$ on the LC-curve (see Figure 2.22). The yield surfaces in $q-p$ space and $q-p-s$ space are shown in Figure 2.23. The critical state line (CSL) is parallel for different suctions with slope $M = (6\sin(\varphi))/(3 - \sin(\varphi))$, as the angle of internal friction φ is assumed constant. The increase in shear strength with suction is therefore incorporated by an increase of apparent cohesion c, realized by a shift p_s of the elliptic yield surface into tension with parameter k and starting from the cohesion at saturated conditions $c(0)$:

$$p_s(s) = \frac{c(0) + k\,s}{\tan(\varphi)}. \tag{2.51}$$

Note that this approach contradicts the findings on shear strength of unsaturated swelling clays later reported by Merchán et al. (2008), Merchan et al. (2011) and Romero et al. (2014), which were presented in Section 2.4.4. The BBM assumes a non-associated flow-rule g:

$$g \equiv \alpha q^2 - M^2(p + p_s)(p_0 - p) = 0, \tag{2.52}$$

in which the factor α ensures that the flow rule yields the stress ratio $K_0 = \sigma_{11}/\sigma_{22} = 1 - \sin(\varphi)$.

In its original formulation, the BBM could not sufficiently predict swelling pressure nor swelling strain (Dieudonne, 2016). The prediction of swelling pressure was only enabled by introducing the suction-dependent definition of the elastic index κ in Equation (2.44) (Vaunat and Gens, 2005). Swelling pressure and swelling strain cannot be accurately predicted with one set of parameters in the original formulation, see e.g. Schoen (2025). The latter was counteracted by defining the elastic index in the suction regime κ_s as a function of suction as shown in Equation (2.45). However, neither the constant κ_{s0}, nor the parameters associated with it, can be derived from laboratory test results. They do not exhibit a direct physical meaning and must

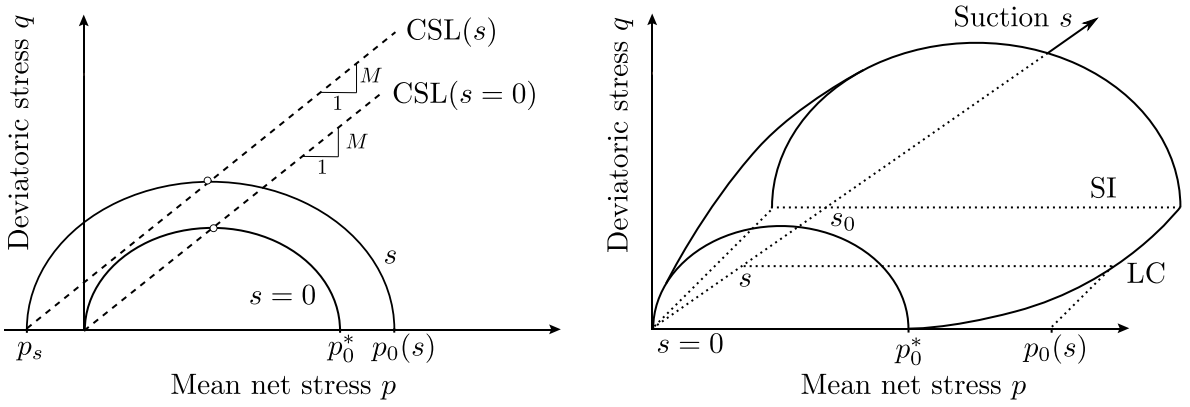

Figure 2.23.: Barcelona Basic Model: Yield surfaces for different suctions in $q - p$ plane (left) and in $q - p - s$ plane (right).

be determined as fitting parameters by back-analysis, i.e. by estimating a value and adjusting it through comparison of numerical simulations with laboratory data. Consequently, the revised BBM is capable of predicting swelling phenomena in expansive materials, but only at the cost of complex and non-straightforward parameter calibration.

2.5.2.2. Double-structure approaches

The underlying assumptions of double porosity approaches were introduced in Sections 2.1.3 and 2.2.1.2. Here, their consideration in constitutive models for the stress-strain-behaviour is shown. The first incorporation of double-structure in a constitutive model was reported with the BExM (Gens and Alonso, 1992) and applied by Alonso et al. (1999). Therein, emphasis was on the material behaviour during wetting-drying cycles, which yields a strain accumulation with increasing number of cycles. The BExM layed the groundwork for the extensions of other models, e.g. the Imperial College Single Structure Model (IC-SSM) to the Imperial College Double structure model (IC-DSM) (Ghiadistri et al., 2019). The double-structure approach divides the pore network into a microstructural level (index: m) and a macrostructural level (index: M), also referred to as the intra-aggregate and inter-aggregate porosity. Deformations on the microstructural level are assumed as a result of clay-water interaction, purely volumetric, reversible and independent of the macrostructural level. They affect, however, the macrostructural deformations. These correspond to the mechanical response measurable in experiments and are computed similarly according to the equations of the BBM. However, coupling between the micro- and macrostructural level is required to enable the evolution of macrostructural, irreversible plastic strains as a result of microstructural deformation.

Microstructural elastic strain increments $\mathrm{d}\epsilon_{vm}^{e}$ are internally generated by changes in a microstructural mean effective stress $\hat{p}$. It is defined as $\hat{p} = p + (S_m^w)^\alpha \; s$ based on the mean net stress p, suction s, the microstructural degree of saturation S_m^w and a material parameter α. Microstructural elastic strain increments are limited by two parallel microstructural yield curves around a neutral line, which are introduced in addition to the macrostructural LC-curve of the BBM. These are valid for shrinkage and expansion and are defined as $\hat{p} - s_i = 0$ (Suction-Increase, SI) and $s_0 - \hat{p} = 0$ (Suction Decrease, SD) with hardening parameters s_i and s_0. The

microstructural yield curves are indicated on the left-hand side of Figure 2.24. However, they are not unique and evolve according to microstructural hardening laws, which depend on coupling functions f_I and f_D between the two structural levels. These same functions are also responsible for the macrostructural plastic strain increments:

$$\mathrm{d}\epsilon^p_{vM} = f_I \, \mathrm{d}\epsilon^e_{vm} \quad \text{for} \quad \text{increasing suction,} \tag{2.53}$$

$$\mathrm{d}\epsilon^p_{vM} = f_D \, \mathrm{d}\epsilon^e_{vm} \quad \text{for} \quad \text{decreasing suction.} \tag{2.54}$$

The schematic development of the coupling functions responsible for the interaction of the two structural levels is shown on the right-hand side of Figure 2.24. The full mathematical formulation can be found in Gens and Alonso (1992) and Alonso et al. (1999). This section is primarily intended to illustrate the complexity of the coupling between the two structural levels and the consequent challenges involved in parameter calibration.

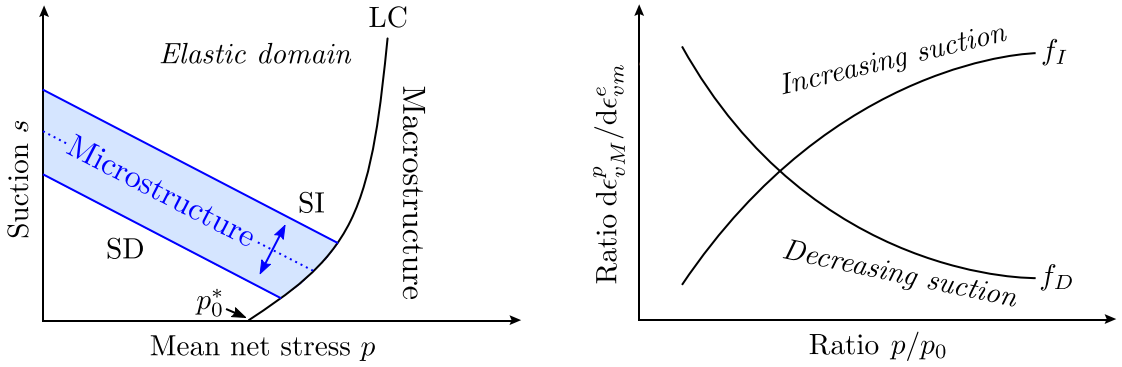

Figure 2.24.: Barcelona Expansive Model: yield curves for micro- and macrostructure (left) and interaction function linking plastic macrostructural and elastic microstructural strain (right).

Double structure approaches exist for the SWRC and relative permeability models as well (see Sections 2.2.1.2 and 2.2.2.2). In general, modelling frameworks exist with considerations of double-porosity on different and multiple levels:

- Double structure in the mechanical model only, as it was applied upon introduction of the BExM (Gens and Alonso, 1992; Alonso et al., 1999, 2005).
- Double structure in the hydraulic model only, as it is implemented e.g. in the FEM code Lagamine (Collin, 2002; Collin et al., 2006), where the BBM can be used with the double-structure water retention model of Dieudonne (2016), see Section 2.2.1.2. Therein, only the macroscopic degree of saturation and void ratio are passed from the hydraulic model to the mechanical model for evaluation of the constitutive equations.
- Double structure in both the mechanical and the hydraulic model: Vecchia and Romero (2013) proposed the consideration of double-porosity effects in the hardening laws of an elasto-plastic mechanical model with generalised hardening in combination with a double-structure hydraulic model.

Introducing micro- and macroporosity in double-structure approaches provides a suitable modelling framework. However, the determination of state variables and model parameters for different structure levels is challenging. It requires microstructural investigations with MIP for the evaluation of the dominant porosity regimes in addition to standard laboratory tests. The

coupling functions between the porosities are arbitrary and have no physical meaning, neither do their parameters. Furthermore, the double porosity concept is not applicable to all unsaturated swelling clays, as e.g. clay shales, less highly compacted bentonites or mixtures tend to have a rather mono-modal pore size distribution (Christ, 2025; Seiphoori et al., 2016; Mohajerani et al., 2011). Finally, the changes in the macrostructural domain are only accounted for at the constitutive level and not at the continuum scale.

2.5.2.3. Degree of saturation as governing variable

In the aforementioned modelling frameworks, several features of the unsaturated behaviour rely on suction: volume change behaviour, hence swelling and compression indices, preconsolidation net stress, yield loci and shear strength. However, an alternative variable is the (effective) degree of saturation, as was proposed e.g. by Zhou et al. (2012a, 2018) or Bosch et al. (2021). Introducing the (effective) degree of saturation as a driving variable in a constitutive model offers two advantages: (1) evolution equations and other mathematical expressions simplify due to its range between 0 and 1.0 and (2) the transition between unsaturated and saturated states is unambiguous, with $S^e = 1$ denoting full saturation. The (effective) degree of saturation and its relation to the suction is given by the hydraulic model at any time. Zhou et al. (2012b) proposed a direct, non-linear dependency of the compressibility index λ on the effective degree of saturation:

$$\lambda = \lambda_0 - (1 - S^e)^{a_1} (\lambda_0 - \lambda_d) , \tag{2.55}$$

wherein $\lambda_0 = \lambda(S^e = 1)$ corresponds to the saturated state and $\lambda_d = \lambda(S^e = 0)$ to the driest state and a_1 is a material parameter. Indirectly, the effective preconsolidation net stress p is thereby also influenced by S^e, as:

$$p = (p_c)^{\frac{\lambda_0 - \kappa}{\lambda(S^e) - \kappa}} , \tag{2.56}$$

with p_c corresponding to the saturated state (Zhou et al., 2012b). Later, a similar dependency of κ on the effective degree of saturation was introduced by Zhou et al. (2018) as well. Bosch et al. (2021) applied the degree of saturation S^w in a similar form of Equation (2.55) for the computation of the compression index λ:

$$\lambda = \lambda_0 - r (\lambda_s - \kappa) \left(1 - S^{w\zeta}\right)^{\xi} , \tag{2.57}$$

wherein ζ and ξ are material parameters, $0 < r < 1$ represents the maximum reduction in compressibility from the saturated state to the dry reference state and the elastic index κ is used as the limit in the dry reference state. Though the volumetric behaviour is dependent on the (effective) degree of saturation, it does not imply a direct coupling between expansion and saturation in the sense of a saturation-induced swelling mechanism.

2.6. Implications for the novel modelling framework and concluding remarks

In this chapter, the clay mineralogy of expansive soils and its significance for swelling processes and phenomena were introduced. The material behaviour under different loading and boundary conditions was shown based on an extensive test campaign on reconstituted Opalinus clay

shale (Nitsch et al., 2023a) and further studies from literature covering a wide range of expansive clay mineral content. Existing modelling frameworks for the mechanical behaviour were presented. Their limitations, which motivate the development of a novel modelling framework, were discussed. This section summarizes the relevant phenomena of the aforementioned material behaviour. When addressing the mechanical and hydraulic phenomena upon swelling, it is essential to determine which aspects of the material behaviour are to be considered at the material level (i.e. in constitutive models). Experimental studies clearly show that the composition of the expansive soil within a control volume changes as a result of swelling, since water transitions from a mobile state to a state attached to the clay minerals. A finite element corresponds to a control volume. Therefore, the change of volume fractions in the expansive soil upon wetting should be represented at the element level (continuum scale) and not the material (constitutive) level. Considering selected effects at the material level may lead to potential violations in the balancing equations.

In this work, a two-level modelling framework is proposed: (1) The soil is described by an extension of the expansive porous medium with a separate swelling water phase. A dedicated mass balance equation tracks the mass transfer between free pore water and water attached to the solid grains on the element level. (2) On the material level, novel constitutive relationships are proposed. For the stress-strain-behaviour, a novel hydro-mechanically coupled constitutive model for expansive soils is introduced, which is formulated in the framework of hypoplasticity. The model includes a dependency of the mechanical response on the saturation changes without relying on the double-porosity concept. It allows for the prediction of the magnitude of both swelling phenomena, swelling strain and net swelling stress, with one single set of material parameters. The flow properties in the soil are governed by the attachment of water in the extended finite element. Thus, the time evolution of swelling lies outside the scope of the mechanical constitutive model and can only be predicted by the overall numerical framework. Figure 2.25 illustrates the underlying concept of the numerical framework, including the division of tasks between the material and element level and the experimental loading paths considered in its development.

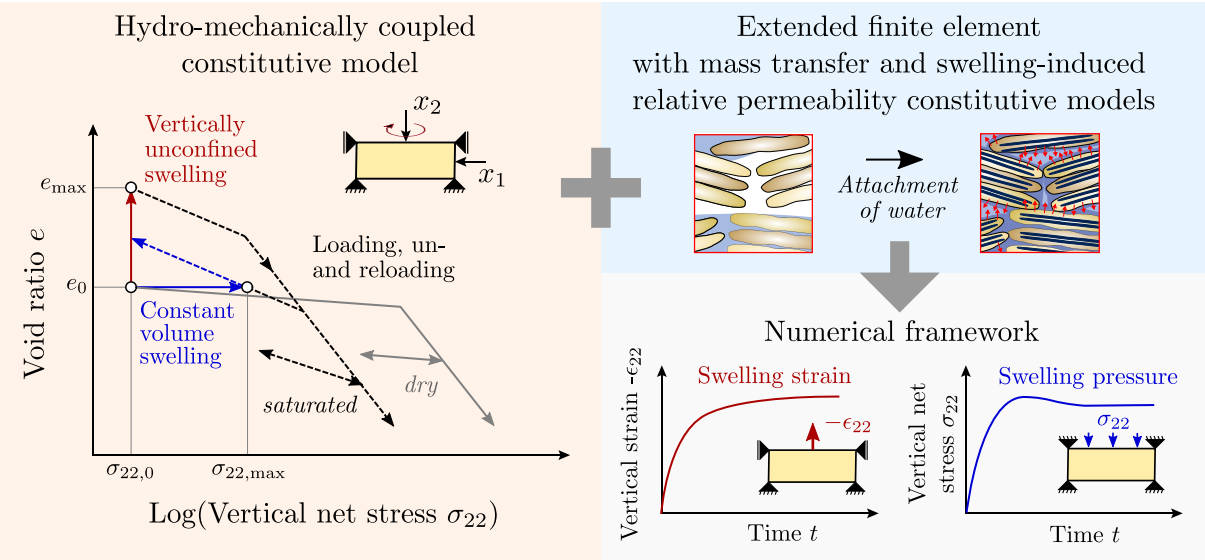

Figure 2.25.: Experimental loading paths and division of tasks in the proposed modelling framework between mechanical constitutive model and extended finite element.

For the formulation of the mass transfer model and the swelling-induced relative permeability model, a change in the internal composition of the soil is considered by the attachement of swelling water, which results in an effective porosity available for flow and is considered in all governing equations.

For the formulation of the mechanical model, the most prominent characteristics of the material behaviour are summarized in the following. Regarding the volumetric behaviour under oedometric conditions they are as follows:

- The material behaviour during monotonic loading (including specimen preparation) is characterised by a unique virgin loading line in the idealized dry reference state. Initial dry density or void ratio correspond to a preloading state on this line.
- Unsaturated and saturated oedometric compression converge to a Normal Compression Curve (NCC) after long monotonic loading, regardless of the initial state, changes in saturation or the prior loading path.
- With increasing water content / degree of saturation, the preloading stress is significantly reduced, indicated by a parallel shift of the virgin loading line to areas of smaller stresses, most pronounced for fully saturated states. Thus, an affinity between the virgin loading line in the idealized dry and saturated state, the NCC, exists.
- The NCC has a fixed position and remains unaffected by the degree of saturation. The elastic stiffness of the material is severely reduced in the saturated state and can be described as a function of the effective degree of saturation. The stress-strain behaviour is continuous and not characterized by a yielding point separating elastic and plastic deformation.
- Equilibrium swelling pressure and swelling strain are always to the left of the preloading line and the NCC in the oedometric $e - \log(\sigma_{22})$ space. An affine trend line is identified for the final, saturated state after swelling at vertically confined and constant volume conditions, independently of the initial state (stress, void ratio) prior to wetting. Thus, the development of expansion and swelling pressure upon wetting depends on the preconsolidation stress and, reciprocally, the preloading stress evolves during swelling.
- The simultaneous development of swelling strain and the progression of the infiltration front for wetting under vertically unconfined conditions indicate a direct coupling between expansion and infiltration. A single swelling mechanism induces either volumetric expansion or stress increase depending on the outer boundary conditions.
- Unloading after constant volume swelling results in a deformation, whose final value can be well described by the wetting-induced reduction of elastic stiffness.

The extension of the volumetric behaviour to triaxial states requires knowledge of the three-dimensional behaviour and strength of the material. For this purpose, the following phenomena are taken into account:

- Upon oedometric loading, radial net stresses evolve and after oedometric unloading to very small vertical net stress, the radial net stress may exceed vertical net stress. In compacted samples the stress state is in extension (negative deviatoric stress) before the start of swelling tests and the stress ratio can exceed the critical one.

- The compaction-induced anisotropy is further reflected in the three-dimensional behaviour during saturation. The volumetric primary phenomena manifest themselves across the spatial directions. Accordingly, for swelling under oedometric conditions, the saturation-dependent swelling mechanism necessitates an anisotropic representation within the full strain space.
- The shear strength decreases significantly with increasing saturation, which is reflected in a decrease in the internal friction angle and not in the existence of an apparent cohesion. Similar to the elastic stiffness, it can be described as a simple function of the effective degree of saturation.

For the constitutive description, net stress and degree of saturation are adopted as primary variables. The degree of saturation is preferred over suction, as swelling is directly coupled to changes in saturation. The use of net stress in the mechanical constitutive model has proven appropriate, as it can be both controlled and measured in laboratory settings.

3. Extended theory of porous media for expansive soils

In this chapter the governing equations for the multi-phase system of an unsaturated expansive soil are derived within the framework of the *Theory of Porous Media* (TPM). The fundamental concept of the TPM is introduced, the classical three-phase description for unsaturated soils is derived and thereafter, the extension of the TPM for expansive soils is presented.

3.1. Theory of porous media for unsaturated soils

The TPM is applied as a macroscopic continuum-based approach for multi-phase materials with complex microstructure. It serves as a theoretical idealisation of the multi-phase material, in which all constituents are assumed to be in a state of ideal disarrangement and thus statistically distributed over the control space. In soil mechanics, these phases classically are the solid (s), pore water (w) and pore air (a) (Schrefler et al., 1990; de Boer, 2000; Ehlers and Blome, 2003). The TPM is based on the *Theory of mixture* (TM) and *Concept of Volume fractions*. All phases of the mixture are averaged over a *Representative Elementary Volume* (REV), hence the constituents and all their geometrical and physical quantities are homogenized. Within the REV, each spatial point is simultaneously occupied by constituents of all phases and the local composition is described by the volume fraction φ^α of each phase α:

$$\varphi^\alpha = \frac{\mathrm{d}V^\alpha}{\mathrm{d}V}, \tag{3.1}$$

wherein $\mathrm{d}V$ denotes the elementary volume of the REV and $\mathrm{d}V^\alpha$ the portion of $\mathrm{d}V$ occupied by phase α. The sum of all volume fractions must satisfy the saturation condition and consequently, the elementary volume $\mathrm{d}V$ is recovered by a summation over the phases:

$$\sum_\alpha \varphi^\alpha = 1 \quad \text{and} \quad \mathrm{d}V = \sum_\alpha \mathrm{d}V^\alpha. \tag{3.2}$$

The approach for a three-phase soil with the phases $\alpha = \{s, w, a\}$ is shown in Figure 3.1 with a simplified visualization of the microstructure (left), the homogenized mixture (centre) and the volume fractions (right).

Consequently, also the pore space is assumed statistically distributed as it equals to the combined volume of the pore fluids $F = \{a, w\}$. Note that the sum of any quantity $\sqcup$ of multiple phases is written in short form as in the following example: $\sqcup^F = \sqcup^{w+a} = \sqcup^w + \sqcup^a$. The porosity n of the porous medium is therefore defined as the proportion of fluid volume $\mathrm{d}V^F$ to the total volume:

$$n = \frac{\mathrm{d}V^F}{\mathrm{d}V} = \frac{\mathrm{d}V^{a+w}}{\mathrm{d}V} = \varphi^a + \varphi^w = 1 - \varphi^s. \tag{3.3}$$

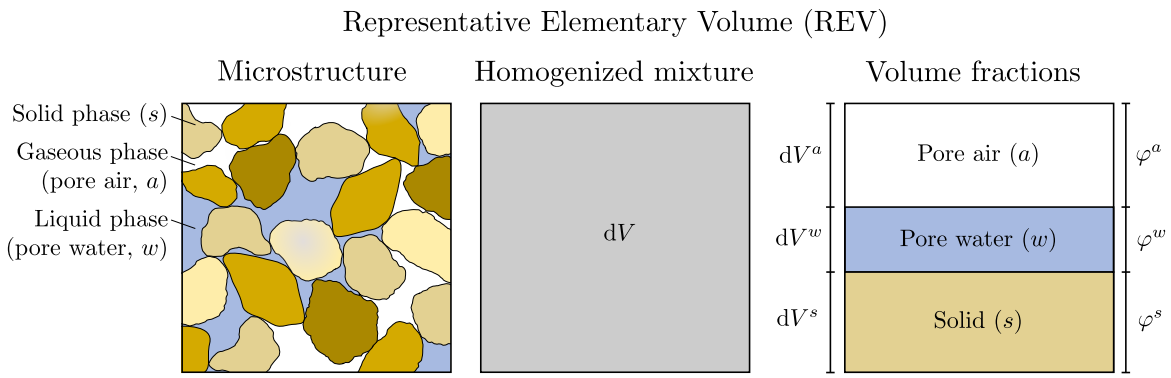

Figure 3.1.: Schematic representation of soil as a three-phase porous medium: microstructure, homogenization and volume fractions in the REV.

Similarly, the degrees of saturation of the fluid phases S^w and S^a are defined as:

$$S^w = \frac{\varphi^w}{\varphi^a + \varphi^w} = \frac{\varphi^w}{1 - \varphi^s} = \frac{\varphi^w}{n} \quad \text{and} \quad S^a = \frac{\varphi^a}{\varphi^a + \varphi^w} = \frac{\varphi^a}{1 - \varphi^s} = \frac{\varphi^a}{n}. \tag{3.4}$$

The condition $S^w + S^a = 1$ holds. The total mass of the mixture m corresponds to the sum of the partial masses m^α in a similar manner as in Equation (3.2):

$$m = \sum_\alpha m^\alpha. \tag{3.5}$$

This allows for the definition of density for the constituents, either as the intrinsic (material) density $\bar{\rho}^\alpha$ (per unit volume of phase α) or as the partial (bulk) density ρ^α (per unit volume of the overall mixture). They are:

$$\bar{\rho}^\alpha = \frac{\mathrm{d}m^\alpha}{\mathrm{d}V^\alpha} \quad \text{and} \quad \rho^\alpha = \frac{\mathrm{d}m^\alpha}{\mathrm{d}V}, \tag{3.6}$$

and can be related to each other by the definition of the volume fraction (Equation (3.1)), i.e. $\rho^\alpha = \varphi^\alpha \bar{\rho}^\alpha$. In general, any physical field $\sqcup$ can either be expressed as an intrinsic ($\bar{\sqcup}^\alpha$) or a partial ($\sqcup^\alpha$) quantity as $\sqcup^\alpha = \varphi^\alpha \bar{\sqcup}^\alpha$. The partial densities ρ^α can be summed to obtain the total density of the mixture:

$$\rho^{tot} = \rho^s + \rho^w + \rho^a = \sum_\alpha \rho^\alpha = \sum_\alpha \varphi^\alpha \bar{\rho}^\alpha, \tag{3.7}$$

or rearranged in terms of the degrees of saturation and the porosity as:

$$\rho^{tot} = (1 - n)\bar{\rho}^s + n\left(S^w \bar{\rho}^w + (1 - S^w)\bar{\rho}^a\right). \tag{3.8}$$

3.1.1. Kinematics

Each spatial point $\boldsymbol{x}$ in the current configuration of the porous medium is simultaneously occupied by material points of all phases α of the mixture at any time t, i.e.

$$\boldsymbol{x} = \boldsymbol{\chi}^\alpha(\boldsymbol{X}^\alpha, t), \tag{3.9}$$

wherein $\boldsymbol{X}^\alpha$ denotes the reference position of each phase. The motion function $\boldsymbol{\chi}^\alpha$ maps the position of the reference configuration $\boldsymbol{X}^\alpha$ to the current position $\boldsymbol{x}$. $\boldsymbol{\chi}^\alpha$ is assumed unique for each phase α, thus $\boldsymbol{X}^\alpha$ may be different for each phase as depicted in Figure 3.2. Any material point can be transformed between the reference configuration at time t_0 and the current configuration at time t using the material deformation gradient $\boldsymbol{F}^\alpha$:

$$\boldsymbol{F}^\alpha = \operatorname{grad}^\alpha(\boldsymbol{x}) = \frac{\partial \boldsymbol{\chi}^\alpha(\boldsymbol{X}^\alpha, t)}{\partial \boldsymbol{X}^\alpha}, \tag{3.10}$$

or its inverse, the spatial deformation gradient $(\boldsymbol{F}^\alpha)^{-1}$:

$$(\boldsymbol{F}^\alpha)^{-1} = \operatorname{grad}^\alpha(\boldsymbol{X}) = \frac{\partial \boldsymbol{X}^\alpha}{\partial \boldsymbol{\chi}^\alpha(\boldsymbol{X}^\alpha, t)}. \tag{3.11}$$

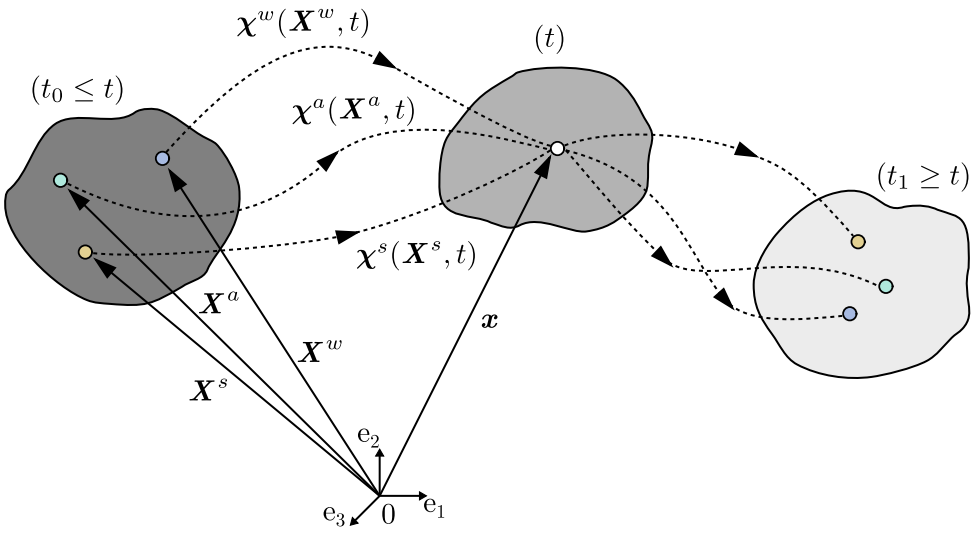

Figure 3.2.: Kinematics for a three-phase mixture.

Note that volumes must be positive and the mapping between the configurations must be unique which requires a positive and non-zero Jacobian determinant $J^\alpha = \det(\boldsymbol{F}^\alpha) > 0$. Different frameworks for the description of the movement of the constituents exist. The *Euler*ian or spatial description provides information about the temporal change of a field function in terms of a fixed spatial position. In contrast, the *Lagrange*an description describes the movement of a field function in terms of a moving phase, measuring the changes in its respective properties with time. The derivative of any quantity $\sqcup = \sqcup(\boldsymbol{x}^\alpha, t)$ of the phase α with respect to its motion in time is referred to as the *material time derivative*. It reads:

$$\frac{\mathrm{d}^\alpha \sqcup(\boldsymbol{x}^\alpha, t)}{\mathrm{d}t} = \frac{\partial \sqcup(\boldsymbol{x}^\alpha, t)}{\partial t} + \operatorname{grad}(\sqcup(\boldsymbol{x}^\alpha, t)) \cdot \bar{\boldsymbol{v}}^\alpha, \tag{3.12}$$

wherein $\bar{\boldsymbol{v}}^\alpha$ is the intrinsic field of velocity of phase α, which is computed by the time derivative of the motion function $\boldsymbol{\chi}^\alpha$:

$$\bar{\boldsymbol{v}}^\alpha = \frac{\mathrm{d}\boldsymbol{\chi}^\alpha(\boldsymbol{X}^\alpha, t)}{\mathrm{d}t}. \tag{3.13}$$

The first part of Equation (3.12) is often called *local* and the second part is called *non-local* or *convective* derivative, accounting for changes of the quantity $\sqcup$ in time and position, respectively.

For solid-fluid mixtures, the solid displacement $\bar{\boldsymbol{u}}^s = \boldsymbol{x}^s - \boldsymbol{X}^s$ is most commonly chosen as the primary kinetic variable in the framework of the TPM. The solid phase is therefore expressed in a Lagrangean description, whereas for the fluid phase β a modified Eulerian description is applied using a relative velocity $\bar{\boldsymbol{w}}^\beta$, usually referred to as the seepage flow velocity, and defined as:

$$\bar{\boldsymbol{w}}^\beta = \bar{\boldsymbol{v}}^\beta - \bar{\boldsymbol{v}}^s, \tag{3.14}$$

wherein $\bar{\boldsymbol{v}}^\beta$ and $\bar{\boldsymbol{v}}^s$ are the intrinsic fields of velocity for the pore fluids and solid respectively. For the pore fluids $\beta = \{w, a\}$ Equation (3.12) thus reads:

$$\frac{\mathrm{d}^\beta \sqcup (\boldsymbol{x}^\alpha, t)}{\mathrm{d}t} = \frac{\mathrm{d}^s \sqcup (\boldsymbol{x}^\alpha, t)}{\mathrm{d}t} + \operatorname{grad}(\sqcup(\boldsymbol{x}^\alpha, t)) \; \bar{\boldsymbol{w}}^\beta. \tag{3.15}$$

The seepage velocity can be transferred into the Darcy velocity $\boldsymbol{w}^\beta$ using the volume fraction φ^β:

$$\boldsymbol{w}^\beta = \varphi^\beta \bar{\boldsymbol{w}}^\beta = \varphi^\beta \left(\bar{\boldsymbol{v}}^\beta - \bar{\boldsymbol{v}}^s \right). \tag{3.16}$$

3.1.2. Governing equations

Balance equations are fundamental in continuum mechanics and include the balance of mass, the balance of linear and angular momentum and the balance of energy. In the TM and TPM, balance equations must be established for both, the mixture and its constituents. For hydro-mechanical processes in soil mechanics, the conservation of mass, linear and angular momentum is generally sufficient for FE implementations. According to Houlsby (1997) amongst others, the balance of energy (or first law of thermodynamics) may be utilized to identify sets of energy-conjugate pairs in the multiphase material, that can contribute to the understanding of coupled processes in the mixture. The following simplifications and resulting implications are considered for the hydro-mechanically coupled framework in this work:

1. No consideration of temperature effects, hence isothermal conditions: $T = \text{const.}$
2. Laminar flow, i.e. low velocities of pore fluid flow and low Reynolds number.
3. Incompressibility of solid grains (s): $\bar{K}^s \to \infty$
4. Homogeneous distribution of the intrinsic density of solid grains: $\operatorname{grad}(\bar{\rho}^s) = 0$

3.1.2.1. Conservation of mass (continuity equation)

The total mass of a body remains constant at all times, if there is no mass exchange across the surface and no increase or loss of mass in the interior of a body. The mass m of a body Ω is determined by the volume integral over the density field $\rho^{tot}(\boldsymbol{x}^\alpha, t)$. For mass continuity of a body, the time derivative of the mass should vanish, yielding:

$$\dot{m} = \frac{\mathrm{d}}{\mathrm{d}t} \int_\Omega \rho^{tot} \, \mathrm{d}V = \int_\Omega \left(\dot{\rho}^{tot} + \rho^{tot} \operatorname{div}(\bar{\boldsymbol{v}}) \right) \mathrm{d}V = 0. \tag{3.17}$$

For an individual phase α of the body, the local form of the conservation of mass for an arbitrary volume reads (Truesdell, 1984):

$$\frac{\mathrm{d}^{\alpha}\rho^{\alpha}}{\mathrm{d}t} + \rho^{\alpha}\,\mathrm{div}\,(\bar{\boldsymbol{v}}^{\alpha}) = \hat{\rho}^{\alpha}, \tag{3.18}$$

wherein $\hat{\rho}^{\alpha}$ denotes mass production of the phase α. For the further derivation, the general case of compressible phases under isothermal conditions is considered. The dependency of the intrinsic density $\bar{\rho}^{\alpha}$ of phase α on the mean pressure $\bar{p}^{\alpha}$ can be expressed with the following constitutive equation (Schrefler et al., 1990; Borja, 2006):

$$\frac{\mathrm{d}\bar{p}^{\alpha}}{\mathrm{d}t} = \frac{\bar{K}^{\alpha}}{\bar{\rho}^{\alpha}}\frac{\mathrm{d}^{\alpha}\bar{\rho}^{\alpha}}{\mathrm{d}t}, \tag{3.19}$$

wherein $\bar{K}^{\alpha}$ is the bulk modulus of phase α. Using $\rho^{\alpha} = \varphi^{\alpha}\bar{\rho}^{\alpha}$ and Equation (3.19), the first part of Equation (3.18) is rewritten as:

$$\frac{\mathrm{d}^{\alpha}\rho^{\alpha}}{\mathrm{d}t} = \varphi^{\alpha}\frac{\bar{\rho}^{\alpha}}{\bar{K}^{\alpha}}\frac{\mathrm{d}\bar{p}^{\alpha}}{\mathrm{d}t} + \frac{\mathrm{d}^{\alpha}\varphi^{\alpha}}{\mathrm{d}t}\bar{\rho}^{\alpha}. \tag{3.20}$$

Consequently, rearrangement of Equation (3.18) and consideration of Equation (3.20) yields:

$$\begin{aligned} &\varphi^{\alpha}\frac{\bar{\rho}^{\alpha}}{\bar{K}^{\alpha}}\frac{\mathrm{d}\bar{p}^{\alpha}}{\mathrm{d}t} + \frac{\mathrm{d}\varphi^{\alpha}}{\mathrm{d}t}\bar{\rho}^{\alpha} + \rho^{\alpha}\,\mathrm{div}\,(\bar{\boldsymbol{v}}^{\alpha}) = \hat{\rho}^{\alpha} \\ \Leftrightarrow\ &\frac{\varphi^{\alpha}}{\bar{K}^{\alpha}}\frac{\mathrm{d}\bar{p}^{\alpha}}{\mathrm{d}t} + \frac{\mathrm{d}\varphi^{\alpha}}{\mathrm{d}t} + \varphi^{\alpha}\,\mathrm{div}\,(\bar{\boldsymbol{v}}^{\alpha}) = \frac{\hat{\rho}^{\alpha}}{\bar{\rho}^{\alpha}}. \end{aligned} \tag{3.21}$$

Equation (3.21) is in general valid for all phases. However, the conservation of mass for the pore fluids β is somewhat more complex, as their motion is described in a modified Eulerian setting with respect to the deformation of the solid phase. For the temporal change of the density field of the fluid phase β, application of the Darcy velocity from Equation (3.16) and differentiation with the product rule results in:

$$\frac{\mathrm{d}^{\beta}\rho^{\beta}}{\mathrm{d}t} = \varphi^{\beta}\frac{\bar{\rho}^{\beta}}{\bar{K}^{\beta}}\frac{\mathrm{d}\bar{p}^{\beta}}{\mathrm{d}t} + \frac{\bar{\rho}^{\beta}}{\bar{K}^{\beta}}\,\mathrm{grad}\left(\bar{p}^{\beta}\right)\cdot\boldsymbol{w}^{\beta} + \frac{\mathrm{d}\varphi^{\beta}}{\mathrm{d}t}\bar{\rho}^{\beta} + \bar{\rho}^{\beta}\,\mathrm{grad}\left(\varphi^{\beta}\right)\cdot\bar{\boldsymbol{w}}^{\beta}. \tag{3.22}$$

With consideration of Equation (3.22), the mass balance from Equation (3.21) reads:

$$\frac{\varphi^{\beta}}{\bar{K}^{\beta}}\frac{\mathrm{d}\bar{p}^{\beta}}{\mathrm{d}t} + \frac{1}{\bar{K}^{\beta}}\,\mathrm{grad}\left(\bar{p}^{\beta}\right)\cdot\boldsymbol{w}^{\beta} + \frac{\mathrm{d}\varphi^{\beta}}{\mathrm{d}t} + \mathrm{grad}\left(\varphi^{\beta}\right)\cdot\bar{\boldsymbol{w}}^{\beta} + \varphi^{\beta}\,\mathrm{div}\left(\bar{\boldsymbol{v}}^{\beta}\right) = \frac{\hat{\rho}^{\beta}}{\bar{\rho}^{\beta}}. \tag{3.23}$$

Equation (3.23) is further rearranged in terms of the Darcy velocity $\boldsymbol{w}^{\beta}$ instead of the seepage velocity $\bar{\boldsymbol{w}}^{\beta}$ (see Equation (3.16)). With consideration of the relation $\mathrm{div}\left(\bar{\boldsymbol{v}}^{\beta}\right) = \mathrm{div}\left(\bar{\boldsymbol{w}}^{\beta}\right) + \mathrm{div}\,(\bar{\boldsymbol{v}}^{s})$ and of the divergence of the Darcy velocity $\mathrm{div}\left(\boldsymbol{w}^{\beta}\right) = \varphi^{\beta}\,\mathrm{div}\left(\bar{\boldsymbol{w}}^{\beta}\right) + \mathrm{grad}\left(\varphi^{\beta}\right)\cdot\bar{\boldsymbol{w}}^{\beta}$ it is:

$$\frac{\varphi^{\beta}}{\bar{K}^{\beta}}\frac{\mathrm{d}\bar{p}^{\beta}}{\mathrm{d}t} + \frac{1}{\bar{K}^{\beta}}\,\mathrm{grad}\left(\bar{p}^{\beta}\right)\cdot\boldsymbol{w}^{\beta} + \frac{\mathrm{d}\varphi^{\beta}}{\mathrm{d}t} + \mathrm{div}\left(\boldsymbol{w}^{\beta}\right) + \varphi^{\beta}\,\mathrm{div}\,(\bar{\boldsymbol{v}}^{s}) = \frac{\hat{\rho}^{\beta}}{\bar{\rho}^{\beta}}. \tag{3.24}$$

When no mass transfer between different phases takes place, the mass production term vanishes ($\hat{\rho}^{\alpha} = 0$ or $\hat{\rho}^{\beta} = 0$).

3.1.2.2. Conservation of linear momentum of the mixture (kinetic force balance)

The conservation of linear momentum for the mixture is the result of the summation of the momenta of all phases α. For each phase, the temporal change of the total linear momentum $\rho^\alpha \bar{\boldsymbol{a}}^\alpha$ is equal to the sum of all forces acting on the body from the outside. The latter comprise the body forces $\rho^\alpha \bar{\boldsymbol{b}}^\alpha$, wherein $\bar{\boldsymbol{b}}^\alpha$ is the intrinsic body force density of the phase, the interaction forces $\boldsymbol{h}^\alpha$ between the phases and the surface forces $\boldsymbol{t}^\alpha$. Surface forces follow from the Cauchy theorem, $\boldsymbol{t}^\alpha = \boldsymbol{\sigma}^\alpha \boldsymbol{n}^\alpha$, with $\boldsymbol{\sigma}^\alpha$ being the partial Cauchy stress tensor and $\boldsymbol{n}^\alpha$ the outward normal. Using the Cauchy theorem and the divergence theorem, which allows to express the surface forces by the divergence of the stress tensor, the conservation of linear momentum for each phase α is obtained as:

$$\rho^\alpha \bar{\boldsymbol{a}}^\alpha = \rho^\alpha \bar{\boldsymbol{b}}^\alpha + \operatorname{div}\left(\boldsymbol{\sigma}^\alpha\right) + \boldsymbol{h}^\alpha, \tag{3.25}$$

wherein $\rho^\alpha \bar{\boldsymbol{b}}^\alpha$ are the body forces with the intrinsic body force density $\bar{\boldsymbol{b}}$ and $\boldsymbol{h}^\alpha$ are interaction forces between the phases. Interaction forces are exerted by the free pore fluids $\beta = \{a, w\}$ on the solid matrix. After Ehlers and Blome (2003) they can be expressed per unit volume as:

$$\boldsymbol{h}^\beta = p^\beta \operatorname{grad}\left(\varphi^\beta\right) - \varphi^\beta \bar{\gamma}^\beta \left(\boldsymbol{k}^\beta\right)^{-1} \cdot \boldsymbol{w}^\beta, \tag{3.26}$$

wherein $\boldsymbol{k}^\beta$ is the hydraulic conductivity tensor (see Section 2.2.2), and $\bar{\gamma}^\beta = \bar{\rho}^\beta g$ the intrinsic unit weight computed by the intrinsic density $\bar{\rho}^\beta$ and the gravity g by phase β. The partial stress of the pore fluids is defined as $\boldsymbol{\sigma}^\beta = -\varphi^\beta \bar{p}^\beta \mathbf{1}$, thus it isotropically depends on the pressure p^β of the respective phase. The conservation of linear momentum for the pore fluids reads as:

$$\rho^\beta \dot{\bar{\boldsymbol{v}}}^\beta = \rho^\beta \bar{\boldsymbol{b}}^\beta + \operatorname{div}\left(\boldsymbol{\sigma}^\beta\right) + \boldsymbol{h}^\beta, \tag{3.27}$$

$$\varphi^\beta \bar{\rho}^\beta \dot{\bar{\boldsymbol{v}}}^\beta = \varphi^\beta \bar{\rho}^\beta \bar{\boldsymbol{b}} + \operatorname{div}\left(-\varphi^\beta \bar{p}^\beta \mathbf{1}\right) + p^\beta \operatorname{grad}\left(\varphi^\beta\right) - \varphi^\beta \bar{\gamma}^\beta \left(\boldsymbol{k}^\beta\right)^{-1} \cdot \boldsymbol{w}^\beta. \tag{3.28}$$

Consideration of a homogeneous distribution of the phase β, thus $\operatorname{grad}\left(\varphi^\beta\right) = 0$, and $\operatorname{div}\left(\mathbf{1}\right) = 0$ allows to derive the so-called generalized Darcy law based on the conservation of linear momentum of the pore fluids:

$$\boldsymbol{w}^\beta = \frac{\boldsymbol{k}^\beta}{\bar{\gamma}^\beta}\left(-\operatorname{grad}\left(\bar{p}^\beta\right) + \bar{\rho}^\beta\left(\bar{\boldsymbol{b}} - \bar{\boldsymbol{a}}^\beta\right)\right), \tag{3.29}$$

or with consideration of Equations (2.18) and (2.19) using the intrinsic permeability tensor $\boldsymbol{K}^s$:

$$\boldsymbol{w}^\beta = \frac{\boldsymbol{K}^s k^{r,\beta}}{\bar{\mu}^\beta}\left(-\operatorname{grad}\left(\bar{p}^\beta\right) + \bar{\rho}^\beta\left(\bar{\boldsymbol{b}} - \bar{\boldsymbol{a}}^\beta\right)\right). \tag{3.30}$$

For the mixture, $\boldsymbol{h}^\alpha$ vanishes. The acceleration $\bar{\boldsymbol{a}}^\alpha = \bar{\boldsymbol{a}}$ and body forces $\bar{\boldsymbol{b}}^\alpha = \bar{\boldsymbol{b}}$ are assumed to be equal for all phases. The following closure conditions apply:

$$\boldsymbol{\sigma}^{tot} = \sum_\alpha \boldsymbol{\sigma}^\alpha \quad , \quad \rho^{tot} \bar{\boldsymbol{b}} = \sum_\alpha \rho^\alpha \bar{\boldsymbol{b}}^\alpha \quad , \quad \rho^{tot} \dot{\bar{\boldsymbol{v}}} = \sum_\alpha \rho^\alpha \dot{\bar{\boldsymbol{v}}}^\alpha \quad \text{and} \quad \mathbf{0} = \sum_\alpha \boldsymbol{h}^\alpha. \tag{3.31}$$

The conservation of linear momentum for the mixture results as follows, considering the conditions presented in Equation (3.31):

$$\rho^{tot} \bar{\boldsymbol{b}} + \operatorname{div}\left(\boldsymbol{\sigma}^{tot}\right) - \sum_\alpha \rho^\alpha \dot{\bar{\boldsymbol{v}}}^\alpha = \mathbf{0}. \tag{3.32}$$

3.1.2.3. Conservation of angular momentum (kinetic equilibrium of moments)

The conservation of angular momentum states that the total angular momentum is constant in closed systems. The temporal change of the angular momentum equals the sum of all external moments acting on the body. The local form of the conservation of angular momentum results in the symmetry of the stress tensor after application of the divergence theorem, the Cauchy theorem and the balance of linear momentum (Equation (3.32)) and reads as:

$$\boldsymbol{\sigma}_{ij}^{tot} = \boldsymbol{\sigma}_{ji}^{tot}. \tag{3.33}$$

3.2. Extension for expansive soils

The attachment of water in different levels of the clay microstructure is indisputably the underlying mechanism of swelling of unsaturated swelling clays. The transition of the wetting fluid, mostly water, from a mobile state during flow through the available porosity, to an immobile state (with respect to water flow), furthermore results in a reduction of hydraulic conductivity, see experimental evidence in Section 2.2.2. However, the framework of the three-phase TPM of classical soil mechanics with the phases $\alpha = \{s, w, a\}$ does not allow to model this transition as only one water phase is considered. In the following, an extension of the three-phase TPM to a four-phase TPM is proposed by including a distinct phase of swelling water $\{ws\}$, thus $\alpha = \{s, wf, af, ws\}$. The extension distinguishes between two water phases: the free water, which can flow through the pore space, and the swelling water, which is attached to the solid by physico-chemical forces. The transition from free water to swelling water (and vice versa) is modelled using a mass transfer model. The indices of the *free* pore fluids $\beta = \{wf, af\}$ are extended with the letter f. Note that extensions of the TPM including mass transfer mechanisms have already been applied in various applications of continuum mechanics, e.g. for swelling gels (Sauerwein and Steeb, 2018; Sauerwein, 2021), cellulose or paperboard (Alexandersson et al. (2016)), or tissues and tumour growth in biomechanics (Humphrey and Rajagopal, 2002; Byrne and Preziosi, 2003). In soil mechanics, especially unsaturated soil mechanics, the work of Machaček (2020) and Machaček et al. (2023) for incorporation of the residual water phase and for air entrapment upon wetting of soils have proved the capability of mass transfer mechanisms.

The findings of this section have been partially published in Machaček et al. (2022), Nitsch et al. (2023b), Nitsch et al. (2023c) and Machaček et al. (2024).

3.2.1. Composition of the mixture

The extension from three to four phases in the porous medium is depicted schematically in Figure 3.3. Note that for dry conditions, when no water phase is present, both porous media are identical. Further, if no swelling occurs, the 4-phase TPM automatically transitions to the 3-phase TPM, hence the proposed extended TPM is fully backwards-compatible. Here, the REV is shown in a circular form to visualise the different levels of kinematics and structure. The whole circle represents the soil as the mixture and from the outside inwards the different phases are sorted according to their composition and motion function:

- Outer circle - **Matter:** both TPM share the same composition, as the expansive soil also consists of solid, water and air.
- Interim circle - **Phase level:** Here, the distinct swelling water phase is introduced, represented by its volume fraction φ^{ws}. The red double arrow indicates the bidirectional mass transfer between free water and swelling water.
- Inner circle - **Motion level:** Two motion levels exist in the soil, the motion of the aggregate (A) and the fluids (F). The term *aggregate* is in accordance with the general nomenclature of clay mineralogy (see Section 2.1.1), in which it describes the largest combination of solid in the fabric of a clay. In the 3-phase TPM, the solid and aggregate are identical. In the extended TPM, the swelling water phase is kinematically attached to the solid, as it is considered as part of the aggregate. In contrast to the aggregate, both mobile pore fluids, free water and free air, move freely in the pore space, though with different velocities (indicated by the dotted line). For both pore fluids, the motion is described in a modified Eulerian framework. Their relative flow with respect to the solid phase is governed by the generalised Darcy law (see Equation (3.16)).

The model decomposition of the 4-phase TPM is thus given by the aggregate $\varphi^A = \varphi^s \cup \varphi^{ws}$ and the pore fluids $\varphi^F = \varphi^{wf} \cup \varphi^{af}$, which form the mixture $\varphi = \varphi^A \cup \varphi^F$. Note that the additive split, e.g. $\sqcup^F = \sqcup^{wf+af} = \sqcup^{wf} + \sqcup^{af}$, applies to all introduced combinations. The saturation condition from Equation (3.2) reads as follows for the extended TPM:

$$\sum_{\alpha} \varphi^{\alpha} = \underbrace{\varphi^s + \varphi^{ws}}_{\varphi^A} + \underbrace{\varphi^{wf} + \varphi^{af}}_{\varphi^F} = 1. \tag{3.34}$$

Figure 3.4 visualises the REV for the extended TPM similar to Figure 3.1. The aforementioned theoretical considerations are linked to the simplified microstructure of an expansive clay. As can be seen, different levels of porosity exist in unsaturated swelling clays due to their specific mineralogy (see Section 2.1.1). Upon wetting, the free water phase (wf) flows through the pore space, which is otherwise filled with free air (af), and a proportion of the water will be attached to the aggregate: as inter-crystalline swelling water within the layers and as an osmotic or diffuse swelling water envelope around the particles in the aggregate. Both kinds of swelling water phases are treated conceptualized as kinematically identical in this work and are summarised as a single phase, the swelling water (ws).

The definition of porosity from Equation (3.3) is still valid for the extended TPM, however, it does not provide any information regarding the swelling water attached to the solid and the associated reduction of the pore space available for flow of the free pore fluids. Therefore, an *effective* porosity with respect to the aggregates n^A is introduced:

$$n = 1 - \varphi^s, \tag{3.35}$$

$$n^A = 1 - \varphi^s - \varphi^{ws} = n - \varphi^{ws}. \tag{3.36}$$

Notice that n^A automatically transitions to n if no swelling occurs and thus no swelling water exists in the porous medium ($\varphi^{ws} = 0$). The same applies for the void ratio with respect to the aggregates:

$$e = \frac{1 - \varphi^s}{\varphi^s} = \frac{n}{1 - n}, \tag{3.37}$$

$$e^A = \frac{1 - \varphi^s - \varphi^{ws}}{\varphi^s + \varphi^{ws}} = \frac{n^A}{1 - n^A}. \tag{3.38}$$

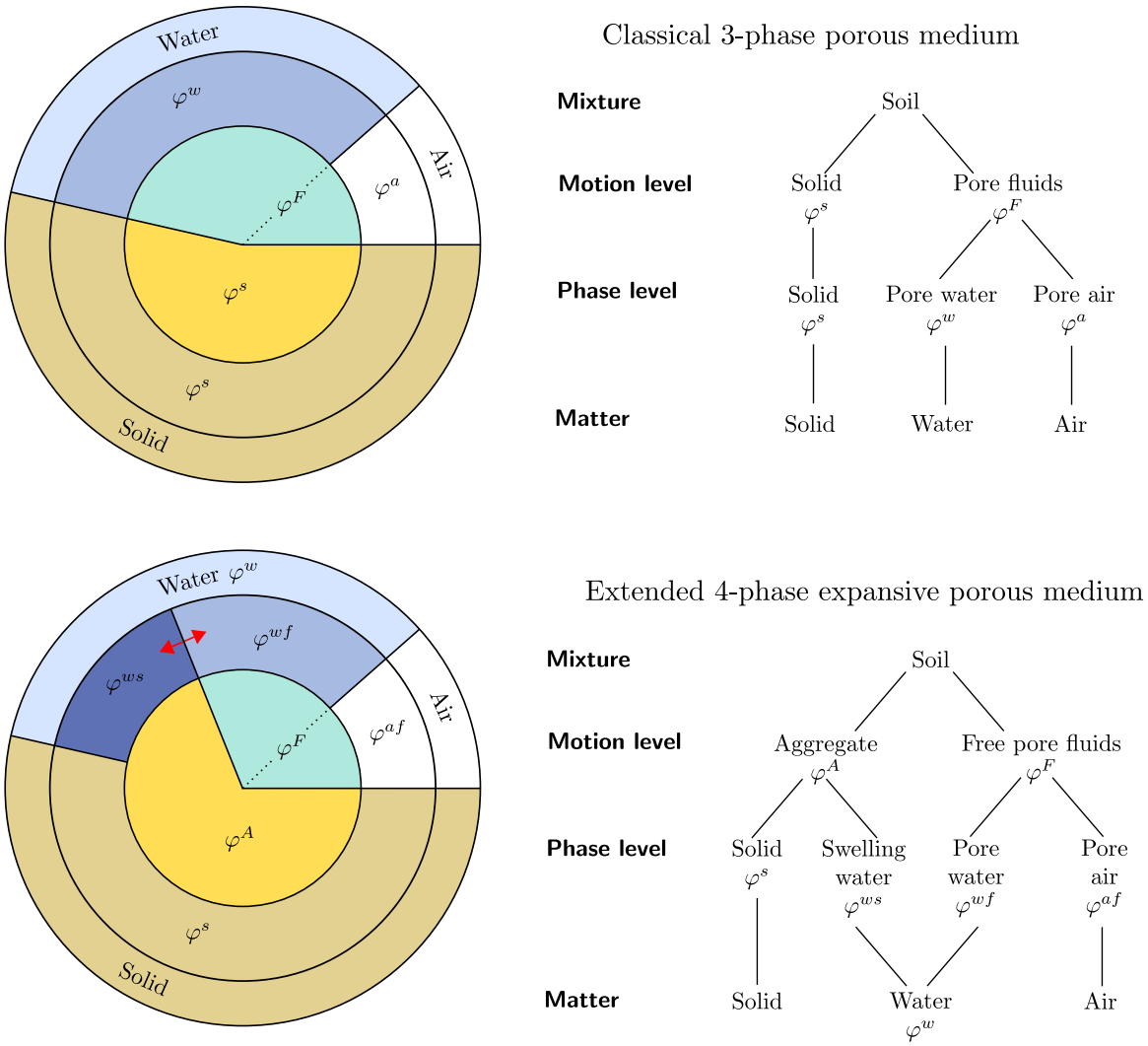

Figure 3.3.: Schematic representation of the volume fractions in the representative elementary volume (REV) of the extended TPM: Decomposition and volume fractions. The red double arrow indicates mass transfer between the free water and the swelling water. Modified from Nitsch et al. (2023b).

Similarly, the definitions of the degree of saturation from Equation (3.4) are still valid for the extended TPM. With the new notation they are:

$$S^w = \frac{\varphi^w}{1-\varphi^s} = \frac{\varphi^{wf+ws}}{1-\varphi^s} \quad \text{and} \quad S^{af} = \frac{\varphi^{af}}{1-\varphi^s}. \tag{3.39}$$

Consequently the volume fractions of water, free water and free air are defined as:

$$\varphi^w = nS^w, \tag{3.40}$$
$$\varphi^{wf} = \varphi^w - \varphi^{ws} = nS^w - \varphi^{ws}, \quad \text{and} \tag{3.41}$$
$$\varphi^{af} = n\left(1 - S^w\right). \tag{3.42}$$

Analogous to Equation (3.7), the total density of the mixture is obtained by summing the partial

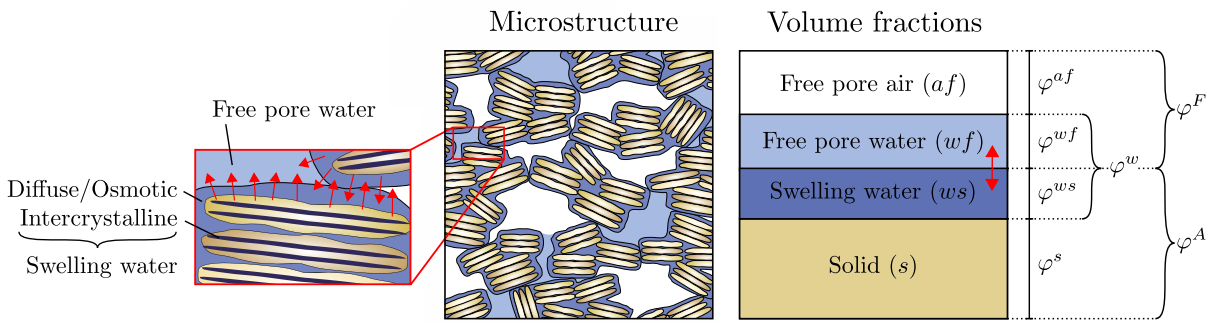

Figure 3.4.: Schematic representation of the simplified microstructure and volume fractions of expansive soils in this work. The red double arrow indicates possible mass transfer between the free water and the swelling water. Modified from Machaček et al. (2022).

densities ρ^α:

$$\rho^{tot} = \sum_\alpha \rho^\alpha = \rho^s + \rho^{wf+ws} + \rho^{af} \tag{3.43}$$

$$= \varphi^s \bar{\rho}^s + \varphi^w \bar{\rho}^w + \varphi^a \bar{\rho}^a \tag{3.44}$$

$$= (1-n)\bar{\rho}^s + n\left(S^w \bar{\rho}^w + (1-S^w)\bar{\rho}^a\right). \tag{3.45}$$

3.2.1.1. Mass transfer

Upon wetting, a mass transfer $\hat{\rho}^\alpha$ between the free water and the swelling water phase takes place. It reads:

$$\hat{\rho}^\alpha = \hat{\rho}^w \hat{\delta}^\alpha \quad \text{with} \quad \hat{\delta}^\alpha = \begin{cases} 1 & \text{for: } \alpha = ws \\ -1 & \text{for: } \alpha = wf \\ 0 & \text{else} \end{cases} \quad \text{or} \quad \hat{\rho}^{wf} = -\hat{\rho}^{ws}. \tag{3.46}$$

Herein $\hat{\rho}^w$ is a scalar function, which shall be described by a suitable constitutive model. The operator $\hat{\delta}^\alpha$ is used to fulfil the constraint $\sum_\alpha \hat{\rho}^\alpha = 0$, as the sum of the mass transfer must vanish for the mixture. Further details on the mass transfer are given in Section 3.2.3.

3.2.1.2. Hydraulic conductivity

For description of fluid flow in the porous medium the hydraulic conductivity tensor of the pore fluids $\boldsymbol{k}^\beta$ is required. Section 2.2.2 introduced the particularities of hydraulic conductivity in an expansive soil, wherein two opposing effects occur simultaneously: the hydraulic conductivity of the free pore water $\boldsymbol{k}^{wf}$ increases due to the increase in saturation, but simultaneously decreases as water becomes adsorbed within the solid phase of the soil. While it may seem intuitive to capture both these effects within a single „swelling relative permeability model“, such an approach cannot be substantiated experimentally. Quantification of the reduction of hydraulic conductivity in the dry and fully saturated states is possible in the laboratory, while the relative permeability arising from partial saturation can be derived from the SWRC. Conceptually, it is more appropriate to superimpose a second relative permeability function to represent the

swelling-induced reduction in hydraulic conductivity. This approach also enables seamless integration into the existing numerical framework for non-swelling clays. Therefore, the relative permeability is defined as a product of both, the relative permeability for unsaturated soils $k^{r,wf}$ and a newly proposed relative permeability due to swelling $k^{r,ws}$. The intrinsic permeability now refers to an unswollen reference state and is denoted as $\boldsymbol{K}^{s}_{\mathrm{ref}}$. Equation (2.20) yields:

$$\boldsymbol{k}^{wf}\left(n, S^{e}\right) = \frac{\boldsymbol{K}^{s}_{\mathrm{ref}}\left(n\right)\,\gamma^{wf}}{\mu^{wf}}\,k^{wf}\left(S^{e}\right) \quad \text{with} \quad k^{wf}\left(S^{e}\right) = k^{r,wf}\left(S^{e}\right)k^{r,ws}. \tag{3.47}$$

The relative permeability due to swelling has the quality of a constitutive relation, which is derived in Section 3.2.4. For free pore air, only the relative permeability for unsaturated states applies:

$$\boldsymbol{k}^{af}\left(n, S^{e}\right) = \frac{\boldsymbol{K}^{s}_{\mathrm{ref}}\left(n\right)\,\gamma^{af}}{\mu^{af}}\,k^{r,af}\left(S^{e}\right). \tag{3.48}$$

3.2.2. Governing equations

The balance equations introduced in Section 3.1.2 are derived for the extended TPM. Note that the balance of angular momentum (Equation (3.33)) is not affected and remains valid. The following simplifications and resulting implications are applied in addition to those specified in Section 3.1.2:

1. Swelling water (ws) is attached to the solid: $\bar{\boldsymbol{v}}^{ws} = \bar{\boldsymbol{v}}^{s}$
2. Incompressibility of swelling water (ws): $\bar{K}^{ws} \to \infty$
3. Homogeneous distribution of the intrinsic density of swelling water (ws): $\operatorname{grad}\left(\bar{\rho}^{ws}\right) = 0$
4. Equal intrinsic density of the water phases: $\bar{\rho}^{ws} = \bar{\rho}^{wf} = \bar{\rho}^{w}$

3.2.2.1. Conservation of mass

The conservation of mass for each individual phase α is derived from Equation (3.21). The conservation of mass of the solid yields the evolution equation of the solid volume fraction φ^{s}:

$$\underbrace{\frac{\varphi^{s}}{\bar{K}^{s}}\frac{\mathrm{d}\bar{p}^{s}}{\mathrm{d}t}}_{\to 0} + \frac{\mathrm{d}\varphi^{s}}{\mathrm{d}t} + \varphi^{s}\operatorname{div}\left(\bar{\boldsymbol{v}}^{s}\right) = 0$$

$$\Leftrightarrow \frac{\mathrm{d}\varphi^{s}}{\mathrm{d}t} = -\left(1-n\right)\operatorname{div}\left(\bar{\boldsymbol{v}}^{s}\right), \tag{3.49}$$

or in terms of the porosity n:

$$\frac{\mathrm{d}n}{\mathrm{d}t} = \left(1-n\right)\operatorname{div}\left(\bar{\boldsymbol{v}}^{s}\right). \tag{3.50}$$

The conservation of mass of the swelling water gives the evolution equation of the swelling water phase φ^{ws} with consideration of the mass transfer from Equation (3.46):

$$\underbrace{\frac{\varphi^{ws}}{\bar{K}^{ws}}\frac{\mathrm{d}\bar{p}^{ws}}{\mathrm{d}t}}_{\to 0} + \frac{\mathrm{d}\varphi^{ws}}{\mathrm{d}t} + \varphi^{ws}\operatorname{div}\left(\bar{\boldsymbol{v}}^{s}\right) = \frac{\hat{\rho}^{w}}{\bar{\rho}^{w}}$$

$$\Leftrightarrow \frac{\mathrm{d}\varphi^{ws}}{\mathrm{d}t} = \frac{\hat{\rho}^{w}}{\bar{\rho}^{w}} - \varphi^{ws}\operatorname{div}\left(\bar{\boldsymbol{v}}^{s}\right). \tag{3.51}$$

As becomes apparent from Equation (3.51), the mass transport represents a density production and must have the quality of a temporal change of a volume fraction, hence a rate. The conservation of mass for the free pore air reads:

$$\frac{\varphi^{af}}{\bar{K}^{af}}\frac{\mathrm{d}\bar{p}^{af}}{\mathrm{d}t} + \frac{1}{\bar{K}^{af}}\operatorname{grad}\left(\bar{p}^{af}\right)\cdot\boldsymbol{w}^{af} + \frac{\mathrm{d}\varphi^{af}}{\mathrm{d}t} + \operatorname{div}\left(\boldsymbol{w}^{af}\right) + \varphi^{af}\operatorname{div}\left(\bar{\boldsymbol{v}}^{s}\right) = 0, \tag{3.52}$$

and the conservation of mass for the free water is obtained by inserting the mass transfer from Equation (3.46) into Equation (3.23):

$$\begin{aligned}
&\frac{\varphi^{wf}}{\bar{K}^{wf}}\frac{\mathrm{d}\bar{p}^{wf}}{\mathrm{d}t} + \frac{1}{\bar{K}^{wf}}\operatorname{grad}\left(\bar{p}^{wf}\right)\cdot\boldsymbol{w}^{wf} + \frac{\mathrm{d}\varphi^{wf}}{\mathrm{d}t} + \operatorname{div}\left(\boldsymbol{w}^{wf}\right) + \varphi^{wf}\operatorname{div}\left(\bar{\boldsymbol{v}}^{s}\right) = \frac{-\hat{\rho}^{w}}{\bar{\rho}^{w}} \\
\Leftrightarrow\ &\frac{\varphi^{wf}}{\bar{K}^{wf}}\frac{\mathrm{d}\bar{p}^{wf}}{\mathrm{d}t} + \frac{1}{\bar{K}^{wf}}\operatorname{grad}\left(\bar{p}^{wf}\right)\cdot\boldsymbol{w}^{wf} + \frac{\mathrm{d}\varphi^{wf}}{\mathrm{d}t} + \operatorname{div}\left(\boldsymbol{w}^{wf}\right) + \varphi^{wf}\operatorname{div}\left(\bar{\boldsymbol{v}}^{s}\right) + \frac{\hat{\rho}^{w}}{\bar{\rho}^{w}} = 0.
\end{aligned} \tag{3.53}$$

The conservation of mass of the aggregates $\varphi^{A} = \varphi^{s+ws}$, hence combining Equations (3.50) and (3.51), gives the evolution equation of the effective porosity with respect to the aggregates n^{A}:

$$\frac{\mathrm{d}n^{A}}{\mathrm{d}t} = \frac{\mathrm{d}n}{\mathrm{d}t} - \frac{\mathrm{d}\varphi^{ws}}{\mathrm{d}t} = \left(1 - n^{A}\right)\operatorname{div}\left(\bar{\boldsymbol{v}}^{s}\right) - \frac{\hat{\rho}^{w}}{\bar{\rho}^{w}}. \tag{3.54}$$

The evolution of the total water phase φ^{w} and pore air phase φ^{af} are obtained by differentiation of Equations (3.40) and (3.42) with respect to time:

$$\frac{\mathrm{d}\varphi^{w}}{\mathrm{d}t} = \frac{\mathrm{d}}{\mathrm{d}t}\left(nS^{w}\right) = \frac{\mathrm{d}n}{\mathrm{d}t}S^{w} + n\frac{\mathrm{d}S^{w}}{\mathrm{d}t} = (1-n)\operatorname{div}\left(\bar{\boldsymbol{v}}^{s}\right)S^{w} + n\frac{\mathrm{d}S^{w}}{\mathrm{d}t}. \tag{3.55}$$

$$\frac{\mathrm{d}\varphi^{af}}{\mathrm{d}t} = \frac{\mathrm{d}}{\mathrm{d}t}\left(n(1-S^{w})\right) = \frac{\mathrm{d}n}{\mathrm{d}t}\left(1-S^{w}\right) - n\frac{\mathrm{d}S^{w}}{\mathrm{d}t} = (1-n)\operatorname{div}\left(\bar{\boldsymbol{v}}^{s}\right)\left(1-S^{w}\right) - n\frac{\mathrm{d}S^{w}}{\mathrm{d}t}. \tag{3.56}$$

With Equations (3.51) and (3.41) the evolution of the free water phase φ^{wf} reads:

$$\frac{\mathrm{d}\varphi^{wf}}{\mathrm{d}t} = \frac{\mathrm{d}\varphi^{w}}{\mathrm{d}t} - \frac{\mathrm{d}\varphi^{ws}}{\mathrm{d}t} = (1-n)\operatorname{div}\left(\bar{\boldsymbol{v}}^{s}\right)S^{w} + n\frac{\mathrm{d}S^{w}}{\mathrm{d}t} - \left(\frac{\hat{\rho}^{w}}{\bar{\rho}^{w}} - \varphi^{ws}\operatorname{div}\left(\bar{\boldsymbol{v}}^{ws}\right)\right). \tag{3.57}$$

3.2.2.2. Conservation of linear momentum

Derivation of the conservation of linear momentum for the mixture obtained from Equation (3.32) includes the contribution of the mass transfer (Equation (3.46)) between the free water phase and swelling water phase. The latter reads:

$$-\sum_{\alpha}\hat{\rho}^{\alpha}\bar{\boldsymbol{v}}^{\alpha} = -\hat{\rho}^{w}\left(-\bar{\boldsymbol{v}}_{i}^{wf} + \bar{\boldsymbol{v}}_{i}^{s}\right) = \hat{\rho}^{w}\left(\bar{\boldsymbol{v}}_{i}^{wf} - \bar{\boldsymbol{v}}_{i}^{s}\right) = \hat{\rho}^{w}\frac{\boldsymbol{w}^{wf}}{\varphi^{wf}}. \tag{3.58}$$

The mass transfer term in Equation (3.58) accounts for the different velocities of free pore water and swelling water and its effect on the linear momentum. Similar momentums from mass transfer were also obtained by e.g. Machaček (2020) and Sauerwein (2021). The balance of linear momentum for the mixture is:

$$\rho^{tot}\boldsymbol{b} + \operatorname{div}\left(\boldsymbol{\sigma}^{tot}\right) - \left(\rho^{s+ws}\right)\bar{\boldsymbol{a}}^{s} - \rho^{wf}\bar{\boldsymbol{a}}^{wf} - \rho^{af}\bar{\boldsymbol{a}}^{af} + \hat{\rho}^{w}\frac{\boldsymbol{w}^{wf}}{\varphi^{wf}} = 0. \tag{3.59}$$

In addition, the conservation of linear momentum for the pore fluids is presented, based on Equation (3.25). Assuming isothermal conditions, they yield the so-called generalised Darcy equations (Schrefler et al., 1990; Ehlers and Bluhm, 2002). They read for the free pore air:

$$\boldsymbol{w}^{af} = \frac{\boldsymbol{K}^{s}_{\mathrm{ref}}\, k^{r,af}}{\bar{\mu}^{\beta}} \left(- \operatorname{grad}\left(\bar{p}^{af}\right) + \bar{\rho}^{af}\left(\bar{\boldsymbol{b}} - \dot{\bar{\boldsymbol{v}}}^{af}\right)\right), \tag{3.60}$$

and for the free pore water:

$$\boldsymbol{w}^{wf} = \frac{\boldsymbol{K}^{s}_{\mathrm{ref}}\, k^{r,wf} k^{r,ws}}{\bar{\mu}^{\beta}} \left(- \operatorname{grad}\left(\bar{p}^{wf}\right) + \bar{\rho}^{wf}\left(\bar{\boldsymbol{b}} - \dot{\bar{\boldsymbol{v}}}^{wf}\right)\right). \tag{3.61}$$

3.2.3. Mass transfer model

The mass transfer mechanism between the free water φ^{wf} and the swelling water φ^{ws} introduced in Section 3.2.1.1 requires the formulation of a suitable constitutive model for the scalar function $\hat{\rho}^{w}/\bar{\rho}^{w}$. Machaček (2020) proposed a simple phenomenological model for the mass transfer in the framework of an extended TPM for air entrapment, which serves as a basis for this work. A ratio of the two phases involved in the mass transfer was formulated, for which in turn an evolution equation is postulated. A similar ratio was introduced by Sauerwein and Steeb (2018) for swelling gels, and referred to as the degree of swelling. The mass transfer appears as a density production term, active only until a target state is reached. This state serves as a limit and is approached asymptotically. The constitutive model is derived considering the following observations and assumptions:

1. The amount of swelling water must never exceed the total amount of water, hence the sum of free water and swelling water must fulfil $\varphi^{ws} \leq \varphi^{wf+ws}$.

2. Mass transfer from free water to swelling water only occurs during swelling processes. Swelling can be induced by either changes in the degree of saturation ($\mathrm{d}S^{w}/\mathrm{d}t \neq 0$) or displacement/stress boundary conditions ($\mathrm{d}n/\mathrm{d}t \neq 0$).

3. During compression of a saturated solid after swelling ($S^{w} = 1$ and $\varphi^{ws} > 0$) any reduction of volume is accompanied by an outflow of water. Free water drains and the amount of swelling water is reduced as the first condition above must apply at all times. Drainage of swelling water is actually a two-step process: first, swelling water transitions to free water, then, it flows through the pore space.

In accordance with the first consideration, for a given state ($\operatorname{div}(\bar{\boldsymbol{v}}^{ws}) = \operatorname{div}(\bar{\boldsymbol{v}}^{s}) = 0$) let ϕ denote the ratio between the swelling water φ^{ws} and the total water volume fraction $\varphi^{w} = \varphi^{wf+ws}$ such that:

$$\varphi^{ws} = \phi \varphi^{w}. \tag{3.62}$$

The rate form of Equation (3.62) is:

$$\frac{\mathrm{d}\varphi^{ws}}{\mathrm{d}t} = \frac{\mathrm{d}\varphi^{w}}{\mathrm{d}t}\phi + \frac{\mathrm{d}\phi}{\mathrm{d}t}\varphi^{w}, \tag{3.63}$$

wherein the first multiplier $\mathrm{d}\varphi^{w}/\mathrm{d}t$ was already derived in Equation (3.55) from the conservation of mass of the water phases wf and ws. The multipliers ϕ and φ^{w} are known for a

given state. Only the second multiplier $\mathrm{d}\phi/\mathrm{d}t$ remains unknown. Based on the aforementioned considerations, a constitutive model based on the following relation is proposed:

$$\frac{\mathrm{d}\phi}{\mathrm{d}t} = c_\phi \left(\phi^{\max} - \phi\right) \left\langle \frac{\mathrm{d}S^w}{\mathrm{d}t} \right\rangle . \tag{3.64}$$

The Macaulay brackets ensure that no swelling water is reduced alongside the drainage of free water during a dewatering process. The amount of swelling water is only reduced by the condition $\varphi^w = \varphi^{wf} + \varphi^{ws}$, which must be maintained at all times. $\phi^{\max} \leq 1$ controls the maximum swelling water content. c_ϕ, a model parameter, controls the evolution of $\mathrm{d}\phi/\mathrm{d}t$. The final mass transfer model reads:

$$\begin{aligned} \frac{\hat{\rho}^w}{\rho^w} &= \frac{\mathrm{d}\varphi^w}{\mathrm{d}t}\phi + c_\phi \left(\phi^{\max} - \phi\right) \left\langle \frac{\mathrm{d}S^w}{\mathrm{d}t} \right\rangle \varphi^w \quad \text{or} \\ \frac{\hat{\rho}^w}{\rho^w} &= \left(\frac{\mathrm{d}S^w}{\mathrm{d}t} n + \frac{\mathrm{d}n}{\mathrm{d}t} S^w \right) \phi + c_\phi \left(\phi^{\max} - \phi\right) \left\langle \frac{\mathrm{d}S^w}{\mathrm{d}t} \right\rangle n S^w . \end{aligned} \tag{3.65}$$

The maximum swelling water content $\phi^{\max}$ may be defined as a parameter or a function depending on the mechanical boundary conditions. The definition of $\phi^{\max}$ is inherently linked to the constitutive description of swelling-induced relative permeability. Accordingly, the concept for the latter is introduced first, before addressing the parameters and performance of the mass transfer model in Section 3.2.5.

3.2.4. Relative permeability due to swelling

The reduction in hydraulic conductivity due to swelling is directly linked to the accumulation of water within the solid structure of the soil and the decrease of the effective porosity available for flow. The extension of the TPM directly allows to quantify this effective porosity, which was introduced as the aggregate porosity in Equation (3.35). Its evolution was derived by considering the mass conservation of the aggregate phase φ^A in Equation (3.54). In this work, a Kozeny-Carman proportionality is used to approximate the swelling-induced relative permeability based on the aggregate porosity n^A. This proportionality was introduced in Equation (2.17) for the saturated hydraulic conductivity of soils as:

$$k^{wf}(S^w = 1, \varphi^{ws} = 0) \propto \frac{n^3}{(1-n)^2}, \tag{3.66}$$

wherein n is the overall porosity. $\varphi^{ws} = 0$ indicates that swelling is not considered yet. Assuming that the same proportionality applies for soils with swelling water ($\varphi^{ws} > 0$) in the saturated state, but taking the reduced aggregate porosity n^A into account, yields:

$$k^{wf}(S^w = 1, \varphi^{ws} > 0) \propto \frac{(n^A)^3}{(1-n^A)^2}. \tag{3.67}$$

The ratio of the reduced hydraulic conductivity due to swelling compared to the non-swollen state is interpreted as a relative permeability for the swollen porous medium $k^{r,ws}$ as:

$$k^{r,ws} = \frac{k^{wf}(S^w = 1, \varphi^{ws} > 0)}{k^{wf}(S^w = 1, \varphi^{ws} = 0)} = \frac{(n^A)^3}{(1-n^A)^2} \frac{(1-n)^2}{n^3}, \tag{3.68}$$

wherein the attachment of water on and in the solid matrix is considered, reducing the pore space available for flow. The reduction refers to the reference value of the intrinsic, saturated

permeability K^s_{ref} in the non-swollen state. The apparent saturated permeability of the swollen material K^s thus reads:

$$K^s = k^{r,ws} K^s_{\mathrm{ref}}. \tag{3.69}$$

In Equation (3.68), both n and n^A must correspond to the same, current (and possibly expanded) state, as the global porosity n may evolve. To consider the global change in volume, two possibilities exist:

1. The evolution of n^A in Equation (3.68) must consider effects from global porosity changes, allowing to use an independent, constant reference permeability $K^s_{\mathrm{ref}}(n_{\mathrm{ref}})$ at all times, which corresponds to the (initial) reference porosity n_{ref} (Machaček et al., 2022; Nitsch et al., 2023c).
2. Alternatively, the global change in volume is considered separately in a more distinctive approach, which uses a double Kozeny-Carman proportionality to scale the reference permeability $K^s_{\mathrm{ref}}(n_{\mathrm{ref}})$ from the initial to the current porosity (Machaček et al., 2024).

The first approach described by Equation (3.68) is denoted with the subscript one, i.e. $k^{r,ws,1}$. In the second approach, denoted with the subscript two, i.e. $k^{r,ws,2}$, changes in the current porosity n are related to the initial porosity n_{ref}, and Equation (3.68) is redefined as:

$$\begin{aligned} k^{r,ws,2} = \frac{k^{wf}(S^w = 1, \varphi^{ws} > 0)}{k^{wf}(S^w = 1, \varphi^{ws} = 0)} &= \underbrace{\left(\frac{(n^A)^3}{(1-n^A)^2} \frac{(1-n)^2}{n^3} \right)}_{\text{attachment of swelling water}} \underbrace{\left(\frac{(n)^3}{(1-n)^2} \frac{(1-n_{\mathrm{ref}})^2}{(n_{\mathrm{ref}})^3} \right)}_{\text{change in volume}}, \\ &= \underbrace{\frac{(n^A)^3}{(1-n^A)^2}}_{\text{attachment of swelling water}} \underbrace{\frac{(1-n_{\mathrm{ref}})^2}{(n_{\mathrm{ref}})^3}}_{\text{change in volume}}. \end{aligned} \tag{3.70}$$

In Equation (3.70), the expression in the first bracket takes into account the attachment of water on and in the solid matrix, while the expression in the second bracket takes into account the change in volume during a swelling process. If no swelling occurs ($\varphi^{ws} = 0$) and constant volume conditions apply ($n = n_{\mathrm{ref}}$), $k^{r,ws,\sqcup} = 1$ holds. Here, n_{ref} is the reference porosity at which the permeability of the non-swollen, but saturated, material was determined. Note further, that contrary to the relative permeability $k^{r,wf}$ introduced to account for the influence of partial saturation, the swelling-induced relative permeability does not yield $k^{r,ws,\sqcup} = 1$ for $S^w = 1$ and thereby leads to the permanent reduction in permeability at full saturation observed in experiments. Equation (3.69) is based on the simplifying assumption that the (an)isotropy of the permeability does not change as a result of the swelling process. Both approaches for the relative permeability due to swelling, $k^{r,ws,1}$ from Equation (3.68) and $k^{r,ws,2}$ from Equation (3.70), are considered in the following. Neither approach requires material parameters, however, they are both governed by the material parameters of the constitutive relation of the mass transfer. The following section discusses their significance and calibration.

3.2.5. Material parameters

This section focusses on the material parameters, which are required for the extended TPM. They refer to the mass transfer model, but are closely linked to the swelling-induced relative permeability. The calibration of the parameters is presented using experimental evidence on the

permeability in different states from the campaign on reconstituted Opalinus clay (Nitsch et al., 2023a) (see Section 2.2.2). As the permeability was determined under oedometric conditions, it is treated as a scalar rather than a tensorial quantity in the subsequent analysis.

The first parameter c_ϕ controls the evolution of the ratio $\mathrm{d}\phi/\mathrm{d}t$ and is required to ensure that $\phi^{\max}$ is reached at full saturation. It can be set to a high value based on experience, e.g. 10. The significance of c_ϕ on the evolution of ϕ is depicted in Figures 3.6 and 3.9. The second parameter, the maximum swelling water ratio $\phi^{\max}$, works as an upper limit for the volume fraction of the swelling water. It must be less than 1 at all times, as a full mass transfer from mobile to adsorbed water would result in an impermeable material. Rather, the permeability of the material is reduced significantly, which indicates a high value estimated between 0.8 and 0.95. Direct quantification in the laboratory remains challenging, thus in this work, the magnitude is deduced from permeability measurements. Experimental evidence presented in Section 2.2.2 showed that the reduction of permeability of the expansive soil is in the order of several magnitudes in comparison to a dry reference state, and more pronounced under constant volume (CV) conditions than under vertically unconfined (VU) conditions. Two approaches for the definition of $\phi^{\max}$ are presented.

Switch approach to $\phi^{\max}$

The switch approach as introduced in Machaček et al. (2022) and Nitsch et al. (2023c) accounts for possible changes of porosity due to expansion upon wetting within the mass transfer mechanism. It must therefore consider the first relative permeability approach $k^{r,ws,1}$ due to swelling in Equation (3.68), in which the reduced aggregate porosity n^A and current porosity n in the same state are used. Based on the above described second observation, the reduced aggregate porosity n^A must be smaller in relation to the total porosity for constant volume than for vertically unconfined conditions and thus, the relative amount of swelling water must be greater for constant volume conditions. Therefore the ratio $\phi^{\max}$ is not constant, but depends on the boundary conditions. It switches between the two extreme states of vertically unconfined and constant volume swelling. The following relationship is proposed:

$$\phi^{\max} = \phi^{\max}_{\mathrm{VU}} - (\phi^{\max}_{\mathrm{CV}} - \phi^{\max}_{\mathrm{VU}}) \left\langle \operatorname{sgn}\left(\frac{\mathrm{d}n}{\mathrm{d}t}\right) \right\rangle . \tag{3.71}$$

Therein, $\phi^{\max}_{\mathrm{CV}} \leq 1$ and $\phi^{\max}_{\mathrm{VU}} \leq \phi^{\max}_{\mathrm{CV}}$ are material parameters controlling the maximum swelling water content. $\phi^{\max}_{\mathrm{VU}}$ corresponds to vertically unconfined conditions and $\phi^{\max}_{\mathrm{CV}}$ to constant volume conditions. The term in Macaulay brackets $\langle \sqcup \rangle$ is an indicator of whether or not constant volume swelling conditions are active and thus controls the maximum achievable swelling water content. $\phi^{\max}_{\mathrm{VU}}$ and $\phi^{\max}_{\mathrm{CV}}$ can be calibrated by either fitting the time evolution of swelling pressure or swelling strain in a transient simulation or by computing the permeability in accordance to experimental results. For this, the aggregate porosity can be computed by solving Equation (3.69) with consideration of Equation (3.68) for n^A. In the (water) saturated state $n = \varphi^w$, $n^A = \varphi^{wf}$ and $\varphi^{ws} = \varphi^w - \varphi^{wf} = n - n^A$ apply. Herein, n is the current porosity. It is:

$$\phi^{\max}_{\mathrm{VU}} = \left.\frac{\varphi^{ws}}{\varphi^w}\right|_{\mathrm{VU}} = \left.\frac{n - n^A}{n}\right|_{\mathrm{VU}} \quad \text{and} \quad \phi^{\max}_{\mathrm{CV}} = \left.\frac{\varphi^{ws}}{\varphi^w}\right|_{\mathrm{CV}} = \left.\frac{n - n^A}{n}\right|_{\mathrm{CV}} . \tag{3.72}$$

For reconstituted Opalinus clay, the relevant experimental evidence and resulting values for ϕ are gathered in Table 3.1. The two model parameters are $\phi^{\max}_{\mathrm{CV}} = 0.871$ for constant volume conditions and $\phi^{\max}_{\mathrm{VU}} = 0.827$ for vertically unconfined conditions.

Table 3.1.: Experimental results of permeability testing on reconstituted Opalinus clay shale (Nitsch et al., 2023a) and derived values for the aggregate porosity n^A and ratio ϕ based on Equation (3.69).

Condition	n	K^s in m^2	n^A	ϕ
Dry	0.2801	1.0×10^{-15}	-	-
Vertically unconfined (VU)	0.3395	2.6×10^{-18}	0.0589	0.827
Constant volume (CV)	0.279	1.2×10^{-18}	0.0360	0.871

With these parameters, the performance of the mass transport and relative permeability approach $k^{r,ws,1}$ was evaluated by means of simulations of swelling tests under vertically unconfined and constant volume conditions as well as constant volume conditions followed by unloading. For this purpose, the initial and final values of the void ratio (or porosity) and effective degree of saturation from the experiments were incremented linearly and Equations (3.62) – (3.65) were evaluated for increments Δn and ΔS^e. The results are shown in Figure 3.5. On the left-hand side of Figure 3.5, the evolution of the swelling-induced relative permeability $k^{r,ws,1}$ is shown from simulations for three loading paths: swelling under vertically unconfined conditions, swelling under constant volume, and constant volume followed by unloading on Opalinus clay. The latter two paths converged upon saturation. Under dry conditions, $k^{r,ws,1}$ was equal to one and decreased as saturation increased. On the right-hand side of Figure 3.5, the apparent permeability K^s is shown, comparing model results (dashed lines) with experimental data (markers). The experiments represent fully saturated states. The permeability of the dry (air-saturated) material is indicated by the black star, from which the dashed lines illustrate the decrease in permeability due to swelling as saturation (and thus swelling) progressed.

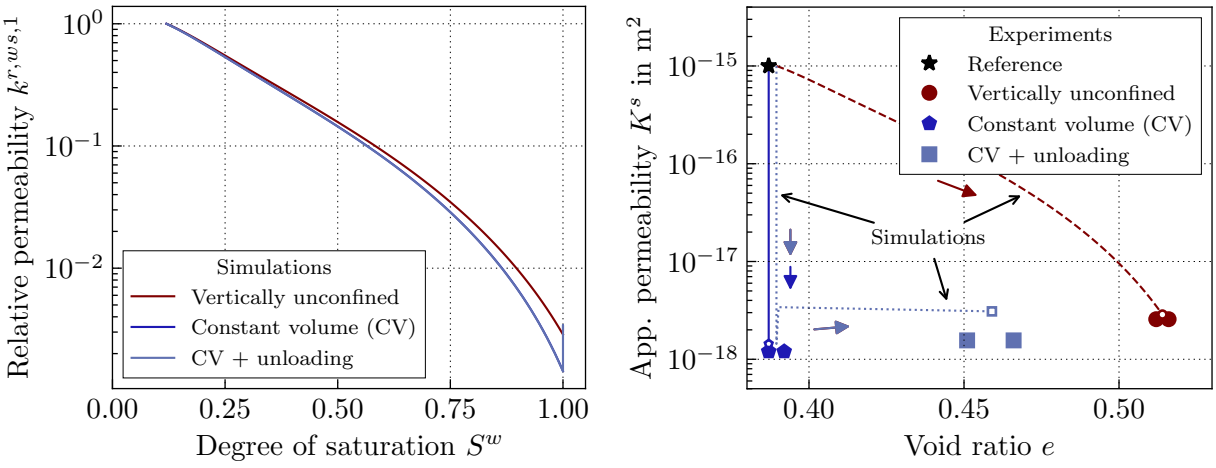

Figure 3.5.: Relative permeability $k^{r,ws,1}$ for the mass transfer model with switch approach $\phi^{\max}$ vs. degree of saturation (left) and saturated, apparent permeability K^s vs. void ratio (right) for the experiments (symbols) and the simulations (lines). Modified from Machaček et al. (2022).

The simulations show very good agreement with the experimental results under both constant volume and vertically unconfined conditions. However, for the unloading case following constant volume conditions, the model underestimated the permeability reduction. This discrepancy arose from a limitation in the switch-based approach and became apparent in the evolution of the swelling water ratio ϕ, shown in Figure 3.6 for all three boundary conditions and for different values of the parameter c_ϕ. For vertically unconfined and constant volume conditions,

ϕ approached $\phi^{\max} = \phi^{\max}_{\mathrm{VU}}$ and $\phi^{\max} = \phi^{\max}_{\mathrm{CV}}$, respectively, and the results demonstrate that a value of $c_\phi = 10$ was sufficiently high to ensure that $\phi^{\max}$ was reached under full saturation.

During unloading after constant volume swelling, the porosity evolved ($\langle \mathrm{sgn}\,(\mathrm{d}n/\mathrm{d}t)\rangle \neq 0$), and ϕ decreased towards the lower limiting value of $\phi^{\max} = \phi^{\max}_{\mathrm{VU}}$. As a result, the associated reduction in permeability was underestimated (see Figure 3.5). From a physical perspective, such behaviour is implausible, as the ratio of swelling water to total water should not change abruptly, however it is inevitable due to the nature of the switch approach.

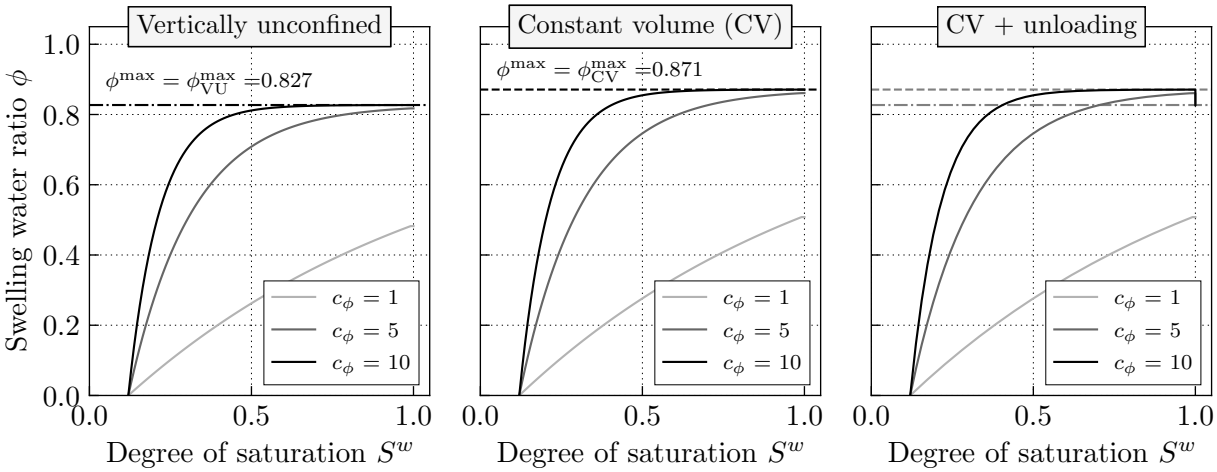

Figure 3.6.: Swelling water ratio ϕ vs. degree of saturation: Influence of c_ϕ on the evolution during saturation for vertically unconfined (left), constant volume (centre) and constant volume conditions with subsequent unloading (right). Modified from Machaček et al. (2022).

Constant approach for $\phi^{\max}$

Application of a constant attractor $\phi^{\max}$ and consideration of the change in global volume within a second proportionality in the relative permeability approach $k^{r,ws,2}$, as was presented in Equation (3.70) and introduced in Machaček et al. (2024), offers several advantages:

- The constitutive model for the mass transfer only requires two parameters in total ($\phi^{\max}$ and c_ϕ).
- For calibration only knowledge of the apparent permeability in the saturated state is required, which can be determined for the experimentally most simple boundary conditions of constant volume.
- Transitional states in between the two limit states of vertically unconfined and constant volume swelling are automatically considered.

The parameter $\phi^{\max}$ is identical to the previous parameter $\phi^{\max}_{\mathrm{CV}}$, and can - due to the consistency of the approach - be evaluated using any pair of swollen saturated permeability and porosity. The aggregate porosity can be determined by solving Equations (3.69) and (3.70) for n^A and computing $\phi^{\max}$ with the knowledge of n:

$$\phi^{\max} = \frac{\varphi^{ws}}{\varphi^{w}} = \frac{n - n^A}{n}. \tag{3.73}$$

The evaluation of the experimental results for reconstituted Opalinus clay is presented in Table 3.2. The values of ϕ computed for the different boundary conditions demonstrate good

agreement within each other, particularly when considering the general uncertainties associated with permeability measurements. Equation (3.69) is illustrated in Figure 3.7 for the experiments on Opalinus clay. On the left-hand side, the good accordance between the Kozeny–Carman relationship for global volume change and the saturated permeabilities from the experiments, as a function of the respective void ratios, is clearly evident. On the right-hand side, the double Kozeny–Carman relationship is depicted against the corresponding aggregate porosity, confirming the applicability of the Kozeny–Carman proportionality across the full range of conditions occurring during swelling.

Table 3.2.: Experimental results of permeability testing on reconstituted Opalinus clay shale (Nitsch et al., 2023a) and derived values for the aggregate porosity n^A and ratio ϕ based on Equation (3.69).

Condition	n	K^s in m^2	n^A	ϕ
Dry	0.2801 (n_{ref})	1.0×10^{-15}	-	-
Vertically unconfined	0.3395	2.6×10^{-18}	0.0461	0.864
Constant volume (CV)	0.2790	1.2×10^{-18}	0.0360	0.871
CV + unloading	0.3144	1.6×10^{-18}	0.0392	0.875

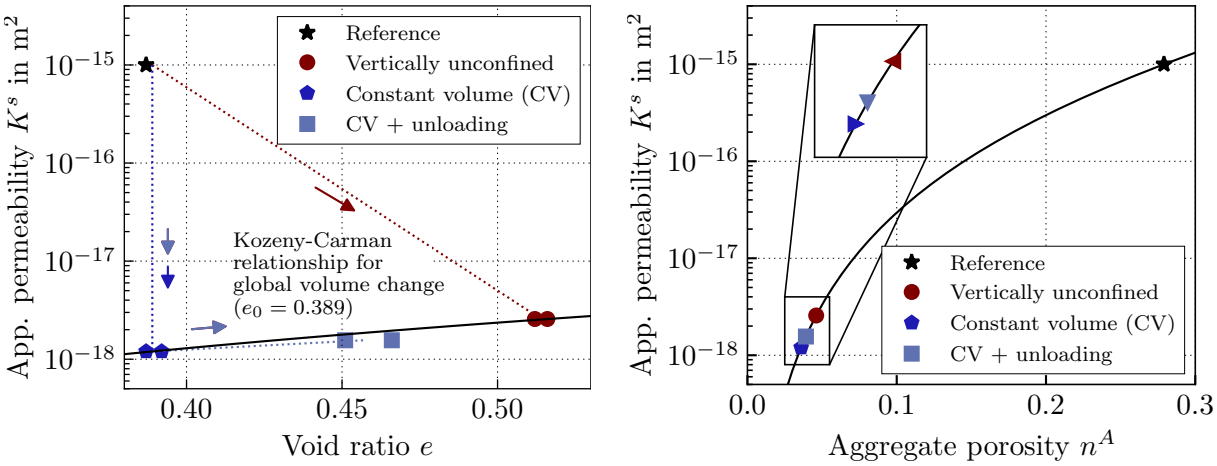

Figure 3.7.: Saturated, apparent permeability K^s vs. void ratio (left) and aggregate porosity (right) using a double Kozeny-Carman proportionality (Equation (3.69)) and for experimental results of reconstituted Opalinus clay.

Analogous to the evaluation of $k^{r,ws,1}$, the mass transport and relative permeability in experiments on Opalinus clay were predicted using the approach of $k^{r,ws,2}$. The maximum swelling water content was set to $\phi^{\max} = 0.871$. On the left-hand side of Figure 3.8, the simulated evolution of the swelling-related relative permeability $k^{r,ws,2}$ is shown for the three boundary conditions. In contrast to Figure 3.5, the relative permeability for both vertically unconfined and constant volume conditions differed not only at full saturation, but also more significantly during the saturation process, as the initial porosity n_{ref} was used as the reference state and n evolved upon vertically unconfined swelling. The model prediction of the saturated permeability is presented on the right-hand side of Figure 3.8, comparing simulation results (dashed lines) with experimental data (markers) plotted against void ratio. Good agreement is achieved for all boundary conditions. For constant volume conditions, the model slightly underestimated the permeability reduction, which was also reflected in the values after unloading. Nevertheless,

the evolution was physically consistent, especially when compared to the behaviour shown in Figure 3.5. Adjusting the parameter $\phi^{\max}$ improved the final predicted values.

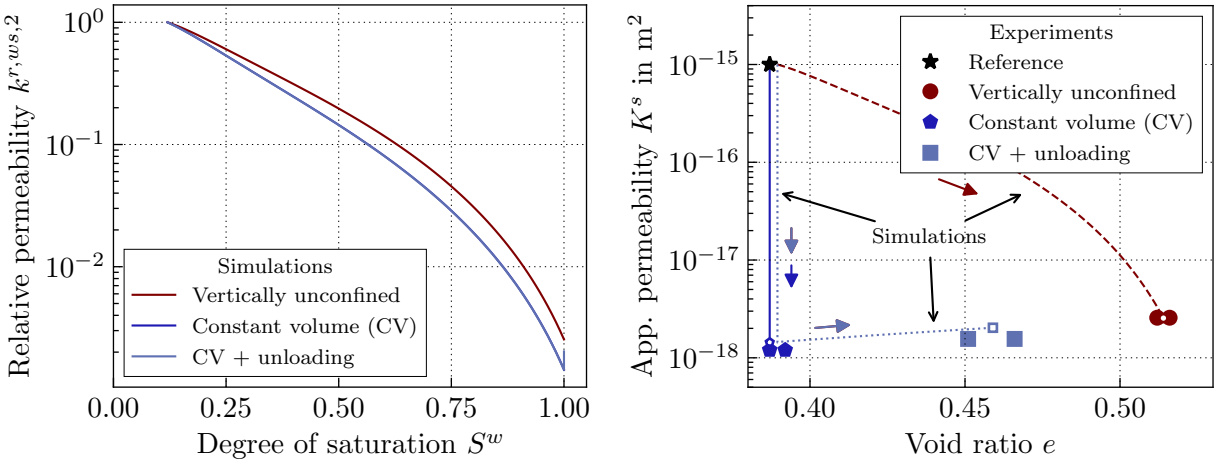

Figure 3.8.: Relative permeability $k^{r,ws,2}$ for the mass transfer model with constant $\phi^{\max}$ vs. degree of saturation (left) and saturated, apparent permeability vs. void ratio (right) for the experiments (symbols) and the simulations (lines). Modified from Machaček et al. (2024).

Figure 3.9 shows the evolution of the ratio ϕ during the simulation of the swelling tests. In contrast to Figure 3.6 ϕ evolved identical for all three boundary and loading conditions due to the nature of the formulation. The previously observed drop in ϕ during unloading (right-hand plot), which is both physically inappropriate and mathematically problematic, was avoided while at the same time the overall prediction of permeability was improved.

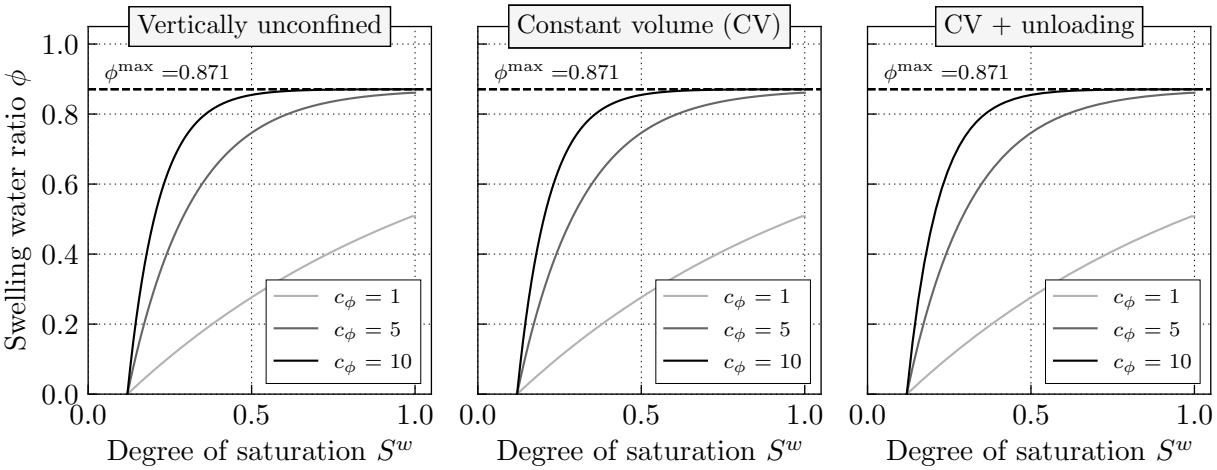

Figure 3.9.: Relative swelling water content ϕ vs. degree of saturation: Influence of c_ϕ on the evolution during saturation for vertically unconfined, constant volume and constant volume conditions with subsequent unloading.

3.2.6. Performance of the mass transfer mechanism

In this section, the performance of the mass transfer mechanism is evaluated for the loading paths being relevant in this work. Therefore, oedometric swelling tests on reconstituted Opalinus clay shale were considered (see Figure 2.10 in Section 2.4.1), and idealized loading paths were

constructed based on the corresponding steady-state states of the experiments in terms of void ratio and vertical stress. In addition, steady-state values in terms of void ratio and vertical stress from the experimental campaign by Villar and Lloret (2008), including constant volume swelling at different void ratios (see Section 2.4.2.1) and vertically unconfined swelling at various stress levels (see Section 2.4.3.1), were used to investigate the influence of these variations on the behaviour of the mass transfer mechanism in idealized loading paths. Although the material response to cyclic wetting and drying is not specifically addressed in this work, the proposed mass transfer model is applicable to such paths and is therefore also illustrated in this section. Therein, the steady-state values of a cyclic wetting and drying test on a bentonite-kaolin mixture by Estabragh et al. (2013) were considered for the definition of the loading path. For all simulations, the parameters of the mass transfer model were set to $\phi^{\max} = 0.871$ and $c_\phi = 10$. The calculation procedure with evaluation of all relevant equations is presented in Algorithm 1.

Algorithm 1: Evaluation of the mass transfer and swelling-induced relative permeability model.

Input: S^w, e, number of increments j
Result: Volume fractions φ^{ws} and φ^{wf}, aggregate porosity n^A, overall relative permeability k^{wf}
Get increments: $\Delta S_i^w = S_{i+1}^w - S_i^w$; $\Delta e_i = e_{i+1} - e_i$
Save initial porosity: $n_{\text{ref}} \leftarrow \dfrac{e_0}{1+e_0}$
for $i = 0 \dots j-1$ **do**
  $\epsilon_i \leftarrow \dfrac{\Delta e_i}{1+e_i}$; $n_i \leftarrow \dfrac{e_i}{1+e_i}$; $\phi_i^s \leftarrow 1 - n_i$; $\phi_i^w \leftarrow n_i\, S_i^w$
end
Initialize: φ^{ws}, ϕ
for each ΔS_i^w **do**
  $\Delta\phi \leftarrow 0$; $\dfrac{\hat{\rho}^w}{\bar{\rho}^w} \leftarrow 0$
  if $i \neq 0$ **then**
    $\Delta\phi \leftarrow c_\phi \left(\phi^{\max} - \phi_{i-1}\right) \langle \Delta S_i^w \rangle$; $\phi_i \leftarrow \phi_{i-1} + \Delta\phi$
    if $\phi_i > \phi_{\max}$ **then**
      $\Delta\phi \leftarrow \phi^{\max} - \phi_{i-1}$; $\phi_i \leftarrow \phi^{\max}$
    end
    $\dfrac{\hat{\rho}^w}{\bar{\rho}^w} \leftarrow \Delta\phi\, \phi_{i-1}^w + \phi_{i-1}\left(\varphi_i^w - \varphi_{i-1}^w\right)$; $\varphi_i^{ws} \leftarrow \varphi_{i-1}^{ws} + \dfrac{\hat{\rho}^w}{\bar{\rho}^w} - \varphi_{i-1}^{ws}\left(\epsilon_i - \epsilon_{i+1}\right)$
    if $\varphi_i^{ws} > \phi^{\max} \varphi_i^w$ **then**
      $\varphi_i^{ws} \leftarrow \phi^{\max} \varphi_i^w$
    end
  end
end
$\varphi^{wf} \leftarrow \varphi^w - \varphi^{ws}$; $n^A \leftarrow n - \varphi^{ws}$; $k^{r,ws} \leftarrow \dfrac{(n^A)^3}{(1-n^A)^2} \dfrac{(1-n)^2}{n^3} \dfrac{n^3}{(1-n)^2} \dfrac{1-n_{\text{ref}}^2}{n_{\text{ref}}^3}$

Oedometric swelling, compression and rebound paths

For the derivation of the mass transfer model and the relative permeability associated with swelling, simulations of experimental results on reconstituted Opalinus clay shale have already been presented in the previous paragraph with respect to the swelling paths. In this section, the complete oedometric loading and unloading paths for the two tests including swelling under both vertically unconfined and constant volume conditions are considered, and the evolution of the

volume fractions is analysed in greater detail. For this purpose, the initial and final values for each segment of the experimental loading paths were incremented linearly. The state variables were the vertical stress σ, void ratio e, and degree of saturation S^w, so the respective increments $\Delta\sigma$, Δe, and ΔS^w were considered for each segment of the loading path.

The results are shown in Figures 3.10 and 3.11. Starting from the initial state (σ_0, e_0) (point 0), wetting was first performed under vertically unconfined conditions (constant net stress, $\Delta\sigma = 0$) and under constant volume conditions ($\Delta e = 0$). The subsequent mechanical loading paths were divided into loading (segments 1-2-3), unloading (segment 3-4), and reloading (segment 4-5-6). The idealised loading paths are shown on the left-hand side of Figures 3.10 and 3.11 in terms of void ratio versus vertical net stress. The wetting is indicated by a wavy colored line. In the centre, the input S^w (solid line) is shown together with the evolution of the swelling water ratio ϕ as the output of the mass transfer model (dashed line) over the simulation steps. On the right-hand side, the evolution of the volume fractions versus the simulation steps is displayed.

For vertically unconfined swelling in Figure 3.10, the solid volume fraction φ^s decreased upon saturation (step 0-1) as the void ratio increased. At the same time, the water volume fraction φ^w increased and the air volume fraction φ^a reached zero. The swelling water ratio ϕ, increased with saturation (see centre plot). As a result, the volume fraction of free water φ^{wf}, which initially constituted a large proportion of the total water, decreased with increasing saturation, while the volume fraction of swelling water φ^{ws} increased significantly. During subsequent mechanical loading, the swelling water ratio ϕ remained at its maximum value (see centre plot of Figure 3.10), as only a positive rate of change in the degree of saturation S^w leads to changes in the ratio ϕ (Equation (3.71)). However, during loading, the total volume fraction of water had to decrease due to drainage of the free water (see right-hand side of Figure 3.10). The swelling water also decreased due to the summation condition $\varphi^w = \varphi^{wf} + \varphi^{ws}$. During unloading, the opposite trend was observed. The solid volume fraction φ^s evolved inversely to the water fraction in all steps.

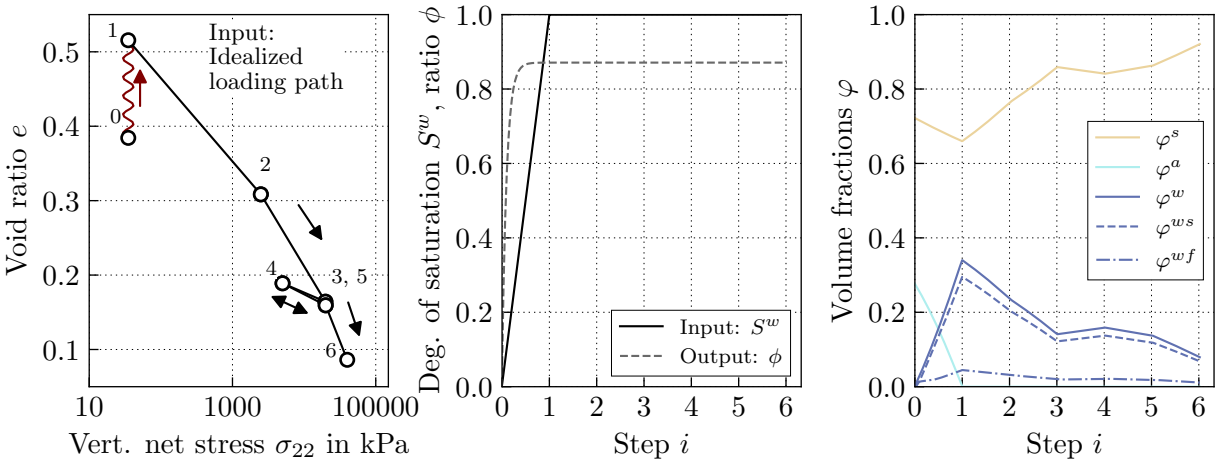

Figure 3.10.: Performance of the proposed mass transfer model for vertically unconfined swelling and subsequent oedometric compression and rebound test: Idealized input path based on test results from Nitsch et al. (2023a) (left), input for S^w and response of the mass transfer model for ϕ (middle) and evolution of volume fractions φ^α during all steps (right).

For constant volume swelling, depicted in Figure 3.11, the observations were similar as observed for vertically unconfined swelling. Here, the solid volume fraction φ^s was constant upon wetting

due to the constant volume conditions. The total volume fraction of water φ^w and of swelling water φ^{ws} were smaller for constant volume swelling, compared for vertically unconfined swelling, where expansion took place. Due to the identical swelling water ratio ϕ (see centre plot of Figures 3.10 and 3.11), the volume fraction of free water φ^{wf} was also slightly higher, which is consistent with the slightly increased permeability for CV conditions observed in experiments.

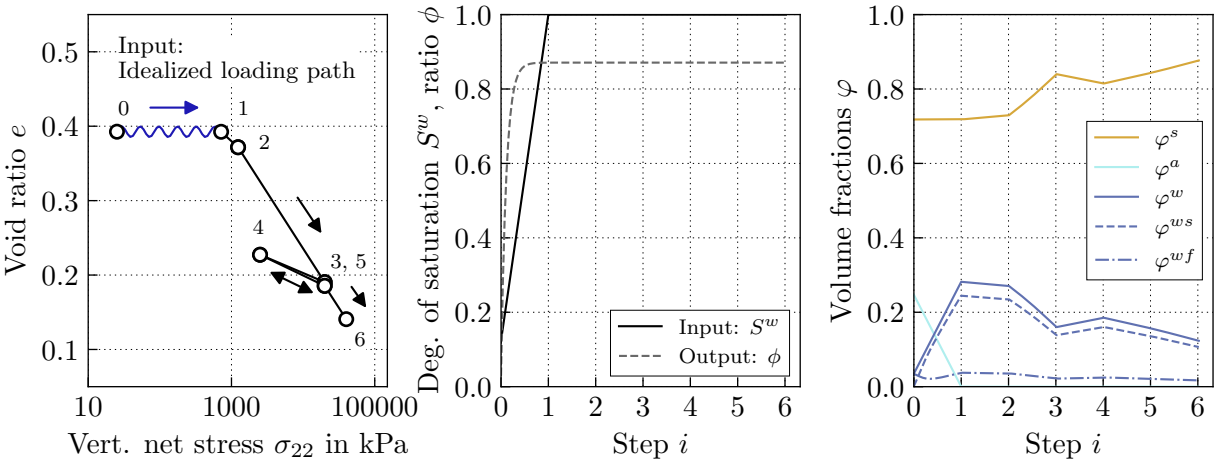

Figure 3.11.: Performance of the proposed mass transfer model for constant volume swelling and subsequent oedometric compression and rebound test: Idealized input path based on test results from Nitsch et al. (2023a) (left), input for S^w and response of the mass transfer model for ϕ (middle) and evolution of volume fractions φ^α during all steps (right).

Oedometric swelling with variation of initial state

Based on the experimental campaign on MX80 bentonite by Villar and Lloret (2008), four swelling tests under vertically unconfined conditions ($\rho_d = 1.5$ g/cm^3, indicated by blue markers in Figure 2.14) and three swelling tests under constant volume (indicated by red markers in Figure 2.18) were considered. The simulation results are presented in Figures 3.12 and 3.13. The wetting paths are indicated by wavy blue lines, with different darkness corresponding to the different initial states. For vertically unconfined swelling, the tests started from similar initial void ratios (positioned on an elastic un- and reloading line), leading to a comparable volume fraction of the solid φ^s, see Figure 3.12. However, at same initial water content, the initial degrees of saturation differed more pronounced in the range $S^w = 0.30 - 0.43$. Upon wetting, greater expansion at lower constant net stress levels (darker line colours) led to a more significant decrease in φ^s, accompanied by an increase in φ^w and φ^{ws}. The volume fraction of free water φ^{wf} also increased with greater expansion, in line with the commonly understood increase in permeability with increasing overall porosity.

The results for constant volume swelling are shown in Figure 3.13. Here, with increasing compaction (lighter line colours), the initial volume fraction of the solid φ^s was higher and remained constant. The increase of all water volume fractions φ^w, φ^{ws} and φ^{wf} was therefore smaller upon wetting. As a result, constant volume conditions would result in a greater reduction in permeability compared to vertically unconfined conditions.

Cyclic drying and wetting

The proposed mass transfer model was applied for cyclic wetting and drying with an idealized

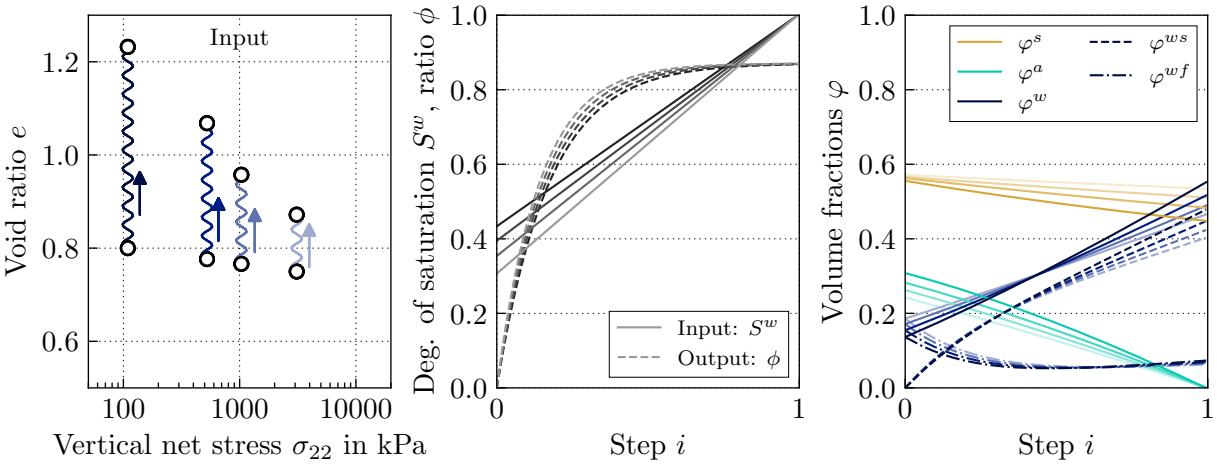

Figure 3.12.: Performance of the proposed mass transfer model for vertically unconfined swelling under different loads based on test results from Villar and Lloret (2008).

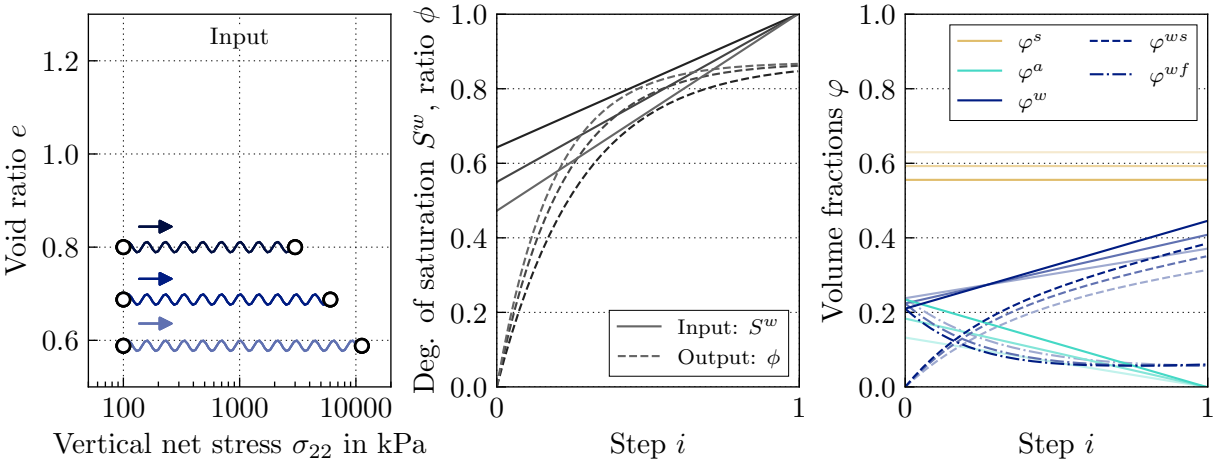

Figure 3.13.: Performance of the proposed mass transfer model for constant volume swelling at different initial void ratios based on test results from Villar and Lloret (2008).

input based on the results of a test reported by Estabragh et al. (2015), which was also referred to in Section 2.4.2.2. At a constant net stress of 6.25 kPa, a sample was subjected to five cycles of wetting and drying with measurement of the volumetric deformation and determination of the degree of saturation. The final states of each wetting and drying path of the cycles in terms of void ratio e and degree of saturation S^w were considered. The results are shown in Figure 3.14. On the left-hand side, the input void ratio e is shown versus the number of cycles and in the centre, the input S^w (solid line) is plotted together with the evolution of the swelling water ratio ϕ as the output of the mass transfer model (dashed line) versus the number of cycles. On the right-hand side, the evolution of all volume fractions versus the number of cycles is presented.

Upon first saturation, the swelling water ratio ϕ increased. However, the maximum value $\phi^{\max}$ was not reached in the first wetting cycle. Upon drying the ratio ϕ remained constant, as only a positive rate of the degree of saturation S^w can produce increases in ϕ, see Equation (3.71). The maximum value was reached in the second wetting cycle (centre of Figure 3.14). In the first cycle the volume fraction of swelling water φ^{ws} increased upon wetting, though slowed down by the evolution of the ratio ϕ. However in the subsequent cycles, in which the degree of saturation

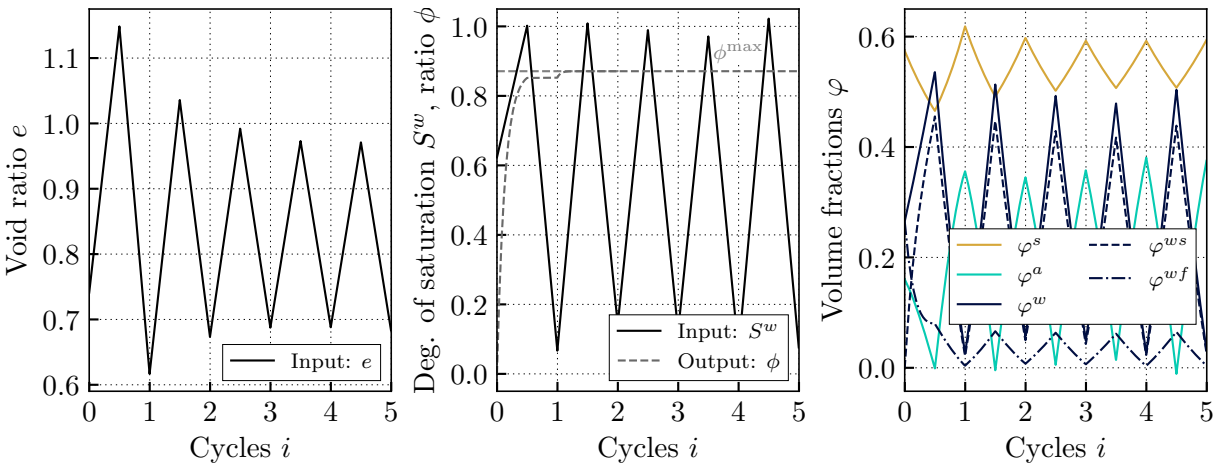

Figure 3.14.: Response of the proposed mass transfer model to a simplified wetting-drying path with five cycles, based on test results from Estabragh et al. (2015): input for S^w and resulting evolution of ϕ (left) and evolution of volume fractions (right).

ranged between 0.06 and 1.0 and the changes in void ratio approximately stabilized, the volume fraction of swelling water increased directly with wetting. Consequently the aggregate porosity n^A (and relative permeability due to swelling $k^{r,ws}$) decreased *faster* as well upon re-wetting compared to first wetting. Further experimental evidence on permeability upon cyclic wetting and drying is required to evaluate the model in this regard. In general, upon drying, the total volume of water decreased, accompanied by a reduction of the volume fraction of free water φ^{wf} and swelling water φ^{ws} by the summation condition $\varphi^w = \varphi^{wf} + \varphi^{ws}$.

3.2.7. Parameter calibration

The mass transport model requires two parameters. The parameter c_ϕ is likely constant, which does not have to be calibrated for different materials, but set to a high value. Throughout this work, $c_\phi = 10$ was used.

For the parameter $\phi^{\max}$ experiments on different materials may help to identify a universally applicable magnitude or to define a correlation with the mineralogical composition of expansive materials. In this work, its calibration based on permeability measurements is recommended. However, advanced methodologies, such as the thermogravimetric analysis proposed by Babiy et al. (2025), could also prove promising for calibrating $\phi^{\max}$ in the future. Currently, as a minimum, the intrinsic permeability in the unswollen (dry) and swollen (saturated) state must be determined, wherein constant volume swelling conditions are sufficient for the latter. Solving Equations (3.69), (3.70) and (3.73) gives the maximum swelling water ratio $\phi^{\max}$ for a known reference and saturated permeability. Exemplary calibration is presented in Sections 7.1.2 and 7.1.3 within application of the framework.

3.3. Concluding remarks

In this chapter, an extended TPM for a four-phase porous medium was derived, suitable for describing expansive soils. The 3-phase TPM of classical soil mechanics, comprising of the solid

phase (s), and the (free) pore fluids water (wf) and air (af), was extended with an additional swelling water phase (ws) to incorporate the effects of swelling within a closed-form numerical framework. The total water phase (w) was proposed to consist of both the swelling water and the free water phase (wf). A mass transfer mechanism is responsible for mass exchange between the two phases. A suitable constitutive relation for the mass transfer was proposed and evaluated together with a swelling-induced relative permeability. The latter uses an aggregate porosity n^A of the swollen porous medium in the extended TPM to account for the reduction of permeability upon swelling. The response of the mass transfer model subjected to different hydro-mechanical loading paths was shown and the calibration of the parameters of the mass transfer model was discussed. The proposed constitutive relation for the swelling-induced relative permeability does not require additional parameters. A set of governing equations based on the extended TPM was derived, which are summarized in Box 3.1.

A) Conservation of linear momentum:

$$\rho^{tot}\boldsymbol{b} + \operatorname{div}\left(\boldsymbol{\sigma}^{tot}\right) - \left(\rho^{s+ws}\right)\bar{\boldsymbol{a}}^{s} - \rho^{wf}\,\bar{\boldsymbol{a}}^{wf} - \rho^{af}\,\bar{\boldsymbol{a}}^{af} + \hat{\rho}^{w}\,\frac{\boldsymbol{w}^{wf}}{\varphi^{wf}} = 0$$

B) Conservation of mass for free pore water:

$$\frac{\varphi^{wf}}{\bar{K}^{wf}}\frac{\mathrm{d}\bar{p}^{wf}}{\mathrm{d}t} + \frac{1}{\bar{K}^{wf}}\operatorname{grad}\left(\bar{p}^{wf}\right)\cdot\boldsymbol{w}^{wf} + \frac{\mathrm{d}\varphi^{wf}}{\mathrm{d}t} + \operatorname{div}\left(\boldsymbol{w}^{wf}\right) + \varphi^{wf}\operatorname{div}\left(\bar{\boldsymbol{v}}^{s}\right) + \frac{\hat{\rho}^{w}}{\bar{\rho}^{w}} = 0$$

C) Conservation of mass for free pore air:

$$\frac{\varphi^{af}}{\bar{K}^{af}}\frac{\mathrm{d}\bar{p}^{af}}{\mathrm{d}t} + \frac{1}{\bar{K}^{af}}\operatorname{grad}\left(\bar{p}^{af}\right)\cdot\boldsymbol{w}^{af} + \frac{\mathrm{d}\varphi^{af}}{\mathrm{d}t} + \operatorname{div}\left(\boldsymbol{w}^{af}\right) + \varphi^{af}\operatorname{div}\left(\bar{\boldsymbol{v}}^{s}\right) = 0$$

D) Conservation of angular momentum:

$$\boldsymbol{\sigma}^{tot} = \left(\boldsymbol{\sigma}^{tot}\right)^{T}$$

Box 3.1.: Governing equations for the four-phase porous medium with a distinct swelling water phase for expansive soils.

All introduced constitutive relations for the extended TPM are gathered in Box 3.2. In soil mechanics, the term „constitutive model“ is often used specifically for the mechanical behaviour, hence deformation of the solid, and referred to as the stress–strain relation. However, constitutive models can be formulated for any (unknown) physical quantity. In addition to those shown in Box 3.2, suitable constitutive relations must be included for the remaining, secondary variables. They are:

- Constitutive stress model: Relates the total stress tensor $\boldsymbol{\sigma}^{tot}$ and the pore fluid pressures p^{af} and p^{wf} of the finite element formulation with the constitutive stress tensor. In this work, net stress $\boldsymbol{\sigma}$ is considered as constitutive stress (in combination with the degree of saturation).

- Mechanical model: Describes the „mechanical“ material behaviour by relating the constitutive net stress tensor $\boldsymbol{\sigma}$ with the strain tensor $\boldsymbol{\epsilon}$. In this work, the mechanical model is

formulated in rate form:

$$\frac{\mathrm{d}\boldsymbol{\sigma}}{\mathrm{d}t} = \frac{\mathrm{d}\boldsymbol{\sigma}}{\mathrm{d}t}\left(\boldsymbol{\sigma}, \frac{\mathrm{d}\boldsymbol{\epsilon}}{\mathrm{d}t}, sv, \frac{\mathrm{d}S^e}{\mathrm{d}t} \dots\right),$$

wherein sv refers to any state variables considered.

- Hydraulic model: Relates the degree of saturation S^w with the suction $s = p^{af} - p^{wf}$ and is also referred to as the soil water retention curve (SWRC). It is also universally formulated in rate form:

$$\frac{\mathrm{d}S^w}{\mathrm{d}t} = \frac{\mathrm{d}S^w}{\mathrm{d}t}\left(S^w, \frac{\mathrm{d}s}{\mathrm{d}t}, sv, \dots\right).$$

- Relative permeability model for unsaturated states: Relates the hydraulic conductivity $\boldsymbol{k}^\beta$ with the effective degree of saturation S^e by a relative permeability model $k^{r,\beta}$ for both pore fluids $\beta = \{wf, af\}$.

a) Conservation of mass for the aggregate (Evolution equation):

$$\frac{\mathrm{d}n^A}{\mathrm{d}t} = \left(1 - n^A\right) \operatorname{div}\left(\bar{\boldsymbol{v}}^s\right)$$

b) Conservation of mass for swelling water (Evolution equation):

$$\frac{\mathrm{d}\varphi^{ws}}{\mathrm{d}t} = \frac{\hat{\rho}^w}{\bar{\rho}^w} - \varphi^{ws} \operatorname{div}\left(\bar{\boldsymbol{v}}^s\right)$$

c) (Generalized) Darcy flow model for the pore fluids (β):

$$\boldsymbol{w}^\beta = \frac{\boldsymbol{K}^s_{\mathrm{ref}}\, k^\beta}{\bar{\mu}^\beta} \cdot \left(-\operatorname{grad}\left(\bar{p}^\beta\right) + \bar{\rho}^\beta\left(\boldsymbol{b} - \boldsymbol{a}^\beta\right)\right) \quad \text{with:} \quad \beta = \{wf, af\}$$

d) Mass transfer model:

$$\frac{\hat{\rho}^w}{\rho^w} = \left(\frac{\mathrm{d}n}{\mathrm{d}t} S^w + n \frac{\mathrm{d}S^w}{\mathrm{d}t}\right) \phi + \varphi^w c_\phi \left(\phi^{\max} - \phi\right) \left\langle \frac{\mathrm{d}S^w}{\mathrm{d}t} \right\rangle$$

e) Compressibility model for the pore fluids (β):

$$\frac{\mathrm{d}^\beta \bar{p}^\beta}{\mathrm{d}t} = \frac{\bar{K}^\beta}{\bar{\rho}^\beta} \frac{\mathrm{d}^\beta \bar{\rho}^\beta}{\mathrm{d}t}$$

f) Relative permeability model due to swelling:

$$k^{r,ws} = \frac{K^w(S^w = 1, \varphi^{ws} > 0)}{K^w(S^w = 1, \varphi^{ws} = 0)} = \frac{(n^A)^3}{(1 - n^A)^2} \frac{(1 - n_{\mathrm{ref}})^2}{n^3_{\mathrm{ref}}}$$

Box 3.2.: Constitutive relations for the four-phase porous medium with a distinct swelling water phase for expansive soils: a)-c) Constitutive relations derived from governing equations and d)-f) empirical constitutive relations.

In general, a hydro-mechanically coupled analysis based on a 3-phase TPM requires a mechanical model, a constitutive stress model, a hydraulic model and a fluid flow model. The unsaturated relative permeability model should be considered in accordance with the hydraulic model (see Section 2.2.3). The compressibility of the pore fluids is often disregarded in hydro-mechanical simulations.

4. Hypoplasticity for expansive soils: one-dimensional formulation

The governing equations derived for the extended TPM (Chapter 3) require several constitutive models, among them one for the hydro-mechanically coupled stress-strain behaviour, which will be referred to as the mechanical model in this work. Based on the observations and conclusions from Chapter 2, a novel constitutive model is proposed. This chapter presents the one-dimensional version of the model together with an assessment of its capabilities. The findings of this chapter have been published in Grandas Tavera et al. (2022), Machaček et al. (2022), Nitsch et al. (2023d), Nitsch et al. (2023c), Nitsch et al. (2023b) and Machaček et al. (2024).

4.1. One-dimensional formulation and equations

The novel mechanical model is formulated in terms of the vertical net stress $\sigma = \sigma^{tot} - p^a$ (excess of total stress over air pressure) and the (effective) degree of saturation $S^{(e)}$. For reasons of readability, the vertical quantities are denoted without their direction indices within this Chapter, thus the vertical net stress σ_{22} is denoted as σ and the vertical strain ϵ_{22} as ϵ. The main features of the mechanical model are: (1) its hypoplastic nature with continuous description of the stress-strain behaviour without distinction of the strain into an elastic and a plastic part, (2) a distinct swelling feature, which can predict deformation (expansion) or development of swelling pressure depending on the mechanical boundary conditions with the same set of parameters and (3) the usage of the (effective) degree of saturation as the main hydraulic variable, as swelling is perceived directly as a consequence of changes in saturation. The effective degree of saturation is related to the suction at any time by the soil water retention curve. This approach simplifies the formulation of the constitutive model and makes the parameter calibration less sensitive to the hydraulic model (as S^w/S^e range from 0 to 1 and not from material and state specific values to 0). Note that even though the degree of saturation determines the current state via the SWRC, it is treated as an input for the mechanical model.

4.1.1. Oedometric compression and rebound behaviour

The oedometric loading, unloading and reloading behaviour can be generally described by the two following equations (Niemunis et al., 2009) using the logarithmic strain definition $\epsilon = \ln \frac{1+e_0}{1+e}$ and geotechnical sign conventions (compressive stress and strain are positive):

$$\begin{cases} \ln \dfrac{1+e_0}{1+e} = \lambda \ln \dfrac{\sigma}{\sigma_0} & \text{or} \quad \dot{\sigma} = \dfrac{\sigma}{\lambda}\dot{\epsilon} \quad \text{for loading,} \\ \ln \dfrac{1+e_0}{1+e} = \kappa \ln \dfrac{\sigma}{\sigma_0} & \text{or} \quad \dot{\sigma} = \dfrac{\sigma}{\kappa}\dot{\epsilon} \quad \text{for unloading/reloading,} \end{cases} \tag{4.1}$$

wherein λ and κ are the virgin loading and un-/reloading indices, respectively. An arbitrary state (σ_0, e_0) is used as the reference point for the deformed state (σ, e) on the same loading (or un-/reloading) branch. The virgin loading line exhibits the slope λ and the un/-reloading line the slope κ in the $\ln(1+e) - \ln(\sigma)$ space. The virgin loading line passes a fixed reference point (σ_d, e_d) and is denoted as the B-line. Facilitating the concept of overstress by Olszak W. (1966), a bounding net stress $\sigma_B(e)$ as the net stress on the B-line corresponding to the current void ratio e is introduced and depicted in Figure 4.1.

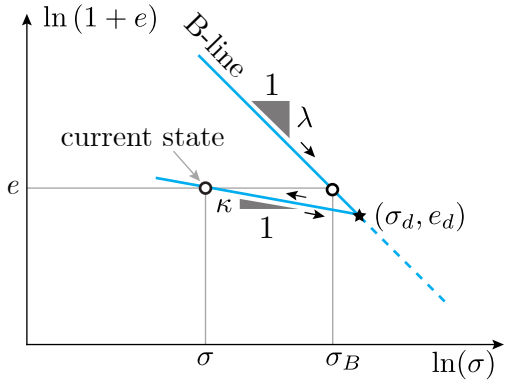

Figure 4.1.: Loading, unloading and reloading paths with reference point (σ_d, e_d) and bounding net stress σ_B corresponding to current void ratio e on the B-line. Modified from Grandas Tavera et al. (2022).

The material response for net stresses $\sigma \leq \sigma_B$ is considered reversible. Loading beyond the bounding net stress evokes anelastic flow. To evaluate the current net stress σ in relation to the bounding net stress σ_B, the overconsolidation ratio $\mathrm{OCR} = \sigma_B/\sigma$ is used. For $\mathrm{OCR} = 1$ the current state is on the B-line and considered as *normally consolidated*, whereas for $\mathrm{OCR} > 1$ the state is *overconsolidated* and located on the left of the B-line. Considering the OCR, Equation (4.1) can be written as a single hypoplastic equation:

$$\dot{\sigma} = \frac{\sigma}{\kappa}\left(\dot{\epsilon} - Y\mathrm{OCR}^{-m}|\dot{\epsilon}|\right) \quad \text{with} \quad Y = \frac{\lambda - \kappa}{\lambda} \quad \text{and} \quad \mathrm{OCR} = \sigma_B/\sigma, \tag{4.2}$$

with the degree of non-linearity Y and the exponent $m > 1$. The factor $Y\mathrm{OCR}^{-m}$ enables simulation of the material behaviour in both, normally consolidated and overconsolidated states, without switching between the equations in Equation (4.1). Upon virgin compression ($\dot{\epsilon} > 0$), OCR is approximately 1, and Equation (4.2) becomes $\dot{\sigma} = \sigma\dot{\epsilon}/\lambda$. For un-/reloading paths, OCR is larger than 1, the factor $Y\mathrm{OCR}^{-m}$ vanishes, and Equation (4.2) becomes $\dot{\sigma} = \sigma\dot{\epsilon}/\kappa$. m is a material constant controlling the sharpness of the transition from the reversible to anelastic material behaviour (larger values for m lead to sharper transitions). An example is shown in Figure 4.13. For oedometric compression up to high stresses, thus significantly exceeding the preloading net stress, Burland (1990), Lloret et al. (2003), Nowamooz and Masrouri (2008) and Monroy et al. (2010) amongst others presented the existence of a unique compression line in the $e - \log(\sigma)$ space. Samples with different degrees of saturation and even dry samples approached this unique compression line for compression under constant suction. The concept of the normal compression (or consolidation) line/curve has often been facilitated in the modelling of unsaturated soils e.g. by Gallipoli and Bruno (2017) and is adopted here as well. In this work the normal compression curve (NCC) serves as an attractor which is reached upon compression, regardless of the initial void ratio or degree of saturation, see left-hand side of Figure 4.2. The

NCC is described by a unique function $\sigma_e(e)$, which gives the equivalent net stress σ_e on the NCC for a given void ratio e. An often used definition of the NCC was proposed by Butterfield (1979) for the compression of clayey materials:

$$\ln \frac{1+e_0}{1+e} = \Lambda \ln \frac{\sigma_e}{\sigma_0}, \tag{4.3}$$

wherein Λ is the slope of the NCC and (σ_0, e_0) is a reference point. This formulation, however, bears the possibility of excessively large or negative void ratios at very low or high stresses, respectively. Furthermore, a curved nature of the NCC was found to be more suitable especially for higher stresses by e.g. Wheeler et al. (2002). Therefore, in this work, the equation proposed by Bauer (1996) was adopted for the vertical net stress:

$$\sigma_e(e) = h_s \left[-\ln(e/e_N)\right]^{1/n}, \tag{4.4}$$

which remains valid over a wide net stress range $0 \leq \sigma_e < \infty$. Therein three material parameters are required, the net stress at the inflection point h_s (in kPa), the void ratio at zero (nil) net stress e_N and the exponent n. For samples with higher degrees of saturation, the NCC is reached *sooner*, meaning at lower net stresses, than compared to samples with a low degree of saturation or even dry samples, see left-hand side of Figure 4.2. In the fully saturated state, the NCC and the virgin loading line (Equation (4.2)) approximately coincide. To account for the attractive nature of the NCC within the model, the B-line must shift towards the NCC when compression occurs at net stresses exceeding the preloading net stress. The right-hand side of Figure 4.2 illustrates the idealised compression of a sample with a low degree of saturation. After elastic reloading (path 0–1) up to the preloading state (σ_{d1}, e_{d1}), which serves as the reference point for the initial B-line (1), the sample undergoes anelastic loading as net stress increases (path 1–2). For the loading path to approach the NCC, the reference point (σ_{d2}, e_{d2}), which defines the shifted B-line (2) in an arbitrary state beyond exceeding the initial preloading net stress σ_{d1}, must move towards the NCC. Hence, the preloading net stress σ_d and corresponding void ratio e_d are state variables, whose evolution equations must depend on (i) the loading path and (ii) the degree of saturation, see Section 4.1.5.

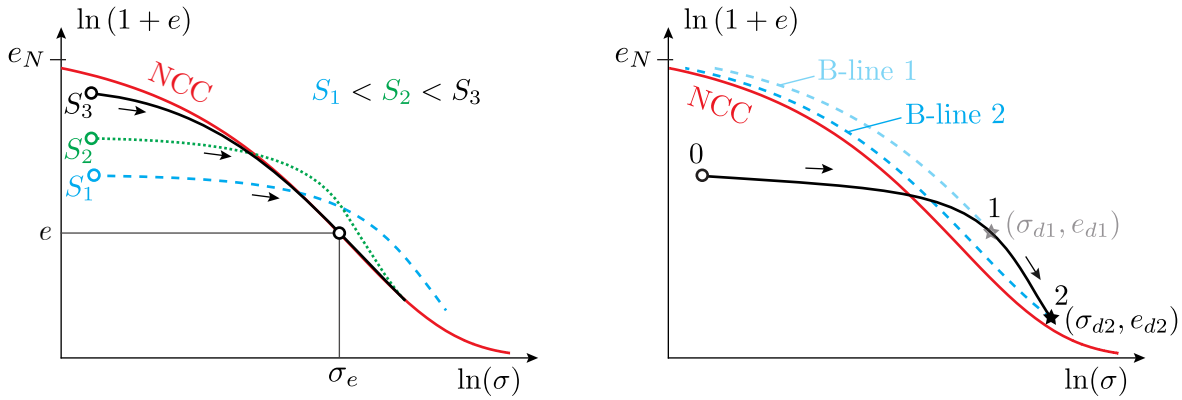

Figure 4.2.: Normal compression curve (red) and idealized loading paths at constant suction for different initial degrees of saturation $S_1 < S_2 < S_3$ (left) and shift of B-line from points 1 to 2 during virgin compression of a sample with very low degree of saturation starting from point 0. Modified from Grandas Tavera et al. (2022).

Along the B-line, virgin loading (beyond the preloading net stress) takes place with a slope $\lambda(e)$. As the virgin loading path is *affine* to the NCC, the virgin loading index $\lambda(e)$ is not defined as a material parameter, but is obtained by Equation (4.4) as:

$$\lambda = \lambda(e) = \lambda_{NCC}(e) = n\,(\sigma_e/h_s)^n\,\frac{e}{1+e} \quad \text{with} \quad \lambda > \kappa. \tag{4.5}$$

Note that contrary to other mechanical constitutive models, e.g. the BBM (Alonso et al., 1990), its successor BExM (Gens and Alonso, 1992; Alonso et al., 1999) and other subsequent models as the Coupled Glasgow Model (Wheeler et al., 2003) or the Imperial College model (Georgiadis et al., 2005), the virgin loading index $\lambda(e)$ is not a direct function of the suction. The shift of the B-line depending on the current loading path and degree of saturation, though, results in an apparent indirect dependency of λ on suction. The un-/reloading index κ, however, is directly depending on the hydraulic state of the material. The pronounced reduction of elastic stiffness with increasing effective degree of saturation (Monroy et al., 2010; Nitsch et al., 2023a) is accounted for with a simple linear interpolation between dry (reference) and fully saturated conditions:

$$\kappa(S^e) = \kappa_{\text{ref}} + S^e\,(\kappa_w - \kappa_{\text{ref}})\,, \tag{4.6}$$

wherein $\kappa_{\text{ref}} = \kappa(S_{\text{ref}})$ and κ_w are the respective un-/reloading indices at dry (reference) and fully saturated conditions. $S^e = (S^w - S_{\text{ref}})/(1 - S_{\text{ref}})$ denotes the effective degree of saturation. The reference degree of saturation S_{ref} corresponds to a nearly dry reference state at which the elastic stiffness can be measured in the laboratory at atmospheric conditions, and is ideally equivalent to the residual degree of saturation ($S_{\text{ref}} = S^{wr}$). In Figure 4.3, the (un-)loading behaviour of two samples with different effective degrees of saturation $S_1^e < S_2^e$ is presented.

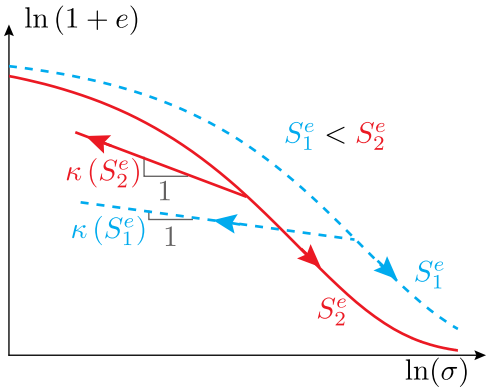

Figure 4.3.: Influence of the effective degree of saturation on the elastic stiffness: $\kappa(S_1^e) < \kappa(S_2^e)$ for $S_1^e < S_2^e$. Modified from Grandas Tavera et al. (2022).

The dependency of the un-/reloading index on the hydraulic variable is in line with the formulations of Sánchez et al. (2012) or Vaunat and Gens (2005), which enhanced the original formulations of the BBM / BExM (Alonso et al., 1990; Gens and Alonso, 1992), where κ was defined as constant.

4.1.2. Vertically unconfined swelling

Wetting of samples at a constant (vertical) net stress ($\dot{\sigma} = 0$) leads to a volume increase (see Section 2.4.2), whereas drying causes a reduction in volume. Observations of the relation between

changes in void ratio e and water content w in wetting-drying tests by Hanafy (1991), Tripathy et al. (2002) and Estabragh et al. (2015) amongst others, provided the basis for incorporating swelling into the proposed model. These studies show, that the wetting and drying paths evolve approximately between two limiting states (w_s, e_s) and (w_w, e_w), wherein w_s is the shrinkage limit at corresponding void ratio e_s and w_w and e_w correspond to the fully saturated state. After several cycles, the samples followed an almost identical path during both wetting and drying. The idealized evolution of void ratio versus water content is presented in Figure 4.4. Upon wetting ($\dot{S}^e > 0$), swelling occurs until a given void ratio e_w is reached. Conversely, upon drying ($\dot{S}^e < 0$), the void ratio reduces again to e_s. The limiting void ratios e_s and e_w are not unique, but functions of the stress state and loading history.

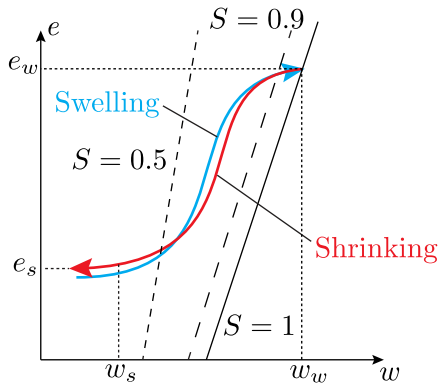

Figure 4.4.: Idealized evolution of the void ratio vs. water content during wetting and drying at constant net stress after Estabragh et al. (2015). Modified from Grandas Tavera et al. (2022).

The volumetric deformation described is governed by changes in the effective degree of saturation rather than by changes in stress. To account for swelling within the mechanical model, the total strain rate $\dot{\epsilon}$ is therefore decomposed as follows:

$$\dot{\epsilon} = \dot{\epsilon}^w + \dot{\epsilon}^h. \tag{4.7}$$

Therein, $\dot{\epsilon}^w$ denotes the saturation-driven strain rate, which will be related to changes in saturation via a constitutive relation $\dot{\epsilon}^w(\dot{S}^e, S^e, e, \dots)$. The remaining portion $\dot{\epsilon}^h$ is referred to as the hypoplastic strain rate and determines the evolution of the net stress. Equation (4.2) changes to:

$$\dot{\sigma} = \frac{\sigma}{\kappa}\left(\dot{\epsilon}^h - Y\mathrm{OCR}^{-m}|\dot{\epsilon}^h|\right) \quad \text{with} \quad \dot{\epsilon}^h = \dot{\epsilon} - \dot{\epsilon}^w. \tag{4.8}$$

For vertically unconfined swelling, $\dot{\epsilon}^w \neq 0$ applies and the portion $\dot{\epsilon}^h$ must be zero to fulfil the condition of constant net stress $\dot{\sigma} = 0$ in Equation (4.8). Consequently, the total strain rate corresponds to the saturation-driven strain rate ($\dot{\epsilon} = \dot{\epsilon}^w + \cancel{\dot{\epsilon}^h}$) following Equation (4.7). The constitutive equation for $\dot{\epsilon}^w$ considers that the volume of a sample (i) increases $\dot{\epsilon}^w > 0$ upon wetting $\dot{S}^e > 0$ until a limit void ratio $e \to e^w$ is reached at full saturation, i.e. $\dot{\epsilon}^w \sim (e - e_w)\dot{S}^e$, and (ii) decreases $\dot{\epsilon}^w < 0$ upon drying $\dot{S}^e < 0$ until the limiting void ratio $e \to e^s$ at nearly dry conditions is reached, i.e. $\dot{\epsilon}^w \sim (e_s - e)\dot{S}^e$. The following evolution equation is proposed:

$$\dot{\epsilon}^w = -b\frac{e}{(1+e)}\left[(e_w - e)\,(S^e)^2\left\langle \dot{S}^e \right\rangle + (e_s - e)\,(1 - S^e)^2\left\langle -\dot{S}^e \right\rangle\right]. \tag{4.9}$$

Therein b is a material constant, which governs the shape of the water content - void ratio - path[1]. To follow the sigmoid-shaped drying/wetting behaviour shown in Figure 4.4, the evolution of

[1]Two different factors b_1 and b_2 may be used for the first and second term within the square brackets of Equation (4.9) to describe drying and wetting paths independently.

$\dot{\epsilon}^w$ must decelerate when reaching nearly dry and fully saturated states, which is realised by introducing the factors $(S^e)^2$ and $(1 - S^e)^2$. Experiments discussed in Section 2.4 showed that the magnitude of the swelling phenomenon under constant net stress depends on the current stress state and the loading history. An increasing final void ratio in the saturated state with decreasing constant net stress upon wetting and an affinity between the bandwidths of the final states and the virgin loading line (unique for each material) was established. To account for this observation in the proposed model, an idealized set of vertically unconfined swelling tests is illustrated in Figure 4.5. All samples are compacted up to the same preloading state (point 0,(σ_d, e_d)) and subsequently unloaded to different vertical net stresses (points 1, 3, 5,...). Here, the samples are wetted. Vertically unconfined swelling at constant net stress occurs until the final void ratio $e = e_w(S^w = 1)$ in the fully saturated state is reached (at points 2, 4, 6,...). A decreasing final void ratio $e_w(\sigma)$ is evident for higher constant net stresses (σ) during wetting. A hypothetical connection between these points shows an affinity to the NCC and the B-line (see Figure 4.5). It enables the prediction of the *maximum swelling strain* $\epsilon_{\max}$ under constant net stress σ for a sample with a known preloading net stress σ_d.

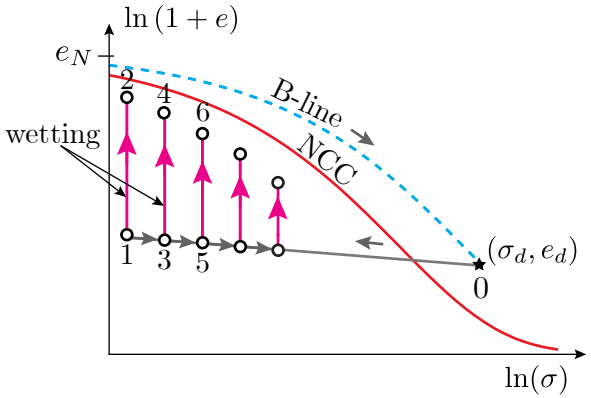

Figure 4.5.: Idealized wetting paths for vertically unconfined swelling tests (swelling strain) of samples compacted to the same preloading net stress, but wetted under different net stresses. Modified from Grandas Tavera et al. (2022).

4.1.3. Constant volume swelling

The introduced decomposition of the strain rate in Equation (4.7) results in the development of swelling pressure ($\dot{\sigma} > 0$) for wetting at constant volume conditions. While the total strain must remain zero ($\dot{\epsilon} = 0$) to satisfy the constant volume conditions in Equation (4.8), the saturation driven strain increases $\dot{\epsilon}^w \neq 0$ due to changes in the effective degree of saturation (see Equation (4.9)). The remaining portion of $\dot{\epsilon}^h = -\dot{\epsilon}^w$ gives the wetting-induced change of net stress until the final void ratio in the saturated state $e = e_w(S^w = 1)$ is reached.

Experimental results of various campaigns presented in Section 2.4 showed the significance of the preloading stress σ_d for the magnitude of swelling pressure σ_w. The very common, exponential relation between the swelling pressure and dry density $\sigma_w \sim \exp(\rho_d)$ (Villar and Lloret, 2008; Zou et al., 2020; Middelhoff et al., 2021; Schanz and Tripathy, 2009) was reinterpreted as the more evident relation between σ_w and σ_d. With increasing preloading stress, swelling pressure increases as well and an affinity between the final states and the virgin compression line (unique for each material) was evident. In a similar manner to Figure 4.5, a set of idealized constant

volume swelling tests is shown in Figure 4.6. The samples are compacted to different preloading net stresses σ_d reaching the void ratios e_d (points a, b, c, d) and subsequently unloaded to the same, low vertical net stress (points 1, 3, 5, 7). Here, the samples are wetted at constant volume conditions and the net stress increases (points 2, 4, 6, 8). The final value of net stress is the maximum swelling pressure. It is directly related to the preloading net stress σ_d (or the density given by the corresponding void ratio e_d), as higher compaction stress results in higher swelling pressure. Analogously to vertically unconfined swelling, the hypothetical connection of the final saturated states is affine to the NCC and the B-line.

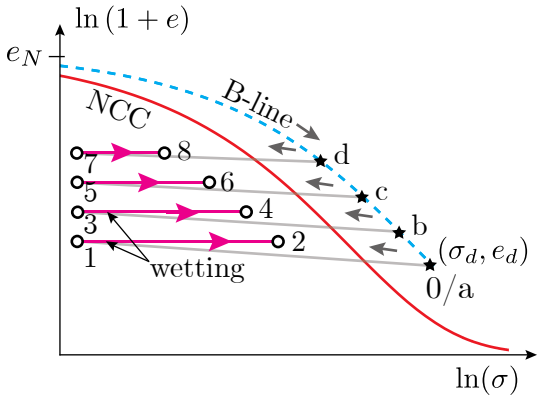

Figure 4.6.: Idealized wetting paths for constant volume swelling tests (swelling pressure) of samples compacted to different preloading net stresses. Modified from Grandas Tavera et al. (2022).

4.1.4. Characteristic curves

The affinity between the final states (σ_w, e_w) of both, vertically unconfined and constant volume swelling tests to the already introduced unique NCC and evolving B-line is introduced to the mechanical model as a conceptualized third line, the w-line. The w-line is not unique, but evolving, and its position is depending on the stress state before wetting and the preloading stress. However, the slope of the individual w-lines is very similar. In the proposed model, swelling is thus modelled by using three characteristic lines, as is shown in Figure 4.7 for idealized wetting paths. Subsequent to an identical loading history (0–1–2), the w-line is reached for vertically unconfined (3a, left) and constant volume (3b, right) conditions upon wetting solely depending on the mechanical boundary condition.

The three characteristic curves are:

- B-line: virgin compression line with bounding net stress $\sigma_B(e, sv)$, evolves with loading,
- NCC: a unique attractor with equivalent net stress $\sigma_e(e)$ reached after compression to high net stresses, and
- w-line: an evolving line with net stress $\sigma_w(e, sv)$, which is reached for full saturation.

Their relative position in the $\ln(1+e) - \ln(\sigma)$ space governs the material behaviour and is shown in Figure 4.8. As the position of the NCC is unique, determined by the material parameters h_s, e_N and n, it is utilized as a reference for the evolving B- and w-line.

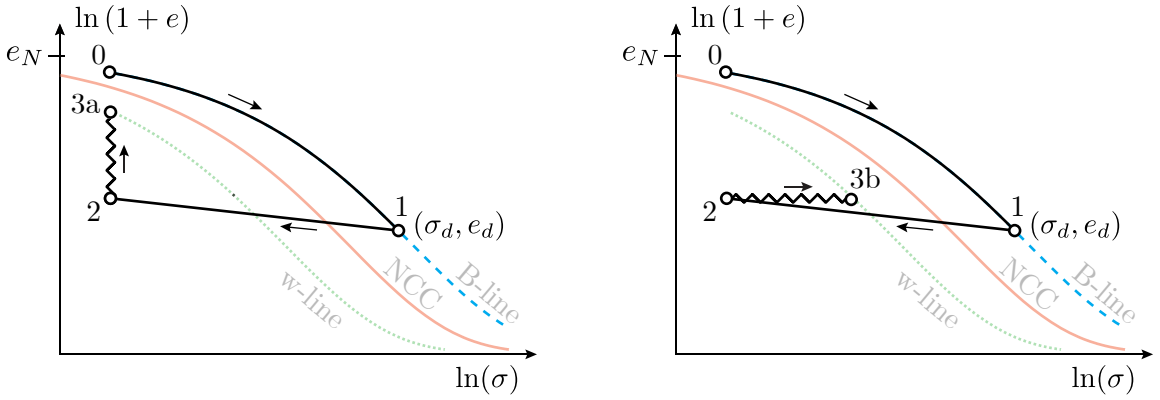

Figure 4.7.: Idealization of swelling processes: at the end stage of wetting, the w-line can be reached either by keeping the net stress (left) or the volume (right) constant. Modified from Grandas Tavera et al. (2022).

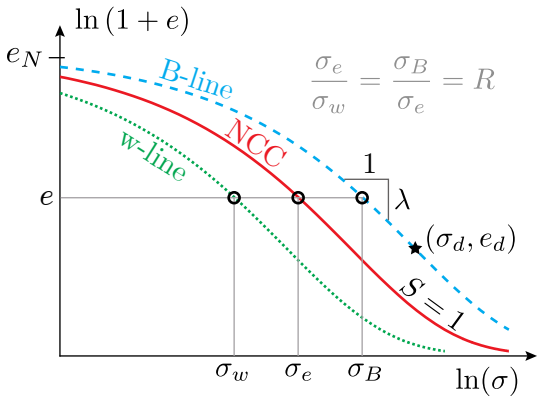

Figure 4.8.: Schematic representation of the three characteristic lines: Normal compression curve (red) with equivalent net stress σ_e, B-line (blue) with bounding net stress σ_B and w-line (green) with net stress σ_w reached at full saturation after wetting for a specific void ratio e. Modified from Grandas Tavera et al. (2022).

Suitable evolution equations for σ_B and σ_w are derived assuming that the B-line is always on the right of the NCC and the w-line is always on the left of the NCC in the $\ln(1+e)-\ln(\sigma)$ space. For a given void ratio e, the following holds:

$$\sigma_w(e) \leq \sigma_e(e) \leq \sigma_B(e). \tag{4.10}$$

Moreover, the three lines are affine to each other in the relevant range of void ratio and vertical net stress, and the relative position of the B- and w-line to the NCC in the $\ln(1+e)-\ln(\sigma)$ space is identical and characterized by the ratio R:

$$R = \frac{\sigma_B}{\sigma_e} = \frac{\sigma_e}{\sigma_w}. \tag{4.11}$$

The position of the B-line is defined by the current preloading state (σ_d, e_d) and the ratio R can be computed using Equation (4.11) and the material parameters h_s, e_N and n of the NCC as:

$$R = \frac{\sigma_d}{h_s}\left[-\ln\left(e_d/e_N\right)\right]^{-1/n} = \frac{\sigma_B}{\sigma_e}. \tag{4.12}$$

This enables computation of the bounding net stress $\sigma_B(e)$ on the B-line for any given void ratio e as:

$$\sigma_B(e) = R\,\sigma_e(e) = R\,h_s\left[-\ln\left(e/e_N\right)\right]^{1/n}. \tag{4.13}$$

The net stress $\sigma_w(e)$ in the saturated state on the w-line for any given void ratio e is derived analogously and yields:

$$\sigma_w(e) = \frac{\sigma_e(e)}{R} = \frac{h_s \left[-\ln\left(e/e_N\right)\right]^{1/n}}{R}. \tag{4.14}$$

The limiting void ratio on the w-line at full saturation $e_w(\sigma)$ for a given net stress is given by:

$$e_w(\sigma) = e_N \exp\left[-\left(\frac{\sigma R}{h_s}\right)^n\right]. \tag{4.15}$$

Finally, the following definition for the limiting void ratio $e_s(\sigma)$ at the shrinkage limit w_s is proposed:

$$e_s(\sigma) = \begin{cases} (1+e_d)\left(\sigma_d/\sigma\right)^{\kappa_{\mathrm{ref}}} - 1 & \text{for } \sigma < \sigma_d, \\ e_d & \text{for } \sigma \geq \sigma_d. \end{cases} \tag{4.16}$$

From Equations (4.13) and (4.14), it follows that all three lines share the same slope λ. For $R = 1$, the B-line and the w-line are identical to the NCC.

4.1.5. Evolution equations and material parameters

The one-dimensional formulation of the proposed model has four state variables: the net stress σ, void ratio e, preloading net stress σ_d and corresponding void ratio e_d. The evolution of the net stress $\dot{\sigma}$ was already given in Equation (4.8). First, the evolution of the void ratio is related to the total strain rate $\dot{\epsilon}$ and given by

$$\dot{e} = -(1+e)\,\dot{\epsilon}. \tag{4.17}$$

In Section 4.1.1, the influence of the loading path and the degree of saturation on the evolution of the preloading net stress σ_d was introduced. To derive a suitable evolution equation for $\dot{\sigma}_d$, the following three effects are accounted for:

1. Increase of σ_d due to an increase in net stress beyond the preloading state:

$$\dot{\sigma}_{d+} = \frac{\sigma_d}{\lambda(e_d)} \left(\frac{\sigma_d}{\sigma}\right)^{-m} \dot{\epsilon}^h. \tag{4.18}$$

2. Reduction of σ_d due to changes in the net stress at constant degree of saturation (shift of the B-line due to attractive nature of the NCC):

$$\dot{\sigma}_{d-,1} = \frac{\sigma_e(e_d) - \sigma_d}{\lambda(e_d)} \left[S^w\ \dot{\epsilon}^h\right]. \tag{4.19}$$

3. Reduction of σ_d related to changes in the degree of saturation:

$$\dot{\sigma}_{d-,2} = \frac{\sigma_e(e_d) - \sigma_d}{\lambda(e_d)} \left[-\dot{\epsilon}^w \frac{S^{w2}}{c\left(e_w - e_s\right)}\right]. \tag{4.20}$$

In Equation (4.20), c is a material parameter, which decelerates the wetting-induced reduction of σ_d. Note that the degree of saturation S^w is used in Equations (4.19) and (4.20), as even samples with a very low degree of saturation approach the NCC for sufficiently high net stresses (Nowamooz and Masrouri, 2008; Nitsch et al., 2023a). Usage of S^e would neglect this. The complete evolution equation for σ_d reads:

$$\dot{\sigma}_d = \dot{\sigma}_{d+} + \dot{\sigma}_{d-,1} + \dot{\sigma}_{d-,2}. \tag{4.21}$$

For the corresponding void ratio e_d the following equation is proposed:

$$\dot{e}_d = -(1+e)\left(\frac{\sigma_d}{\sigma}\right)^{-m} \dot{\epsilon}^h. \tag{4.22}$$

Therein, the factor $(\sigma_d/\sigma)^{-m}$ controls the different evolution of e_d for normally consolidated and overconsolidated states. Upon un/-reloading e_d is nearly constant as the factor becomes negligible. Upon virgin loading beyond the preloading net stress the factor is approximately 1 and e_d evolves similarly as the void ratio e in Equation (4.17).

The proposed model requires seven material parameters which are listed in Table 4.1 and can be determined from standard laboratory tests. The exponent m for OCR is not considered as a model parameter, but as constant for all materials in the scope of this work. The calibration of the parameters is explained in further detail in Section 4.3. Therein, the influence of m is also addressed and a recommended value of $m \approx 6$ is proposed. In addition to the material parameters, the initial state of the material described in Table 4.2 must be defined for every simulation. Note that the initial degree of saturation S_0 is required for the description of the current state.

Table 4.1.: Material parameters of the one-dimensional constitutive model and their meaning.

Symbol	Domain	Description
e_N	Normal Compression Curve (NCC)	Void ratio at nil net stress, $\sigma = 0$
h_s		Net stress at inflection point of NCC, in kPa
n		Exponent of Bauer equation
κ_{ref}	Elastic stiffness	Unloading/Reloading slope for $S^w = S^w_{\mathrm{ref}}$
κ_w		Unloading/Reloading slope for $S^w = 1$
b	Wetting	Curvature for wetting and drying
c	Yielding	Factor for reduction of preloading $\dot{\sigma}_{d-}$

Table 4.2.: Initial conditions of the one-dimensional model.

Symbol	Description
σ_{d0}	Initial preloading net stress
e_{d0}	Initial void ratio corresponding to σ_{d0}
σ_0	Initial net stress
e_0	Initial void ratio corresponding to σ_0
S_0	Initial degree of saturation

4.2. Discussion and capabilities of the one-dimensional formulation

The capabilities of the one-dimensional model for an arbitrary parameter set, shown in Table 4.3, are presented in the following. Different complex hydro-mechanical loading paths were considered. All sets of loading paths included an identical reference test (A-B-A*), which represents

loading and unloading at *nearly* dry conditions. Most simulations included sample preparation in the laboratory, which consists of loading (compaction) up to a certain net stress σ_d at which the target void ratio e_d is reached. This state (σ_{d0}, e_{d0}) represents the preloading state of the sample, whose evolution upon wetting and deformation is tracked by the model. Subsequently, the sample was unloaded to a net stress $\sigma < \sigma_d$, which equals the initial net stress at the start of the actual test or simulation. The corresponding void ratio after unloading corresponds to the void ratio at the shrinkage limit (as the material is *nearly* dry).

Table 4.3.: Parameters for discussion of the one-dimensional formulation of the proposed model.

Parameter	e_N	h_s in MPa	n	κ_{ref}	κ_w	b	c
Value	1.615	1.2	0.40	0.002017	0.02647	17	2.6

4.2.1. Oedometric compression: influence of saturation

The material response to oedometric loading and unloading for different constant degrees of saturation is presented in Figure 4.9. Note that S^w was considered as given and thus not evolves upon compaction. For the reference test (A–B–A*), elastic reloading was evident up to the preloading state (σ_{d0}, e_{d0}), through which the current B-line passed. For vertical net stresses exceeding the preloading net stress, the slope of the subsequent virgin loading is affine to the slope $\lambda(e)$ of the NCC. For increasing degrees of saturation, stress paths approached the NCC at smaller net stress levels due to the reduction of σ_d (see Equation (4.21)). In the fully saturated state, the virgin loading path (I–J) nearly coincided with the NCC. The reduction of the elastic stiffness with increasing degree of saturation following Equation (4.6) became evident in the unloading paths ($\sigma \leq \sigma_d$).

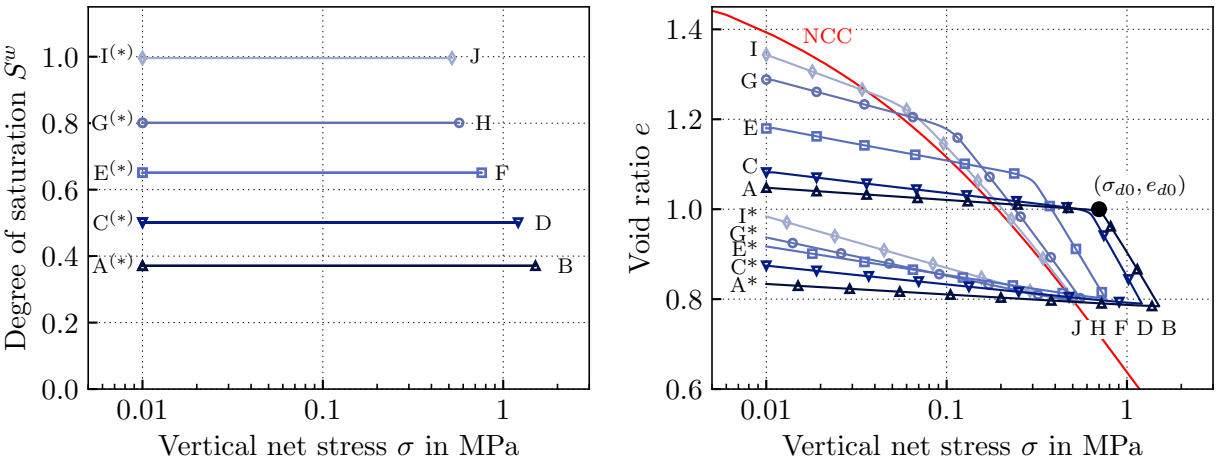

Figure 4.9.: Oedometric loading and unloading at different degrees of saturation: Net stress and wetting paths (left) and response of the model (right). Modified from Grandas Tavera et al. (2022).

4.2.2. Vertically unconfined swelling: swelling strain

The saturation-induced deformation at constant net stress (swelling under load) is shown for different stress states prior to wetting in Figure 4.10. For very small net stresses this refers to

vertically unconfined swelling. Starting at the identical preloading state (σ_{d0}, e_{d0}), the vertical net stress was reduced to points A, D, F and H and at constant vertical net stress the degree of saturation was increased. At full saturation the void ratio corresponded to $e = e_w$ according to Equation (4.15), as the deformation was determined by the position of the w-line. With increasing vertical net stress at wetting, the deformation decreased. The affinity of the final states (at points C, E, G and I) and the NCC was apparent. The w-line (green) and the B-line (medium blue) are shown in Figure 4.10 for the simulation with the smallest vertical net stress (path A–C) for the state before swelling (faint lines) and the final state after completion of swelling (opaque lines). The evolution of the characteristic lines upon swelling was evident. Furthermore, the uniqueness of the final w-line (and B-line) for each simulation was apparent, as not all final states (C, E, G and I) were located on the same w-line.

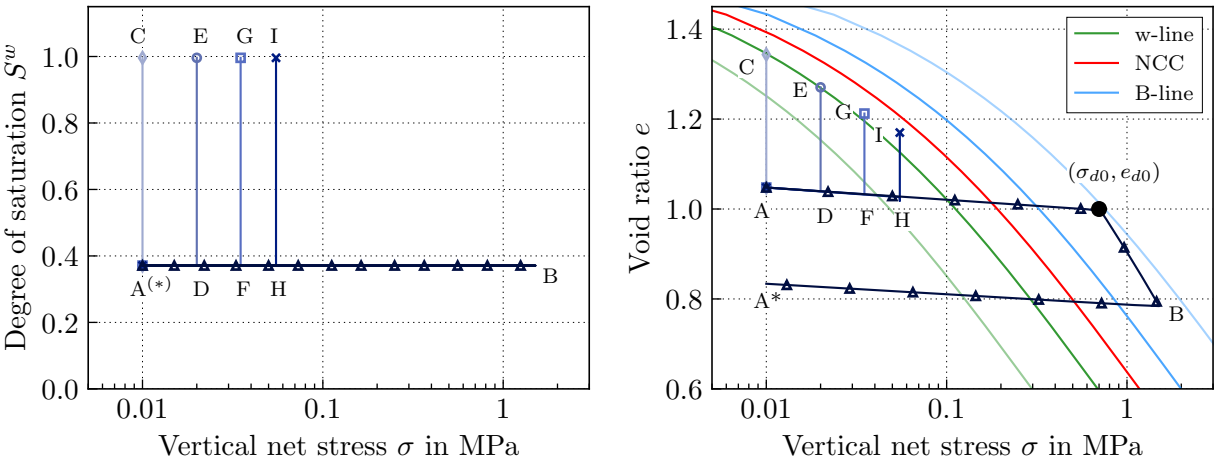

Figure 4.10.: Saturation-induced deformation at different vertical net stress: Net stress and wetting paths (left) and response of the model (right). Modified from Grandas Tavera et al. (2022).

4.2.3. Constant volume swelling: swelling pressure

At constant volume conditions, the model response is shown for different net preloading stresses (or initial void ratios) in Figure 4.11. The unloading paths from each preloading state (σ_{d0}, e_{d0}) are shown as dashed lines, ending at points A, D, F and H. At constant volume, thus constant void ratio, the degree of saturation was increased. At full saturation the vertical net stress corresponded to $\sigma = \sigma_w$ and was again determined by the position of the w-line (at points C, E, G and I). The affinity of the w-line and the NCC can clearly be seen. Note that the final position of the w-line was slightly different for each test, as it was determined by the loading history. For the simulation with the smallest void ratio (path A–C), the w-line (green) and the B-line (medium blue) are shown in Figure 4.11 for the state before swelling (faint lines) and the final state after completion of swelling (opaque lines). The evolution of the characteristic lines upon swelling and the uniqueness of the final w-line (and B-line) for each simulation was again apparent.

Comparison between the final states of vertically unconfined (Figure 4.10) and constant volume (Figure 4.11) swelling tests revealed different distances between the w-line at full saturation and the NCC, thus different magnitudes of the ratio R (see Equation (4.12)). For constant

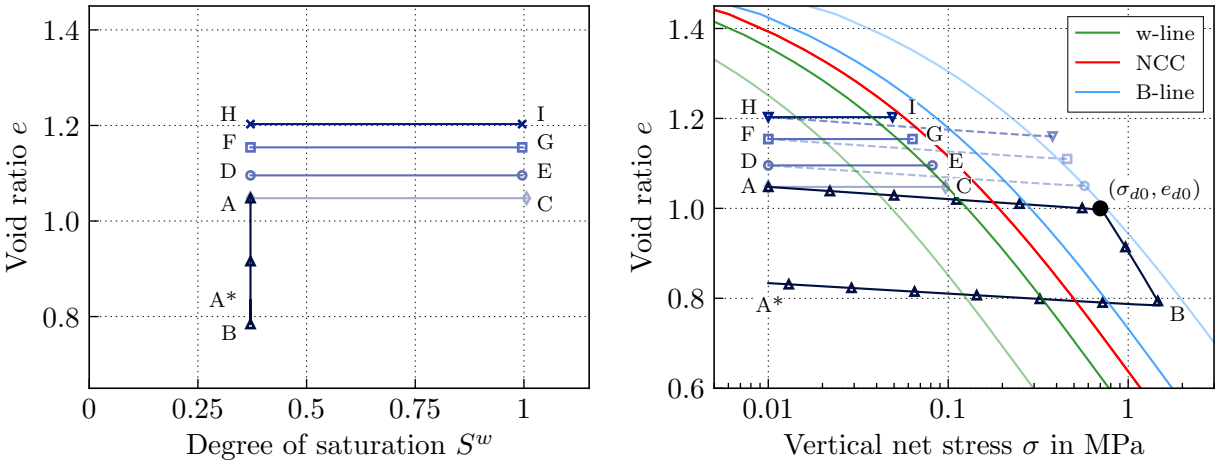

Figure 4.11.: Saturation-induced swelling pressure for different initial void ratios: Void ratio and wetting paths (left) and response of the model (right). Modified from Grandas Tavera et al. (2022).

volume swelling, the ratio R was smaller. The reason becomes clear on closer examination of the evolution equations (4.19) and (4.20): the degradation of σ_d was influenced by both $\dot{\epsilon}^w$ and $\dot{\epsilon}^h$. As $\dot{\epsilon}^h = 0$ had to be fulfilled for vertically unconfined swelling to ensure $\dot{\sigma} = 0$ (see Section 4.1.2), consequently, the degradation of σ_d was less pronounced and the ratio R stayed larger: thus, the w-line showed a slightly larger distance to the NCC at full saturation.

4.2.4. Collapse upon wetting

At a certain net stress level, the soil behaviour upon wetting at constant net stress changes from swelling to collapse. In the proposed constitutive model this phenomenon occurs, when the current vertical net stress is larger than the respective net stress on the w-line, hence $\sigma > \sigma_w$. As a consequence, the current void ratio is larger than the respective void ratio on the w-line, hence $e > e_w$ and the sign of the saturation-driven strain rate changes in Equation (4.9). The model response for one exemplary loading path is shown in Figure 4.12. From its preloading state (σ_{d0}, e_{d0}), the sample was only partially unloaded and the degree of saturation was increased at constant vertical net stress. During wetting (path C–D), the deformation increased until the final void ratio reached the w-line (at point D), hence $e = e_w$. The position before saturation (faint lines) and the final position (opaque lines) of the w-line (green) and B-line (medium blue) are displayed as well to show their evolution upon collapse.

4.3. Determination of material parameters

The proposed one-dimensional model requires seven parameters and four state variables, see Tables 4.1 and 4.2. All parameters can be determined by common laboratory tests under oedometric conditions. The parameters b and c must be iteratively calibrated by repeated back-calculation of these tests. The significance of these two parameters for the model response is therefore shown in more detail. Note that the parameter calibration does not require any microstructural investigations. The full parameter calibration was described in detail in Grandas Tavera et al. (2022). A simplified approach was proposed in Nitsch et al. (2023d)

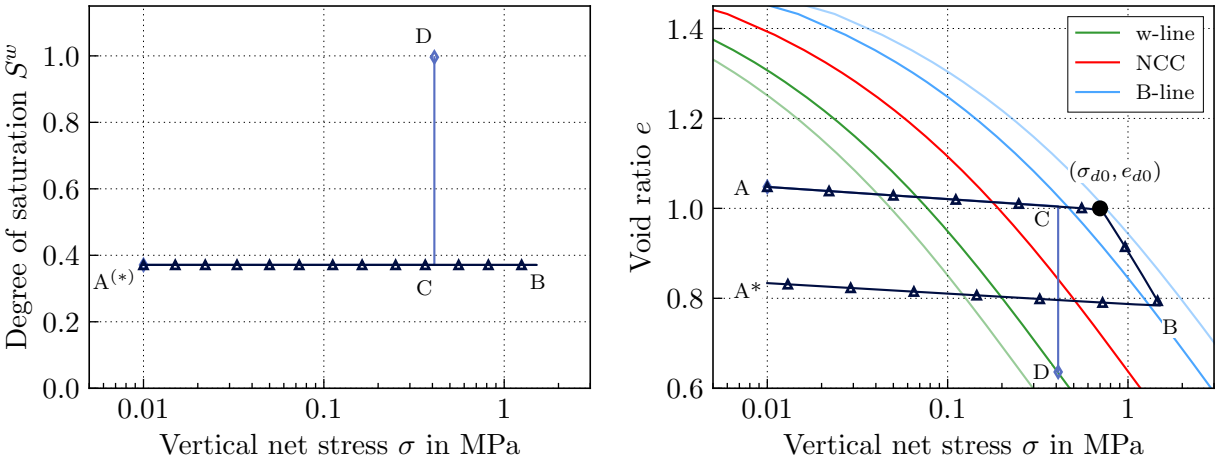

Figure 4.12.: Saturation-induced collapse: Net stress and wetting paths (left) and response of the model (right). Modified from Grandas Tavera et al. (2022).

and is presented in Section 4.5. In addition to the material parameters, the initial state of the material must be defined for every simulation. The exponent m is not considered as a material parameter in this work and chosen as a fixed value of $m = 6$. For the dry reference test a variation of the exponent m is presented in Figure 4.13. For a relatively small value of $m = 2$, a very subtle transition between elastic and anelastic material behaviour can be seen. For a large value of $m = 10$, the transition was unnaturally sharp. A medium value of $m = 6$ resulted in a distinct, yet still gradual transition. From a numerical point of view, an overly sharp transition can be challenging, while a too subtle transition may lead to inaccurate solutions.

The initial net stress, void ratio and degree of saturation are known by default. For the preloading state, ideally the net compaction stress is measured upon sample preparation. With knowledge of the reference un-/reloading index κ_{ref}, the corresponding void ratio can be computed. Alternatively, the net compaction stress can be determined with the results of a dry oedometer test or approximated and confirmed by back-calculations of experiments with the model.

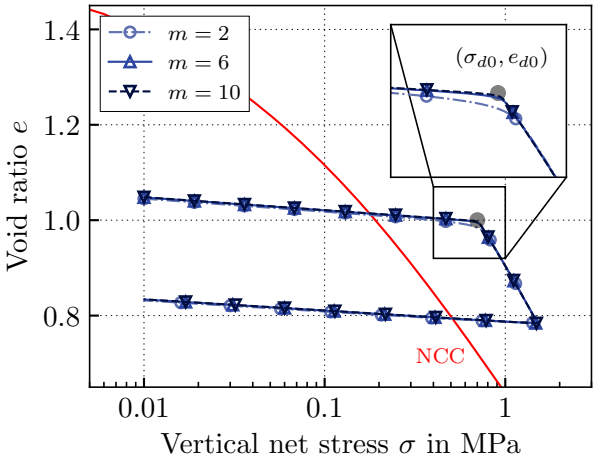

Figure 4.13.: Influence of the choice of the exponent m on the sharpness of the transition between elastic and anelastic material behaviour.

4.3.1. Parameters h_s, e_N and n of the normal compression curve

The position of the NCC is state-independent and acts as an attractor for any loading (mechanical or hydraulic) path. It can be best estimated by curve-fitting of Equation (4.4) to the compression path in the saturated state after vertically unconfined swelling. The magnitude of the void ratio e_N at very small stresses should be slightly larger than the void ratio on the w-line after vertically unconfined swelling (e_w). The parameters h_s and n can be determined simultaneously from the compression path at high net stresses. Since the preloading net stress has not yet been completely reduced by saturation in most materials, it is to be expected that the NCC will intersect the oedometric compression path in the area of low net stresses. If the results of a swelling pressure test exist, the plausibility of the position of the NCC can further be confirmed by ensuring that the swelling pressure for a specific void ratio $\sigma_{\max}(e)$ is smaller than the equivalent net stress $\sigma_e(e)$. Note that also a combination of one vertically unconfined swelling test and a saturated compression path from another test is feasible for a good calibration of e_N, h_s and n. Figure 4.14 shows the parameter calibration of the NCC for reconstituted Opalinus clay. The data used for fitting Equation (4.4) is shown in dark red solid markers. It represents the largest void ratio from a vertically unconfined swelling test decisive for e_N and the compression path required for the fit of h_s and n. The more load steps are available in the low-stress range after swelling, the more reliably the parameters can be determined. The magnitude of swelling pressure is depicted with a white filled square marker in Figure 4.14.

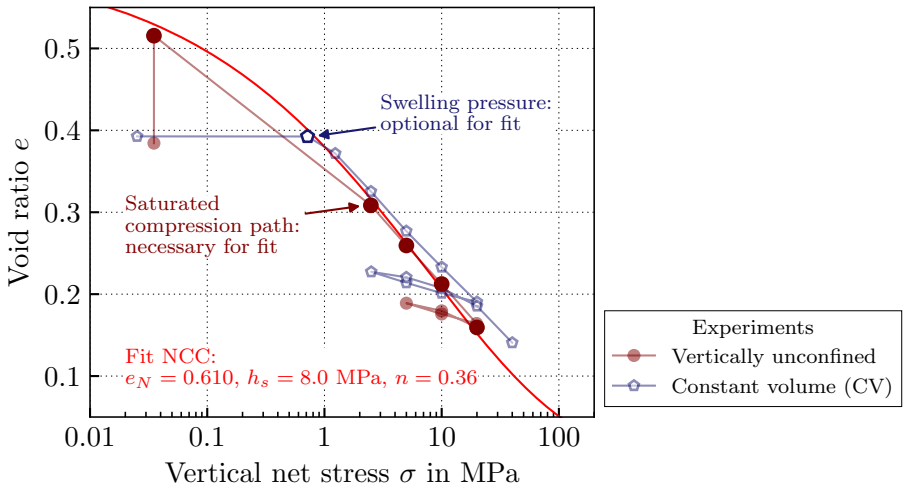

Figure 4.14.: Curve fitting of Equation (4.4) to experimental data for reconstituted Opalinus clay for calibration of the parameters of the NCC.

4.3.2. Elastic indices κ_{ref} and κ_w

The results of two oedometric tests with un- and reloading paths in the nearly dry ($S^e = 0$) and fully saturated state ($S^e = 1$) are required for the determination of the un-/reloading indices κ_{ref} and κ_w as the slope of the branches, respectively. A representative segment of the un-/reloading branch passing two point pairs (σ_a, e_a) and (σ_b, e_b) yields:

$$\kappa = \frac{\ln\left(\dfrac{1+e_a}{1+e_b}\right)}{\ln\left(\dfrac{\sigma_b}{\sigma_a}\right)}. \tag{4.23}$$

Figure 4.15 shows the representative segments of the un-/reloading branches for two oedometric compression and rebound tests on Opalinus clay in the dry, reference state and in the fully saturated state following vertically unconfined swelling. The elastic indices κ_{ref} and κ_w are calibrated with the indicated point pairs using Equation (4.23).

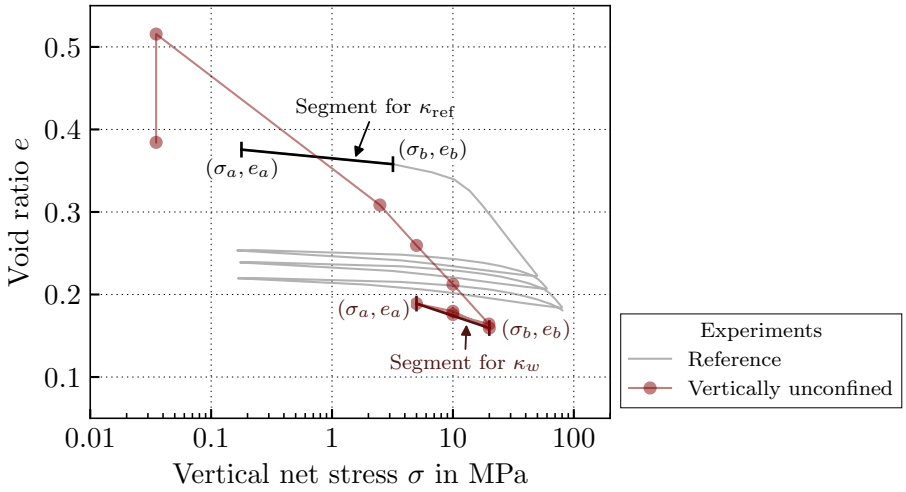

Figure 4.15.: Point pairs on representative segments on the un-/reloading branches from oedometric compression tests in the dry reference and fully saturated state on Opalinus clay for calibration of κ_{ref} and κ_w with Equation (4.23).

Alternatively, κ_w can also be determined from the slope of a multi-step swelling test with unloading following e.g. the method of Huder and Amberg (1970) or ISRM (1979), as these represent the saturated elastic stiffness.

4.3.3. Parameter b for the evolution of the saturation driven strain

The material parameter b determines the curvature of the sigmoid-shaped relationship between void ratio and water content for the evolution of the saturation-driven strain rate in Equation (4.9). It should be selected such that the inflection point of the mechanism is reached after approx. 50 % of the amount of water required during saturation. If b is selected too small, the inflection point occurs at high degrees of saturation and the maximum expansion cannot be achieved. A premature decay of the swelling mechanism by choosing too large values for b, which shifts the inflection points to small degrees of saturation, should be avoided as well, as the amount of swelling expansion will be underestimated. The recalculation of a vertically unconfined swelling test and the verification of the predicted development of the void ratio vs. the water content thus enables the estimation of b. Note that the limit void ratio e_w is also influenced by the parameter c as it depends on the evolution of the preloading stress σ_d. Thus, these two parameters should ideally be determined together. As a starting point it is recommended to choose a value of $c = 1.0$ and optimize it thereafter. The non-unique trend for the parameter b is shown in Figure 4.16. Therein b was varied, while the parameter for yielding was chosen arbitrarily as $c = 2.6$. The maximum void ratio upon wetting e_w (left), the evolution of $R = \sigma_B/\sigma_e$ (centre) and the sigmoid swelling mechanism (right) are presented. With increasing b, the inflection point was shifted to smaller water contents in the diagram on the right-hand side of Figure 4.16. For a small value of $b = 5$, the inflection point was not yet reached and the e–w curve did not yet flatten. For a large value of $b = 50$, a pronounced plateau

in the e–w curve is evident. Both extreme values underestimate the evolution of deformation upon swelling and are not able to reproduce vertically unconfined swelling correctly. The medium value of $b = 17$ results in a well-shaped sigmoid-curve for e–w and consequently for the evolution of the ratio $R = \sigma_B/\sigma_e$ as well.

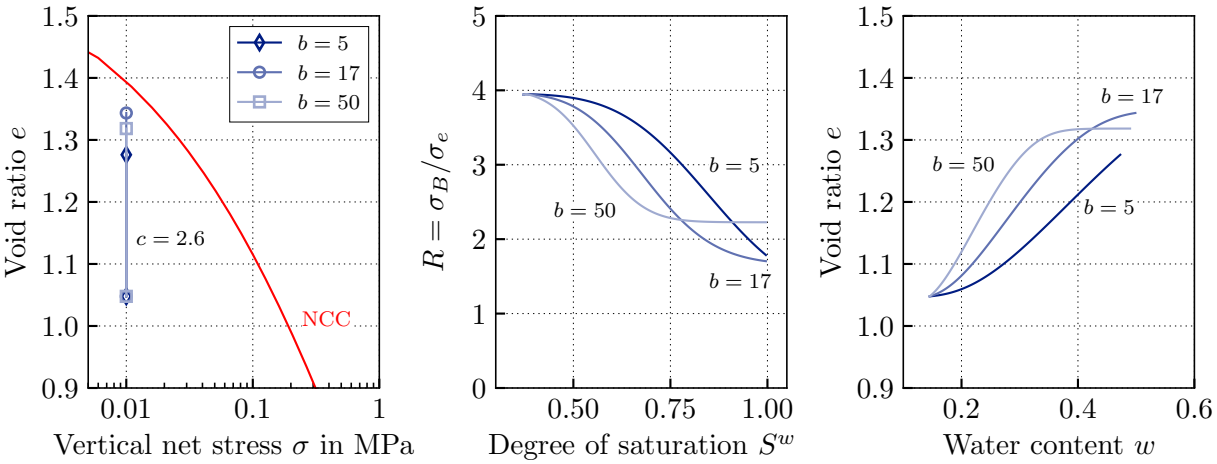

Figure 4.16.: Influence of parameter b during vertically unconfined swelling: void ratio versus vertical net stress and NCC (left), horizontal distance $R = \sigma_B/\sigma_e$ between B-line/w-line and NCC (centre) and void ratio vs. water content (right). Modified from Grandas Tavera et al. (2022).

4.3.4. Parameter c for the evolution of preloading net stress

The parameter c mainly controls the evolution of the preloading net stress σ_d. However, it also affects the position of the w-line and therefore the magnitude of the swelling phenomena. Thus, it must be optimised together with the previous parameter b. Most decisive for the value of c is the slope of the compression line after saturation, especially after vertically unconfined swelling. Contrary to b, a unique trend for the value of c exists and is shown in Figure 4.17 for the maximum void ratio upon wetting e_w (left), the evolution of $R = \sigma_B/\sigma_e$ (centre) and the sigmoid swelling mechanism (right). The subsequent compression paths after saturation are shown as dashed lines in the $e - \log(\sigma)$ diagram of Figure 4.17. Note that the medium dark paths ($c = 2.6$ and $b = 17$) in Figure 4.16 and 4.17 correspond to each other.

For $c = 1$, which is equivalent to omitting the parameter, the reduction of the bounding net stress σ_B, preloading net stress σ_d and ratio R during saturation was very pronounced and the loading path coincided with the NCC. With increasing c, the reduction was slowed down and smaller deformation took place upon wetting. Special attention has to be given to the simulation of unsaturated states, when calibrating c. If R does not decrease sufficiently, the transition from elastic to anelastic material behaviour might be underestimated for unsaturated states and already coincide with the fully saturated state. The characteristic behaviour of a *hook* in the $e - \log(\sigma)$ space, as reported e.g. by Nowamooz and Masrouri (2008), cannot be simulated in that case. However, an overly strong reduction of R may lead to an underestimation of the swelling phenomena, since the w-line does not sufficiently approach the NCC.

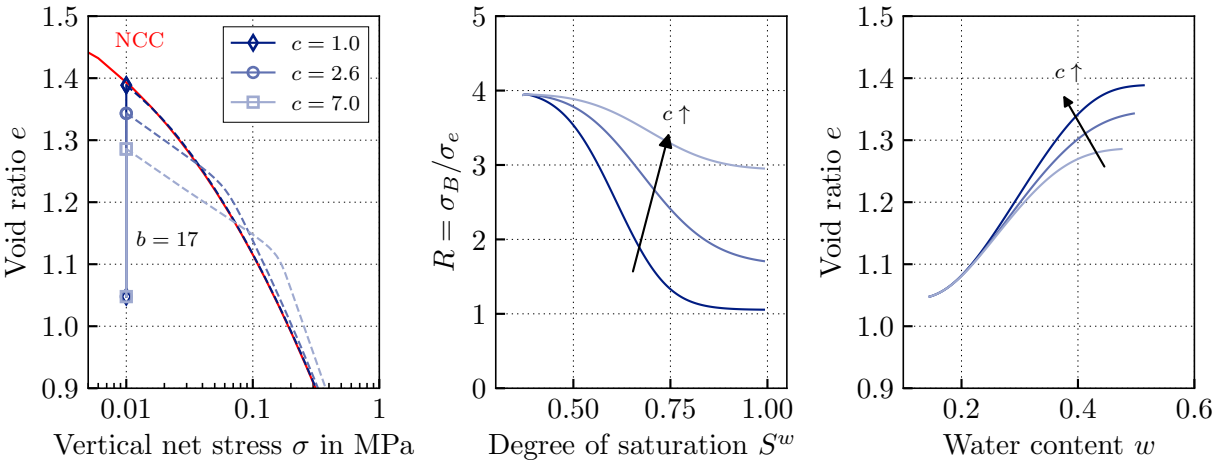

Figure 4.17.: Influence of parameter c during vertically unconfined swelling: void ratio versus vertical net stress and NCC (left), horizontal distance $R = \sigma_B/\sigma_e$ between B-line/w-line and NCC (centre) and void ratio vs. water content (right). Modified from Grandas Tavera et al. (2022)

4.4. Comparison with experimental results

The performance of the proposed one-dimensional model was validated by simulating the experimental results of different expansive soils. The integration of the constitutive equations is performed in a single point in terms of strain or saturation increments. Time dependency is not considered. In addition to the campaign on reconstituted Opalinus clay (Nitsch et al., 2023a), studies on a silt-bentonite mixture (Nowamooz and Masrouri, 2008) and a sand-bentonite mixture (Lang, 2019) were used, covering relevant hydro-mechanical loading paths in unsaturated and saturated conditions including vertically unconfined and constant volume swelling. The parameters for these materials were calibrated based on available tests for each material. A single set of parameters was used to simulate the experiments for each material. These parameters are summarized in Table 4.4. The considered materials represent a relatively wide range of unsaturated swelling clays with respect to their smectite content x_{sc} and thus the magnitude of the swelling phenomena.

Table 4.4.: Typical range of the model parameters of the one-dimensional hypoplastic model and model parameters for three different expansive soils.

Parameter	Range	Reconstituted Opalinus clay (Nitsch et al., 2023a)	Bentonite-sand mixture (Lang, 2019)	Bentonite-silt mixture (Nowamooz and Masrouri, 2008)
x_{sc} in wt-%	–	5*	30-35	62
e_N	0.5 – 1.8	0.610	0.895	1.615
h_s in MPa	1 – 25	8.0	18.0	1.2
n	0.3 – 0.6	0.36	0.31	0.40
κ_{ref} (10^{-3})	1 – 15	3.792	1.103	2.017
κ_w (10^{-3})	0.5 – 35	15.37	7.044	26.47
b	15 – 60	55	15	17
c	2 – 10	4.5	5.0	2.6

* Additionally, 30% illite content is present in the material.

For simulations of unsaturated suction-controlled laboratory tests, the soil water retention curve of the respective materials was applied to determine the respective degree of saturation.

4.4.1. Reconstituted Opalinus clay

Starting from very similar initial states, samples of reconstituted Opalinus clay were fully saturated and subsequently subjected to oedometric loading and unloading (Nitsch et al., 2023a). Different boundary conditions were investigated during saturation prior to the mechanical loading paths: (a) constant volume (CV, swelling pressure test OPA-0-34), (b) constant volume followed by unloading (OPA-0-07) and (c) vertically unconfined swelling (VU, OPA-0-24). A test on a dry sample serves as reference (OPA-0-33). The initial conditions for the simulations are gathered in Table 4.5 and the material parameters[1] were already summarized in Table 4.4. Figure 4.18 shows the results of the simulations (right) and the experiments (left).

Table 4.5.: Initial conditions for the simulations of experiments on reconstituted Opalinus clay shale from Nitsch et al. (2023a).

	σ_{d0} (MPa)	e_{d0}	σ_0 (MPa)	e_0	$S_0^w = S^{\text{ref}}$
Reference	:	:	0.18	0.376	:
Constant volume (CV), CV + unloading	10.535	0.359	0.035	0.388	0.13
Vertically unconfined (VU)	:	:	0.025	0.387	:

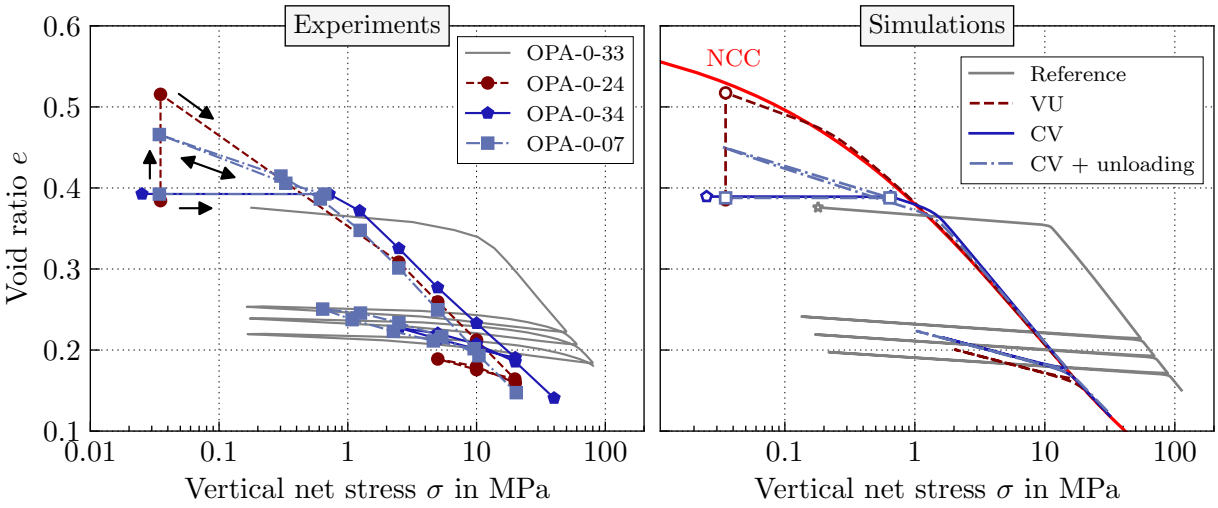

Figure 4.18.: Simulation of oedometric compression tests in the reference state and preceded by saturation at different boundary conditions on reconstituted Opalinus clay (right) and experimental results (left, Nitsch et al. (2023a)). The NCC is shown in red. Modified from Grandas Tavera et al. (2022).

As can be seen, the model was able to predict the magnitude of the swelling phenomena effectively as well as the material response in the dry and saturated state under oedometric loading

[1]Note that the void ratio e in the experimental campaign on reconstituted Opalinus clay was computed linearized in reference to its initial state e_0 in Nitsch et al. (2023a), Nitsch et al. (2023d), Grandas Tavera et al. (2022) and Machaček et al. (2024). In this work, however, it was evaluated incrementally using the current strain increment to ensure consistency with evaluation within FE simulations. This refinement in the evaluation method enhanced the comparability between experimental and numerical results. As a result, selected material properties differed slightly and constitutive model parameters were recalibrated.

and unloading. The larger discrepancies between experiment and simulation at low net stress levels in the swelling test under vertically unconfined conditions are attributable to the limited experimental data, such that linear connection between points does not necessarily represent the true material response. The affinity of the NCC and the B-line, hence the first loading path of the reference test, could be clearly identified. Further, the pronounced decrease of the elastic stiffness on the un-/reloading branches with increasing saturation was well reproduced by the simulations. The magnitude of expansion and swelling pressure was predicted very well by the model with a single set of parameters.

4.4.2. Bentonite-silt mixture

Nowamooz and Masrouri (2008) carried out vertically unconfined swelling tests starting from unsaturated conditions with subsequent oedometric loading and unloading. At constant net stress and starting from comparable initial void ratios, one sample was fully saturated (M1) while two samples were partially saturated by suction control. The respective final degrees of saturation for the latter two tests were determined by fitting the van Genuchten (1980) model to the experimentally determined SWRC shown in Figure 4.19. Samples M4 and M5 reached $S^w = 0.79$ and $S^w = 0.54$, respectively. One further sample M0 was subjected to loading and unloading without prior saturation (Nowamooz, 2007). The initial conditions for the simulations are listed in Table 4.6 and the materials parameters are summarized in Table 4.4.

Table 4.6.: Initial conditions for the simulations of experiments on a bentonite-silt mixture from Nowamooz and Masrouri (2008).

	σ_{d0} (MPa)	e_{d0}	σ_0 (MPa)	e_0	S_0^w
M1 ($S^w = 1.0$)	0.700	1.001	:	1.047	:
M4 ($S^w = 0.79$)	0.540	1.051	0.010	1.095	0.371
M5 ($S^w = 0.54$)	0.488	1.071	:	1.102	:
M0 (reference)	0.700	1.080	:	1.128	:

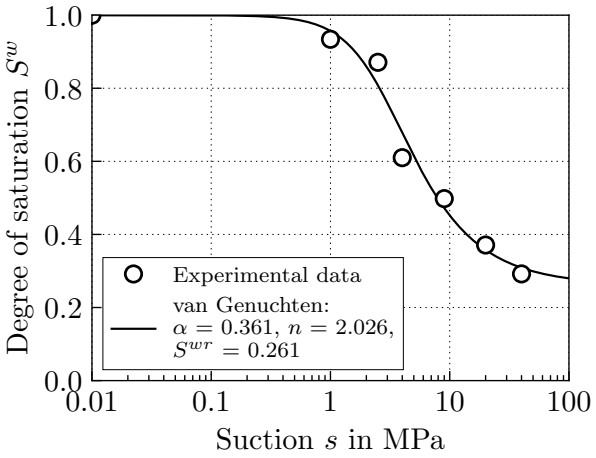

Figure 4.19.: Soil water retention curve of a bentonite-silt mixture for vertically unconfined conditions: experimental data (Nowamooz and Masrouri, 2008) and van Genuchten fit. Modified from Grandas Tavera et al. (2022).

Figure 4.20 compares the results of the simulations (right) with the experiments (left). The results show that all tests approached the NCC upon monotonic loading in the simulations. The

magnitude of the stiffness as well as the preloading net stress and the decrease of elastic stiffness with increasing saturation were very well reproduced by the model for different unsaturated states. Furthermore, the model predicted the magnitude of expansion at full saturation (M1) well. For swelling at unsaturated conditions, the model was able to reproduce the increasing deformation with increasing final degree of saturation, but the magnitude of expansion was slightly overestimated (for test M4). This may be improved by sacrificing the accuracy in the prediction of the loading behaviour (by reducing the model parameter c). Note that the determination of the final degree of saturation by application of the SWRC further introduced some uncertainties. Nevertheless, an overall good agreement between the experimental data and the simulations was evident.

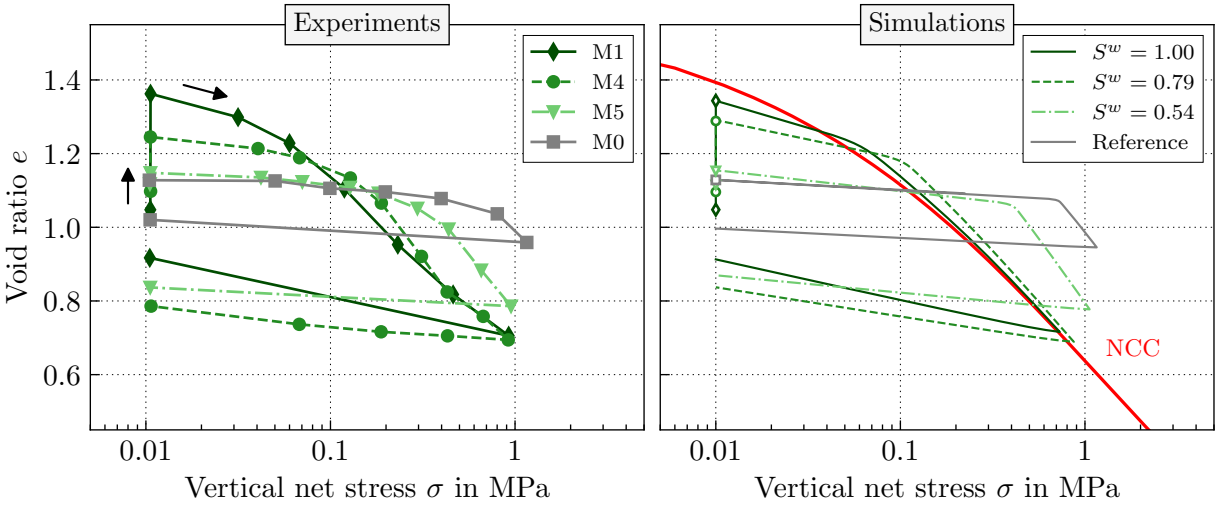

Figure 4.20.: Simulation of vertically unconfined swelling and subsequent oedometric compression tests under unsaturated and fully saturated conditions on a bentonite-silt mixture (right) and experimental results (left, Nowamooz and Masrouri (2008)). The NCC is shown in red. Modified from Grandas Tavera et al. (2022).

4.4.3. Bentonite-sand mixture

The experimental campaign of Lang (2019) included constant volume swelling tests and vertically unconfined swelling tests with subsequent oedometric loading and unloading starting from unsaturated and saturated conditions. This allowed to evaluate the prediction capability of the model with one parameter set for not solely the magnitude of both, swelling strain and swelling pressure, but also for the compression behaviour in unsaturated conditions. Starting from the same initial state, one sample was directly subjected to the mechanical loading (BS-SCR-4). In addition, one sample was fully saturated at vertically unconfined conditions (BS-SCR-4) and one sample at constant volume conditions (BS-WCV-1). Further, for both mechanical boundary conditions, two samples each were saturated by controlling the suction at constant net stress (BS-SCR-2 and -3) and at constant volume conditions (BS-WCV-5 and -7), resulting in different degrees of saturation upon the subsequent compression.

The final degrees of saturation for the partially saturated tests were again determined by evaluation of the van Genuchten (1980) model which was fitted to experimental data. Lang (2019) investigated the dependency of the SWRC on the net stress. Therefore, two SWRCs were chosen, which are shown in Figure 4.21: one for vertically unconfined conditions (black line,

$\alpha = 2.976, n = 1.269$) and one for confined conditions (grey line, $\alpha = 0.401, n = 1.482$). The residual degree of saturation was $S^{wr} = 0.26$. The vertically unconfined swelling tests were carried out under a load of $\sigma = 2.5$ kPa (ensuring contact to the load cell), whereas the SWRC measurements refer to zero net stress. On that account, the van Genuchten fit for vertically unconfined conditions also takes data for load of $\sigma = 2.5$ kPa into account. For vertically unconfined swelling tests, the final degrees of saturation for the unsaturated samples were determined to $S^w = 0.55$ (BS-SCR-3) and $S^w = 0.64$ (BS-SCR-2). For constant volume swelling tests, depending on the choice of the SWRC, the respective degrees of saturation were $S^w = 0.54$ and $S^w = 0.64$ for the vertically unconfined fit and $S^w = 0.61$ and $S^w = 0.80$ for the constant volume fit each for sample BS-WCV-5 and BS-WCV-7. To illustrate the influence of the chosen SWRC on the model's performance, both SWRCs are employed. A significant difference in the values from the different SWRC fits becomes apparent. The material parameters and the initial conditions for the simulations are listed in Table 4.4 and Table 4.7.

Table 4.7.: Initial conditions for the simulation of tests on a bentonite-sand mixture from Lang (2019).

	σ_{d0} (MPa)	e_{d0}	σ_0 (MPa)	e_0	S_0^w
All tests	10.2	0.498	0.025	0.530	0.468

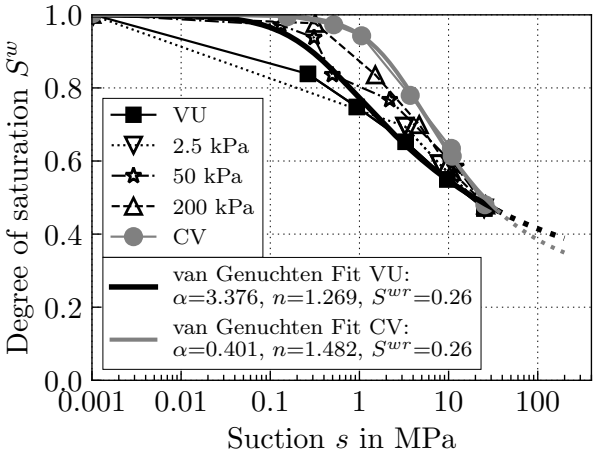

Figure 4.21.: Soil water retention curves of a bentonite-sand mixture: experimental data from Lang (2019) and two van Genuchten fits representing constant volume conditions (grey) and vertically unconfined conditions (black). Modified from Grandas Tavera et al. (2022).

The simulation results for vertically unconfined conditions are shown in Figure 4.22 (right) together with the experimental results (left). Similar to the previously presented materials, the magnitude of expansion upon saturation and the material response upon mechanical loading were well reproduced by the model. The NCC was approached in all simulations and the reduction of elastic stiffness with increasing degree of saturation can be clearly seen. The simulation results for constant volume conditions, however, showed some differences from the experimental data, see Figure 4.23. The magnitude of swelling pressure in the fully saturated state was predicted well, but in the unsaturated states both approaches show some deficits, either under- or overestimating the magnitude of swelling pressure.

These results show that transferring the known hydraulic property of suction into a final degree of saturation achieved at unsaturated conditions bears a certain inaccuracy. If no exact pairs

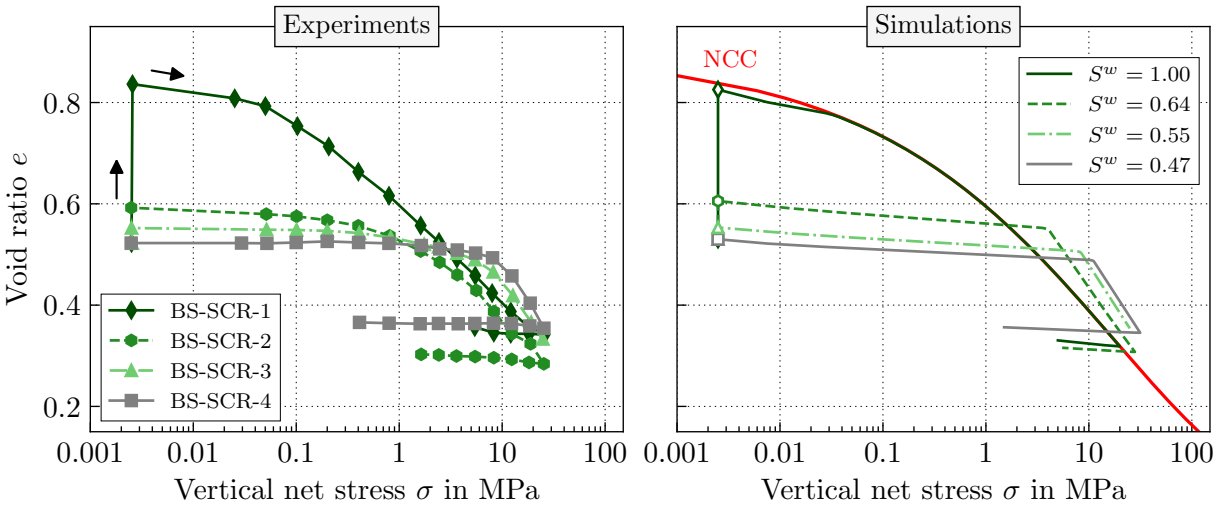

Figure 4.22.: Simulation of vertically unconfined swelling and subsequent oedometric compression tests under unsaturated and fully saturated conditions on a bentonite-sand mixture (right) and experimental results (left, Lang (2019)). The NCC is shown in red. Modified from Grandas Tavera et al. (2022).

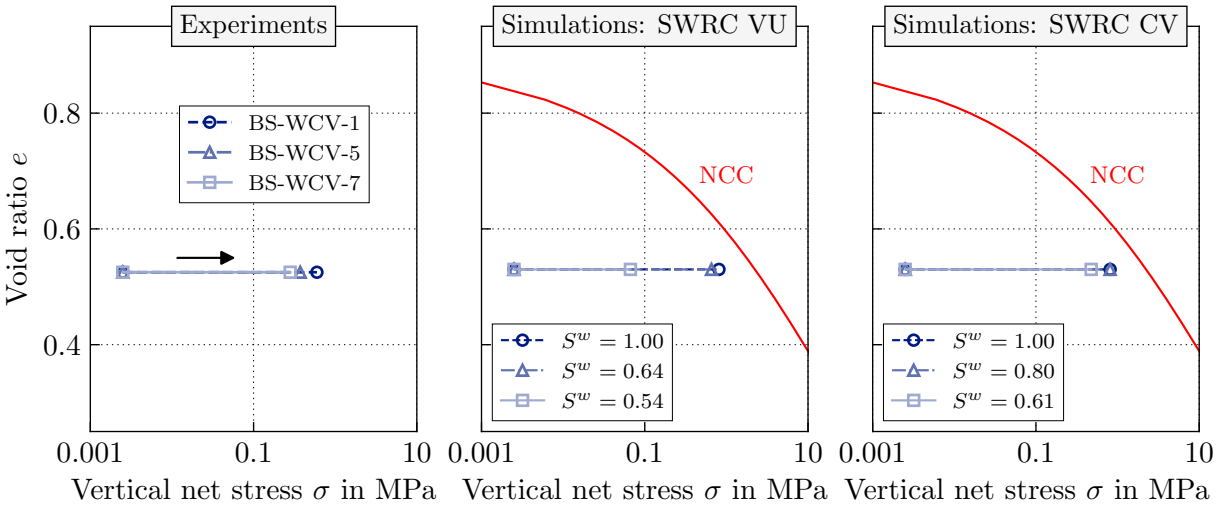

Figure 4.23.: Simulation of constant volume swelling tests under unsaturated and fully saturated conditions on a bentonite-sand mixture using the SWRC corresponding to vertically unconfined data (middle) and constant volume data (right) and experimental results (left, Lang (2019)). The NCC is shown in red. Modified from Grandas Tavera et al. (2022).

of values for the corresponding suction and degree of saturation are known, but the prediction is based on the application of a hydraulic model, which in turn is subject to uncertainties, the accuracy of the predicted material response is reduced. Determining the degree of saturation via the final water content after completion of lab tests avoids this and would enable a more accurate prediction of the material behaviour in unsaturated states. The limited prediction quality for the swelling pressure is also attributable to another aspect of the model formulation. For the material under investigation, the NCC was clearly defined by vertically unconfined swelling followed by oedometric loading. The swelling pressure was of a comparatively low magnitude and thus, the ratio R between the swelling pressure, i.e. net stress σ_w on the w-line after constant volume swelling, and the corresponding net stress σ_e on the NCC had to remain high. A reliable

prediction of the swelling pressure was only possible by a significantly delayed reduction of R, i.e., σ_d. As a consequence, the development of swelling pressure did not persist throughout the entire saturation process but instead diminished before full saturation was reached. The results indicate, that the shape of the NCC, defined by Equation (4.4), may not be suitable for all expansive materials. Nevertheless, an overall good performance of the model with a single set of parameters was again shown, especially for the material behaviour upon vertically unconfined swelling and subsequent oedometric loading.

4.5. Simplified parameter calibration

Experiments on expansive soils are often very time-consuming and therefore typically address only selected aspects of hydro-mechanical behaviour, usually the magnitude of swelling strain or swelling pressure, and the oedometric compression and rebound response after saturation (swelling). Experimental studies in the literature have shown that swelling pressure correlates with mineralogical composition, particularly smectite or bentonite content (Komine and Ogata, 2003; Agus and Schanz, 2008; Zeng et al., 2022). In the proposed model, swelling pressure is governed by the material parameters. Therefore, correlations observed for swelling pressure in experiments may also extend to the parameters themselves, allowing a direct link to the amount of expansive clay minerals in the material. Validation of the constitutive model against three reference materials (Table 4.4) indicated that typical parameter ranges could be established across a broad span of expansive clay mineral contents. For instance, the void ratio e_N at zero stress scaled with the montmorillonite/smectite fraction (5–62 % in the examined materials), whereas other parameters, such as the curvature parameter n of the NCC, appeared largely independent of clay mineralogy. These considerations motivated the development of a simplified calibration procedure, which is proposed in the following. In addition to basic mineralogical information, it requires only one vertically unconfined oedometric swelling test followed by compression (Nitsch et al., 2023d). The simplified calibration targeted the un-/reloading index κ, which is decisive for the elastic stiffness, and the parameter c together with the initial state (σ_{d0}, e_{d0}). It was evaluated against experimental data from three further studies (Wang et al., 2013b; Monroy et al., 2015; Zhang et al., 2022) and is discussed in detail below. These materials contain different smectite contents x_{sc} than those previously investigated.

4.5.1. Procedure

The loading history of compacted samples is essential for their material behaviour, but is often not sufficiently investigated or documented in the context of experimental campaigns. As a result, the elastic stiffness or the un-/reloading index of the compacted material before saturation is often unknown. However, the elastic stiffness in the unsaturated state can often be estimated from the oedometric behaviour in the saturated state. Experience from Section 4.4 has shown, that the ratio of the un-/reloading indices in the dry and saturated state correlated with the smectite content x_{sc} in the expansive soil. The respective data for the three different materials studied in Section 4.4 are presented as black markers in Figure 4.24. The illustrated correlation can be described by the following exponential function (with x_{sc} in wt-%):

$$\frac{\kappa_{\mathrm{ref}}}{\kappa_w} = 0.29 \exp(-0.021\, x_{\mathrm{sc}}). \tag{4.24}$$

The blue markers correspond to additional materials, where only the un-/reloading index κ_w in the saturated state was known. The elastic un-/reloading index κ_{ref} in the almost dry state was estimated using the ratio from Equation (4.24).

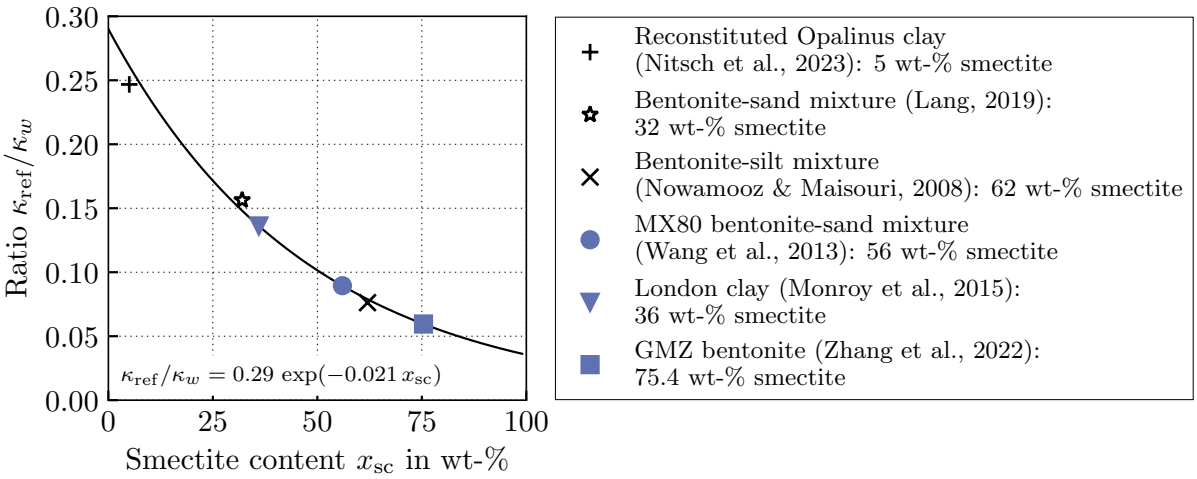

Figure 4.24.: Correlation of the ratio of the values of the un-/reloading indices in the dry and saturated states with the smectite content x_{sc} of expansive soils: Known experimental data (black symbols), trend line and estimated data (blue symbols). Modified from Nitsch et al. (2023c).

For the calibration of the parameter c, the left-hand side of Figure 4.25 shows the relevant decision aid: the parameter should be selected according to the shape of the compression path after determining the position of the NCC and parameter b. With c approaching 1, the *hook* in the transition zone from elastic to plastic behaviour becomes less pronounced. Note that the preloading state (σ_{d0}, e_{d0}) must be known or otherwise iteratively approximated and optimized together with the parameter c by back-calculating the experiment. In general, it must be located to the right of the NCC and on a straight line with the gradient κ_{ref} in relation to the state (σ_0, e_0) of the sample prior to saturation, see right-hand side of Figure 4.25. According to the author's experience, an initial ratio between the bounding net stress on the B-line σ_{B0} and the equivalent net stress σ_{e0} on the NCC in the magnitude of $2 < R < 4$ can be applied for approximation.

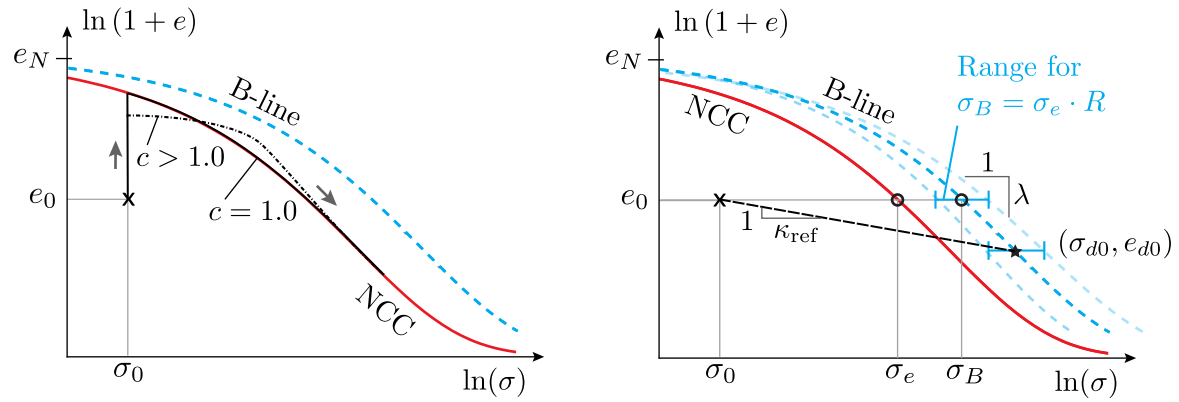

Figure 4.25.: Idealized influence of the parameter c on the prediction of the material behaviour in a swelling test with subsequent compression (left) and idealized approximation of the initial preloading state (σ_{d0}, e_{d0}) with a range of $2 < R < 4$ (right). Modified from Nitsch et al. (2023a).

4.5.2. Application

The material parameters and initial conditions of the materials used in this section can be found in Table 4.8. Note that for the calibration of the material parameters, no tests other than those presented were used. The simulation results are displayed together with the experimental results in Figure 4.26. Therein, the experiments are shown with markers and the simulations with solid lines. The NCC is again shown in red. In addition, the initialized preloading state (σ_{d0}, e_{d0}) and the unloading path reaching the state prior to wetting are visualized with an „x“ and dashed line as well (on κ_{ref}).

Table 4.8.: Model parameters and initial conditions for simulation of three different materials.

	London Clay (36%) (Monroy et al., 2015)	MX80 Bentonite-Sand (56%) (Wang et al., 2013b)	GMZ Bentonite (75.4%) (Zhang et al., 2022)
x_{sc} in %	36	56	75.4
Parameter			
e_N	1.186	1.118	1.38
h_s in MPa	2.2	29.1	17.6
n	0.620	0.388	0.380
κ_{ref} (10^{-3})	1.930	0.8375	2.052
κ_w (10^{-3})	13.9569	9.361	34.476
b	21	22	20
c	6.0	9.0	5.5
Initial state			
σ_{d0} in MPa	13.94	8.12	0.616
e_{d0}	0.6366	0.810	0.949
σ_0 in MPa	0.1	0.11	0.07
e_0	0.6428	0.824	0.949
S_0^w	0.474	0.388	0.671

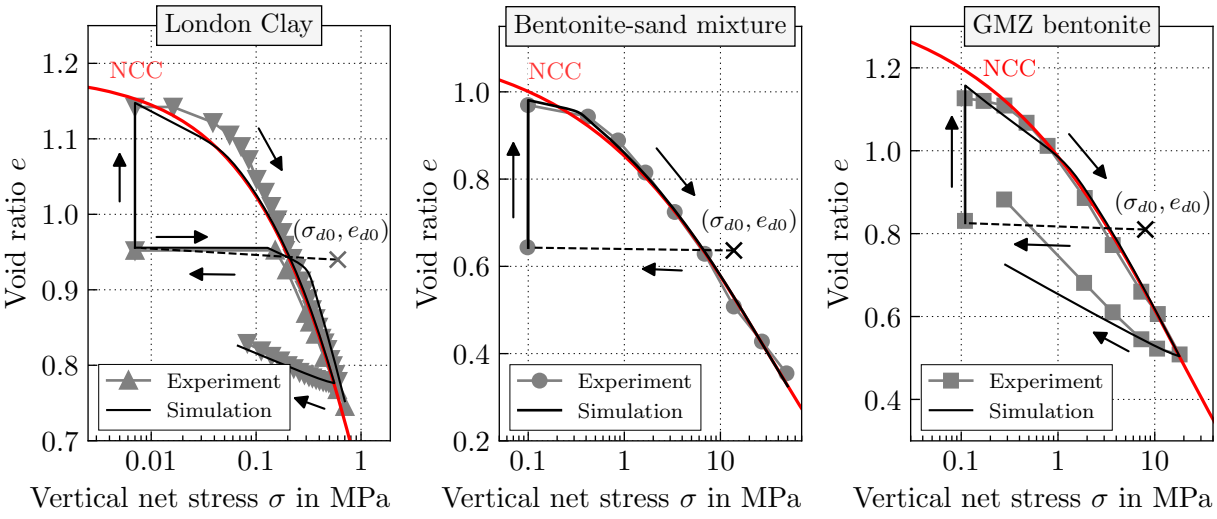

Figure 4.26.: Simulation of swelling tests followed by oedometric loading paths on a MX80-bentonite-sand mixture (Wang et al., 2013b), GMZ bentonite (Zhang et al., 2022) and London Clay (Monroy et al., 2015).

The results highlight that the constitutive model in combination with the simplified parameter calibration were able to reproduce the experiments well. The magnitude of all swelling phenomena and the compression paths were predicted in very good accordance with the experiments. Some deviations are visible for the unloading path of GMZ bentonite. This was accepted by choosing the saturated un-/reloading index κ_w in a manner to match the reloading part on the loading path preferably. Only minor deviations are seen for London Clay. These were attributed to the overall relatively loose state of the material and thus small area of net stress and void ratio. As the NCC was formulated to match a range of net stress and void ratio, as wide as possible, the prediction is less precise in this case. For the bentonite-sand mixture, excellent agreement between simulation results and experimental results was evident. Overall, the prediction can be enhanced by a more detailed parameter calibration. However, also with the simplified procedure, the model was able to reproduce the main characteristics of the material behaviour well.

4.6. Concluding remarks

This chapter presented a novel hypoplastic constitutive model for the mechanical behaviour of expansive soils. It is capable of capturing the key features as observed in oedometric swelling and oedometric compression and rebound tests. The model is formulated in terms of net stress and degree of saturation. The total strain rate is decomposed into two components: one associated with changes in saturation, and the other with variations in net stress. No distinction is made between elastic and plastic strains.

Through this decomposition, the model successfully reproduces maximum swelling strains under constant net stress (vertically unconfined) and maximum net swelling stresses under constant volume conditions. In addition to the void ratio, two scalar variables are introduced to account for the loading history of the material, the preloading net stress and its corresponding void ratio. The calibration of model parameters based on standard laboratory tests has been outlined.

The model showed good agreement with experimental results from swelling tests under oedometric conditions, including loading and unloading cycles, for three different materials. In addition, a simplified parameter calibration was presented, which provides a first step towards identifying potential correlations between material parameters and the mineralogical composition of expansive clays.

5. Hypoplasticity for expansive soils: full formulation

For the application in engineering boundary value problems, the proposed one-dimensional constitutive model „Hypoplasticity for expansive soils“ is generalised as a full tensorial formulation. The first version of the full formulation of the model was published in Machaček et al. (2024) and is further developed and discussed in this work. It is formulated using the net stress tensor $\boldsymbol{\sigma}$ and strain tensor $\boldsymbol{\epsilon}$ and effective degree of saturation S^e. In this work, the following features are introduced to the model for the generalisation:

- The preloading net stress for the current void ratio σ_B, which is a point in the one-dimensional model, is now represented by a surface in the three-dimensional stress space. States within this surface have a nearly elastic, hence reversible response, while states exceeding the surface have an irreversible response. This surface is referred to as the preconsolidation surface and is described by a generalized version of the yield surface of the Modified Cam Clay model (MCC, Burland (1990)).
- The total strain rate $\dot{\boldsymbol{\epsilon}}$ and both components, the hypoplastic strain rate $\dot{\boldsymbol{\epsilon}}^h$ and the saturation-driven strain rate $\dot{\boldsymbol{\epsilon}}^w$, are now three-dimensional strain tensors with six independent components.
- Upon monotonic shearing, the full formulation of the model must reach the critical state, at least asymptotically.

In this chapter, the requirements necessary for the generalisation of the model are introduced and additional equations are discussed. The capabilities of the full formulation of the model are presented, remarks on the parameters are given and the formulation is validated against the results from the same experimental campaigns used for the demonstration of the one-dimensional formulation in single element simulations.

5.1. Full formulation and equations

The main evolution equation of the one-dimensional model, Equation (4.8), is extended to a full tensorial formulation. Analogously to the one-dimensional formulation, the total strain rate tensor $\dot{\boldsymbol{\epsilon}}$ is decomposed into two portions: $\dot{\boldsymbol{\epsilon}} = \dot{\boldsymbol{\epsilon}}^h + \dot{\boldsymbol{\epsilon}}^w$:

$$\dot{\boldsymbol{\sigma}} = \mathsf{E} : \left(\dot{\boldsymbol{\epsilon}}^h - \Lambda \mathbf{m} \left\| \dot{\boldsymbol{\epsilon}}^h \right\| \right) \quad \text{with} \quad \dot{\boldsymbol{\epsilon}}^h = \dot{\boldsymbol{\epsilon}} - \dot{\boldsymbol{\epsilon}}^w. \tag{5.1}$$

Therein, $\mathbf{m}$ denotes the direction of anelastic flow and Λ is the plastic multiplier. The latter may be defined as $\Lambda = \mathrm{OCR}^{-m}$, analogously to the one-dimensional formulation, however, it is very sensitive to changes in net stress, even for small strain increments. To improve the robustness of the numerical time integration, it can be alternatively expressed with the help of

the preconsolidation surface as $\Lambda = \exp(m_O\, F)$. Both, the overconsolidation ratio OCR and preconsolidation surface F are introduced in Section 5.1.1, The factor $m_O \approx 100$ differs from the original formulation in Equation (4.2) ($m \approx 6$) and is renamed for the sake of clarity. In Equation (5.1), E is a fourth-order tensor and denotes the barotropic elastic stiffness similar to the one used in the anisotropic and isotropic versions of viscohypoplasticity (Niemunis, 2003; Niemunis et al., 2009):

$$\mathsf{E} = \frac{-\mathrm{tr}\,\boldsymbol{\sigma}}{3\kappa}\hat{\mathsf{L}}, \tag{5.2}$$

with the un-/reloading index κ and the hypoplastic linear stiffness $\hat{\mathsf{L}}$ defined as:

$$\hat{\mathsf{L}} = a_M^2 \left(\left[\frac{F_M}{a_M}\right]^2 \mathsf{I} + \hat{\boldsymbol{\sigma}}\hat{\boldsymbol{\sigma}} \right). \tag{5.3}$$

Therein I is the symmetric fourth order identity tensor and $\hat{\boldsymbol{\sigma}}$ is the normalised net stress $\hat{\boldsymbol{\sigma}} = \boldsymbol{\sigma}/\mathrm{tr}\,\boldsymbol{\sigma}$. The expression $\hat{\boldsymbol{\sigma}}\hat{\boldsymbol{\sigma}}$ indicates dyadic multiplication, i.e. $(\hat{\boldsymbol{\sigma}}\hat{\boldsymbol{\sigma}})_{ijkl} = \hat{\sigma}_{ij}\hat{\sigma}_{kl}$. a_M and F_M are coefficients defined as:

$$F_M = \sqrt{\frac{1}{8}\tan^2\Psi + \frac{2-\tan^2\Psi}{2+\sqrt{2}\tan\Psi\cos 3\theta}} - \frac{1}{2\sqrt{2}}\tan\Psi \tag{5.4}$$

$$\text{with} \quad \tan\Psi = \sqrt{3}\,\|\hat{\boldsymbol{\sigma}}^*\| \tag{5.5}$$

$$\text{and} \quad \cos 3\theta = -3\sqrt{6}\det\left(\boldsymbol{\sigma}^*\right)^{\rightarrow}, \tag{5.6}$$

$$a_M = \frac{\sqrt{3}\,(3-\sin\varphi_{\mathrm{ref}})}{2\sqrt{2}\sin\varphi_{\mathrm{ref}}}, \tag{5.7}$$

wherein $(\sqcup)^{\rightarrow} = \sqcup/\,\|\sqcup\|$ means normalization of the tensor $\sqcup$, $\boldsymbol{\sigma}^* = \boldsymbol{\sigma} - \mathrm{tr}\boldsymbol{\sigma}/3\,\mathbf{1}$ is the deviatoric part of the net stress tensor, θ is the Lode angle and φ_{ref} is the angle of internal friction in the reference (dry) state and a material constant of the full formulation of the model. In Equation (5.2), κ denotes the unloading/reloading index under *isotropic* deformation according to Butterfield (1979):

$$\ln\left(\frac{1+e_0}{1+e}\right) = \kappa \ln\left(\frac{p}{p_0}\right) \quad \text{with} \quad p = \frac{-\mathrm{tr}\,\boldsymbol{\sigma}}{3} = -\frac{(\sigma_{11}+\sigma_{22}+\sigma_{33})}{3}, \tag{5.8}$$

wherein the void ratio e_0 and the mean net stress p_0 correspond to a reference point on the current unloading/reloading branch and e and p denote the current state (compression is positive). Analogous to Equation (4.6) of the one-dimensional formulation, the un- and reloading index κ is saturation-dependent and defined by means of a linear interpolation between the fully saturated state (κ_w) and the nearly dry state (κ_{ref}):

$$\kappa(S^e) = \kappa_{\mathrm{ref}} + S^e\,(\kappa_w - \kappa_{\mathrm{ref}})\,. \tag{5.9}$$

Consequently, the barotropic elastic stiffness in Equation (5.2) is saturation-dependent.

5.1.1. Preconsolidation surface ($F = 0$) and overconsolidation ratio

In Equation (5.1), the intensity of anelastic flow $\mathrm{OCR}^{-m_O}\left\|\dot{\boldsymbol{\epsilon}}^h\right\|$ increases as the current net stress $\boldsymbol{\sigma}$ approaches the preconsolidation surface. To describe this surface in the stress space, a generalized version of the MCC yield surface (Roscoe and Burland, 1968) was adopted:

$$F \equiv \frac{1}{\beta^2}\left(\frac{p}{a}-1\right)^2 + \left(\frac{q}{Ma}\right)^2 - 1 = 0, \tag{5.10}$$

wherein q is the second Roscoe invariant defined as $q = \sqrt{3/2}\,\|\boldsymbol{\sigma}^*\|$. β is a material constant that changes the shape of the preconsolidation surface for subcritical stress ratios $|q/p| < M$ and $a = p_B/(1+\beta)$ is an auxiliary variable. p_B is the net preconsolidation pressure on the isotropic axis at the apex of the preconsolidation surface and therefore governs its size. For $\beta = 1.0$, the original formulation of Roscoe and Burland (1968) is recovered with $a = p_B/2$. The reason for adopting the generalized version of the preconsolidation surface is discussed in Section 5.2. In Equation (5.10), M is the slope of the critical state line in the stress space and depends on the angle of internal friction φ and on the Lode angle θ according to Grandas Tavera et al. (2020):

$$M = 6\sin\varphi \frac{(3 + \sin\varphi\cos 3\theta)}{9 - \sin^2\varphi}. \tag{5.11}$$

The preconsolidation surface is shown in the $q-p$ space in Figure 5.1. The current net stress state $\boldsymbol{\sigma}$ is located on a pseudo preconsolidation surface $F_+(\boldsymbol{\sigma}, p_{B+}) = 0$, which passes through the pseudo preconsolidation net stress p_{B+} on the isotropic axis, intersects the critical state line (CSL) at the apex a_+ and has the same material parameters φ and β. Equation (5.11) yields $M_c = 6\sin\varphi/(3 - \sin\varphi)$ in compression for $\cos 3\theta = 1$ ($\theta = 0$) and $M_e = -6\sin\varphi/(3 + \sin\varphi)$ in extension for $\cos 3\theta = -1$ ($\theta = 60°$).

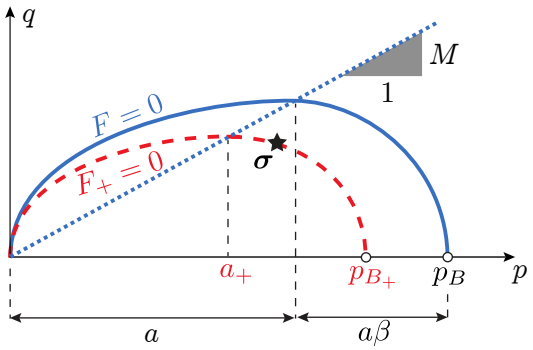

Figure 5.1.: Pseudo preconsolidation surface $F_+ = 0$ with size p_{B+} passing through the current net stress $\boldsymbol{\sigma}$, preconsolidation surface $F = 0$ with size p_B and critical state line with slope M passing through the maximum of both surfaces. Modified from Machaček et al. (2024).

Thereby, the overconsolidation ratio OCR is computed by comparing the preconsolidation pressure p_B, i.e. the size of the surface $F(\boldsymbol{\sigma}, p_B) = 0$, with the size p_{B+} of the pseudo preconsolidation surface $F_+(\boldsymbol{\sigma}, p_{B+}) = 0$ for the current state:

$$\mathrm{OCR} = p_B/p_{B+}. \tag{5.12}$$

The pseudo preconsolidation pressure $p_{B+} = a_+(1+\beta)$ can be obtained from the intersection of $F_+(\boldsymbol{\sigma}, p_{B+}) = 0$ with the isotropic axis by defining the pseudo auxiliary variable a_+:

$$a_+ = \begin{cases} -\dfrac{\sqrt{M^2\beta^2\left(M^2p^2 + q^2\left(\beta^2 - 1\right)\right)} + M^2p}{M^2\left(\beta^2 - 1\right)} & \text{for } \; q/p < M, \\ \dfrac{p}{2}\left[1 + \left(\dfrac{q}{Mp}\right)^2\right] & \text{for } \; q/p \geq M. \end{cases} \tag{5.13}$$

In Figure 5.1, the (pseudo) preconsolidation surface is shown for a specific state, i.e. according to the current net stress $\boldsymbol{\sigma}$, void ratio, degree of saturation and angle of internal friction φ. Experiments have shown that the angle of internal friction is not constant, but a function of the

effective degree of saturation for swelling clays. The proportion of expansive clay minerals in the soil affects the extent of the influence of the effective degree of saturation. The influence of saturation on the critical state is displayed in Figure 5.2 for two identical bounding pressures p_B at the apex of the surface on the isotropic axis and two different effective degrees of saturation $S_1^e < S_2^e$. The inclination of the critical state line is reduced with increasing S^e due to the influence of saturation on the friction angle φ and the preconsolidation surface $F_2 = 0$ is reduced in height in comparison to $F_1 = 0$ as $\varphi(S_2^e) < \varphi(S_1^e)$ and thus $M(S_2^e) < M(S_1^e)$ for $S_1^e < S_2^e$ apply. For the dependency of φ on S^e, a linear interpolation between the fully saturated state (φ_w) and the nearly dry state (φ_{ref}), similar to the un- and reloading index $\kappa\,(S^e)$, is assumed:

$$\varphi\,(S^e) = \varphi_{\text{ref}} + S^e\,(\varphi_w - \varphi_{\text{ref}}) \tag{5.14}$$

Both, φ_w and φ_{ref} are material parameters of the full formulation of the model. The dependency of the friction angle on the effective degree of saturation was not yet included in Machaček et al. (2024).

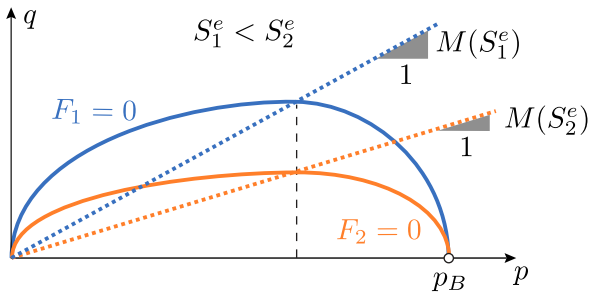

Figure 5.2.: Influence of the effective degree of saturation on the friction angle φ, critical state line with slope M and preconsolidation surface $F = 0$: $\varphi(S_1^e) > \varphi(S_2^e)$ for $S_1^e < S_2^e$.

5.1.2. Flow rule

The direction of the anelastic flow in Equation (5.1) is given by the unit tensor $\mathbf{m}$ with the magnitude of $||\mathbf{m}|| = 1$. As anelastic flow occurs not only on the preconsolidation surface $F = 0$, the flow rule $\mathbf{m}$ should be defined for arbitrary net stresses and not only for those on $F = 0$ or outside the preconsolidation surface $F > 0$. Therefore, a flow rule associated to the pseudo preconsolidation surface $F_+ = F(\boldsymbol{\sigma}, p_{B+}) = 0$ is used, i.e.:

$$\mathbf{m} \sim \frac{\partial F_+}{\partial \boldsymbol{\sigma}} = \left.\frac{\partial F_+}{\partial \boldsymbol{\sigma}}\right|_{pB_+}. \tag{5.15}$$

The flow rule is displayed in Figure 5.3 for a specific stress state $\boldsymbol{\sigma}$ at a constant water content. In the graphical representation, the direction of flow $\mathbf{m}$ is always perpendicular to the corresponding pseudo preconsolidation surface passing through the current stress state. It is:

$$\frac{\partial F_+}{\partial \boldsymbol{\sigma}} = -\frac{(2p - 2a_+)}{3\beta^2}\mathbf{1} + \frac{3}{M^2}\boldsymbol{\sigma}^* - \frac{2q^2}{M^3}\frac{\partial M}{\partial \boldsymbol{\sigma}} \quad \text{and} \quad \mathbf{m} = \left(\frac{\partial F_+}{\partial \boldsymbol{\sigma}}\right)^{\rightarrow}. \tag{5.16}$$

For simplicity, the dependency of M on the stress is neglected, i.e. $\left(\dfrac{\partial M}{\partial \boldsymbol{\sigma}} = \mathbf{0}\right)$ and the last summand of Equation (5.16) vanishes.

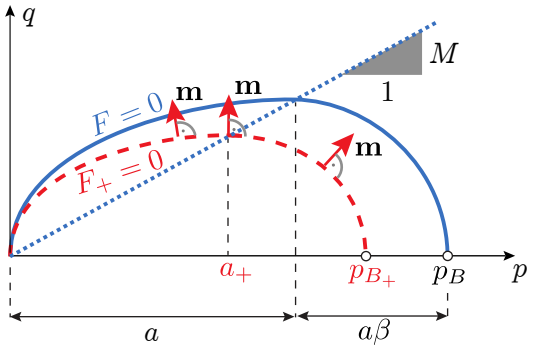

Figure 5.3.: Associated flow rule $\mathbf{m}$ for arbitrary net stresses. Modified from Machaček et al. (2024).

5.1.3. Direction of saturation-driven strain rate

In the general form the saturation-driven strain rate $\dot{\boldsymbol{\epsilon}}^w$ reads:

$$\dot{\boldsymbol{\epsilon}}^w = -\dot{\epsilon}^w \mathbf{m}^w, \tag{5.17}$$

where $\dot{\epsilon}^w$ is the scalar, saturation-driven strain rate proposed in the one-dimensional model (Equation (4.9)) and $\mathbf{m}^w$ is a second order tensor controlling its direction with $||\mathbf{m}^w|| = 1$. The evolution equation for the saturation-driven strain rate is repeated for the sake of clarity:

$$\dot{\epsilon}^w = -b\frac{e}{(1+e)}\left[(e_w - e)\,(S^e)^2\left\langle \dot{S}^e \right\rangle + (e_s - e)\,(1 - S^e)^2\left\langle -\dot{S}^e \right\rangle\right], \tag{5.18}$$

wherein b is a material parameter and e is the current void ratio. The void ratio at full saturation e_w and the void ratio in the shrinkage state e_s are considered as variables of the model, which evolve with the material state. For an isotropic material response, expansion takes place in the same extent across the directions in space. Experimental evidence, however, shows that isotropic conditions do not generally apply for the swelling strain, see Section 2.4.2.2, but a preferred direction of swelling exists. For a general definition of $\mathbf{m}^w$, the preferred direction might not align with a coordinate axis. In this work, the direction of the swelling strain is expressed in a simplified manner by the normalized diagonal tensor:

$$\mathbf{m}^w = \frac{\mathrm{diag}(1,\, m^w,\, 1)}{\|\mathrm{diag}(1,\, m^w,\, 1)\|}. \tag{5.19}$$

The factor m^w controls the extent of swelling in the vertical direction relative to the orthogonal (radial) directions. Normalization ensures that only the direction of the tensor $\dot{\boldsymbol{\epsilon}}^w$ is affected in Equation (5.17), while its magnitude is governed by the scalar, saturation-driven strain rate $\dot{\epsilon}^w$. In this work, $m^w = 5/3$ is used as a first approximation, but it may be introduced as a material constant in the future. Isotropic conditions correspond to $m^w = 1$.

5.1.4. Characteristic curves

In the full formulation of the model, the characteristic curves, which were introduced for the one-dimensional model, namely the NCC, B-line and w-line, are written as functions of the mean net stress p, see Figure 5.4.

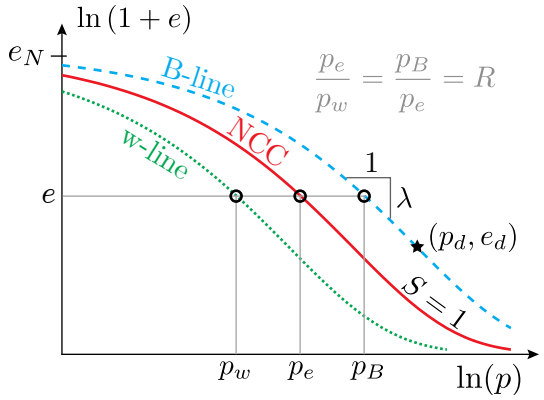

Figure 5.4.: Three characteristic curves of the model and their relative position described by the equivalent pressure p_e on the Normal Compression Curve NCC, the bounding pressure p_B on the B-line and the pressure p_w reached after a full saturation process for a given void ratio e. Modified from Machaček et al. (2024).

The NCC is therefore defined for the equivalent mean net stress p_e by:

$$p_e = h_s[-\ln(e/e_N)]^{1/n}, \tag{5.20}$$

wherein h_s, e_N and n are material parameters. The slope λ for a given void ratio e is:

$$\lambda = \lambda(e) = \lambda_{NCC}(e) = n\,(p_e/h_s)^n\,\frac{e}{1+e} \quad \text{with} \quad \lambda > \kappa. \tag{5.21}$$

Analogously to the one-dimensional formulation, the distance R between the B-line and the NCC is assumed to be the same as the distance between the NCC and the w-line:

$$R = \frac{p_d}{h_s}\,[-\ln\,(e_d/e_N)]^{-1/n} = \frac{p_B}{p_e} = \frac{p_e}{p_w}. \tag{5.22}$$

Therein p_d and e_d denote the preconsolidation state on the B-line and p_w is the mean net stress on the w-line for the current void ratio e. The void ratio at full saturation on the w-line is therefore:

$$e_w = e_N \exp\left[-\left(\frac{pR}{h_s}\right)^n\right], \tag{5.23}$$

and the void ratio at nearly dry conditions is:

$$e_s = \begin{cases} (1+e_d)\,(p_d/p)^{\kappa_{\text{ref}}} - 1 & \text{for } p < p_d, \\ e_d & \text{for } p \geq p_d. \end{cases} \tag{5.24}$$

5.1.5. Evolution equations

The evolution equations of the one-dimensional model (Equations (4.17) - (4.22)) are rewritten in terms of mean net stress for the full formulation of the model as well. The evolution of the preloading pressure p_d is:

$$\dot{p}_d = \dot{p}_{d+} + \dot{p}_{d-}, \tag{5.25}$$

wherein the build-up term due to loading beyond the preloading state is defined as:

$$\dot{p}_{d+} = -\frac{p_d}{\lambda(e_d)} \left(\frac{p_d}{p} \right)^{-m_O} \operatorname{tr} \dot{\boldsymbol{\epsilon}}^h, \tag{5.26}$$

and the degradation due to loading under constant saturation and related to changes in the degree of saturation reads:

$$\dot{p}_{d-} = \frac{p_e(e_d) - p_d}{\lambda(e_d)} \left\langle \operatorname{tr} \dot{\boldsymbol{\epsilon}}^w \frac{S^{w2}}{c\,(e_w - e_s)} - S^w \operatorname{tr} \dot{\boldsymbol{\epsilon}}^h \right\rangle. \tag{5.27}$$

Therein c is a material parameter. Finally, the evolution of the void ratio e_d corresponding to the preloading pressure p_d is rewritten as follows:

$$\dot{e}_d = (1 + e) \left(\frac{p_d}{p} \right)^{-m} \operatorname{tr} \dot{\boldsymbol{\epsilon}}^h. \tag{5.28}$$

5.1.6. Parameters of the model

In addition to the seven material parameters of the one-dimensional formulation, the full formulation requires three more parameters: the shape parameter β of the preconsolidation surface (1) and the friction angles in the reference state φ_{ref} (2) and saturated state φ_w (3). All material parameters are given in Table 5.1.

Table 5.1.: Material parameters of the full formulation of the hypoplastic hydro-mechanical model and their meaning.

Symbol	Domain	Description
e_N	Normal Compression Curve (NCC)	Void ratio at $p = 0$
h_s		Net stress at inflection point of NCC
n		Exponent of Bauer equation
κ_{ref}	Elastic stiffness	Un-/reloading index for $S^w = S^w_{\text{ref}}$
κ_w		Un-/reloading index for $S^w = 1$
b	Wetting	Curvature for wetting and drying
c	Yielding	Factor for degradation of preloading net stress $\dot{p}_{d-}$
β	Three-dimensional extension	Shape parameter of the preconsolidation surface
φ_{ref}		Angle of internal friction for $S^w = S^w_{\text{ref}}$
φ_w		Angle of internal friction for $S^w = 1$

Note that the factor m_O of the plastic multiplier and the scalar variable m^w for the direction of the saturation-driven strain rate are not considered as model parameters, but as constant for all materials in the scope of this work. The calibration of the model parameters is explained in further detail in Section 5.4.

5.2. Challenges of the generalisation to the full formulation

The one-dimensional formulation was developed to describe oedometric behaviour. Extending the model to three dimensions posed several challenges. These included transferring the core of the model, the three characteristic curves, from oedometric to isotropic compression and thus

from σ to p, selecting an appropriate preconsolidation surface and flow rule capable of accurately reproducing oedometric loading paths, and initializing the generalized preconsolidation state in a consistent way. Alongside the stress state p, the evolution of the preconsolidation state, which is represented by the preconsolidation pressure p_d, is essential for predicting the material response of expansive soils. As was discussed in Section 2.4, little experimental evidence exists regarding the evolution of radial net stresses during oedometric compression, rebound and swelling tests. During virgin vertical loading, the radial net stress component and thus the mean net stress p and preconsolidation pressure p_d develop proportionally to the vertical net stress component, however, they are no longer proportional upon unloading. The full stress state after preparation of compacted samples is unknown and can not be accurately initialized for simulations.

In simulations with the one-dimensional version, the one-dimensional preloading state (σ_d, e_d) is initialized based on experimental evidence and thus simulations start with unloading from this state. For the full formulation, however, even this state cannot be initialised and thus the complete compaction process is simulated. The material is initialised with a small isotropic pressure and subjected to loading up to the desired vertical net preloading net stress, which is known from experiments, and to unloading to the *as-compacted* state at a certain vertical net stress level. During this process, both p and p_d evolve in accordance with the predicted stress ratio $K_0 = \sigma_{11}/\sigma_{22}$, also known as the lateral earth pressure coefficient, which depends on the shape of the preconsolidation surface and the formulation of the flow rule. The original MCC yield surface without the modification by the shape parameter β and associated flow rule shows significant shortcoming for a loading path starting from a normally consolidated state, as the resulting stress ratio K_0 is very large during loading. Owing to the elliptic preconsolidation surface and associated flow rule, unloading to a low vertical net stress prior to wetting in oedometric swelling tests results in a stress state deep in extension in the $q-p$ space, wherein $q = \sigma_{22} - \sigma_{11}$ applies for the axially symmetric case in oedometric conditions. This state is characterized by a substantial residual radial net stress and a high mean net stress p. From a graphical perspective, see Figure 5.5, the stress state is too close to the NCC and the resulting w-line, resulting in the loss of applicability of the three characteristic lines. This is crucial, as the nature of the w-line as an attractor is essential for reproducing the correct magnitude of swelling and the associated swelling pressure.

Figure 5.5 presents the conceptual issue: a nearly dry sample is compressed under oedometric conditions by control of the vertical net stress σ_{22} (from point 0 to 1), resulting in a preloading pressure p_d at corresponding void ratio e_d. Upon unloading by control of the vertical net stress σ_{22} (from point 1 to 2*), the mean net stress p^* is overestimated due to the incorrect K_0 prediction upon loading. When subjected to wetting, the w-line ($e = e_w$) is reached either at constant vertical net stress (from 2* to 3a*, left) or constant volume (from 2* to 3b*, right) conditions. The magnitude of either swelling phenomenon is wrongly predicted in comparison to the path 0-1-2-3/3b (in grey) with a better K_0 prediction for the idealised concept of the three characteristic lines. The loading and unloading path in the $q-p$ space is also indicated in Figure 5.5. Note that in contrast to Figure 4.7, which shows the idealised swelling paths for the one-dimensional formulation, the swelling path upon wetting in Figure 5.5 at constant *vertical* net stress is not vertical, as the mean net stress p evolves differently upon swelling. More details are given in Section 5.3.4 in exemplary simulations.

The objective of the three-dimensional generalisation is to retain the ability to calibrate the model solely based on oedometric loading paths, avoiding the necessity of radial net stress mea-

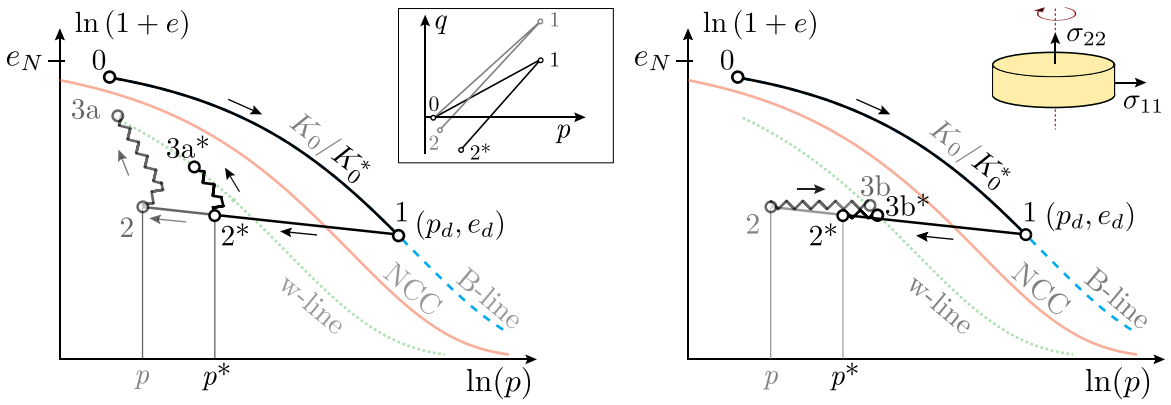

Figure 5.5.: Wrong prediction of swelling at constant vertical net stress (left) and constant volume (right) conditions due to incorrect K_0 prediction upon loading, resulting in an overestimation of mean net stress after unloading to the state prior to wetting.

surements or triaxial testing (for parameter calibration). In this way, the direct correlation between the experiments and model parameters remains. A suitable definition of the preconsolidation surface and / or flow rule must ensure realistic material behaviour upon oedometric loading paths. To this end, either the shape of the preconsolidation surface or the formulation of the flow rule can be modified, e.g. by application of a non-elliptic yield surface after Matsuoka and Nakai (1974), which includes a smaller opening angle near the $q-p$ origin and a more curved subcritical portion. In this way, a steeper loading path in the $q-p$ space can be achieved, resulting in the stress state less in extension after unloading. Moreover, a non-associated flow rule can be applied, e.g. with the coefficient α, which is also applied in the BBM (see Section 2.5.2.1). In this work, a modification of the MCC yield surface with the shape parameter β on the *subcritical* side as introduced in Equation (5.10) was chosen. With this modification, the material constant β can be adjusted so that the desired ratio $K_{0,NC} = \sigma_{11}/\sigma_{22}$ corresponds to a flow direction $\mathbf{m} = (\partial F/\partial \boldsymbol{\sigma}) \sim \text{diag}[0, -1, 0]$ for $\boldsymbol{\sigma} \sim \text{diag}[-K_0, -1, -K_0]$ under oedometric conditions. This approach allows direct control of the loading direction under normally consolidated conditions and, indirectly, of the unloading stress path, thus providing a suitable initial state prior to swelling in a simulation of the material preparation. The flow rule remains associated, which is advantageous from a numerical standpoint, but its relative direction in the $q-p$ space is altered through the modification of the preconsolidation surface. A smaller value of β results in a more compressed elliptic arc on the wet side. This approach is also implemented in Abaqus for clay plasticity (Dassault Systèmes, 2024).

5.3. Discussion and capabilities of the full formulation

In this section, the capabilities and features of the full formulation of the model are examined for different loading paths with a single, arbitrary parameter set in single-element simulations. First, the material behaviour is shown without explicit consideration of swelling processes to verify the general functionality of the formulation. The model response to triaxial loading paths and in simple shear and oedometric compression and rebound tests is presented. Then, the overall discussion of the full formulation of the model regarding swelling-relevant loading paths under oedometric conditions is taken on. The parameters used in the simulations are gathered in

Table 5.2. Note that instead of the angle of internal friction in the saturated state, the expansive clay mineral content x_{ecm} is stated in Table 5.2, as an alternative approach for estimating the dependence of the friction angle on the effective degree of saturation is used here, which is explained in more detail in the description of the parameter calibration in Section 5.4. Both approaches are interchangeable.

Table 5.2.: Model parameters of the mechanical model for discussion of its full formulation.

e_N	h_s in kPa	n	κ_{ref}	κ_w	b	c	β	φ_{ref} in °	x_{ecm} in wt-%	S_{ref}
0.58	9000	0.40	0.003792	0.02	55	2.0	{1.0, 0.5, 0.3} and 0.36 (for swelling)	37	35	0.126

In addition to the mechanical model, the simulation of the coupled material behaviour in `numgeo` requires a hydraulic model. Here, the model of Fredlund and Xing (1994) is applied with the parameters determined to match the experimental data of Opalinus clay (Figure 2.5.), see Section 5.5.1 for further details. The parameter are given in Table 5.3. The dry, reference state corresponds to a pore water pressure $p^w = -s = -106700$ kPa at $S_{\text{ref}} = 0.126$.

Table 5.3.: Model parameters of the hydraulic model of Fredlund and Xing (1994) for discussion of the full formulation of the mechanical model.

h_r in kPa	a_f in kPa	n_f	m_f
17826	4000	0.896	1.26

5.3.1. Triaxial response

Figure 5.6 shows the representation of monotonic triaxial tests using a single finite element. An axisymmetric rectangular element with linear interpolation of the displacement and pore water pressure was used, which was vertically fixed at the bottom and radially fixed on the symmetry axis. Pressure was initially applied from the top (σ^0_{22}) and the radially unconstrained side (σ^0_{11}). For drained loading, a constant increment of vertical displacement Δu_{22} was applied, while for undrained loading, a constant increment of vertical displacement Δu_{22} was applied along with a constant increment of radial displacement $\Delta u_{11} = -0.5\, r\, \Delta u_{22}$. r is the radius of the sample, hence the width of the element. Results are reported in geotechnical sign convention, i.e. compressive strains and stresses are positive. The material was saturated and the pore water pressure was fixed to $p^w = 0$ kPa at all nodes.

Four sets of simulations are shown for drained triaxial compression and extension and undrained triaxial compression and extension. In each set, three simulations with different initial void ratios at the same initial pressure, i.e. different overconsolidation ratios, were carried out. The initial state was achieved by isotropically loading the samples to the preconsolidation pressure for normally consolidated (NC) conditions, followed by unloading for overconsolidated (OC) initial conditions. The normally consolidated initial state (OCR = 1.0) corresponded to a void ratio of $e_0 = 0.424$. For the overconsolidated states, the initial void ratios were $e_0 = 0.352$ and $e_0 = 0.307$, corresponding to overconsolidation ratios of OCR = 3.2 and OCR = 5.8. An isotropic initial pressure of 500 kPa was applied. The results are plotted in Figures 5.7 – 5.10 as void ratio versus mean net stress (top left plot each), volumetric strain versus vertical strain (top right plot each), deviatoric stress versus mean net stress (bottom left plot each) and deviatoric

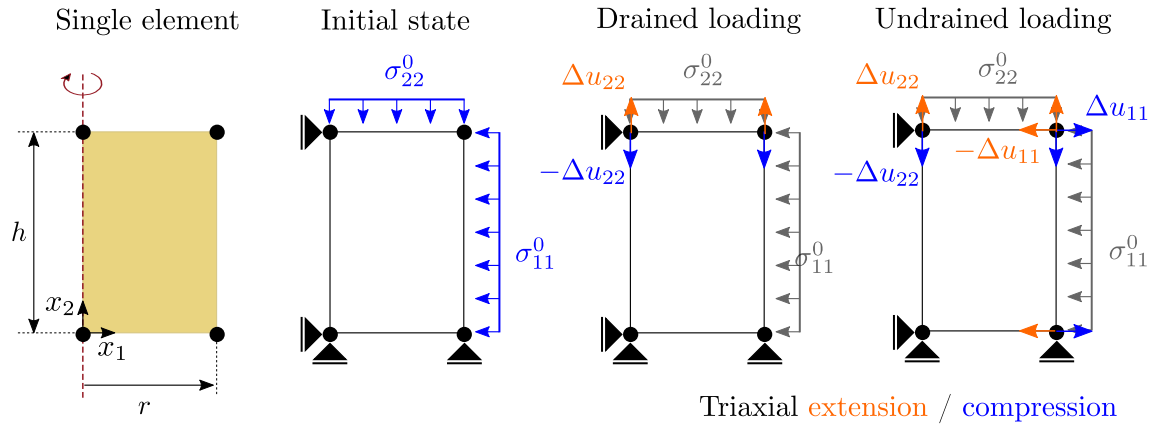

Figure 5.6.: Single-element representation of monotonic triaxial tests: Initial state, boundary conditions and loading for drained and undrained compression and extension.

stress versus vertical strain (bottom right plot each). The definition of $q = \sigma_{22} - \sigma_{11}$ applies. In the $q-p$ diagram, the preconsolidation surfaces are plotted for the initial (lower saturated solid line) and final state (saturated dotted line). In all plots, the initial state is indicated by a solid circle, the final state is indicated by a white filled circle and the direction of the paths is indicated by arrows. In the $e-p$ diagram, the NCC evaluated according to Equation (5.20) is shown. In addition, the CSL, representing the critical void ratio $e_c(p)$, is depicted by a shift in p with the factor $1/(1+\beta)$ from the NCC. In the $q-p$ diagram, the CSL is visualized using the slope M (Equation (5.11)).

Drained loading

The upper part of Figure 5.7 shows the model response under drained triaxial compression (blue). Under NC initial conditions (3, bright blue) the stress path started on the preconsolidation surface (PCS) and during triaxial compression the stress increased and the PCS expanded. Compressive volumetric strain developed and the critical state was reached when the volumetric deformation subsided. For OC initial conditions (1,2, darker blues), the stress state was located inside the PCS. Upon compression, the soil showed a reversible material response until the PCS was met. In the $e-p$ diagram, compressive volumetric strain developed and the point of intersection of the stress path with the PCS was clearly visible at the reversal of direction. In the $q-p$ diagram this state was found to the left of the CSL and marked with a smaller solid circle for easier recognition in Figure 5.7. With further loading, the soil response was associated with volume expansion. It was accompanied by softening until the critical state was reached, visible in the decrease of the deviatoric stress q. For higher initial OCR, larger deviatoric stress was generated before softening. In comparison to their initial state, the size of the PCSs was reduced. Overall, the results in Figure 5.7 show that the same critical void ratio $e_c(p)$ was reached regardless of the initial state prior to shearing.

The results for the drained triaxial extension tests are presented in the lower part of Figure 5.7 (green) and show a similar behaviour to that observed for compression. Under NC initial conditions (3, bright green), the critical state was reached at lower volumetric strains, i.e. with less expansion of the PCS, compared to the response observed under drained triaxial compression. In contrast, for OC initial states (1,2, brighter green), the trend was reversed: the PCS

contracted more pronounced due to softening, and the critical state was reached at higher volumetric strains. In the $e-p$ diagram it is clearly visible, that for initially OC conditions, the current state moved along an elastic unloading line in expansion. Overall less deviatoric strain q developed for extension than for compression. The same critical void ratio in $e_c(p)$ was reached regardless of the initial state prior to shearing.

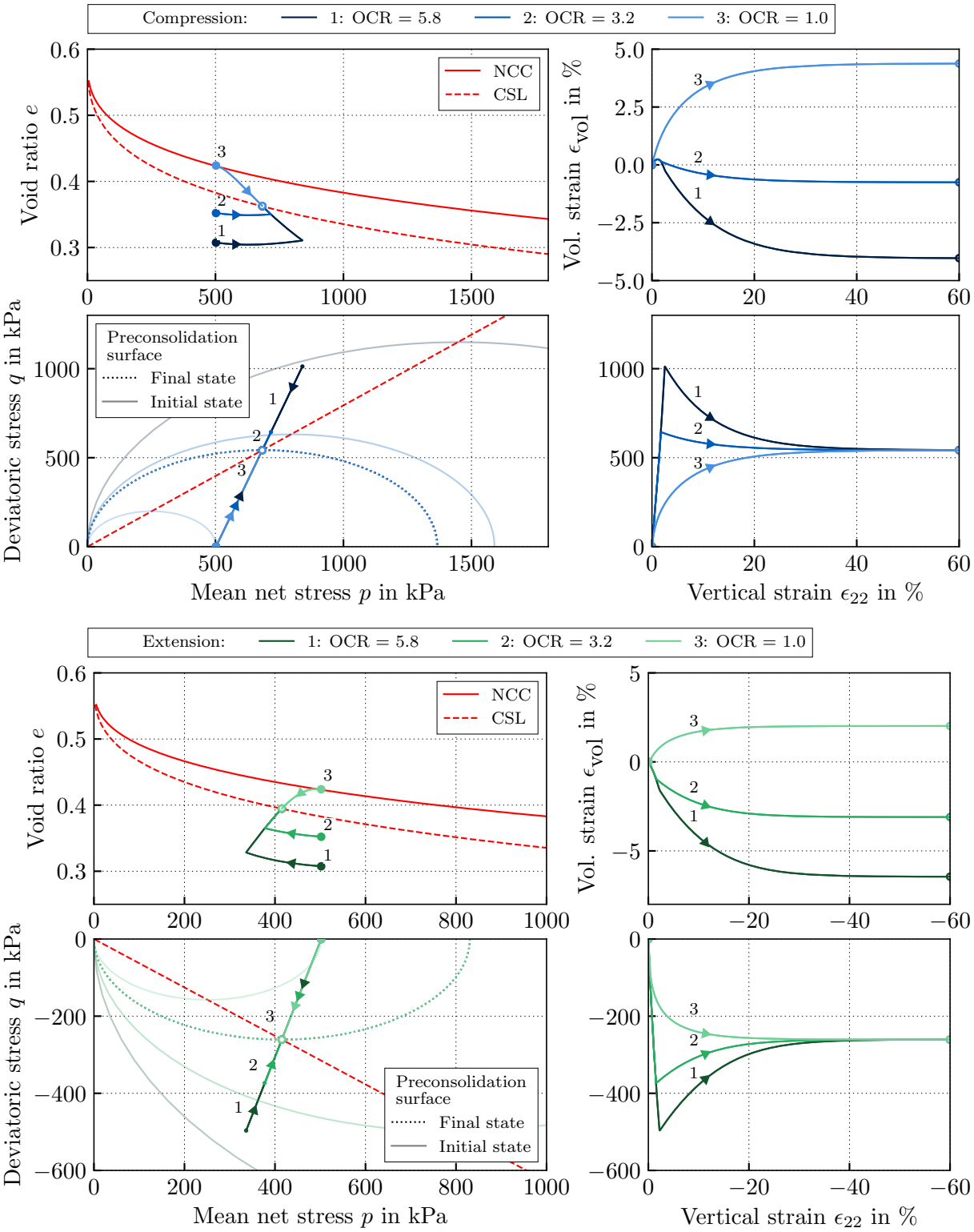

Figure 5.7.: Single element simulations: Drained triaxial compression and extension for different initial states.

Undrained loading

The model response for undrained triaxial compression is shown in the upper part of Figure 5.8 (blue). Starting from NC conditions (3, bright blue), the PCS did not evolve and the stress path followed it until the critical state was reached. For initial OC conditions, the stress state laid within the PCS, and upon triaxial compression, the strain was initially reversible until the PCS was reached. The stress path then followed the PCS, accompanied by a slight further increase in deviatoric stress, until the critical state was reached (1,2, darker blue). As no volumetric deformation occurred under undrained triaxial compression, the final critical void ratio $e_c(p)$ differed for the three simulations; however, the critical state line was reached regardless of the initial state prior to shearing. The results for undrained triaxial extension are shown in the lower part of Figure 5.8 (green). As critical state had to be reached under constant volume conditions as well, the same critical void ratio in $e_c(p)$ was reached in triaxial extension as in triaxial compression. The deviatoric stress q developed in the opposite direction and to a slightly reduced magnitude for triaxial extension compared to triaxial compression. The shear strength at critical state was reduced in triaxial extension relative to triaxial compression due to the dependence of the CSL slope M on the Lode angle.

Influence of shape parameter β

Up to this point, simulations have been conducted with the shape parameter β set to 1, corresponding to the original MCC yield surface. However as discussed in Section 5.2, the subcritical portion of the preconsolidation surface ($|q/p| < M$) can be modified by selecting $\beta < 1$. This section investigates the influence of β on the triaxial response. Drained and undrained triaxial compression for NC initial conditions (OCR = 1.0, simulation 3 in Figure 5.7 and 5.8) and OC initial conditions (OCR = 5.8, simulation 1 respectively) were repeated for values of $\beta = 0.5$ and $\beta = 0.3$. In the $e-p$ diagram the CSL is shown for each preconsolidation surface individually, though they coincide in the $q-p$ diagram.

For drained triaxial compression, the results are shown in Figure 5.9 for OCR = 5.8 (green lines, 1-3) and for OCR = 1.0 (blue lines, 4-6). Under NC conditions, a decrease in β leads to reduced volumetric strain, and hence less axial strain was required to reach the critical state. The compression of the subcritical portion of the preconsolidation surface reduced the distance between the apex (p_B) and the peak (at $|q/p| = M$) of the surface. In the graphical representation, this implied a closer proximity between the NCC and the CSL in the $e-p$ diagram, as can be seen in the upper left plot in Figures 5.9 and 5.10. In the $q-p$ space, the same critical state was reached regardless of β. The CSL in the $e-p$ space moved towards the NCC for decreasing β. For OC conditions, the trend was reversed, as shown in Figure 5.9: Decreasing β resulted in increased volumetric strain during loading. The larger volumetric material response was accompanied by a more pronounced increase of deviatoric strain prior to reaching the preconsolidation surface, followed by softening and volumetric expansion. Again, the same critical state was reached in the $q-p$ space regardless of the magnitude of β.

For undrained triaxial compression the results for OCR = 5.8 (green lines, 1-3) and for OCR = 1.0 (blue lines, 1-3) are shown in Figure 5.10. For NC conditions, the stress path followed the preconsolidation surface, which differed for different values of β, until the CSL was met. With decreasing β, the subcritical part of the preconsolidation surface was compressed more pronounced and the peak (at $|q/p| = M$) of the surface was located at larger net stresses. In the graphical representation, this can be seen by a larger distance between the NCC and the CSL in

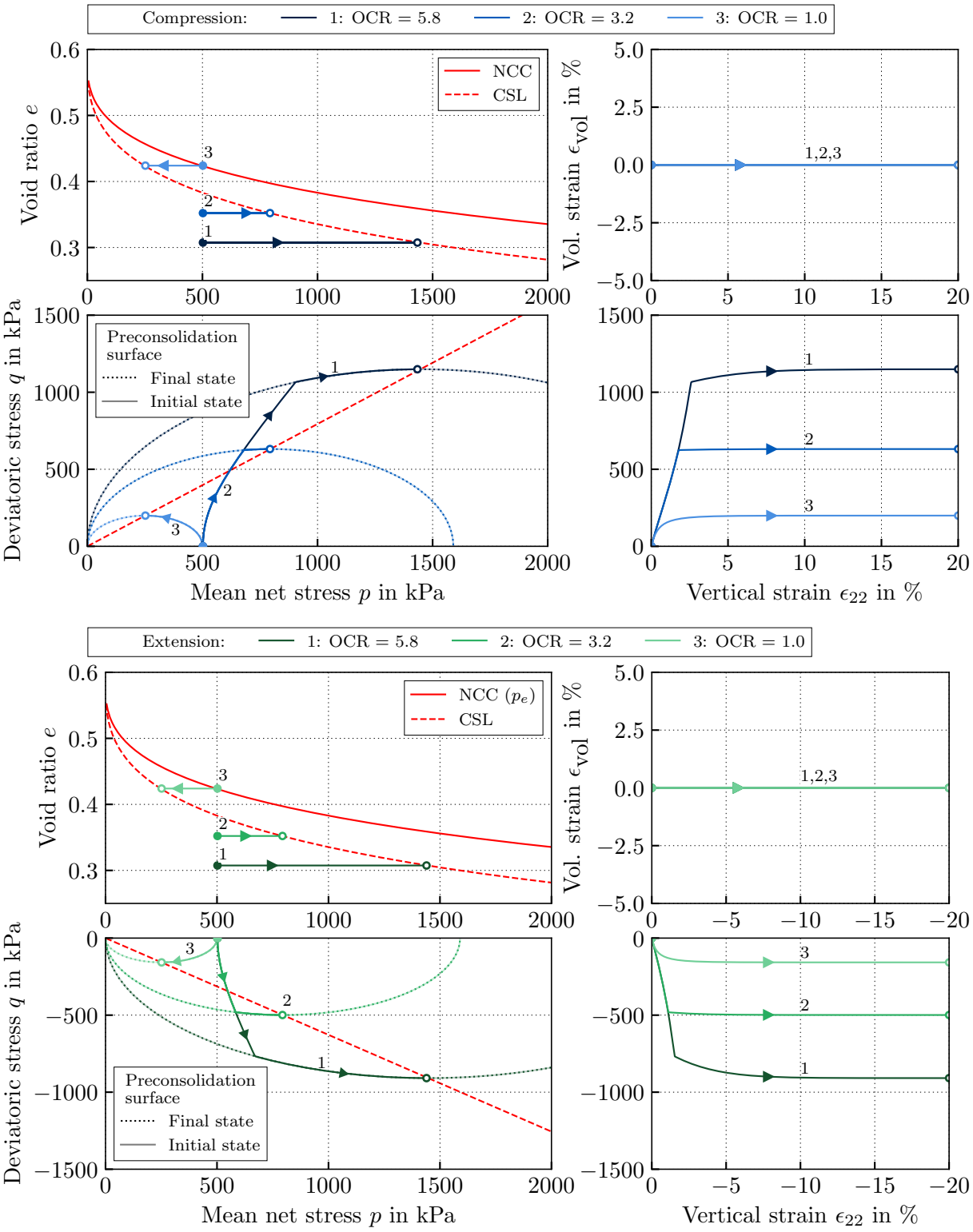

Figure 5.8.: Single element simulations: Undrained triaxial compression and extension for different initial states.

the $e-p$ diagram with increasing β. With decreasing β, more deviatoric stress was required for smaller changes in mean net stress to reach the critical state. However, as the stress path was „longer“ in the $q-p$ diagram, slightly greater vertical strain was required to reach the critical state with increasing β.

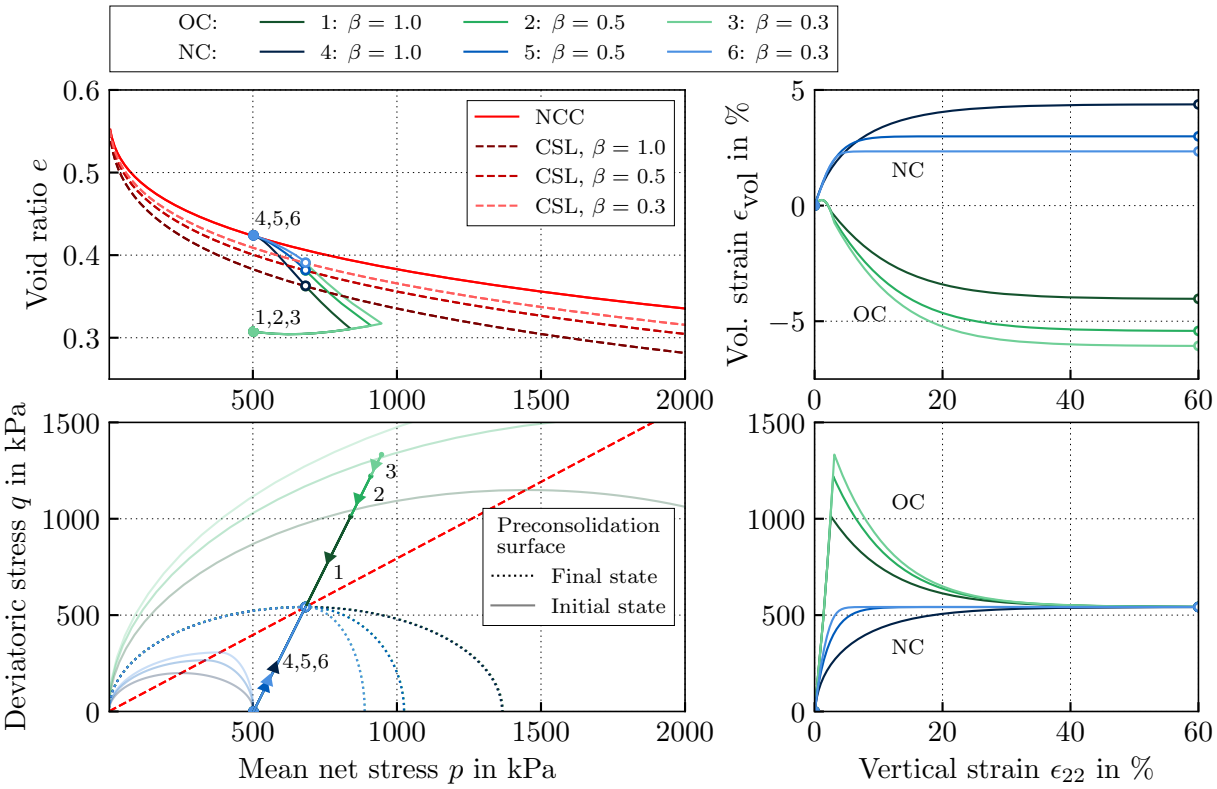

Figure 5.9.: Single element simulations: Drained triaxial compression with varying β for OCR = 1.0 and OCR = 5.8.

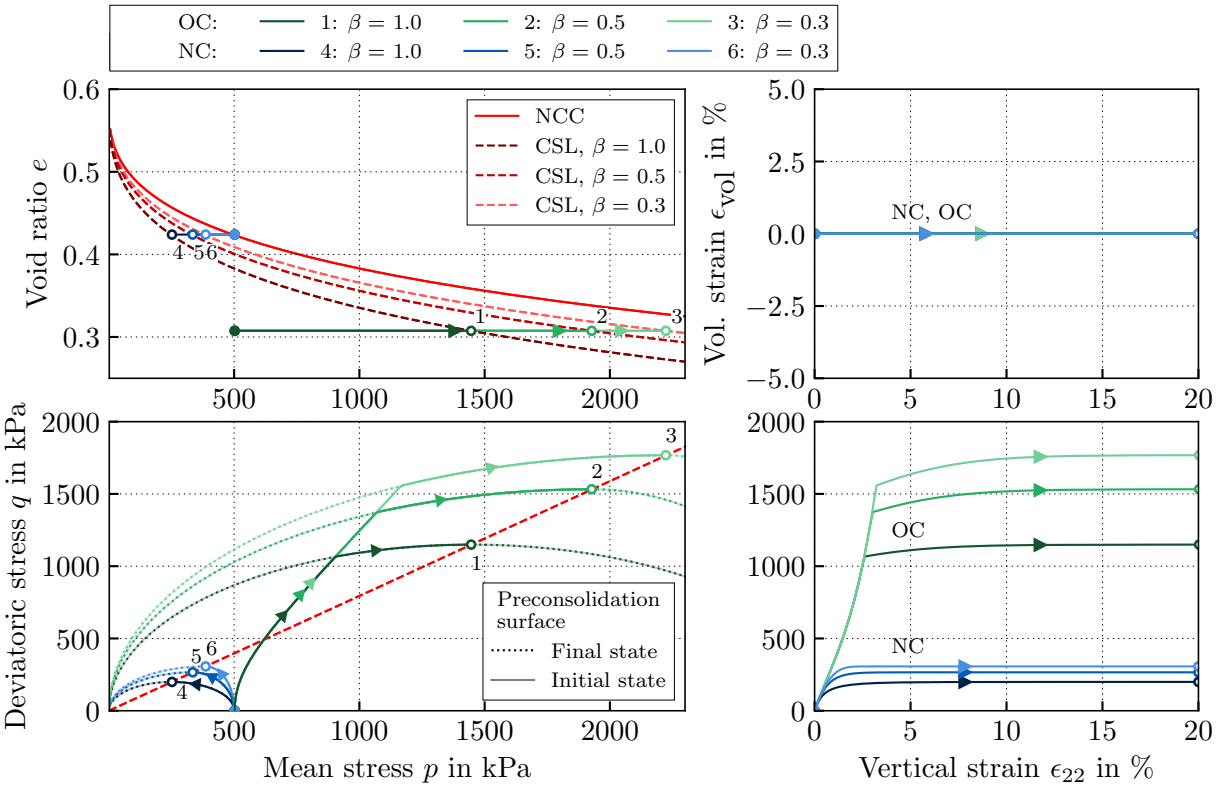

Figure 5.10.: Single element simulations: Undrained triaxial compression with varying β for OCR = 1.0 and OCR = 5.8.

For OC conditions, the stress path initially evolved within the preconsolidation surface and then followed it once reached, ultimately approaching the critical state from the overcritical side ($|q/p| > M$). With decreasing β greater deviatoric stress was generated as the apex of the surface was located at higher stresses. In the $e-p$ diagram, the constant volume conditions resulted in a horizontal path, and with decreasing β this path became longer as the distance between the initial state and the CSL increased. In contrast to NC conditions, OC conditions exhibited slightly greater vertical strain to reach the critical state as β decreased. In conclusion, the simulations demonstrate that β influenced the stress path prior to reaching the critical state and the critical state itself. The model response after reaching the critical state was independent of β.

5.3.2. Simple shear response

In addition to triaxial loading paths, simple shear tests were simulated for dry and fully saturated conditions. Figure 5.11 shows the representation of a simple shear test in a single element simulation. A plane strain rectangular element with linear interpolation of the displacement and pore water pressure was used, which was vertically fixed at the bottom and horizontally fixed at both sides. Analogous to the procedure in the laboratory, the material was not initialised isotropically; instead specimen preparation by applying a vertical load at constrained horizontal deformation was simulated. A vertical net stress (σ^0_{22}) was maintained prior to shearing. For loading upon the simple shear test itself, the horizontal constraint was removed and a constant increment of horizontal displacement Δu_{11} was applied to both top nodes. The vertical displacement u_{22} of both top nodes was enforced equally upon shearing via a multi point constraint. Compressive strains and stresses were positive. The pore water pressure was fixed at all nodes to $p^w = 0$ kPa for fully saturated and to $p^w = -106700$ kPa for dry conditions.

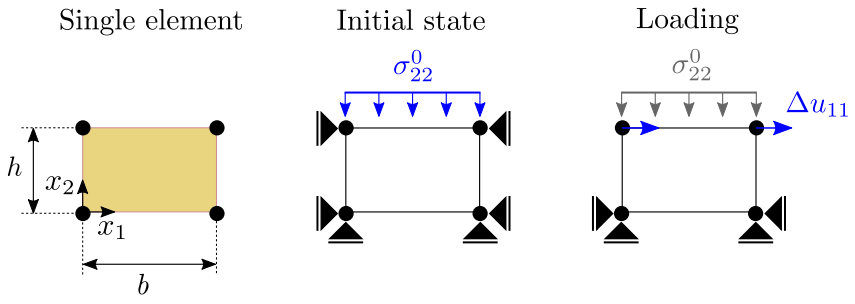

Figure 5.11.: Single-element representation of simple shear tests: Initial state, boundary conditions and loading.

Three sets of simulations were carried out: Shearing under different vertical loads for NC and OC initial conditions in the saturated state and for NC initial conditions in the dry state. The initial state was reached by vertical loading at dry or saturated conditions to the preconsolidation net stress for NC conditions, followed by unloading from higher preconsolidation stresses for OC initial conditions. The overconsolidation ratio was OCR = 3.2 in the latter case. The results are shown in terms of volumetric strain ϵ_{vol} versus shear strain ϵ_{12} and shear stress σ_{12} versus shear strain. Furthermore, the final (residual) state of the shear stress $\tau = \sigma_{12}$ versus vertical net stress σ_{22} is shown and evaluated in terms of the Mohr-Coulomb failure envelope.

Figure 5.12 compares the results of shearing in the saturated state for initially NC (solid lines, round markers) and OC conditions (dashed lines, square markers). For NC conditions, the evolution of volumetric strain and shear stress asymptomatically approached a final value, whereas for OC conditions, a peak value of shear stress was reached first, followed by softening to a final, residual value. For higher vertical net stress during shearing, a higher shear stress was reached and more volumetric strain occurred upon shearing, which was in compression for NC and in extension for OC conditions. With increasing vertical net stress, increasing shear strain was required to reach the critical state. The final state of all tests formed a linear shear strength envelope with a residual angle of internal friction of $\varphi = 22.3°$ with no cohesion component, see the plot on the right-hand side of Figure 5.12. Initially normally consolidated and overconsolidated conditions resulted in the same residual shear strength at the same vertical net stress level.

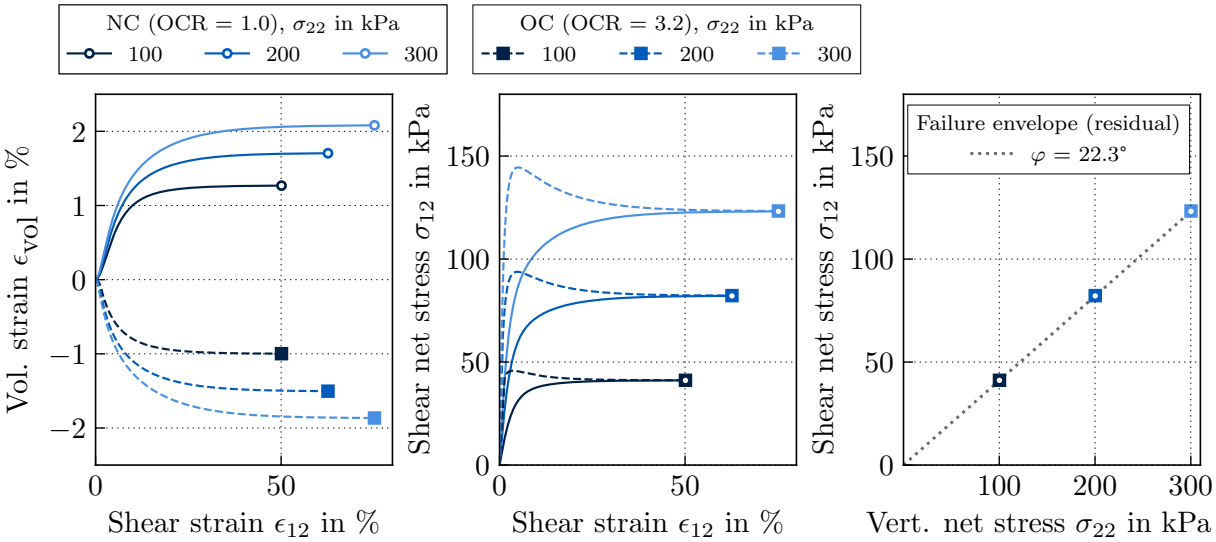

Figure 5.12.: Single element simulations: Simple shear tests under three different vertical loads at initially normally consolidated and overconsolidated conditions in the saturated state.

The results at initially NC conditions in the saturated state from Figure 5.12 are shown again in comparison to tests at initially NC conditions in the dry state at identical vertical net stress levels in Figure 5.13. Here too, the shear stress asymptotically approached the final state and the volume deformation was in compression. However, an increased shear strength was evident in the dry state due to the dependency of the friction angle on the effective degree of saturation. This was reflected in a larger slope of the linear shear strength envelope with no cohesion component and a residual angle of internal friction of $\varphi_{ref} = 35.7°$ in the plot on the right-hand side of Figure 5.13.

To evaluate the influence of the shape parameter β, which compresses the subcritical portion of the preconsolidation surface, simulations with $\beta = 0.5$ and $\beta = 0.3$ were additionally carried out for initially normal and overconsolidated conditions in the saturated state at a vertical net stress of 200 kPa. The results are shown in Figure 5.14. For NC conditions, with decreasing β less volumetric strain (in compression) was generated upon shearing, and critical state was reached at lower shear strain, thus the critical void ratio $e_c(p)$ depended on β. However, the final shear strength was not influenced by β. For OC initial conditions, the trend was opposite, as with decreasing β a higher peak in shear stress was evident and more volumetric strain (in extension) was generated upon shearing. Again, the final state was not influenced by β. All

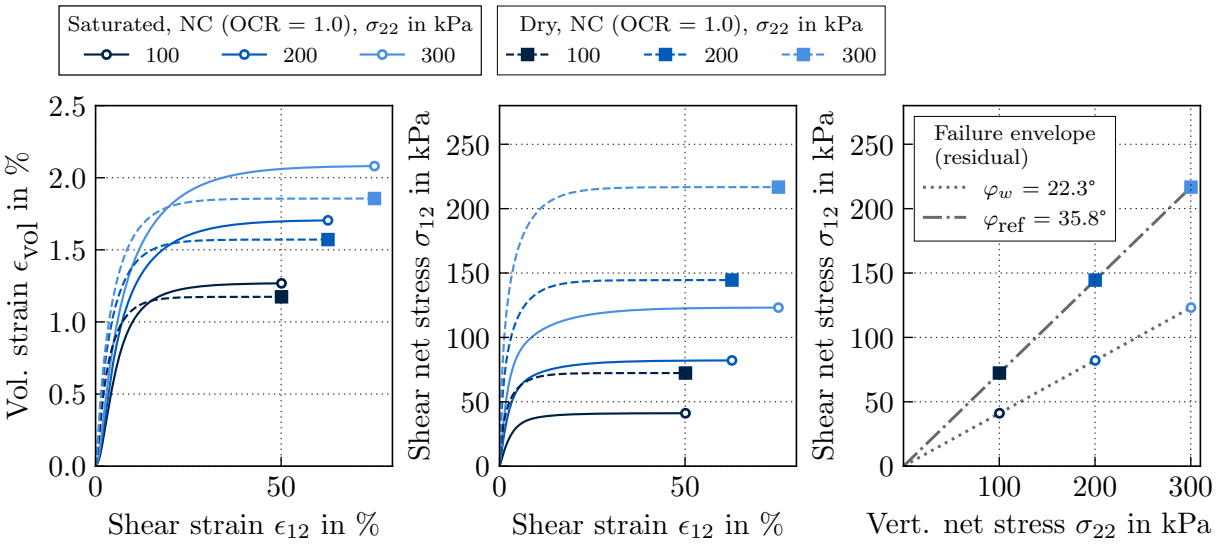

Figure 5.13.: Single element simulations: Simple shear tests at three different vertical loads at initially normally consolidated conditions in the dry and saturated state.

simulations resulted in the same residual shear strength. The results were in line with those from the simulations of the triaxial material response: β influenced the path before reaching the critical state line, but the model response thereafter was independent of β.

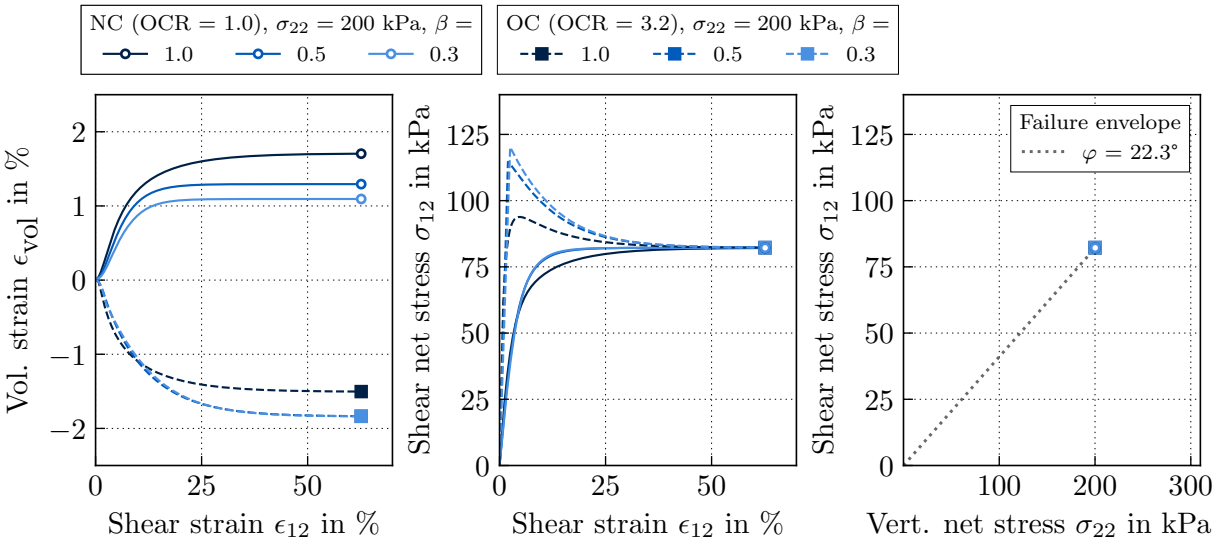

Figure 5.14.: Single element simulations: simple shear tests under identical vertical load at initially normally consolidated and overconsolidated conditions with varying β.

5.3.3. Oedometric compression and rebound behaviour

The material response regarding compressibility was assessed in simulations of oedometric compression tests in the fully saturated and dry state. Figure 5.15 shows the representation of oedometric compression tests in a single element simulation. An axisymmetric rectangular element with linear interpolation for displacement and pore water pressure was used, whose displacements were vertically fixed at the bottom and radially fixed at both sides. As described for simple shear tests, the specimen preparation was simulated as well to initialize the non-isotropic

initial state. A vertical net stress (σ_{22}^0) was maintained prior to loading. For loading, an additional vertical net stress increment $\Delta\sigma_{22}$ was applied. Compressive strains and stresses are positive. Two sets of simulations are shown for oedometric compression in dry and saturated

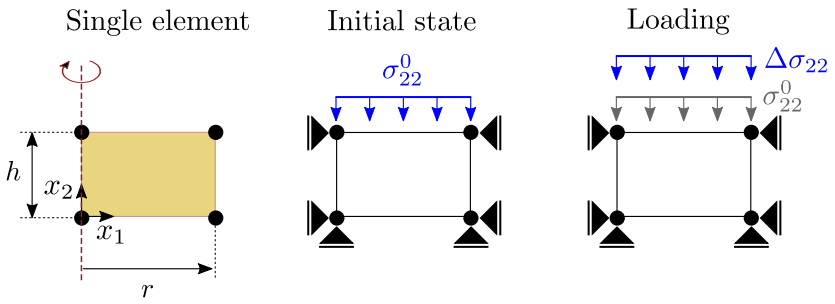

Figure 5.15.: Single-element representation of an oedometric compression test: Initial state, boundary conditions and loading.

conditions. In each set, three simulations were carried out starting from different initial void ratios at the same initial stress, i.e. different overconsolidation ratios. The initial state was reached by initial loading to the preconsolidation stress for normally consolidated conditions, followed by unloading from higher preconsolidation stresses for overconsolidated initial conditions. The maximum vertical net stress upon the subsequent oedometric compression path was identical in all simulations. The pore water pressure was fixed at all nodes to $p^w = 0$ kPa for fully saturated and to $p^w = -106700$ kPa for dry conditions. The results are plotted as void ratio over net stress in a semi-logarithmic representation (left plot) and deviatoric stress over mean net stress (right plot). In the $e-\log(\sigma)$ diagram, both the mean net stress p (solid lines) and the vertical net stress σ_{22} (dotted lines) are shown. In the $q-p$ diagram, the preconsolidation surfaces are plotted for the initial state (saturated dash-dotted line) and the maximum value of p (lower saturated solid line). In all plots, the initial state is indicated by a solid circle, the final state by a white filled circle, and arrows indicate the direction of the paths.

The upper row of Figure 5.16 shows the results of element tests for oedometric compression in the dry state. For the NC initial state (1, dark blue), the loading path followed the virgin loading line, corresponding to the B-line, right to the NCC. Starting from an OC initial state (2,3, brighter blue) the material response was initially elastic before the B-line was reached and followed upon loading, see upper left-hand plot in Figure 5.16. The effect of the original MCC preconsolidation surface with $\beta = 1.0$ became evident, as after unloading of the vertical net stress, the mean net stress p remained high and was merely located on the left of the NCC. In the $q-p$ diagram on the upper right-hand side of Figure 5.16, the loading path was below the critical state line. During virgin loading, the preconsolidation surface expanded with increasing load to accommodate the stress state, $\{p, q\}$, which was always located on the surface to fulfil the consistency condition. Upon un- and reloading, the preconsolidation surface remained constant and the stress path inside of the preconsolidation surface was reversible. The associated flow rule governed the direction of the stress path, resulting in a stress state in extension.

A similar material response is shown for oedometric compression in the saturated state in the bottom row of Figure 5.16. Therein, virgin loading for the NC initial state (1, dark green) almost coincided with the NCC, see lower left-hand side of Figure 5.16. Due to the reduced friction angle in the saturated state, the stress path upon virgin loading in the lower right-hand side of Figure 5.16 was less steep than for dry conditions. Starting from an OC initial

state (2,3, brighter green) the material response was initially elastic. However, due to the saturation-dependent un- and reloading index κ, which was larger in the saturated state, the volumetric deformation was greater under saturated conditions compared to the dry state. Upon unloading, the combination of the reduced saturated elastic stiffness and the associated flow rule of the preconsolidation surface with $\beta = 1.0$ resulted in a stress state $\{p, q\}$ that shifted deep into extension, even reaching the critical state surface.

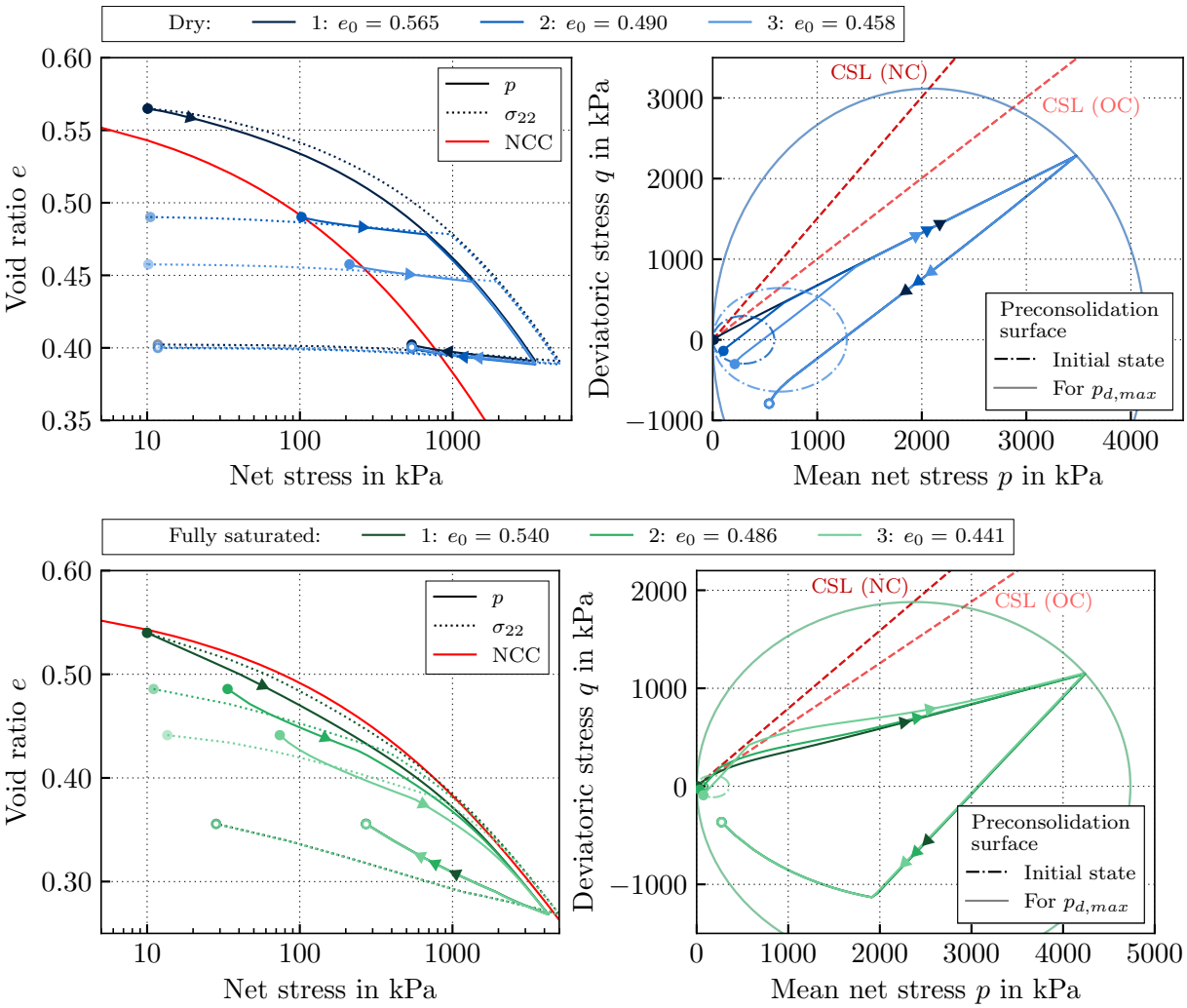

Figure 5.16.: Single element simulations: Oedometric compression in the dry and fully saturated state for initially normally consolidated and overconsolidated conditions.

The shape parameter β was introduced for the preconsolidation surface to improve the material response upon oedometric compression. Therefore, in the following the influence of β is analysed for loading and unloading from initially normally consolidated conditions in the dry and saturated state for $\beta = 0.5$ and $\beta = 0.3$. The dry material response for vertical loading and unloading is shown in the upper part of Figure 5.17. In the $q-p$ diagram on the right-hand side, the subcritical part of the preconsolidation surface was compressed more pronounced with decreasing β and the peak (at $|q/p| = M$) of the surface was located at smaller mean net stress and larger deviatoric stress. Upon vertical loading, the surface expanded to accommodate the stress state and with decreasing β (depicted in brighter blues in Figure 5.17), the desired steeper loading path was achieved. Upon vertical unloading, the corresponding steeper direction of the associated flow rule led to a more pronounced decrease of radial net stress and resulted in a stress state

lying less in extension upon unloading. In the upper left-hand side of Figure 5.17, the reduced difference between the final mean net stress p and the vertical net stress σ_{22} with decreasing β becomes evident. Thus, with decreasing β, the discrepancy between the one-dimensional and full formulation of the model was less pronounced and the three-line concept of the mechanical model enabled the development of expansion or swelling pressure upon wetting.

The material response for vertical loading and unloading for different values of β in the saturated state is shown in the bottom part of Figure 5.17. Due to the reduced friction angle in the saturated state, the overall difference in the shape of the preconsolidation surface for different values of β was less pronounced. However, similar behaviour as for the dry material can be seen and with decreasing β a steeper loading and unloading path and a reduced difference between the final mean net stress p and the vertical net stress σ_{22} after unloading became evident. With decreasing β, the preconsolidation surface was only just met upon unloading in extension.

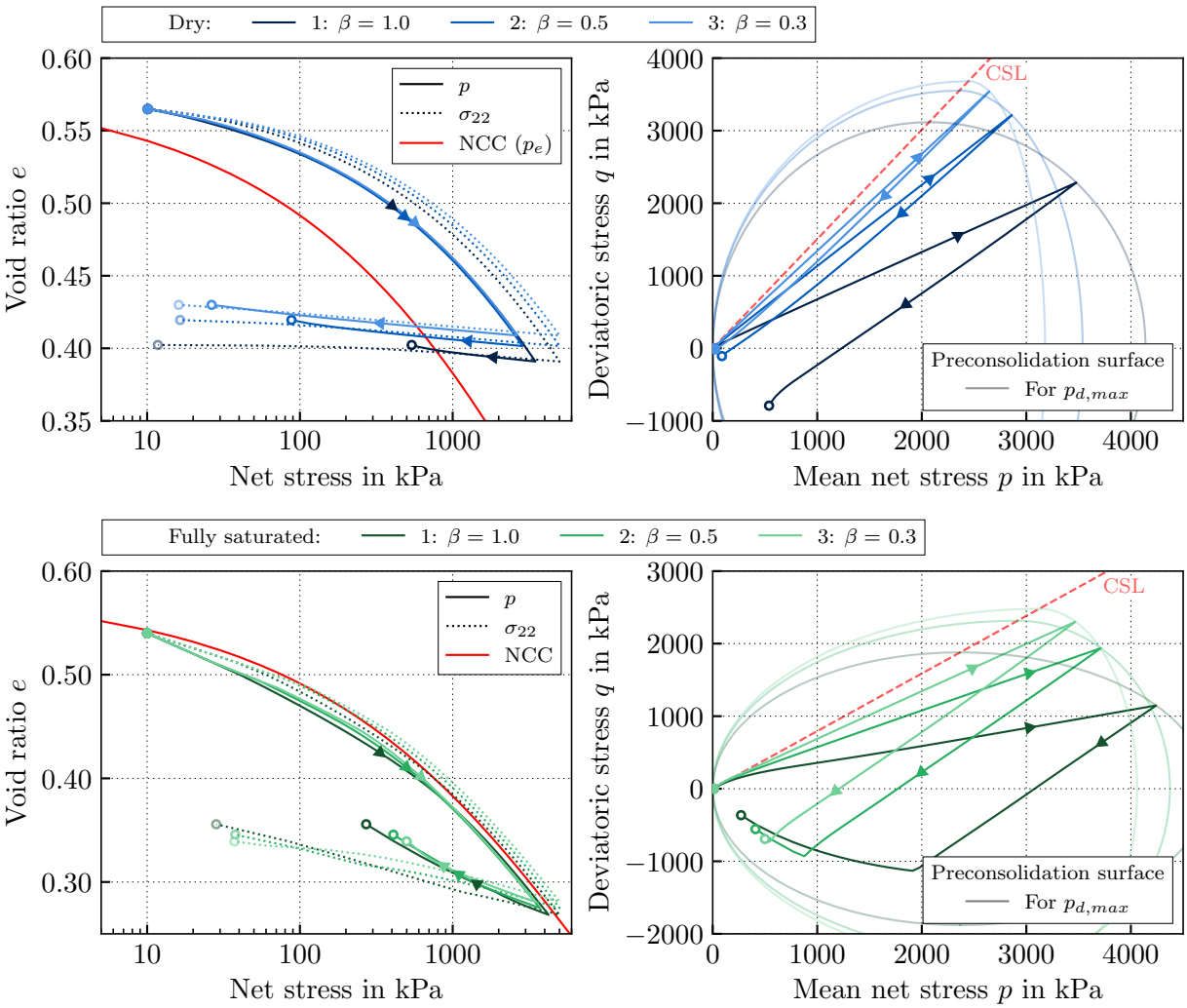

Figure 5.17.: Single element simulations: Oedometric compression in the dry and fully saturated state for initially normally consolidated conditions with varying β.

The results show that the shape parameter β significantly influenced the model response upon oedometric loading and unloading. The compression of the subcritical part of the preconsolidation surface was essential to ensure realistic stress states especially after unloading and to prevent an overestimation of radial net stresses.

5.3.4. Oedometric swelling behaviour

In this section, the features of the proposed model are examined for relevant loading paths of oedometric swelling behaviour and its performance is discussed analogously to the discussion of the one-dimensional formulation in Section 4.2. The loading paths include oedometric compression for different initial degrees of saturation, saturation-induced deformation and stress, hence swelling strain and swelling pressure, and saturation-induced collapse. All loading paths were simulated with a single set of material parameters given in Table 5.2. The shape parameter was chosen to $\beta = 0.36$ based on the angle of internal friction in the reference state, see Section 5.4 for details on the parameter calibration. The single-element representation for the simulations together with the boundary conditions for swelling tests is depicted in Figure 5.18. For oedometric compression in the (un)saturated state, an additional loading and unloading sequence was simulated after infiltration. For wetting, the pore water pressure was applied to all four nodes of the element simultaneously. An axisymmetric rectangular element with linear interpolation for displacement and pore water pressure was used, whose displacements were vertically fixed at the bottom and radially fixed at both sides. For simulation of constant volume swelling, the vertical displacement of the upper nodes was constrained as well.

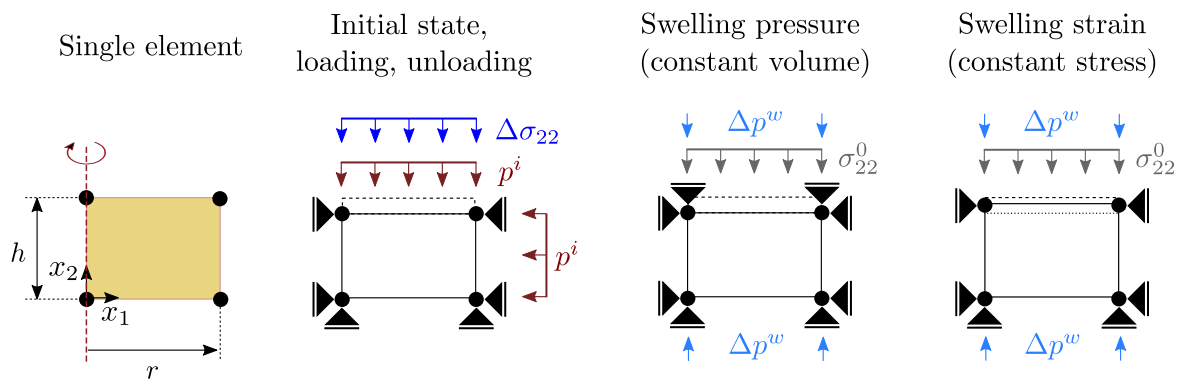

Figure 5.18.: Single-element representation of oedometric swelling tests: Initial state, boundary conditions and loading.

Compressibility at different water contents

The response of the model to loading and unloading paths at constant water content for different initial degrees of saturation is shown in Figure 5.19. The initial state was reached by dry loading and unloading to the same vertical preconsolidation net stress $\sigma_{22,d0}$ and subsequent wetting to different degrees of saturation by increasing the pore water pressure at the model boundary as depicted in Figure 5.18. Herein, the influence of swelling on the material behaviour was explicitly considered, however, for the sake of clarity, only the oedometric loading and unloading path after wetting is shown. The maximum vertical net stress was identical in all simulations. The preloading is indicated by a grey line and x-marker on the right-hand side of Figure 5.19. The target pore water pressures for wetting were $p^w = -\{100, 20, 10, 5, 3, 0\}$ MPa, corresponding to degrees of saturation of $S^w = \{0.13, 0.35, 0.49, 0.63, 0.73, 1.0\}$.

The results are reported in Figure 5.19 and show that the full formulation of the model can reproduce the same material behaviour as the one-dimensional formulation, see Section 4.2.1. With increasing degree of saturation, the NCC (red) was approached sooner upon monotonic

compression by the reduction of the preloading pressure p_d, see Equation (5.25). The slope of the virgin loading line was affine to the slope $\lambda(e)$ of the NCC and a decrease in elastic stiffness during unloading with increasing degree of saturation was visible, though being only moderately pronounced with the chosen parameters. Since the elastic index κ referred to the pressure p in the full formulation (see Equation 5.9) and the radial net stress did not decrease proportionally to the vertical net stress during unloading, the decrease in elastic stiffness for σ_{22} was less pronounced than in the one-dimensional formulation, especially for unloading to small vertical net stresses.

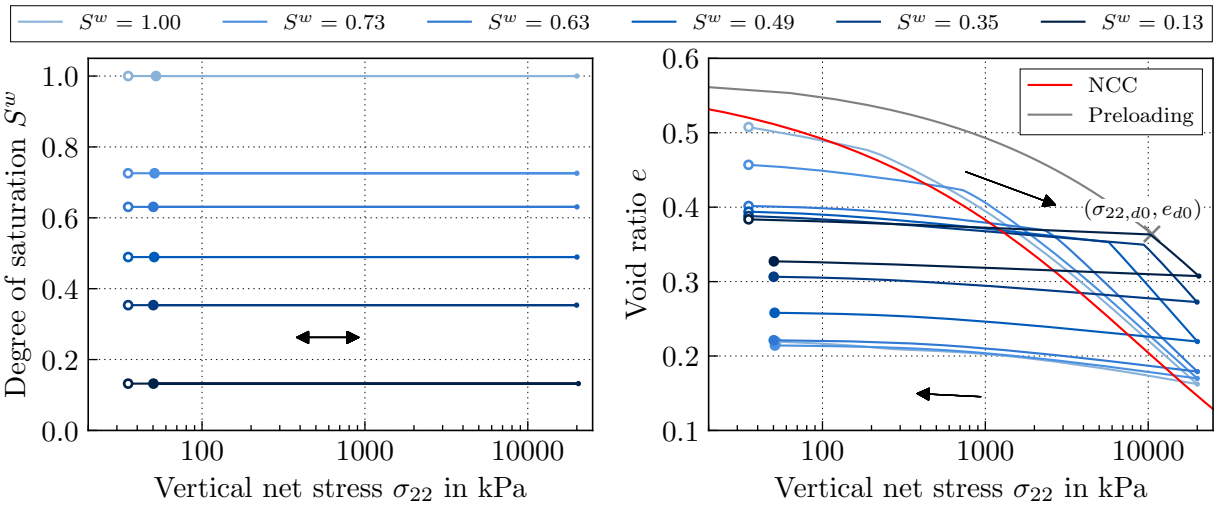

Figure 5.19.: Oedometric loading and unloading for different degrees of saturation: Vertical net stress and wetting paths (left) and response of the model in terms of void ratio e versus vertical net stress σ_{22} (right).

The plot on the right-hand side of Figure 5.19 represents the results in the commonly used semi-logarithmic $e - \log(\sigma_{22})$ diagram. As the depicted NCC was formulated for mean net stress p in the full formulation of the model, the saturated loading path and the NCC do not coincide for oedometric conditions. Figure 5.20 shows two of the above presented compression tests, for fully saturated and nearly dry conditions, in terms of void ratio versus net stress and deviatoric stress versus mean net stress. For the sake of completeness, the stress paths during saturation are depicted as well. In the plot on the left-hand side both, the mean net stress p and vertical net stress σ_{22} are depicted. The different evolution of mean net stress and vertical net stress was evident. Upon loading in the fully saturated state, p was slightly to the left of the NCC, while σ_{22} was to the right due to the shape parameter β, which compressed the subcritical portion of the preconsolidation surface. In the plot on the right-hand side of Figure 5.20 the stress path upon oedometric loading and unloading for both simulations is shown with the CSL and the preconsolidation surface for the maximum pressure p. With increasing saturation, the CSL was less inclined due to the reduction of the angle of internal friction upon saturation and as a result the stress path was less inclined as well.

Vertically unconfined swelling: swelling strain

Figure 5.21 presents the response of the model to full saturation at constant-stress conditions at different vertical net stresses. The preloading sequence with the maximum, vertical preloading pressure $\sigma_{22,d0}$ and corresponding void ratio e_{d0} and subsequent unloading to different vertical net stresses $\sigma_{22} = \{169, 100, 60, 35\}$ kPa is shown on the right-hand side of Figure 5.21. During

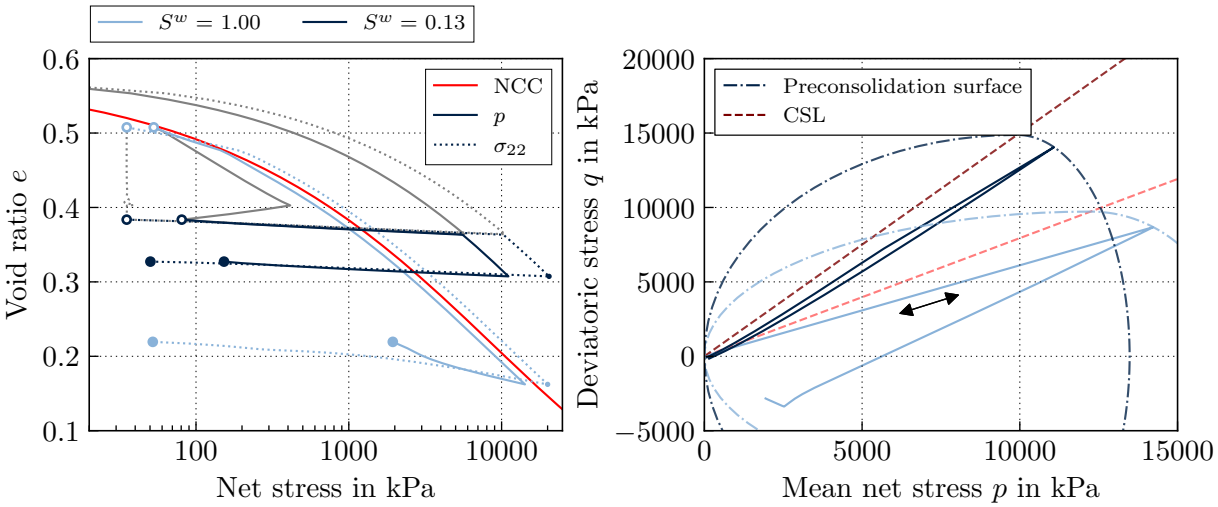

Figure 5.20.: Oedometric loading and unloading in the fully saturated and dry state: Void ratio e versus vertical net stress σ_{22} and mean net stress p (left) and deviatoric stress q versus mean net stress (right).

wetting at constant vertical net stress, an expansion was evident, see right-hand side of Figure 5.21. The maximum deformation reached in the fully saturated state for each simulation was determined by the position of the w-line. Swelling stopped when $e = e_w$ applied according to Equation (5.23). With increasing vertical net stress upon wetting, the saturation-induced deformation decreased due to the affinity of the w-line and the NCC.

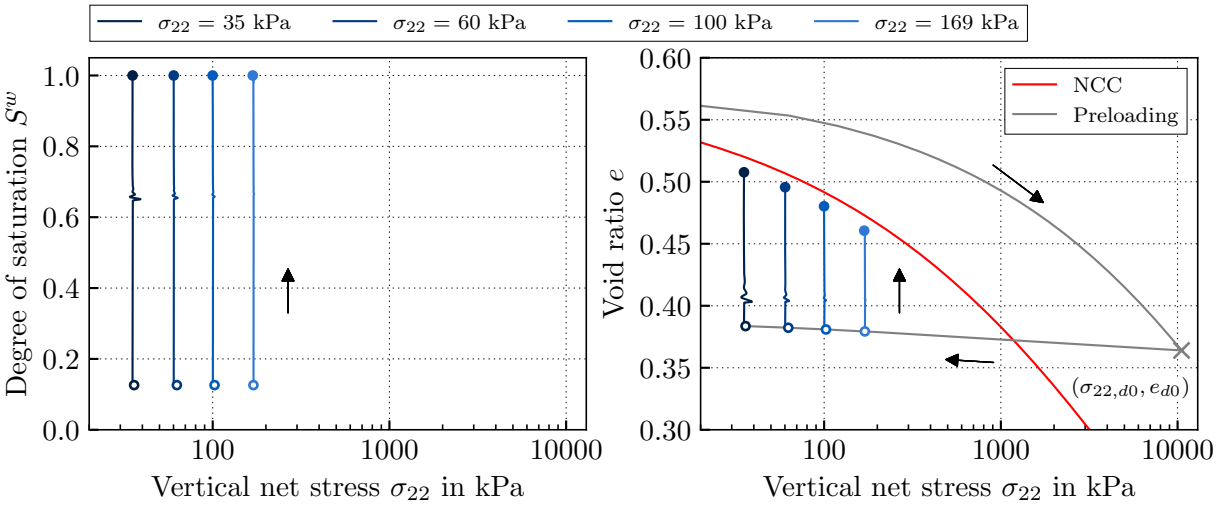

Figure 5.21.: Saturation-induced deformation at different stresses: Vertical net stress and wetting paths (left) and response of the model in terms of void ratio e versus vertical net stress σ_{22} (right).

The stress path of one simulation (at constant vertical net stress $\sigma_{22} = 35$ kPa) is shown in Figure 5.22 in terms of void ratio versus net stress (left) and deviatoric stress versus mean net stress (right). In the plot on the left-hand side both, the mean net stress p and the vertical net stress σ_{22} are displayed. The position of the w-line (green) and B-line (light blue) is shown for the start and end of saturation. The evolution of both lines upon saturation, which yielded the magnitude of expansion, was evident. While σ_{22} remained constant during saturation upon from minor oscillations, the mean net stress initially increased before sharply changing its direction and decreasing into a lower stress regime. This directional change caused the oscillations in σ_{22} and

is more clearly seen in the plot on the right-hand side of Figure 5.22, which also shows the CSL and the preconsolidation surface at various stages of the wetting. As swelling strain evolved, the stress path first followed a loading direction and, after intersecting the preconsolidation surface, exhibited a change of direction in extension. The preconsolidation surface itself contracted during saturation due to a reduction in both the preloading net stress (softening) and the internal friction angle. The latter was indicated by the movement of the CSL, shown by the dark red arrow.

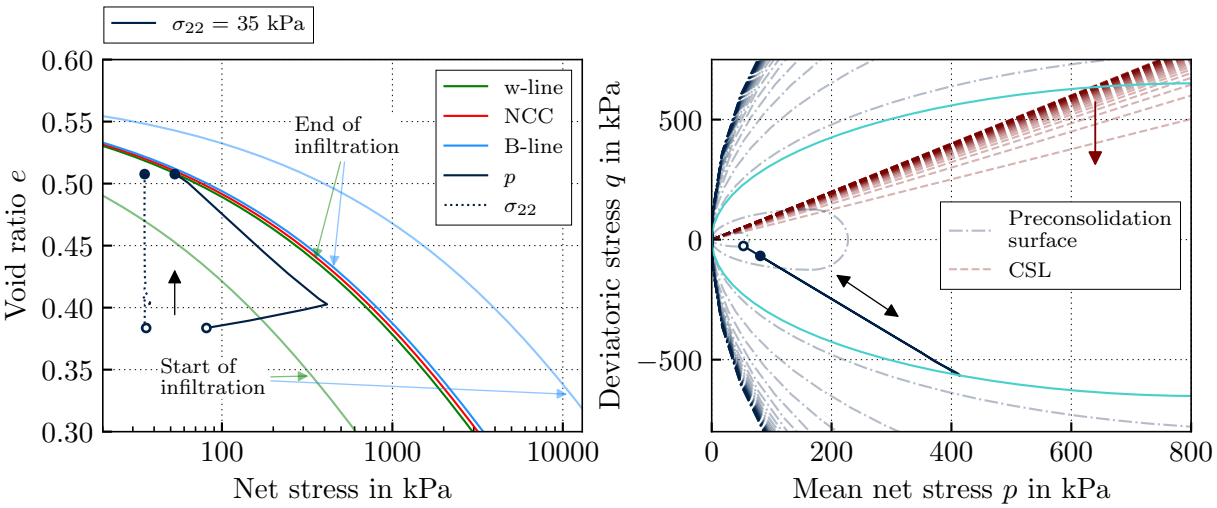

Figure 5.22.: Saturation-induced deformation: Void ratio e versus vertical net stress σ_{22} and mean net stress p (left) and deviatoric stress q versus mean net stress (right). The arrows indicate the stress path and movement of the CSL upon wetting.

Constant volume swelling: swelling pressure

Figure 5.23 presents the model response to wetting under constant volume conditions for different initial void ratios. The preloading sequence, characterized by varying maximum vertical preloading net stresses $\sigma_{22,d0}$ and corresponding void ratios e_{d0}, is illustrated on the right-hand side of the figure. For each simulation, the state is marked with a grey x, followed by unloading to the same vertical net stress level of $\sigma_{22} = 35$ kPa. Lower preloading net stresses resulted in higher void ratios. During wetting, represented on the left-hand side of Figure 5.23, as the degree of saturation increased to $S^w = 1.0$, an increase in stress was observed under constant volume conditions. The magnitude of the maximum swelling pressure in the fully saturated state was governed by the position of the w-line.

Again, the stress path of one simulation (for $e_0 = 0.384$) is shown in Figure 5.24 in terms of void ratio versus net stress (left) and deviatoric stress versus mean net stress (right). In the full formulation of the model, the development of swelling pressure exhibited a simpler path than swelling strain: under constant volume conditions, both vertical net stress and mean net stress increased proportionally, as can be seen on the left-hand side of Figure 5.24. Therein, the position of the w-line (green) and the B-line (medium blue) are shown for the start and the end of saturation as well. The evolution of both lines upon saturation, which determined the magnitude of swelling pressure, was evident. In the $q-p$ space, shown on the right-hand side of Figure 5.24, it was evident that the stress path during the development of swelling pressure remained entirely within the preconsolidation surface. The preconsolidation surface also contracted during saturation, due to the simultaneous reduction of both, the preloading net

stress and the angle of internal friction. The latter was indicated by the movement of the CSL, shown by the dark red arrow.

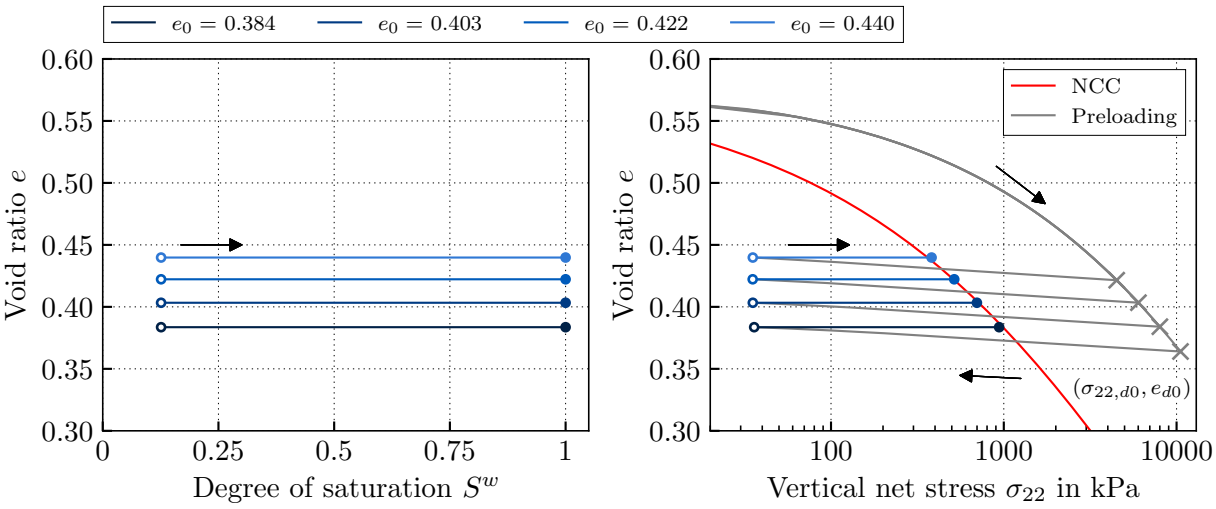

Figure 5.23.: Saturation-induced stress changes at different initial void ratios: Void ratio and wetting paths (left) and response of the model in terms of void ratio e versus vertical net stress σ_{22} (right).

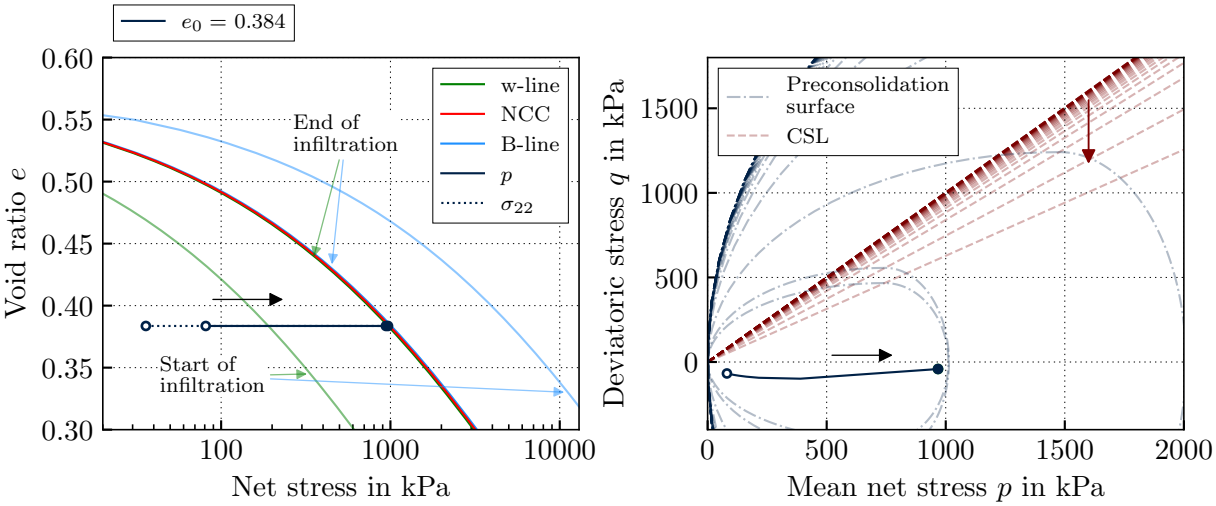

Figure 5.24.: Saturation-induced stress: void ratio e versus vertical net stress σ_{22} and mean net stress p (left) and deviatoric stress q versus mean net stress (right). The arrows indicate the stress path and movement of the CSL upon wetting.

Collapse upon wetting

For the sake of completeness, the capability of the full formulation of the model to predict saturation-induced collapse is illustrated in Figure 5.25. Note that the term collapse refers to a transient, saturation-dependent deformation. Collapse occurs when wetting takes place at a stress state that lies above the w-line corresponding to the current void ratio. In this case, the sign of the saturation-induced strain rate reverses. Figure 5.25 shows the model response for a representative loading path. The preloading sequence was identical to that in Figure 5.21, but unloading was terminated at a higher vertical net stress level. At constant stress, the degree of saturation was increased to $S^w = 1.0$ (see left-hand side of Figure 5.25), and the resulting

deformation progressed in compression until the void ratio reached its limiting value $e = e_w$ on the w-line, as defined by Equation (5.23). Therefore, the position of the w-line (green) and B-line (medium blue) for the start and end of saturation are shown as well.

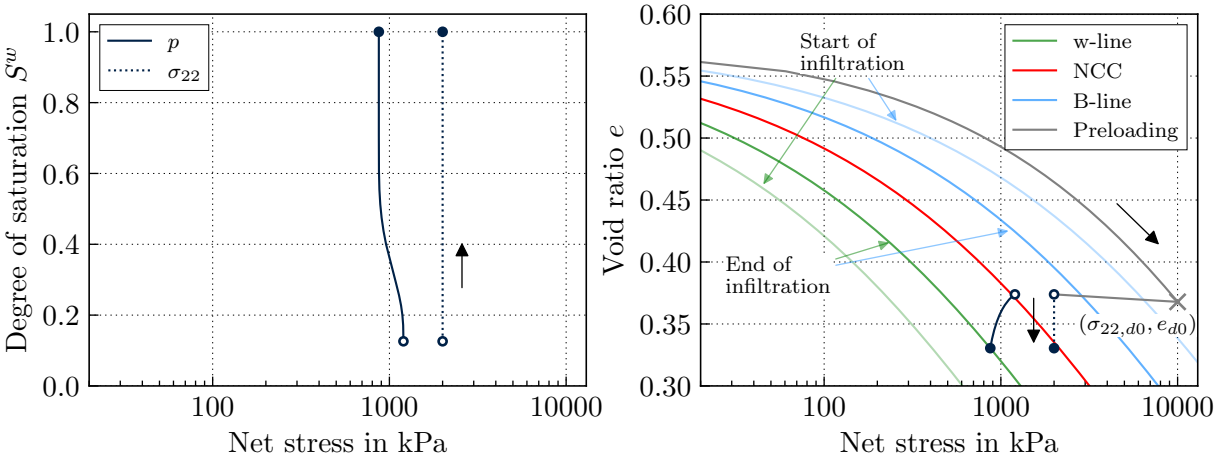

Figure 5.25.: Saturation-induced collapse upon wetting: vertical net stress and wetting paths (left) and response of the model in terms of void ratio e versus vertical net stress σ_{22} (right).

5.4. Determination of material parameters

The full formulation requires ten material parameters in total, which were given in Table 5.1. In addition to the seven material parameters required for the one-dimensional formulation, which are the parameters h_s, n and e_N for the NCC, the un-/reloading indices κ_{ref} and κ_w, the parameter b for the evolution of the saturation-driven strain rate and the parameter c for the reduction of preloading net stress, the three additional parameters are the friction angle in the reference state φ_{ref}, the friction angle in the saturated state φ_w, and the shape parameter β of the preconsolidation surface. The parameter calibration for the one-dimensional formulation (see Section 4.3)) is essentially still valid for the full formulation, as most parameters can be calibrated directly from experimental results. However, parameters calibrated for the one-dimensional formulation must be adjusted for usage within the full formulation, as the material behaviour is now determined by the mean net stress p and deviatoric stress q and not only by the vertical net stress component σ_{22}. In this section, the calibration of the additional parameters of the three-dimensional generalisation and the adjustment of the remaining parameters is discussed. Finally, a schematic overview for the calibration of the full formulation is given.

5.4.1. Angles of internal friction φ_{ref} and φ_w

The friction angle φ is linearly interpolated between its values in the saturated state and a dry, reference state according to Equation (5.14). Thus, both friction angles φ_{ref} and φ_w are material parameters. Analogously to the un- and reloading slope κ, the degree of saturation in the reference state can be regarded equivalent to the residual degree of saturation $S^w_{\mathrm{ref}} = S^{wr]}$. In general, the angle of internal friction can be determined in the laboratory, e.g. using direct shear tests, simple shear tests or triaxial compression tests. The execution of suitable tests on the saturated material is, however, not trivial and requires advanced testing equipment and small

(shear) displacement rates, as drainage must be ensured upon shearing. Therefore, an alternative calibration procedure was developed, which requires the knowledge of only one friction angle, ideally in the dry, reference state and the expansive clay mineral content. The friction angle in the saturated state can be estimated based on a correlation derived from experimental results for the four materials presented in Chapter 2, Section 2.4.4. The results were reevaluated in terms of the ratio $\varphi\left(S^e\right)/\varphi_w$. They are shown versus the effective degree of saturation on the left-hand side of Figure 5.26. All materials coincide for $\varphi\left(S^e=1\right)/\varphi_w = 1.0$ and exhibit an approximately linear increase with decreasing degree of saturation. The slope m of the linear trends, which are shown as dashed lines on the left-hand side of Figure 5.26, is itself linearly dependent on the content of expansive clay minerals in the soils x_{ecm} (smectite and illite). The values for the four studied materials are displayed on the right-hand side of Figure 5.26. The expansive clay mineral content is $x_{\mathrm{ecm}} = \{16, 35, 40, 92\}$ wt-% for Barcelona silt (Barrera, 2002), Opalinus clay (see Appendix A), Boom clay (Romero, 1999) and Febex bentonite (Villar and Lloret, 2008).

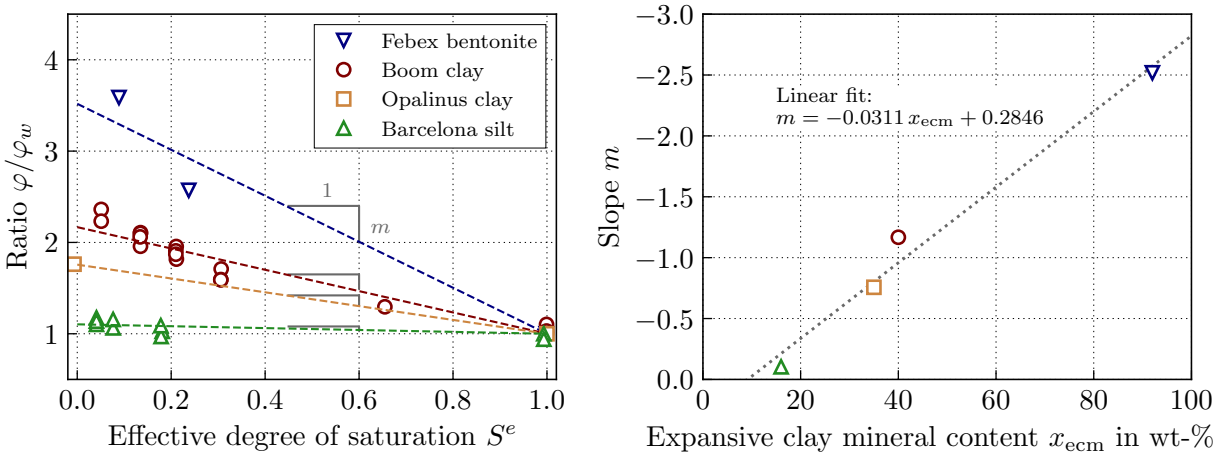

Figure 5.26.: Ratio φ/φ_w of Febex bentonite, Boom clay, Opalinus clay and Barcelona silt vs. effective degree of saturation with linear trend lines (left) and slope m of linear trends vs. content of expansive clay minerals (right).

As can be seen, a linear relation between the slope m and the expansive clay mineral content of the materials exists, which represents the intensity of the influence of saturation on the friction angle. The more expansive the soil, the more pronounced is its dependency of the friction angle on the degree of saturation or suction. Equation (5.14) can be rewritten as:

$$\begin{aligned} \varphi\left(S^e\right) &= \varphi_{\mathrm{ref}} + S^e\left(\varphi_w - \varphi_{\mathrm{ref}}\right) \\ \Leftrightarrow \frac{\varphi\left(S^e\right)}{\varphi_w} &= m\, S^e + (1-m) \quad \text{or} \qquad (5.29) \\ \Leftrightarrow \varphi\left(S^e\right) &= \left(m\, S^e + (1-m)\right)\varphi_w. \qquad (5.30) \end{aligned}$$

The evaluation of the linear fit for the slope m depending on the expansive clay mineral content x (in wt-%) on the right-hand side of Figure 5.26 is undertaken with a lower limit of $m < 0$:

$$m = \max\left(0, -0.0311\, x_{\mathrm{ecm}} + 0.2846\right). \qquad (5.31)$$

Consequently, instead of providing both friction angles φ_{ref} and φ_w, the expansive clay mineral content x_{ecm} can be used as a material parameter in addition to the reference friction angle

φ_{ref}. The total number of material parameters remains, while the experimental effort reduces. This alternative procedure should be regarded as a simplification. Providing both friction angles based on laboratory tests yields more accurate results.

5.4.2. Shape parameter β

The shape parameter β can be computed based on the friction angle. Its magnitude must guarantee a stress ratio $K_{0,NC} = \sigma_{11}/\sigma_{22}$ corresponding to the flow direction $\mathbf{m} \sim \mathrm{diag}[0, -1, 0]$ for $\boldsymbol{\sigma} \sim \mathrm{diag}[-K_0, -1, -K_0]$ under oedometric conditions, hence $m_1 = m_3 = 0$ for the vertical net stress σ_{22}. Any state $\{p, q\}$ upon virgin loading must fulfil the consistency condition $F = 0$ (Equation (5.10)). Considering K_0, the invariants $\{p, q\}$ are:

$$p = -\frac{\sigma_{22}(1 + 2K_0)}{3} \quad \text{and} \quad q = -\sigma_{22}(1 - K_0). \tag{5.32}$$

The condition of the associated flow rule for $m_1 = m_3 = 0$ is:

$$m_1 = \frac{\partial F}{\partial p}\frac{\partial p}{\partial \sigma_{11}} + \frac{\partial F}{\partial q}\frac{\partial q}{\partial \sigma_{11}} = 0. \tag{5.33}$$

With algebraic transformation of $K_0 = K_0(F(\beta, M))$, Equation (5.33) results in:

$$K_0(\beta, M) = \frac{-81\beta^2 + 81\beta^4 - 9M^2 + 9\beta^2M^2 - 2M^4 + 9M^2\sqrt{9\beta^2 + M^2}}{-81\beta^2 + 81\beta^4 - 9M^2 + 36\beta^2M^2 + 4M^4}, \tag{5.34}$$

wherein $M = (6\sin\varphi)/(3 - \sin\varphi)$, thus neglecting the influence of the Lode angle θ, is applied for reasons of simplicity. Figure 5.27 shows the resulting approximation for β for given values of the friction angle φ. For calibration of β from Figure 5.27, the friction angle in the reference state φ_{ref} should be used to guarantee the intended material response during dry loading and unloading upon specimen preparation. For unloading in the saturated state, merely the parameter κ_w is decisive (see subsequent paragraph).

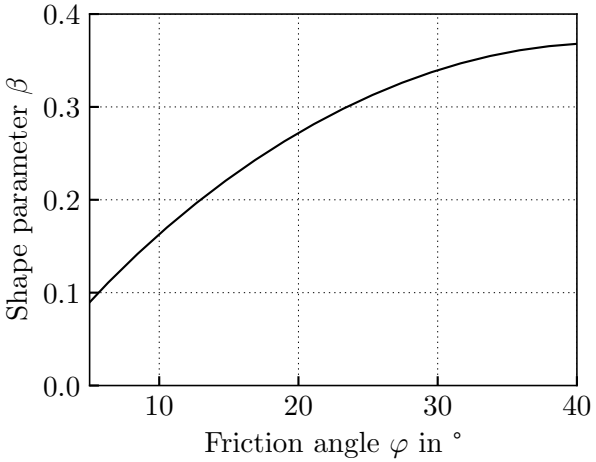

Figure 5.27.: Calibration curve for approximation of the shape parameter β for given values of the friction angle φ.

5.4.3. Parameters h_s, e_N and n of the normal compression curve

The parameters h_s, e_N and n of the NCC remain unchanged in the full formulation and can be determined as described in Section 4.3. However, it is recommended to ensure a certain vertical distance between the NCC and the maximum void ratio $e_{\max}$ observed in vertically unconfined swelling in the $e - \log(p)$ diagram by choosing e_N accordingly. Due to the increased radial net stress in oedometric conditions, the mean net stress p and its target value on the w-line are generally larger than their vertical counterparts. As a result, the stress path in the $e - \log(p)$ space starts closer to the NCC, increasing the possibility that e reaches the w-line prematurely before the full range of void ratio evolution has been mobilised upon wetting, thus constraining the achievable $e_{\max}$ during the simulation of vertically unconfined swelling.

5.4.4. Elastic indices κ_{ref} and κ_w

The parameters responsible for the elastic stiffness must be partly adjusted. In the one-dimensional case, κ directly relates the volumetric deformation to the vertical net stress, and the differences in the elastic stiffness are directly reflected in an increased κ_w in the saturated state in comparison to the dry, reference state κ_{ref}. In the full formulation, however, the magnitude of the volumetric deformation during elastic loading relates to the mean net stress p. As the model is well calibrated for the dry state (see Section 5.4.2), the deformation for oedometric unloading in the saturated state, i.e., for a given change in vertical net stress, is underestimated when κ_w from the one-dimensional model is used. Therefore, κ_w must be manually increased in simulations to ensure a good prediction of the material behaviour. κ_{ref} must not be adopted and can be determined as described in Section 4.3.

5.4.5. Parameters b for the evolution of the saturation driven strain and c for the evolution of preloading net stress

The parameters b and c, which are responsible for the evolution of the saturation-driven strain rate $\dot{\epsilon}^w$ and the degradation of the preloading pressure p_d, respectively, must be re-examined for the full formulation. They should still be determined simultaneously by simulating vertically unconfined swelling tests, as recommended for the one-dimensional model in Section 4.3, since both parameters impact $\dot{\epsilon}^w$: b directly in Equation (5.18) and c indirectly via the preloading state in the limiting void ratio e_w in Equation (5.23). Moreover, the preloading net stress p_d directly governs the size and shape of the preconsolidation surface, which can be met by the stress path for any stress state in the full formulation of the model and impacts the material response. In case of vertically unconfined swelling, the stress path first follows a loading path until it meets the preconsolidation surface and afterwards follows an unloading path in extension. If the parameter c is too large, p_d decreases less pronounced upon wetting, resulting in a shallower preconsolidation surface (in extension), that is met for smaller mean net stress, however, after infiltration has progressed further. From a graphical point of view, the sigmoid shaped evolution of the void ratio in relation to the water content for the saturation-driven strain rate is initially not steep enough until the preconsolidation surface is met. As a result, volumetric deformation is underestimated. Reduction of c can help to recover the characteristic sigmoid shape of the void ratio-water content curve, particularly by ensuring that the initial portion of the curve is not overly flat. This adjustment improves the prediction of volumetric expansion upon wetting

under vertically unconfined conditions. Based on the author's experience, a suitable choice for c is approximately 50 % of the value used in the one-dimensional formulation. However, this reduction must still allow for an accurate representation of the preloading net stress, i.e., the transition from reversible to irreversible material behaviour during oedometric compression. Moreover, a too severe reduction results in an overestimation of the expansion. As an alternative, the parameter b can be increased, which accelerates the increase of e upon infiltration and thus also leads to less initial flattening of the e-w curve. However, an increase of b may also result in a premature decay of deformation, as the influence on the e-w curve is point-symmetrical. Swelling under constant volume conditions is less sensitive to the magnitude of c, as long as the stress path remains within the preconsolidation surface and follows a purely elastic loading path. Nevertheless, it cannot be assumed that this behaviour generalizes to all materials and initial conditions. Given the current state of the full formulation and the available experimental evidence for three-dimensional behaviour, recalibration must be performed individually for each material.

Figure 5.28 studies the influence of b and c on the model response for vertically unconfined swelling in single-element simulations. On the left-hand side, the e–$\log(\sigma_{22})$ paths are shown, including oedometric loading for the simulations with variation of c, and the plots in the centre and on the right-hand side present the evolution of e over the water content for both variations.

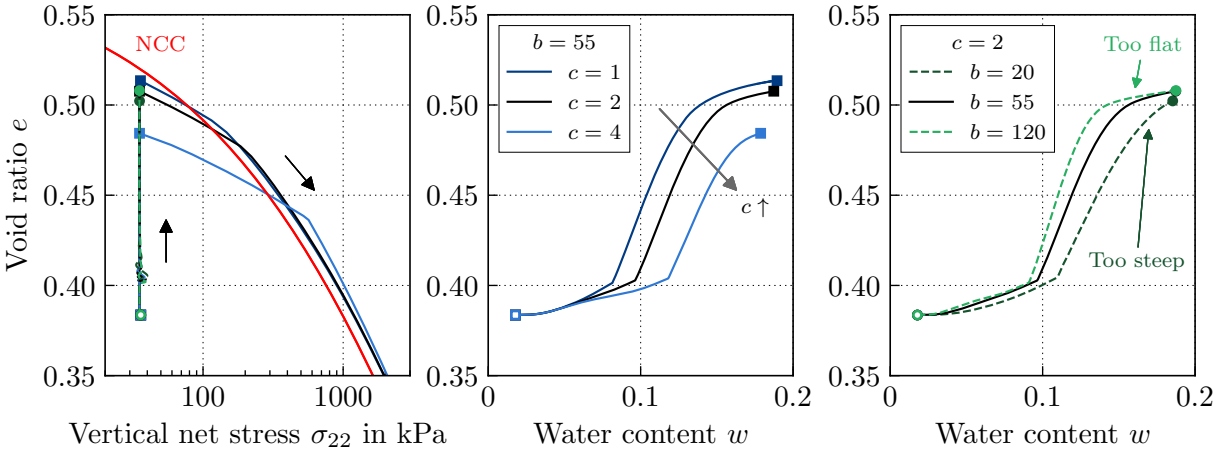

Figure 5.28.: Influence of parameters b and c during vertically unconfined swelling: void ratio versus vertical net stress (left) and void ratio versus water content (centre an right).

For variations of b, a decrease from the reference value of $b = 55$ to $b = 20$ resulted in a delayed increase of void ratio and consequently in an underestimation of expansion, as the e-w curve was still rising at the end of infiltration. An increase to $b = 120$ had less impact on the predicted expansion at full saturation, however, resulted in a rather flat final section of the e-w curve, which can create difficulties in the accurate prediction of unsaturated swelling. The results in Figure 5.28 highlight the more pronounced impact of c on the material response, which follows unique trends: With decreasing c, the point-symmetry of the e-w curve was improved, increasing final expansion was predicted and the transition from reversible to irreversible material response upon loading occurred at smaller stresses due to the reduced preloading net stress.

5.4.6. Overview of parameter calibration

A schematic overview of the recommended parameter calibration for the full model formulation including required laboratory tests and decision aids is given in Figure 5.29.

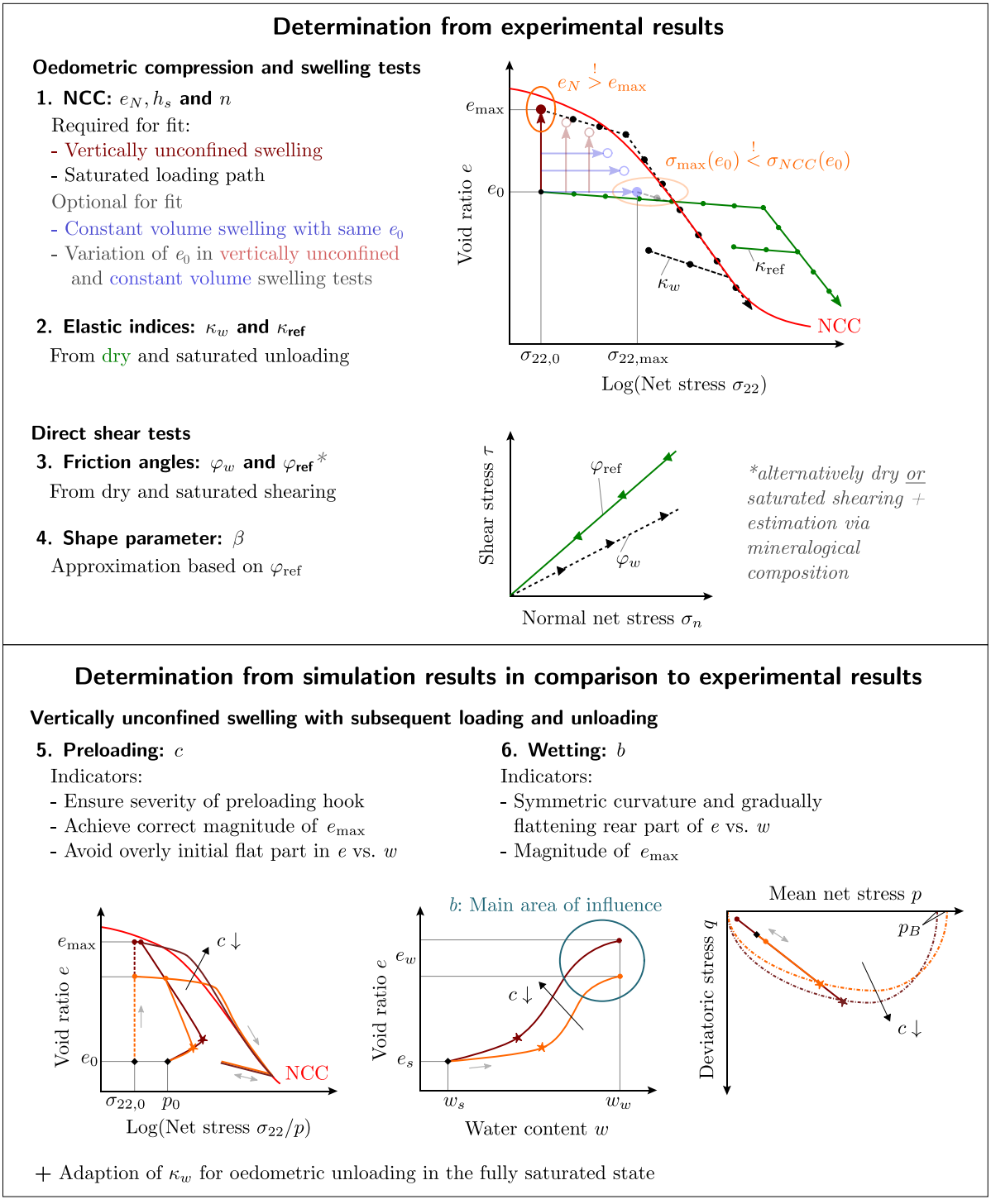

Figure 5.29.: Overview of the recommended material parameter calibration for the full formulation of the mechanical constitutive model.

To summarize:

- The parameters h_s, e_N and n for the NCC and κ_{ref} can be determined directly from experimental results. As a minimum, a swelling test under vertically unconfined conditions and subsequent oedometric loading in the saturated state is required. Additional results from constant volume swelling starting at the same initial void ratio and swelling tests starting from different initial conditions improve the fit of the NCC.

- The reference friction angle φ_{ref}, the associated shape parameter β and the friction angle in the fully saturated state φ_w can be evaluated from results of direct shear tests. As an alternative to the latter, a correlation between the proportion of expansive clay minerals (illite and smectite) and the ratio of friction angles φ/φ^w can be applied to approximate the friction angle in the fully satuarted state based on the reference friction angle (or any known friction angle). The expansive clay mineral content must be determined by mineral analysis (using x-ray diffraction), which is routinely performed as part of experimental campaigns.

- The parameters b and c must be calibrated by simulating swelling under vertically unconfined conditions and should be assessed in relation to each other. The parameter c for the evolution of the preloading pressure has the more pronounced impact of these parameters, affects the final magnitude and the overall shape of the stress path in p, which follows a loading and unloading path in extension. It is therefore recommended to initially assume a value for c and to calibrate the parameter b first to ensure an adequate shape of the e–w curve at the end of infiltration. The value of c should then be determined to meet the magnitude of expansion and preloading net stress, with minor readjustments of b if necessary.

- Finally, for application of the full formulation κ_w can be optimized by simulation of an unloading path in the fully saturated state. However, determining the index from experimental results serves as a good starting point.

In theory, β could be excluded as a parameter by incorporating the evaluation underlying Figure 5.27 into the full formulation of the model, thereby further reducing the number of required model parameters. In this work, however, β is retained as a parameter to preserve flexibility. It should also be noted that the model requires a reference degree of saturation S_{ref}. If specified independently of the hydraulic model, S_{ref} also functions as a material parameter.

5.5. Comparison with experimental results

The experimental validation is presented for the materials intensively discussed in Section 4.4 for the one-dimensional formulation. The revised parameters for the full formulation are given in Table 5.4. Parameters in brackets refer to those calibrated for the one-dimensional model, which were adjusted for the full model formulation. For all three materials, the parameter κ_w had to be increased as discussed in the previous Section 5.4. For reconstituted Opalinus clay and the bentonite-silt mixture (Nowamooz and Masrouri, 2008), only the parameter c was adjusted additionally, while for the bentonite-sand mixture (Lang, 2019), an adjustment of parameter b was undertaken as well. The parameters were calibrated with a focus on the prediction of the

fully saturated behaviour and therefore, the parameters were selected to capture swelling strain and swelling pressure under full saturation best, where available.

Table 5.4.: Model parameters for the full formulation for three different expansive materials.

Parameter	Reconstituted Opalinus clay (Nitsch et al., 2023a)	Bentonite-sand mixture (Lang, 2019)	Bentonite-silt mixture (Nowamooz and Masrouri, 2008)
e_N	0.610	0.895	1.615
h_s in kPa	8000	18000	1200
n	0.36	0.31	0.40
κ_{ref}	0.003792	0.001013	0.002017
κ_w	0.02 (0.01537)	0.03 (0.007044)	0.04 (0.02647)
b	55	25 (15)	17
c	2.2 (4.5)	3.5 (5.0)	1.4 (2.6)
β	0.35	0.25	0.33
φ_{ref} in $^\circ$	37	17	30
x_{ecm}	0.35	0.32	0.62
S_{ref}	0.126	0.26	0.27

The preparation of the compacted specimens was simulated starting from an initial isotropic pressure of $p^i = 10$ kPa. The specimens were loaded to the known vertical preloading net stress $\sigma_{22,d0}$ and corresponding void ratio e_{d0} and subsequently unloaded to the known initial vertical net stress $\sigma_{22,0}$ before wetting. The initial void ratio e^i corresponding to the initial isotropic pressure was unknown and had to be determined iteratively by matching the known void ratio e_0 at the beginning of infiltration after loading and unloading for the given vertical net stress $\sigma_{22,0}$. A void ratio just smaller than the material parameter e_N from the NCC served as a suitable starting point. The initial values of the preloading net stress and its corresponding void ratio were chosen identical to the initial state, hence $p^i = p^i_d$ and $e^i = e^i_d$.

5.5.1. Reconstituted Opalinus clay

Oedometric compression tests on reconstituted Opalinus clay shale (Nitsch et al., 2023c) with different hydro-mechanical prior loading paths were simulated in Section 4.4.1. Starting from nearly dry states, samples with similar void ratios were fully saturated and then subjected to oedometric loading and unloading paths. The saturation occurred under different conditions: (a) constant volume (swelling pressure test, OPA-0-34); (b) constant volume (swelling pressure test, OPA-0-07) followed by unloading; and (c) constant-stress (unconfined axial swelling strain test, OPA-0-24). For comparison, another sample was loaded at dry conditions (without the saturation stage, OPA-0-33).

The initial conditions are summarized in Table 5.5. Therein the initial state of the simulations, and both the target vertical preloading net stress $\sigma_{22,d0}$ and corresponding void ratio e_{d0} upon preparation and the state of the tests prior to wetting or the oedometric compression for the reference test are given. The material parameters were given in Table 5.4. The hydraulic model, required for the hydro-mechanically coupled simulation in `numgeo`, is shown in Figure 5.30. Here, the model of Fredlund et al. (1994) was fitted to the experimental data. The experimental value close to $S^w = 1$ was not taken into account. The hydraulic initial state is marked with an asterisk in Figure 5.30 and also included in Table 5.5. The angle of internal friction in the

reference state was determined to $\varphi_{\text{ref}} = 37°$, see Section 2.4.4 and Appendix A. Based on the known content of expansive clay minerals of $x_{\text{ecm}} = 35$ wt-%, the angle of internal friction in the saturated state was estimated as $\varphi_w = 20.5°$, which was in good accordance with the reported experimental value. The shape parameter was determined to $\beta = 0.36$ based on the procedure discussed in Section 5.4.2.

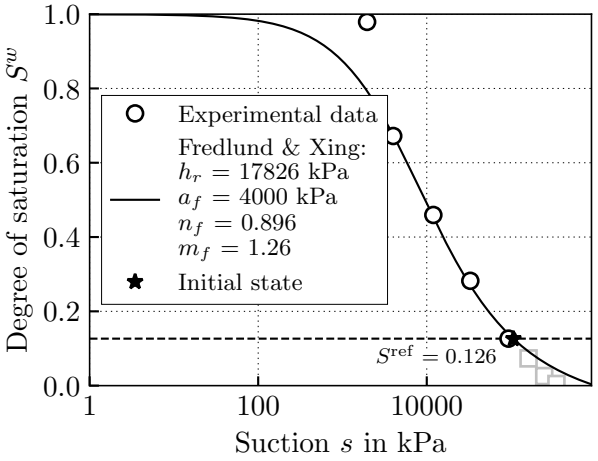

Figure 5.30.: Soil water retention curve: experimental data for Opalinus clay and fit using the hydraulic model of Fredlund et al. (1994).

Table 5.5.: Initial and target conditions for the simulations on Opalinus clay shale from Nitsch et al. (2023a).

	$p^i = p^i_d$ in kPa	$e^i = e^i_d$	$\sigma_{22,d0}$ in kPa	e_{d0}	$\sigma_{22,0}$ in kPa	e_0	$S^w_0 = S_{\text{ref}}$	$p^w_0 = -s_0$ in kPa
Reference	10	0.587	10535	0.359	180	0.374	0.126	-106700
Constant volume	:	0.589	:	0.376	25	0.396	:	:
CV + unloading	:	0.588	:	0.374	35	0.392	:	:
Vertically unconfined	:	0.588	:	0.364	35	0.384	:	:

Figure 5.31 shows the simulations (right) of the experiments (left) on reconstituted Opalinus clay shale. The full formulation of the model was able to predict the mechanical response in the dry reference state and after different wetting paths with subsequent oedometric loading and unloading in a similar manner as the one-dimensional model in Section 4.4.1. The unique NCC was reached after long monotonic loading regardless of the prior loading path and the reduced elastic stiffness from the reference state to the saturated conditions was well simulated. The generalised model was able to reproduce both the maximum swelling pressure and the maximum swelling strain with a single set of material parameters.

5.5.2. Bentonite-silt mixture

Three suction-controlled oedometric swelling tests under vertically unconfined conditions, followed by oedometric loading, as well as one reference oedometric compression test, were reported by Nowamooz and Masrouri (2008) for a bentonite-silt mixture and back-calculated in Section 4.4.2. The initial conditions for the simulations with the full formulation are summarized in Table 5.6, and the corresponding model parameters are listed in Table 5.4. The soil water retention curve used was identical to that in Section 4.4.2 (van Genuchten model), which was employed to

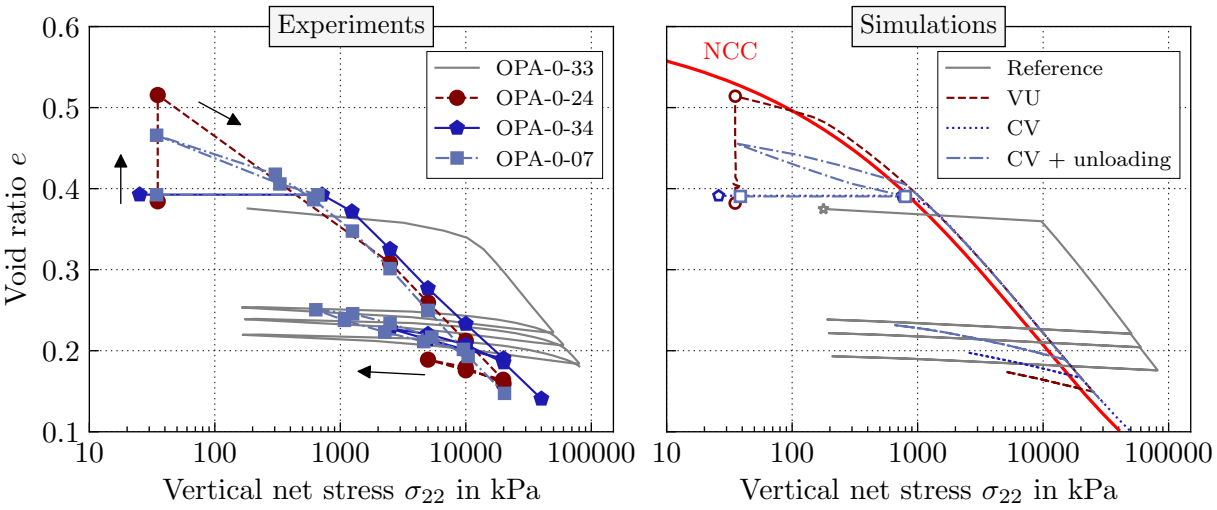

Figure 5.31.: Simulation of oedometric compression tests in the reference state and preceded by saturation at different boundary conditions on reconstituted Opalinus clay (right) and experimental results (left, Nitsch et al. (2023a)).

estimate the target degree of saturation in the unsaturated tests. For completeness, it is shown again in Figure 5.32, with the initial conditions marked by an asterisk. In the simulations, the target pore water pressure was directly prescribed to match the experimental conditions. The applied suctions were $s = 0$ kPa (full saturation) for sample M1, $s = 3000$ kPa for M4, and $s = 8000$ kPa for M5, all starting from an initial suction of $s = 20000$ kPa, which applied to the reference sample M0. Since the reference internal friction angle of the material was not reported, a value of $\varphi_{\text{ref}} = 30°$ was estimated, resulting in $\beta = 0.34$ based on the procedure discussed in Section 5.4.2. This corresponded to a reduced friction angle of $\varphi_w \approx 11.5°$ in the saturated state, based on the known content of expansive clay minerals of $x_{\text{ecm}} = 62$ wt-%.

Table 5.6.: Initial and target conditions for the simulations on a bentonite-silt mixture from Nowamooz and Masrouri (2008).

	$p^i = p^i_d$ in kPa	$e^i = e^i_d$	$\sigma_{22,d0}$ in kPa	e_{d0}	$\sigma_{22,0}$ in kPa	e_0	S^w_0	$p^w_0 = -s_0$ in kPa
M1	10	1.535	700	1.001	10	1.047	0.36	-20000
M4	:	1.538	540	1.051	:	1.095	:	:
M5	:	1.539	488	1.071	:	1.102	:	:
M0 (reference)	:	1.560	700	1.080	:	1.128	:	:

Figure 5.33 presents the simulation results (right) alongside the experimental data (left) for the bentonite-silt mixture. The full formulation of the model successfully reproduced the attracting nature of the NCC, as higher degrees of saturation led to a more rapid approach toward the NCC during compression. The evolution of vertical preconsolidation stress and elastic stiffness with saturation was well captured. The magnitude of expansion during swelling was generally well predicted, with only minor deviations, most notably in test M5, where the vertical swelling strain was slightly underestimated.

The unsaturated swelling tests under vertically unconfined conditions reveal one challenge in applying the three-dimensional generalisation of the model: due to the characteristic stress path, which exhibited a change of direction in extension, the relationship between volumetric

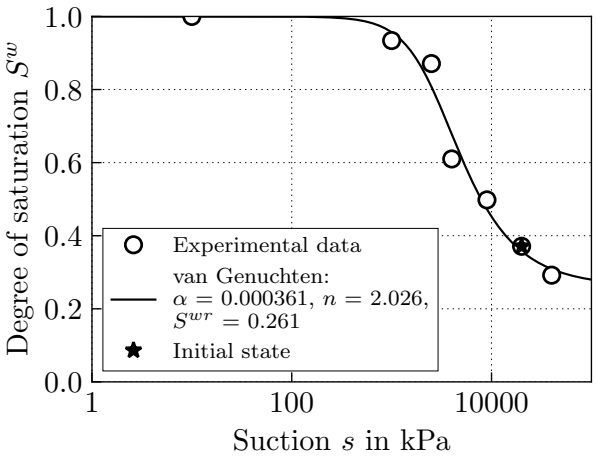

Figure 5.32.: Soil water retention curve: experimental data for vertically unconfined samples from Nowamooz and Masrouri (2008) with fit using the hydraulic model after van Genuchten (1980).

deformation induced by the saturation-driven strain rate and the increment in the effective degree of saturation was less direct than in the one-dimensional formulation. Nevertheless, this did not compromise the overall predictive capability of the full formulation of the model.

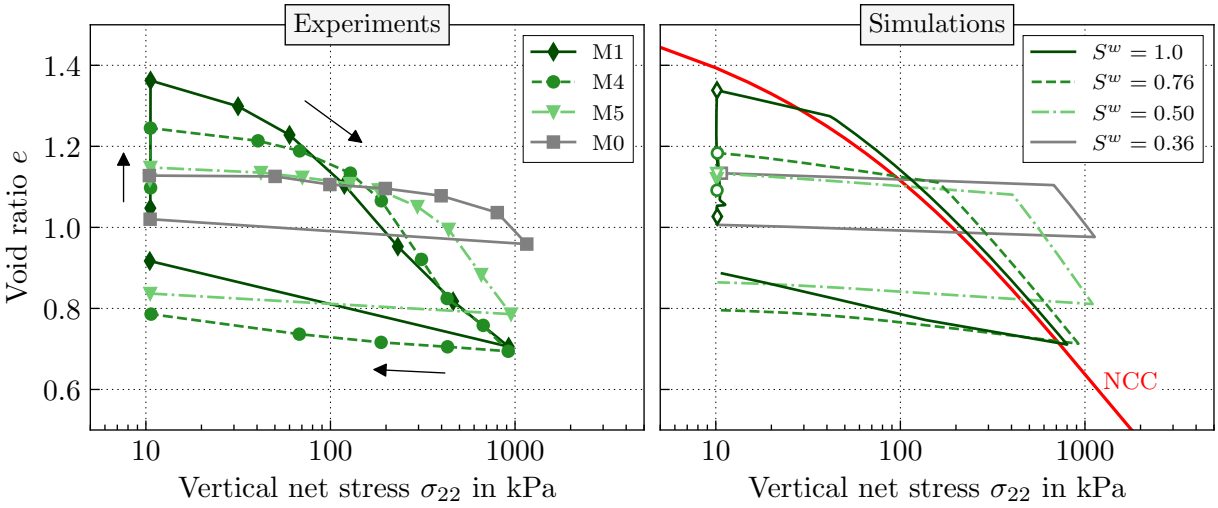

Figure 5.33.: Simulation of vertically unconfined swelling and subsequent oedometric compression tests under unsaturated and fully saturated conditions on a bentonite-silt mixture (right) and experimental results (left, Nowamooz and Masrouri (2008)). The NCC is shown in red.

5.5.3. Bentonite-sand mixture

In Section 4.4.3, several swelling tests under both vertically unconfined and constant volume conditions, followed by oedometric compression tests and a reference oedometric compression test reported by Lang (2019) were simulated using the one-dimensional formulation. For simulations with the full formulation, the initial conditions are summarized in Table 5.7, and the corresponding model parameters are listed in Table 5.4. The soil water retention curves used for the simulations are shown alongside the experimental data from Lang (2019) in Figure 5.34, with the initial state marked by an asterisk. As in Section 4.4.3, two fits using the model of

van Genuchten (1980) were applied, reflecting the different boundary conditions in the experiments.

Table 5.7.: Initial and target conditions for the simulations on a bentonite-sand mixture from Lang (2019).

	$p^i = p^i_d$ in kPa	$e^i = e^i_d$	$\sigma_{22,d0}$ in kPa	e_{d0}	$\sigma_{22,0}$ in kPa	e_0	S^w_0	$p^w_0 = -s_0$ in kPa
All tests	10	0.883	10200	0.498	25	0.530	0.47	-27000

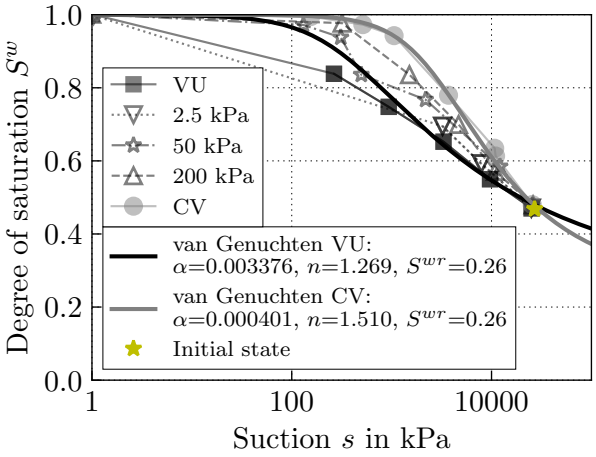

Figure 5.34.: Soil water retention curve: experimental data from Lang (2019) and two van Genuchten fits representing constant volume conditions (grey) and vertically unconfined conditions (black). Modified from Grandas Tavera et al. (2022).

Figure 5.35 compares the experimental results (left) with the simulations (right) performed using the proposed full formulation of the model for vertically unconfined swelling followed by oedometric compression. The van Genuchten fit for vertically unconfined conditions (bold black line in Figure 5.34) was applied. The target suctions were $s = 0$ kPa for test BS-SCR-1 (full saturation), $s = 8000$ kPa for BS-SCR-2, and $s = 10000$ kPa for BS-SCR-3, all starting from an initial suction of $s = 27000$ kPa, which applied to the reference test BS-SCR-4. The reference internal friction angle of the material was unknown and set to $\varphi_{\text{ref}} = 17°$ to avoid excessive radial net stresses after sample preparation in the reference state. Based on the procedure described in Section 5.4.2, $\beta = 0.25$ was determined. Given the known content of expansive clay minerals ($x_{\text{ecm}} = 32$ wt-%), a reduced friction angle of $\varphi_w \approx 10.0°$ was applied in the saturated state.

Overall, the material behaviour upon vertically unconfined swelling and oedometric compression was well reproduced by the model, including the reduction of stiffness with increasing degree of saturation upon unloading paths and of the vertical preconsolidation stress. The magnitude of deformation upon swelling was slightly underestimated in the fully saturated state, however, predicted well for unsaturated conditions, with increasing deformation for higher final degrees of saturation. The fluctuations in vertical net stress visible in Figure 5.35 during the evolution of swelling strain were numerical instabilities due to the comparatively small vertical net stress level of $\sigma_{22} = 2.5$ kPa upon saturation. The difference between radial and vertical net stresses was very pronounced, which resulted in large horizontal nodal forces and made convergence of the simulation more demanding. However, the fluctuation only occurred with a small range $2.0 - 3.5$ kPa and appears more pronounced due to the logarithmic scale of the horizontal axis in Figure 5.35.

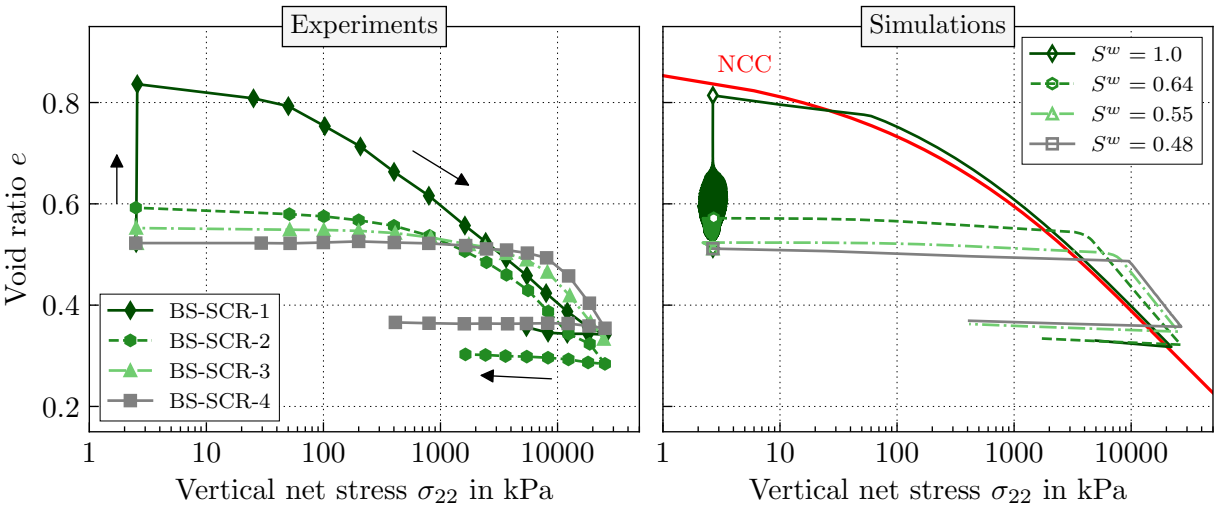

Figure 5.35.: Simulation of vertically unconfined swelling and subsequent oedometric compression tests under unsaturated and fully saturated conditions on a bentonite-sand mixture (right) and experimental results (left, Lang (2019)). The NCC is shown in red.

Figure 5.36 compares the results of the swelling pressure tests (left) with the corresponding simulations (middle and right). In line with Section 4.4.3, the simulations were carried out using the van Genuchten fits for both vertically unconfined and constant volume conditions. The target suctions were $s = 0$ kPa for BS-WCV-1 (full saturation), $s = 3780$ kPa for BS-WCV-5, and $s = 11450$ kPa for BS-WCV-7. The swelling pressure under fully saturated conditions was satisfactorily reproduced by the model. However, the predictive accuracy for the final unsaturated tests is deficient, as the differences in the swelling pressure dependent on the final degrees of saturation are not adequately captured by the model, only partially in the case of the vertically unconfined SWRC. An accurate assessment of the prediction quality required knowledge of the final water content or degree of saturation, which was not available. Overall, the model captured the material behaviour satisfactory though further improvements remain possible. A more advanced hydraulic model that evolves with deformation is required to further optimise the overall modelling framework for unsaturated conditions, as the evolution of the hydraulic constitutive equations also influences the mechanical material response in unsaturated states.

As already discussed in Section 4.4.3, the swelling pressure of the material was comparably small in comparison to the swelling strain and in a graphical representation, its saturated final state was positioned in a rather large distance to the well-defined NCC in the $e - \log \sigma_{22}$ diagram. The result was a premature ceasing of the development of swelling pressure prior to full saturation in the simulations. This issue reduces the predictive quality for constant volume swelling, especially in a discretised boundary value problem, wherein the saturation front progresses and interaction effects between neighbouring elements impact the material response. Overall, there is considerable uncertainty regarding the model parameters of this material. The friction angle, for instance, has already been set relatively low for a bentonite–sand mixture in order to minimise the remaining radial net stress following the simulation of sample preparation. However, due to the low vertical net stress, the initial state prior to swelling remains unfavourably located deep within the extensional domain, beyond the critical state line.

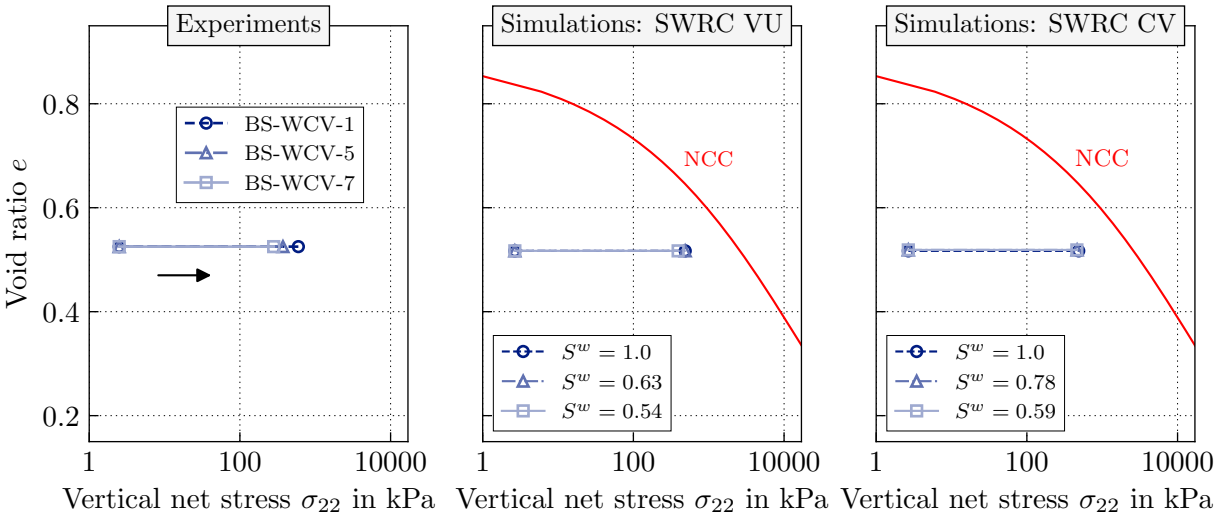

Figure 5.36.: Simulation of constant volume swelling tests under unsaturated and fully saturated conditions on a bentonite-sand mixture using the SWRC corresponding to vertically unconfined data (middle) and constant volume data (right) and experimental results (left, Lang (2019)). The NCC is shown in red.

5.6. Concluding remarks

In this chapter, the generalisation of the one-dimensional mechanical constitutive model to three-dimensional stress paths was presented through the adoption of the Modified Cam Clay (MCC) yield surface and flow rule. The generalized model is capable of reproducing key aspects of the behaviour of expansive soils under oedometric conditions, including a consistent representation of shear strength. Swelling under both vertically unconfined and constant volume conditions, monotonic loading, and reversible unloading and reloading at various degrees of saturation can be simulated using a single set of material parameters. The model also captures volumetric collapse, that is, the reduction in void ratio upon wetting. While the model accurately predicts the maximum swelling strain and swelling pressure, further improvement of the mechanical formulation is limited by the uncertainties inherent in the hydraulic model. In particular, the simulation of swelling pressures under partially saturated final conditions depends strongly on the quality of the hydraulic representation, which currently constrains refinement of the mechanical response. Nonetheless, the overall predictive capability of the full formulation of the model is sound and in good agreement with experimental results from campaigns on three different materials.

The full formulation introduces three additional material parameters compared to the one-dimensional model: the internal friction angles in the reference and saturated states, φ_{ref} and φ_w, and the shape parameter β, which adjusts the shape of the MCC yield surface in the subcritical stress range. As an alternative to specifying both friction angles, an interpolation based on the expansive clay mineral content can be used, where the latter then serves as an alternate material constant. This approach considers smectite and illite clay minerals. In this work, selected material parameters show dependency on the mineralogical composition whereas others appear to be relatively independent of it. Similar observations were reported for other constitutive models for unsaturated swelling clays, e.g. by Dieudonne (2016). A reliable indicator based on the proportion of expansive clay minerals has yet to be identified, since different

parameters may respond to distinct mineralogical features or remain largely unaffected. For example, the parameter e_N of NCC is closely linked to the maximum void ratio upon vertically unconfined swelling, which is in turn larger for materials with a higher amount of expansive clay minerals. A recommendation for the parameter calibration of the full model formulation based on standard laboratory tests and selected simulations was presented in this chapter. Development of relationships between clay mineralogy and constitutive parameters may simplify the parameter estimation based on selected mineralogical indicators where direct experimental calibration is not feasible.

6. Finite element implementation of the numerical framework

The governing equations are discretised in space using the finite element method (FEM). For the modelling of fully coupled processes in unsaturated soil mechanics, three kinematic variables are generally involved: the solid displacements $\boldsymbol{u}^s = u_i^s$ and the pore pressures of water and air, p^{wf} and p^{af}. In the present formulation, the primary variables are chosen as the solid displacements u_i^s and the pore water pressure p^{wf}, leading to a two-phase $\boldsymbol{u}p$ formulation. This reduction is justified by assuming a passive air phase, as commonly adopted in the literature (Forsyth, 1988; Zienkiewicz et al., 1997). The system is considered open to the atmosphere, such that the pore air pressure remains constant and no air flow occurs. Thus, the conservation of mass for the pore air can be neglected. In addition, the relative acceleration between the pore water and the solid phase is assumed negligible, i.e. $\bar{a}_i^{wf} = \bar{a}_i^s$. This chapter presents the implementation of the governing equations and all required constitutive models. The variational (weak) forms of the conservation of linear momentum of the mixture and the conservation of mass for the free pore water are derived. Their spatial discretisation is described, and the corresponding element contributions to the system of equations within the FE solution procedure, including time integration, are discussed. Subsequently, the implementation is examined with respect to element performance, time-stepping, and the integration of the mechanical material model.

6.1. Constitutive relations and material models

Several constitutive models are required to solve the governing equations. Details on the implementation of all applied constitutive models in this work are given in the following. Within FEM, the equations of any constitutive model have to be expressed in terms of finite increments instead of rates. Therefore, a time increment Δt from time t to $t + \Delta t$ is considered. Any quantity at the beginning of the increment at time t is denoted as $\sqcup^{(t)}$, whereas the superscript $\sqcup^{(t+\Delta t)}$ denoting the current value at the end of the increment at time $t + \Delta t$ is omitted for the sake of clarity, such that any updated quantity is written without an additional index.

6.1.1. Mechanical model

The mechanical material model is responsible for returning an updated stress net tensor σ_{ij} and updated solution-dependent state variables sv^{sol}. The solution is based on the state of the net stress, all state variables ($sv^{\mathrm{sol}} \subseteq sv$) and the suction at the beginning of the increment

$\left\{\sigma_{ij}^{(t)}, sv^{(t)}, s^{(t)}\right\}$ and on the strain increment $\Delta\epsilon_{kl}$, the suction increment Δs and time increment Δt:

$$\sigma_{ij} = \sigma_{ij}\left(\sigma_{ij}^{(t)}, sv^{(t)}, s^{(t)}, \Delta\epsilon_{kl}, \Delta s, \Delta t\right) \quad \text{and} \tag{6.1}$$

$$sv^{\text{sol}} = sv^{\text{sol}}\left(\sigma_{ij}^{(t)}, sv^{(t)}, s^{(t)}, \Delta\epsilon_{kl}, \Delta s, \Delta t\right). \tag{6.2}$$

Furthermore the mechanical model is responsible to return the Jacobians $J_{ijkl}^{\sigma,\epsilon}$ and $J_{ij}^{\sigma,s}$, hence the derivative of the stress with respect to the strain and suction[1]:

$$J_{ijkl}^{\sigma,\varepsilon} = \frac{\partial\sigma_{ij}}{\partial\epsilon_{kl}} \quad \text{and} \quad J_{ij}^{\sigma,s} = \frac{\partial\sigma_{ij}}{\partial s}. \tag{6.4}$$

The mechanical model proposed in Chapters 4 and 5 is written using the effective degree of saturation instead of suction. From the hydraulic model, the suction increment Δs, and the degree of saturation at the beginning and end of the increment, $S^{w,(t)}$ and S^w are passed to the mechanical model. The increment of the effective degree of saturation ΔS^e is computed as:

$$\Delta S^e = S^e - S^{e,(t)} \quad \text{with} \quad S^{e,(t)} = \frac{S^{w,(t)} - S^w_{\text{ref}}}{1 - S^w_{\text{ref}}}, \tag{6.5}$$

wherein S^w_{ref} is the reference degree of saturation, which corresponds to the nearly dry state and can be equivalent to the residual degree of saturation S^{wr}. The computation of the rate $\dot{S}^e$ is addressed in the next section. Consequently, the computation of the Jacobian of stress with respect to the hydraulic variable is also with respect to the effective degree of saturation:

$$J_{ij}^{\sigma,S^e} = \frac{\partial\sigma_{ij}}{\partial S^e}. \tag{6.6}$$

Computation of the Jacobian of the stress with respect to suction from Equation (6.4) follows the chain rule:

$$J_{ij}^{\sigma,s} = J_{ij}^{\sigma,S^e} J^{S^e,s} = \frac{\partial\sigma_{ij}}{\partial S^e}\frac{\partial S^e}{\partial s}\frac{1}{1 - S^w_{\text{ref}}}, \tag{6.7}$$

wherein the derivative $\partial S^e/\partial s$ is also passed from the hydraulic model.

6.1.1.1. Integration

Time integration within the mechanical model can compute the stress increment and increment of state variables (1) either based on the known values of the stress and state variables from the beginning of the increment $\left\{\sigma_{ij}^{(t)}, sv^{(t)}\right\}$ with an explicit integration scheme or (2) with consideration of the change of state variables and stress upon the increment $\{\sigma_{ij}, sv\}$ with an implicit integration scheme. In this work, two explicit integration schemes are used, a Forward

[1] Formally, in an incremental formulation the derivatives are $\partial\Delta\sigma_{ij}/\partial\Delta\epsilon_{kl}$ and $\partial\Delta\sigma_{ij}/\partial\Delta s$ with $\Delta\sigma_{ij} = \sigma_{ij} - \sigma_{ij}^{(t)}$, $\Delta\epsilon_{kl} = \epsilon_{kl} - \epsilon_{kl}^{(t)}$ and $\Delta s = s - s^{(t)}$. However, it is common practice to use the simplified notation, i.e. $\partial\sigma_{ij}/\partial\epsilon_{kl}$ and $\partial\sigma_{ij}/\partial s$. The difference is purely notational, since the incremental variables at the beginning of the increment remain known and constant, thus their contributions in the derivative vanish, which is exemplary shown for the Jacobian $J_{ijkl}^{\sigma,\epsilon}$:

$$J_{ijkl}^{\sigma,\epsilon} = \frac{\partial\Delta\sigma_{ij}}{\partial\Delta\epsilon_{kl}} = \frac{\partial\sigma_{ij}}{\partial\Delta\epsilon_{kl}} - \underbrace{\frac{\partial\sigma_{ij}^{(t)}}{\partial\Delta\epsilon_{kl}}}_{=0} = \frac{\partial\sigma_{ij}}{\partial\epsilon_{kl}}\underbrace{\frac{\partial\epsilon_{kl}}{\partial\Delta\epsilon_{kl}}}_{=0} = \frac{\partial\sigma_{ij}}{\partial\epsilon_{kl}}. \tag{6.3}$$

Euler integration and a Modified Euler scheme. Let $\boldsymbol{y}$ denote the solution and $\boldsymbol{F}(t, \boldsymbol{y})$ its time derivative. In the Forward Euler integration, the solution $\boldsymbol{y}^{(1)}$ at the end of the increment $t + \Delta t$ is approximated by a single forward step with the current value $\boldsymbol{y}^{(t)}$ and time derivative $\boldsymbol{F}(t, \boldsymbol{y}^{(t)})$ evaluated at the beginning of the increment as $\boldsymbol{y}^{(1)} = \boldsymbol{F}(t, \boldsymbol{y}^{(t)})\Delta t$. The Modified Euler method extends this approach by introducing an intermediate evaluation. Following the computation of the first forward Euler step, the time derivative $\boldsymbol{F}(t, \boldsymbol{y}^{(1)})$ is evaluated for the previous solution $\boldsymbol{y}^{(1)}$ at the end of the increment t. With the average of both derivatives, the final solution $\boldsymbol{y} = 0.5 \left[\boldsymbol{F}(t, \boldsymbol{y}^{(t)}) + \boldsymbol{F}(t, \boldsymbol{y}^{(1)})\right] \Delta t$ at the end of the increment is then computed and yields a more accurate approximation.

For hypoplasticity of expansive soils, the solution vector $\boldsymbol{y}$ consists of all entries of the stress tensor σ_{ij}, the solution-dependent state variables $sv^{\mathrm{sol}} = \{p_d, e_d, e\}$ and the hydraulic variable. In this work, the (effective) degree of saturation S^e is chosen as the hydraulic variable, see Section 6.6.3.3 for discussion. The remaining state variables are directly computed in the constitutive equations. The integration scheme evaluates the net stress increment $\Delta\sigma$ and the increments of the solution-dependent state variables Δsv^{sol} from the strain increment $\Delta\epsilon_{ij}$ and the increment of the effective degree of saturation ΔS_e. Over a time increment Δt, the strain rate and the rate of effective degree of saturation are assumed constant and linearised as

$$\dot{\epsilon}_{kl} = \frac{\Delta\epsilon_{kl}}{\Delta t} \quad \text{and} \quad \dot{S}^e = \frac{\Delta S^e}{\Delta t}. \tag{6.8}$$

The stress and state variable rates are obtained from the constitutive rate equations and integrated in time, resulting in their increments:

$$\Delta\sigma_{ij} = \dot{\sigma}_{ij}\,\Delta t \quad \text{and} \quad \Delta sv^{\mathrm{sol}} = \dot{sv}^{\mathrm{sol}}\,\Delta t. \tag{6.9}$$

Due to the high non-linearity of the material behaviour and the usage of explicit time integration, a subincrementation is applied within the integration of the mechanical model. The single time increment Δt is divided into a number of small subincrements. The number of subincrements n_{sub} is estimated using the norm of the current strain increment $\Delta\epsilon_{kl}$ and increment of effective degree of saturation ΔS^e:

$$n_{\mathrm{sub}} = \min\left\{ \max\left\{ \frac{\|\Delta\epsilon_{kl}\|}{\underbrace{1 \times 10^{-5}}_{\text{strain}}}, 1.0 \right\}, \max\left\{ \frac{|\Delta S^e|}{\underbrace{5 \times 10^{-4}}_{\text{saturation}}}, 1.0 \right\}, 1500 \right\}, \tag{6.10}$$

where a minimum of 1500 subincrements was determined empirically to achieve good accuracy. The subincrements of time Δt_{sub}, strain $\Delta\epsilon_{kl,\mathrm{sub}}$ and the effective degree of saturation $\Delta S^e_{\mathrm{sub}}$ are computed as:

$$\Delta\epsilon_{kl,\mathrm{sub}} = \frac{\Delta\epsilon_{kl}}{n_{\mathrm{sub}}} \quad , \quad \Delta S^e_{\mathrm{sub}} = \frac{\Delta S^e}{n_{\mathrm{sub}}} \quad \text{and} \quad \Delta t_{\mathrm{sub}} = \frac{\Delta t}{n_{\mathrm{sub}}} \tag{6.11}$$

Consequently, the subincrements of the strain and effective degree of saturation are constant. Due to the non-linearity of the hydraulic model, the subincrement of suction it, however, not constant. The significance of the hydraulic variable used within the subincrementation of the mechanical model is discussed in detail in Section 6.6.3.3.

6.1.1.2. The Jacobians

Accurate Jacobians are required for rapid convergence of the Newton-Raphson iteration (see Section 6.5.1) during the solution of the global governing equations. The most accurate Jacobian is obtained analytically, but it can be difficult and tedious to find the analytical expressions and to implement them correctly. When forming the analytical derivation, it is generally necessary to use the chain rule, however, some inner derivations are omitted to simplify the analytical expressions. A different method is obtaining the Jacobian numerically, wherein a numerical perturbation is applied to the independent variables. In hydro-mechanically coupled analysis, the strain rate and rate of effective degree of saturation must be perturbed separately from each other, while holding the other variable fixed. Regardless of its determination method, the Jacobians can either be taken as the tangent at the end of the increment or smoothed over all subincrements, which based on the experience gained in this work, results in better convergence.

Numerical differentiation

For a good estimation, the perturbation should be carried out at each subincrement of the integration and averaged for the whole increment. A computationally less costly approach is to only take the Jacobian from the last subincrement in a tangent approach, however, at reduced accuracy. In coupled analysis, the magnitude of the perturbation should be a tiny portion of the independent variable. Since the magnitude of the strain rate and the rate of the effective degree of saturation differ greatly, two perturbations ϑ_ϵ and ϑ_{S^e} are introduced. For the strain, the scalar of the perturbation ϑ_ϵ is computed according to Miehe (1996) and Fellin and Ostermann (2002) and for the effective degree of saturation the scaling approach from Collin (2002) and Dieudonne (2016) is adopted:

$$\vartheta_\epsilon = \max\left(\|\dot{\epsilon}_{kl}\|, 1.0\right) \vartheta_{\text{ctrl}} \quad \text{and} \quad \vartheta_{S^e} = \vartheta_\epsilon \, S^e, \tag{6.12}$$

wherein ϑ_{ctrl} is a control parameter, see Table 6.1. A value of $\vartheta_{\text{ctrl}} = 1 \times 10^{-6}$ is applied as default. For perturbation of $\Delta\epsilon_{kl}$, a perturbation tensor ϑ_{kl} is defined:

$$\vartheta_{kl} = \begin{cases} \vartheta_\epsilon & \text{for} \quad k = l, \\ 0.5\,\vartheta_\epsilon & \text{for} \quad k \neq l, \end{cases} \tag{6.13}$$

which considers the different mapping of the strain and stress tensors into Voigt notation. Shear strains are stored with a factor 2, whereas shear stresses are not and thus, the factor must be considered in perturbation of the shear strain increments. In three dimensions, the Voigt notations read $\sigma_{ij} = (\sigma_{11}, \sigma_{22}, \sigma_{33}, \sigma_{23}, \sigma_{13}, \sigma_{12})^{\mathrm{T}}$ and $\epsilon_{ij} = (\epsilon_{11}, \epsilon_{22}, \epsilon_{33}, 2\epsilon_{23}, 2\epsilon_{13}, 2\epsilon_{12})^{\mathrm{T}}$. Independent of the magnitude of perturbation and the moment of evaluation in the material model, different accuracies can be applied. According to Fellin and Ostermann (2002) and Dieudonne (2016), a central finite difference scheme with the accuracy of $O(h^2)$ with two perturbations $+\vartheta_\sqcup, -\vartheta_\sqcup$ yields satisfactory results without being overly computationally costly. In `numgeo`, a single forward step $O(h)$ and finite difference step are implemented for the Jacobian of stress with respect to both, strain and effective degree of saturation. For the finite difference scheme the numerical differentiation is computed according to:

$$\frac{\partial \sigma_{ij}}{\partial \epsilon_{kl}} \approx \frac{\sigma_{ij}(\Delta\epsilon_{kl} + \vartheta_{kl}, \Delta S^e) - \sigma_{ij}(\Delta\epsilon_{kl} - \vartheta_{kl}, \Delta S^e)}{2\vartheta_\epsilon}, \tag{6.14}$$

$$\frac{\partial \sigma_{ij}}{\partial S^e} \approx \frac{\sigma_{ij}(\Delta\epsilon_{kl}, S^e + \vartheta_{S^e}) - \sigma_{ij}(\Delta\epsilon_{kl}, \Delta S^e - \vartheta_{S^e})}{2\vartheta_{S^e}}. \tag{6.15}$$

In standard implementations, the perturbation is applied around the current increments of strain and effective degree of saturation. In the case of a deeply coupled hydro-mechanical constitutive model, where strain and saturation influence each other directly and enter into the evolution equations, the perturbation of one quantity while keeping the other quantity constant, can lead to inconsistent internal states. This is particularly problematic for the perturbation of strain, when the current state lies on the moving preconsolidation surface. Perturbations may then deviate from the physically admissible direction and result in a degraded or misleading Jacobian. To improve robustness, the numerical derivative may instead be evaluated from a reference configuration of the zero-state of strain, which is applied in this work.

Analytical Jacobian

Computation of the analytical Jacobian is challenging due to the deep hydro-mechanical coupling of the evolution equations. In this work, the implementation of the analytical Jacobian is limited to its most fundamental form, which is equivalent to the barotropic elastic stiffness. For readability, the analytical Jacobian is derived for the one-dimensional formulation and subsequently rewritten for the full, tensorial formulation at the end. To be consistent with the integration scheme of the mechanical constitutive model, explicit time integration is applied for derivation of the analytical Jacobian. Based on the evolution equation for net stress (see Equation (4.8)), the unknown stress σ is integrated with consideration of the known stress $\sigma^{(t)}$ at the beginning of the increment and the known barotropic elastic stiffness $E^{(t)} = \sigma^{(t)}/\kappa$ as:

$$\sigma = \sigma^{(t)} + \frac{\sigma^{(t)}}{\kappa}\left(\Delta\epsilon^h - Y\mathrm{OCR}^{-m}|\Delta\epsilon^h|\right) = \sigma^{(t)} + E^{(t)}\left(\Delta\epsilon^h - Y\mathrm{OCR}^{-m}|\Delta\epsilon^h|\right). \tag{6.16}$$

The Jacobian follows as:

$$\frac{\partial\sigma}{\partial\epsilon} = \frac{\partial}{\partial\epsilon}\left(E^{(t)}\left(\Delta\epsilon^h - Y\mathrm{OCR}^{-m}|\Delta\epsilon^h|\right)\right) \tag{6.17}$$

$$= \underbrace{\frac{\partial E^{(t)}}{\partial\epsilon}\left(\Delta\epsilon^h - Y\mathrm{OCR}^{-m}|\Delta\epsilon^h|\right)}_{(1)\to 0} + \underbrace{E^{(t)}\frac{\partial}{\partial\epsilon}\left(\Delta\epsilon^h - Y\mathrm{OCR}^{-m}|\Delta\epsilon^h|\right)}_{(2)}. \tag{6.18}$$

Since the known stiffness is independent of the strain increment, the first part of Equation (6.18) vanishes. The second part is rewritten as:

$$\frac{\partial\sigma}{\partial\epsilon}^{(2)} = \underbrace{E^{(t)}\frac{\partial}{\partial\epsilon}\left(\Delta\epsilon^h\right)}_{(2a)} - \underbrace{E^{(t)}\frac{\partial}{\partial\epsilon}\left(Y\mathrm{OCR}^{-m}|\Delta\epsilon^h|\right)}_{(2b)}. \tag{6.19}$$

The barotropic elastic stiffness as the simplest approximation is recovered by neglecting term $(2b)$ and the contribution of the saturation-driven strain rate in term $(2a)$:

$$\frac{\partial\sigma}{\partial\epsilon}^{(2a)} = E^{(t)}\frac{\partial}{\partial\epsilon}\left(\Delta\epsilon - \Delta\epsilon^w\right) \approx E^{(t)}\frac{\partial}{\partial\epsilon}\left(\Delta\epsilon\right) = E^{(t)}. \tag{6.20}$$

As the subtractive components in Equation (6.19) are not taken into account, application of the barotropic elastic stiffness overestimates the precise analytical value. On the one hand, this may necessitate reduced time increments, consequently increasing the computational cost. The accuracy of the solution is not affected. On the other hand, the calculation of a more sophisticated analytical Jacobian results in elevated computational cost as well due to carrying

out higher order mathematical operations. For the full, tensorial formulation the Jacobian from Equation (6.20) reads:

$$\frac{\partial \sigma_{ij}}{\partial \epsilon_{kl}} = E^{(t)}_{ijmn} \frac{\partial \epsilon_{mn}}{\partial \epsilon_{kl}} = E^{(t)}_{ijmn} J_{mnkl} = E^{(t)}_{ijkl}. \tag{6.21}$$

wherein the barotropic elastic stiffness $E^{(t)}_{ijkl}$ is computed following Equations (5.2)–(5.7).

6.1.1.3. Input: Parameters and integration controls

The parameters of the mechanical model were already presented and discussed in Chapter 5. The input in `numgeo` takes the following form:

```
*Material, name = <name>, phases = 3
*Mechanical = hypoplasticity-swelling
e_N, h_s in kPa, n, κ_ref, S(κ_ref), κ_w, c, b, m_O1, m_O2, S_ref, φ in °,
S(φ), β, x_ecm in %
```

Note that m_{O1}, m_{O2} are not strictly material parameters and are set to $m_{O1} = 100$ and $m_{O2} = 8$ as default in all simulations. However, the implementation offers the flexibility to adjust them. Furthermore, if the reference state is consistently used for parameter calibration, the reference degree of saturation applies for κ_{ref} and $\varphi_{(\mathrm{ref})}$, hence $S_{\mathrm{ref}} = S(\kappa_{\mathrm{ref}}) = S(\varphi)$.

Several optional integration controls are implemented for the mechanical constitutive model, which were presented in the preceding sections. Table 6.1 gives an overview of the keywords and options for the available controls.

Table 6.1.: Integration controls: keywords and options implemented for the mechanical model.

Keyword	Explanation and options (def = default option)
*integration	Choice of integration scheme (Section 6.1.1.1): 0: Forward Euler (def), 1: Modified Euler
*jacobi	Method for evaluation of the Jacobians (Section 6.1.1.2): 1: Tangent at the end of the increment, 2: Smoothed over subincrements (def)
*num_diff	Method for determination of the Jacobians (Section 6.1.1.2): 1: Numerical differentiation with forward step $O(h)$, 2: Numerical differentiation with finite difference step $O(h^2)$ (def), 3: Barotropic elastic stiffness (simplified analytical Jacobian, only for $\partial\sigma_{ij}/\partial\epsilon_{ij}$)
*Pert_eps	Value of the perturbation $\vartheta_{\mathrm{ctrl}}$ in Equation (6.12): <value> (1×10^{-6} def)
*coupled	Consideration of $\partial\sigma_{ij}/\partial s$ in the global Newton–Raphson iteration: 0: no (uncoupled), 1: yes (coupled, def)
*nd_mm	Perturbation of strain in $\partial\sigma_{ij}/\partial\epsilon_{ij}$: 0: $\Delta\epsilon_{ij} = 0$ (def), 1: $\Delta\epsilon_{ij}$
*nd_hm	Perturbation of strain in $\partial\sigma_{ij}/\partial s$: 0: $\Delta\epsilon_{ij} = 0$ (def), 1: $\Delta\epsilon_{ij}$

The input in `numgeo` takes the following form:

```
*Optional mechanical parameter
*<keyword>, <value>
```

6.1.2. Hydraulic model: Saturation-suction relation

In the hydraulic model the (unknown) degree of saturation S^w at time $t + \Delta t$ is computed by the (known) degree of saturation $S^{w(t)}$, the increment of suction Δs and the void ratio $e^{(t)}$ and other state variables $sv^{(t)}$ at time t:

$$S^w = S^w \left(S^{w(t)}, \Delta s, e^{(t)}, sv^{(t)} \right). \tag{6.22}$$

The general rate form for $\dot{S}^w$ reveals two dependencies of S^w:

$$\dot{S}^w = \frac{\partial S^w}{\partial s} \dot{s} + \frac{\partial S^w}{\partial e} (1 + e) \dot{\varepsilon}_v, \tag{6.23}$$

which are also referred to as the Jacobians of the degree of saturation with respect to the solid strain $J_{ij}^{S^w,\varepsilon}$ and the suction $J^{S^w,s}$:

$$J_{ij}^{S^w,\varepsilon} = \frac{\partial S^w}{\partial \varepsilon_{jk}} \quad \text{and} \quad J^{S^w,s} = \frac{\partial S^w}{\partial s}. \tag{6.24}$$

To account for the residual degree of saturation S^{wr}, the effective degree of saturation S^e and its time derivative are evaluated and passed on by the hydraulic model. S^e is calculated via:

$$S^e = \frac{S^w - S^{wr}}{1 - S^{wr}},$$

and the Jacobian of the effective degree of saturation read as:

$$J_{ij}^{S^e,\varepsilon} = \frac{\partial S^e}{\partial S^w} \frac{\partial S^w}{\partial \varepsilon_{jk}} = \frac{1}{1 - S^{wr}} \frac{\partial S^w}{\partial \varepsilon_{jk}}, \tag{6.25}$$

$$J^{S^e,s} = \frac{\partial S^e}{\partial S^w} \frac{\partial S^w}{\partial s} = \frac{1}{1 - S^{wr}} \frac{\partial S^w}{\partial s}. \tag{6.26}$$

In this work, no dependency of the SWRC on deformation is considered, hence $J_{ij}^{S^e,\varepsilon} = 0$. The Jacobians can be evaluated in various ways, which is illustrated in Figure 6.1. For the hydraulic models employed here, the derivative with respect to suction can, in general, be obtained analytically (1). The chord slope approach (2), using the secant of the SWRC, approximates the Jacobian, if the analytical derivative of the SWRC is not available. Evaluation of the analytical derivative solely at the end of the time increment may lead to numerical instabilities due to the pronounced nonlinearity of the SWRC. This effect is particularly significant near full saturation, where small changes in suction induce large variations in saturation, and the permeability is already substantially increased compared to more unsaturated states. Alternatively, a time-step centred Jacobian (3) can be applied, however, owing to the nonlinearity of the SWRC, this method does not necessarily yield a representative average over the increment and may under- or overestimate the true Jacobian. Consequently, the smoothed analytical Jacobian (4), provides a more accurate approximation that accounts for the underlying nonlinearity. A sensitivity

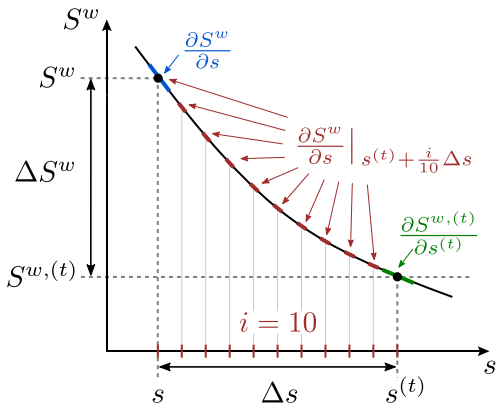

1. Analytical derivative: $J^{S^w,s} = \frac{\partial S^w}{\partial s}$
2. Chord-slope (secant): $J^{S^w,s} = \frac{\Delta S^w}{\Delta s}$
3. Time-step centred, analytical: $J^{S^w,s} = \frac{1}{2}\left(\frac{\partial S^{w,(t)}}{\partial s^{(t)}} + \frac{\partial S^w}{\partial s}\right)$
4. Smoothed analytical (default): $J^{S^w,s} = \frac{1}{10}\sum_{i=0}^{10} \frac{\partial S^w}{\partial s}\Big|_{s^{(t)}+\frac{i}{10}\Delta s}$

Figure 6.1.: Different approaches for evaluation of the Jacobian of the SWRC in `numgeo`.

analysis has shown that $i = 10$ subincrements are sufficient for this purpose and the smoothed analytical Jacobian is used as default in this work.

In this work, mainly the models after Van Genuchten and Fredlund & Xing are applied. The functions were already introduced in Section 2.2.1.1. Here, the analytical derivatives of both models are additionally presented in terms of degree of saturation S^w.

1. **Van Genuchten model**
   The model of van Genuchten (1980) is implemented as:

$$S^w = S^{wr} + (1 - S^{wr}) \left(\frac{1}{1 + (\alpha \frac{s}{\gamma^w})^n} \right)^{1-1/n}, \tag{6.27}$$

   wherein α, n and S^{wr} are material parameters and γ^w is the unit weight of water. Further $m = 1 - 1/n$ applies. The Jacobian of Equation (6.27) with respect to the suction reads as:

$$\frac{\partial S^w}{\partial s} = -(1 - S^{wr}) \frac{\alpha m n}{\gamma^w} \left(\alpha \frac{s}{\gamma^w} \right)^{-1+n} \left(\frac{1}{1 + \left(\alpha \frac{s}{\gamma^w} \right)^n} \right)^{1+m}. \tag{6.28}$$

2. **Fredlund & Xing**
   The model of Fredlund et al. (1994, 2012) is implemented as:

$$S^w = \left(1 - \frac{\ln\left(1 + \frac{s}{h_r}\right)}{\ln\left(1 + \frac{1\times10^6}{h_r}\right)} \right) \frac{1}{\ln\left(e + \left(\frac{s}{a_f}\right)^{n_f}\right)^{m_f}}, \tag{6.29}$$

   wherein h_r (in kPa), a_f (in kPa), n_f and m_f are material parameters. The contributions of Equation 6.29 to the Jacobian read:

$$\begin{aligned} \frac{\partial S}{\partial s} = &-m_f n_f \left(\frac{s}{a_f}\right)^{-1+n_f} \left(1 - \frac{\ln\left(1 + \frac{s}{h_r}\right)}{\ln\left(1 + \frac{1\times10^6}{h_r}\right)} \right) \frac{\ln\left(e + \left(\frac{s}{a_f}\right)^{n_f}\right)^{-1-m_f}}{a_f \left(e + \left(\frac{s}{a_f}\right)^{n_f}\right)} \\ &- \frac{\ln\left(e + \left(\frac{s}{a_f}\right)^{n_f}\right)^{m_f}}{h_r \left(1 + \frac{s}{h_r}\right) \ln\left(1 + \frac{1\times10^6}{h_r}\right)}. \end{aligned} \tag{6.30}$$

6.1.3. Relative permeability model

The hydraulic conductivity tensor k_{ij}^{wf} is evaluated in the integration of the finite element. Considering the relative permeability for both, unsaturated soils $k^{r,wf}$ and due to swelling $k^{r,ws}$, the hydraulic conductivity is defined as:

$$k_{ij}^{wf} = \frac{K_{ij,\mathrm{ref}}^{s}\,\gamma^{wf}}{\mu^{wf}}\,k^{r,wf}\,k^{r,ws}. \tag{6.31}$$

For the unsaturated relative permeability coefficient, which ranges between 0 and 1, a lower limit $k_{\min}^{w}$ is considered in `numgeo` to avoid quasi-impermeability and resulting convergence issues and numerical instabilities:

$$k^{r,wf} = (1 - k_{\min}^{w})\,k^{r,wf^*} + k_{\min}^{w}, \tag{6.32}$$

wherein k^{r,wf^*} refers to the model equations given below. It can be considered as an additional parameter. For the relative permeability of the unsaturated state $k^{r,wf} = k^{r,wf}(S^e)$, the partial derivative with respect to the effective degree of saturation $J^{k^{r,wf},s}$ reads:

$$J^{k^{r,wf},s} = \frac{\partial k^{wf}}{\partial S^e} = \frac{\partial k^{wf}}{\partial S^e}\frac{\partial S^e}{\partial s}. \tag{6.33}$$

Note that in the two-phase $\mathbf{u}p-$formulation with passive pore air, the relative permeability of the pore air phase $k^{r,af}$ is not required. Since in this work the relative permeability is applied consistently with the hydraulic model, the formulations by van Genuchten and by Fredlund and Xing are of particular relevance. Analytical expressions for the Jacobian may not be possible for all hydraulic models. In those cases, the Jacobian can be found by numerical differentiation. A sensitivity analysis using the Van Genuchten model showed, however, that consideration of the Jacobian $J^{k^{r,wf},s}$ at the element level has no influence on numerical accuracy or computational performance. This simplification is consistent with the standard linearised formulation used in Abaqus, where the derivative of the relative permeability with respect to saturation is also omitted in the Jacobian (Dassault Systèmes, 2024). The mathematical models were already introduced in Section 2.2.1.1. For completeness, the analytical Jacobian for the van Genuchten model is provided here.

1. **Van Genuchten-Mualem model**
   Mualem (1976) evaluated the SWRC of van Genuchten (1980) on the basis of Equation (2.21) and derived the following closed-form analytical equation for pore water and pore air:

   $$k^{r,wf^*} = \sqrt{S^e}\left(1 - \left(1 - (S^e)^{\frac{n}{n-1}}\right)^{\frac{n-1}{n}}\right)^2. \tag{6.34}$$

   The Jacobian of Equation (6.32) with consideration of Equation (6.34) reads as:

   $$\frac{\partial k^{r,wf}}{\partial S^e} = (1 - k_{\min}^{w})\left(\frac{\left(1 - \zeta^{\frac{1}{m}}\right)^2}{2\sqrt{S^e}} + 2\big(S^e\big)^{m-\frac{1}{2}}\zeta^{\frac{1}{m}-1}\Big(1 - \zeta^{\frac{1}{m}}\Big)\right), \tag{6.35}$$

   wherein $\zeta = 1 - (S^e)^m$. Note that division by zero for completely dry ($S^e = 0$) and fully saturated states ($S^e = 1$) is prevented in the implementation.

2. **Fredlund & Xing**
   The relative permeability is derived as an integral solution of the SWRC, see Figure 2.8 in Section 2.2.1.1:

$$k^{r,wf*}(S^w, s) = \frac{\int_{\ln(s)}^{\ln(10^6)} \frac{S^w(e^y)-S^w(s)}{e^y} S'(e^y)\,\mathrm{d}y}{\int_{\ln(s_i)}^{\ln(10^6)} \frac{S^w(e^y)-S^w(s_i)}{e^y} S'(e^y)\,\mathrm{d}y}. \tag{6.36}$$

   The lower limit s_i is a material parameter in addition to the parameters of the SWRC itself. The Jacobian cannot be derived analytically.

The relative permeability associated with swelling is a function of the aggregate porosity n^A, hence $k^{r,ws} = k^{r,ws}(n^A)$, and is therefore indirectly depending on the effective degree of saturation as well. The implicit dependence of the swelling-induced relative permeability on saturation renders the analytical expression for the derivative difficult, if not impossible. In line with the treatment of the derivative of the relative permeability for unsaturated soils, the corresponding contribution is not taken into account. For the sake of completeness, the relative permeability due to swelling, see Equation (3.68), is defined as:

$$k^{r,ws} = \frac{K^w(S^e = 1, \varphi^{ws} > 0)}{K^w(S^e = 1, \varphi^{sw} = 0)} = \frac{(n^A)^3}{(1-n^A)^2} \frac{(1-n_{\mathrm{ref}})^2}{n_{\mathrm{ref}}^3}, \tag{6.37}$$

wherein n_{ref} is the reference porosity corresponding to the reference permeability $K^s_{ij,\mathrm{ref}}$ from Equation (6.31).

6.1.4. Mass transfer model

The mass transfer model returns the (unknown) density production ($\hat{\rho}^w/\bar{\rho}^w$) at the time at the end of the increment $t + \Delta t$ according to Equation (3.65), which is rewritten here for the sake of clarity:

$$\frac{\hat{\rho}^w}{\rho^w} = \frac{\mathrm{d}\varphi^w}{\mathrm{d}t}\phi + \frac{\mathrm{d}\phi}{\mathrm{d}t}\varphi^w, \tag{6.38}$$

wherein the rate of the volume fraction of water $\mathrm{d}\varphi^w/\mathrm{d}t = \mathrm{d}S^w/\mathrm{d}t\; n + \mathrm{d}n/\mathrm{d}t\; S^w$ and its quantity $\varphi^w = n\, S^w$ at the end of the increment are known by the hydraulic and mechanical model. The rate of the swelling water ratio $\mathrm{d}\phi/\mathrm{d}t$ and its (unknown) quantity ϕ at the end of the increment are computed within the mass transfer model as:

$$\frac{\mathrm{d}\phi}{\mathrm{d}t} = c_\phi\,(\phi^{\max} - \phi) \left\langle \frac{\mathrm{d}S^w}{\mathrm{d}t} \right\rangle, \tag{6.39}$$

and

$$\phi = \phi^{(t)} + \Delta\phi \quad \text{with} \quad \Delta\phi = \frac{\mathrm{d}\phi}{\mathrm{d}t}\,\Delta t. \tag{6.40}$$

In this work, the mass transfer is considered explicitly at time t, however, the general dependency is given here. It considers the contributions of the degree of saturation S^w, which depends on changes in void ratio e and suction s in the general formulation, see Equation (6.23). These dependencies apply for the Jacobians of the mass transfer itself as well. They read as:

$$J^{\hat{\rho}^w/\bar{\rho}^w,\epsilon}_{ij} = \frac{\partial \hat{\rho}^w/\bar{\rho}^w}{\partial \epsilon_{jk}} = \frac{\partial \hat{\rho}^w/\bar{\rho}^w}{\partial S^w} \frac{\partial S^w}{\partial \varepsilon_{jk}}, \tag{6.41}$$

$$J^{\hat{\rho}^w/\bar{\rho}^w,s} = \frac{\partial \hat{\rho}^w/\bar{\rho}^w}{\partial s} = \frac{\partial \hat{\rho}^w/\bar{\rho}^w}{\partial S^w} \frac{\partial S^w}{\partial s}. \tag{6.42}$$

6.1.5. Constitutive stress approach

The mechanical material model is formulated in net stress $\sigma_{ij} = \sigma_{ij}^{tot} - p^a 1_{ij}$ for partial saturation ($S^e < 1$) and in effective stresses $\sigma'_{ij} = \sigma_{ij}^{tot} - p^w 1_{ij}$ for full saturation ($S^e = 1$, see Equation (2.32)). To switch the constitutive stress from net to effective stress in the transition from partial to full saturation, the Bishop parameter χ is formulated as:

$$\chi = \begin{cases} 1 & \text{for } S^e = 1, \\ 0 & \text{else.} \end{cases} \tag{6.43}$$

Note that the partial derivative with respect to the effective degree of saturation is zero in all cases, hence $\partial\chi/\partial S^e = 0$. The input of the switch takes the following form:

```
*Bishop effective stress = Crude-Switch
```

6.1.6. Pore fluid flow

The generalized Darcy's law was derived from the conservation of linear momentum for the free water, see Equation (3.61), as:

$$w_i^{wf} = \frac{k^{wf}}{\bar{\mu}^{wf}} K_{ij}^{s,\mathrm{ref}} \left(-\bar{p}_{,j}^{wf} + \bar{\rho}^{wf} \left(b_j - a_j^s \right) \right), \tag{6.44}$$

wherein $K_{ij}^{s,\mathrm{ref}}$ is the (intrinsic) permeability tensor of the solid in the unswollen state, μ^{wf} is the dynamic viscosity of the free water and $k^{wf} = k^{r,wf}\, k^{r,ws}$ the collective relative permeability due to swelling and partial saturation. Equation (6.44) is a constitutive relation linking the velocity of the free water w_i^{wf} to the driving force for flow, composed of the pore pressure gradient and gravity. This driving force corresponds to the seepage force acting on the solid matrix.

6.1.7. Pore fluid compressibility

The relation between the intrinsic density $\bar{\rho}^{wf}$ of the free water phase and the mean pressure $\bar{p}^{wf}$ (Schrefler et al., 1990; Borja, 2006) was introduced already in Section 3.1.2.1 as:

$$\frac{\mathrm{d}^{wf}\bar{p}^{wf}}{\mathrm{d}t} = \frac{\bar{K}^{wf}}{\bar{\rho}^{wf}} \frac{\mathrm{d}^{wf}\bar{\rho}^{wf}}{\mathrm{d}t}, \tag{6.45}$$

wherein $\bar{K}^{wf}$ is the bulk modulus of the free pore water phase. It also acts as a constitutive relation.

6.2. Finite element library based on the extended theory of porous media

Within this work, different types of two-dimensional, quadrilateral $\mathbf{u}p-$elements with consideration of swelling have been implemented, which are summarized in Table 6.2 and displayed in Figure 6.2. They are referred to as `up-sw`-elements in the following. Each implemented element type exists as a plane strain and axi-symmetric element. The number of nodes, number of degrees of freedom (DOF) and the number and location of the integration points are listed as well.

Therein, the absolute value of the respective coordinates (ζ, η) referring to the local system of coordinates is given, see Figure 6.2. Details regarding the numerical integration of the elements are beyond the scope of this work and are given in the `numgeo` documentation (Machaček, 2026). The library includes Taylor-Hood elements and stabilised equal order elements. For coupled, hence mixed, elements, the *inf-sup* or Ladyshenskaya-Babuška-Brezzi (LBB) (Babuška, 1973; Brezzi and Fortin, 1991) condition must be fulfilled, to avoid non-physical oscillations of the pore fluid pressures and volumetric locking behaviour (Zienkiewicz et al., 2005; Preisig and Prévost, 2011; Boffi et al., 2013). These occur especially in low permeability media, as is the case for expansive soils, near the undrained limit. To overcome this, so-called Taylor-Hood elements are usually used, in which pore fluids are discretised with shape functions that are one order lower than the solid displacements. Mostly quadratic shape functions are chosen for the solid displacement and linear functions for the pore fluids. Alternatively, elements of the same order, so-called equal order elements, can be used, which are enhanced with stabilization techniques (Zienkiewicz et al., 2005; White and Borja, 2008). Various methods have been presented in the past, the most prominent of which are the Galerkin/least-squares (GLS) method and the Fluid-Pressure-Laplacian (FPL) method, wherein generally compressibility of the fluid phase is added to the fluid mass conservation equation. In the framework of this thesis, a modified version of the FPL-stabilisation, first presented by Brezzi and Pitkäranta (1984) and further developed by Truty and Zimmermann (2006) is applied. Linear equal order elements with reduced integration require an additional stabilisation with an artificial element stiffness to prevent so-called hourglass modes, wherein certain characteristic deformation patterns develop with no stresses resisting the deformation (zero-energy modes). In `numgeo`, the method of Flanagan and Belytschko (1981) is applied to provide hourglass stiffness.

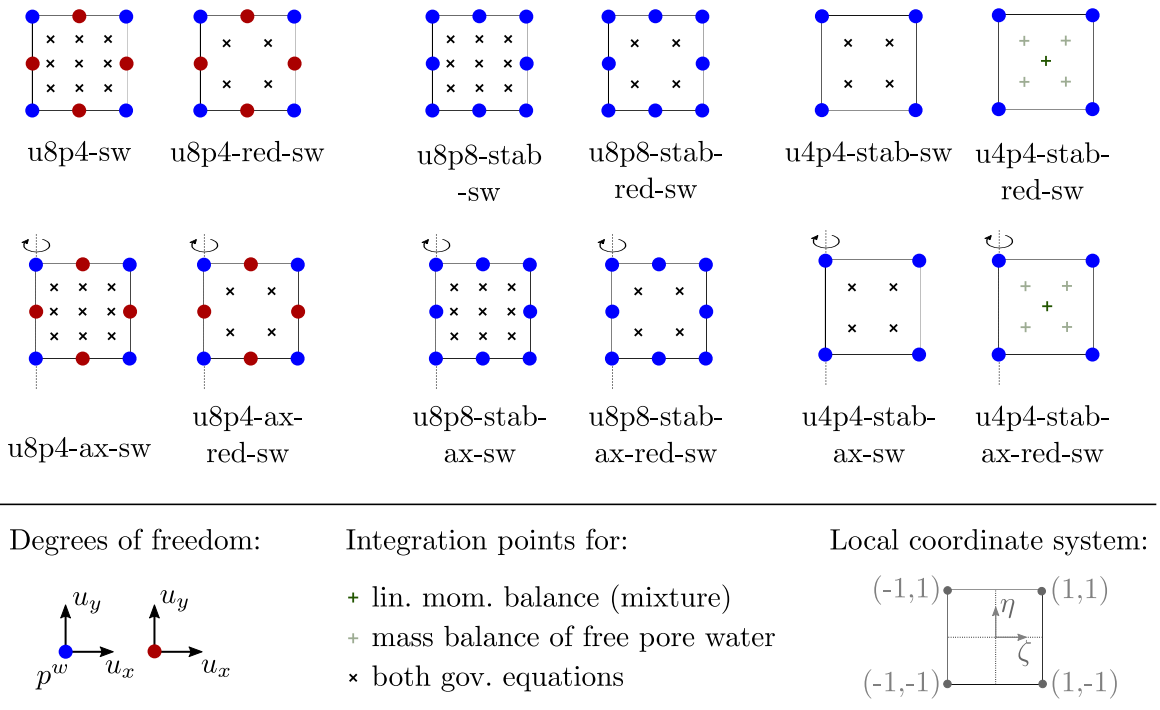

Figure 6.2.: Library of `up-sw`-elements implemented in `numgeo`.

Table 6.2.: Implemented elements with extended TPM and their characteristics.

Element Label	Interpolation	Nodes	DOF	Integration Points	
				No.	Abs. coordinates (ζ, η)
u8p4-(ax-)sw[1]	quadratic	8	20	9	$\frac{\sqrt{15}}{5} \approx 0.7746$
u8p4-(ax-)red-sw[1]	quadratic	8	20	4	$\frac{1}{\sqrt{3}} \approx 0.5774$
u8p8-stab-(ax-)sw [2]	quadratic	8	24	9	$\frac{\sqrt{15}}{5} \approx 0.7746$
u8p8-stab-(ax-)red-sw [2]	quadratic	8	24	4	$\frac{1}{\sqrt{3}} \approx 0.5774$
u4p4-stab-(ax-)sw[2]	linear	4	12	4	$\frac{1}{\sqrt{3}} \approx 0.5774$
u4p4-stab-(ax-)red-sw[2,3]	linear	4	12	1 / 4*	0.0 — $\frac{1}{\sqrt{3}} \approx 0.5774$

[1] Taylor-Hood elements: biquadratic displacement, bilinear pore pressure
[2] Stabilised equal order elements, see Section 6.5.4
[3] Reduced equal order elements require additional stiffness to prevent hourglass modes, currently only available for linear elements, see Section 6.5.5.
* Reduced integration applies only to the conservation of linear momentum of the mixture, whereas full integration is applied for the conservation of mass for free pore water.

The element type is declared within the mesh definition in numgeo. The parameters $\phi^{\max}$ and c_ϕ of the mass transfer and the porosity n_{ref} for the swelling-induced relative permeability must be defined within the material declaration of the corresponding part of the mesh. If no parameters are given, the elements of the `up-sw`-library simplify to elements of the standard `up`-library of `numgeo`. Inside the extended elements, the swelling water content is initialized as $\varphi_0^{ws} = 0$ as no swelling or attachment of water prior to the initial state is considered in this work. The input in `numgeo` takes the following form:

```
*Element, Type = <element type of up-sw>
...
*Swelling
φ^max, c_φ, n_ref
```

6.3. Variational and weak form of governing equations

The strong form of the governing equations, which were given in Box 3.1, are multiplied with the selected test functions δu_i^s and δp^{wf} and integrated over the current volume Ω. Required theorems are Green's first integral theorem (integration by parts):

$$\operatorname{div}(a\sqcup) = a \operatorname{div}(\sqcup) + \operatorname{grad}(a)\,\sqcup \qquad \text{or} \qquad (a\sqcup)_{,i} = a\,\sqcup_{,i} + a_{,i}\sqcup, \tag{6.46}$$

wherein a is an arbitrary multiplier, and the Gaussian integral theorem to transform an integral over Ω into an integral on surface Γ with its normal vector n_i:

$$\int_\Omega \sqcup_{,i}\, \mathrm{d}\Omega = \int_\Gamma \sqcup\, n_i \; d\Gamma \,. \tag{6.47}$$

Conservation of linear momentum of the mixture

The strong form of the conservation of linear momentum without consideration of the relative acceleration between the pore water and the solid phase reads:

$$\sigma_{ij,j}^{tot} + \rho^{tot} b_i - \rho^{tot} \bar{a}_i^s + \hat{\rho}^w \frac{w_i^{wf}}{\varphi^{wf}} = 0. \tag{6.48}$$

The variational form is achieved by multiplication with the test function for displacement of the solid δu_i^s and integration over the volume Ω:

$$\underbrace{\int_\Omega \delta u_j^s \sigma_{ij,j}^{tot}\,\mathrm{d}\Omega}_{(1)} + \int_\Omega \delta u_i^s \rho^{tot} b_i\,\mathrm{d}\Omega - \int_\Omega \delta u_i^s \rho^{tot} a_i\,\mathrm{d}\Omega + \int_\Omega \hat{\rho}^w \frac{w_i^{wf}}{\varphi^{wf}}\,\mathrm{d}\Omega = 0. \tag{6.49}$$

Summand (1) of Equation (6.49) can be rewritten by applying integration by parts and further transformed with the Gaussian integral theorem for its first sub-summand:

$$\underbrace{\int_\Omega \delta u_j^s \sigma_{ij,j}^{tot}\,\mathrm{d}\Omega}_{(1)} = \int_\Omega \left(\delta u_j^s \sigma_{ij}^{tot}\right)_{,j}\,\mathrm{d}\Omega - \int_\Omega \delta u_{i,j}^s \sigma_{ij}^{tot} = \int_\Gamma \delta u_j^s \sigma_{ij}^{tot} n_j\,d\Gamma - \int_\Omega \delta u_{i,j}^s \sigma_{ij}^{tot}\,\mathrm{d}\Omega\,. \tag{6.50}$$

Considering $t_j^{tot} = \sigma_{ij}^{tot} n_j$, the effective stress principle (Equation (2.32)), the Biot constant equal to $\alpha = 1.0$ and the passive air phase ($p^{af} = 0$), the weak form of the conservation of linear momentum of the mixture reads:

$$\begin{aligned}\int_\Gamma \delta u_i^s t_i^{tot}\,d\Gamma - \int_\Omega \delta u_{i,j}^s \sigma_{ij}\,\mathrm{d}\Omega + \int_\Omega \delta u_{i,j}^s \chi p^w \delta_{ij}\,\mathrm{d}\Omega + \int_\Omega \delta u_i^s \rho^{tot} b_i\,\mathrm{d}\Omega \\ - \int_\Omega \delta u_i^s \rho^{tot} a_i^s\,\mathrm{d}\Omega + \int_\Omega \delta u_i^s \hat{\rho}^w \frac{w_i^{wf}}{\varphi^{wf}}\,\mathrm{d}\Omega = 0.\end{aligned} \tag{6.51}$$

Conservation of mass for the free pore water

The weak form of the conservation of mass for the free pore water is deduced similarly. The strong form reads:

$$\frac{\varphi^{wf}}{\bar{K}^{wf}} \frac{d\bar{p}^{wf}}{dt} + \frac{1}{\bar{K}^{wf}} \bar{p}_{,i}^{wf} w_i^{wf} + \dot{\varphi}^{wf} + w_{i,i}^{wf} + \varphi^{wf} \bar{v}_{i,i}^s - \frac{\hat{\rho}^w}{\bar{\rho}^w} = 0, \tag{6.52}$$

and multiplication with the test function for the (free) pore water pressure δp^{wf} and integration over Ω results in the variational form:

$$\begin{aligned}&\int_\Omega \delta p^{wf} \frac{\varphi^{wf}}{\bar{K}^{wf}} \frac{d\bar{p}^{wf}}{dt}\,\mathrm{d}\Omega + \int_\Omega \delta p^{wf} \frac{1}{\bar{K}^{wf}} \bar{p}_{,i}^{wf} w_i^{wf}\,\mathrm{d}\Omega + \int_\Omega \delta p^{wf} \dot{\varphi}^{wf}\,\mathrm{d}\Omega \\ &+ \underbrace{\int_\Omega \delta p^{wf} w_{i,i}^{wf}\,\mathrm{d}\Omega}_{(4)} + \int_\Omega \delta p^{wf} \varphi^{wf} \bar{v}_{i,i}^s\,\mathrm{d}\Omega - \int_\Omega \delta p^{wf} \frac{\hat{\rho}^w}{\bar{\rho}^w}\,\mathrm{d}\Omega = 0.\end{aligned} \tag{6.53}$$

Inserting the Darcy-Flux from Equation (3.61) with the assumption of $\bar{a}_i^{wf} = \bar{a}_i^s$ to summand (4) of Equation (6.53), separation of terms, integration by parts and the application of the Gaussian

integral theorem to each summand gives:

$$\begin{aligned}
\underbrace{\int_\Omega \delta p^{wf} w^{wf}_{i,i}\,\mathrm{d}\Omega}_{(4)} &= \int_\Omega \delta p^{wf} \frac{\partial}{\partial x_i}\left(\frac{k^{wf}}{\bar\mu^{wf}} K^s_{ij}\left(-\frac{\partial \bar p^{wf}}{\partial x_j} + \bar\rho^w\left(b_j - \bar a^s_j\right)\right)\right)\mathrm{d}\Omega \\
&= -\int_\Omega \frac{\partial}{\partial x_i}\left(\delta p^{wf}\frac{k^{wf}}{\bar\mu^{wf}} K^s_{ij}\frac{\partial p^{wf}}{\partial x_j}\right)\mathrm{d}\Omega + \int_\Omega \frac{\partial \delta p^{wf}}{\partial x_i}\frac{k^{wf}}{\bar\mu^{wf}} K^s_{ij}\frac{\partial \bar p^{wf}}{\partial x_j}\,\mathrm{d}\Omega \\
&\quad + \int_\Omega \frac{\partial \delta p^{wf}}{\partial x_i}\frac{k^{wf}}{\bar\mu^{wf}} K^s_{ij}\bar\rho^w b_j\,\mathrm{d}\Omega - \int_\Omega \frac{\partial \delta p^{wf}}{\partial x_i}\frac{k^{wf}}{\bar\mu^{wf}} K^s_{ij}\bar\rho^w \bar a^s_j\,\mathrm{d}\Omega \\
&= -\int_\Gamma n_i \delta p^{wf}\frac{k^{wf}}{\bar\mu^{wf}} K^s_{ij}\frac{\partial \bar p^{wf}}{\partial x_j}\,d\Gamma + \int_\Omega \frac{\partial \delta p^{wf}}{\partial x_i}\frac{k^{wf}}{\bar\mu^{wf}} K^s_{ij}\frac{\partial \bar p^{wf}}{\partial x_j}\,\mathrm{d}\Omega \\
&\quad + \int_\Gamma n_i \delta p^{wf}\frac{k^{wf}}{\bar\mu^{wf}} K^s_{ij}\bar\rho^w b_j\,d\Gamma - \int_\Omega \frac{\partial \delta p^{wf}}{\partial x_i}\frac{k^{wf}}{\bar\mu^{wf}} K^s_{ij}\bar\rho^w b_j\,\mathrm{d}\Omega \\
&\quad - \int_\Gamma n_i \delta p^{wf}\frac{k^{wf}}{\bar\mu^{wf}} K^s_{ij}\bar\rho^w \bar a^s_j\,d\Gamma + \int_\Omega \frac{\partial \delta p^{wf}}{\partial x_i}\frac{k^{wf}}{\bar\mu^{wf}} K^s_{ij}\bar\rho^w \bar a^s_j\,\mathrm{d}\Omega\,. \qquad (6.54)
\end{aligned}$$

Therein n_i is the normal vector. All surface integrals in Equation (6.54) can be grouped and simplified by taking the definition of flux $q^w = -n_i w^w_i$ (inflow is positive) into account:

$$\int_\Gamma n_i \delta p^{wf}\frac{k^{wf}}{\bar\mu^{wf}} K^s_{ij}\left(-\frac{\partial \bar p^w}{\partial x_j} + \bar\rho^w\left(b_j - \bar a^s_j\right)\right)d\Gamma = -\int_\Gamma n_i w^w_i \delta p^w\,d\Gamma = +\int_\Gamma q\delta p^w\,d\Gamma\,.$$

The volume integrals of Equation (6.54) remain and the final weak form of the conservation of mass for the free pore water reads:

$$\begin{aligned}
&\int_\Omega \delta p^{wf}\frac{\varphi^{wf}}{\bar K^{wf}}\frac{d\bar p^{wf}}{dt}\,\mathrm{d}\Omega + \int_\Omega \delta p^{wf}\frac{1}{\bar K^{wf}}\bar p^{wf}_{,i} w^{wf}_i\,\mathrm{d}\Omega + \int_\Omega \delta p^{wf}\dot\varphi^{wf}\,\mathrm{d}\Omega + \int_\Omega \frac{\partial \delta p^{wf}}{\partial x_i}\frac{k^{wf}}{\bar\mu^{wf}} K^s_{ij}\frac{\partial \bar p^{wf}}{\partial x_j}\,\mathrm{d}\Omega \\
&- \int_\Omega \frac{\partial \delta p^{wf}}{\partial x_i}\frac{k^{wf}}{\bar\mu^{wf}} K^s_{ij}\bar\rho^w b_j\,\mathrm{d}\Omega + \int_\Omega \frac{\partial \delta p^{wf}}{\partial x_i}\frac{k^{wf}}{\bar\mu^{wf}} K^s_{ij}\bar\rho^w a^s_j\,\mathrm{d}\Omega + \int_\Gamma q\delta p^w\,d\Gamma \\
&+ \int_\Omega \delta p^{wf}\varphi^{wf}\bar v^s_{i,i}\,\mathrm{d}\Omega - \int_\Omega \delta p^{wf}\frac{\hat\rho^w}{\bar\rho^w}\,\mathrm{d}\Omega = 0. \qquad (6.55)
\end{aligned}$$

6.4. Spatial discretisation

Spatial discretisation is applied for the numerical solution of the unknown nodal variables, the displacement of the solid u^s_i and the pore pressure of the free water p^{wf}. The test functions δu^s_i and δp^{wf} are approximated as follows:

$$u^s_i \approx N^{u^s}_I \bar u^s_{Ii} \qquad \text{and} \qquad \delta u^s_i \approx N^{u^s}_I \delta\bar u^s_{Ii}, \qquad (6.56)$$

$$p^{wf} \approx N^{p^w}_K \bar p^{wf}_K \qquad \text{and} \qquad \delta p^{wf} \approx N^{p^{wf}}_K \delta\bar p^{wf}_K, \qquad (6.57)$$

wherein $N^{u^s}_i$ denotes the shape function for the solid displacement and $N^{p^{wf}}_K$ for the pore water pressure. For readability reasons in the following $N^{u^s}_I = N^s_I$ and $N^{p^{wf}}_K = N^p_K$ apply. Different capital indices I, K are chosen as the interpolation order of the pore fluid pressures is commonly chosen differently from the solid displacement. The small caption index i denotes the dimension in space and only applies to the solid displacement. The governing equations are non-linear with respect to their primary unknowns and have to be solved iteratively. Therefore the residuum r is introduced, which has to be minimised during the Newton-Raphson iteration. With elimination of the arbitrary test functions, the residual functions of the governing equations are derived.

Conservation of linear momentum of the mixture

In addition to the spatial discretisation of the test functions and the primary variables (Equation (6.56)), further discretisation is needed:

$$\frac{\partial \delta u_i^s}{\partial x_j} = \delta u_{i,j}^s \approx \frac{\partial N_I^s}{\partial x_j} \delta \bar{u}_{Ij}^s \quad \text{and} \quad \bar{a}_i^s = \bar{a}_i \approx N_I^s \bar{a}_{Ii}^s. \tag{6.58}$$

The discretised residuum of Equation (6.51) with disregard of the test function $\delta \bar{u}_{Ii}^s$ reads:

$$\begin{aligned} r_{Ii}^s = &\int_\Gamma N_I^s t_i^{tot} \, d\Gamma - \int_\Omega \frac{\partial N_I^s}{\partial x_j} \sigma_{ij} \, d\Omega + \int_\Omega \frac{\partial N_I^s}{\partial x_j} \alpha \chi N_K^p \bar{p}_K^w \delta_{ij} \, d\Omega + \int_\Omega N_I^s \rho^{tot} b_i \, d\Omega \\ &- \int_\Omega N_I^s \rho^{tot} N_J^s \bar{a}_{Ji}^s \, d\Omega + \int_\Omega N_I^s \hat{\rho}^w \frac{w_i^{wf}}{\varphi^{wf}} \, d\Omega \,. \end{aligned} \tag{6.59}$$

Conservation of mass for the free pore water

For the discretisation of the conservation of mass for the free pore water, in addition to the spatial discretisation of the test functions and the primary variables (Equation (6.57)) further discretisation is needed:

$$\frac{\partial v_i^s}{\partial x_i} = v_{i,i}^s \approx \frac{\partial N_I^s}{\partial x_i} \bar{v}_{Ii}^s \quad \text{and} \quad \frac{\partial p^{wf}}{\partial x_j} \approx \frac{\partial N_K^p}{\partial x_j} \bar{p}_K. \tag{6.60}$$

The discretised residuum of Equation (6.55) with disregard of the test function $\delta \bar{p}_K^{wf}$ reads:

$$\begin{aligned} r_K^{p^w} = &\int_\Omega N_K^p \frac{\varphi^{wf}}{K^{wf}} N_L^p \dot{\bar{p}}_L^w \, d\Omega + \int_\Omega N_K^p \frac{1}{K^{wf}} \frac{\partial N_L^p}{\partial x_i} \bar{p}_L w_i^{wf} \, d\Omega + \int_\Omega N_K^p \dot{\varphi}^{wf} \, d\Omega \\ &+ \int_\Omega \frac{\partial N_K^p}{\partial x_i} \frac{k^{wf}}{\bar{\mu}^{wf}} K_{ij}^s \frac{\partial N_L^p}{\partial x_j} \bar{p}_L \, d\Omega - \int_\Omega \frac{\partial N_K^p}{\partial x_i} \left(\frac{k^{wf}}{\bar{\mu}^{wf}} K_{ij}^s \bar{\rho}^w b_j \right) d\Omega \\ &+ \int_\Omega \frac{\partial N_K^p}{\partial x_i} \left(\frac{k^{wf}}{\bar{\mu}^{wf}} K_{ij}^s \bar{\rho}^w N_I^s \bar{a}_{Ij}^s \right) d\Omega + \int_\Gamma q N_K^p \, d\Gamma \\ &+ \int_\Omega N_K^p \varphi^{wf} \frac{\partial N_I^s}{\partial x_i} \bar{v}_{Ii}^s \, d\Omega - \int_\Omega N_K^p \frac{\hat{\rho}^w}{\bar{\rho}^w} \, d\Omega \,. \end{aligned} \tag{6.61}$$

6.5. Solution procedure and time integration

The overall matrix differential equation of the system for the degrees of freedom (DOFs) is:

$$\mathbf{M} \ddot{\boldsymbol{d}} + \boldsymbol{C} \dot{\boldsymbol{d}} + \boldsymbol{K} \boldsymbol{d} + \boldsymbol{f} = \mathbf{0}, \tag{6.62}$$

wherein $\boldsymbol{M}$ is the mass matrix, $\boldsymbol{C}$ is the damping matrix, $\boldsymbol{K}$ is the static Jacobian, $\boldsymbol{f}$ is the load vector, $\boldsymbol{d}$ is the vector with all DOFs and $\dot{\boldsymbol{d}}$ and $\ddot{\boldsymbol{d}}$ are its first and second derivatives with respect to time. If dynamic behaviour is not considered, the first summand of Equation (6.62) vanishes and the equation for the DOFS $\boldsymbol{d} = [\boldsymbol{u}, p^w]^T$ with indices s and w reads:

$$\begin{bmatrix} \boldsymbol{C}^{s,s} & \boldsymbol{C}^{s,w} \\ \boldsymbol{C}^{w,s} & \boldsymbol{C}^{w,w} \end{bmatrix} \begin{bmatrix} \dot{\boldsymbol{u}} \\ \dot{p}^w \end{bmatrix} \begin{bmatrix} \boldsymbol{K}^{s,s} & \boldsymbol{K}^{s,w} \\ \boldsymbol{K}^{w,s} & \boldsymbol{K}^{w,w} \end{bmatrix} \begin{bmatrix} \boldsymbol{u} \\ p^w \end{bmatrix} + \begin{bmatrix} \boldsymbol{f}^s \\ \boldsymbol{f}^w \end{bmatrix} = \begin{bmatrix} \mathbf{0} \\ \mathbf{0} \end{bmatrix}. \tag{6.63}$$

Note that in textbooks the coupling matrix $\boldsymbol{C}^{w,s}$ of the pore water pressure field to the solid displacement is also referred to as $\boldsymbol{Q}$, the matrix $\boldsymbol{C}^{w,w}$ as the compressibility matrix for the

pore water as $\boldsymbol{S}$ and one part of $\boldsymbol{K}^{w,w}$ is referred to as the permeability matrix $\boldsymbol{H}$. In this work, all respective contributions regarding the pore water pressure are gathered in $\boldsymbol{K}^{w,w}$. The remaining contributions do not receive specific designations.

Based on the current solution $\boldsymbol{d}^t$, the solution of the DOFs $\boldsymbol{d}$ at time $t + \Delta t$ must be solved for incrementally as $\boldsymbol{d} = \boldsymbol{d}^t + \Delta\boldsymbol{d}$, wherein the total solution increment $\Delta\boldsymbol{d}$ itself is solved for iteratively. During the iteration process the estimated solution is improved with each iteration by adding a correction $\boldsymbol{c}^{(i+1)}$:

$$\Delta\boldsymbol{d}^{(i+1)} = \Delta\boldsymbol{d}^i + \boldsymbol{c}^{(i+1)} \quad \text{or} \quad \boldsymbol{c}^{(i+1)} = \Delta\boldsymbol{d}^{(i+1)} - \Delta\boldsymbol{d}^i, \tag{6.64}$$

wherein the state $\sqcup^i$ is assumed known and the unknown state $\sqcup^{i+1}$ will be computed at iteration $(i+1)$. Note that for a linear problem, a single „iteration“ gives the exact solution. The iterative correction $\boldsymbol{c}^{(i+1)}$ is solved for with the Newton-Raphson method.

6.5.1. Newton-Raphson Method

The Newton-Raphson method is applied as an approximation algorithm for the numerical solution of the non-linear system of equations (SOE), thus the SOE is linearised. The aim of the non-linear FEM overall is to determine the unknown state $\boldsymbol{d}$ in a way, that the residuum $\boldsymbol{r}$ is minimised. The Newton-Raphson method is derived from a Taylor series expansion around the previous iteration value $\boldsymbol{d}^{(i)}$, which is aborted after the linear term:

$$\boldsymbol{r}\left(\boldsymbol{d}^{(i+1)}\right) = \boldsymbol{r}\left(\boldsymbol{d}^{(i)}\right) + \frac{\partial \boldsymbol{r}\left(\boldsymbol{d}^{(i)}\right)}{\partial \boldsymbol{d}^{(i)}}\left(\boldsymbol{d}^{(i+1)} - \boldsymbol{d}^{(i)}\right). \tag{6.65}$$

Solving for $\boldsymbol{r}\left(\boldsymbol{d}^{(i+1)}\right) \overset{!}{=} 0$ iteratively with consideration of the correction $\boldsymbol{c}^{(i+1)}$ from Equation (6.64) yields:

$$\frac{\partial \boldsymbol{r}\left(\boldsymbol{d}^{(i)}\right)}{\partial \boldsymbol{d}^{(i)}}\boldsymbol{c}^{(i+1)} = -\boldsymbol{r}\left(\boldsymbol{d}^{(i)}\right). \tag{6.66}$$

The SOE is solved for until predefined convergence criteria are met. For a detailed description of the convergence criteria, the reader is kindly referred to Machaček (2020) and the `numgeo` documentation. In general, convergence criteria exist on a global level and for each DOF separately and are either based on the residuum $\boldsymbol{r}$, the solution $\boldsymbol{d}$ or are a combination of both. In matrix notation, Equation (6.66) reads for DOFs $\boldsymbol{d} = [\boldsymbol{u}^s, p^w]^T$:

$$\begin{bmatrix} \dfrac{\partial \boldsymbol{r}^{u^s}}{\partial \boldsymbol{u}^s} & \dfrac{\partial \boldsymbol{r}^{u^s}}{\partial p^{wf}} \\ \dfrac{\partial \boldsymbol{r}^{p^{wf}}}{\partial \boldsymbol{u}^s} & \dfrac{\partial \boldsymbol{r}^{p^{wf}}}{\partial p^{wf}} \end{bmatrix} \begin{bmatrix} \boldsymbol{c}^{u^s} \\ \boldsymbol{c}^{p^{wf}} \end{bmatrix} = - \begin{bmatrix} \boldsymbol{r}^{u^s} \\ \boldsymbol{r}^{p^{wf}} \end{bmatrix}. \tag{6.67}$$

6.5.2. System of equations

The residuum $\boldsymbol{r}\left(\boldsymbol{d}^{(i)}\right)$ is referred to as the *right-hand-side* (RHS):

$$\text{RHS} = -\boldsymbol{r}\left(\boldsymbol{d}^{(i)}\right) = -\boldsymbol{f}, \tag{6.68}$$

and $\partial \boldsymbol{r}\left(\boldsymbol{d}^{(i)}\right)/\partial \boldsymbol{d}$ as the *left-hand-side* (LHS). In (geo)static analysis, the LHS only includes the static Jacobian $\boldsymbol{K}$ whereas it also includes contributions regarding the first derivative $\dot{\boldsymbol{d}}$ of the unknown nodal variables $\boldsymbol{d}$ with respect to time in transient analysis:

$$\dot{\boldsymbol{d}} = \frac{\boldsymbol{d} - \boldsymbol{d}^{(t)}}{\Delta t} \quad \text{and} \quad \frac{\partial \dot{\boldsymbol{d}}}{\partial \boldsymbol{d}} = \frac{\partial}{\partial \boldsymbol{d}} \left(\frac{\boldsymbol{d} - \boldsymbol{d}^{(t)}}{\Delta t} \right) = \frac{1}{\Delta t}, \tag{6.69}$$

and consequently the respective contributions of the damping matrix $\boldsymbol{C}$ have to be scaled by the time increment Δt in Equation (6.67):

$$\text{LHS} = \frac{\partial \boldsymbol{r}\left(\boldsymbol{d}^{(i)}\right)}{\partial \boldsymbol{d}^{(i)}} = \boldsymbol{C}\frac{\partial \dot{\boldsymbol{d}}}{\partial \boldsymbol{d}} + \boldsymbol{K}, \tag{6.70}$$

$$\Leftrightarrow \text{LHS} = \frac{\partial \boldsymbol{r}\left(\boldsymbol{d}^{(i)}\right)}{\partial \boldsymbol{d}^{(i)}} = \frac{\boldsymbol{C}}{\Delta t} + \boldsymbol{K}. \tag{6.71}$$

6.5.3. Element contributions

The element contributions of the discretised residuums $\boldsymbol{r}$ and required derivatives of the Jacobian $\partial \boldsymbol{r}/\partial \boldsymbol{d}$ from the conservation of linear momentum of the mixture and the conservation of mass for the pore water phase for the extended porous medium are presented in the following. They are given in their full extent, thus valid for constitutive models and problems beyond the scope of this work. The derivatives considered for the respective constitutive models were stated in Section 6.1. Note that time derivatives of the DOFs with respect to themselves contribute to the damping matrix $\boldsymbol{C}$ within the Jacobian $\partial \boldsymbol{r}/\partial \boldsymbol{d}$ (see Equation (6.70)). During the collection of the derivatives, these contributions are written explicitly including the factor $1/\Delta t$. For the definition of the individual summands of the governing equations, the factor is omitted in contributions to $\boldsymbol{C}$ and accounted for globally in the Jacobian assembly, yielding the standard form given in Equation (6.71).

The secondary unknowns from the SOE are described by constitutive models for the mechanical and hydraulic behaviour. They are linearized as:

$$\sigma_{ij} = \sigma_{ij}^{(t)} + \Delta\sigma_{ij} \approx \sigma_{ij}^{(t)} + J_{ijkl}^{\sigma,u}\Delta\varepsilon_{kl} + J_{ij}^{\sigma,s}\Delta s, \tag{6.72}$$

$$S^{e} = S^{e(t)} + \Delta S^{e} \approx S^{e(t)} + J_{ij}^{S^e,\varepsilon}\Delta\varepsilon_{ij} + J^{S^e,s}\Delta s, \tag{6.73}$$

$$S^{w} = S^{w(t)} + \Delta S^{w} \approx S^{w(t)} + J_{ij}^{S^w,\varepsilon}\Delta\varepsilon_{ij} + J^{S^w,s}\Delta s, \tag{6.74}$$

$$k^{r,wf} = k^{r,wf(t)} + \Delta k^{r,wf} \approx k^{r,wf(t)} + J^{k^{r,wf},S^e}\left(J_{ij}^{S^e,\varepsilon}\Delta\varepsilon_{ij} + J^{S^e,s}\Delta s\right). \tag{6.75}$$

wherein $\sqcup^{(t)}$ are the known values of the variables at the beginning of the increment at time t. The superscript $\sqcup^{(t+\Delta t)}$ denoting the current value at the end of the increment at time $t + \Delta t$ is omitted for the sake of clarity. The strain increment $\Delta\varepsilon_{ij}$ is computed from the incremental nodal displacement Δu_{kl} via the strain-displacement matrix B_{ijkl}, using the respective derivatives of the shape functions:

$$\Delta\varepsilon_{ij} = B_{ijkI}\Delta u_{Ik}. \tag{6.76}$$

With the increments of the pore water pressure $\Delta\bar{p}^w_K$ and pore air pressure $\Delta\bar{p}^a_K$, using Equation (6.57) and the assumption of the passive air phase, the suction increment $\Delta s = \Delta\bar{p}^a - \Delta\bar{p}^w = -\Delta\bar{p}^w$ results in:

$$\Delta s = -N^p_K \Delta\bar{p}^w_K \tag{6.77}$$

. Inserting Equations (6.76) and (6.77), the linearized forms of Equations (6.72) − (6.75) are:

$$\sigma_{ij} \approx \sigma^{(t)}_{ij} + J^{\sigma,\varepsilon}_{ijkl} B_{klmI} \Delta u_{mI} + J^{\sigma,s}_{ij} \left(-N^p_K \Delta\bar{p}^w_K\right), \tag{6.78}$$

$$S^e \approx S^{e(t)} + J^{S^e,\varepsilon}_{ij} B_{ijmI} \Delta u_{mI} + J^{S^e,s} \left(-N^p_K \Delta\bar{p}^w_K\right), \tag{6.79}$$

$$S^w \approx S^{w(t)} + J^{S^w,\varepsilon}_{ij} B_{ijmI} \Delta u_{mI} + J^{S^w,s} \left(-N^p_K \Delta\bar{p}^w_K\right), \tag{6.80}$$

$$k^{r,wf} \approx k^{wf(t)}_r + J^{k^{wf},S^e} \left(J^{S^e,\varepsilon}_{ij} B_{ijmI} \Delta u_{mI} + J^{S^e,s} \left(-N^p_K \Delta\bar{p}^w_K\right)\right). \tag{6.81}$$

The discretised derivatives with respect to the unknowns u^s_i and $\bar{p}^w$ are:

$$J^{\sigma,u}_{ijmI} = J^{\sigma,\varepsilon}_{ijkl} B_{klmI}, \qquad J^{\sigma,p^w}_{ijK} = -J^{\sigma,s}_{ij} N^p_K, \tag{6.82}$$

$$J^{S^e,u}_{mI} = J^{\Delta S^e,u}_{mI} = J^{S^e,\varepsilon}_{ij} B_{ijmI}, \qquad J^{S^e,p^w}_K = J^{\Delta S^e,p^w}_K = -J^{S^e,s} N^p_K, \tag{6.83}$$

$$J^{S^w,u}_{mI} = J^{\Delta S^w,u}_{mI} = J^{S^w,\varepsilon}_{ij} B_{ijmI}, \qquad J^{S^w,p^w}_K = J^{\Delta S^w,p^w}_K = -J^{S^w,s} N^p_K, \tag{6.84}$$

$$J^{k^{wf},u}_{mI} = J^{k^{wf},S^e} J^{S^e,\varepsilon}_{ij} B_{ijmI}, \qquad J^{k^{wf},p^w}_K = -J^{k^{wf},S^e} J^{S^e,s} N^p_K. \tag{6.85}$$

The derivatives $J^{S^\sqcup,\varepsilon}_{ij}$ are computed based on the derivatives $J^{S^\sqcup,e}$ of $S^\sqcup$ with respect to the void ratio e, which are passed from the hydraulic model. The void ratio is the volumetric part of the strain increment and linearized as:

$$e \approx e^{(t)} + \left(1 + e^{(t)}\right) \delta_{ij} \Delta\epsilon_{ij}. \tag{6.86}$$

For the derivative $J^{S^\sqcup,\varepsilon}_{ij}$ follows:

$$J^{S^\sqcup,\varepsilon}_{ij} = J^{S^\sqcup,e} J^{e,\epsilon}_{ij} \quad \text{with} \quad J^{e,\epsilon}_{ij} = (1 + e^{(t)})\delta_{ij}. \tag{6.87}$$

Moreover, linearization of the porosity, volume fractions and mass transfer and the derivatives with respect to the unknowns u^s_i and $\bar{p}^w$ is required. The porosity $n = n\,(u^s_i)$ is linearized analogously to the void ratio in Equation (6.86):

$$n \approx n^{(t)} + \left(1 - n^{(t)}\right) \delta_{ij} B_{ijmI} \Delta u_{mI}. \tag{6.88}$$

The derivatives of the current value of the total porosity n and its increment Δn with respect to the unknowns u^s_i and $\bar{p}^w$ are:

$$J^{n,u}_{mI} = J^{\Delta n,u}_{mI} = \left(1 - n^{(t)}\right) \delta_{ij} B_{ijmI}, \quad J^{n,p^w} = 0. \tag{6.89}$$

With Equation (6.88), the derivative of the volume fraction of the solid $\varphi^s = (1-n)$ with respect to the unknowns u^s_i and $\bar{p}^w$ follows as:

$$J^{\varphi^s,u}_{mI} = -\left(1 - n^{(t)}\right) \delta_{ij} B_{ijmI} = -J^{n,u}_{mI}, \qquad J^{\varphi^s,p^w} = 0. \tag{6.90}$$

The derivatives of the rate of the degree of saturation and porosity are required as well. They scale with $1/\Delta t$ with respect to their incremental counterparts. Moreover, since a first-order

linearization is assumed, the derivatives of the increments of S^w and n coincide with those for the quantities evaluated at time t and the Jacobians are written without distinction:

$$J_{mI}^{\dot{S}^w,u} = J_{mI}^{S^w,u}\frac{1}{\Delta t}, \qquad J_{K}^{\dot{S}^w,p^w} = J_{K}^{S^w,p^w}\frac{1}{\Delta t}. \tag{6.91}$$

$$J_{mI}^{\dot{n},u} = J_{mI}^{n,u}\frac{1}{\Delta t}, \qquad J^{\dot{n},p^w} = 0. \tag{6.92}$$

Thereon based, the derivatives of the total water fraction of water $\varphi^w = nS^w$, its increment $\Delta\varphi^w = \Delta n S^w + n\Delta S^w$ and its rate $\dot{\varphi}^w = \dot{n}S^w + n\dot{S}^w$ with respect to the unknowns u_i^s and $\bar{p}^w$ are:

$$J_{mI}^{\varphi^w,u} = J_{mI}^{\Delta\varphi^w,u} = J_{mI}^{n,u}S^w + J_{mI}^{S^w,u}n, \tag{6.93}$$

$$J_{K}^{\varphi^w,p^w} = J_{K}^{\Delta\varphi^w,p^w} = J^{n,p^w}S^w + J_{K}^{S^w,p^w}n = J_{K}^{S^w,p^w}n, \tag{6.94}$$

$$\begin{aligned} J_{mI}^{\dot{\varphi}^w,u} &= J_{mI}^{\dot{n},u}S^w + J_{mI}^{S^w,u}\,\dot{n} + J_{mI}^{n,u}\,\dot{S}^w + J_{mI}^{\dot{S}^w,u}n \\ &= J_{mI}^{n,u}\frac{1}{\Delta t}S^w + J_{mI}^{S^w,u}\dot{n} + J_{mI}^{n,u}\dot{S}^w + J_{mI}^{S^w,u}\frac{1}{\Delta t}n, \end{aligned} \tag{6.95}$$

$$\begin{aligned} J_{K}^{\dot{\varphi}^w,p^w} &= J^{\dot{n},p^w}S^w + J_{K}^{S^w,p^w}\,\dot{n} + J^{n,p^w}\,\dot{S}^w + J_{K}^{\dot{S}^w,p^w}n \\ &= J_{K}^{S^w,p^w}\dot{n} + J_{K}^{S^w,p^w}\frac{1}{\Delta t}n. \end{aligned} \tag{6.96}$$

In addition, the partial derivatives of the mass transfer model $\hat{\rho}^w/\bar{\rho}^w$ are derived, which are required for the derivatives for the volume fraction of swelling water φ^{ws} and the volume fraction of free water φ^{wf}. Note that the mass transfer has the *quality of a rate* and the derivatives also correspond to the *rate*. The mass transfer from Equation (3.65) is linearized as:

$$\Delta\frac{\hat{\rho}^w}{\bar{\rho}^w} \approx \Delta\varphi^w\phi^{(t)} + \varphi^{w,(t)}\Delta\phi \tag{6.97}$$

$$\approx \left(\Delta n S^{w,(t)} + n^{(t)}\Delta S^w\right)\phi + \varphi^{w,(t)}\left(c_\phi\left(\phi^{\max} - \phi^{(t)}\right)\langle\Delta S^w\rangle\right). \tag{6.98}$$

The derivatives of the mass transfer with respect to the unknowns u_i^s and $\bar{p}^w$ in turn consist of the derivatives of $\dot{\phi}$ and $\Delta\phi$ with respect to the unknowns u_i^s and $\bar{p}^w$, which are defined as:

$$J_{mI}^{\Delta\phi,u} = c_\phi\left(\phi^{\max} - \phi^{(t)}\right)J_{mI}^{S^w,u}\Big|_{\dot{S}^w>0}, \tag{6.99}$$

$$J_{K}^{\Delta\phi,p^w} = c_\phi\left(\phi^{\max} - \phi^{(t)}\right)J_{K}^{S^w,p^w}\Big|_{\dot{S}^w>0}, \tag{6.100}$$

$$J_{mI}^{\dot{\phi},u} = c_\phi\left(\phi^{\max} - \phi^{(t)}\right)J_{mI}^{S^w,u}\frac{1}{\Delta t}\Big|_{\dot{S}^w>0}, \tag{6.101}$$

$$J_{K}^{\dot{\phi},p^w} = c_\phi\left(\phi^{\max} - \phi^{(t)}\right)J_{K}^{S^w,p^w}\frac{1}{\Delta t}\Big|_{\dot{S}^w>0}. \tag{6.102}$$

For the derivatives of the mass transfer and its increment, denoted as $\Delta\hat{\rho}^w$, with respect to the unknowns u_i^s and $\bar{p}^w$ follows:

$$J_{mI}^{\Delta\hat{\rho}^w,u} = J_{mI}^{\varphi^w,u}\,\phi^{(t)} + J_{mI}^{\Delta\phi,u}\varphi^{w,(t)}, \tag{6.103}$$

$$J_{K}^{\Delta\hat{\rho}^w,p^w} = J_{K}^{\varphi^w,p^w}\,\phi^{(t)} + J_{K}^{\Delta\phi,p^w}\varphi^{w,(t)}, \tag{6.104}$$

$$J_{mI}^{\hat{\rho}^w,u} = J_{mI}^{\dot{\varphi}^w,u}\,\phi^{(t)} + J_{mI}^{\dot{\phi},u}\varphi^{w,(t)}, \tag{6.105}$$

$$J_{K}^{\hat{\rho}^w,p^w} = J_{K}^{\dot{\varphi}^w,p^w}\,\phi^{(t)} + J_{K}^{\dot{\phi},p^w}\varphi^{w,(t)}. \tag{6.106}$$

Linearisation of the volume fraction of swelling water φ^{ws} based on Equation (3.51) results in:

$$\varphi^{ws} \approx \varphi^{ws,(t)} + \Delta\frac{\hat{\rho}^w}{\bar{\rho}^w} - \varphi^{ws,(t)}\delta_{ij}B_{ijmI}\Delta u_{mI}, \tag{6.107}$$

and the derivatives with respect to the unknowns u_i^s and $\bar{p}^w$ are:

$$\begin{aligned} J_{mI}^{\varphi^{ws},u} = J_{mI}^{\Delta\varphi^{ws},u} &= J_{mI}^{\Delta\hat{\rho}^w,u} - \varphi^{ws(t)}\delta_{ij}B_{ijmI} \\ &= J_{mI}^{\varphi^w,u}\,\phi^{(t)} + J_{mI}^{\Delta\phi,u}\varphi^{w,(t)} - \varphi^{ws,(t)}\delta_{ij}B_{ijmI}, && (6.108) \\ J_K^{\varphi^{ws},p^w} = J_K^{\Delta\varphi^{ws},p^w} &= J_K^{\Delta\hat{\rho}^w,p^w} = J_K^{\varphi^w,p^w}\,\phi^{(t)} + J_K^{\Delta\phi,p^w}\varphi^{w,(t)}, && (6.109) \\ J_{mI}^{\dot{\varphi}^{ws},u} &= J_{mI}^{\hat{\rho}^w,u} - \varphi^{ws}\delta_{ij}B_{ijmI}\frac{1}{\Delta t} \\ &= J_{mI}^{\dot{\varphi}^w,u}\,\phi^{(t)} + J_{mI}^{\dot{\phi},u}\varphi^{w,(t)} - \varphi^{ws,(t)}\delta_{ij}B_{ijmI}\frac{1}{\Delta t}, && (6.110) \\ J_K^{\dot{\varphi}^{ws},p^w} &= J_K^{\hat{\rho}^w,p^w} = J_K^{\dot{\varphi}^w,p^w}\,\phi^{(t)} + J_K^{\dot{\phi},p^w}\varphi^{w,(t)}. && (6.111) \end{aligned}$$

The derivatives of the volume fraction of free water $\varphi^{wf} = \varphi^w - \varphi^{ws}$ and its rate $\dot{\varphi}^{wf} = \dot{\varphi}^w - \dot{\varphi}^{ws}$ (Equation (3.57)) with respect to the unknowns u_i^s and $\bar{p}^w$ are not stated here, as they comprise of the difference between the derivatives of the volume fraction of water and swelling water and their rates respectively.

Conservation of linear momentum of the mixture

The discretised residuum of the conservation of linear momentum of the mixture (Equation (6.59)) consists of six summands, whose contributions to the RHS f_{Ii}^s and to the LHS in matrices $K_{IimJ}^{s,s}$, $K_{IiK}^{s,w}$, $C_{IimJ}^{s,s}$ and $C_{IiK}^{s,w}$ of the SOE are presented in the following. Note that summand (0) does not yield any contributions to the RHS or the LHS.

$$\begin{aligned} r_{Ii}^u = &\underbrace{-\int_\Gamma N_I^s t_i^{tot}\,d\Gamma}_{(0)} \underbrace{+\int_\Omega \frac{\partial N_I^s}{\partial x_j}\sigma_{ij}\,\mathrm{d}\Omega}_{(1)} \underbrace{-\int_\Omega \frac{\partial N_I^s}{\partial x_j}\alpha\chi N_K^p\bar{p}_K^w\delta_{ij}\,\mathrm{d}\Omega}_{(2)} \underbrace{-\int_\Omega N_I^s\rho^{tot}b_i\,\mathrm{d}\Omega}_{(3)} \\ &\underbrace{+\int_\Omega N_I^s\rho^{tot}N_J^s\bar{a}_{Ji}^s\,\mathrm{d}\Omega}_{(4)} \underbrace{-\int_\Omega N_I^s\hat{\rho}^w\frac{w_i^{wf}}{\varphi^{wf}}\,\mathrm{d}\Omega}_{(5)}. \end{aligned} \tag{6.112}$$

Summand (1): Contributions of effective stresses

$$f_{Ii}^s = +\int_\Omega \frac{\partial N_I^s}{\partial x_j}\sigma_{ij}\,\mathrm{d}\Omega\,,$$

with the corresponding partial derivatives based on Equation (6.82):

$$\begin{aligned} K_{IimJ}^{s,s} &= +\int_\Omega \frac{\partial N_I^s}{\partial x_j}J_{ijkI}^{\sigma,\varepsilon}B_{klmJ}\,\mathrm{d}\Omega\,, \\ K_{IiK}^{s,w} &= -\int_\Omega \frac{\partial N_I^s}{\partial x_j}J_{ij}^{\sigma,s}N_K^p\,\mathrm{d}\Omega\,. \end{aligned}$$

Summand (2): Contributions from the difference between total and effective stress

The Bishop parameter is kept as χ as different effective stress approaches may be used. However, as they all depend on the effective degree of saturation, the dependency $\chi = \chi\,(S^e, p^w)$ applies

and solely the derivative $J_K^{\chi,p^w} = -J^{\chi,S^e} J^{S^e,s} N_K^p$ with respect to the pore water pressure is considered:

$$f_{Ii}^s = -\int_\Omega \frac{\partial N_I^s}{\partial x_j} \chi N_K^p \bar{p}_K^w \delta_{ij} \, \mathrm{d}\Omega \,,$$

with the corresponding partial derivative:

$$K_{IiK}^{s,w} = -\int_\Omega \frac{\partial N_I^s}{\partial x_i} \left(J^{\chi,S^e} J^{S^e,s} N_K^p \left(N_L^p \bar{p}_L^w \right) \right) \mathrm{d}\Omega \, - \int_\Omega \frac{\partial N_I^s}{\partial x_i} \chi N_K^p \, \mathrm{d}\Omega \,.$$

Summand (3): Contributions of the body forces due to gravity

For the total density the air density is assumed negligible ($\bar{\rho}^a = 0$) and the density of all water phases identical ($\bar{\rho}^{sw} = \bar{\rho}^{wf} = \bar{\rho}^w$), hence the total density is defined by the volume fractions of solid and water as $\rho^{tot} = \varphi^s \bar{\rho}^s + \varphi^w \bar{\rho}^w = (1-n)\, \bar{\rho}^s + n S^w \bar{\rho}^w$:

$$f_{Ii}^s = -\int_\Omega N_I^s \rho^{tot} b_i \, \mathrm{d}\Omega = -\int_\Omega N_I^s \left(\varphi^s \bar{\rho}^s + \varphi^w \bar{\rho}^w \right) b_i \, \mathrm{d}\Omega = -\int_\Omega N_I^s \left((1-n)\, \bar{\rho}^s + n S^w \bar{\rho}^w \right) b_i \, \mathrm{d}\Omega \,,$$

with the corresponding partial derivatives based on Equations (6.90), (6.93) and (6.94):

$$K_{IimJ}^{s,s} = -\int_\Omega N_I^s \left(J_{mJ}^{\varphi^s,u} \bar{\rho}^s + J_{mJ}^{\varphi^w,u} \bar{\rho}^w \right) b_i \, \mathrm{d}\Omega = -\int_\Omega N_I^s \left[-J_{mJ}^{n,u} \bar{\rho}^s + \left(J_{mJ}^{n,u} S^w + J_{mJ}^{S^w,u} n \right) \bar{\rho}^w \right] b_i \, \mathrm{d}\Omega \,,$$
$$K_{IiK}^{s,w} = -\int_\Omega N_I^s \left(J_K^{\varphi^s,p^w} \bar{\rho}^s + J_K^{\varphi^w,p^w} \rho^w \right) b_i \, \mathrm{d}\Omega = -\int_\Omega N_I^s \left(J_K^{S^w,p^w} n \, \rho^w \right) b_i \, \mathrm{d}\Omega \,.$$

Summand (4): Dynamic contribution

Note that this work does not consider dynamic processes, however, for the sake of completeness, the contributions of inertia forces are still presented:

$$f_{Ii}^s = +\int_\Omega N_I^s \rho^{tot} N_J^s \bar{a}_{Ji}^s \, \mathrm{d}\Omega \,,$$

with the corresponding partial derivative in the mass matrix $M_{IimJ}^{s,s}$ (see Equation (6.62)):

$$M_{IimJ}^{s,s} = \int_\Omega N_I^s \rho^{tot} N_J^s \delta_{im} \, \mathrm{d}\Omega \,.$$

Summand (5): Contributions from the mass transfer between free water and swelling water

The darcy velocity $w_i^{wf,(t)}$ and the volume fraction of free water $\varphi^{wf,(t)}$ are considered in an explicit manner at (known) time t.

$$f_{Ii}^s = -\int_\Omega N_I^s \hat{\rho}^w \frac{w_i^{wf,(t)}}{\varphi^{wf,(t)}} \, \mathrm{d}\Omega = -\int_\Omega N_I^s \bar{\rho}^w \frac{\hat{\rho}^w}{\bar{\rho}^w} \frac{w_i^{wf,(t)}}{\varphi^{wf,(t)}} \, \mathrm{d}\Omega \,,$$

with the corresponding partial derivatives based on Equations (6.105) and (6.106), wherein the superscripts K and C indicate the portion of the respective derivatives considered in the static Jacobian and damping matrix:

$$
\begin{aligned}
K^{s,s}_{IimJ} &= -\int_\Omega N^s_I \bar{\rho}^w \frac{w_i^{wf,(t)}}{\varphi^{wf,(t)}} \left(J^{\hat{\rho}^w,u}_{mJ}\right)^K \mathrm{d}\Omega - \int_\Omega N^s_I \bar{\rho}^w \frac{w_i^{wf,(t)}}{\varphi^{wf,(t)}} \left(J^{S^w,u}_{mJ}\dot{n} + J^{n,u}_{mJ}\dot{S}^w\right)\phi^{(t)}\,\mathrm{d}\Omega\,,\\
C^{s,s}_{IimJ} &= -\int_\Omega N^s_I \bar{\rho}^w \frac{w_i^{wf,(t)}}{\varphi^{wf,(t)}} \left(J^{\hat{\rho}^w,u}_{mJ}\right)^C \mathrm{d}\Omega\\
&= -\int_\Omega N^s_I \bar{\rho}^w \frac{w_i^{wf,(t)}}{\varphi^{wf,(t)}} \left[\left(J^{n,u}_{mJ}S^w + J^{S^w,u}_{mJ}n\right)\phi^{(t)} + \left(c_\phi\left(\phi^{\max}-\phi^{(t)}\right)J^{S^w,u}_{mJ}\Big|_{\dot{S}^w>0}\right)\varphi^{w,(t)}\right]\mathrm{d}\Omega\,,\\
K^{s,w}_{IiK} &= -\int_\Omega N^s_I \bar{\rho}^w \frac{w_i^{wf,(t)}}{\varphi^{wf,(t)}} \left(J^{\hat{\rho}^w,w}_{K}\right)^K \mathrm{d}\Omega = -\int_\Omega N^s_I \bar{\rho}^w \frac{w_i^{wf,(t)}}{\varphi^{wf,(t)}} \left(J^{S^w,p^w}_{K}\dot{n}\,\phi^{(t)}\right)\mathrm{d}\Omega\,,\\
C^{s,w}_{IiK} &= -\int_\Omega N^s_I \bar{\rho}^w \frac{w_i^{wf,(t)}}{\varphi^{wf,(t)}} \left(J^{\hat{\rho}^w,w}_{K}\right)^C \mathrm{d}\Omega\\
&= -\int_\Omega N^s_I \bar{\rho}^w \frac{w_i^{wf,(t)}}{\varphi^{wf,(t)}} \left[J^{S^w,p^w}_{K}\,n\,\phi^{(t)} + \left(c_\phi\left(\phi^{\max}-\phi^{(t)}\right)J^{S^w,p^w}_{K}\Big|_{\dot{S}^w>0}\right)\varphi^{w,(t)}\right]\mathrm{d}\Omega\,.
\end{aligned}
$$

Conservation of mass for the free pore water

The discretised residuum of the conservation of mass for the free pore water (Equation (6.61)) is rearranged and nine summands are identified, whose contributions to the RHS f^w_K and to the LHS in matrices $K^{w,s}_{KIi}$, $K^{w,w}_{KL}$, $C^{w,s}_{KIi}$ and $C^{w,w}_{KL}$ of the SOE are presented in the following. Summand (0) does not yield any contributions to RHS or LHS. Superscripts K and C indicate the portion of the respective derivatives considered in the static Jacobian and damping matrix.

$$
\begin{aligned}
r^{p^w}_K = &\underbrace{-\int_\Gamma q N^p_K\,\mathrm{d}\Gamma}_{(0)} \underbrace{-\int_\Omega N^p_K \dot{\varphi}^{wf}\,\mathrm{d}\Omega}_{(1)} \underbrace{-\int_\Omega N^p_K \frac{\varphi^{wf}}{\bar{K}^{wf}} N^p_L \dot{\bar{p}}^w_L\,\mathrm{d}\Omega}_{(2)} \underbrace{-\int_\Omega N^p_K \varphi^{wf}\frac{\partial N^s_I}{\partial x_i}\bar{v}^s_{Ii}\,\mathrm{d}\Omega}_{(3)}\\
&\underbrace{+\int_\Omega \frac{\partial N^p_K}{\partial x_i}\frac{k^{wf}}{\bar{\mu}^{wf}} K^s_{ij}\bar{\rho}^w b_j\,\mathrm{d}\Omega}_{(4)} \underbrace{-\int_\Omega \frac{\partial N^p_K}{\partial x_i}\frac{k^{wf}}{\bar{\mu}^{wf}} K^s_{ij}\frac{\partial N^p_L}{\partial x_j}\bar{p}^w_L\,\mathrm{d}\Omega}_{(5)}\\
&\underbrace{-\int_\Omega N^p_K \frac{1}{\bar{K}^{wf}}\frac{\partial N^p_L}{\partial x_i}\bar{p}_L w_i^{wf}\,\mathrm{d}\Omega}_{(6)} \underbrace{-\int_\Omega \frac{\partial N^p_K}{\partial x_i}\frac{k^{wf}}{\bar{\mu}^{wf}} K^s_{ij}\bar{\rho}^w N^s_I \bar{a}^s_{Ij}\,\mathrm{d}\Omega}_{(7)} \underbrace{+\int_\Omega N^p_K \frac{\hat{\rho}^w}{\bar{\rho}^w}\,\mathrm{d}\Omega}_{(8)}\,.
\end{aligned}
\tag{6.113}
$$

Summand (1): Contributions of the storage of water

Changes in the degree of saturation and in the porosity influence the water content.

$$
f^w_K = -\int_\Omega N^p_K \dot{\varphi}^{wf}\,\mathrm{d}\Omega = -\int_\Omega N^p_K\left(\dot{\varphi}^w - \dot{\varphi}^{ws}\right)\mathrm{d}\Omega\,,
$$

with the corresponding partial derivatives from Equations (6.95), (6.96), (6.110) and (6.111):

$$
\begin{aligned}
K_{KIi}^{w,s} &= -\int_\Omega N_K^p \left(J_{Ii}^{\dot{\varphi}^w,u}\right)^K \mathrm{d}\Omega - \int_\Omega N_K^p \left(-J_{Ii}^{\dot{\varphi}^{ws},u}\right)^K \mathrm{d}\Omega \\
&= -\int_\Omega N_K^p \left(J_{Ii}^{S^w,u}\dot{n} + J_{Ii}^{n,u}\dot{S}^w\right) \mathrm{d}\Omega + \int_\Omega N_K^p \left(J_{Ii}^{S^w,u}\dot{n} + J_{Ii}^{n,u}\dot{S}^w\right) \phi^{(t)}\,\mathrm{d}\Omega\,, \\
C_{KIi}^{w,s} &= -\int_\Omega N_K^p \left(J_{Ii}^{\dot{\varphi}^w,u}\right)^C \mathrm{d}\Omega - \int_\Omega N_K^p \left(-J_{Ii}^{\dot{\varphi}^{ws},u}\right)^C \mathrm{d}\Omega \\
&= -\int_\Omega N_K^p \left(J_{Ii}^{n,u}S^w + J_{Ii}^{S^w,u}n\right) \mathrm{d}\Omega + \int_\Omega N_K^p \left(J_{Ii}^{n,u}S^w + J_{Ii}^{S^w,u}n\right) \phi^{(t)}\,\mathrm{d}\Omega \\
&\quad + \int_\Omega N_K^p \left[\left(c_\phi \left(\phi^{\max} - \phi^{(t)}\right) J_{Ii}^{S^w,u}\Big|_{\dot{S}^w>0}, \right) \varphi^{w,(t)} - \varphi^{ws,(t)}\delta_{kl}B_{klIi}\right] \mathrm{d}\Omega\,, \\
K_{KL}^{w,w} &= -\int_\Omega N_K^p \left(J_L^{\dot{\varphi}^w,p^w}\right)^K \mathrm{d}\Omega - \int_\Omega N_K^p \left(-J_L^{\dot{\varphi}^{ws},p^w}\right)^K \mathrm{d}\Omega \\
&= -\int_\Omega N_K^p \left(J_L^{S^w,p^w}\dot{n}\right) \mathrm{d}\Omega + \int_\Omega N_K^p \left(J_L^{S^w,p^w}\dot{n}\right) \phi^{(t)}\,\mathrm{d}\Omega\,, \\
C_{KL}^{w,w} &= -\int_\Omega N_K^p \left(J_L^{\dot{\varphi}^w,p^w}\right)^C \mathrm{d}\Omega - \int_\Omega N_K^p \left(-J_L^{\dot{\varphi}^{ws},p^w}\right)^C \mathrm{d}\Omega \\
&= -\int_\Omega N_K^p \left(J_L^{S^w,p^w}n\right) \mathrm{d}\Omega \\
&\quad + \int_\Omega N_K^p \left[\left(J_L^{S^w,p^w}n\right) \phi^{(t)} + \left(c_\phi \left(\phi^{\max} - \phi^{(t)}\right) J_L^{S^w,p^w}\Big|_{\dot{S}^w>0}\right) \varphi^{w,(t)}\right] \mathrm{d}\Omega\,.
\end{aligned}
$$

Summand (2): Contributions of the compressibility of pore water due to pore water pressure gradients.

Note that this term vanishes for incompressible pore fluids.

$$
f_K^w = -\int_\Omega N_K^p \frac{\varphi^{wf}}{\bar{K}^{wf}} N_L^p \dot{\bar{p}}_L^w \,\mathrm{d}\Omega = -\int_\Omega N_K^p \frac{(\varphi^w - \varphi^{ws})}{K^{wf}} N_L^p \dot{\bar{p}}_L^w \,\mathrm{d}\Omega\,,
$$

with the corresponding partial derivatives from Equations (6.93), (6.94), (6.108) and (6.109):

$$
\begin{aligned}
K_{KIi}^{w,s} &= -\int_\Omega N_K^p \frac{1}{\bar{K}^{wf}} \left(J_{Ii}^{\varphi^w,u}\right)^K N_L^p \dot{\bar{p}}_L^w \,\mathrm{d}\Omega - \int_\Omega N_K^p \frac{1}{\bar{K}^{wf}} \left(-J_{Ii}^{\varphi^{ws},u}\right)^K N_L^p \dot{\bar{p}}_L^w \,\mathrm{d}\Omega \\
&= -\int_\Omega N_K^p \frac{1}{K^{wf}} \left(J_{Ii}^{n,u}S^w + J_{Ii}^{S^w,u}n\right) N_L^p \dot{\bar{p}}_L^w \,\mathrm{d}\Omega + \int_\Omega N_K^p \frac{1}{\bar{K}^{wf}} \left[\left(J_{Ii}^{n,u}S^w + J_{Ii}^{S^w,u}n\right) \phi^{(t)}\right. \\
&\quad \left. + \left(c_\phi \left(\phi^{\max} - \phi^{(t)}\right) J_{Ii}^{S^w,u}\Big|_{\dot{S}^w>0}\right) \varphi^{w,(t)} - \varphi^{ws,(t)}\delta_{kl}B_{klIi}\right] N_L^p \dot{\bar{p}}_L^w \,\mathrm{d}\Omega\,, \\
K_{KL}^{w,w} &= -\int_\Omega N_K^p \frac{1}{\bar{K}^{wf}} \left(J_L^{\varphi^w,p^w}\right)^K N_M^p \dot{\bar{p}}_M^w \,\mathrm{d}\Omega - \int_\Omega N_K^p \frac{1}{\bar{K}^{wf}} \left(-J_L^{\varphi^{ws},p^w}\right)^K N_M^p \dot{\bar{p}}_M^w \,\mathrm{d}\Omega \\
&= -\int_\Omega N_K^p \frac{1}{\bar{K}^{wf}} \left(J_L^{S^w,p^w}n\right) N_M^p \dot{\bar{p}}_M^w \,\mathrm{d}\Omega + \int_\Omega N_K^p \frac{1}{\bar{K}^{wf}} \left[\left(J_L^{S^w,p^w}n\right) \phi^{(t)}\right. \\
&\quad \left. + \left(c_\phi \left(\phi^{\max} - \phi^{(t)}\right) J_L^{S^w,p^w}\Big|_{\dot{S}^w>0}\right) \varphi^{w,(t)}\right] N_M^p \dot{\bar{p}}_M^w \,\mathrm{d}\Omega\,, \\
C_{KL}^{w,w} &= -\int_\Omega N_K^p \frac{(\varphi^w - \varphi^{ws})}{K^{wf}} N_L^p \,\mathrm{d}\Omega
\end{aligned}
$$

Summand (3): Contribution of consolidation processes

Volumetric strain of the solid influences the pore water pressure evolution.

$$
f_K^w = -\int_\Omega N_K^p \varphi^{wf} \frac{\partial N_I^s}{\partial x_i} \bar{v}_{Ii}^s \,\mathrm{d}\Omega = -\int_\Omega N_K^p \left(\varphi^w - \varphi^{ws}\right) \frac{\partial N_I^s}{\partial x_i} \bar{v}_{Ii}^s \,\mathrm{d}\Omega\,,
$$

with the corresponding partial derivatives from Equations (6.93), (6.94), (6.108) and (6.109):

$$\begin{aligned}
K^{w,s}_{KIi} &= -\int_\Omega N^p_K \left(J^{\varphi^w,u}_{Ii}\right)^K \frac{\partial N^s_J}{\partial x_j}\bar{v}^s_{Jj}\,\mathrm{d}\Omega - \int_\Omega N^p_K \left(-J^{\varphi^{ws},u}_{Ii}\right)^K \frac{\partial N^s_J}{\partial x_j}\bar{v}^s_{Jj}\,\mathrm{d}\Omega \\
&= -\int_\Omega N^p_K \left(J^{n,u}_{Ii}S^w + J^{S^w,u}_{iI}n\right)\frac{\partial N^s_J}{\partial x_j}\bar{v}^s_{Jj}\,\mathrm{d}\Omega + \int_\Omega N^p_K \Big[\left(J^{n,u}_{Ii}S^w + J^{S^w,u}_{Ii}n\right)\phi^{(t)} \\
&\quad + \left(c_\phi\left(\phi^{\max}-\phi^{(t)}\right)J^{S^w,u}_{Ii}\Big|_{\dot{S}^w>0}\right)\varphi^{w,(t)} - \varphi^{ws,(t)}\delta_{kl}B_{klIi}\Big]\frac{\partial N^s_J}{\partial x_j}\bar{v}^s_{Jj}\,\mathrm{d}\Omega\,, \\
C^{w,s}_{KIi} &= -\int_\Omega N^p_K\left(\varphi^w-\varphi^{ws}\right)\frac{\partial N^s_I}{\partial x_i}\,\mathrm{d}\Omega\,, \\
K^{w,w}_{KL} &= -\int_\Omega N^p_K \left(J^{\varphi^w,p^w}_{L}\right)^K \frac{\partial N^s_I}{\partial x_i}\bar{v}^s_{Ii}\,\mathrm{d}\Omega - \int_\Omega N^p_K \left(-J^{\varphi^{ws},p^w}_{L}\right)^K \frac{\partial N^s_I}{\partial x_i}\bar{v}^s_{Ii}\,\mathrm{d}\Omega \\
&= -\int_\Omega N^p_K \left(J^{S^w,p^w}_{L}n\right)\frac{\partial N^s_I}{\partial x_i}\bar{v}^s_{Ii}\,\mathrm{d}\Omega + \int_\Omega N^p_K \Big[\left(J^{S^w,p^w}_{L}n\right)\phi^{(t)} \\
&\quad + \left(c_\phi\left(\phi^{\max}-\phi^{(t)}\right)J^{S^w,p^w}_{L}\Big|_{\dot{S}^w>0}\right)\varphi^{w,(t)}\Big]\frac{\partial N^s_I}{\partial x_i}\bar{v}^s_{Ii}\,\mathrm{d}\Omega\,.
\end{aligned}$$

Summand (4): Contributions of gravitational forces on water flow

The dependency $k^{r,wf} = k^{r,wf}\left(S^e\right)$ is considered for the relative permeability of the soil due to partial saturation, whereas the relative permeability due to swelling $k^{r,ws}$ is considered explicitly at time t:

$$f^w_K = +\int_\Omega \frac{\partial N^p_K}{\partial x_i}\left(\frac{k^{wf}}{\bar{\mu}^{wf}}K^s_{ij}\bar{\rho}^w b_j\right)\mathrm{d}\Omega\,,$$

with the corresponding partial derivatives from Equation (6.85):

$$\begin{aligned}
K^{w,w}_{KL} &= +\int_\Omega J^{k^{wf},p^w}_K \frac{\partial N^p_L}{\partial x_k}\frac{K^s_{kl}\,k^{r,ws(t)}}{\bar{\mu}^{wf}}\bar{\rho}^w b_l\,\mathrm{d}\Omega\,, \\
K^{w,s}_{KIi} &= +\int_\Omega J^{k^{wf},u}_{Ii} \frac{\partial N^p_K}{\partial x_k}\frac{K^s_{kl}\,k^{r,ws(t)}}{\bar{\mu}^{wf}}\bar{\rho}^w b_l\,\mathrm{d}\Omega\,.
\end{aligned}$$

Summand (5): Contributions of Darcy flow

Pore water pressure gradients result in Darcy water flow. Again the dependency of the relative permeability on the effective degree of saturation is considered and the relative permeability due to swelling is considered explicitly:

$$f^w_K = -\int_\Omega \frac{\partial N^p_K}{\partial x_i}\frac{k^{wf}}{\bar{\mu}^{wf}}K^s_{ij}\frac{\partial N^p_L}{\partial x_j}\bar{p}^w_L\,\mathrm{d}\Omega\,,$$

with the corresponding partial derivatives from Equation (6.85):

$$\begin{aligned}
K^{w,w}_{KL} &= -\int_\Omega J^{k^{wf},pw}_K \frac{\partial N^p_K}{\partial x_i}\frac{K^s_{ij}\,k^{r,ws(t)}}{\bar{\mu}^{wf}}\frac{\partial N^p_L}{\partial x_j}\bar{p}^w_L\,\mathrm{d}\Omega - \int_\Omega \frac{\partial N^p_K}{\partial x_i}\frac{k^{wf}}{\bar{\mu}^{wf}}K^s_{ij}\frac{\partial N^p_L}{\partial x_j}\,\mathrm{d}\Omega\,, \\
K^{w,s}_{KIi} &= -\int_\Omega J^{k^{wf},u}_{Ii}\frac{\partial N^p_K}{\partial x_k}\frac{K^s_{kl}\,k^{r,ws(t)}}{\bar{\mu}^{wf}}\frac{\partial N^p_L}{\partial x_l}\bar{p}^w_L\,\mathrm{d}\Omega\,.
\end{aligned}$$

Summand (6): Contributions of the compressibility of pore water due to Darcy velocity

Note that this term vanishes for incompressible pore fluids. The Darcy velocity is considered explicit at known time t:

$$f^w_K = -\int_\Omega N^p_K\frac{1}{\bar{K}^{wf}}\frac{\partial N^p_L}{\partial x_i}\bar{p}_L w^{wf,(t)}_i\,\mathrm{d}\Omega\,,$$

with the corresponding partial derivative:

$$K_{KL}^{w,w} = -\int_\Omega N_K^p \frac{1}{\bar{K}^{wf}} \frac{\partial N_L^p}{\partial x_i} w_i^{wf,(t)} \,\mathrm{d}\Omega\,.$$

Summand (7): Dynamic contribution

Note that this work does not consider dynamic processes, however, for the sake of completeness, the contributions of inertia forces are still presented. The dependency of the relative permeability on the effective degree of saturation is considered and the relative permeability due to swelling is considered explicitly:

$$f_K^w = -\int_\Omega \frac{\partial N_K^p}{\partial x_i} \left(\frac{k^{wf}}{\bar{\mu}^{wf}} K_{ij}^s \bar{\rho}^w N_I^s \bar{a}_{Ij}^s \right) \mathrm{d}\Omega\,,$$

with the corresponding partial derivatives from Equation (6.85):

$$\begin{aligned}
K_{KL}^{w,w} &= -\int_\Omega J_L^{k^{wf},p^w} \frac{\partial N_K^p}{\partial x_i} \frac{K_{ij}^s\, k^{r,ws(t)}}{\bar{\mu}^{wf}} N_I^s \bar{a}_{Ij}^s \,\mathrm{d}\Omega\,,\\
K_{KIi}^{w,s} &= -\int_\Omega J_{Ii}^{k^{wf},u} \frac{\partial N_K^p}{\partial x_k} \frac{K_{kl}^s\, k^{r,ws(t)}}{\bar{\mu}^{wf}} N_J^s \bar{a}_{Jl}^s \,\mathrm{d}\Omega\,,\\
M_{KIj}^{w,s} &= -\int_\Omega \frac{\partial N_K^p}{\partial x_i} \frac{k^{wf}}{\bar{\mu}^{wf}} K_{ij}^s N_I^s \,\mathrm{d}\Omega\,.
\end{aligned}$$

Summand (8): Contributions from the mass transfer between free water and swelling water

$$f_K^w = \int_\Omega N_K^p \frac{\hat{\rho}^w}{\bar{\rho}^w} \,\mathrm{d}\Omega\,,$$

with the corresponding partial derivatives from Equation (6.105) and (6.106):

$$\begin{aligned}
K_{KIi}^{w,s} &= \int_\Omega N_K^p \left(J_{Ii}^{\hat{\rho}^w,u} \right)^K \mathrm{d}\Omega = \int_\Omega N_K^p \left(J_{Ii}^{S^w,u} \dot{n} + J_{Ii}^{n,u} \dot{S}^w \right) \phi^{(t)} \,\mathrm{d}\Omega\,,\\
C_{KIi}^{w,s} &= \int_\Omega N_K^p \left(J_{Ii}^{\hat{\rho}^w,u} \right)^C \mathrm{d}\Omega\\
&= \int_\Omega N_K^p \left(J_{Ii}^{n,u} S^w + J_{Ii}^{S^w,u} n \right) \phi^{(t)} + \left(c_\phi \left(\phi^{\max} - \phi^{(t)} \right) J_{Ii}^{S^w,u} \Big|_{\dot{S}^w>0} \right) \varphi^{w,(t)} \,\mathrm{d}\Omega\,,\\
K_{KL}^{w,w} &= \int_\Omega N_K^p \left(J_L^{\hat{\rho}^w,p^w} \right)^K \mathrm{d}\Omega = \int_\Omega N_K^p \left(J_L^{S^w,p^w} \dot{n} \right) \phi^{(t)} \,\mathrm{d}\Omega\,,\\
C_{KL}^{w,w} &= \int_\Omega N_K^p \left(J_L^{\hat{\rho}^w,p^w} \right)^C \mathrm{d}\Omega\\
&= \int_\Omega N_K^p \left(J_L^{S^w,p^w} n \right) \phi^{(t)} + \left(c_\phi \left(\phi^{\max} - \phi^{(t)} \right) J_L^{S^w,p^w} \Big|_{\dot{S}^w>0} . \right) \varphi^{w,(t)} \,\mathrm{d}\Omega\,.
\end{aligned}$$

6.5.4. Stabilisation

To overcome the violation of the LBB condition, equal order element formulations are enhanced with a stabilisation in this work. A fluid pressure Laplacian approach as described by Truty and Zimmermann (2006) is applied. The stabilisation concerns the compressibility matrix for the pore water $C_{KL}^{w,w}$ and the RHS f_K^{wf} of the $\boldsymbol{u}p-$(sw$-$)formulation in order to ensure adequate

diffusivity. This is done to stabilise the mass balance equation of the pore water pressure (Equation (6.113)) without overly smoothing the pressure field. The contributions of the stabilisation read as:

$$f_K^{wf,\mathrm{stab}} = -\int_\Omega \frac{\partial N_K^p}{\partial x_i}\,\tau^{FPL}\,\frac{\partial N_L^p}{\partial x_i}\dot{\bar{p}}_L^{wf}\,\mathrm{d}\Omega\,, \tag{6.114}$$

$$C_{KL}^{w,w,\mathrm{stab}} = -\int_\Omega \frac{\partial N_K^p}{\partial x_i}\,\tau^{FPL}\,\frac{\partial N_L^p}{\partial x_i}\,\mathrm{d}\Omega\,, \tag{6.115}$$

with the stabilisation factor τ^{FPL} defined as (Truty and Zimmermann, 2006):

$$\tau^{FPL} = \alpha\left(\frac{(S^w\,l_e)^2}{4M_{\mathrm{el}}} + \frac{l_e^2\,c^P}{6} - \frac{\Delta t\;k^{wf}}{\rho^w g}\right), \tag{6.116}$$

wherein Δt is the time increment, l_e is the characteristic element length, M_{el} is the constrained modulus of the material and k^{wf} is the representative hydraulic conductivity. With the stabilisation factor $0 \leq \alpha^{FPL} \leq 1.0$, the amount of diffusivity added to the balance of mass is controlled. It depends on the boundary value problem and must be chosen iteratively. c^P is the storage capacity and is:

$$c^P = \frac{\varphi^{wf}}{\bar{K}^{wf}} + \frac{\partial \varphi^w}{\partial \bar{p}^w}, \tag{6.117}$$

with the assumption of incompressibility of the solid particles and the swelling water ($K^s = K^{ws} \to \infty$). The characteristic element size l_e is approximated as the longest distance from the first node to any other node n of a finite element:

$$l_e = \max_{k=2,\ldots,n} \|x_i^{(1)} - x_i^{(k)}\|. \tag{6.118}$$

The constraint modulus M_{el} is approximated from the current material tangent stiffness $\boldsymbol{D}$ (in Voigt-notation) assuming incremental linear elasticity with $\boldsymbol{\epsilon} = [1\;1\;1\;0\;0\;0]^T$:

$$M_{\mathrm{el}} = K_{\mathrm{el}} + \frac{4}{3}G_{\mathrm{el}} \quad \text{with} \quad K_{\mathrm{el}} = \frac{1}{9}\left(\mathbf{1}^T\,\boldsymbol{D}\right)\boldsymbol{\epsilon} \quad \text{and} \quad G_{\mathrm{el}} = D_{44}. \tag{6.119}$$

The representative hydraulic conductivity is estimated following Truty (2001) in parallel direction of the pore water pressure gradient, however, modified to account for the presence of swelling water:

$$k^{wf} = \frac{\bar{p}_{,i}^w}{\|\,\bar{p}_{,i}^w\,\|}\,\frac{k^{r,wf}k^{r,ws}K_{ij}^s\gamma^{wf}}{\mu^{wf}}\,\frac{\bar{p}_{,j}^w}{\|\,\bar{p}_{,j}^w\,\|}. \tag{6.120}$$

Note that no fixed value for α can be recommended, as it strongly depends on the hydraulic regime and hydro-mechanical coupling of the specific boundary value problem (Truty and Zimmermann, 2006; Leon Bal, 2023). However, it should be chosen as small as possible to only create required stability without artificially accelerating the infiltration process.

6.5.5. Hourglass stiffness

Reduced integration in linear equal order elements leads to rank deficiency of the stiffness matrix and zero-energy modes, since characteristic deformation patterns without energy contribution cannot be recognized. So-called hourglass modes can be addressed with hourglass control

schemes. The element stiffness $K^{s,s,e}_{IimJ}$ is stabilised by the addition of an artificial stiffness K^{HG}_{IimJ} (Flanagan and Belytschko, 1981):

$$\begin{aligned} K^{s,s,e}_{IimJ} &= K^{s,s,e1Pt}_{IimJ} + K^{HG}_{IimJ} \\ &= K^{s,s,e,1Pt}_{IimJ} + \kappa^{HG} \mathrm{d}\Omega^e \sum^{\alpha} \gamma_{\alpha I} \gamma_{\alpha J} \delta_{im}, \end{aligned} \tag{6.121}$$

wherein $K^{s,s,e1Pt}_{IimJ}$ is the element stiffness evaluated at one integration point and $\gamma_{\alpha I/J}$ are the hourglass shape vectors for each hourglass mode α according to (Flanagan and Belytschko, 1981). The parameter κ^{HG} has the physical meaning of a stiffness, which controls the hourglass resistance. It is assumed constant throughout the simulation and is calculated as follows:

$$\kappa^{HG} = c^{HG} G_{\mathrm{el}} \frac{\partial N^s_I}{\partial x_i} \frac{\partial N^s_I}{\partial x_i}, \tag{6.122}$$

wherein c^{HG} is typically in the range of $0.01\, G_{\mathrm{el}}$.

6.5.6. Time stepping algorithm

In `numgeo`, an automatic time-stepping scheme adjusts the time increment Δt based on solution convergence. It applies to all analysis types. If convergence requires fewer than seven iterations, the time increment Δt^i from the previous (converged) increment i is increased by 25%; if more than twelve iterations are required, it is reduced by 25%. The prescribed minimum time increment $\Delta t_{\min}$ and maximum time increment $\Delta t_{\max}$ act as limits:

$$\Delta t = \begin{cases} \min\left(1.25\Delta t^i, \Delta t_{\max}\right) & \text{if: } n_j < 7, \\ \max\left(0.75\Delta t^i, \Delta t_{\min}\right) & \text{if: } n_j > 12, \\ \Delta t_n & \text{else.} \end{cases} \tag{6.123}$$

A minimum of two iterations is carried out. If convergence fails at a prescribed number of iterations j in the current increment (default $j = 24$), the analysis reverts to the previous converged increment and retries with half the previous time step. This process continues until convergence is achieved or the minimum time step $\Delta t_{\min}$ is reached.

6.5.6.1. Critical time steps

In transient hydro-mechanically coupled pore water pressure and stress analysis, time stepping is not trivial. Spurious, non-physical oscillations in the pore water pressure evolution may occur due to small time increments, if a minimum critical time increment Δt_{crit} is undercut, cf. Vermeer and Verruijt (1981) and Thomas and Zhou (1997). These oscillations may lead to convergence difficulties. Therefore, criteria for critical time increments exist for saturated flow in consolidation analysis and unsaturated flow analysis upon infiltration, wherein the latter is of higher importance for the simulation of swelling. Large time increments are generally not considered critical for convergence, although they may compromise the accuracy of the solution and should be chosen with care as well, see e.g. Li et al. (2022), who gives recommendations on determining the maximum time increment.

During unsaturated flow, the (minimum) critical time increment is not constant, but inversely proportional to the diffusion coefficient D (in m^2/s), which itself is a function of the porosity n, the specific weight of water γ^w, the current hydraulic conductivity as a product of saturated hydraulic conductivity k^w and relative permeability $k^{r,wf}$, and the partial derivative of the degree of saturation with respect to suction $\partial S^w / \partial s$ (see Equation (6.24)):

$$\Delta t_{\mathrm{crit}} \sim \frac{1}{D} \quad \text{with} \quad D = \frac{k^{r,wf}\, k^w}{\gamma^w\, n \dfrac{\partial S^w}{\partial s}}. \tag{6.124}$$

To avoid undershooting of the critical time increment in a transient FE analysis, the initial time increment and the minimum time increment of the respective simulation step should be chosen as $\Delta t_0 > \Delta t_{\mathrm{crit}}$ and $\Delta t_{\mathrm{min}} > \Delta t_{\mathrm{crit}}$ respectively, and the critical time increment must be determined analytically in advance. As it is non-constant upon infiltration, the conservative choice may be to consider the expected maximum value of Δt_{crit} during the analysis, which corresponds to the expected minimum value of the diffusion coefficient (D_{min}). However, this effectively cancels out convergence-based time stepping in the analysis, whenever the current critical time increment is smaller than this maximum value. In some cases, it completely negates convergence and the analysis terminates. To account for the variation of the diffusion coefficient, which may span over several orders of magnitude, Li et al. (2022) proposed to use the geometric mean value of the diffusion coefficient (D_{mean}) to compute a representative value of the critical time increment Δt_{crit} over the course of infiltration. It computes as $D_{\mathrm{mean}} = \sqrt{D_{\mathrm{min}} D_{\mathrm{max}}}$, wherein D_{min} and D_{max} correspond to the expected minimum and maximum value of the diffusion coefficient. However, the choice of D_{mean} can still negate convergence. Contrary, Karthikeyan et al. (2001) amongst others, recommend to compute D for the highest suction, thus corresponding to the driest, initial state and denoted as D_0. However, this approach results in a rather small Δt_{crit} and carries the highest risk of undershooting the critical time increment in the further course of the analysis as the convergence-based time stepping does not allow for a sufficiently fast increase of Δt. This risk, however, applies to any choice for D except that of D_{min}, as Δt_{crit} is not actively considered in the automatic time-stepping.

In `numgeo`, the critical time increments for unsaturated flow during infiltration and saturated flow in consolidation were added as element output. In this way, the user can track their evolution during an analysis, compare the actual time incrementation and evaluate the choices made for Δt_0 and Δt_{min}. Their computation is based on the following criteria:

- Unsaturated flow: The critical time increment $\Delta t_{\mathrm{unsat}}$ is a function of the representative nodal distance Δl_n of the finite element and the diffusion coefficient D (Equation (6.124)). It was derived from the mass balance equation for unsaturated flow in diffusion problems (Reed, 1984; Thomas and Zhou, 1997) and seepage analysis (Karthikeyan et al., 2001; Cui et al., 2024) and reads as (Dassault Systèmes, 2024):

$$\Delta t_{\mathrm{unsat}} = \frac{1}{6\,D} \left(\Delta l_n\right)^2 = \frac{\gamma^w\, n}{6\, k^{r,wf}\, k^w} \frac{\partial S^w}{\partial s} \left(\Delta l_n\right)^2. \tag{6.125}$$

- Unsaturated flow, extended for swelling: The additional consideration of swelling adds to the spatially and temporally varying conditions. Equation (6.125) must be expanded to include the relative permeability $k^{r,ws}$ induced by swelling and the aggregate porosity n^A:

$$\Delta t_{\mathrm{unsat},ws} = \frac{\gamma_w\, n^A}{6\, k^{r,ws}\, k^{r,wf}\, k^w} \frac{\partial S^w}{\partial s} \left(\Delta l_n\right)^2. \tag{6.126}$$

- Fully saturated flow (in consolidation analysis): The critical time increment Δt_{sat} is estimated based on an analytical expression of the one-dimensional consolidation problem of a homogeneous elastic saturated porous medium (Vermeer and Verruijt, 1981; Dassault Systèmes, 2024):

$$\Delta t_{\text{sat}} = \frac{\gamma^w}{6 M_{\text{el}}\, k^w} \left(\Delta l_n\right)^2 , \tag{6.127}$$

  wherein M_{el} is the constraint modulus of the soil, which is approximated from the current material tangent stiffness $\boldsymbol{D}$ assuming incremental linear elasticity, see Equation (6.119).

The representative hydraulic conductivity k^w and representative nodal distance Δl_n in Equations (6.125) – (6.127) are defined consistently with the governing direction, i.e. parallel to the pore water pressure gradient for $\Delta t_{\text{unsat}(,ws)}$ (similar to Equation (6.120)) or parallel to the solid velocity for Δt_{sat}:

$$k^w = \frac{d_i}{\|d\|} \frac{K^s_{ij}\, \gamma^{wf}}{\mu^{wf}} \frac{d_j}{\|d\|}, \qquad \text{with} \quad d_i = \begin{cases} p^w_{,i} & \text{for } \Delta t_{\text{unsat}(,ws)}, \\ v^s_i & \text{for } \Delta t_{\text{sat}}. \end{cases} \tag{6.128}$$

For computation of Δl_n , first the characteristic element length Δl_e is evaluated with a projection of the coordinates x^n_j of all nodes n of the finite element in the governing direction:

$$\Delta l_e = \max_{k=1,\dots,n} \left(x^{(k)}_j \frac{d_j}{\|d\|} \right) - \min_{k=1,\dots,n} \left(x^{(k)}_j \frac{d_j}{\|d\|} \right), \quad \text{with} \quad d_j = \begin{cases} \bar{p}^w_{,j} & \text{for } \Delta t_{\text{unsat}(,ws)}, \\ \bar{v}^s_j & \text{for } \Delta t_{\text{sat}}, \end{cases} \tag{6.129}$$

and subsequently, the order of interpolation of the pore water pressure is considered:

$$\Delta l_n = \begin{cases} \Delta l_e & \text{for linear interpolation of } p^w, \\ \Delta l_e / 2 & \text{for quadratic interpolation of } p^w. \end{cases} \tag{6.130}$$

Δt_{unsat} and $\Delta t_{\text{unsat},ws}$ are evaluated for unsaturated conditions, i.e. if $\left|\dot{S}^e\right| > 0$ and $S^e \leq 0.999$, and Δt_{sat} is evaluated otherwise, however, only if a sufficiently large velocity of the solid phase, indicating a consolidation process ($v^s > 1 \times 10^{-4}$ m/s), is present. In any other cases, all critical time increments are set to zero. They are evaluated in every integration point of the respective element and averaged for output. Table 6.3 gives an overview of the corresponding element output variables.

6.5.6.2. Extended time stepping algorithm

In `numgeo`, a novel analysis type called *transient critical* has been introduced to ensure that a meaningful minimum time increment, based on the critical time increment Δt_{crit}, is considered at any time of the transient analysis. This approach enables continuous, convergence-based time stepping and prevents spurious hydraulic behaviour resulting from inadequate time increments, which could otherwise significantly affect the convergence and accuracy of hydro-mechanically coupled material responses. Moreover, it reduces the user's effort, as the quality of the time stepping becomes less dependent on the selection Δt_{min} and Δt_0. The minimum time increment Δt_{min} of the automatic time stepping algorithm in Equation (6.123) was redefined as:

$$\Delta t_{\text{min}} = f_{t_{\text{min}}} \Delta t_{\text{crit}} \tag{6.131}$$

Table 6.3.: Additional element output variables regarding the critical time increment for unsaturated and saturated flow.

Keyword	Variable	Remark
`DT-UNSAT`	$\frac{1}{n_{\mathrm{gp}}} \sum_{i=1}^{n_{\mathrm{gp}}} \left(\Delta t_{\mathrm{unsat}} \vert_i \right)$	Average value of the critical time increment of all integration points for unsaturated conditions (Equation (6.125))
`DT-UNSAT-SW`	$\frac{1}{n_{\mathrm{gp}}} \sum_{i=1}^{n_{\mathrm{gp}}} \left(\Delta t_{\mathrm{unsat},sw} \vert_i \right)$	Average value of the critical time increment of all integration points for unsaturated conditions with consideration of swelling (Equation (6.126)). Only available in `up-sw` elements.
`DT-SAT`	$\frac{1}{n_{\mathrm{gp}}} \sum_{i=1}^{n_{\mathrm{gp}}} \left(\Delta t_{\mathrm{sat}} \vert_i \right)$	Average value of the critical time increment of all integration points for saturated conditions (Equation (6.127))

wherein Δt_{crit} is the critical time increment of the current calculation step, determined within `numgeo`, and $f_{t_{\mathrm{min}}}$ is a factor, which enables scaling of the critical time increment within the automatic time stepping. It must be defined by the user in the input file in addition to the initial time increment Δt_0, the overall step time t_{step} and the maximum time increment Δt_{max}. The input of the novel analysis type takes the following form:

```
*Transient-critical
Δt0 , tstep , f_tmin , Δtmax
```

The defined maximum time increment is not a hard upper limit at all times. If the critical time increment is smaller than the defined maximum time increment, the latter acts as an upper ceiling to prevent uncontrolled increase of the time increment (similar to as in normal transient analysis). However, if the critical time increment exceeds this ceiling, the latter is ignored and the time step is increased according to the critical value. Equation (6.123) changes to:

$$\Delta t = \begin{cases} \max\left(\min\left(1.25\,\Delta t^i,\, \Delta t_{\mathrm{max}}\right),\, \Delta t_{\mathrm{min}}\right) & \text{if: } n_j < 7, \\ \max\left(0.75 \Delta t^i, \Delta t_{\mathrm{min}}\right) & \text{if: } n_j > 12, \\ \max\left(\Delta t^i, \Delta t_{\mathrm{min}}\right) & \text{else.} \end{cases} \tag{6.132}$$

The critical time increment Δt_{crit} of the respective calculation step is decisive for the subsequent calculation step and is governed by the critical element el_{crit} of the FE model. For unsaturated flow, the critical element el_{crit} is the one that exhibits the most significant increment in pore water pressure for the subsequent calculation step. Otherwise, it is the element with the largest critical time increment. The critical element el_{crit} is identified in the following manner:

1. In each element, the maximum value of the critical time increments Δt_{sat} and $\Delta t_{\mathrm{unsat}(,ws)}$ in all integration points is determined, and the critical time increment $\Delta t^{el}_{\mathrm{crit}}$ of the element is returned:

$$\Delta t^{el}_{\mathrm{crit}} = \begin{cases} \max\limits_{k=1,\ldots,n_{\mathrm{gp}}} \left(\Delta t_{\mathrm{unsat}(,ws)} \big\vert_k \right), & \text{if } \left(\left| \dot{S}^e \right| > 0 \ \wedge \ S^e \leq 0.999 \right), \\ \max\limits_{k=1,\ldots,n_{\mathrm{gp}}} \left(\Delta t_{\mathrm{sat}} \vert_k \right), & \text{else if } v^s > 1 \times 10^{-4}\mathrm{m/s}, \\ 0, & \text{else.} \end{cases} \tag{6.133}$$

Furthermore, for unsaturated flow, the critical increment of pore water pressure is computed in each integration point of an element based on the maximum value of $\Delta t_{\mathrm{unsat},(ws)}$ and the corresponding rate of pore water pressure $\mathrm{d}p^w/\mathrm{d}t$:

$$\Delta p^{w,el}_{\mathrm{crit}} = \begin{cases} \left(\max\limits_{k=1,\dots,n_{\mathrm{gp}}} \left(\dfrac{\mathrm{d}p^w}{\mathrm{d}t}\, \Delta t_{\mathrm{unsat}} \right) \Big|_k \right), & \text{if } \left(\left| \dot{S}^e \right| > 0 \ \wedge \ S^e \leq 0.999 \right), \\ 0, & \text{else.} \end{cases} \tag{6.134}$$

2. The critical element el_{crit} is identified in the element assembly based on the largest critical increment of pore water pressure $\Delta p^{w,el}_{\mathrm{crit}}$, if unsaturated flow takes place anywhere in the model, or else based on the largest critical time increment $\Delta t^{el}_{\mathrm{crit}}$:

$$el_{\mathrm{crit}} = \begin{cases} \underset{i=1,\dots,n_{\mathrm{elem}}}{\arg\max} \left(\Delta p^{w,el}_{\mathrm{crit}} \Big|_i \right), & \text{if } \Delta p^{w,el}_{\mathrm{crit}} > 0, \\ \underset{i=1,\dots,n_{\mathrm{elem}}}{\arg\max} \left(\Delta t^{el}_{\mathrm{crit}} \Big|_i \right), & \text{else.} \end{cases} \tag{6.135}$$

3. The critical time increment $\Delta t^{el_{\mathrm{crit}}}_{\mathrm{crit}}$ of the critical element is returned as the significant critical time increment of the whole FE model, thus $\Delta t_{\mathrm{crit}} = \Delta t^{el_{\mathrm{crit}}}_{\mathrm{crit}}$ and applied in Equation (6.131). For a vanishing critical time increment ($\Delta t_{\mathrm{crit}} = 0$), the previous time increment is recovered to avoid empty quantities after evaluation of Equation (6.131).

The critical time increment Δt_{crit} of the whole FE model and the respective element number el_{crit} are provided in the statistics file of the `numgeo` calculation. Furthermore, the critical time increment and the critical increment of pore water pressure are added as element output in addition to the variables already introduced in Table 6.3. Table 6.4 provides an overview of the additional element output variables. The element output is not only available for the novel analysis type, but also available for the normal transient analysis procedure. In the latter, however, it is solely for the purpose of output and evaluating the simulation results, and is not employed in the time-stepping algorithm.

Table 6.4.: Additional element output variables regarding the critical time increment and critical pore water pressure element increment.

Keyword	Variable	Remark
`DELTA-T`	$\Delta t^{el}_{\mathrm{crit}}$	Critical time increment of the element (Equation (6.133))
`DELTA-PW`	$\Delta p^{w,el}_{\mathrm{crit}}$	Critical increment of pore water pressure (Equation (6.134))

6.6. Discussion and performance of the implementation

In this section, the implementation of the finite element library based on the extended TPM and the required constitutive models in `numgeo`are discussed. Particular attention is given to the numerical validation of the element performance and the novel time-stepping procedure for transient infiltration problems. The objective is to verify the correctness and robustness of the implementation and to establish a solid numerical basis for subsequent simulations of swelling tests in boundary value problems. First, the implementation of the mass transport model and relative permeability model due to swelling is examined in single-element simulations using the complete numerical framework including the finite elements based on the extended TPM and

the novel hydro-mechanical constitutive model. Thereafter, the capability of the `up-sw` element library to reproduce unsaturated flow in porous media decoupled from the mechanical constitutive model is demonstrated. An analytical solution of a one-dimensional infiltration problem serves as a reference benchmark. Subsequently, a comparative analysis under relevant hydraulic boundary conditions is presented, comparing the performance of the `up-sw` elements and the novel time-stepping procedure with corresponding formulations in the commercial FE software Abaqus Standard (Dassault Systèmes, 2024). Finally, the numerical aspects of the implementation „Hypoplasticity for expansive soils“ are examined, with emphasis on the integration of the constitutive equations and the evaluation of the consistent Jacobians within the coupled hydro-mechanical framework.

6.6.1. Performance of the mass transport model and relative permeability model due to swelling

The one-dimensional response of the proposed mass transport model for idealized loading paths based on experimental results was presented in Section 3.2.6. Herein, the performance of the mass transport model in the `up-sw` element library and the relative permeability model is shown for coupled FE simulations with consideration of the mechanical constitutive model in single element simulations. The parameters corresponded to those previously applied in the discussion and were given in Tables 5.2 and 5.3. The unsaturated relative permeability model of Fredlund & Xing was used in a consistent manner with the hydraulic model. The additionally required parameters were $k^w_{\min} = 1 \times 10^{-6}$ and $s_i = 5$ kPa (see Equations (6.32) and (6.36)). For the mass transfer model, the parameters $\phi^{\max} = 0.88$ and $c_\phi = 10$ were applied. The reference permeability was $K^s_{\text{ref}} = 1 \times 10^{-15}$ m^2 at $n_{\text{ref}} = 0.288$. The single-element representation for the simulations corresponds to that used for the discussion of the mechanical constitutive model in Figure 5.18. One axisymmetric rectangular element with linear interpolation and selective reduced integration was used. The simulations consisted of a geostatic step and a transient infiltration step. Specimen preparation giving the initial conditions in Table 6.5 was simulated separately. For infiltration, the pore water pressure was described as $\Delta p^w = 0$ at the bottom and top nodes at either vertically unconfined conditions or constant volume conditions with additional consideration of a small vertical load.

Table 6.5.: Initial conditions for single element simulations of vertically unconfined and constant volume swelling.

p_{d0} in kPa	e_{d0}	$\sigma_{22,0}$ in kPa	K_0	e_0	$S^w_0 = S_{\text{ref}}$	p^w_0 in kPa
5684	0.377	-35	2.9	0.383	0.126	-106700

Figures 6.3 and 6.4 show the simulation results of vertically unconfined and constant volume swelling. On the left-hand side, the mechanical material response in terms of void ratio e and vertical net stress σ_{22} is shown. In the centre, the evolution of the swelling water ratio ϕ and the volume fractions of the solid, air, water, free water and swelling water are displayed, thus ϕ^α for $\alpha = \{s, a, w, wf, ws\}$. The maximum ratio $\phi^{\max}$ is indicated as well. On the right-hand side the evolution of the contributions of the relative permeabilities are presented. Therein, the relative permeability for unsaturated soils $k^{r,wf}$ is drawn in a dash-dotted line and the relative permeability due to swelling $k^{r,ws}$ as a dashed line. For the latter, the two components according

to Equation (3.70) are distinguished: the contribution by the change in volume (purple) and the contribution by the attachment of swelling water (green).

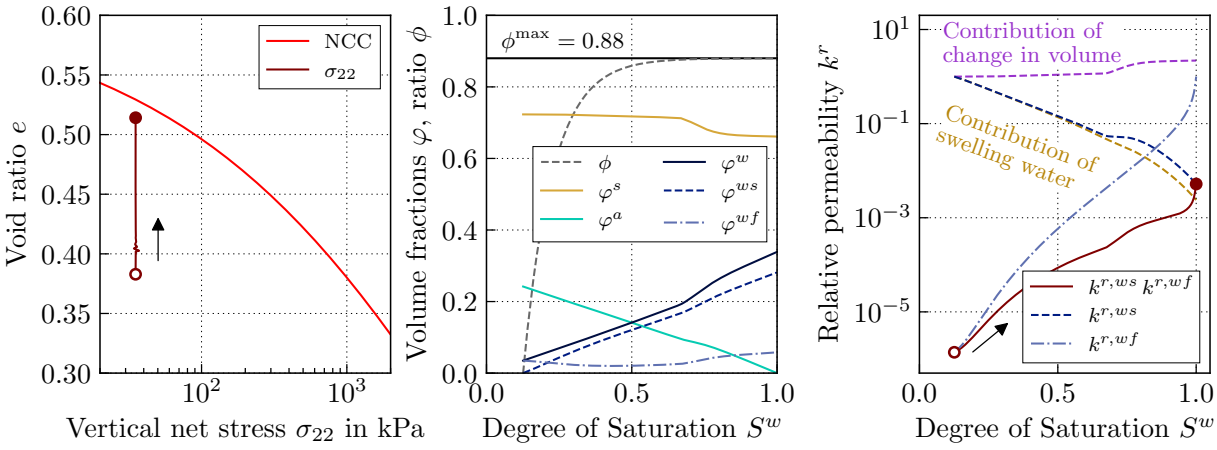

Figure 6.3.: Performance of the mass transfer and relative permeability model for vertically unconfined swelling in single-element simulations.

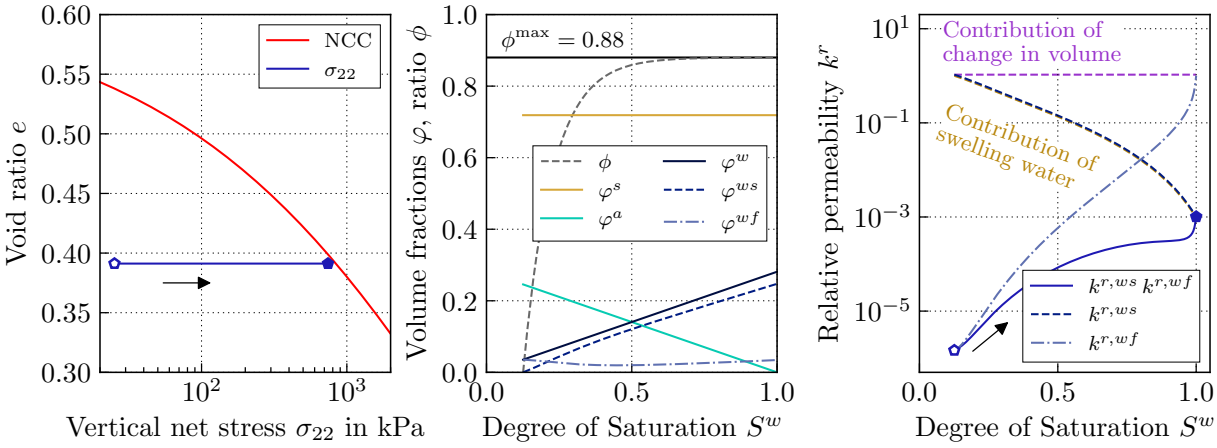

Figure 6.4.: Performance of the mass transfer and relative permeability model for constant volume swelling in single-element simulations.

For vertically unconfined swelling, the void ratio increased upon infiltration at constant vertical net stress (Figure 6.3) and for constant volume swelling, the stress increased at constant void ratio (Figure 6.4). In both simulations, the volume fraction of pore air decreased and the total volume fraction of water increased due to the infiltration. The mass transport mechanism developed upon saturation until the maximum ratio ϕ was reached. As a result the volume fraction of the swelling water increased. Due to the expansion for vertically unconfined swelling (Figure 6.3), the volume fraction of the solid decreased with increasing degree of saturation while it was constant upon the evolution of swelling pressure at constant volume conditions (Figure 6.4). The influence of swelling on the permeability can also be assessed in Figures 6.3 and 6.4. In both simulations, the swelling-induced relative permeability was initially $k^{r,ws} = 1$, whereas the unsaturated relative permeability was $k^{r,wf} = k^w_{\text{min}} = 10^{-6}$. As saturation increased, both processes occurred simultaneously: the unsaturated relative permeability increased up to $k^{r,wf} = 1$ at full saturation ($S^w = 1$), while the swelling-induced relative permeability decreased. For vertically unconfined conditions, the swelling-induced decrease was less pronounced due to the expansion, which is evident as the contribution of change in volume in both Figures

6.3 and 6.4 (purple dashed line). Consequently, the apparent permeability at the end of the simulation $K^{s,\mathrm{VU}} = 6.2 \times 10^{-18}$ m^2 was slightly higher than in the simulation with constant volume conditions $K^{s,\mathrm{CV}} = 1.3 \times 10^{-18}$ m^2. Thus, the simulation results in terms of permeability are consistent with the experimentally observed trends.

6.6.2. Numerical validation of element performance and time-stepping in infiltration problems

6.6.2.1. Analytical solution of column infiltration

Srivastava and Yeh (1991) proposed an analytical solution for the transient pore water pressure distribution during one-dimensional, vertical infiltration in a homogeneous soil column toward the water table. Herein, a soil layer with a total height l and initial hydrostatic pore water pressure distribution, infiltrated with a constant infiltration rate q from the top, was considered. An exponential approach was chosen for the relative permeability model and hydraulic model of the soil layer:

$$k^{r,w} = e^{-\zeta s} \quad \text{and} \quad S^w = \left(1 - S^{wr}\, e^{-\zeta s}\right) + S^{wr}, \tag{6.136}$$

wherein ζ is a material parameter (in kPa^{-1}.) The solution for the suction $s = -p^w$ at an elevation z and time t was proposed as follows:

$$s = \frac{1}{\zeta} \ln B, \tag{6.137}$$

wherein:

$$\begin{aligned} B =& \frac{q}{K^w} - \left(\frac{q}{K^w} - 1\right) e^{-z^*} \\ &- \frac{4q}{K^w}\, e^{(L^* - z^*)/2}\, e^{-t^*/4} \sum_{i=1}^{\infty} \frac{\sin\left(\lambda_i z^*\right) \sin\left(\lambda_i\, L^*\right) e^{-\lambda_i^2\, t^*}}{1 + L^*/2 + 2\lambda_i^2\, L^*}, \\ t^* =& \frac{n\, \zeta\, K^w\, t}{1 - S^{wr}}, \quad z^* = s z \quad \text{and} \quad L^* = s\, L. \end{aligned} \tag{6.138}$$

In Equation (6.138), λ_i is the i^{th} root of the solution of the characteristic equation:

$$\tan\left(\lambda L^*\right) + 2\ \lambda \stackrel{!}{=} 0. \tag{6.139}$$

To evaluate the analytical solution at specified heights and times, the roots λ_i of the characteristic equation (6.139) were determined. Only positive and real values and all roots in the specified range were considered. Investigations on the number of roots showed that the quality of the analytical prediction did not improve for numbers greater than a couple 100. A range of $0 < x < 500$ was considered here, yielding a number of 795 roots. Abed and Sołowski (2017) showed a back-calculation of the analytical formulation for a specific infiltration problem, which was adopted for simulations with the `up-sw` element library in `numgeo`. An axisymmetric soil column with a total height of $h = 1.0$ m and radius of $r = 0.1$ m was infiltrated from the top with a rate of $q = 0.005$ m/day $= 5.787 \times 10^{-8}$ m/s and modelled for a duration of 10 days. The ground water table was located at the bottom with a hydrostatic pore water pressure distribution above. The saturated hydraulic conductivity of the soil was $k^w = 0.1$ m/day, which corresponds to $K^s = 1.157 \times 10^{-13}$ m^2. The residual degree of saturation was $S^{wr} = 0.23$. The

porosity was $n = 0.400$, corresponding to a void ratio of $e = 0.667$. The material parameter for the hydraulic and relative permeability model in Equation (6.136) was $\zeta = 5.0\ \mathrm{m}^{-1}$. Within the relative permeability model, a minimum value of $k^w_{\mathrm{min}} = 1 \times 10^{-3}$ was used. Fig. 6.5 shows the soil water retention curve and relative water permeability following Equation (6.136) compared to more widely used approaches.

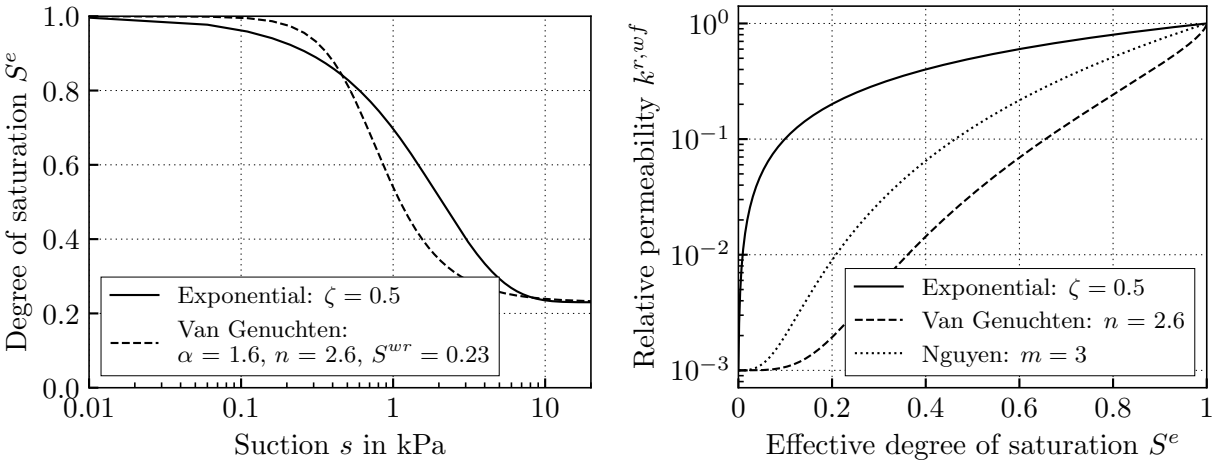

Figure 6.5.: Soil water retention curve and water relative permeability after Equation (6.136).

For the solid, a linear elastic constitutive model with a Young's modulus of $E = 1 \times 10^5$ kPa and a Poisson's ratio of $\nu = 0.4$ was chosen. This problem concerned fluid flow only and the degrees of freedom for the solid displacement u_1 and u_2 of all nodes were constrained during the simulation. Thus, as no soil deformation was considered, this choice of the mechanical constitutive model was arbitrary. The simulation was carried out in two steps: (1) the static geostatic step and (2) the transient infiltration step, wherein the flow boundary condition at the upper surface of the column was prescribed.

The simulations were carried out with three different FE meshes, which are displayed with the initial pore water pressure distribution on the left-hand side of Figure 6.6. The standard mesh consisted of 30 elements in height, whereas a coarser (10 elements in height) and finer (66 elements in height) mesh were studied additionally. For visualisation of the results, the analytical solution was always evaluated with the same resolution as the FE mesh. The right-hand side of Figure 6.6 shows the simulation results using these three meshes and the u4p4-stab-ax-red-sw-element. The pore water distribution $p^w = f(t, z)$ is shown for $t = \{0, 0.1, 0.3, 0.5, 1.0, 3.0, 10.0\}$ days at all corner nodes analogously to the validation done by Abed and Sołowski (2017).

To compare the simulation results with the analytical solution, the relative Root Mean Squared Error (RMSE) was evaluated. It quantifies the average deviation of the simulation from the exact analytical values, with lower RMSE indicating higher accuracy. Note that the computed RMSE depends on the number and distribution of support points used for the evaluation. Coarser meshes, with fewer evaluation points, smooth out local deviations, whereas finer meshes include more evaluation points and thus capture additional discrepancies, which can increase the global error measure. For a meaningful comparison between different meshes, the simulation results from all three simulations in Figure 6.6 were evaluated with the identical number of evaluation points from the coarse mesh. The uppermost node was excluded from error calculation. Overall excellent agreement between the analytical solution and simulation in `numgeo` is evident. Disre-

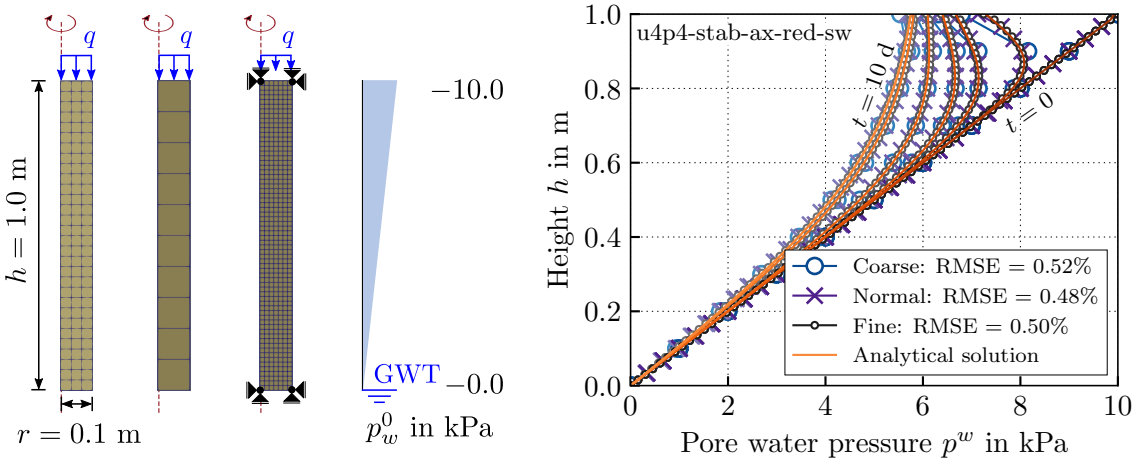

Figure 6.6.: FE model and pore water pressure distribution (right) and simulation results versus analytical solution (right) for vertical infiltration of a soil column using three different meshes.

garding the uppermost node, all three meshes show the same distribution of pore water pressure over height at different times and exhibit a negligibly small RSME.

The simulation with the standard mesh was repeated with different element types, whose results are shown in terms of the pore water pressure distribution over the height of the column in Figure 6.7. Taylor-Hood elements (u8p4-) and linear (u4p4-) and quadratic (u8p8-) equal order

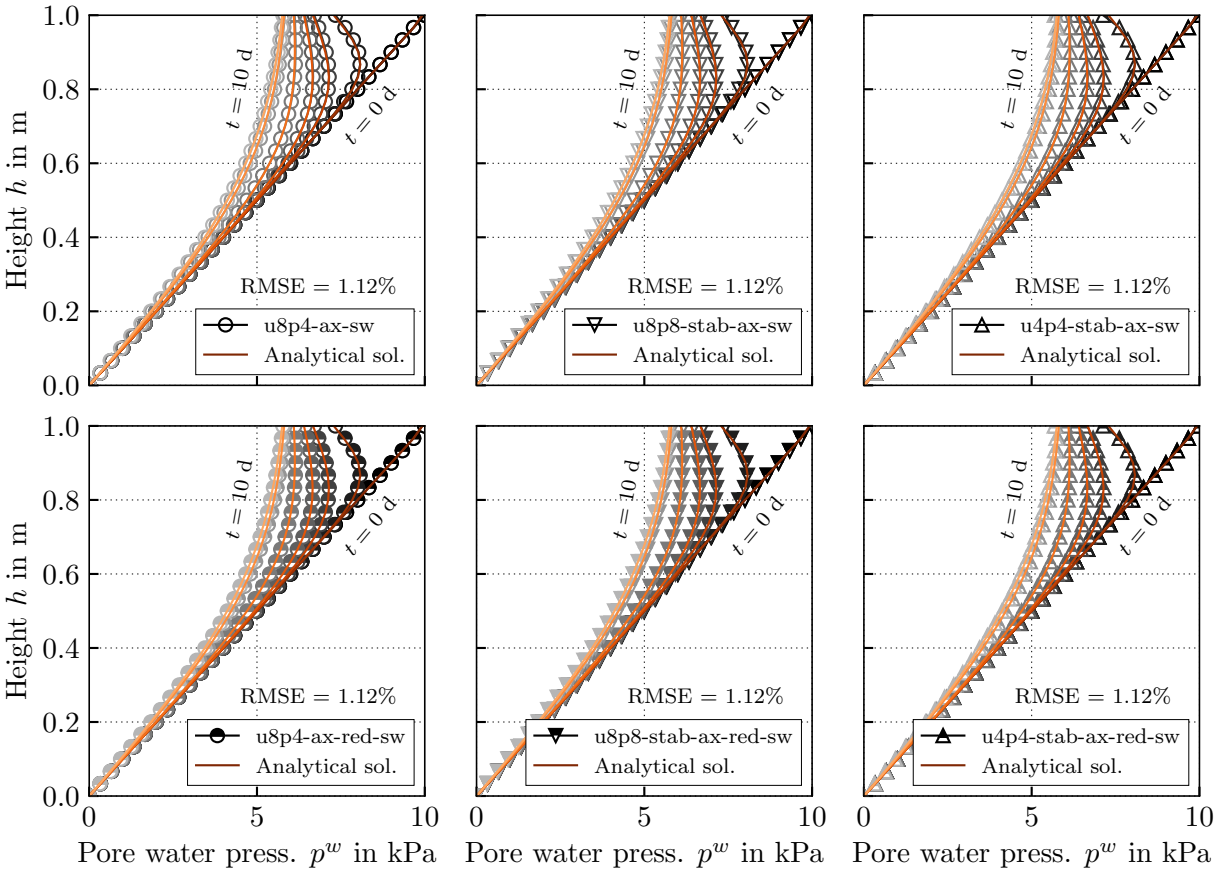

Figure 6.7.: Numerical results versus analytical solution for vertical infiltration of a soil column using different element types.

elements with full and reduced integration each were considered. In the upper row of Figure 6.7, the results using fully integrated elements are shown with white filled markers and in the lower row, the results using the corresponding reduced elements are shown. The RMSE was computed for all simulations based on all corner nodes of the normal mesh as evaluation points. With increasing number of nodes, the deviations for the RMSE are not only sampled more frequently, but also arise at additional locations between the support points and as a result, the RMSE in Figure 6.7 was slightly higher than in Figure 6.6. Overall, the results obtained with different element types showed no significant differences. Minor deviations from the analytical solution are observed for the fully integrated linear elements at the upper node, where infiltration progressed marginally faster in the simulation. Overall, however, these deviations are negligible, and it can be concluded that the various element types performed equally well.

The simulation of the infiltration was repeated with two variations: (1) with the saturated permeability reduced by one order of magnitude, hence $k^w = 0.01$ m/day, which corresponds to $K^w = 1.157 \times 10^{-14}$ m^2 and (2) with the infiltration rate increased by one order of magnitude, hence $q = 0.05$ m/day $= 5.787 \times 10^{-7}$ m/s. All other initial and boundary conditions each remained. The analytical solution was evaluated with the adapted conditions as well. Again, the results are shown in terms of the pore water pressure distribution over the height of the column for the simulations and analytical solution in Figure 6.8. Therein the evaluation was done for arbitrary points in time. With reduced permeability, the infiltration needed longer time to reach an equilibrium state while the higher infiltration rate yielded the opposite trend. The calculated RSME indicates very good agreement between the simulation results and the analytical solution.

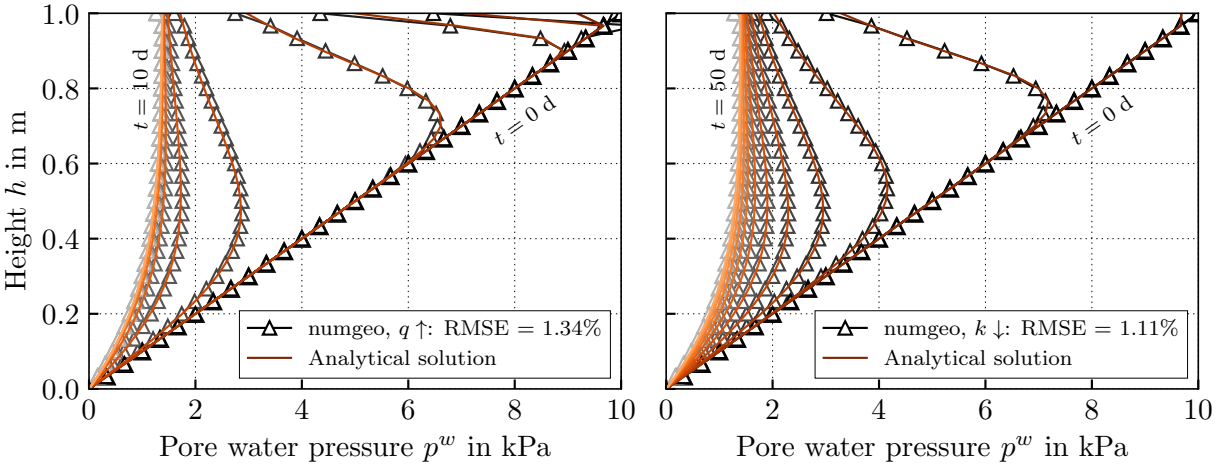

Figure 6.8.: Numerical results versus analytical solution for vertical infiltration of a soil column with increased infiltration rate (left) and reduced permeability (right).

Application of the novel analysis type 'transient-critical'

In addition, the novel analysis type *transient-critical* was applied to the infiltration problem. The coarse mesh was selected for the simulation to facilitate understanding of the critical element based on the maximum increment of the pore water pressure occurring during infiltration. $f_{t_{\min}} = 1.0$ was chosen, thus the global time increment Δt must never undercut the critical time increment Δt_{crit} (see Section 6.5.6.2). The maximum time increment was $\Delta t_{\max} = 500$ s. Figure 6.9 shows the results in terms of pore water pressure distribution over the height of

the column for the simulations and analytical solution (left) and the evolution of the critical pore water pressure increment (centre) and critical time increments (right) versus calculation increments. The elements are numbered in descending order from top to bottom, wherein the element number 10 is the uppermost element, at whose upper edge the infiltration boundary conditions is applied. Only the critical elements are depicted here and only 70 calculation increments (corresponding to $t \approx 1.70$ d) are shown, as element number 7 remained the critical element in the further course of the calculation.

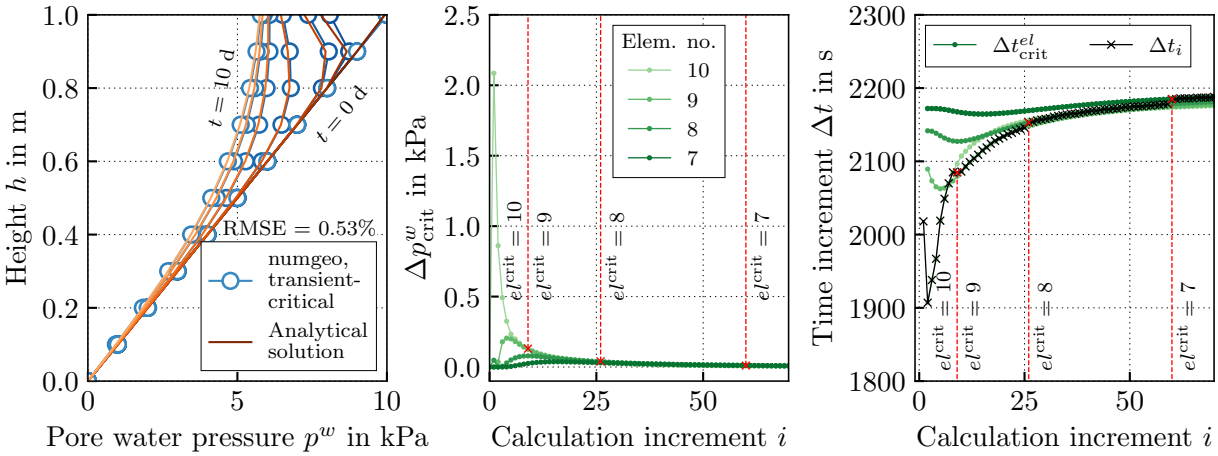

Figure 6.9.: Application of the novel analysis type *transient-critical* to vertical infiltration of a soil column: numerical results and analytical solution (left) and critical pore water pressure increment (centre) and time increment (right) over the first 70 calculation increments.

The centre plot of Figure 6.9 displays red vertical lines and x-markers denoting the instances at which the critical increment of pore water pressure Δp^w_{crit} arose in a different element. These lines are likewise represented in the right-hand side plot. First, the uppermost element number 10 was critical and as infiltration progressed, the critical element moved downward through the column ($\rightarrow 9 \rightarrow 8 \rightarrow 7$), determined by the largest Δp^w_{crit}. It becomes evident, that the global time increment during infiltration Δt evolved corresponding with the critical time increment of the critical element $\Delta t^{el_{\text{crit}}}_{\text{crit}}$. Overall, the critical time increment increased with advancing calculation increment, thus progressing infiltration. The maximum time increment is not decisive in this case. The computed RSME for the simulation shown in Figure 6.9 corresponds to that from the simulation with the coarse mesh shown in Fig. 6.6. The results demonstrate that the novel analysis type performs as intended, without any loss of predictive accuracy relative to the analytical solution, when compared with the simulations performed using the standard transient analysis.

6.6.2.2. Comparative analysis under relevant hydraulic boundary conditions

In this section, the infiltration behaviour of the `up-sw` element library implemented in `numgeo` is evaluated for hydraulic boundary conditions with parameter magnitudes representative of expansive soils. A comparison of simulation results obtained with `numgeo` and Abaqus Standard allows to assess the general predictive capability of the implementation. The suitability of different element formulations for highly non-linear infiltration processes is evaluated with regard to the order of interpolation of pore water pressure and discretisation. The limitations and

influence of the time-stepping procedure are demonstrated. Swelling is not considered, neither in the mechanical constitutive model, which is chosen as linear elastic, nor in the element formulation, as mass transfer is omitted and the focus is placed solely on the hydraulic response and numerical stability of the coupled `up-sw` formulation. Effective stresses using $\chi = S^e$ are considered. Identical mesh, material parameters for the mechanical and hydraulic behaviour, and boundary and initial conditions enable a direct comparison between both software packages.

The FE model represents an oedometric soil specimen ($h = 2$ cm, $b = 5$ cm), modelled in front view using plane strain elements. Infiltration occurred solely from the bottom through a pore water pressure boundary condition on the outer nodes of a porous stone. Regardless of the soil mesh, the porous stone was discretised with four elements over its height to allow uniform application of the infiltration boundary conditions and to prevent numerical instabilities such as pressure oscillations at the model edge. Figure 6.10 shows the FE model for a mesh with $n_{el} = 10$ elements over height for the soil, corresponding to a representative nodal distance (pore water pressure as the relevant degree of freedom) of $\Delta l_{n,\text{quadratic}} = 1$ mm and $\Delta l_{n,\text{linear}} = 2$ mm, and the initial distribution of pore water pressure.

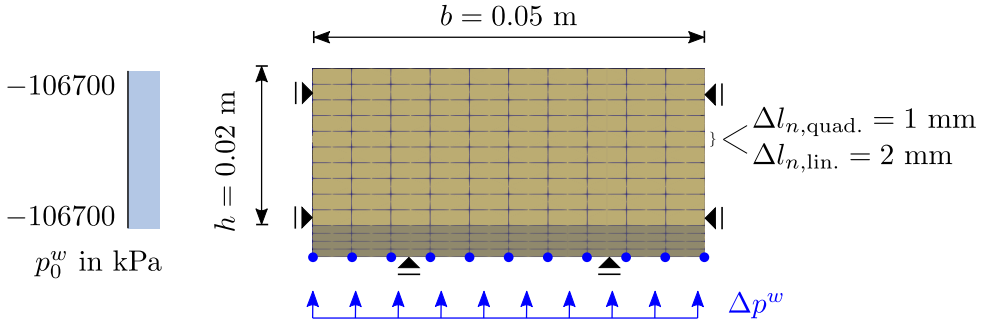

Figure 6.10.: Finite element model of the infiltration BVP: Exemplary mesh for the soil (10 elements in height, beige) and porous stone (grey), initial distribution of pore water pressure p_0^w and infiltration boundary condition Δp^w at the bottom nodes.

Further discretisation of the model were with $n_{el} = 20$ elements in height ($\Delta l_{n,\text{quadratic}} = 0.5$ mm, $\Delta l_{n,\text{linear}} = 1$ mm) and with $n_{el} = 40$ elements in height ($\Delta l_{n,\text{linear}} = 0.5$ mm).

For the soil the initial conditions of the simulation and the material parameters of the linear-elastic mechanical model and the hydraulic and relative permeability model after Fredlund et al. (1994) are given in Tables 6.6 and 6.7, respectively. The permeability of the soil was $K = 1.0 \times 10^{-15}$ m^2. For the unsaturated relative permeability a minimum value of $k^w_{\text{min}} = 1 \times 10^{-4}$ was applied and the lower integration limit was chosen as $s_i = 5$ kPa. Figure 6.11 shows the hydraulic model (left) and the relative permeability model (right), which were applied for the soil.

In Abaqus, the hydraulic and relative permeability models must be defined using tabular input. These tables were generated with high resolution to accurately capture the highly non-linear behaviour of the models. However, since the internal interpolation scheme used by Abaqus for tabular data is not publicly documented, differences in the simulated infiltration behaviour cannot be ruled out. Linear elasticity with high stiffness was assigned to the porous stone, together with a permeability of $K^s = 1 \times 10^{-12}$ m^2. Its hydraulic behaviour was described using the van Genuchten model van Genuchten (1980), with parameters representative of a highly

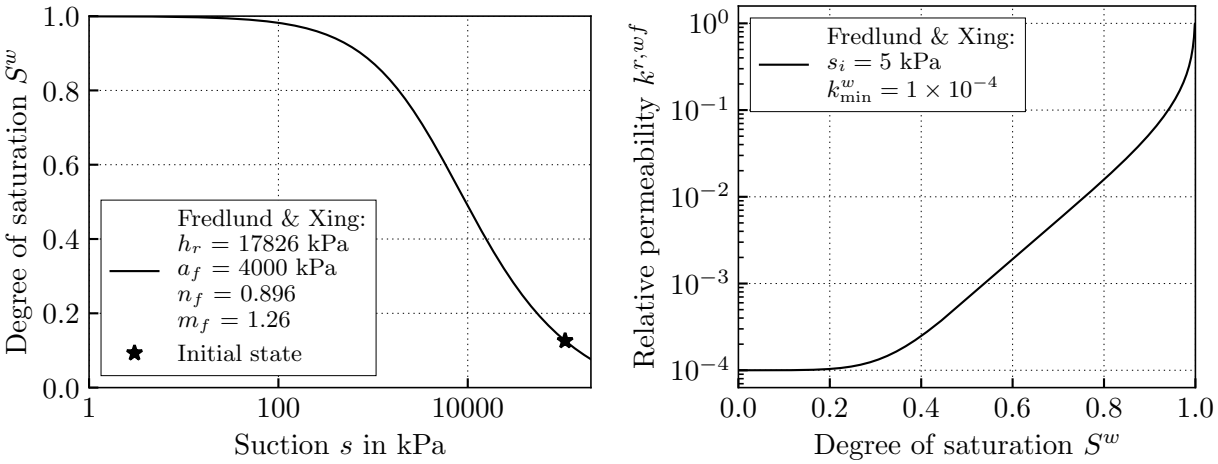

Figure 6.11.: Soil water retention curve and relative water permeability after Fredlund et al. (1994) for infiltration benchmark.

permeable soil and without a relative permeability model. The initial state corresponded to that of the soil apart from a higher initial void ratio of $e = 1.0$. The initial conditions and material properties are gathered in Tables 6.6 and 6.8, respectively. The analysis consisted of two steps: (1) the geostatic step ($t_{\text{step}} = 1$ s) and (2) the infiltration step ($t_{\text{step}} = 400$ s). The infiltration was prescribed as an increment of pore water pressure Δp^w at the bottom nodes via a ramp function spanning 10 seconds. For the infiltration step, the analysis types 'consolidation' and 'transient' were applied in Abaqus and `numgeo` respectively.

Table 6.6.: Initial state in comparative infiltration simulations in numgeo and Abaqus Standard.

e_0	p_0^w in kPa	S_0^w	$\sigma_{22,0}$ in kPa	K_0
0.3834 (soil), 1.0 (porous stone)	-106700	0.126	-13500	0.667

Table 6.7.: Material parameters for the soil in comparative infiltration simulations in numgeo and Abaqus Standard.

Mechanical model		Hydraulic and rel. permeability model			
E in kPa	ν	h_r in kPa	a_f in kPa	n_f	m_f
1×10^6	0.4	17826	4000	0.896	1.26

Table 6.8.: Material parameters for the porous stone in comparative infiltration simulations in numgeo and Abaqus Standard.

Mechanical model		Hydraulic model	
E in kPa	ν	α in kPa^{-1}	n
1×10^{10}	0.3	0.383	1.377

For the infiltration step, identical nominal time-stepping parameters were applied in both software packages. However, this does not guarantee numerical equivalence, since the underlying algorithms for adaptive time-stepping may differ. To ensure a consistent definition of the initial time step Δt_0 and minimum time increment $\Delta t_{\min}$, Equation (6.125) was evaluated for different characteristic nodal distances ($\Delta l_n = \{0.5, 1.0, 2.0\}$ mm) and material parameters applied in the simulations. The evolution of the critical time increment for unsaturated flow Δt_{unsat} is shown versus the degree of saturation in Figure 6.12. The critical time-increment is not constant and

proportional to the square of the element length. Three values are noted for each Δl_n: (i) the maximum time increment, corresponding to the minimum diffusion coefficient ($\Delta t_{D_{\min}}$), (ii) the time increment corresponding to the mean value of the diffusion coefficient ($\Delta t_{D_{\text{mean}}}$) and (iii) the time increment corresponding to the initial diffusion coefficient (Δt_{D_0}). The difficulty of selecting a suitable value is evident from the wide range of orders in magnitude for each characteristic nodal distance.

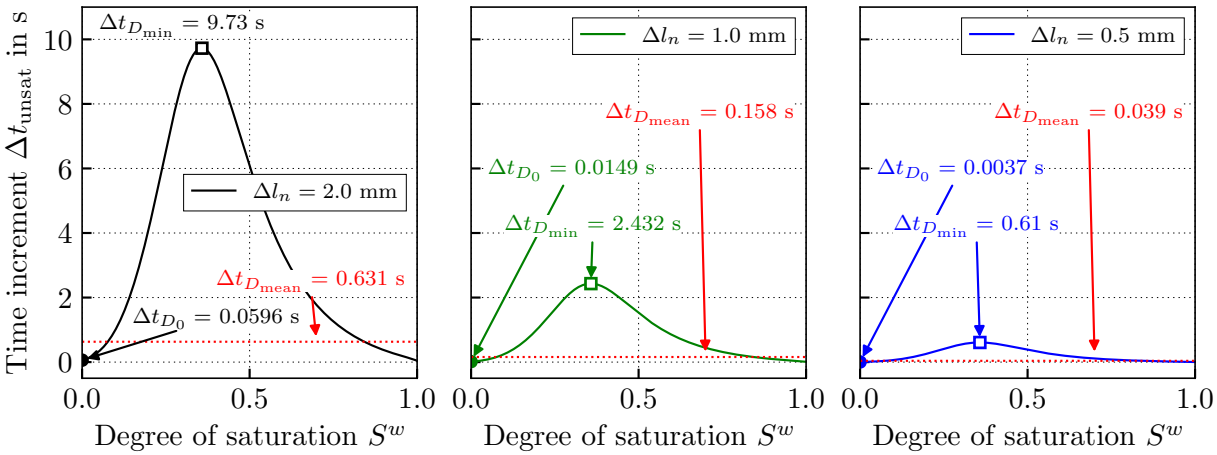

Figure 6.12.: Evaluation of Equation (6.125) for the critical time increment Δt_{unsat} depending on characteristic nodal distance with three distinctive values given for the initial (D_0), minimum ($\Delta t_{D_{\min}}$) and average ($\Delta t_{D_{\text{mean}}}$) diffusion coefficient.

Comparison of different element formulations in numgeo and Abaqus

Direct comparison between numgeo and Abaqus is only meaningful for the same element types and thus Taylor-Hood (TH) elements, namely u8p4-sw(-red) and CPE8P(R), and linear equal order elements with reduced integration, namely u4p4-stab-red and CPE4PR, were compared. Note that in `numgeo`, selected higher integration applies for the degree of freedom of pore water in the reduced formulation of the linear equal order element, however, not for the solid displacement. The characteristic nodal distance $\Delta l_n = 2$ mm was identical for all three element types for the same mesh ($n_{el} = 10$). The number of integration points agrees between the u8p4-red- and u4p4-stab-elements. The critical time increment corresponding to the initial state ($\Delta t_{\text{crit}} = \Delta t_{D_0} = 0.0596$, see Figure 6.12 left) was applied to prioritise simulation convergence over potential instabilities. The maximum time increment was chosen as $\Delta t_{\max} = 10$ s.

The results are shown in Figure 6.13 in terms of the evolution of pore water pressure, degree of saturation and the vertical component of the Darcy velocity, hence in direction of flow, versus time. The pore water pressure is nodal output (only visualised at the corner nodes) and the degree of saturation and Darcy velocity are element output. The results of simulations in `numgeo` are depicted in solid lines, whereas for results from Abaqus dashed lines are used. The colour gradient indicates elements on the symmetry axis from the bottom (dark) to the top (bright) of the model.

The simulation results using the fully integrated TH element (u8p4-sw / CPE8P) in the first row of Figure 6.13 show excellent agreement between `numgeo`and Abaqus. The mixed interpolation ensured stable up-coupling, minimized pore water pressure oscillations and offered a good resolution for unsaturated flow due to its high number of integration points. However, some

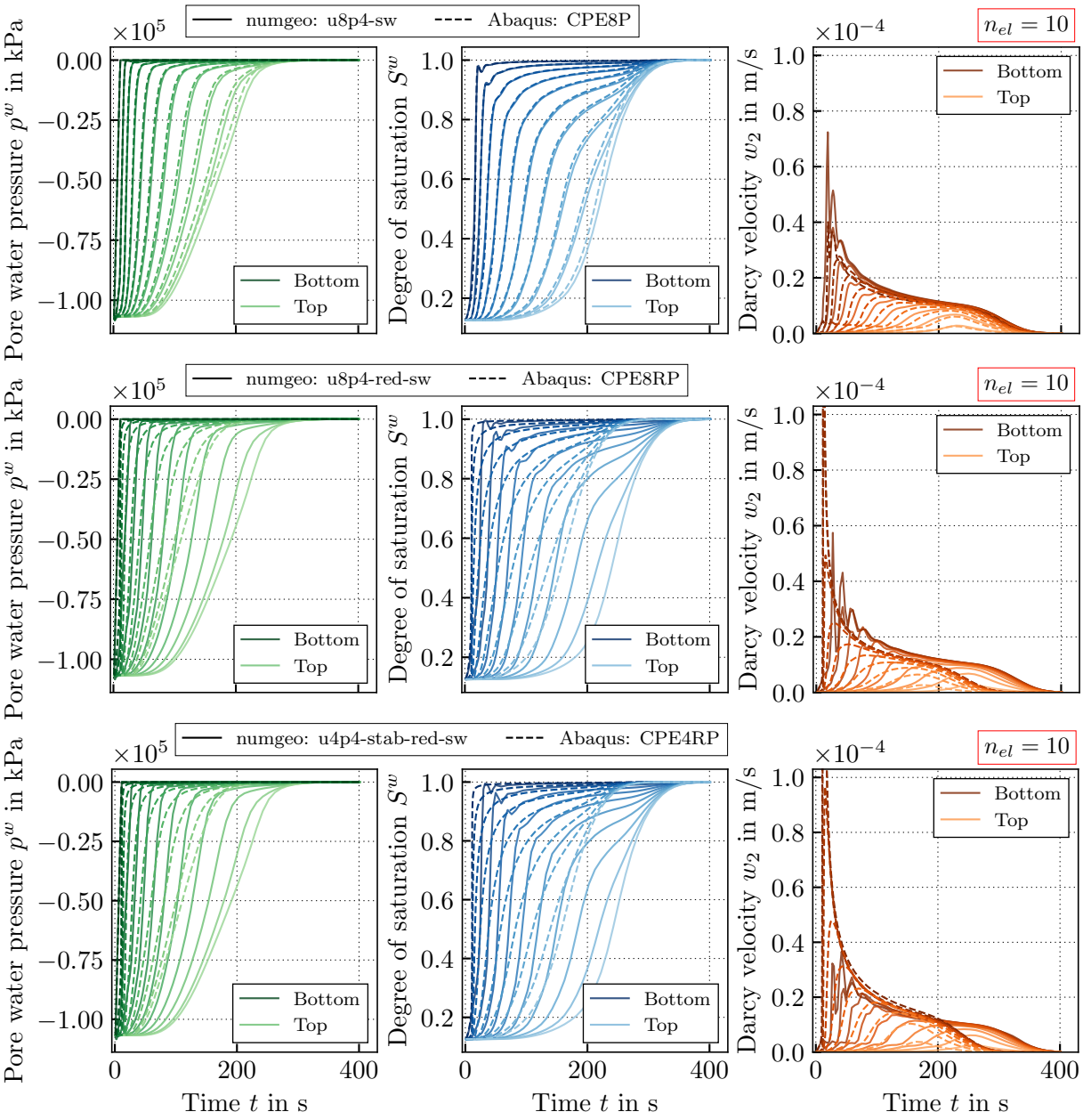

Figure 6.13.: Evolution of pore water pressure, degree of saturation and vertical Darcy velocity from simulations with different element types in `numgeo` in comparison to Abaqus: Taylor-Hood element with full integration (upper row) and with reduced integration (centre row) and linear equal order element (bottom row).

irregularities existed in the evolution of the degree of saturation. In contrast, the simulation results using TH elements with reduced integration (u8p4-red-sw / CPE8RP) in the second row of Figure 6.13 showed significant discrepancies in the simulation results. Therein, the simulation in `numgeo` exhibited physically plausible behaviour in terms of time evolution, however, also more pronounced numerical instabilities. The reduced number of integration points yields a lower spatial resolution for the evaluation of the permeability, which delayed the propagation of the saturation front. The simulation in Abaqus, however, showed a reverse, implausible trend; a faster propagation of the saturation front and no numerical instabilities were evident. Both observations indicate an internal smoothing of the pore pressure field in the CPE8RP element,

which effectively averaged the permeability within the element, leading to artificially higher flow rates compared to the fully integrated CPE8P element. The simulation results with the linear equal order element with reduced integration are shown in the bottom row of Figure 6.13. Their performance was very similar to those of the reduced TH element, which is expected due to the identical interpolation order for pore water pressure and number of integration points.

From the results in Figure 6.13, it is evident that regardless of the identical characteristic nodal distance Δl_n in different element types, the number of integration points must be sufficiently large to accurately capture the infiltration behaviour. Therefore the simulations were repeated with additional configurations: Firstly, using the same mesh with a quadratic equal order element (only available in numgeo, u8p8-stab), which offers the same resolution in terms of integration points as the previously used Taylor Hood element, and secondly, using a finer mesh with linear equal order elements, which doubles the integration points in comparison to the previously used mesh. Both configurations cut the characteristic nodal distance in half ($\Delta l_n = 1$ mm). For the sake of completeness, a simulation with the quadratic equal order element with reduced integration was carried out as well (only available in numgeo, u8p8-stab-red). The critical time increment was again chosen corresponding to the initial state ($\Delta t_{\text{crit}} = \Delta t_{D_0} = 0.0149$ s, see Figure 6.12).

The results are shown in Figure 6.14 in terms of the evolution of pore water pressure, degree of saturation and the vertical component of the Darcy velocity versus time. Note that in the upper and centre row, the simulation results from the TH element were employed for comparison, as Abaqus does not provide a quadratic equal order element. In general, a similar pattern is evident as for the TH elements in Figure 6.13. The fully integrated element in the upper row of Figure 6.14 yielded a good prediction with slightly less irregularities in the evolution of the degree of saturation, while noticeable deviations occur with the reduced formulation in the centre row of Figure 6.14. Therein, the numerical instabilities in the simulation with `numgeo` were slightly more pronounced than in the simulation with the TH element. Finally, the simulations results using the linear equal order element and finer mesh are presented in the bottom row of Figure 6.14. They showed improved agreement between Abaqus and `numgeo`, and the temporal evolution closely matches the simulation results of the fully integrated Taylor–Hood elements (upper row in Figure 6.13).

The simulations indicate that a sufficient number of integration points across the infiltration height is crucial for the prediction of the time evolution of unsaturated flow. Reduced-integration and low-order elements can yield consistent results, if the mesh is sufficiently refined to resolve hydraulic gradients. The numerical formulation of the element remains decisive for stability and convergence. On the one hand, the quadratic equal order element with full integration performs comparably to the TH element, however, with reduced integration, the number of integration points is insufficient to properly integrate the quadratic interpolation functions and does not offer a stable solution. On the other hand, the linear equal order element achieves solutions equivalent to the TH element, even without irregularities in the fields of pore water pressure or degree of saturation for increased mesh resolution. Despite the higher number of elements, the overall computational effort remains comparable. For strongly coupled hydro-mechanical analyses, the u4p4-elements represent a reliable and efficient choice to the TH elements.

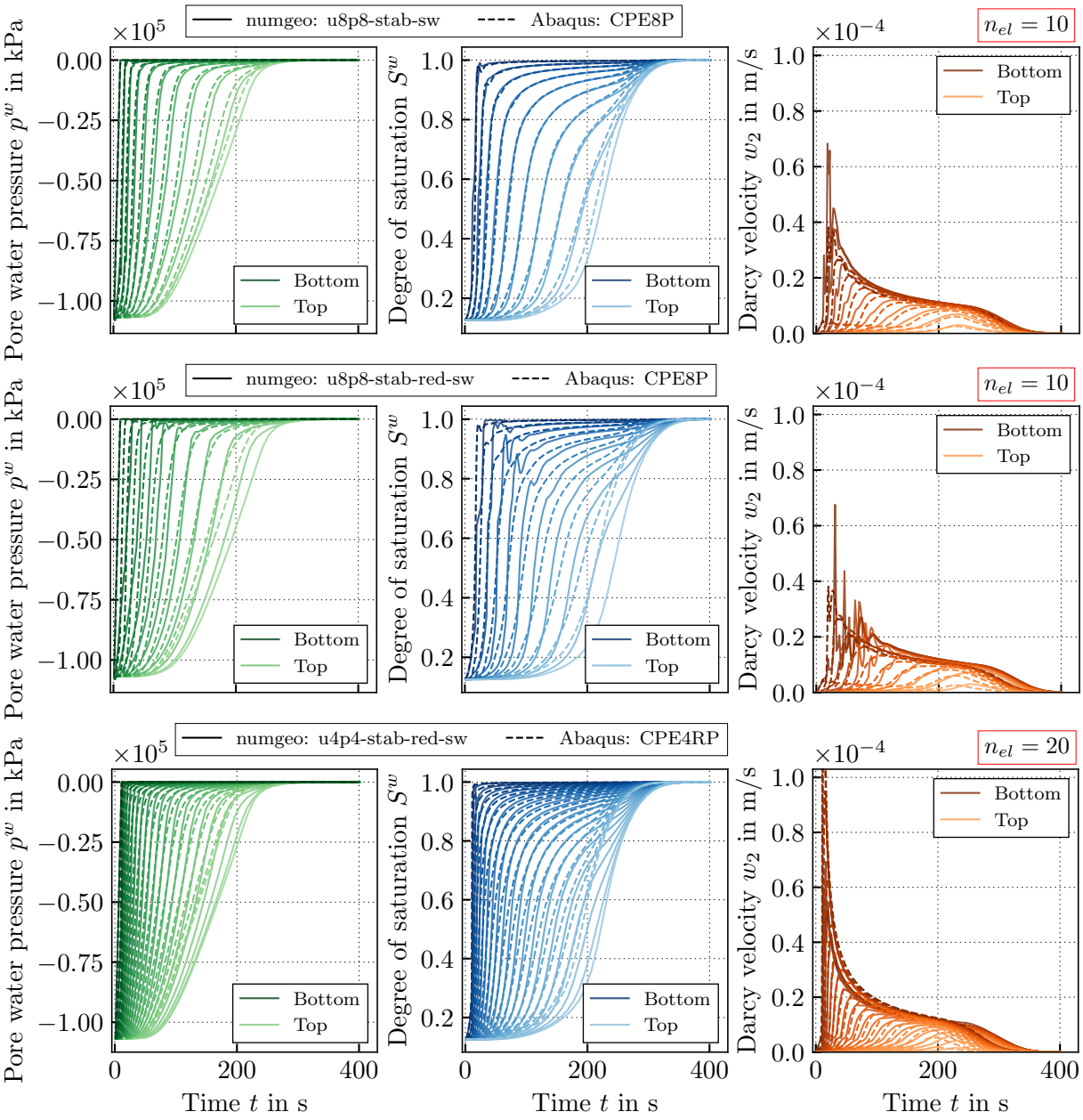

Figure 6.14.: Evolution of pore water pressure, degree of saturation and vertical Darcy velocity from simulations with different element types in `numgeo` in comparison to Abaqus: Quadratic equal order element with full integration (upper row) and with reduced integration (centre row) and bilinear equal order element for finer mesh (bottom row).

Significance of time-stepping

In the previous simulations, the minimum and initial time increment were chosen corresponding to the critical time increment of the initial state. This allowed the automatic time stepping to possibly undercut the required critical time increments with progressing flow. Therefore, the simulations in numgeo were repeated using the novel analysis type *transient critical* using the u8p4-sw-elements ($n_{el} = 10$) and u4p4-stab-sw-elements ($n_{el} = 20$). Therein, the minimum factor was set to $f_{t_{\min}} = 1.0$, thereby enforcing a strict lower bound that excludes any undercutting of the critical time increment, and the maximum time increment remained as $\Delta t_{\max} = 10$ s.

Figure 6.15 illustrates the evolution of time increments in the simulations with u8p4-sw-elements using the transient (top left) and transient-critical (top right) analyses procedure and the evolution of pore water pressure, degree of saturation and vertical Darcy velocity (bottom). Within the transient analysis, it is evident that the actual time increment Δt_i in numgeo remained smaller than the critical time increment computed in the elements $\Delta t^{el}_{\text{crit}}$ for most part of the infiltration. The evolution of the time increment from the corresponding Abaqus simulation is shown for comparison in the top left plot of Figure 6.15. It is similar, yet distinct from the numgeo simulation despite the definition of similar criteria for time stepping in both software. For the transient critical analysis, the actual time increment in numgeo consistently remained above the critical value, which is presented in the top right plot of Figure 6.15. The progression of pore water pressure, degree of saturation, and vertical Darcy velocity shown in the lower row of Figure 6.15 demonstrate an overall similar temporal evolution between both procedures. However, the minor irregularities in pore water pressure and degree of saturation could be further reduced in the transient-critical simulation, marked with ellipses in Figure 6.15.

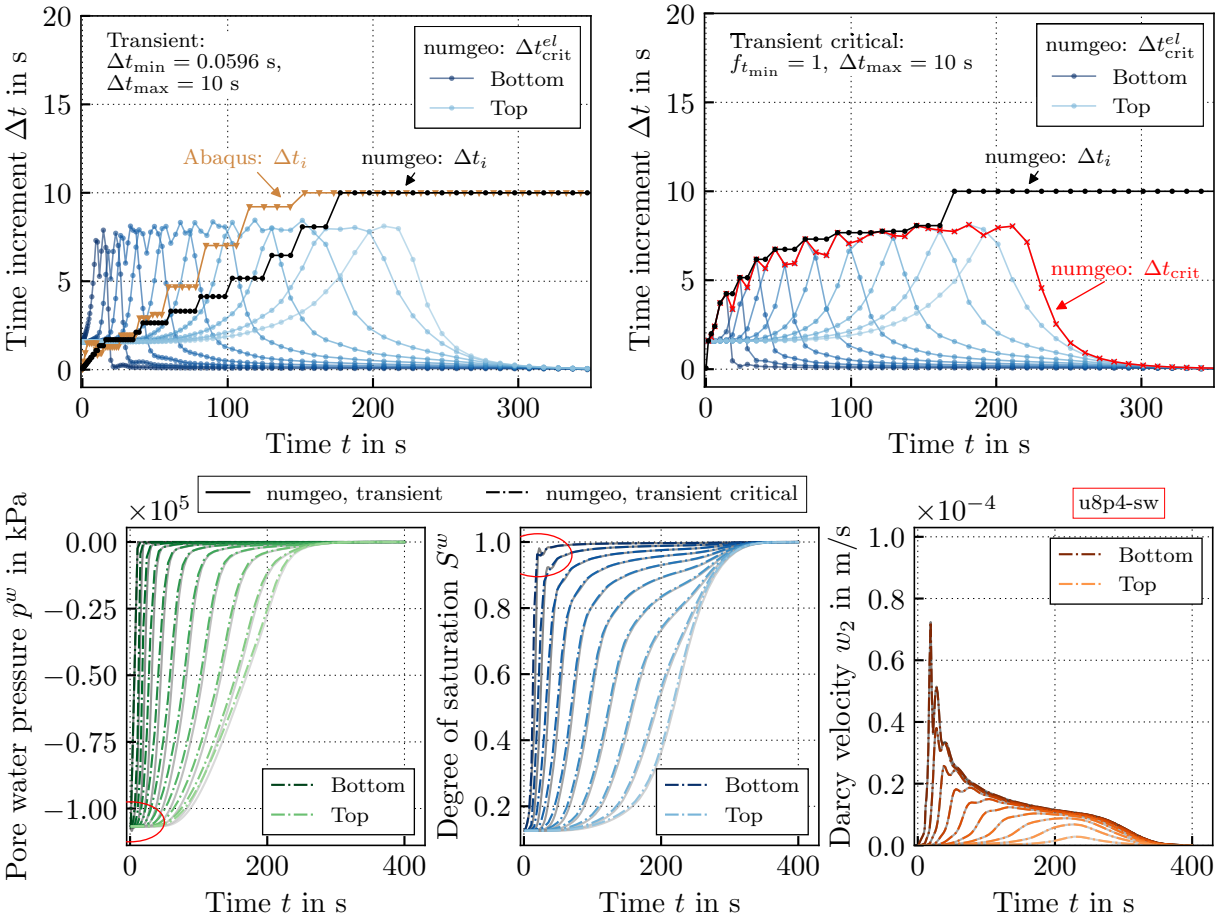

Figure 6.15.: u8p4-sw-element: Evolution of the time increment in `numgeo` for „transient“ (top left) and „transient-critical“ (top right) simulations, with Abaqus results shown for reference. Evolution of pore water pressure, degree of saturation, and vertical Darcy velocity from `numgeo` simulations using the analysis types „transient“ and „transient-critical“ (bottom).

Similar observations are apparent in Figure 6.16 for simulations with u4p4-stab-sw-elements and refined mesh for both procedures. In the transient analysis (upper left plot) it is evident, that the critical time increment $\Delta t^{el}_{\text{crit}}$ computed in the elements is smaller overall due to the

reduced characteristic nodal distance in comparison to the mesh used in simulations with u8p4-sw-elements (Figure 6.15). Consequently, the critical time increment is only undercut by the current time increment Δt_i in the first part of the infiltration. The transient-critical analysis (upper right plot) ensures a time increment larger than the critical one at all times. As a result, almost no irregularities persist in the evolution of pore water pressure and degree of saturation, which are shown with the evolution of the Darcy velocity in the bottom row of Figure 6.16.

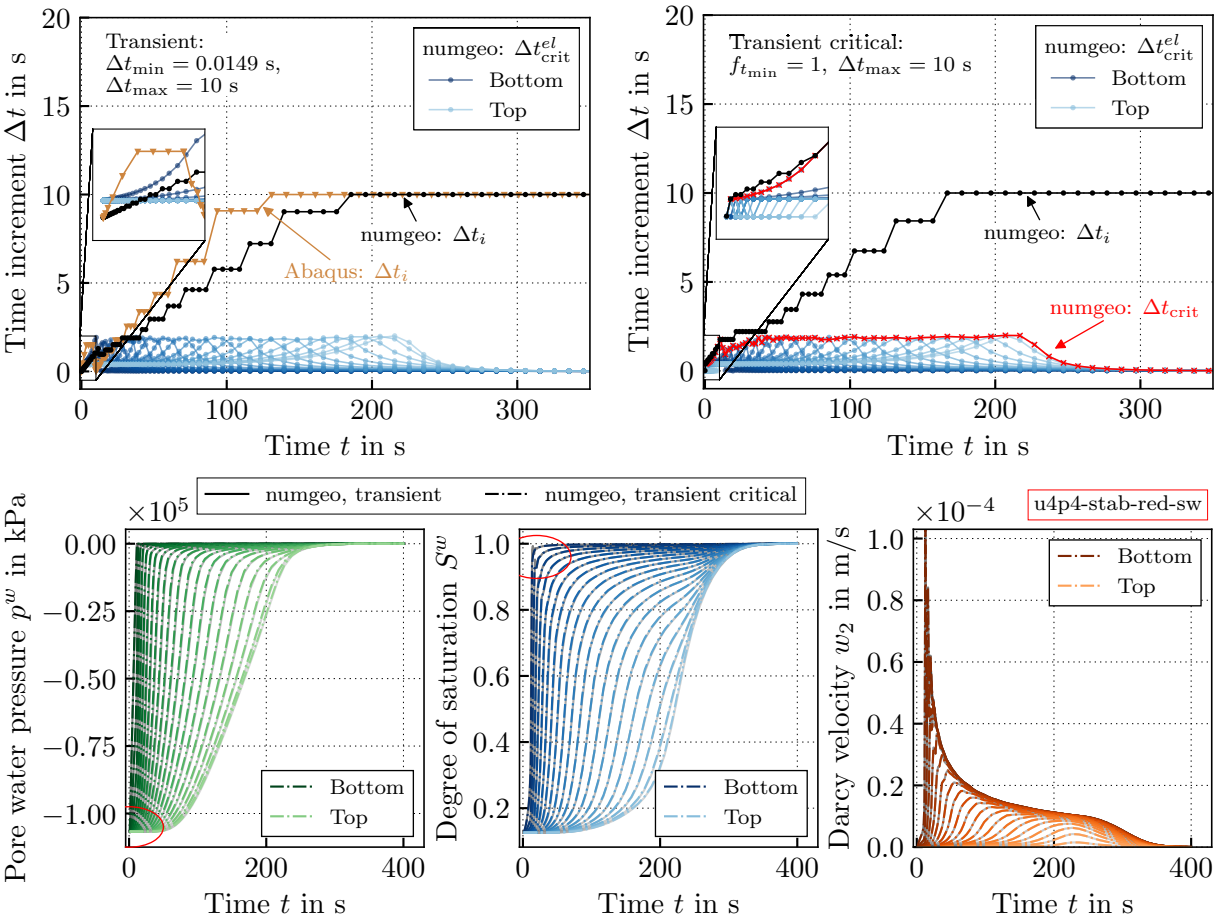

Figure 6.16.: u4p4-stab-red-element: Evolution of the time increment in `numgeo` „transient“ (top left) and „transient-critical“ (top right) simulations, with Abaqus results shown for reference. Evolution of pore water pressure, degree of saturation, and vertical Darcy velocity from `numgeo` simulations using the analysis types „transient“ and „transient-critical“ (bottom).

The results indicate that employing the novel procedure *transient-critical* can prevent fluctuations in the evolution of pore water pressure and degree of saturation, and enhance user-friendliness, as the user is no longer required to determine a critical time increment in advance of the simulation, nor to iteratively identify a time step that yields accurate results while maintaining convergence. Although the influence on the results appears minor or even negligible in the simulations presented here, it may become crucial when considering strongly hydro-mechanically coupled material behaviour as in this work, wherein the constitutive models for both the mechanical response and the mass transfer directly depend on the degree of saturation.

Significance of element types: meshing, interpolation and integration

Further simulations with the element length cut in half were carried out in `numgeo` for selected

element types in order to quantify the significance of mesh resolution, interpolation and integration in simulations with different element types. Meshes with $n_{el} = 20$ were used for the u8p4-sw- and u8p8-stab-sw-elements and with $n_{el} = 40$ for u4p4-stab-sw-elements. The novel analysis type *transient critical* was applied with a minimum factor of $f_{t_{\min}} = 0.9$, thus allowing slight undercutting of the critical time increment. The maximum time increment remained as $\Delta t_{\max} = 10$ s. For the sake of brevity, the evolution of pore water pressure, degree of saturation, and Darcy velocity is not shown in individual plots again. Instead, the simulations are evaluated based on the time required to reach full saturation and the required number of (global) equilibrium iterations. Both quantities are presented in Figure 6.17 against the characteristic nodal distance Δl_n on the left-hand side and against the element length Δl_e on the right-hand side. The time at which the topmost element (i.e. the one farthest from the infiltration boundary) reached a degree of saturation of $S^w > 0.995$ was taken as the criterion for full saturation.

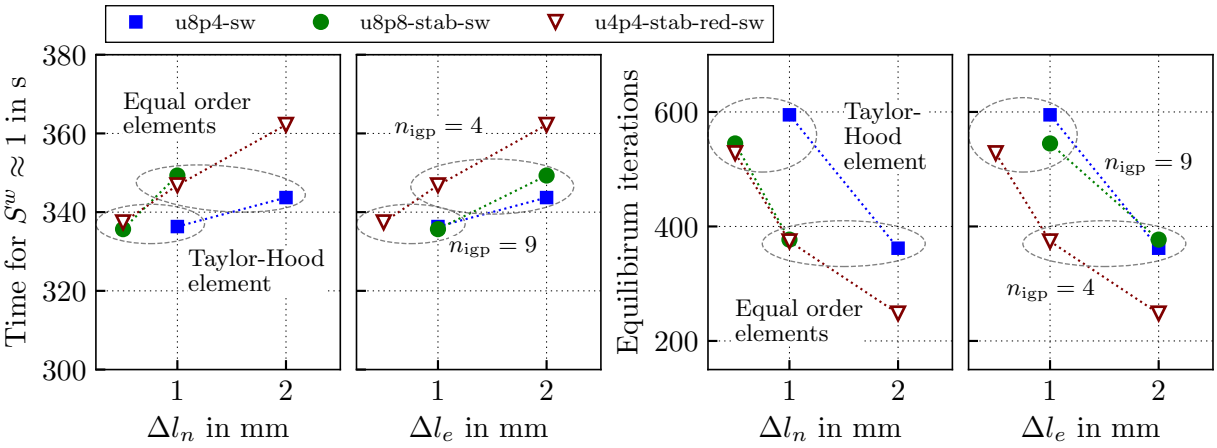

Figure 6.17.: Comparison of numerical performance for simulations with different, robust element types in `numgeo`: Time to reach full saturation (left) and (global) equilibrium iterations (right) versus nodal distance (top row).

It is evident, that neither the nodal distance nor the element length provide a single measure to compare qualitative trends across elements with different interpolation orders for simulation of infiltration. While equal order elements can be compared via nodal distance, the element length is suitable for elements with identical number of integration points. As an example, simulations with equal order elements require the same time to reach full saturation for identical nodal distance, e.g. $t \approx 340$ s for $\Delta l_n = 0.5$ mm. However, with a Taylor-Hood element, double the nodal distance, thus $\Delta l_n = 1$ mm, shows approximately that infiltration time (leftmost plot in Figure 6.17). On the other hand, elements with 9 integration points exhibit similar infiltration times for the same element length, e.g. $t \approx 340$ s for $\Delta l_e = 1$ mm, wherein this infiltration time is exhibited by the equal order element with 4 integration points for half the element length, thus $\Delta l_e = 0.5$ mm (second plot to the left in Figure 6.17). The same trends apply for the number of required equilibrium iterations and are indicated with ellipses in all plots of Figure 6.17. Overall, the time to reach full saturation decreased with increasing mesh refinement amongst all element types. However, increasing mesh refinement also requires an increasing number of iterations. With further mesh refinement, the element responses will likely converge even more closely in terms of time to reach full saturation, however, additional refinement must be weighed against computational cost.

Interim conclusion

The simplified infiltration benchmark presented in this section suggests that the u4p4-stab-red-sw element, in combination with the novel analysis type, proves particularly advantageous for the simulation of infiltration (and thus swelling) processes. Through the use of selective reduced integration, the mechanical response remains constant within each element, while the hydraulic processes are resolved with sufficient accuracy to reproduce realistic infiltration behaviour. Moreover, the novel analysis type enhances the numerical stability of the coupled problem by ensuring a smooth and oscillation-free field of the degree of saturation. For simulation of swelling, artificial stress or strain concentrations within one element can be avoided, which may arise from the direct coupling of swelling and saturation in the evolution equation of both, the mass transfer model and the mechanical constitutive model. However, for more complex boundary value problems, a mesh refinement study should still be performed, and the time incrementation should be carefully monitored.

6.6.3. Numerical integration of the mechanical constitutive model

In this section, the integration scheme, the evaluation of the Jacobians and the choice of the hydraulic variable for integration of „Hypoplasticity for expansive soils“are investigated in simulations of vertically unconfined swelling on the laboratory scale, thus including swelling in both, the mass transfer model and the mechanical constitutive model. The axial-symmetric finite element model represents an oedometric soil specimen, see Figure 6.18. Infiltration occurs from the bottom and top through porous stones. Estimation of the critical time step is not possibly analytically due to the consideration of swelling-induced relative permeability and mass transfer. Therefore, the analysis type *transient-critical* is used. A discretisation of $n_{el} = 20$ elements in height is chosen for the soil sample. However, different meshes with $n_{el} = 10$ and $n_{el} = 1$ elements in height are used in this section as well. The material parameters for the soil correspond to those previously applied in Section 5.3. For the sake of clarity, they are summarized in Table 6.9. The hydraulic and relative permeability model of Fredlund and Xing (1994) are applied with a minimum value for the unsaturated relative permeability of $k^w_{\text{min}} = 1 \times 10^{-4}$ and a lower integration limit of $s_i = 5$ kPa. The material parameters of the mechanical and hydraulic model for the porous stones correspond to Table 6.8.

Table 6.9.: Material parameters of all constitutive models for the soil in simulations regarding the numerical integration of the mechanical constitutive model.

Mechanical model										
e_N	h_s in kPa	n	κ_{ref}	κ_w	c	b	β	φ_{ref} in °	x_{ecm}	S_{ref}
0.58	9000	0.40	0.003792	0.02	2.0	55	0.36	37	0.35	0.126

Hydraulic and rel. permeability model				Mass transfer model	
h_r in kPa	a_f in kPa	n_f	m_f	$\phi^{\max}$	c_ϕ
17826	4000	0.896	1.26	0.88	10

All simulations consist of four steps (see Section 5.5): (1) the geostatic step, (2) a loading step, (3) an unloading step and (4) the infiltration step. For infiltration, the pore water pressure is prescribed as $\Delta p^w = 0$ at the bottom and top nodes (of the porous stones). The duration of the infiltration step is $t = 8000$ s. A vertical load corresponding to a net vertical stress $\Delta\sigma_v$ is applied on the top of the sample. The initial conditions and target conditions after sample preparation are summarized in Table 6.10. Simulations are carried out with the axisymmetric

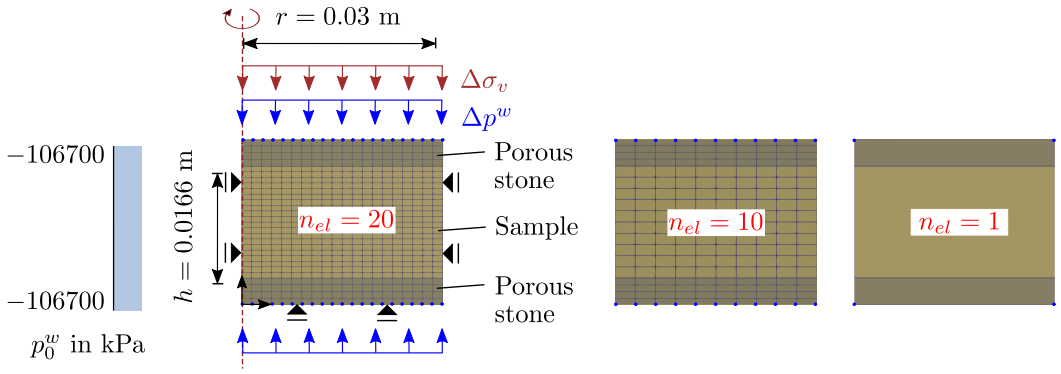

Figure 6.18.: Finite element model with different number of elements in height n_{el} and initial pore water distribution used for discussion of the integration of the mechanical material model.

stabilised reduced equal order linear element (u4p4-stab-ax-red-sw). A stabilisation factor of $\alpha^{FPL} = 0.15$ and an hourglass stiffness of $c^{HG} = 1000$ kPa were applied to stabilise the solution to a sufficiently small extent.

Table 6.10.: Initial and target conditions for all simulations regarding the integration of the mechanical material model.

$p^i = p_d^i$ in kPa	$e^i = e_d^i$	$\sigma_{22,d0}$ in kPa	e_{d0}	$\sigma_{22,0}$ in kPa	e_0	$S_0^w = S_{\text{ref}}$	p_0^w in kPa
10	0.588	10535	0.364	35	0.384	0.126	-106700

6.6.3.1. Integration scheme and maximum time increment

In this section, the performance of the integration schemes from Section 6.1.1.1 is studied. The minimum factor for scaling the critical time increment is chosen as $f_{t_{\min}} = 0.9$ to allow for a slight undershoot. Simulations are carried out using the finite element model from Figure 6.18 with 20 elements over height with both, the Forward Euler (FE) and Modified Euler (ME) integration scheme. The maximum time increment is varied within $\Delta t_{\max} = 5 - 100$ s and and its impact on the material response is discussed. Exemplary results for $\Delta_{t_{\max}} = \{5, 25, 50, 100\}$ are shown in Figure 6.19 in terms of void ratio versus vertical stress and the evolution of pore water pressure and degree of saturation with time. In the plots, each curve represents the solution of one representative element along the sample height for the void ratio, vertical stress and degree of saturation and its corner nodes for the pore water pressure, respectively. In the centre and right-hand side plot of Figure 6.19, no pronounced differences between the evolution of pore water pressure and degree of saturation are apparent in the predicted material response of both integration schemes.

The solution is stable without any oscillations by complying with the critical time increment in the simulations. In the left-hand plot of Figure 6.19 the simulation path exhibits some variations around the idealized vertical swelling path under vertically unconfined conditions. These depend on the maximum time increment allowed during infiltration. For $\Delta t_{\max} = 5$ s, the most stable prediction of the mechanical material response upon infiltration was achieved. With increasing $\Delta t_{\max}$, the mechanical material response exhibited more oscillations without significant changes in the infiltration behaviour.

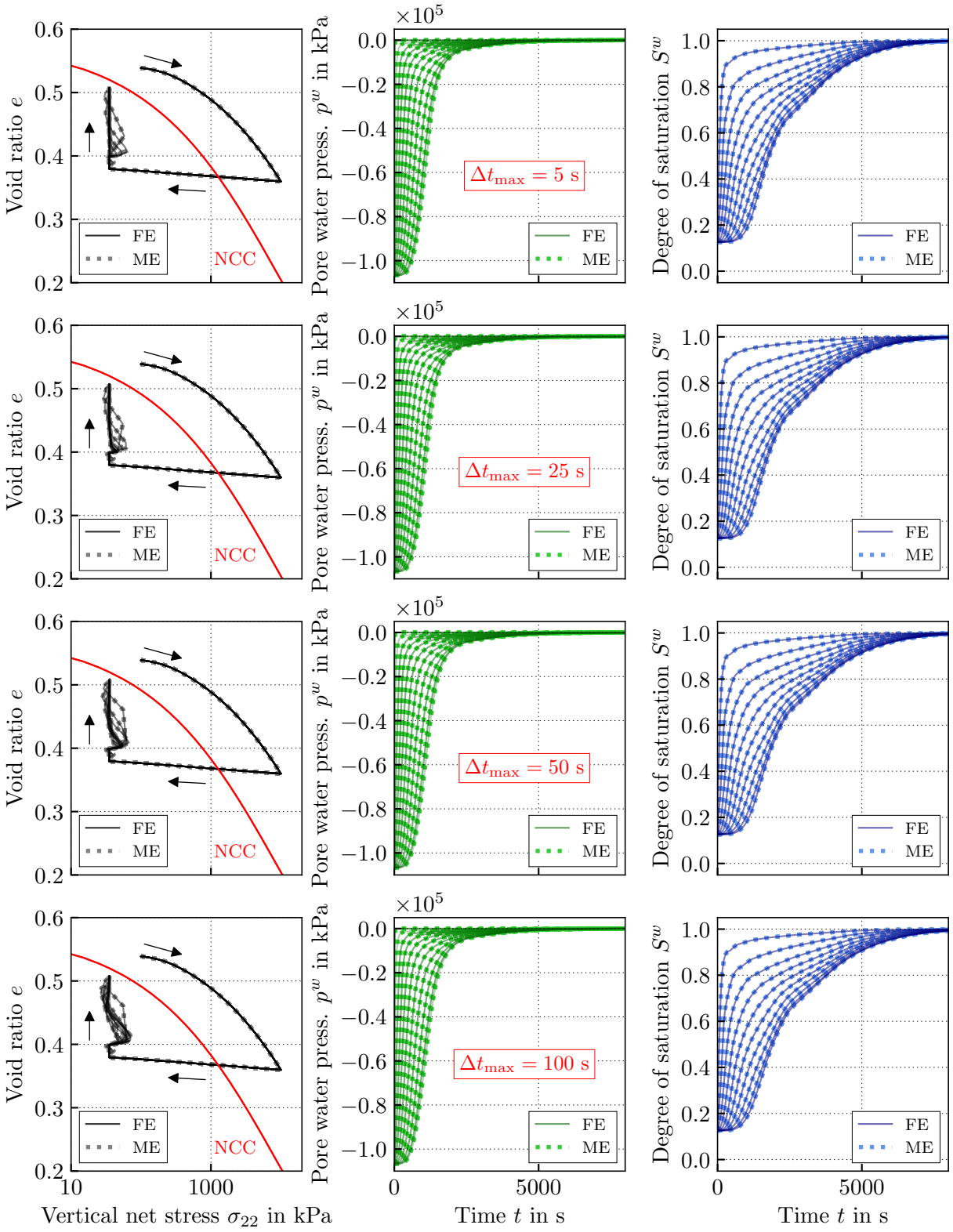

Figure 6.19.: Simulation results for a Forward Euler (FE) and a Modified Euler (ME) integration scheme with variation of maximum time increment during infiltration: void ratio versus vertical stress (left) and evolution of pore water pressure (centre) and degree of saturation (right).

To assess the infiltration behaviour in more detail, the left-hand plot in Figure 6.20 shows the time at which full saturation ($S^w > 0.99$) was reached in the simulations depending on $\Delta t_{\max}$.

The points in time are shown for the outermost element (white filled markers) and centre (element). The right-hand plot in Figure 6.20 presents the number of equilibrium iterations required in the infiltration step for the corresponding simulations. Figure 6.20 illustrates that infiltration behaviour was indeed affected by the maximum time increment, despite the distributions of the hydraulic variables in Figure 6.19 appeared nearly identical. Below a certain maximum time increment at around $\Delta t_{\max} = 20-25$ s, which is indicated in grey in Figure 6.20, the time to reach full saturation was approximately constant. In this zone, the mechanical material response was the most stable. For increasing maximum time increments, the time required to reach full saturation increased and an asymptotic threshold appears to exist, beyond which further increase of $\Delta t_{\max}$ has negligible influence. Nearing this threshold, the mechanical behaviour exhibited pronounced oscillations or inaccuracy of the constitutive equations, as was evident in Figure 6.19. The number of equilibrium iterations exponentially increased with decreasing maximum time increment from $\Delta t_{\max} = 20 - 25$ s. This effect can be related to the time incrementation and evolution of the critical time increment in the simulations.

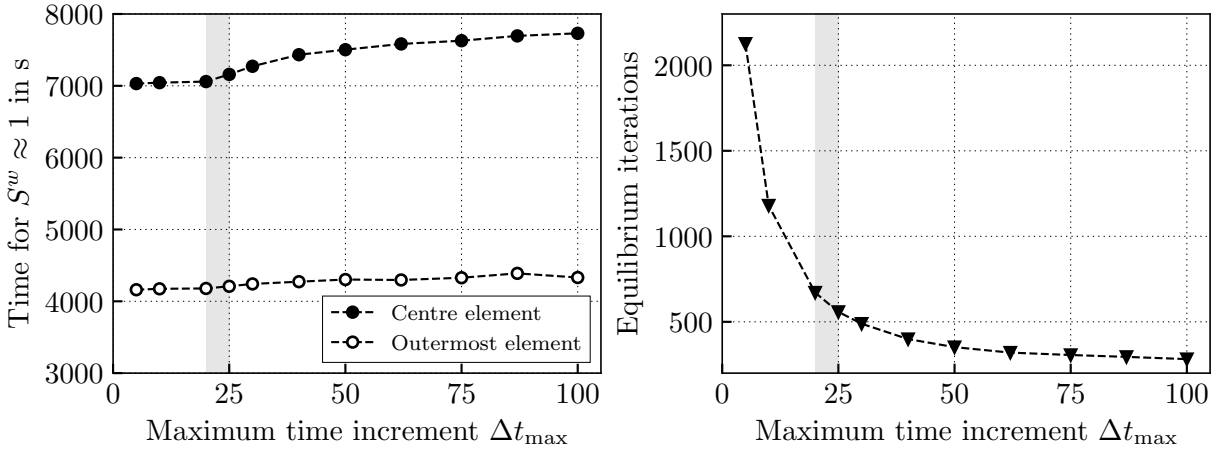

Figure 6.20.: Time to reach full saturation (left) and number of equilibrium iterations (right) versus the maximum time increment $\Delta t_{\max}$ in simulations of vertically unconfined swelling. The minimum factor is constant with a value of $f_{t_{\min}} = 0.9$.

Therefore Figure 6.21 shows the evolution of the time increment Δt_i and the critical time increment $\Delta t_{\text{crit}}^{(el)}$ for the four exemplary simulations using the Forward Euler integration scheme already shown in Figure 6.19. For $\Delta t_{\max} = 5$ s, the current time increment is mostly governed by the minimum scaling factor $f_{t_{\min}}$ during the first part of the infiltration, in which the critical time increment is increasing. It is later reduced to 5 s, explaining the well resolved hydro-mechanically accurate behaviour, however, at the cost of many iterations. For $\Delta t_{\max} = 25$ s, the current time increment is simultaneously governed by $f_{t_{\min}}$ and $\Delta t_{\max}$, yielding a good compromise between accuracy and computational cost. For $\Delta t_{\max} = 50$ s and $\Delta t_{\max} = 100$ s, the time increment rapidly increases, thus though the infiltration is stable, the hydro-mechanically coupled behaviour is poorly resolved, leading to both, rather inaccurate mechanical response and increased infiltration time (see Figure 6.19). However, the computational cost is low. Consequently, when simulatingswelling (with the currently available integration schemes), a trade-off must be made between the solution accuracy and computational cost.

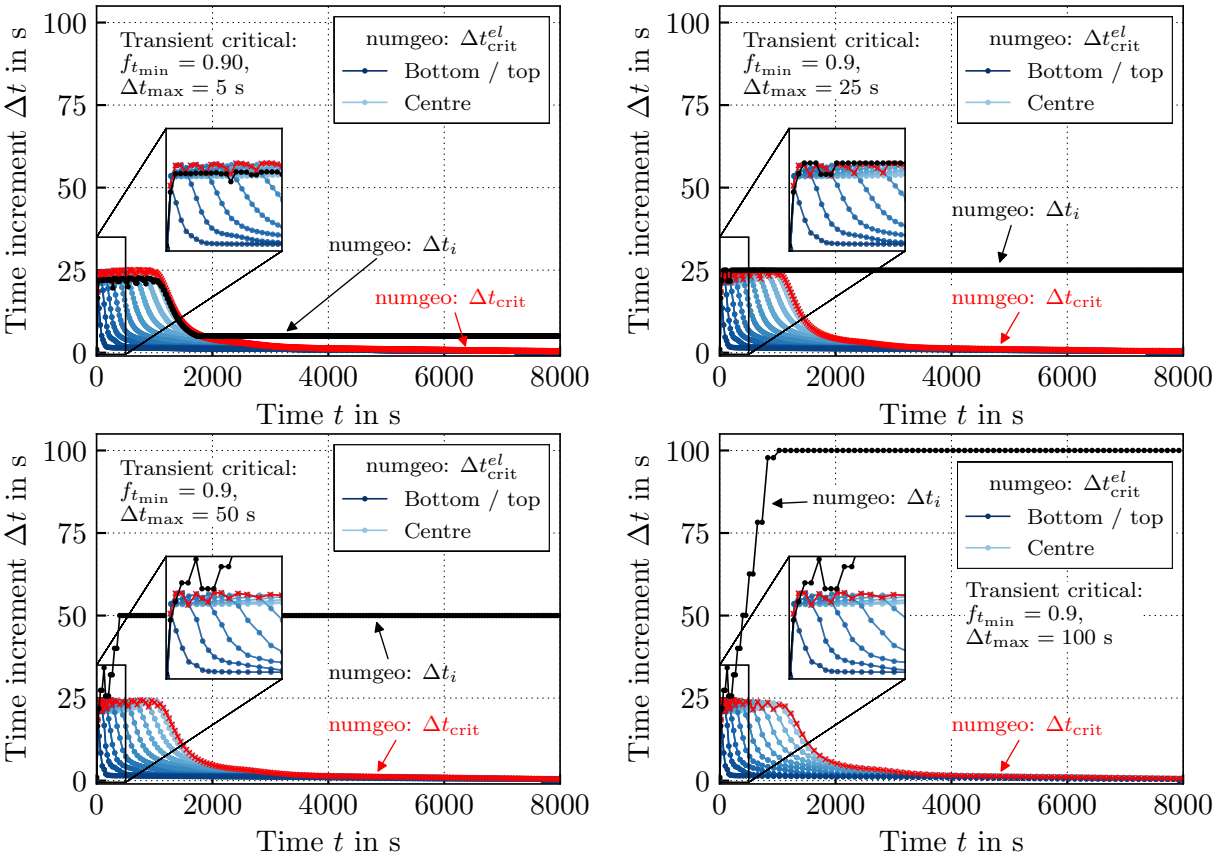

Figure 6.21.: Evolution of the current and critical time increments in simulations of vertically unconfined swelling with different maximum time increments $\Delta_{t_{\max}} = \{5, 25, 50, 100\}$.

6.6.3.2. Jacobian evaluation

Different methods for the evaluation of the Jacobians of the coupled analysis are studied in this section on the same problem as in the previous section. The simulation with the Forward Euler integration scheme using a maximum time increment of $\Delta t_{\max} = 25$ s (Figure 6.19, second row) serves as reference. Therein, the numerical differentiation of the Jacobian was carried out with a finite difference scheme. The system was coupled, thus the Jacobian $\partial \sigma_{ij} / \partial s$ was active. Three variations of the computation of the Jacobian were carried out employing (1) an uncoupled system with no consideration of the Jacobian $\partial \sigma_{ij} / \partial s$, (2) lower accuracy of numerical differentiation with only single forward step and (3) the barotropic elastic stiffness as approximated analytical Jacobian for $\partial \sigma_{ij} / \partial \epsilon_{kl}$. The results are presented in Figure 6.22. They indicate that the infiltration behaviour and the final state of the simulations are largely unaffected by the specific treatment of the Jacobians. However, the evolution towards the final state in terms of the mechanical material response shows some sensitivity. Variants 1–3 exhibit comparable fluctuations along the idealised vertical path, although with varying magnitudes. The uncoupled formulation tends to exhibit stronger oscillations, as does the use of less accurate numerical differentiation schemes for the Jacobians. Notably, the application of the barotropic elastic stiffness for $\partial \sigma_{ij} / \partial \epsilon_{kl}$ yields an equivalent response to that of the reference simulation. The simplified approximated Jacobian and the numerical Jacobian have similar accuracy. Consequently, simulations on the coupled system and higher order numerical Jacobian are recommended. However, different options may be chosen, if they lower e.g. the computational cost.

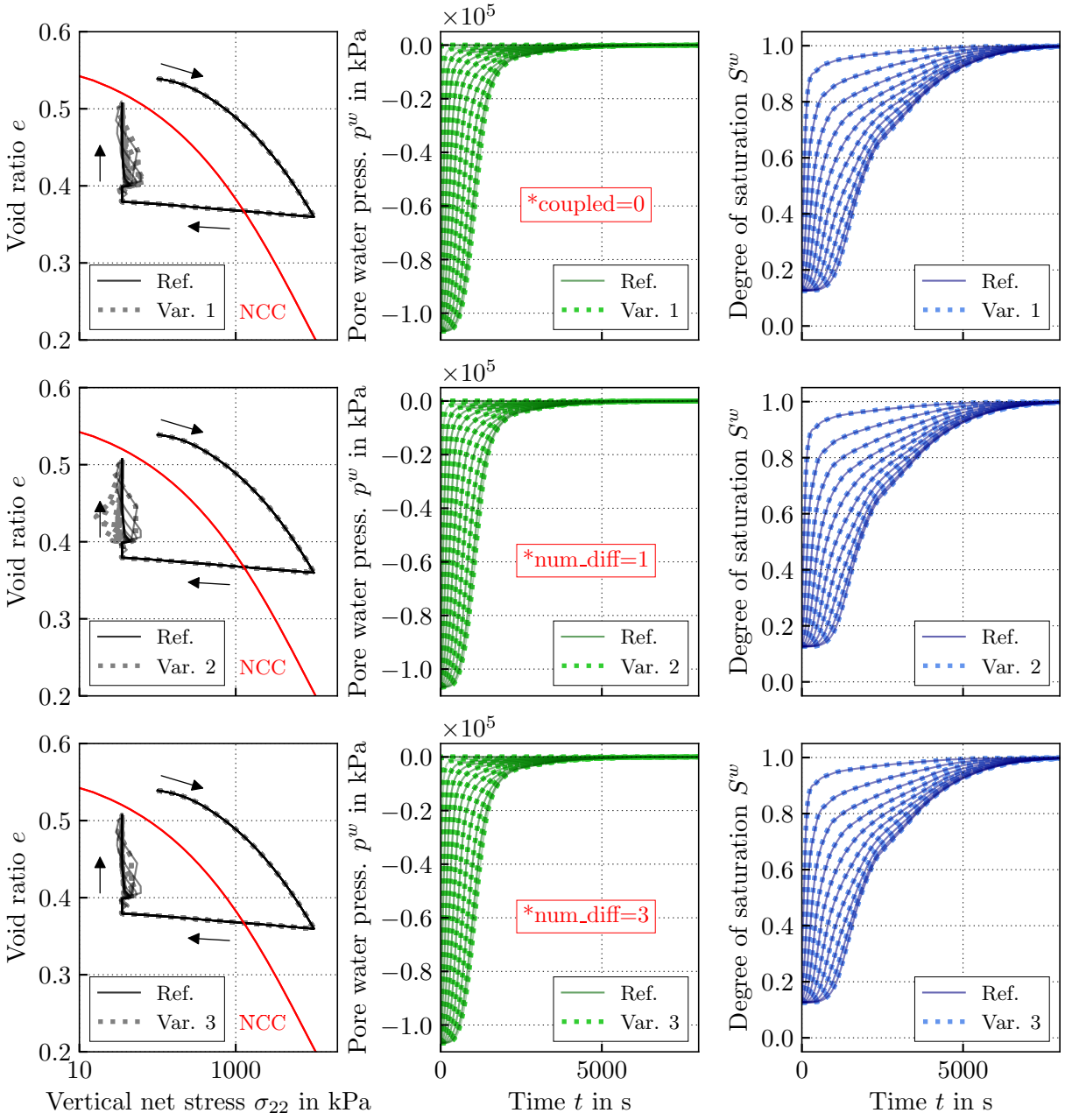

Figure 6.22.: Void ratio versus vertical stress (left) and evolution of pore water pressure (middle) and degree of saturation (right) with time: Variation 1, uncoupled system (top), variation 2 with forward step in numerical differentiation (centre) and variation 3 using the barotropic stiffness for the Jacobian $\partial\sigma_{ij}/\partial\epsilon_{kl}$.

6.6.3.3. Choice of hydraulic variable

In Section 6.1.1, the computation of the increment of the effective degree of saturation, ΔS^e, was introduced, based on the suction increment Δs, the degree of saturation at the beginning and end of the increment, S_n^w and S^w, and a reference saturation S_{ref}^w. The resulting increment ΔS^e is required for the computation of the constitutive rates, in conjunction with the strain increment

$\Delta\epsilon_{kl}$. In a standard time increment of size Δt, both $\Delta\epsilon_{kl}$ and ΔS^e (or ΔS^w) are assumed constant. When subincrementation is applied during the integration of the constitutive equations, these increments are typically subdivided using equidistant steps, such that $\Delta\epsilon_{kl,\text{sub}} = \text{const.}$ and $\Delta S^e_{\text{sub}} = \text{const.}$ However, due to the non-linear relationship between suction and saturation, this results in $\Delta s_{\text{sub}} \neq \text{const.}$, as illustrated on the left-hand side of Figure 6.23. For the sake of simplicity, the effective degree of saturation is chosen for visualisation in Figure 6.23, although the hydraulic model is formulated in terms of the degree of saturation. From a theoretical standpoint, the aforementioned approach is not entirely consistent with the underlying structure of the coupled hydro-mechanical finite element formulation. The primary field variables are the displacement u_i and pore water pressure p^w (or, equivalently, suction $s = -p^w$). Consequently, the physically consistent choice for material integration is the pair $\Delta\boldsymbol{\epsilon}$ and Δs. Using ΔS^e instead corresponds to a non-linear transformation of the primary hydraulic variable and thus represents a derived, rather than a fundamental, integration path. To address this, an alternative subincrementation scheme based directly on Δs has been implemented in `numgeo`. Here, the suction is subdivided into equal increments Δs_{sub} and the increment of the effective degree of saturation ΔS^e is recomputed in each sub step from the hydraulic model. This results in a non-constant increment ΔS^e_{sub} across the subincrements. This approach, illustrated on the right-hand side of Figure 6.23, aligns more directly with the structure of the global solution process. It is expected that numerical integration based on constant ΔS^e is viable, provided that the material model supplies consistent tangent operators, i.e., accurate Jacobians $\partial\sigma_{ij}/\partial\boldsymbol{\epsilon}$ and $\partial\sigma_{ij}/\partial s$ that reflect the true dependence of the stress on both mechanical and hydraulic variables.

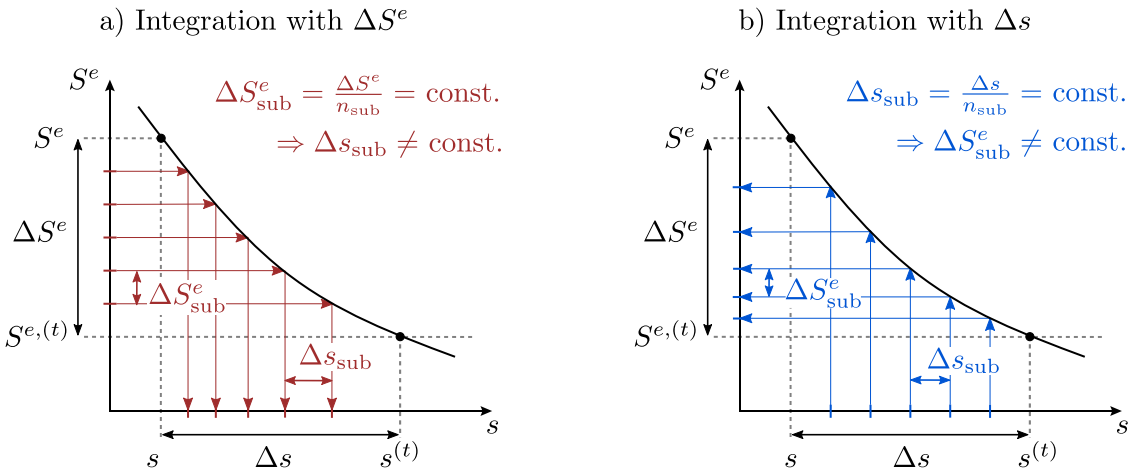

Figure 6.23.: Differences in subincrementation by choice of hydraulic variable, visualised with $n_{\text{sub}} = 6$ for a) integration with ΔS^e (left) and b) integration with Δs (right).

To confirm the viability of integration with ΔS^e, comparative simulations were carried out with both approaches in an element test and boundary value problem with two different discretisations of 10 and 20 elements in height in `numgeo`, see Figure 6.18. The duration and incrementation of the infiltration step were chosen differently for the boundary value problems as for the modified element test. All other conditions, including time stepping, integration controls and subincrementation within the integrator where identical. In these simulations, the dependency of the friction angle on the effective degree of saturation $\varphi = \varphi(S^e)$ was not yet considered and simulations were carried out with transient analysis. A minimum value of $k^w_{\text{min}} = 1 \times 10^{-4}$ was

applied for the unsaturated relative permeability and the hydraulic parameters correspond to those in Figure 6.11). The parameter set for the mechanical behaviour corresponds to the one used in Machaček et al. (2024), see Table 6.11.

Table 6.11.: Material parameters of the mechanical and mass transfer model.

e_N	h_s in MPa	n	κ_{ref}	κ_w	c	b	β	φ in °	S_{ref}	$\phi^{\max}$	c_ϕ	n_{ref}
0.58	9.0	0.40	0.003792	0.013590	1.8	80	0.30	37	0.126	0.88	10	0.280

The results are shown in terms of void ratio versus vertical stress and pore water pressure and degree of saturation versus time in Figure 6.25. In the upper row, the results of the element tests are shown and the middle and bottom row present the results of the BVP with 10 and 20 elements in height, repsecitvely. In each row, both the results of simulations with ΔS^e (darker colour, round markers, solid lines) and Δs (brighter colours, triangle markers, dashed lines) are shown. The markers do not have any physical meaning, but are solely for better differentiation.

The results highlight, that the material response is almost identical for both integration methods regardless of the discretisation of the FE model. Minor differences exist in the middle and bottom left-hand plot of Figure 6.25 for void ratio e versus logarithmic vertical stress σ_{22}. Interestingly, the simulations using Δs exhibited slightly more pronounced oscillations for the mesh with 20 elements in height. However, these oscillations are not decisive for the overall material response. Although similar results, the simulations differ in terms of their performance, which is analysed in Figure 6.24.

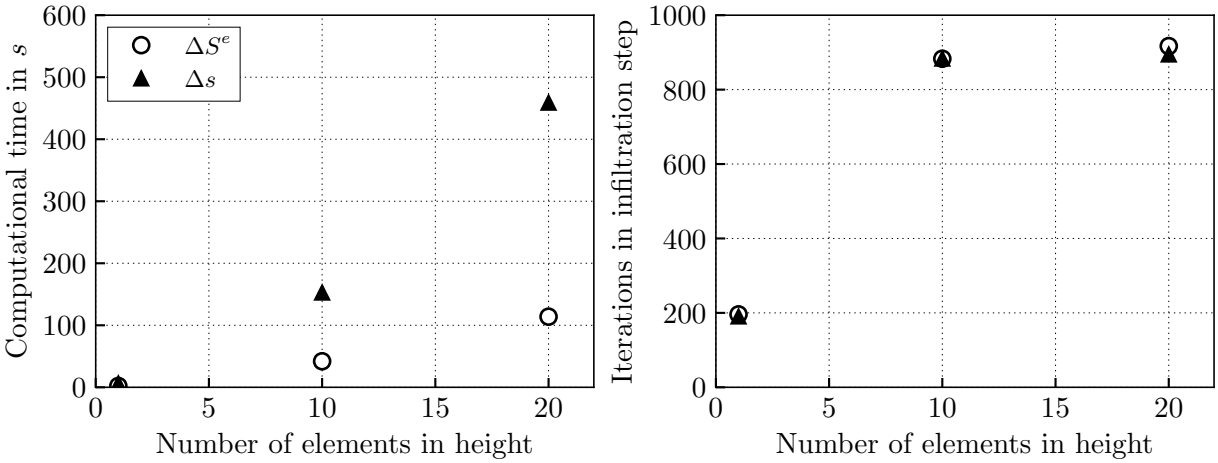

Figure 6.24.: Comparison of numerical performance for simulations with ΔS^e and Δs as hydraulic variable in integration: Total computational time (left) and (global) equilibrium iterations in the infiltration step (right) versus number of elements in height.

On the left-hand side of Figure 6.24, the total computational time (including all steps) and on the right-hand side, the (global) iterations during the infiltration step are shown for integration with ΔS^e (round marker) and Δs (triangle marker) versus the number of elements in height. Note that the simulations were carried out on a 6-core Intel Core processor i8-9700 @ 3.9 GHz with 24 GB RAM. The number of iterations is approximately the same, regardless of the variable chosen for integration. However, the computational cost increases significantly when using Δs in the integration procedure. For example, for $n_{el} = 10$, the computation time is already 3.6 times higher, and this trend continues, reaching a factor of 3.9 for $n_{el} = 20$. Based on these

results, the integration with ΔS^e is preferred, as it provides comparable convergence behavior at significantly lower computational cost.

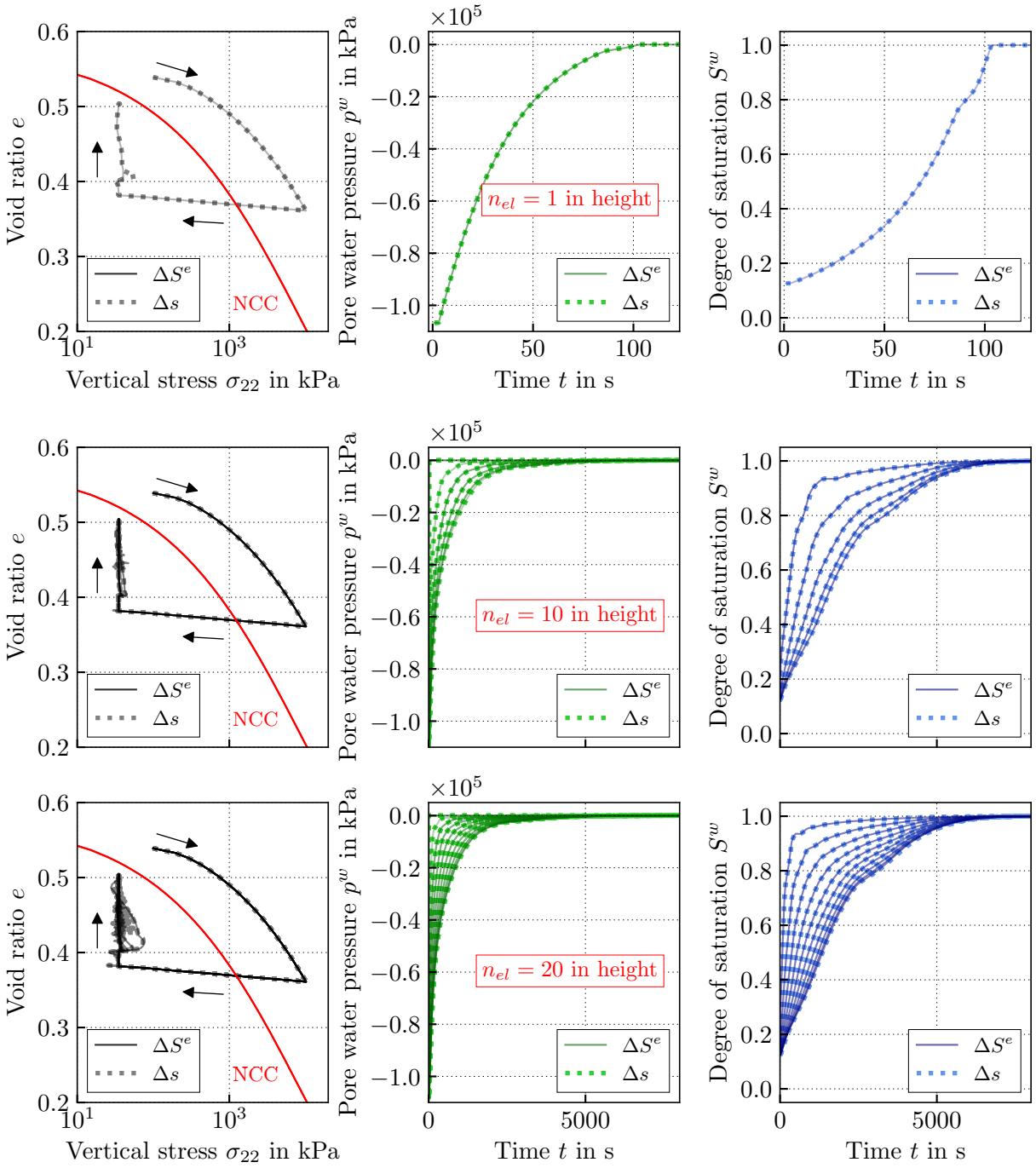

Figure 6.25.: Results of simulations with ΔS^e and Δs as hydraulic variable in integration: void ratio versus vertical stress (left) and evolution of pore water pressure (middle) and degree of saturation (right) with time.

6.7. Concluding remarks

In this chapter, the implementation of the previously introduced novel numerical framework has been presented and selected aspects have been discussed. For the application of the framework

to the simulation of swelling in boundary value problems, the principal conclusion is that time incrementation has the strongest influence on numerical stability when a sufficiently fine mesh is employed. By contrast, factors previously regarded as critical, such as details of the integration scheme, are of limited relevance provided that an appropriate time increment is selected. The application of the novel analysis type with consideration of the transient critical time increment facilitates reliable time integration and a stable material response.

7. Application of the numerical framework to boundary value problems

In this chapter, the previously developed modelling approach is applied to various boundary value problems (BVP) in `numgeo`. In the first part, laboratory tests from the three experimental campaigns, which were already utilised in Chapters 4 and 5 to develop the mechanical constitutive model, are simulated. Focus is placed on the author's own experiments on reconstituted Opalinus clay. In previous chapters, the hydro-mechanical material behaviour was described for a single material point or element. Therefore, only final magnitudes of swelling strain and swelling pressure could be simulated, however, not their evolution over time. The implementation of the complete numerical framework within a FE software enables spatial discretisation and thus investigation into the temporal evolution of the swelling behaviour as well. In the second part, the numerical framework is applied to a large-scale example scenario representing an emplacement tunnel in a deep geological repository for high-level radioactive waste, wherein expansive material seals the tunnel cross-section. The objective is to demonstrate the overall applicability of the framework to a BVP with a large-scale geometry.

7.1. Simulation of laboratory tests as boundary value problems

Discretization of the laboratory tests for simulations as boundary value problems enables the numerical model to replicate the actual experimental setup including specimen geometry and boundary conditions. Consequently, it is possible to capture the temporal evolution of the numerical material response and compare it to experimental results.

In the following, quantities evaluated at any location within the FE model of the specimen, whether at integration points, such as stress, strain, void ratio and degree of saturation, or at nodes, i.e. pore water pressure or displacement, will be referred to as *local quantities*. Quantities evaluated specifically at the models's outer boundaries reflect the integrated effect of the local response. These can be used to compare the numerical response to measurements from the laboratory, where the evolution of deformation or stress is captured outside of the specimen by measurements of the vertical deformation with a displacement transducer and of the vertical force with a load cell (see Chapter 2 and Appendix A.1). These quantities will be referred to as so-called *external quantities*. Figure 7.1 shows the exemplary front view of oedometric swelling tests for vertically unconfined (left) and constant volume (right) conditions, both in the laboratory and in FE simulations, illustrating the evaluation of external quantities (in colour). In the simulations, the vertical displacement of the upper nodes $u_{2,\mathrm{node}}$ is related to a reference height to compute the vertical strain, and the sum of the reaction forces RF_{node} at the vertical boundary is related to the cross section to compute the vertical net stress corresponding to the swelling pressure. For axisymmetric models, the cross section is $A = \pi d^2/4$, and for plane strain, $A = b$, where d is the diameter and b the width. From the vertical strain, the void ratio can also

be determined. The local quantities, shown in black in Figure 7.1, represent a view inside the sample, which is not available from the laboratory unless stress and strain measurement were to be installed inside the sample.

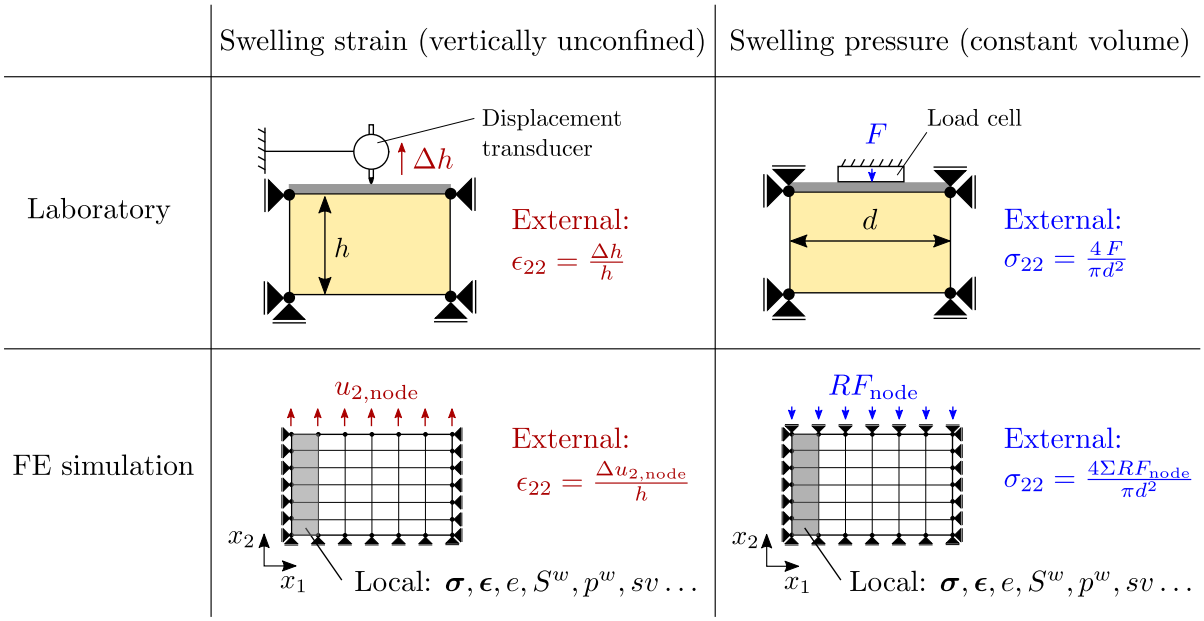

Figure 7.1.: Front view of oedometric swelling tests: Evaluation of mechanical swelling phenomena in the laboratory and in FE simulations in terms of local quantities and external quantities.

In addition to the information provided in Chapters 2 to 5, the geometric dimensions of the samples are required for the simulation of the laboratory tests as boundary value problems. To initialize the preconsolidation net stress p_d correctly, the sample preparation is simulated starting from a small initial isotropic pressure $p^i = 10$ kPa. To ensure the correct height h_0 prior to the actual loading known from the experiments, the compression and slight rebound behaviour of the material upon preparation must be considered in the initial height h^i of the FE model. From simulations of the element tests, which also included specimen preparation (see Section 5.5), the initial void ratio e^i corresponding to p^i in order to reach the target void ratio e_0 at a specific vertical net stress $\sigma_{22,0}$ prior to loading, is already known. Thereon based, the height h^i for specimen preparation starting from p^i is approximated. Note that the simulation results are shown without specimen preparation in the following sections.

7.1.1. Reconstituted Opalinus clay

In this section, several tests from the experimental campaign conducted on reconstituted Opalinus clay (Nitsch et al., 2023a) are simulated including those already presented in Chapter 3 for the derivation of the mass transfer and relative permeability model and Chapters 4 and 5 for the calibration of the mechanical constitutive model. Note that the experimental results are also shown in Figures 2.10, 2.12 and 2.16. In addition, swelling tests in perspex oedometric rings, see experimental results in Figures 2.13 and 2.17, are simulated as well. The axisymmetric FE model is shown in Figure 7.2 with the initial pore water pressure of $p_0^w = -106.7$ MPa corresponding to an initial degree of saturation of $S_0^w = 0.126$. The initial conditions are summarized in Table 7.1 and correspond to those of Table 5.5 applied in single-element simulations. An initial height of $h^i \approx 17.8$ mm at a void ratio of $e^i \approx 0.588$ and small isotropic net stress of $p_i = 10$ kPa was

determined based on the height of $h_0 = 15.6$ mm determined at the start of the experiments at a void ratio of $e_0 \approx 0.387$. The diameter of the samples was $d = 60$ mm. For the sample, a standard discretisation with $n_{el} = 30$ elements over height was chosen, corresponding to a nodal distance of $\Delta l_n \approx 0.5$ mm. The effect of mesh size is discussed in Section 7.1.1.3. Axisymmetric, four node selectively reduced integrated elements with bilinear interpolation functions for both displacement and pore water pressure of the `up-sw`-element library were used. Below and above the soil sample, porous stones were simulated, which consist of `up`-elements without swelling. Four elements in height were used regardless of the discretisation of the sample. Linear elasticity with a high stiffness was chosen for their mechanical constitutive model and their weight was not considered. To account for the high porosity and hydraulic conductivity of the porous stones, an initial void ratio of $e = 1.0$, isotropic permeability of $K = 1 \times 10^{-12}$ m^2, the hydraulic model of van Genuchten (1980) with parameters for a coarse-grained soil and the simple relative permeability model of Nguyen et al. (2006) were applied. The initial state corresponded to that of the soil sample. Their material properties are gathered in Table 7.2. Infiltration via a pore water pressure boundary condition on the outer nodes of the porous stones meets the infiltration boundary conditions of the laboratory.

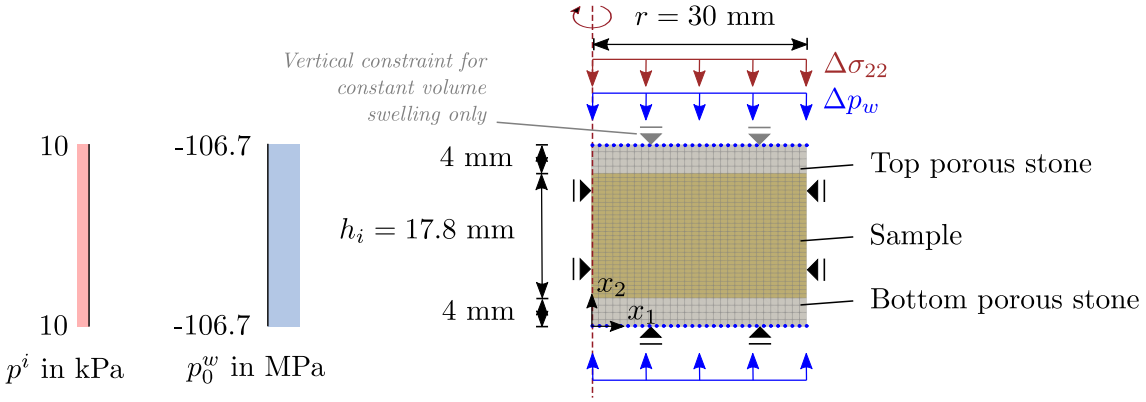

Figure 7.2.: FE model for simulations of laboratory tests on reconstituted Opalinus Clay.

Table 7.1.: Initial and target conditions for the simulations on Opalinus clay shale from Nitsch et al. (2023a) as boundary value problems.

	$p^i = p^i_d$ in kPa	$e^i = e^i_d$	$\sigma_{22,d0}$ in kPa	e_{d0}	$\sigma_{22,0}$ in kPa	e_0	$S^w_0 = S_{\text{ref}}$	$p^w_0 = -s_0$ in kPa
Reference	10	0.587	10535	0.359	180	0.374	0.126	-106700
Constant volume	:	0.589	:	0.376	25	0.396	:	:
CV + unloading	:	0.588	:	0.374	35	0.392	:	:
Vertically unconfined	:	0.588	:	0.364	35	0.384	:	:

Table 7.2.: Material parameters of the mechanical and hydraulic model for the porous stones.

Mechanical model		Hydraulic model	
E in kPa	ν	α in kPa^{-1}	n
1×10^{10}	0.3	0.383	1.377

For the soil, the parameter set determined in Chapters 4 and 5 is considered for the mechanical model. The hydraulic model of Fredlund & Xing was already calibrated for the soil water

retention curve of Opalinus clay (see Figure 5.30) and is applied for the relative permeability model for unsaturated soils in a consistent manner as well, with an upper integration limit $s_i = s(S^{w,sat}) = 5$ kPa and a minimum value of $k^w_{\min} = 1 \times 10^{-3}$ (see Section 7.1.1.2 for further details). The reference permeability in the saturated, but unswollen state, is set isotropically as $K^s_{\text{ref}} = 1.0 \times 10^{-15}$ m^2 for $n_{\text{ref}} = 0.280$. The residual degree of saturation is chosen as $S^{wr} = 0.05$. Although it is not required for the definition of the hydraulic model itself, it is necessary to compute the effective degree of saturation S^e for the unsaturated relative permeability. All materials parameters are gathered in Table 7.3.

Table 7.3.: Material parameters of all constitutive models for reconstituted Opalinus clay shale.

Mechanical model										
e_N	h_s in kPa	n	κ_{ref}	κ_w	c	b	β	φ_{ref} in °	x_{ecm}	S_{ref}
0.610	8000	0.36	0.003792	0.02	2.2	55	0.36	37	0.35	0.126

Hydraulic and rel. permeability model				Mass transfer model	
h_r in kPa	a_f in kPa	n_f	m_f	$\phi^{\max}$	c_ϕ
17826	4000	0.896	1.26	0.88	10

The simulations comprised of a geostatic step (0), specimen preparation in loading and unloading steps (1 and 2), an infiltration step (3), and subsequent vertical loading and unloading steps (4 ff.). For the simulation of the reference test (OPA-0-33) the infiltration step was omitted. The infiltration was realized via a pore water pressure boundary condition of $\Delta p^w = 0$ kPa at the upper and lower nodes. A constant vertical seating load was applied at the top nodes. For constant volume swelling (OPA-0-34 and -07), the vertical displacement of the upper nodes was constrained, while it was not constrained for vertically unconfined swelling (OPA-0-24). An additional unloading step after the infiltration step was considered for simulation of constant volume swelling with unloading prior to the oedometric loading path (OPA-0-07). For infiltration, the novel transient-critical analysis type was applied with $f_{t_{\min}} = 0.90$ and $\Delta t_{\max} = 10$ s, whereas all other steps were simulated as static.

7.1.1.1. Simulation results

Constant volume swelling with subsequent compression and rebound test

Figure 7.3 presents the simulation results of constant volume swelling followed by an oedometric compression and rebound test. A stress ratio of $K_0 \approx 4.0$ was evident before the onset of infiltration as the result of the simulation of specimen preparation. In the upper row, the evolution of the vertical net stress σ_{22} over time, and in the lower row, the material response in terms of void ratio versus vertical net stress is shown. Local quantities are each presented on the left-hand side and external quantities on the right-hand side in comparison with experimental results from constant volume swelling tests (OPA-0-04, -07 and -34), one with subsequent oedometric loading. The colour gradient in blue indicates elements on the symmetry axis from the outer boundary (darker) to the centre (brighter) of the model. The local results on the left-hand side of Figure 7.3 indicate that the external constant volume condition did not hold for the individual element rows. Instead, elements near the outer boundary expanded during infiltration, leading to a slight compression of the inner elements and a non-uniform evolution of swelling pressure. The inner elements tended to develop higher swelling pressures due to the additional load imposed by the expanding outer elements, which themselves generated comparatively less swelling pressure, see upper left plot of Figure 7.3. Some variation of the local, vertical net stress among elements

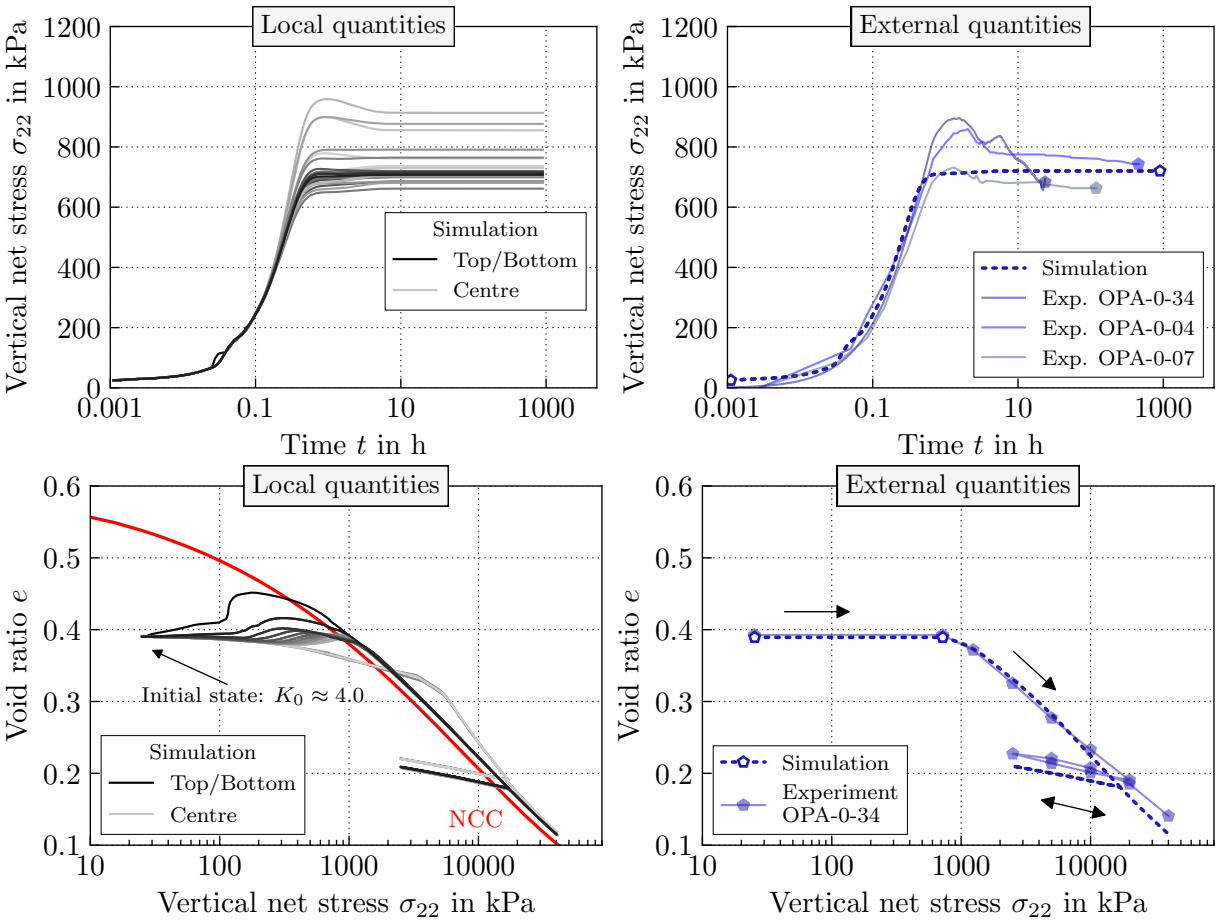

Figure 7.3.: Mechanical response in the simulation of a constant volume swelling and oedometric compression and rebound test on reconstituted Opalinus clay: Local quantities (left) and external quantities (right) versus experimental results from Nitsch et al. (2023a).

along the specimen height was observed, reflecting small numerical shear stresses required to maintain equilibrium of the total stress. These variations arise from the strong nonlinearity of the mechanical constitutive model, where minor rounding errors can lead to numerical inaccuracies, and do not indicate any physical inhomogeneity. The resulting external vertical net stress $\sigma_{22} = 720$ kPa showed very good agreement with the average swelling pressure $\sigma_{22} \approx 700$ kPa from the three experiments. Due to the locally varying behaviour within the FE model, the final stress was however smaller than in the single-element simulations (Section 5.5.1), in which a final value of $\sigma_{22} = 746$ kPa was reached in the fully saturated state. Furthermore, the model successfully reproduced the time evolution, especially the initial increase, of the vertical net stress upon swelling, see upper right plot of Figure 7.3. After completion of swelling, the material behaviour upon subsequent vertical loading and unloading was predicted well in the simulations, as can be seen in the lower right-hand side plot of Figure 7.3. In the local results in the lower left-hand plot, the differences within the element rows are evident and the expansion of the outer element rows and compression of the inner element rows is clearly visible. A void ratio gradient from outer to centre elements existed while constant volume persisted in the external behaviour. The paths of selected elements upon wetting are discussed in more detail in Section 7.1.1.2 and Figure 7.8 shows contour plots of the simulation.

The hydraulic material response during the infiltration step is shown in Figure 7.4 in terms of the evolution of pore water pressure over time (upper left), effective degree of saturation over time (upper right), evolution of apparent permeability with degree of saturation (lower right) and contributions of the relative permeabilities $k^{r,wf}$ and $k^{r,ws}$ with degree of saturation (lower left). For $k^{r,ws}$, the two components according to Equation (3.70) are shown separately as well: the contribution of the change in volume and the contribution of the attachment of swelling water.

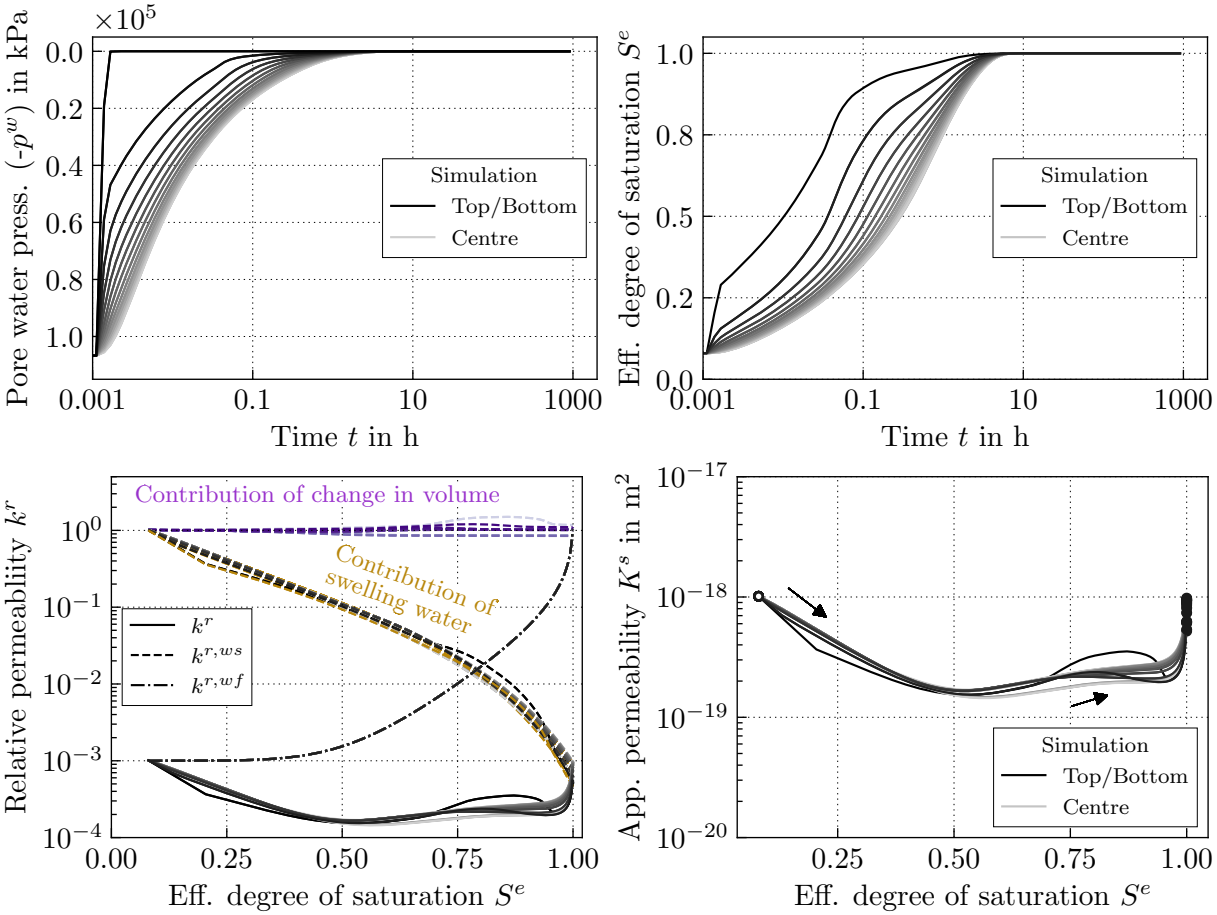

Figure 7.4.: Hydraulic response in the simulation of constant volume swelling on reconstituted Opalinus clay: evolution of pore water pressure, effective degree of saturation, permeability and relative permeabilities.

In the outermost elements, the pore water pressure and the degree of saturation instantaneously increased with the onset of the infiltration boundary condition. With increasing distance from the infiltration end, a delayed increase of both variables became evident over time. However, the onset of infiltration was rather immediate in all elements, see upper left and right plot of Figure 7.4. With increasing saturation, the unsaturated relative permeability increased up to $k^{r,wf} = 1$ at full saturation ($S^e = 1$), while the swelling-induced relative permeability decreased upon wetting from a value of 1 at dry conditions to avlue of 0 in the fully saturated state, see lower left plot of Figure 7.4 The product of both relative permeabilities exhibited first a decrease and later an increase. Note that this trend depends on the minimum value k^w_{min}, which will be addressed in Section 7.1.1.2. The same trend applied to the evolution of the apparent permeability and is indicated by arrows in the lower right plot of Figure 7.4. The mean vertical permeability over the height of the sample at the end of infiltration in the simulations was

estimated to $K^s_{22} \approx 8.0 \times 10^{-19}$ m^2 for a void ratio of $e = 0.389$, which is smaller than the experimentally determined value of $K^s \approx 1.3 \times 10^{-18}$ m^2. The difference can be attributed to the non-linear dependence of permeability on the void ratio, which led to variations caused by the inhomogeneous void ratio distribution in the simulation. The swelling-induced relative permeability and consequently the overall permeability as well reflected the inhomogeneous void ratio distribution in the simulation. For constant volume conditions, ideally, only the attachment of swelling water contributes to the swelling-induced relative permeability. In Figure 7.4, however, contributions of the change in volume are evident as well.

Figure 7.5 presents the simulation results of a constant volume swelling test with additional unloading prior to the main oedometric compression and rebound tests. The results of both constant volume swelling tests in Figures 7.3 and 7.5 differ slightly during infiltration as well as the subsequent loading and unloading phases due to small differences in initial stress, but overall show good agreement.

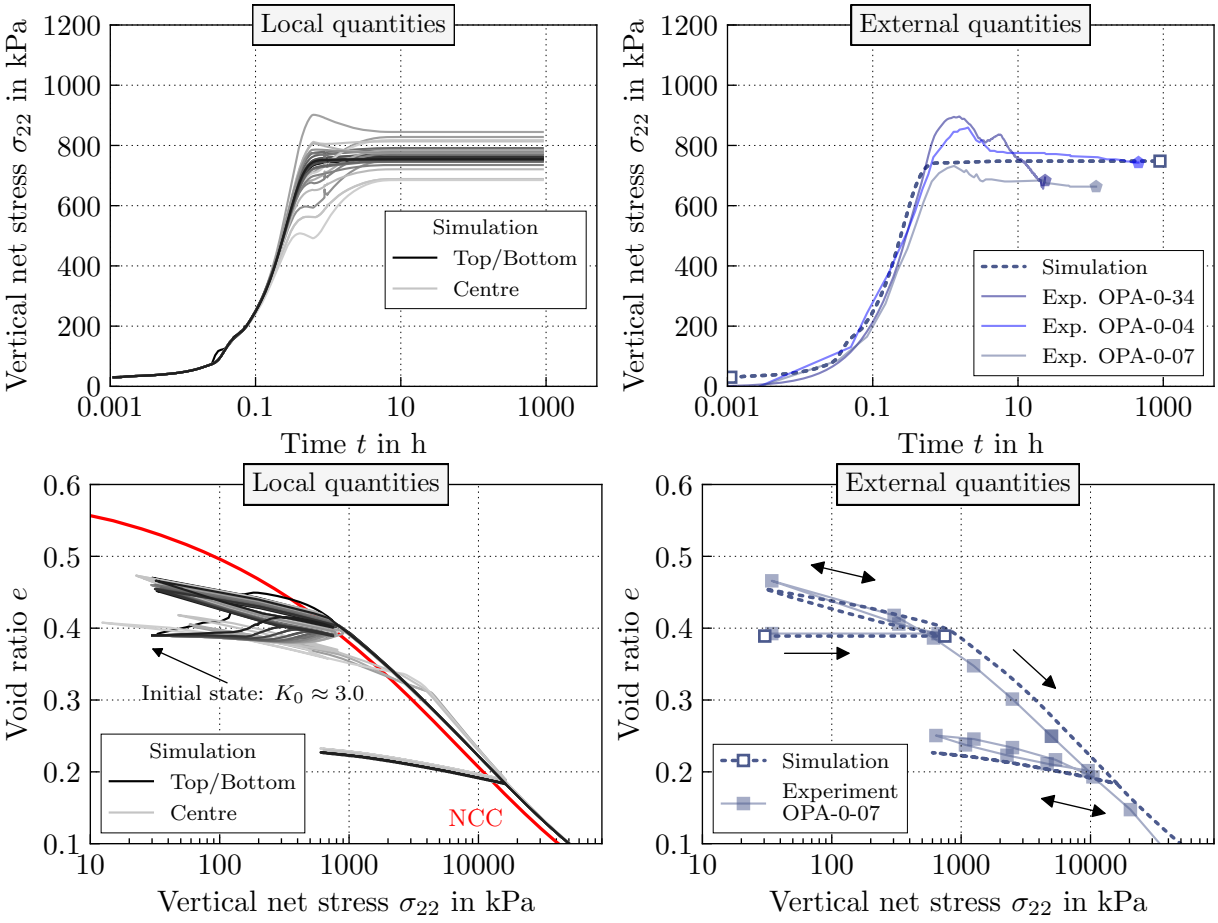

Figure 7.5.: Mechanical response in the simulation of a constant volume swelling with unloading and oedometric compression and rebound test on reconstituted Opalinus clay: Local quantities (left) and external quantities (right) versus experimental results from Nitsch et al. (2023a).

The evolution of local vertical net stress σ_{22} in the upper left plot of Figure 7.5 shows different scattering among the elements along the model height than was evident in Figure 7.3, highlighting the numerical nature of these variations rather than a physical response. Due to the inhomogeneous state in terms of stress and void ratio in the element rows after swelling at the end of the infiltration step, the deformation during unloading differed significantly among the

elements, as is visible in the lower left-hand side plot of Figure 7.5. The simulation underestimated the magnitude of deformation observed in test OPA-0-07 to some extent, see lower right plot of Figure 7.5. Overall, the experimental path was captured adequately well.

Vertically unconfined swelling with subsequent compression and rebound test

Figure 7.6 presents the simulation results of a vertically unconfined swelling test, followed by an oedometric compression and rebound test. A stress ratio of $K_0 \approx 3.0$ was evident before the onset of infiltration as the result of the simulation of specimen preparation. In the upper row, the evolution of the expansion over time is shown, and in the lower row, the material response in terms of void ratio versus vertical net stress is presented. Local quantities are each presented on the left-hand side and external quantities on the right-hand side in comparison with experimental results from vertically unconfined swelling tests (OPA-0-24 and 32), one with subsequent oedometric loading. The colour gradient in blue again indicates elements on the symmetry axis from the outer boundary (darker) to the centre (brighter) of the model.

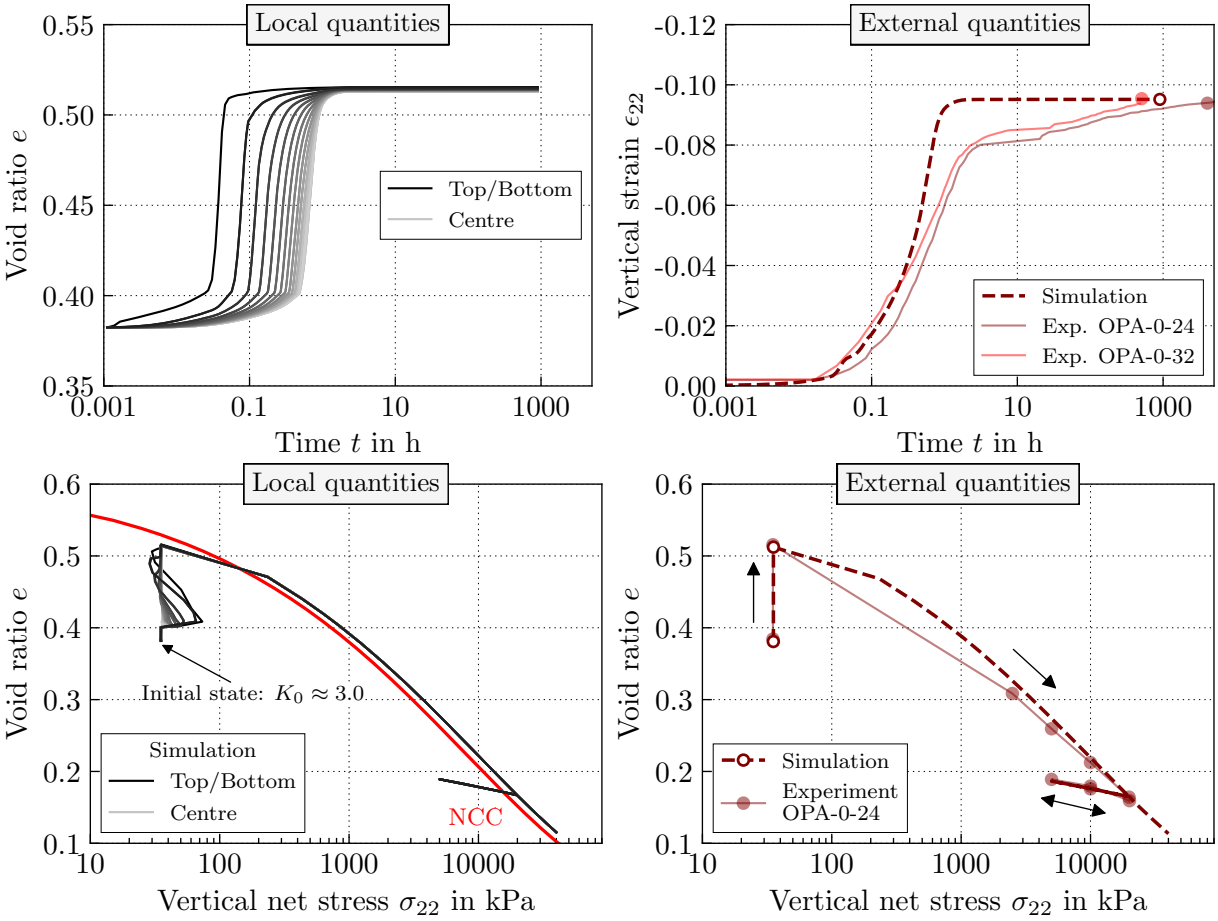

Figure 7.6.: Mechanical response in the simulation of a vertically unconfined swelling and oedometric compression and rebound test on reconstituted Opalinus clay: Local quantities (left) and external quantities (right) versus experimental results from Nitsch et al. (2023a).

Good agreement between the simulation and experimental results is observed in terms of the temporal evolution in the upper plot on the right-hand side of Figure 7.6. In particular, the initial increase in vertical strain due to swelling was reproduced accurately by the simulation, however with a slightly higher rate. With increasing time, the simulation progressed faster than

the experiments. It should be noted that the experiments were conducted using a simple testing device (see Appendix A.1), in which the stress level acting on the sample was adjusted manually during the test to compensate for system deformation. During the intervals between manual corrections, the sample experienced a slightly elevated load, which hindered the expansion and slowed down the overall evolution of deformation. Taking this effect into account, the model's predictive quality is considered as very good. The final magnitude of vertical strain upon swelling in the simulation was $\epsilon_{22} = -0.0932$ and in excellent agreement with the average value of $\epsilon_{22} = -0.0943$ of the experiments. It was found marginally smaller than the final magnitude from the single element simulations, which was $\epsilon_{22} = -0.0953$ in the fully saturated state (see Section 5.5.1). The local results in the bottom plot on the left-hand side of Figure 7.6 revealed some fluctuations of vertical net stress in the response of individual elements, which were more pronounced for the outer elements than for the inner elements of the simulation. As shown in Section 6.6.3.1, these fluctuations were a result of the simple integration schemes of the mechanical constitutive model. However, they were not decisive for the quality of the external response, shown in the bottom plot on the right-hand side of Figure 7.6. Upon the subsequent loading and unloading path, the experimental results were very well reproduced in the simulation.

The hydraulic material response during the infiltration step is shown in Figure 7.7. Analogously to Figure 7.4, the evolution of pore water pressure over time (upper left), effective degree of saturation over time (upper right), evolution of apparent permeability with degree of saturation (lower right) and contributions of the relative permeabilities $k^{r,wf}$ and $k^{r,ws}$ with the degree of saturation (lower left) are presented. For the latter, the two components according to Equation (3.70) are shown separately as well: the contribution by the change in volume and the contribution by the attachment of swelling water. The hydraulic behaviour is very similar to that of constant volume conditions (see Figure 7.4) apart from the change in volume, which is evident on the lower left-hand side of Figure 7.7 for vertically unconfined conditions. The swelling-induced relative permeability reduces less pronounced and the final apparent permeability is slightly increased, see lower right-hand side of Figure 7.7. Consequently, the saturation process is completed slightly faster than for constant volume swelling. The mean vertical permeability over the height of the sample at the end of infiltration in the simulations was estimated to $K^s_{22} \approx 4.4 \times 10^{-18}$ m^2 for a void ratio of $e = 0.513$, which is slightly larger than the experimentally determined value of $K^s \approx 2.8 \times 10^{-18}$ m^2.

Comparison of vertically unconfined and constant volume swelling

Figure 7.8 presents the distribution of the (local) void ratio, the degree of saturation and the volume fraction of swelling water for five time steps upon wetting in vertically unconfined (upper part) and constant volume swelling (bottom part). For the latter, the distribution of vertical net stress is also shown. The corresponding simulation results were shown in Figures 7.3 and 7.6 respectively. The points in time for the contour plots were chosen identical for both simulations and are indicated qualitatively in the evolution of both swelling phenomena in the centre of Figure 7.8. For vertically unconfined swelling, the progressive expansion of the elements over time with the increasing degree of saturation is clearly visible. The expansion of the outer elements did not significantly affect the void ratio of the inner elements, which remained unchanged until changes in degree of saturation took place in these elements. The volume fraction of swelling water increased simultaneously with the increasing degree of saturation from both infiltration ends. As time progressed, homogenisation occurred within the model for all three shown vari-

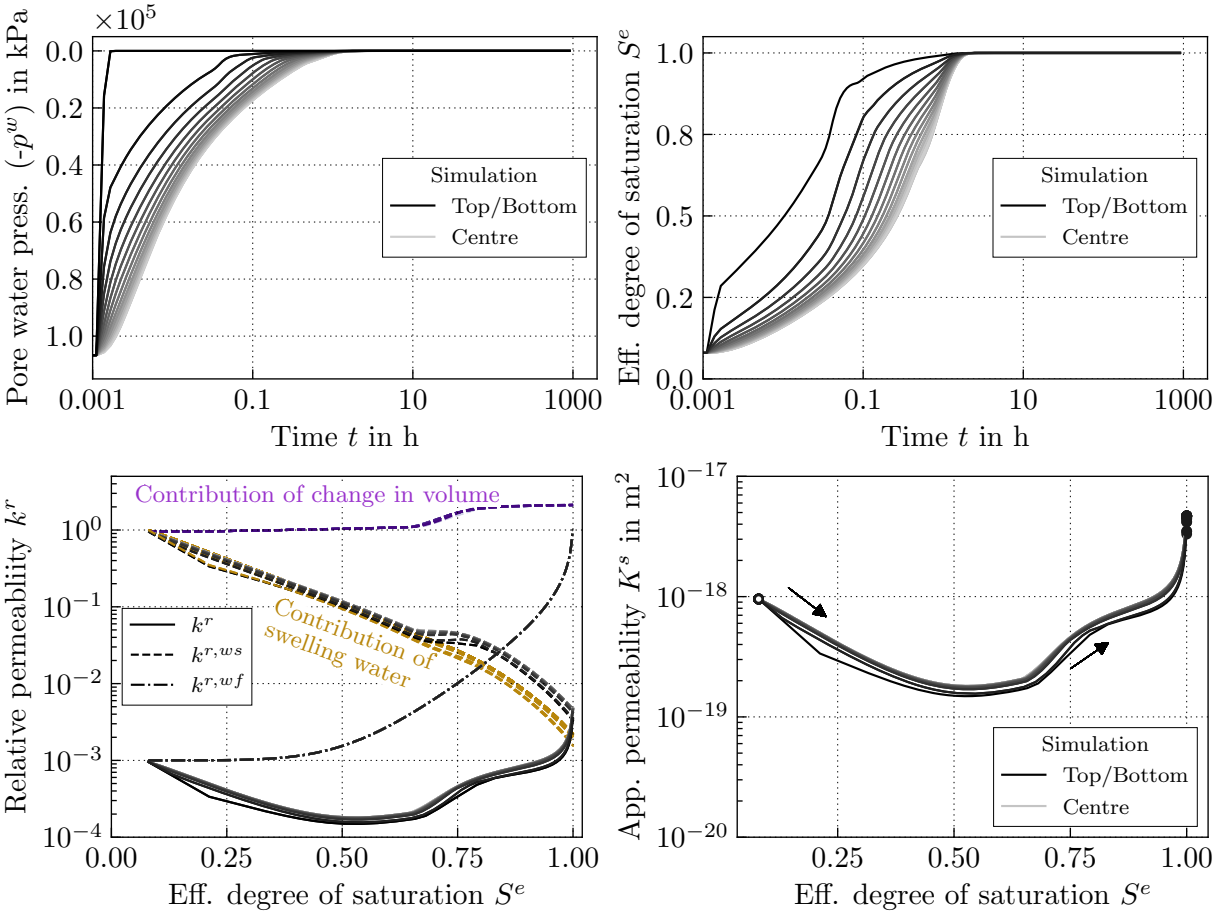

Figure 7.7.: Hydraulic response in the simulation of vertically unconfined swelling on reconstituted Opalinus clay: evolution of pore water pressure, effective degree of saturation, permeability and relative permeabilities.

ables. At full saturation, the final void ratio was $e_{\max} \approx 0.515$ and the final swelling water content amounted $\varphi^{ws}_{\max} \approx 0.290$.

For constant volume swelling, the locally varying behaviour is evident: the outer elements first experienced an expansion, which was subsequently reduced due to swelling of the inner elements. However, the void ratio did not homogenise completely within the model upon further saturation and an inhomogeneous distribution, also within the element rows, persisted. These were also evident in the distribution of vertical net stress and of the volume fraction of swelling water. The degree of saturation showed a very uniform distribution over the model height, with nearly constant values in each row. At full saturation, the final void ratio ranged between $e = 0.366$ and 0.411 and the final swelling water content between $\varphi^{ws}_{\max} = 0.239$ and 0.264. The distribution of the (local) vertical net stress for constant volume swelling in the lower part of Figure 7.8 provides insight into the extent of the net stress scatter previously discussed in the context of Figures 7.3 and 7.5. For the first two time steps, the vertical net stress develops uniformly across the height of the model. However, as the infiltration progresses, the varying response of individual elements becomes apparent. Contrary to the distribution of void ratio, which homogenized with increasing saturation, the variations intensify for the vertical net stress, resulting in values fluctuating between $\sigma_{\max} = 1040$ kPa and $\sigma_{\min} = 320$ kPa. Accordingly, the responses of radial net stress and shear stress also became inhomogeneous (not shown).

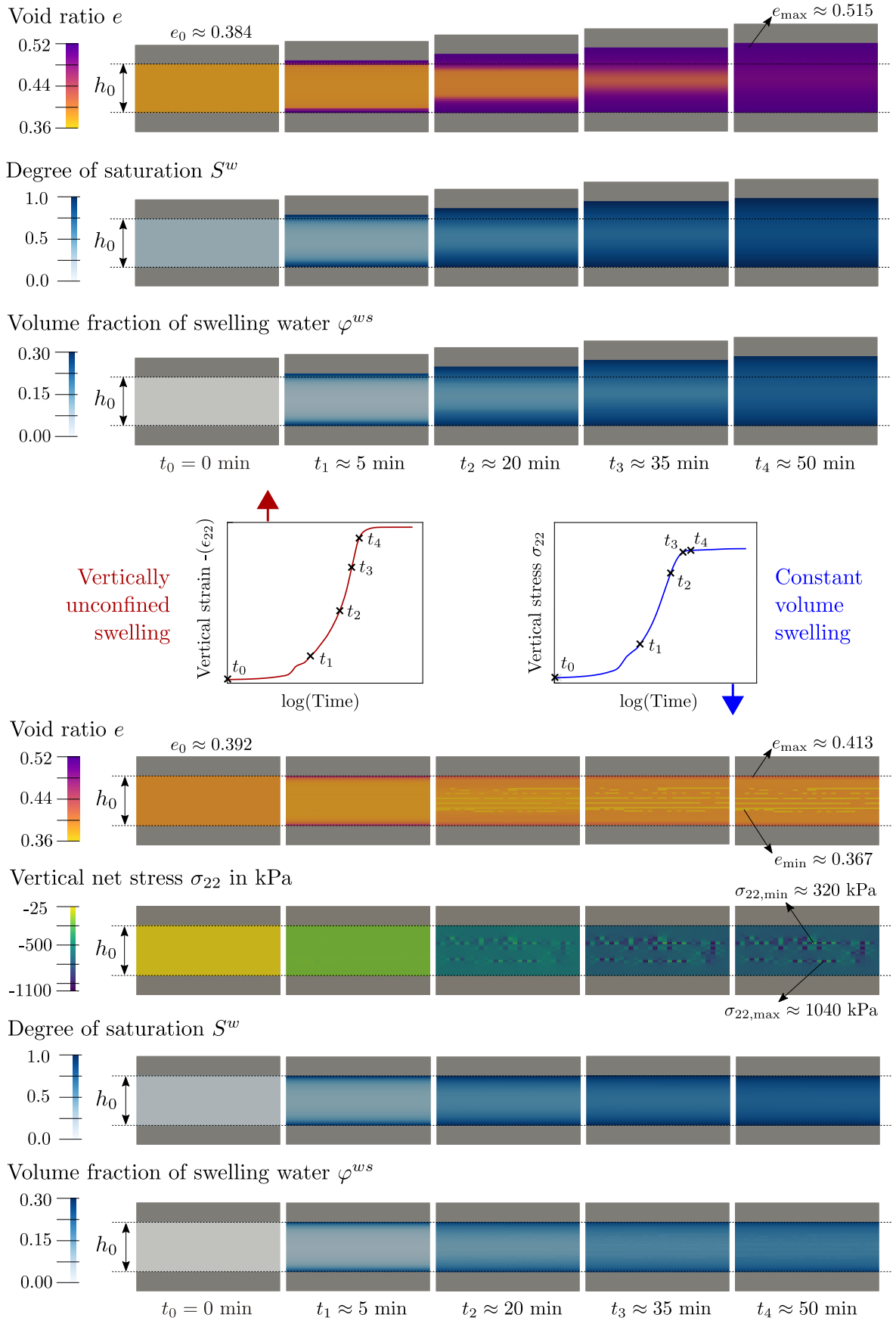

Figure 7.8.: Distribution of void ratio, degree of saturation and volume fraction of swelling water in simulation of swelling tests at different times upon infiltration for vertically unconfined swelling (upper part) and constant volume swelling (lower part). The distribution of vertical net stress is shown additionally for constant volume swelling. Deformation scale factor: 3.

Figure 7.8 underlines the different response in simulations of vertically unconfined and constant volume swelling. To emphasize it further, Figure 7.9 presents the evolution of local void ratio for vertically unconfined and of local vertical net stress for constant volume swelling from the simulations shown in Figures 7.3 and 7.6 respectively, however, here over the effective degree of saturation. For vertically unconfined swelling on the left-hand side of Figure 7.9, all elements exhibit an identical increase of void ratio with effective degree of saturation. The response of each element in the BVP closely matches that of single-element simulations, and expansion developed over the entire range of S^e. Although the externally measurable vertical strain results from the combined contributions of all elements, each element's mechanical response is independent of its neighbouring elements and only governed by local changes in saturation. Swelling evolves while the idealized boundary condition of $\dot{\sigma}_{22} = 0$ holds. In contrast, for constant volume swelling on the right-hand side of Figure 7.9, the elements show a significantly different evolution along the model height. The increase in vertical net stress within each element arose from a combination of load transfer from neighbouring elements and its own mechanical response from changes in saturation. The externally measurable reaction force resulted from the interaction of all element responses. Locally, the idealized boundary condition $\dot{\epsilon}_{22} = 0$ does not hold, and the mechanical response of every element in the BVP was no longer comparable to single-element results. With increasing distance of an element from the infiltration end, the onset of saturation became less dominant for the swelling pressure evolution and even a decrease of vertical net stress occurred. Challenges in the simulation of swelling pressure will be further addressed in Section 7.1.1.2 based on the evolution paths of individual elements.

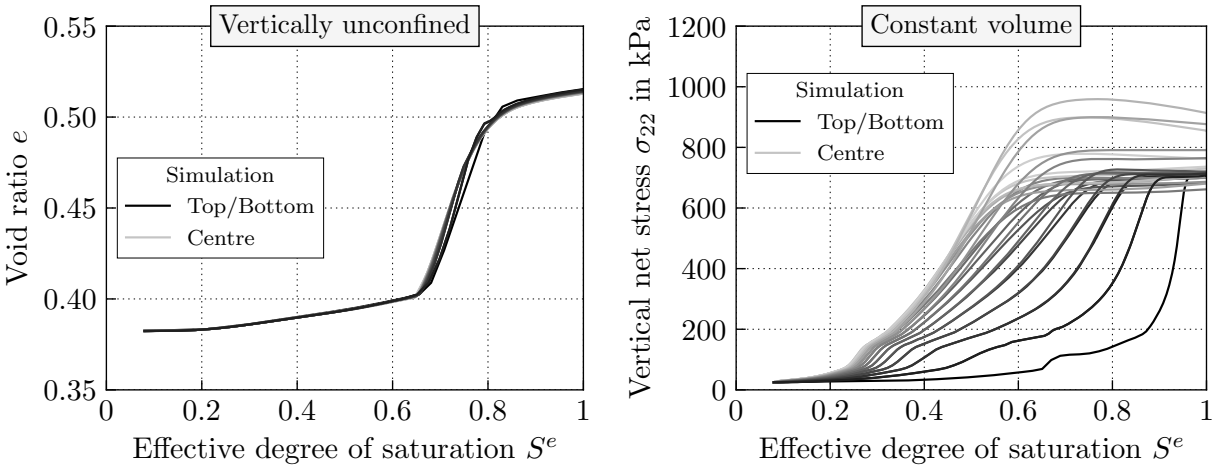

Figure 7.9.: Local void ratio for vertically unconfined swelling and vertical net stress for constant volume swelling versus effective degree of saturation.

Overview of results from simulations and experiments

With the extended finite element formulation and the novel constitutive model, both the magnitude and temporal evolution of swelling were captured in the simulations. Figure 7.10 presents the externally evaluated simulation results in comparison to the experiments in a similar manner as in Sections 4.4.1 and 5.5. In addition to the results from the previously discussed simulations of the oedometric swelling tests, the results of a simulation of the reference oedometric compression and rebound test in the nearly dry reference state (OPA-0-33) are presented as well. For the latter, very good agreement between simulation and experiment was evident. The simulations exhibited a sharper transition from reversible to irreversible material behaviour upon the

reloading branches than was measured in the experiment. However, the simulation was able to capture the magnitude of the transitional point corresponding to the net preloading stress $\sigma_{d,22}$ and to predict the stiffness from the experiment for normally consolidated and overconsolidated conditions. In general, the model accurately reproduced the magnitude of swelling and the material response in both dry and saturated states under oedometric loading and unloading.

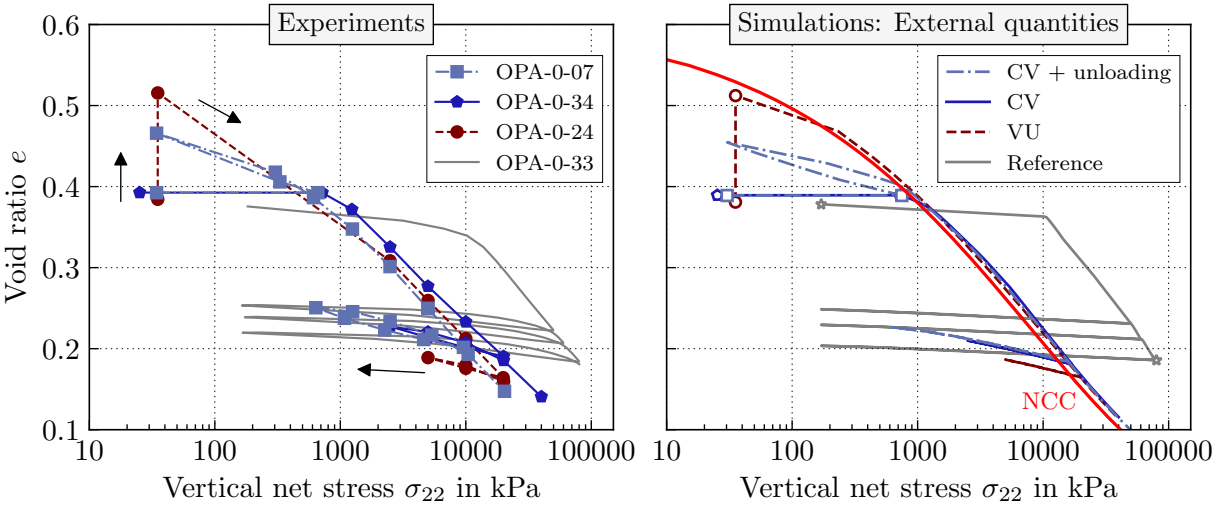

Figure 7.10.: Oedometric compression tests in the reference state and preceded by hydraulic loading at different boundary conditions on reconstituted Opalinus clay (Nitsch et al., 2023a): experimental results (left) and simulation results in terms of external behaviour (right).

Comparative simulation without extended TPM

To show the impact of the up-sw-element formulation, the simulation of vertically unconfined swelling from Figure 7.6 is repeated with the corresponding element of the `up`-library. The results of three simulations are presented in Figure 7.11 in terms of the external evaluation of vertical strain upon infiltration versus time. The up-element only considers the relative permeability for partial saturation, however, not the swelling-induced relative permeability. The

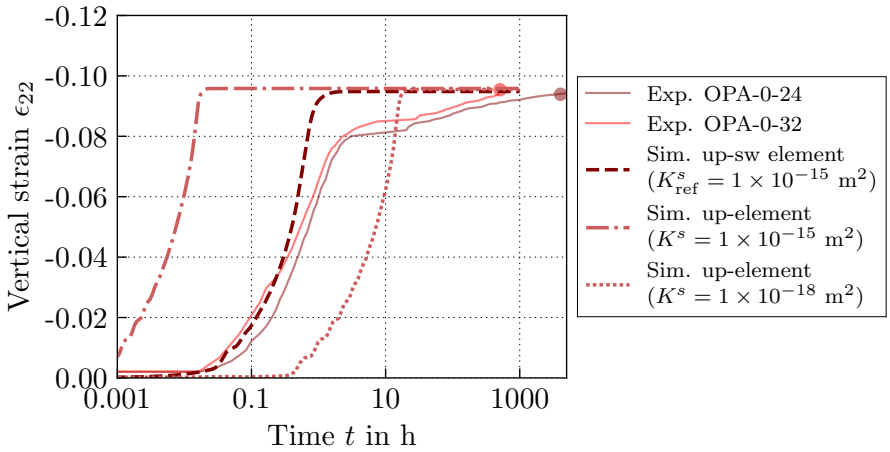

Figure 7.11.: Impact of the extended TPM on the time evolution of strain upon swelling: Simulation results of vertically unconfined swelling in terms of external quantities with a `up-sw`-element and `up`-element.

initial permeability of the simulation was set to $K = 1.0 \times 10^{-18}$ m^2, which corresponds to the saturated permeability from the experiments. For the sake of clarity, a simulation without this adjustment was conducted as well ($K = 1.0 \times 10^{-15}$ m^2). Both simulations with the up-element failed to accurately reproduce the time evolution of strain. The final magnitude was not affected by the choice of the element type and predicted accurately by the mechanical constitutive model. The time evolution however, was significantly delayed in the simulation with the up-element and the saturated permeability (dashed bright line) compared to experimental results and the simulation with the up-sw-element (solid dark line). Performing the simulation with the reference permeability of the saturated, unswollen state and the up-element drastically overestimated the time evolution and swelling was complete after just a few seconds (dash-dotted bright line). The results show the importance of considering both, the swelling-induced and unsaturated relative permeability.

Oedometric swelling tests in perspex ring

In this section, the swelling tests under oedometric conditions in perspex rings on reconstituted Opalinus clay shale are simulated, see Figures 2.13 and 2.17. In the infiltration step, the pore water pressure boundary condition of $\Delta p^w = 0$ kPa was applied at the bottom nodes only. In the simulations, the final magnitude of strain and stress was approximately reached, whereas the experiments were terminated before. The results are shown in terms of the evolution of the height of saturation front and the evolution of vertical strain upon swelling for vertically unconfined conditions and vertical net stress upon swelling for constant volume conditions in Figures 7.12 and 7.13, respectively.

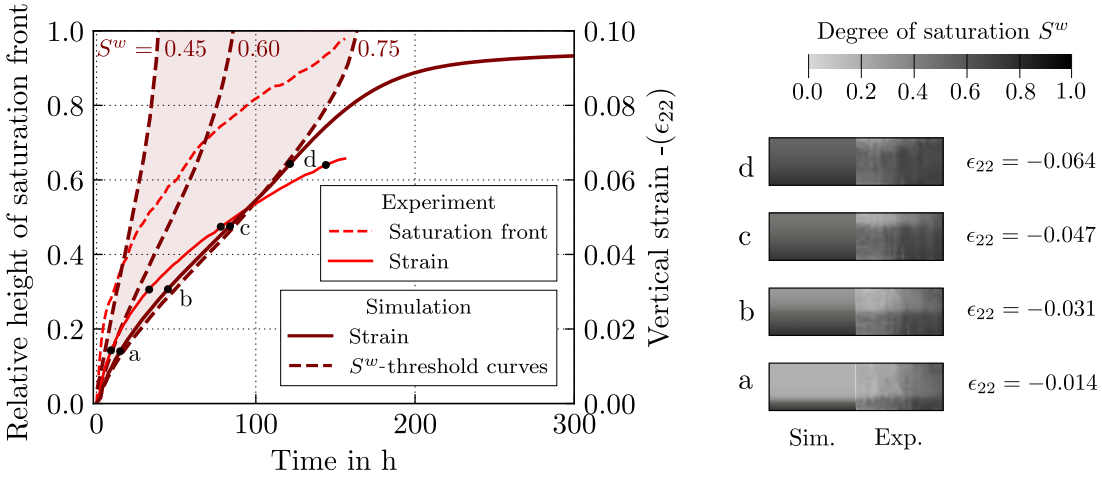

Figure 7.12.: Vertically unconfined swelling in a perspex oedometric ring: Relative height of the saturation front and evolution of vertical strain from experiment and simulation. A bandwidth for the saturation front propagation from simulations is shown.

In the evaluation of the experiments, the height of the saturation front was determined by visually distinguishing between bright and dark material in the perspex ring. However, the transition of dry to saturated state is not sharp in the material and the visible edge does not correspond to $S^w = 1.0$. Rather, an apparent dry part of the specimen is to some extent already saturated, while the apparent dark part is not fully saturated everywhere. Therefore, in the simulations the propagation of the saturation front is evaluated with different threshold values and a bandwidth is shown in Figures 7.12 and 7.13. In addition at four points in time

each, photographs from the experiment and contour plots of the degree of saturation from the simulation are presented next to each other (marked by a-d).

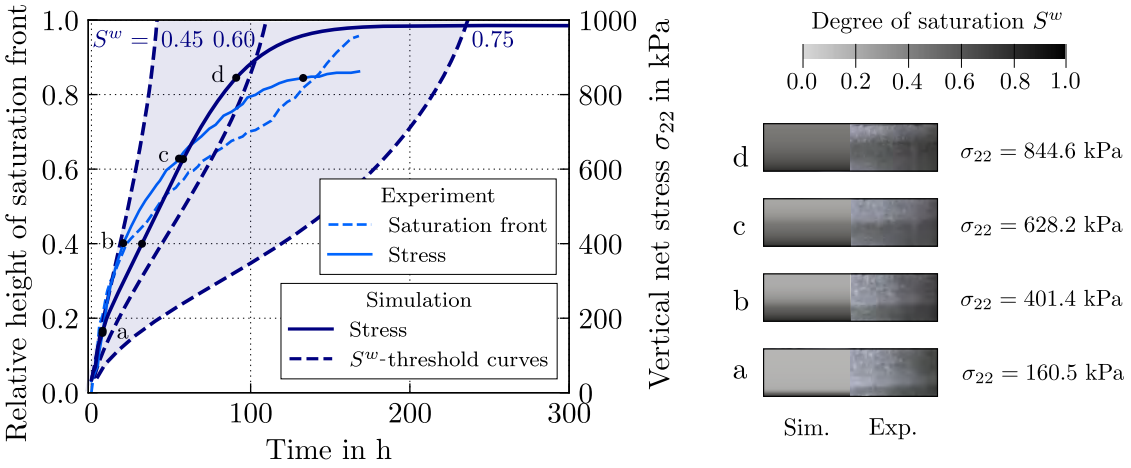

Figure 7.13.: Constant volume swelling in a perspex oedometric ring: Relative height of the saturation front and evolution of vertical net stress from experiment and simulation. A bandwidth for the saturation front propagation from simulations is shown.

For vertically unconfined swelling, the evolution of vertical strain in the simulation for the one-sided infiltration corresponded well to the experimental results, see solid lines in Figure 7.12. Experimental results only exist up to the time, when the saturation front had visually propagated through the sample, where the final deformation was not yet reached. In the simulation, however, the final value was reached. Similar to the simulation results for double-sided infiltration in Figure 7.6, the strain evolution was faster in the simulation than in the experiment. Comparing the progression of saturation between the simulation and the experiment is challenging due to the exclusively qualitative nature of the experimental results. A clear threshold value of S^w could not be established for defining the saturation front in the simulation, which aligned well with the experimental data for the complete progression of the front. The comparison between the photographs and the contour plots from the simulations shows, that an overall good agreement between the qualitative distribution of the degree of saturation within the sample was predicted with the modelling framework. Especially for early stages of the simulation, the infiltrated area was well differentiable, while the distribution of the degree of saturation became more homogeneous with increasing duration.

For constant volume swelling, the evolution of vertical net stress for one-sided infiltration in the experiments is captured reasonably well by the model, see solid lines in Figure 7.13. The magnitude of the experiment was slightly overestimated by the simulation, while the time evolution was well met. Here, as well, a comparison of the infiltration front in simulation and experiment was difficult and the overall trend could not be predicted by a single threshold value in the simulation. The photographs and simulation contour plots show a similar qualitative agreement as observed for vertically unconfined swelling. With increasing saturation, the simulation showed a more uniform infiltration behaviour than the experiment, while the visible differences between low- and highly-saturated material at the infiltration front were well reproduced in the earlier stages. Finally, the simulations confirm the slightly slower infiltration for constant volume swelling compared to vertically unconfined swelling observed in the experiments, as the evaluation of the threshold values of S^w in the simulations showed a broader bandwidth for

constant volume swelling. The transition between unsaturated and saturated zones in the simulation of BVPs depends on the choice of the minimum unsaturated relative permeability $k^w_{\min}$. The smaller $k^w_{\min}$, the more isolated is the hydraulic response of different parts of an FE model upon infiltration. Difficulties associated with the isolated hydraulic response are addressed in the following Section.

7.1.1.2. Influence of minimum permeability

The simulations of vertically unconfined and constant volume swelling are repeated with a smaller value of the minimum value of the unsaturated relative permeability to illustrate the influence of the hydraulic variables on the material response of BVPs. A value of $k^w_{\min} = 1 \times 10^{-6}$ is chosen, which gives a reasonable lower limit for the apparent permeability K, which should be larger than the threshold between liquid water and vapour permeability approximated at $K \approx 1 \times 10^{-21}$ m^2 (Fredlund et al., 2012).

Constant volume swelling

Figure 7.14 shows the mechanical response of the simulation of constant volume swelling with application of $k^w_{\min} = 1 \times 10^{-6}$ for the minimum unsaturated relative permeability. The hydraulic response of the simulation is presented in Figure 7.15. The results are shown analogously to the sections before, including the evolution of pore water pressure over time (upper left), effective degree of saturation over time (upper right), evolution of apparent permeability with degree of saturation (lower right) and contributions of the relative permeabilities $k^{r,wf}$ and $k^{r,ws}$ with degree of saturation (lower left). On the right-hand side of the bottom row of Figure 7.14, the externally evaluated evolution of vertical swelling pressure is additionally displayed for the simulation with $k^w_{\min} = 1 \times 10^{-3}$ (bright line, see Figure 7.3). A pronounced difference in the material behaviour as a result of the different values of $k^w_{\min}$ is evident. The swelling pressure for the simulation with $k^w_{\min} = 1 \times 10^{-3}$ resulted in 320 kPa, which was well below the magnitude observed in the experiments and the simulation with $k^w_{\min} = 1 \times 10^{-3}$. Furthermore, the net stress evolution diminished earlier, at a point in time, where the FE model was far from full saturation. The results in the upper row of Figure 7.15 demonstrate a delayed increase of the pore water pressure and effective degree of saturation with distance from the infiltration ends.

The vertical net stress, however, increased almost identically in all elements, as is evident in the lower row of Figure 7.14. In the upper row of Figure 7.14, an insufficient reduction of the vertical net preloading stress is evident, as the transition from reversible to irreversible behaviour occurred at a larger vertical net stress than in Figure 7.3. Consequently, the simulation does not agree with the experimental results. The evolution of the relative permeability of the simulation with $k^w_{\min} = 1 \times 10^{-6}$ in the lower left plot of Figure 7.15 differs significantly from that of the simulation with $k^w_{\min} = 1 \times 10^{-3}$ in Figure 7.4. While the swelling-induced relative permeability is unaffected by $k^w_{\min}$, the initial unsaturated relative permeability $k^{r,wf}$ is reduced and the product of both shows a unidirectional trend, i.e. apart from a small initial decline, it is increasing during the entire infiltration process. As a result, the apparent permeability (lower right plot of Figure 7.15) increases from its initial value of $K^s = 1 \times 10^{-21}$ m^2, however, decreasing to smaller values intermediately. The significantly reduced apparent permeability in comparison to the previously encountered value of $K^s = 1 \times 10^{-18}$ m^2 caused the isolated hydraulic material response.

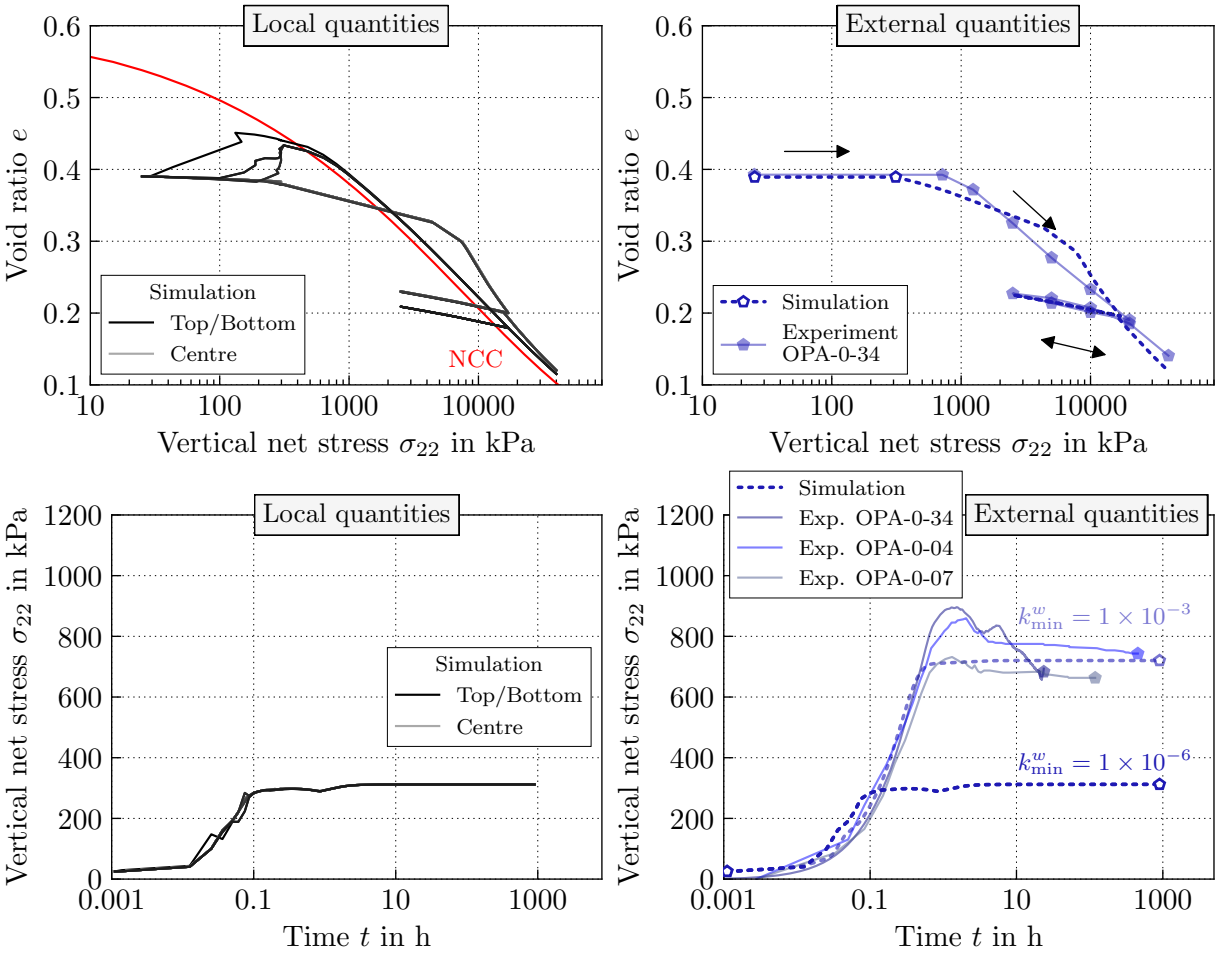

Figure 7.14.: Mechanical response in the simulation of a constant volume swelling and oedometric compression and rebound test on reconstituted Opalinus clay with application of $k^w_{\min} = 1 \times 10^{-6}$. Experimental results from Nitsch et al. (2023a).

For a deeper investigation of the material response in the simulations, the paths of several material variables in the outermost and centre element are examined in more detail in Figures 7.16 and 7.17 for both simulations with $k^w_{\min} = 1 \times 10^{-3} \mathrel{\hat{=}} K^s = 1 \times 10^{-18}$ m^2 and $k^w_{\min} = 1 \times 10^{-6} \mathrel{\hat{=}} K^s = 1 \times 10^{-21}$ m^2, respectively. On the left-hand side each, the evolution of the void ratio $e(p)$ and the void ratio $e_w(p)$ on the w-line is shown versus the degree of saturation. In the centre plot, both are presented over the mean net stress p for the complete infiltration step of the simulation. The w-line, B-line and the respective stresses $p_w(e)$, $p_B(e)$ and $p_e(e)$ on the NCC are depicted for the start and end of the infiltration as well. The right-hand side plot each shows the stress path in the $q-p$ diagram during infiltration including the preconsolidation surface (PS) and critical state line (CSL) at the start and the end of the infiltration. On the isotropic axis, the net stresses of the three characteristic lines are marked. The movement of all shown variables is indicated with arrows. For the simulation with $k^w_{\min} = 1 \times 10^{-3}$, whose full results were shown in Figure 7.3, an expansion of the outermost and compression of the centre elements were evident. The consequences of the locally varying behaviour become apparent in the paths of the respective elements in Figure 7.16.

At the start of the infiltration step, the initial state was identical in both elements. The path of the outermost element (upper row in Figure 7.16) first resembled that of vertically unconfined

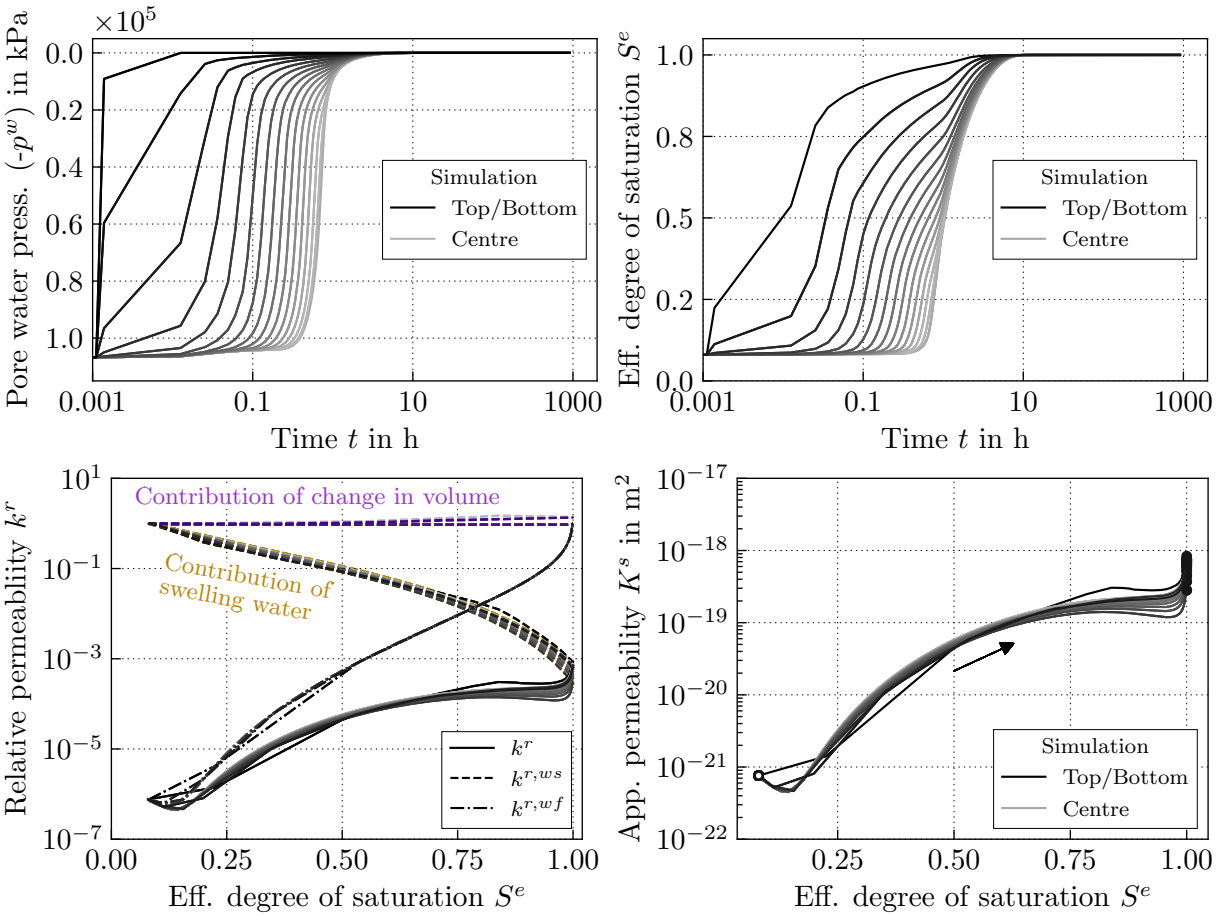

Figure 7.15.: Hydraulic response in the simulation of a constant volume swelling and oedometric compression and rebound test on reconstituted Opalinus clay with application of $k^w_{\min} = 1 \times 10^{-6}$. Experimental results from Nitsch et al. (2023a).

swelling. Upon saturation, the void ratio first increased slightly while the stress path moved in extension in the q–p diagram until the preconsolidation surface was met. Simultaneously with the first increase in p, the void ratio e_w on the w-line decreased (see Equation (5.23)), however, it was always greater than e. Afterwards, the direction of the stress path reversed and a more significant increase of the void ratio took place. At a certain point, however, the compliant deformation boundary conditions imposed by the surrounding elements first limited the expansion of the element and then led to a compression. The latter was evident in the decrease of e and the change of the direction of the stress path towards compression. The saturation-driven strain rate diminished for $e = e_w$ on the w-line very close to the NCC, where the void ratio was larger than its initial value. As a result, the bounding stress p_B on the B-line was also reduced towards the final state and the preconsolidation surface compressed on the isotropic axis. Up to that point, e_w was always larger than e and the saturation strain rate, responsible for the evolution of the swelling phenomena, developed (see Equation (5.18)). Consequently, wetting led to a partial manifestation of both swelling phenomena, a volumetric expansion and a swelling pressure build-up in the outermost element. In the centre element, a different path can be observed in the lower row of Figure 7.16. In the beginning, the element was slightly compressed, which is evident in the decrease of e and the stress path in compression in the q–p diagram. However, the volumetric deformation was small and the element behaviour is similar to that of idealized constant volume conditions. As a result p_B is comparably larger

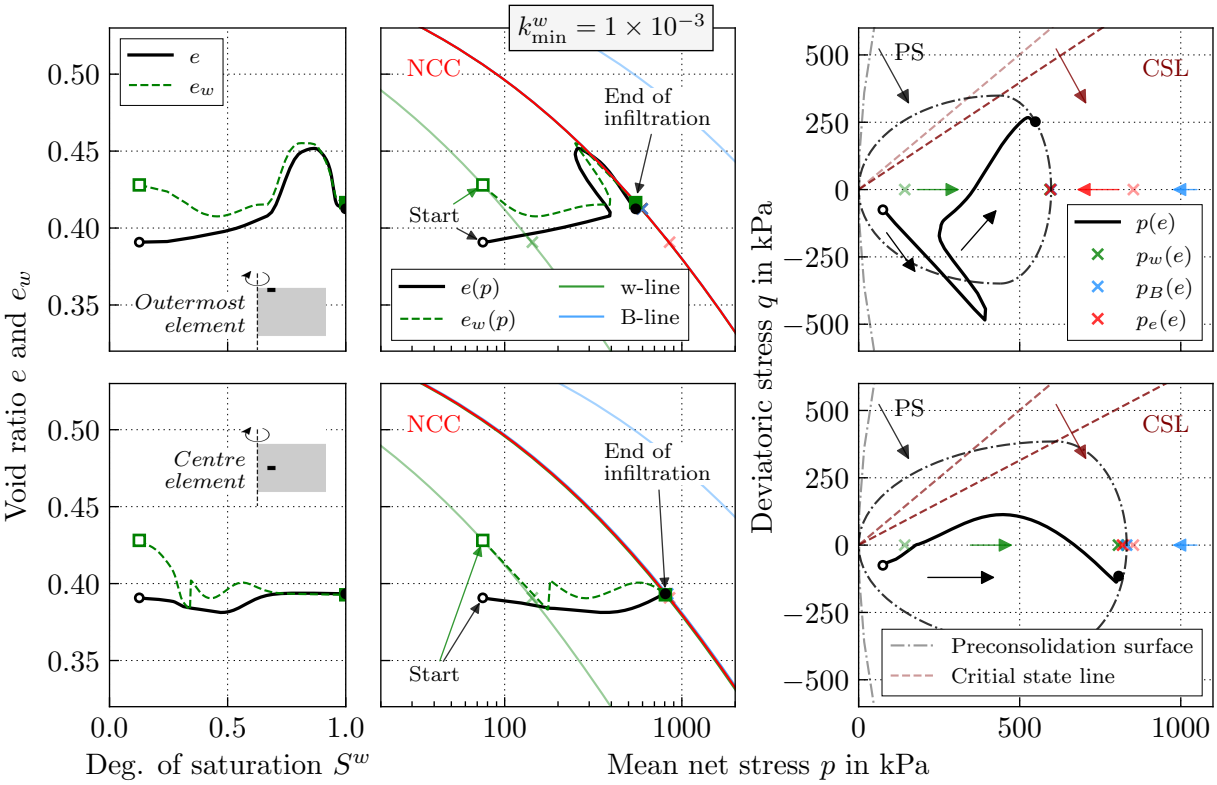

Figure 7.16.: Material response of outermost (top row) and centre (bottom row) element in simulation of constant volume swelling with $k^w_{\min} = 1 \times 10^{-3}$: Evolution of void ratios e and e_w during saturation (left), path in void ratio versus mean net stress diagram (centre) and stress path in q–p diagram (right). The arrows indicate the stress path and movement of CSL, PS and the net stresses on the isotropic axis during infiltration.

than in the outer element and p increases until $e = e_w$ on the w-line. Upon swelling, the element again expanded and the final void ratio is similar to its initial value.

For the simulation with $k^w_{\min} = 1 \times 10^{-6}$, significantly different paths of the material variables can be seen in Figure 7.17. At the start of the infiltration step, the initial state is again identical in both elements. The behaviour in the outermost element in Figure 7.17 is similar to that described in Figure 7.16. The slightly uneven path in the outer element is due to a comparatively larger critical time increment resulting from the very low initial permeability of $K = 1 \times 10^{-21}$ m^2. Wetting led to a manifestation of both swelling phenomena, first a volumetric expansion followed by a stress build-up. However, the final state of $e = e_w$ on the w-line was reached before a recompression of the element took place. Consequently, the void ratio remained large and the reduced bounding stress p_B resulted in an even smaller preconsolidation surface, reducing the final value of p. The missing recompression of the outer element was due to the absence of expansion in the inner elements. The latter behaviour is however a consequence of the behaviour of the outer elements, meaning that a pronounced interaction took place. Figure 7.17 shows, that the swelling of the outer elements resulted in a compaction and severe increase in p due to a load transfer before the degree of saturation S^w evolved within the centre element. As a consequence, the void ratio $e_w(p)$ on the w-line is smaller than the void ratio $e(p)$, when the first increase of saturation occurs in the element, see right-hand side plot of Figure 7.17. This state is additionally visualized by asterisks in the centre plot of Figure 7.17. The evolution of the saturation-driven strain rate (see Equation (5.18)) evoked a slight compaction, however

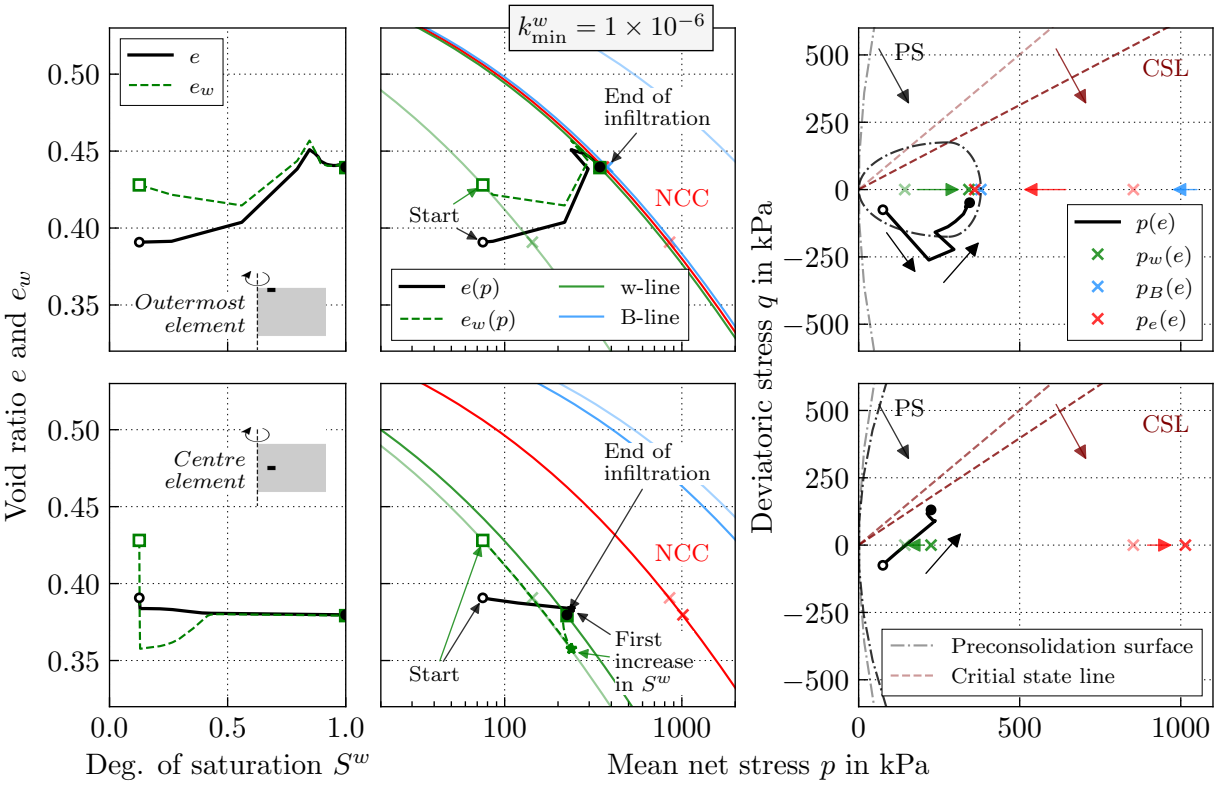

Figure 7.17.: Material response of outermost (top row) and centre (bottom row) element in simulation of constant volume swelling with $k^w_{\min} = 1 \times 10^{-6}$: Evolution of void ratios e and e_w during saturation (left), path in void ratio versus mean net stress diagram (centre) and stress path in q–p diagram (right). The arrows indicate the stress path and movement of CSL, PS and the net stresses on the isotropic axis during infiltration.

it vanished ($e = e_w$) without pronounced expansion or build-up of swelling pressure. The final stress state in the element was only due to load transfer from the outer element and consequently, the vertical net stress σ_{22} and the vertical reaction force were identical in all elements. Due to the reverse evolution of e_w, the preloading stress was not reduced (see Equation (5.27)), and the bounding stress p_B for the current void ratio remained large. The preconsolidation surface did not shrink upon swelling, which was also evident in the larger vertical net stress at the transition of reversible to irreversible material behaviour in the $e - \log(\sigma)$ diagram in Figure 7.14.

Vertically unconfined swelling

Analogously to the presentation of the results for constant volume swelling, Figures 7.18 and 7.19 show the mechanical and hydraulic response of the simulation of vertically unconfined swelling using $k^w_{\min} = 1 \times 10^{-6}$ for the minimum unsaturated relative permeability. On the right-hand side of the lower row of Figure 7.18, the externally evaluated evolution of the vertical strain is additionally displayed for the previously used value of $k^w_{\min} = 1 \times 10^{-3}$ (bright line, see Figure 7.6 for the full results).

In contrast to constant volume swelling, only a small influence of the magnitude of $k^w_{\min}$ and consequently of the magnitude of the apparent permeability was evident: The final magnitude of deformation is identical for $k^w_{\min} = 1 \times 10^{-3} \mathrel{\hat{=}} K^s = 1 \times 10^{-18}$ m^2 and $k^w_{\min} = 1 \times 10^{-6} \mathrel{\hat{=}} K^s = 1 \times 10^{-21}$. The time evolution was slightly affected, as the externally evaluated strain develops

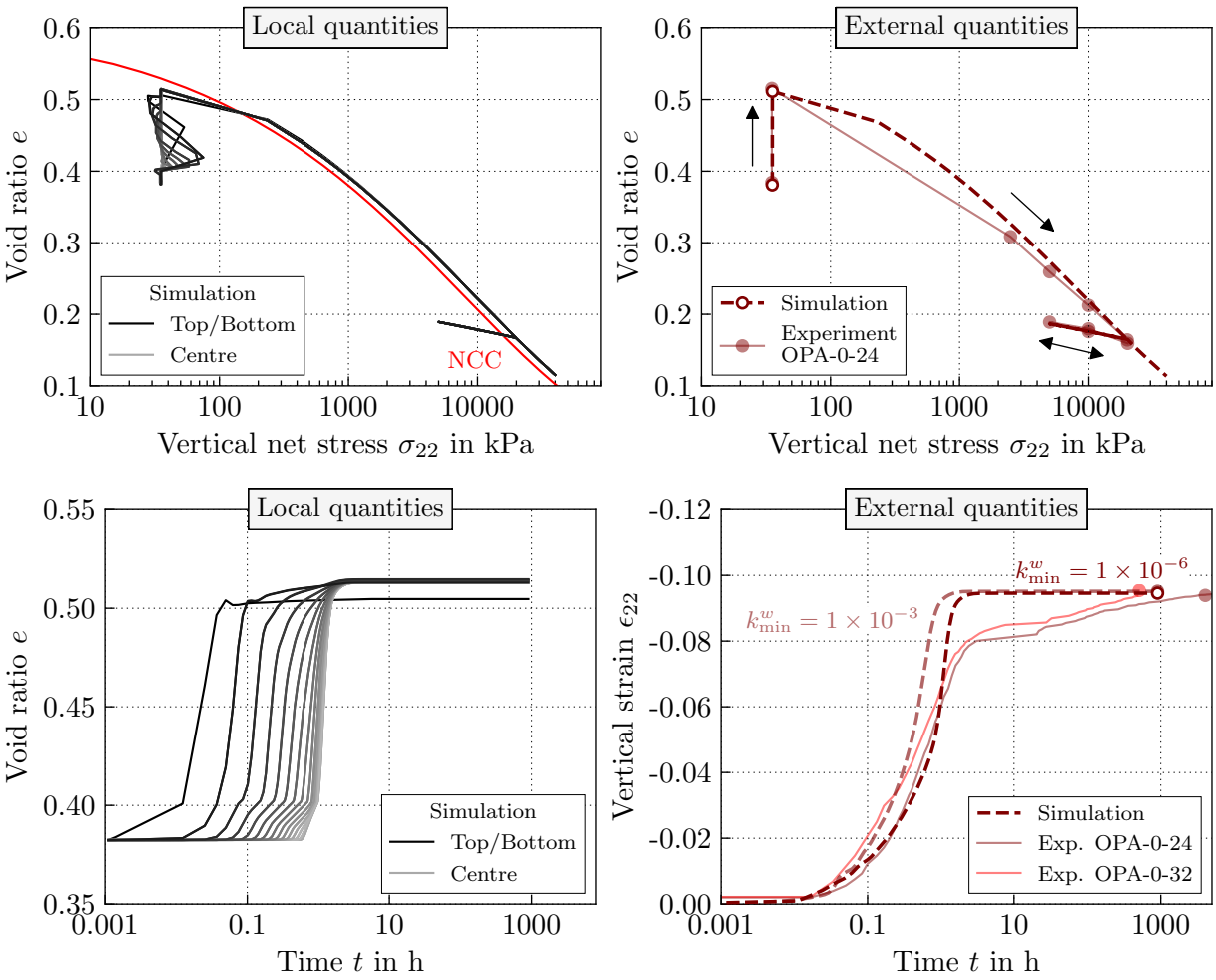

Figure 7.18.: Mechanical response in the simulation of a vertically unconfined swelling and oedometric compression and rebound test on reconstituted Opalinus clay with application of $k^w_{\min} = 1 \times 10^{-6}$. Experimental results from Nitsch et al. (2023a).

marginally slower for $k^w_{\min} = 1 \times 10^{-6}$ due to the delayed progression of the saturation front from the outer to the inner elements, which is evident in the lower right plot of Figure 7.18. The local results of the simulation with $k^w_{\min} = 1 \times 10^{-6}$ exhibited slightly more fluctuations of vertical net stress in the response of individual elements as well as in the void ratio evolution of the outermost element, which was smaller than in all other elements, see lower left plot of Figure 7.18. However, the time evolution of the vertical strain in both simulations is in similar good agreement with the experimental results. The hydraulic material behaviour in the simulation of vertically unconfined swelling in Figure 7.19 is also very similar to that of the simulation of constant volume swelling (Figure 7.15). The evolution of pore water pressure and effective degree of saturation (upper row) exhibited a significant delay with increasing distance from the infiltration ends. The evolution of the apparent permeability in the simulation with $k^w_{\min} = 1 \times 10^{-6}$ (lower right plot) was comparably less influenced by the contribution of the change in volume of the swelling-induced relative permeability (lower left plot) than in the simulation with $k^w_{\min} = 1 \times 10^{-3}$.

The paths of several material variables in the outermost and centre element are also examined for both simulations with $k^w_{\min} = 1 \times 10^{-3}$ and $k^w_{\min} = 1 \times 10^{-6}$ of vertically unconfined swelling in Figures 7.20 and 7.21, respectively. For the simulation with $k^w_{\min} = 1 \times 10^{-3}$, whose full results

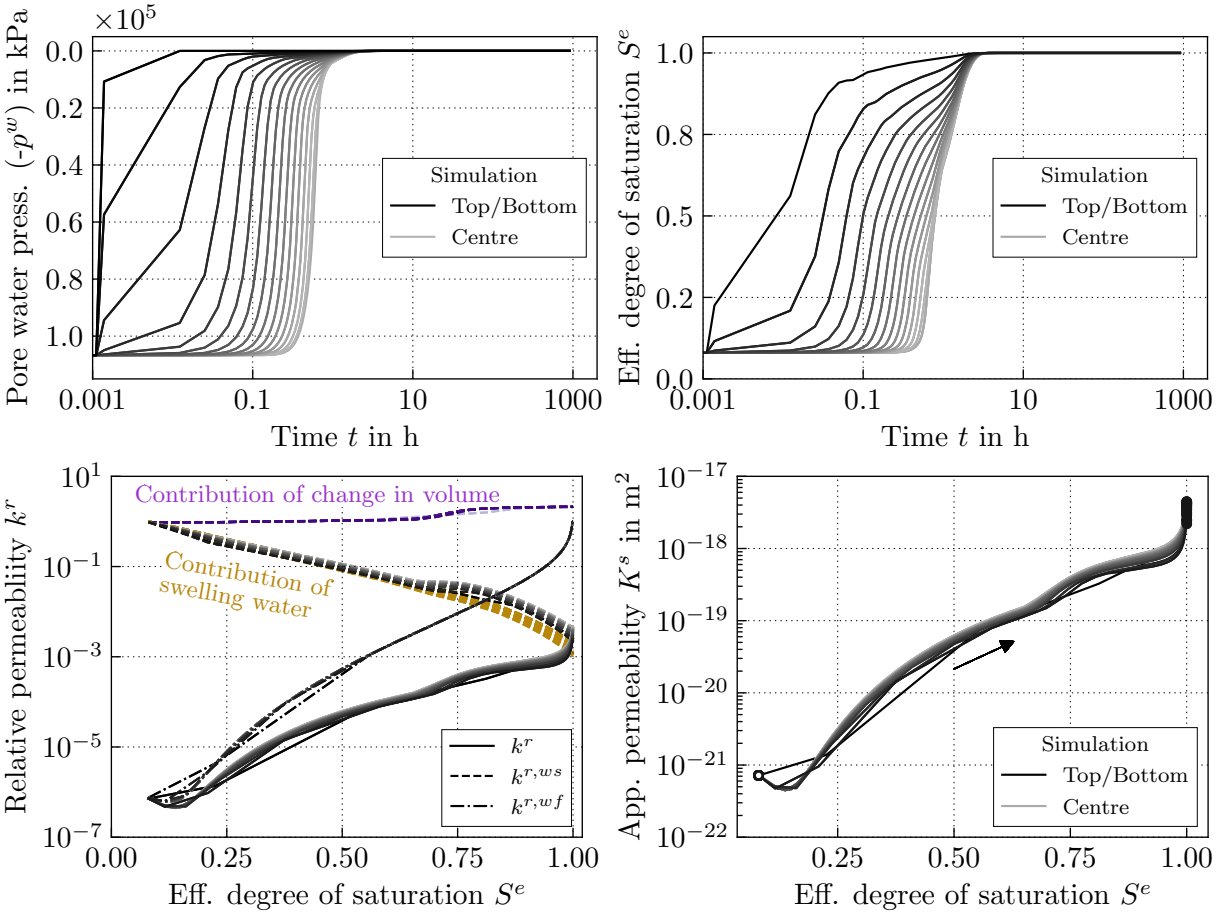

Figure 7.19.: Hydraulic response in the simulation of a vertically unconfined swelling and oedometric compression and rebound test on reconstituted Opalinus clay with application of $k^w_{\min} = 1 \times 10^{-6}$. Experimental results from Nitsch et al. (2023a).

were shown in Figure 7.6, no pronounced differences in the responses of different elements were evident. This observation is confirmed by the paths in Figure 7.20 for the outermost (upper row) and centre element (bottom row), which are almost identical.

Upon saturation, the void ratio increased while the stress path moved first in extension in the q–p diagram until the preconsolidation surface was met and the path exhibited a change of direction in extension. This corresponds to softening, hence plastic reduction of the net stress and preconsolidation surface. The void ratio e_w on the w-line was always larger than e and thus the saturation-driven strain rate evolved (see Equation (5.18)) and resulted in a pronounced expansion due to the outer boundary condition of vertically unconfined displacement, which was valid in each element. The saturation-driven strain rate vanished for $e = e_w$ on the w-line close to the NCC. Due to the large final void ratio, the bounding stress p_B on the B-line was very small and consequently the preconsolidation surface as well.

Figure 7.21 presents the paths for the simulation with $k^w_{\min} = 1 \times 10^{-6}$ for the outermost (upper row) and centre element (bottom row). Therein, the deviating behaviour of the outermost element row can be seen, which was due to the very small initial permeability of approximately $K = 1 \times 10^{-21}$ m^2, resulting in a comparatively larger critical time increment. As a result, the mechanical behaviour is less well resolved in the very beginning, resulting in the uneven path and premature change of the direction of the stress path in the q–p diagram. With progressing

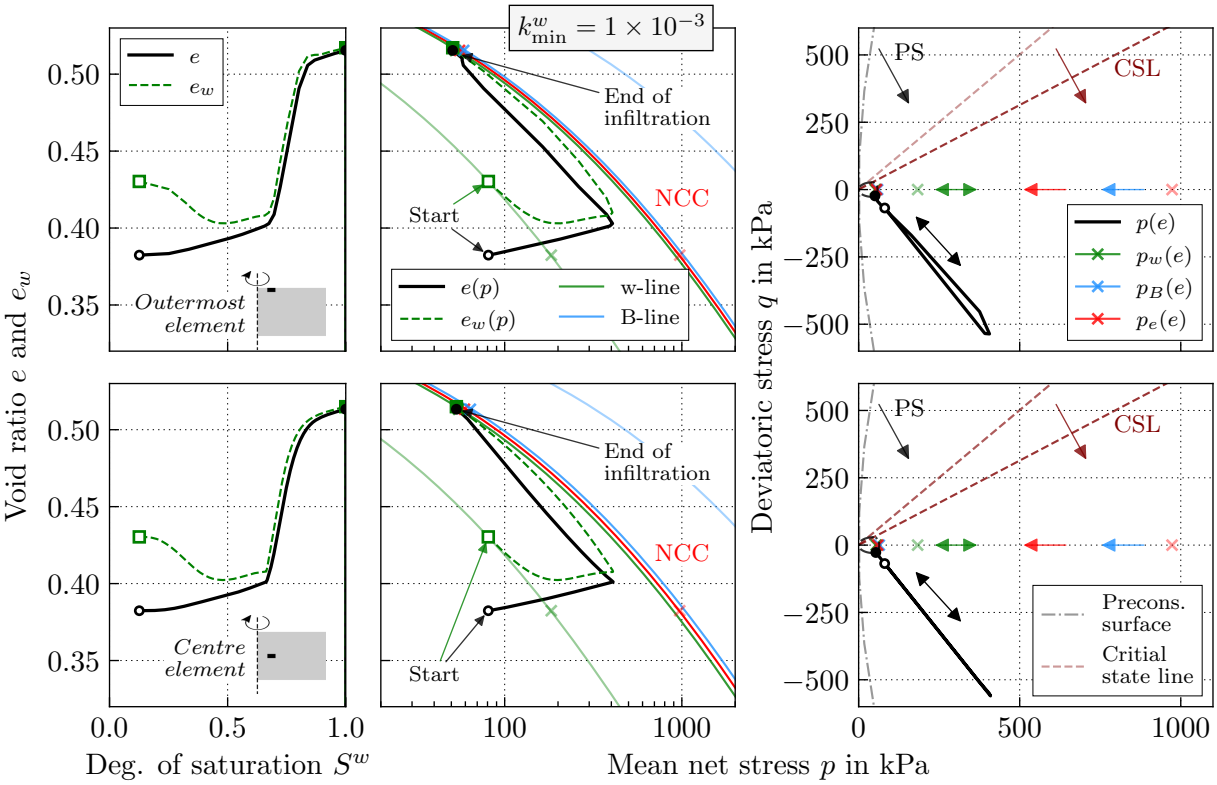

Figure 7.20.: Material response of outermost (top row) and centre (bottom row) element in simulation of vertically unconfined swelling with $k^w_{\min} = 1 \times 10^{-3}$: Evolution of void ratios e and e_w during saturation (left), path in void ratio versus mean net stress diagram (centre) and stress path in q–p diagram (right). The arrows indicate the stress path and movement of CSL, PS and the net stresses on the isotropic axis during infiltration.

infiltration, the saturation-driven strain rate vanished in the element ($e = e_w$) at a slightly reduced void ratio. This issue is not present in the centre element, whose state variables and stress path evolved analogously to those shown for the simulation with $k^w_{\min} = 1 \times 10^{-3}$ in Figure 7.20.

Concluding remarks

The simulations of this section demonstrated the influence of the minimum unsaturated relative permeability $k^w_{\min}$, which governs the propagation of infiltration and evolution of the degree of saturation upon wetting. For decreasing values of $k^w_{\min}$, elements located at larger distances from the infiltration front became hydraulically isolated. For swelling under vertically unconfined conditions, this isolation had little influence on the global swelling response, as the expansion of currently infiltrated elements did not impact the mechanical state of the neighbouring elements. In contrast, for swelling at constant volume conditions, the deformation of elements near the infiltration boundary compacted the remaining material and altered its stress state prior to wetting. This behaviour results from the interaction of elements in discretised boundary value problems. Single-element simulations preserve a uniform hydraulic and mechanical state consistent with the assumptions of the constitutive model and the boundary conditions of displacement and pore water pressure, and external loads apply uniformly across the element. In multi-element simulations, each element's response is influenced by its adjacent elements. Consequently, the hydraulic and mechanical state within the elements evolve heterogeneously.

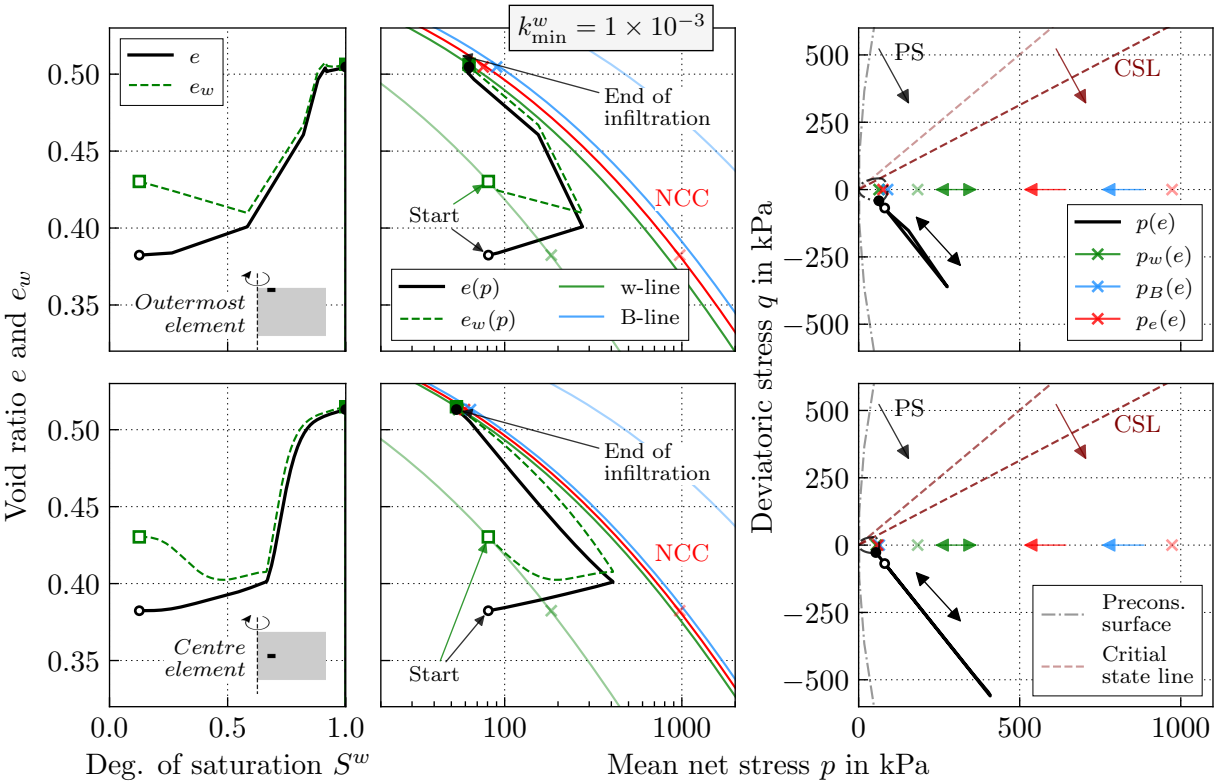

Figure 7.21.: Material response of outermost (top row) and centre (bottom row) element in simulation of vertically unconfined swelling with $k^w_{\min} = 1 \times 10^{-6}$: Evolution of void ratios e and e_w during saturation (left), path in void ratio versus mean net stress diagram (centre) and stress path in q–p diagram (right). The arrows indicate the stress path and movement of CSL, PS and the net stresses on the isotropic axis during infiltration.

The more inhomogeneous the distribution of the degree of saturation across the elements of the mesh is, the more likely is a diverging response of individual elements from the global material behaviour. Hydraulically isolated elements may therefore undergo significant mechanical changes induced by neighbouring elements before any increase in saturation occurs. with respect to the constitutive model, such changes in the initial mechanical state can substantially reduce the predicted magnitude of swelling or even lead to a further compaction. Moreover, the low initial permeability associated with small values of $k^w_{\min}$ also has numerical implications on the time stepping algorithm. Since permeability appears in the denominator of the criterion for unsaturated flow (see Equation (6.126)), the critical time step increases accordingly. This may lead to a less well-resolved hydraulic response and, in hydro-mechanically coupled analyses, to a reduced accuracy of the mechanical response at the onset of infiltration.

7.1.1.3. Influence of discretisation

In this section, the influence of the discretisation on the time evolution of swelling is discussed. For that purpose, in addition to the mesh applied in the previously analysed simulations, five alternative meshes are used in the simulations of vertically unconfined and constant volume swelling: meshes comprising 10, 30 and 40 elements over height with a constant element length as was the case for the previously used mesh with 20 elements over height, and two gradually spaced meshes comprising 20 and 30 elements over height, with the element size increasing from

the infiltration ends to the centre of the mesh. The FE meshes are depicted in Figure 7.22. All simulations were carried out with the minimum relative permeability of $k^w_{\text{min}} = 1 \times 10^{-3}$. Figure 7.23 presents the simulation results in terms of the externally evaluated material response for vertically unconfined swelling on the left-hand side and constant volume swelling on the right-hand side.

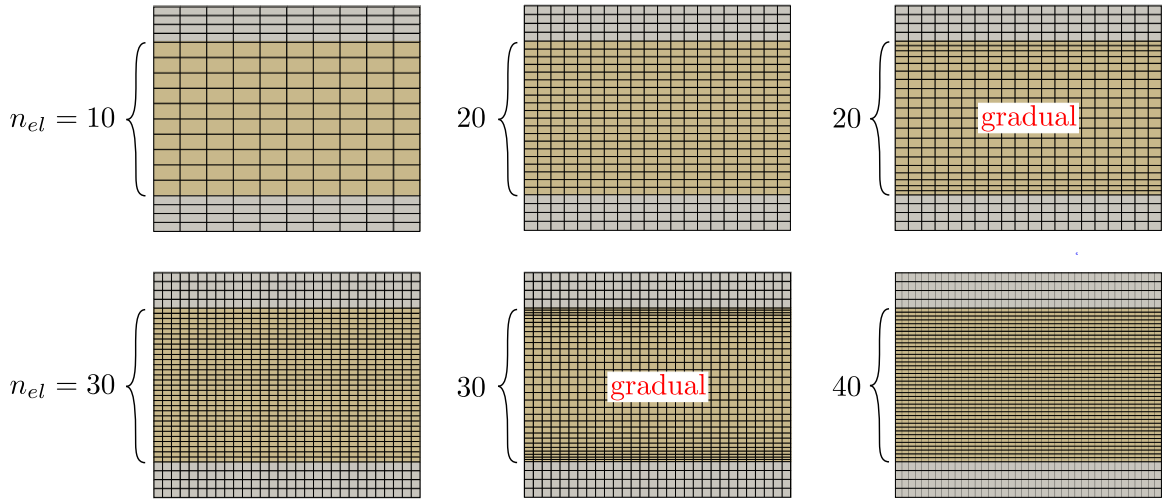

Figure 7.22.: Six finite element meshes applied in the discretisation study.

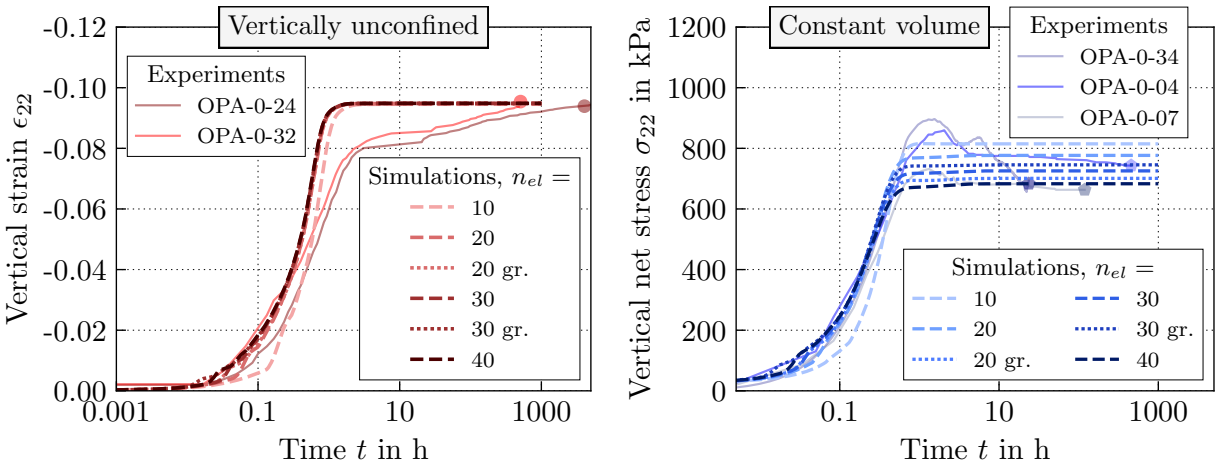

Figure 7.23.: Influence of discretisation on swelling behaviour for vertically unconfined swelling (left) and constant volume swelling (right) for six different meshes with 10, 20, 30 and 40 elements over height (gr. = gradually spaced mesh).

For vertically unconfined swelling the mesh study revealed that the final magnitude of vertical strain was independent of the discretisation, while the time evolution slightly accelerated with an increasing number of elements. This trend agrees with the findings of the infiltration studies in Section 6.6.2. The discretisation mainly affected the onset of deformation in Figure 7.23, as the finer meshes had integration points closer to the infiltration end. Afterwards, all meshes exhibited a similar time evolution. The mesh with 10 elements in height was too coarse to accurately capture the first onset of deformation.

For constant volume swelling the mesh size influenced both, the time evolution and magnitude of swelling pressure (right-hand side of Figure 7.23). With increasing mesh resolution, the swelling

pressure decreased, except for the gradually spaced 20-elements mesh, which was an outlier. The final vertical net stress ranged within $\sigma_{22} = 683 - 814$ kPa (approx. 18% variation). The time evolution accelerated with increasing number of elements, similar to the vertically unconfined case. The coarsest mesh (10 elements) exhibited a delayed onset of stress increase, while the finer meshes exhibited almost identical time evolution in good agreement with the experimental results.

The reduction in swelling pressure with increasing mesh resolution arises from the same mechanisms observed for the influence of the minimum relative permeability: a finer mesh led to a more heterogeneous local response during constant volume swelling and to stronger interaction between elements. This is illustrated in Figure 7.24, comparing the evolution of vertical net stress within the elements over time and effective degree of saturation.

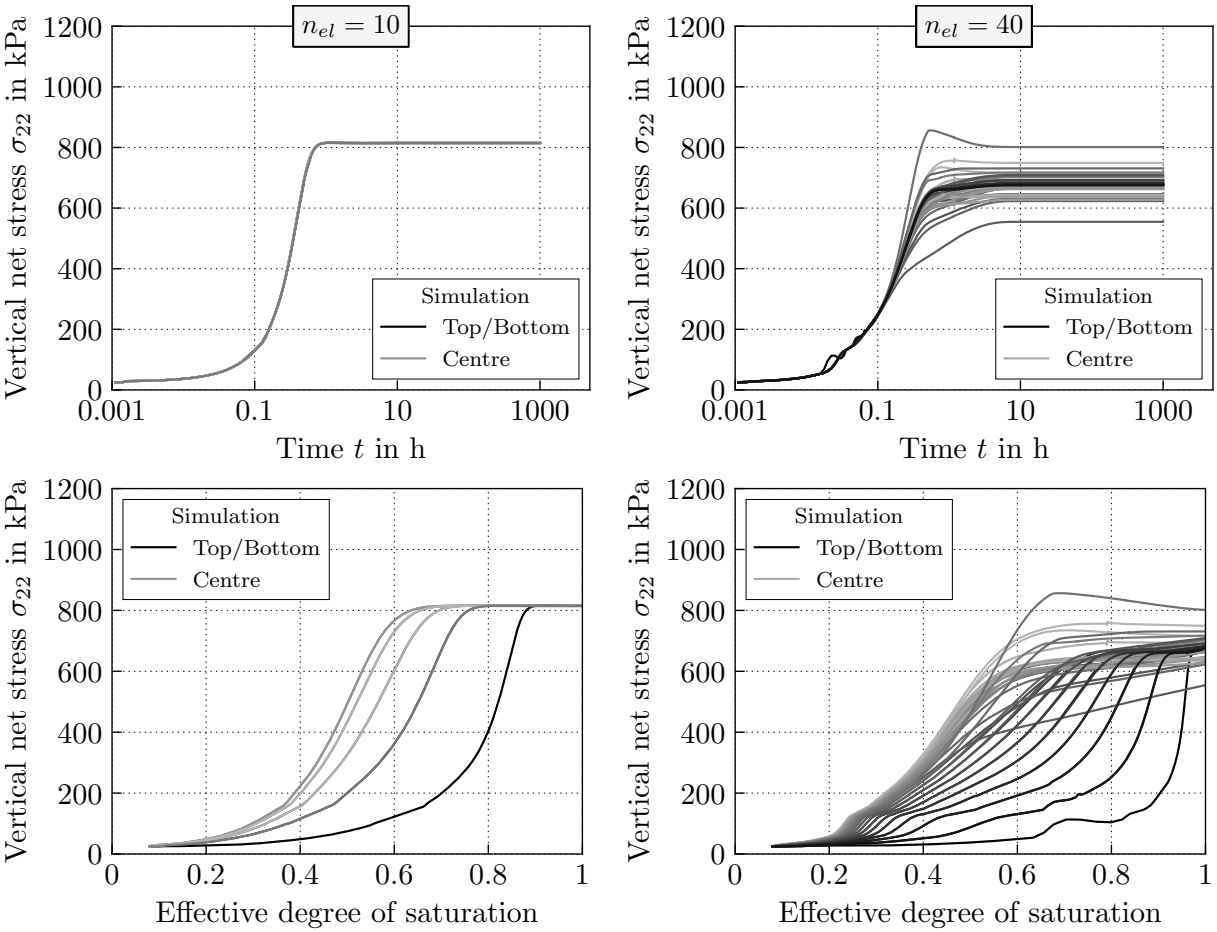

Figure 7.24.: Internal response of simulation of constant volume swelling: vertical net stress versus time (top row) and effective degree of saturation (bottom row), exemplary shown for $n_{el} = 10$ (left) and $n_{el} = 40$ (right).

In the simulation with 10 elements over height (left-hand side), the evolution with time was uniform across all elements. Over the effective degree of saturation, however, the behaviour discussed in Figure 7.9, which differed significantly from the single-element simulations, becomes apparent: with increasing distance from the infiltration end, the swelling pressure evolution diminished even though full saturation was not yet reached. However, a gradient in the mechanical response existed from the outer to the inner elements and the inner elements are less isolated for the coarse discretisation. This was not the case for the simulation with 40 elements

over height (right-hand side), where a non-uniform evolution of swelling pressure and stronger interaction between the neighbouring elements prevailed, which reduced the overall measurable external increase in vertical net stress. The mesh dependency of the swelling pressure magnitude is undesirable and must be addressed in future work.

7.1.2. Bentonite-silt mixture

The numerical framework was applied for simulations of the unsaturated swelling tests on a bentonite-silt mixture at vertically unconfined conditions and oedometric compression and rebound tests reported by Nowamooz and Masrouri (2008). The experiments were carried out suction-controlled and no data on the time evolutions was reported. The permeability of the material was not reported as well. Consequently, no comparison between the temporal evolution of the measured swelling strain and simulations was possible and the parameter $\phi^{\max}$ of the mass transfer model could not be calibrated. Therefore, both, $\phi^{\max}$ and K^s_{ref} were varied to assess their influence on the temporal evolution of the swelling strain. To calculate the reference permeability, two rather small values of the saturated permeability were chosen, $K^s = 1 \times 10^{-19}$ m^2 and $K^s = 5 \times 10^{-20}$ m^2. Furthermore, $\phi^{\max} = 0.88$ and an increased value of $\phi^{\max} = 0.92$ were applied in the following equation, which was derived in Section 3.2.7 with the assumption of constant volume conditions:

$$K^s_{\text{ref}} = \frac{(n_{\text{ref}})^3}{(1-n_{\text{ref}})^2} \frac{(1-n^A)^2}{(n^A)^3} K^s \quad \text{with} \quad n^A = (1-\phi^{\max})\, n_{\text{ref}}. \tag{7.1}$$

In this way, the influence of the saturated permeability and the mass transfer could be evaluated in a systematic manner complying to the recommended parameter calibration of the mass transfer model. However, as this results in four different reference permeabilities, another simulation is carried out, wherein K^s_{ref} is kept and only $\phi^{\max}$ is varied (decoupled from the calculation in Equation (7.1)). All combinations a)–e) are listed in Table 7.4. They were applied in simulation of vertically unconfined swelling up to full saturation (test M1). The simulations of the remaining test were carried out with parameter set c).

Table 7.4.: Variations of $\phi^{\max}$ and K^s in simulations of a bentonite–silt mixture and resulting reference permeabilities K^s_{ref}.

$\phi^{\max}$ \ K^s in m^2	1×10^{-19}	5×10^{-20}
0.88	a) 2.2×10^{-16} m^2	c) 1.1×10^{-16}m^2
0.92	b) 7.5×10^{-16} m^2	d) 3.8×10^{-16} m^2
Additional case: e) $K^s_{\text{ref}} = 1.1 \times 10^{-16}$ m^2 from case c), however with variation of $\phi^{\max} = 0.92$		

The minimum relative permeability was chosen as $k^w_{\min} = 1 \times 10^{-3}$ to avoid reaching the threshold of liquid to vapour permeability for the initial conditions. The hydraulic model of van Genuchten (1980) was already calibrated for the soil water retention curve for the material (see Figure 5.32) and the corresponding relative permeability model was used consistently. The initial height of the samples was $h_0 = 10 \pm 0.5$ mm and their diameter was $d = 70$ mm. The initial height of the FE model was determined to $h^i \approx 12.4$ mm for $e^i \approx 1.535$ and $e_0 \approx 1.047$ (sample M1). The initial (reference) porosity was $n_{\text{ref}} = 0.512$. All parameters corresponded to those determined

Table 7.5.: Initial and target conditions for the simulations on a bentonite-silt mixture from Nowamooz and Masrouri (2008).

	$p^i = p^i_d$ in kPa	$e^i = e^i_d$	$\sigma_{22,d0}$ in kPa	e_{d0}	$\sigma_{22,0}$ in kPa	e_0	S^w_0	$p^w_0 = -s_0$ in kPa
M1	10	1.535	700	1.001	10	1.047	0.36	-20000
M4	:	1.538	540	1.051	:	1.095	:	:
M5	:	1.539	488	1.071	:	1.102	:	:
M0 (reference)	:	1.560	700	1.080	:	1.128	:	:

Table 7.6.: Parameters of all constitutive models for simulations of a bentonite-silt mixture (Nowamooz and Masrouri, 2008).

Mechanical model										
e_N	h_s in kPa	n	κ_{ref}	κ_w	c	b	β	φ_{ref} in °	x_{ecm}	S_{ref}
1.615	1200	0.40	0.002017	0.04	1.4	17	0.33	30	0.62	0.27

Hydraulic and rel. permeability model			Mass transfer model	
α in kPa^{-1}	n	S^{wr}	$\phi^{\max}$	c_ϕ
0.000361	2.026	0.261	varying	10

in Chapters 4 and 5 and are summarized in Table 7.6. The initial conditions are presented in Table 7.5 for all four simulations.

The axisymmetric FE model is shown in Figure 7.25. The FE model consists of two porous stones below and above the sample. The material parameters for the porous stone correspond to those already defined in Table 7.2. For the sample, a discretisation with $n_{el} = 20$ elements over the height was chosen, corresponding to a nodal distance of $\Delta l_n = 0.0005$ m. Axisymmetric, linear equal order elements with reduced integration were used. For infiltration, the novel transient-critical analysis type was applied with $f_{t_{\min}} = 0.95$ and $\Delta t_{\max} = 10$ s, whereas all other steps were simulated as static. The simulations comprised a geostatic step (0), specimen preparation in loading and unloading steps (1 and 2), an infiltration step (3) and subsequent vertical loading and unloading steps (4 and 5). For simulation of the reference test (M0) the infiltration step was omitted. The infiltration was realized via a pore water pressure boundary conditions at the lower nodes at constant vertical net stress. For infiltration, the pore water pressure boundary is $\Delta p^w = 0$ kPa for test M1, $\Delta p^w = -3000$ kPa for test M4 and $\Delta p^w = -8000$ kPa for test M5.

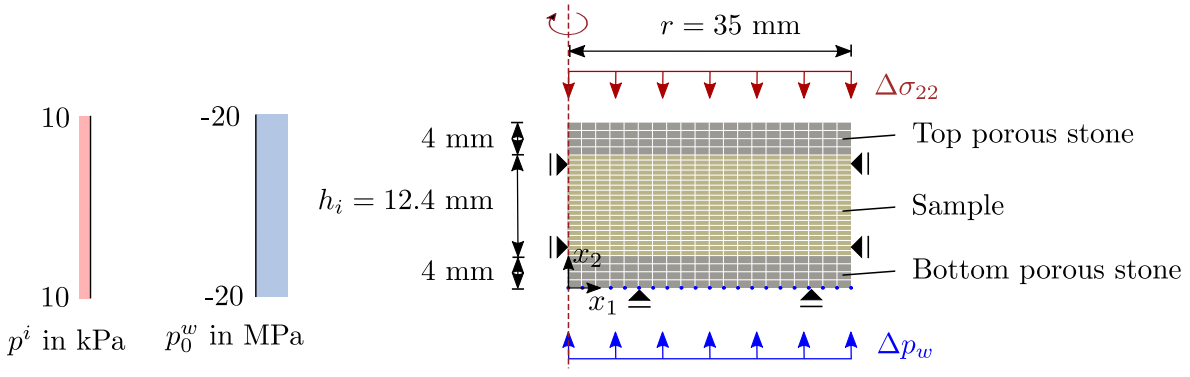

Figure 7.25.: FE model for simulations of bentonite-sand mixture.

Figure 7.26 shows the detailed results of the simulation c) of vertically unconfined swelling with a subsequent oedometric compression and rebound test (M1). Before the onset of infiltration, the stress ratio was $K_0 \approx 2.0$ as a result of the simulation of specimen preparation. The material response upon infiltration is presented with local quantities in terms of void ratio over time (left) as well as with external quantities (right), corresponding to the evolution of vertical strain over time, in the upper row. Here, the final value of strain computed from the final given void ratio from the experiment is given for the sake of comparison. In the lower row of Figure 7.26, the void ratio is presented over vertical net stress for local (left) and external (right) quantities in comparison to the experimental results. The colour gradient in blue indicates elements on the symmetry axis from the bottom (darker) to the top (brighter) of the model.

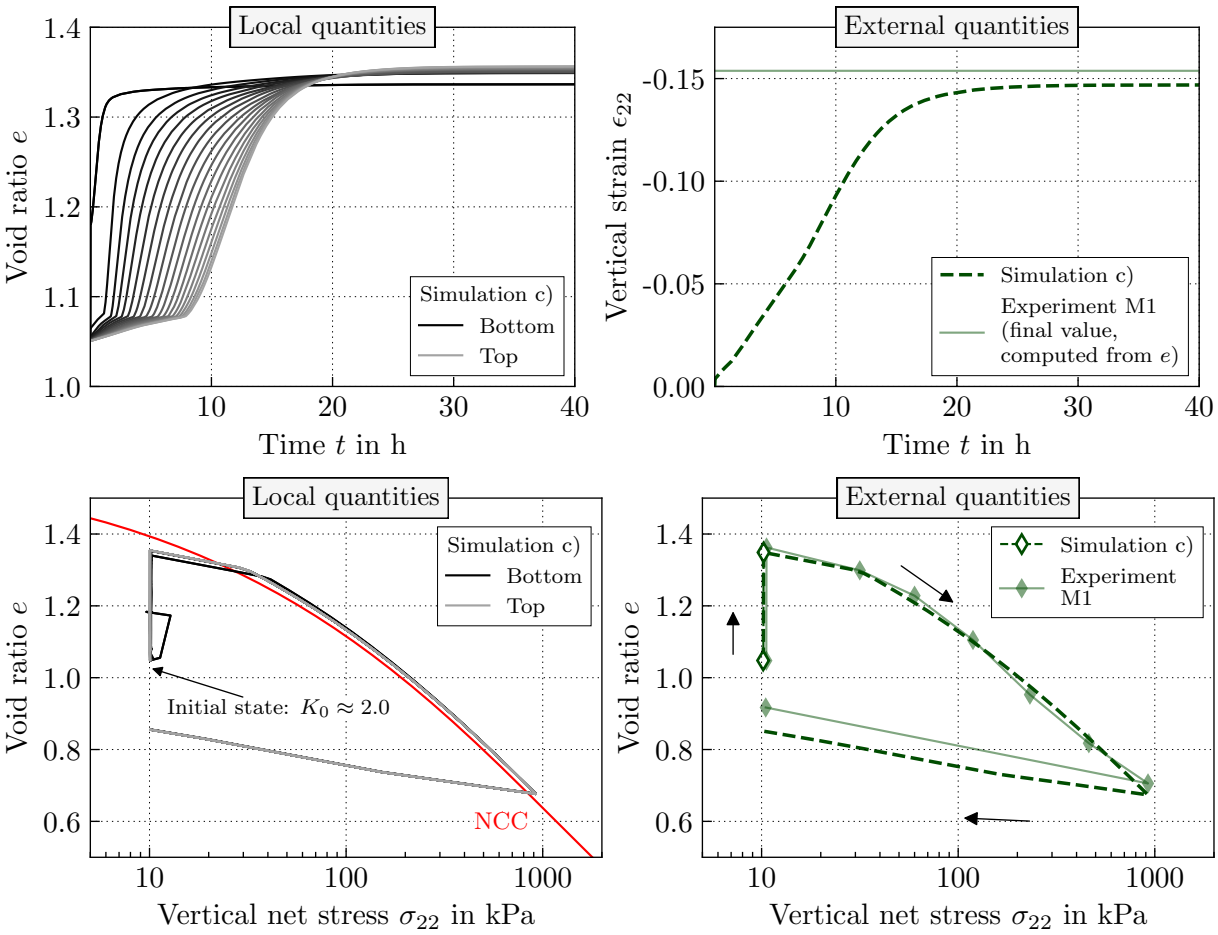

Figure 7.26.: Mechanical response in simulations of vertically unconfined swelling up to full saturation and oedometric compression and rebound test (M1) on a bentonite-silt mixture: Local quantities (left) and external quantities (right). Experimental data from Nowamooz and Masrouri (2008).

The results show that the modelling framework could be successfully applied to a boundary value problem for this material. The magnitude of swelling and the general mechanical behaviour were well represented, consistent with the element test simulations (see Section 5.5.2), wherein the swelling strain was slightly underestimated as well. In the local quantities, a different behaviour was found for the most bottom element row of the soil sample, see the plots on the left-hand side of Figure 7.26 (local quantities). The mechanical response of this element row took place instantly due to the very low permeability, which evoked a rather large critical time increment.

It resulted in the sharp increase of the void ratio, which is evident in the externally evaluated time evolution as well (upper right plot), before wetting could progress into the next element rows. With progressing infiltration, the element row was not able to produce the same swelling strain as the remaining elements in the sample. Due to the fine discretisation, however, the reduced local void ratio of the bottom most element row did not affect the magnitude of the externally evaluated response in a pronounced way.

The hydraulic behaviour is presented in Figure 7.27 in terms of the evolution of pore water pressure over time (upper left), effective degree of saturation over time (upper right) and evolution of permeability (lower right) and relative permeability contributions with effective degree of saturation (lower left). The aforementioned instant increase of the degree of saturation in the bottom element row is evident. The swelling-induced relative permeability and the overall permeability reflected the difference in void ratio of the elements over height via the contribution of swelling water, which evolves depending on porosity, thus void ratio. The mean apparent permeability over the height of the sample at the end of infiltration in the simulations was estimated to $K^s \approx 3.3 \times 10^{-19}$ m^2 for a void ratio of $e = 1.351$. Compared to the reference permeability of $K^s_{\text{ref}} = 1.1 \times 10^{-16}$ m^2 for the unswollen, saturated state, this corresponds to a swelling-induced permeability reduction by a factor of approximately 333.

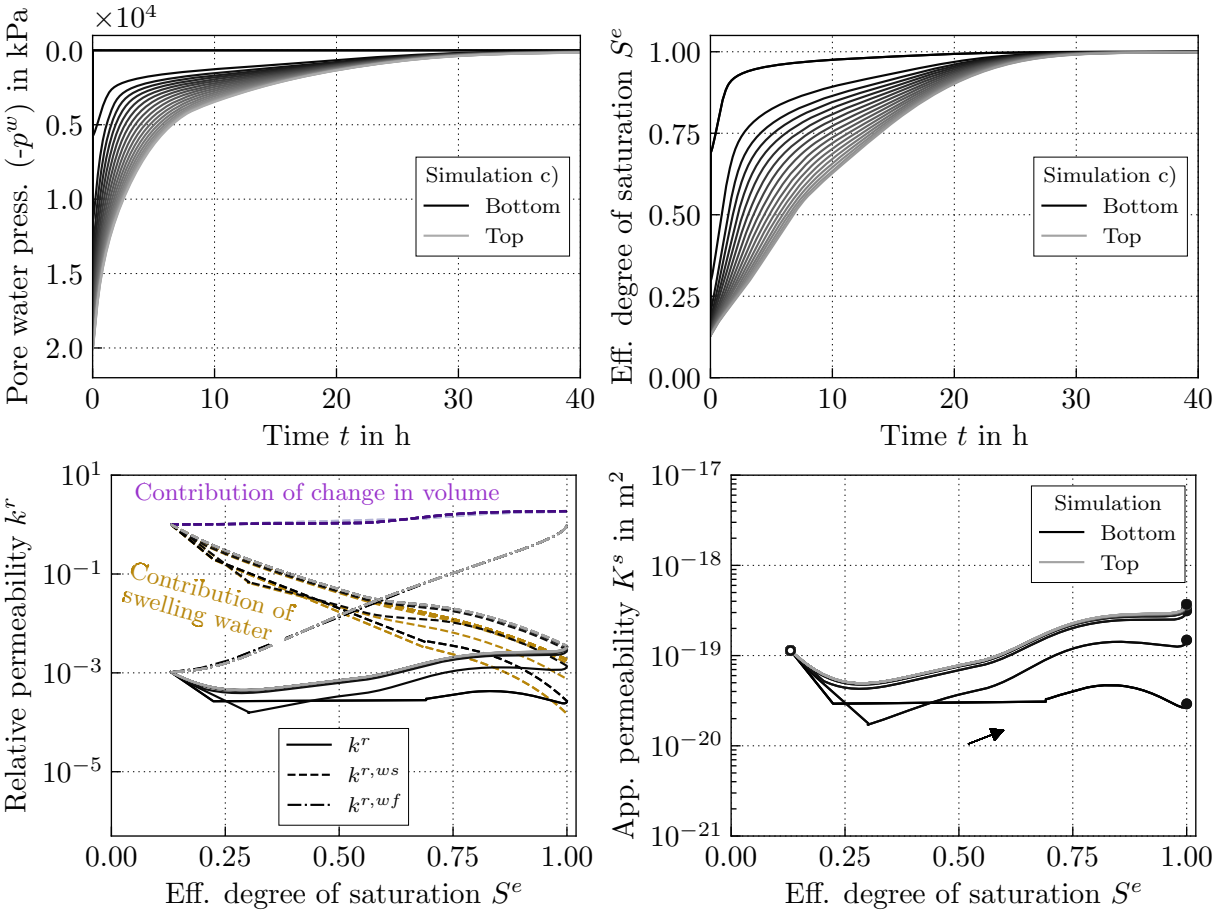

Figure 7.27.: Hydraulic response in simulations of vertically unconfined swelling up to full saturation and oedometric compression and rebound test (M1) on a bentonite-silt mixture.

In Figure 7.28 the influence of the reference permeability and maximum swelling water ratio on the time evolution of the vertical strain upon infiltration is shown using the parameter variations a) – e). The solid lines refer to a value of $\phi^{\max} = 0.88$, and the dash-dotted lines to $\phi^{\max} = 0.92$.

The darkest lines depict simulations referring to a constant volume saturated permeability of $K^s = 1 \times 10^{-19}$ m^2, thus simulations a) and b), and medium green correspond to $K^s = 5 \times 10^{-20}$ m^2, thus simulations c) and d), and the additional variation e) is shown with the bright dash-dotted line. The wider lines indicate simulations a), c), and e). These simulations were selected to separate the effects of the two parameters: simulations a) and c) differ only in K^s_{ref}, while simulations c) and e) differ only in $\phi^{\max}$.

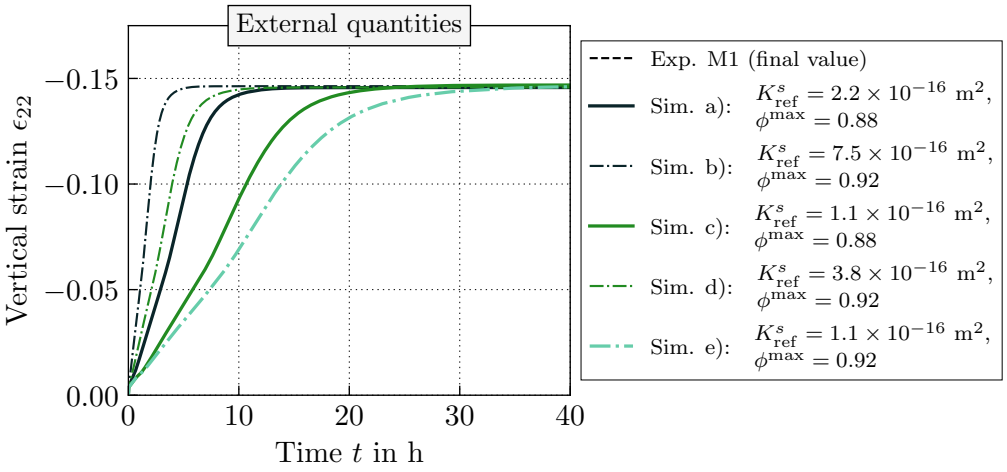

Figure 7.28.: Time evolution of vertical strain upon infiltration for vertically unconfined swelling: Influence of choice of K^s_{ref} and $\phi^{\max}$.

The parameters for simulation pairs a) and b), and c) and d), respectively, were computed based on an identical saturated permeability in the saturated state, however for constant volume conditions (see matrix in Table 7.4). The results in Figure 7.28 indicate that the saturated permeability is not decisive for a similar time evolution, which differed significantly for each pair. Rather, the magnitude of the (initial) reference permeability was decisive for the temporal evolution: higher initial permeabilities accelerated the development over time (dash-dotted lines for the same colour), despite a larger maximum swelling water ratio. This is also evident when comparing simulations a) and e) to simulation c), wherein only one quantity was varied each. The increase of $\phi^{\max}$ in case e) slowed down the temporal evolution relative to simulation c), yet this effect is overall less pronounced than the acceleration caused by the increased K^s_{ref} in case a). Consequently, accurate knowledge of the reference permeability value is required for application of the modelling framework to calibrate $\phi^{\max}$ and to predict the unknown time evolution of expansion correctly. If the time evolution and the saturated permeability are known, the reference permeability and swelling water ratio can be determined by matching the experimental results in simulations. This approach is applied in Section 7.1.3.

The time evolution of expansion for the unsaturated tests M4 and M5 and the fully saturated test M1 (Simulation c)) are shown in terms of the externally evaluated evolution of vertical strain on the left-hand side of Figure 7.29. On the right-hand side, the evolution of permeability from all three simulations is shown versus the effective degree of saturation. It mostly overlaps for the three simulations, thus the final states are indicated with vertical dotted lines at their respective final value of S^e. As is evident on the left-hand side of Figure 7.29, reaching a steady value under unsaturated conditions requires more time in the simulation due to the overall smaller permeability, superimposed by both relative permeabilities. For the simulations of the unsaturated tests M4 and M5, the mean vertical permeability had only increased to $K^{s,\text{M4}} \approx 1.5 \times 10^{-19}$ m^2 at a void ratio of $e^{M4} = 1.225$ and $K^{s,\text{M5}} \approx 5.7 \times 10^{-20}$ m^2 at a void ratio of $e^{M5} = 1.140$ in

comparison to the final value of $K^{s,\mathrm{M1}} \approx 3.3 \times 10^{-19}$ m^2 in the simulation of the fully saturated test M1. The results show that the variations in the relative permeability due to swelling and overall permeability were less pronounced for simulations of tests M4 and M5, depicted by the green dots at their final states on the right-hand side plot of Figure 7.29. Consequently, the smaller increment of pore water pressure, which was applied in those simulations, did result in a less isolated hydraulic behaviour of the bottom most element row of the soil sample. This implies that localisation effects are a consequence of the combination of unfavourable hydraulic conditions, thus very low permeabilities, and comparatively high pore water pressure gradients. The magnitude of swelling-induced expansion was predicted satisfactorily in the simulations, with a slight underestimation of the experimental results.

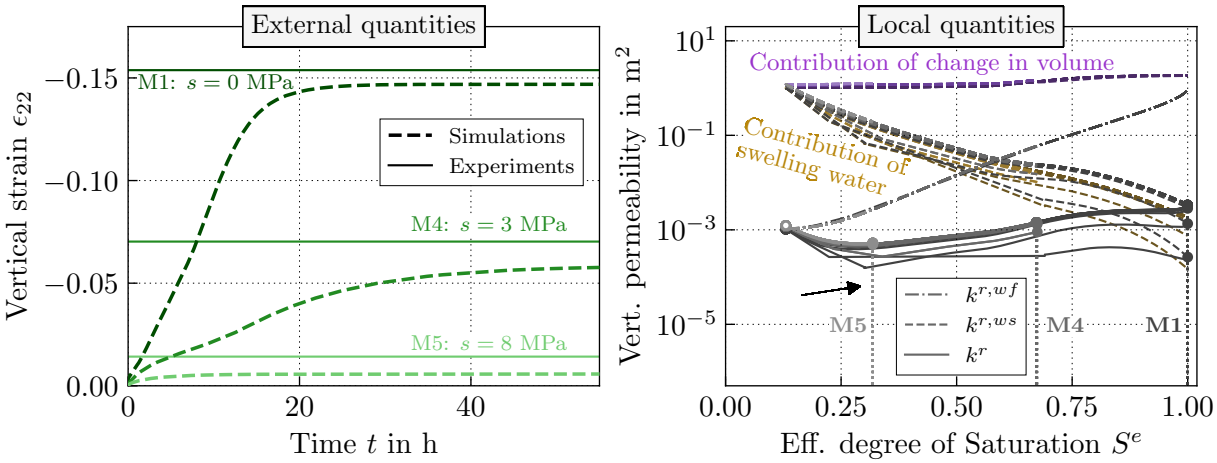

Figure 7.29.: Vertically unconfined swelling at different suctions: Time evolution of vertical strain upon infiltration (external quantities, left) and evolution of relative permeability versus degree of saturation (local quantities, right).

The simulation results of all four tests of the experimental campaign, including the reference compression and rebound test (M0) and the unsaturated tests (M4 and M5) are shown in Figure 7.30 in terms of external results on the right-hand side with the experimental results on the left-hand side. The reference permeability of $K^s_{\mathrm{ref}} = 1.1 \times 10^{-16}$ m^2 and maximum swelling water ratio of $\phi_{\max} = 0.88$ were applied. As was the case within the single-element simulations (see Sections 4.4.2 and 5.5.2), for test M0 the transition from reversible to irreversible material behaviour is sharper in the simulation than in the experiment. Overall, very good agreement between the simulation and the test results is apparent. The reduction of elastic stiffness and preloading net stress with increasing degree of saturation is well captured in the simulations as well as the increasing expansion with increasing degree of saturation in the partially saturated tests. Permeability measurements, swelling pressure tests and data on the temporal development of the swelling phenomena are necessary in order to make a more comprehensive assessment of the predictive capabilities. Based on the existing data, the modelling approach demonstrates good applicability, plausible trends and promising results.

7.1.3. Bentonite-sand mixture

Vertically unconfined swelling and subsequent oedometric compression and rebound tests on a bentonite-sand mixture reported by Lang (2019) were simulated with the numerical framework as boundary value problems. The majority of the experimental campaign were carried out

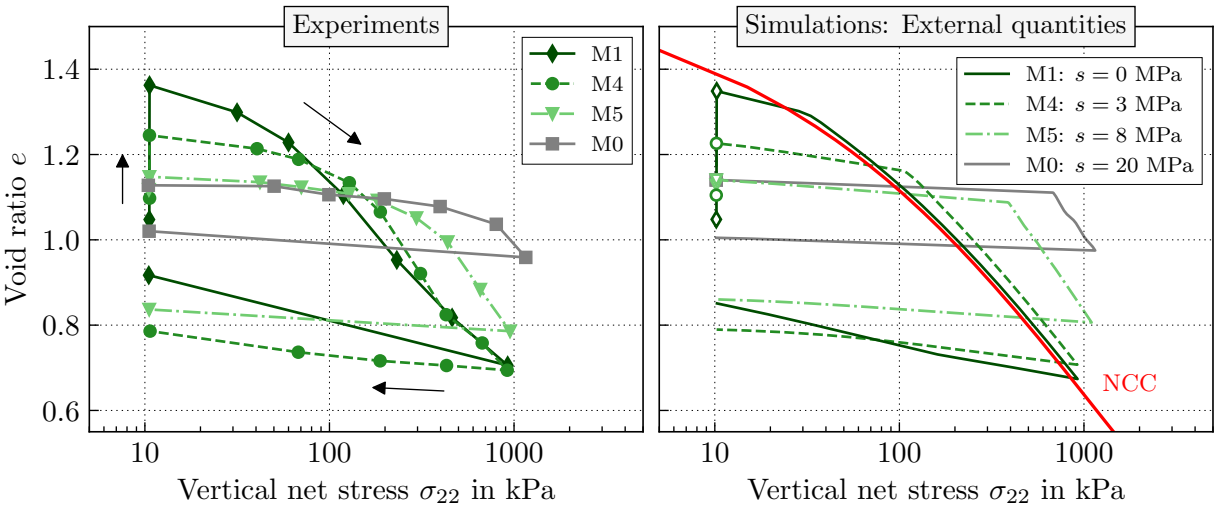

Figure 7.30.: Vertically unconfined swelling and oedometric compression and rebound tests on a bentonite-silt mixture at different suctions (Nowamooz and Masrouri, 2008): experimental results (left) and simulation results in terms of external behaviour (right).

suction-controlled and the time evolution is only reported for one test (BS-SCR-1), which is a swelling test under vertically unconfined conditions wetted up to full saturation with water supplied at the bottom. For the other tests, a comparison of the time scales between experiments and simulations is therefore not possible. The reference permeability in the saturated, but non-swollen state is not reported for the material, but the saturated permeability at constant volume conditions is given in Lang (2019). For the initial (reference) porosity of $n_{\text{ref}} = 0.344$, it is $K^s = 1.2 \times 10^{-19}$ m^2. With an assumption of $\phi^{\max}$ and the known swollen, saturated permeability, the reference permeability in the saturated, but unswollen state could be approximated using Equation (7.1). The maximum swelling water ratio and reference permeability were established as $\phi^{\max} = 0.93$ and $K^s_{\text{ref}} = 9.2 \times 10^{-17}$ m^2 by iteratively comparing the time evolution in simulations for different values with the experimental results of test BS-SCR-1. The second parameter of the mass transfer model remained at $c_\phi = 10$. For verification of the parameters, further swelling tests with time evolution or permeability measurements are required. The hydraulic model of van Genuchten was applied with the parameter set corresponding to vertically unconfined conditions (VU, see Figure 5.34). For the relative permeability model for unsaturated soils, the approach of van Genuchten is used in a consistent manner with a minimum relative permeability of $k^w_{\min} = 1 \times 10^{-4}$. Table 7.8 summarizes all material parameters, which correspond to those determined in Chapters 4 and 5. The samples had a height of $h_0 = 15 \pm 0.2$ mm and a diameter of $d = 50$ mm, resulting in an initial height of the FE model of $h^i \approx 18.5$ mm for $e^i \approx 0.883$ and $e_0 \approx 0.530$. The initial conditions are stated in Table 7.7.

Table 7.7.: Initial and target conditions for the simulations on a bentonite–sand mixture from Lang (2019).

	$p^i = p^i_d$ in kPa	$e^i = e^i_d$	$\sigma_{22,d0}$ in kPa	e_{d0}	$\sigma_{22,0}$ in kPa	e_0	S^w_0	$p^w_0 = -s_0$ in kPa
All tests	10	0.883	10200	0.498	25	0.530	0.47	-27000

Figure 7.31 shows the axisymmetric FE model, which considers of two porous stones below and above the sample. The material parameters for the porous stone correspond to those already

Table 7.8.: Material parameters for simulations of swelling tests on a bentonite-sand mixture by Lang (2019).

Mechanical model										
e_N	h_s in kPa	n	κ_{ref}	κ_w	c	b	β	φ_{ref} in °	x_{ecm}	S_{ref}
0.895	18000	0.31	0.001013	0.03	5.0	35	0.34	28	0.32	0.37

Hydraulic and rel. permeability model			Mass transfer model	
α in kPa^{-1}	n	S^{wr}	$\phi^{\max}$	c_ϕ
0.00383	1.269	0.26	0.93	10

defined in Table 7.2. For the sample, a nodal distance of $\Delta l_n = 0.0005$ m was chosen by a discretisation with $n_{el} = 30$ elements over height. Axisymmetric, linear equal order elements with selected reduced integration were used. For infiltration, the novel transient-critical analysis type was applied with $f_{t_{\min}} = 0.95$ and $\Delta t_{\max} = 20$ s. The simulations comprised a geostatic step (0), specimen preparation in loading and unloading steps (1 and 2), an infiltration step (3) and subsequent vertical loading and unloading steps (4 and 5). For simulation of the reference test (M0) the infiltration step was omitted. The infiltration was realized via a pore water pressure boundary conditions at the lower nodes at constant vertical net stress. For infiltration, the pore water pressure boundary is $\Delta p^w = \{0, 3400, 10000\}$ kPa for tests BS-SCR-1, BS-SCR-2 and BS-SCR-3 respectively.

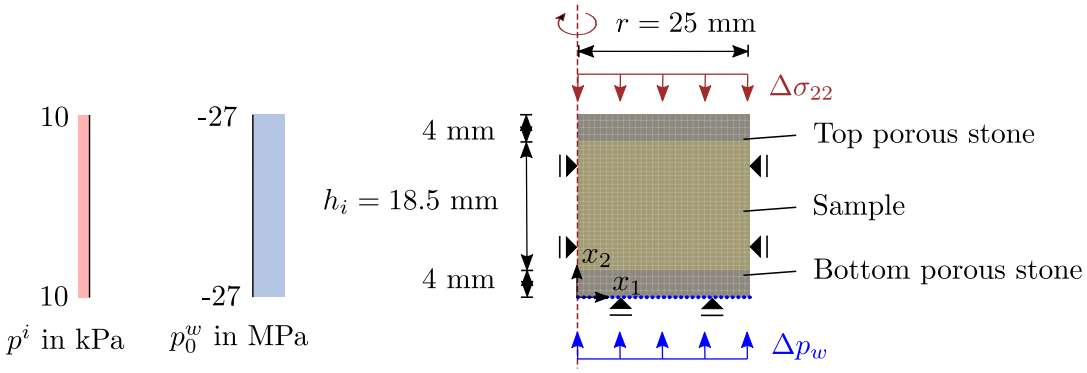

Figure 7.31.: FE model for simulations of bentonite-sand mixture.

Figure 7.32 shows the detailed results of the simulation of test BS-SCR-1, which was wetted up to full saturation and subjected to oedometric loading and unloading afterwards. The results are presented as local quantities (left) as well as external quantities (right) in terms of void ratio versus vertical net stress (upper row) and evolution of void ratio and vertical strain over time (lower row). The externally evaluated material response is compared to the experimental results. The colour gradient in blue indicates elements on the symmetry axis from the bottom (darker) to the top (brighter) of the model. In the local results, pronounced fluctuations of both, vertical net stress and void ratio were evident. These were due to the very small vertical seating stress of $\Delta\sigma_{22} = 2.5$ kPa, which is on the one hand numerically challenging for convergence, and on the other hand caused an initial unfavourable stress state in extension with a stress ratio of $K_0 \approx 24$ (corresponding to a mobilised friction angle of $\varphi^{\text{mob}} = \arcsin((1-K_0)/(1+K_0)) \approx 67°$). The latter was also evident for the single-element simulations in Section 5.5.3. However, a more favourable initialisation of the stress state prior to loading could only limit the fluctuations to a certain extent. Comparative simulations with an increased vertical seating stress revealed lower

fluctuations. Figure 7.33 displays the evolution of void ratio over vertical net stress for the local and external response for a vertical seating stress of $\Delta\sigma_{22} = 10$ kPa. The reduced stress ratio of $K_0 \approx 7$ reduced the fluctuations, however, the vertical displacement due to saturation was reduced as well. Note that in comparison to the simulations on reconstituted Opalinus clay and the bentonite-silt mixture in Sections 7.1.1 and 7.1.2, the stress ratio is still comparably high. For the sake of comparison of the simulation with the time evolution of the experiment, the fluctuations for $\Delta\sigma_{22} = 2.5$ kPa were accepted here. The external behaviour of this simulation exhibited very good agreement with the experimental results as shown on the right-hand side of Figure 7.32 with respect to both, the magnitude of swelling strain as well as the time evolution. For the latter, the parameter $\phi^{\max}$ of the mass transfer model was calibrated with knowledge of the saturated permeability.

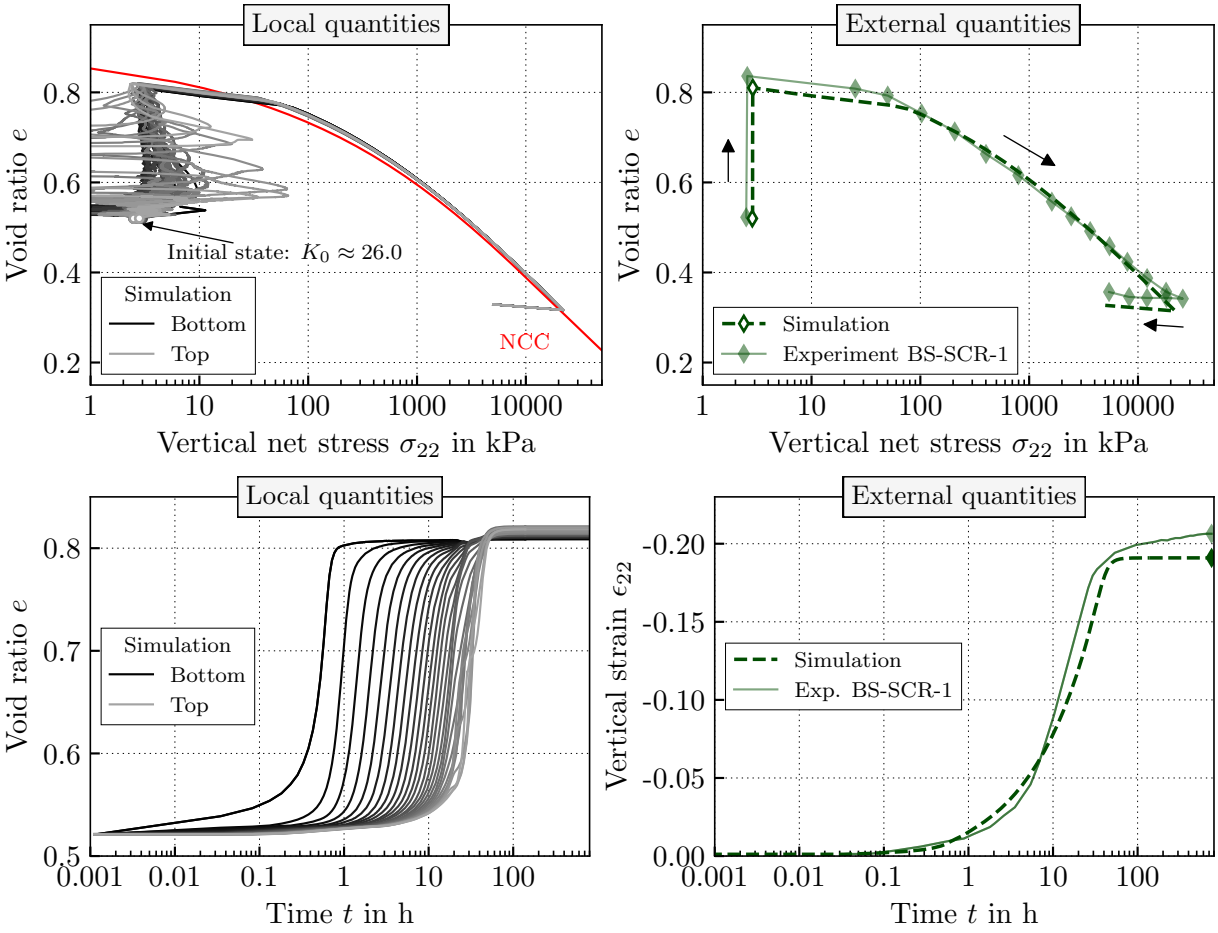

Figure 7.32.: Mechanical response in simulations of vertically unconfined swelling and oedometric compression and rebound test on a bentonite-sand mixture: Local quantities (left) and external quantities (right) for vertical seating stress of $\Delta\sigma_{22} = 2.5$ kPa during wetting. Experimental data from Lang (2019).

The hydraulic behaviour is presented in Figure 7.34 in terms of the evolution of pore water pressure over time (upper left), effective degree of saturation over time (upper right) and evolution of permeability (lower right) and relative permeability contributions with effective degree of saturation (lower left). A very homogeneous infiltration behaviour becomes apparent in the evolution of pore water pressure and effective degree of saturation from the bottom to the top elements. The irregular evolution of the void ratio is reflected in both the relative permeability

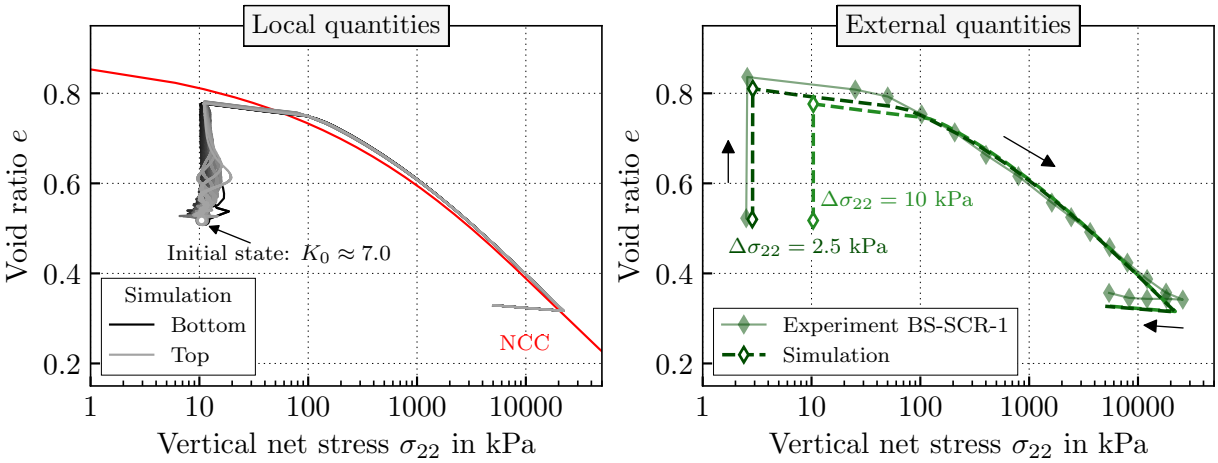

Figure 7.33.: Mechanical response in simulations of vertically unconfined swelling and oedometric compression and rebound test on a bentonite-sand mixture: Local quantities (left) and external quantities (right) for a vertical seating stress of $\Delta\sigma_{22} = 10$ kPa during wetting. Experimental data from Lang (2019).

due to swelling and the apparent permeability, see lower row of Figure 7.34. The product of both relative permeabilities and the resulting apparent permeability first decreased and subsequently increased with progressing infiltration. The mean vertical permeability over the height of the sample at the end of infiltration in the simulations was estimated to $K_{22}^s \approx 1.6 \times 10^{-18}$ m^2 for a void ratio of $e = 0.813$. Compared to the reference permeability of $K_{\text{ref}}^s = 7.7 \times 10^{-16}$ m^2 for the unswollen, saturated state, this corresponds to a swelling-induced permeability reduction by a factor of approximately 412.

Figure 7.35 shows the time evolution of expansion for the simulations of the unsaturated tests BS-SCR-2 and -3 and the previously shown saturated test BS-SCR-1 in terms of the externally evaluated vertical strain on the left-hand side. For the experiments, the final value was computed from the known final void ratios. On the right-hand side, the evolution of relative permeability is shown versus the effective degree of saturation for all three simulations. The final states of the simulations are indicated with vertical dotted lines at their respective effective degree of saturation. For the simulations of the unsaturated tests BS-SCR-2 and BS-SCR-3, the product of both relative permeabilities and consequently the apparent permeability had decreased, see right-hand side of Figure 7.35. The mean vertical permeabilities were only $K_{22}^{\text{BS-SCR-2}} \approx 1.46 \times 10^{-20}$ m^2 at a void ratio of $e^{\text{BS-SCR-2}} = 0.5695$ and $K_{22}^{\text{BS-SCR-3}} \approx 2.7 \times 10^{-20}$ m^2 at a void ratio of $e^{\text{BS-SCR-3}} = 0.531$. Note that this reversed trend is due to the minimum value of relative permeability, which results first in a decrease and subsequently in an increase of the permeability overall. As a result, the simulation of test BS-SCR-2 required the longest time to reach a steady state. Similar to the simulations of the bentonite-silt mixture in Section 7.1.2, the smaller pore water pressure gradients led to less variations in the permeability evolution and thus in the evolution of void ratio. The magnitude of expansion on the left-hand side of Figure 7.35 was underestimated in all simulations. However this was the case for the single-element simulations with the same parameter set in Section 5.5.3 as well. The trend of increasing deformation with decreasing suction was captured well.

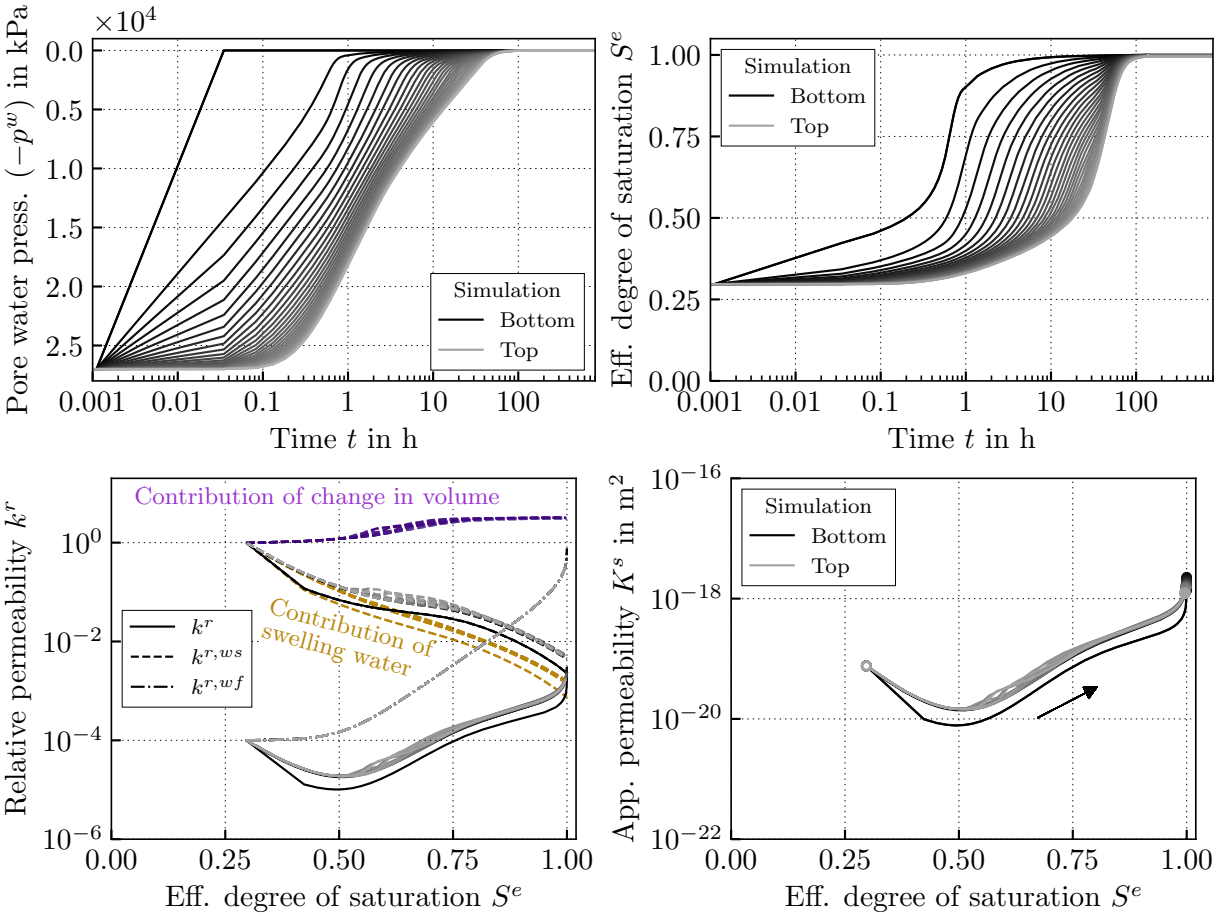

Figure 7.34.: Hydraulic response in simulations of vertically unconfined swelling and oedometric compression and rebound test on a bentonite-sand mixture for a vertical seating stress of $\Delta\sigma_{22} = 2.5$ kPa during wetting.

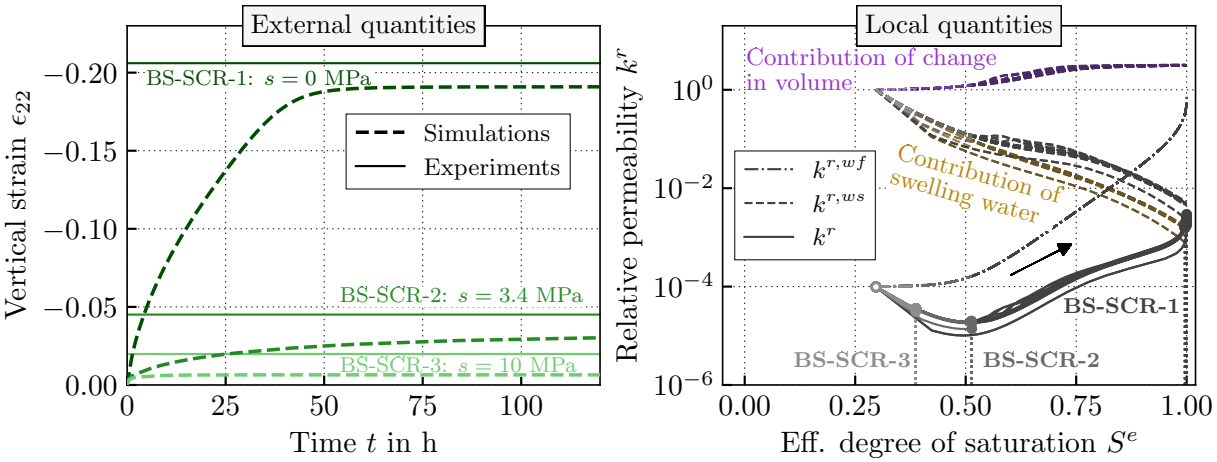

Figure 7.35.: Vertically unconfined swelling at different suctions: Time evolution of vertical strain upon infiltration (external quantities, left) and evolution of relative permeability versus degree of saturation (internal quantities, right).

The results of all simulations of the four tests including the reference oedometric compression and rebound test (BS-SCR-4) are compared to the experimental results in terms of the external response in Figure 7.36, showing the experiments on the left-hand side and the corresponding

simulations on the right-hand side. Overall, good agreement is evident. The decreasing vertical preloading stress with decreasing suction or increasing degree of saturation and corresponding faster approach of the NCC is captured well. Moreover, the simulations accurately captured the decreasing elastic stiffness with decreasing suction or increasing degree of saturation. The simulation results shown in this section highlight that the modelling framework is able to predict the material behaviour of the bentonite-sand mixture in terms of magnitude and temporal evolution. The parameters of the mass transfer model could be successfully calibrated by back-calculation of the experimental results in simulations with the knowledge of the saturated permeability.

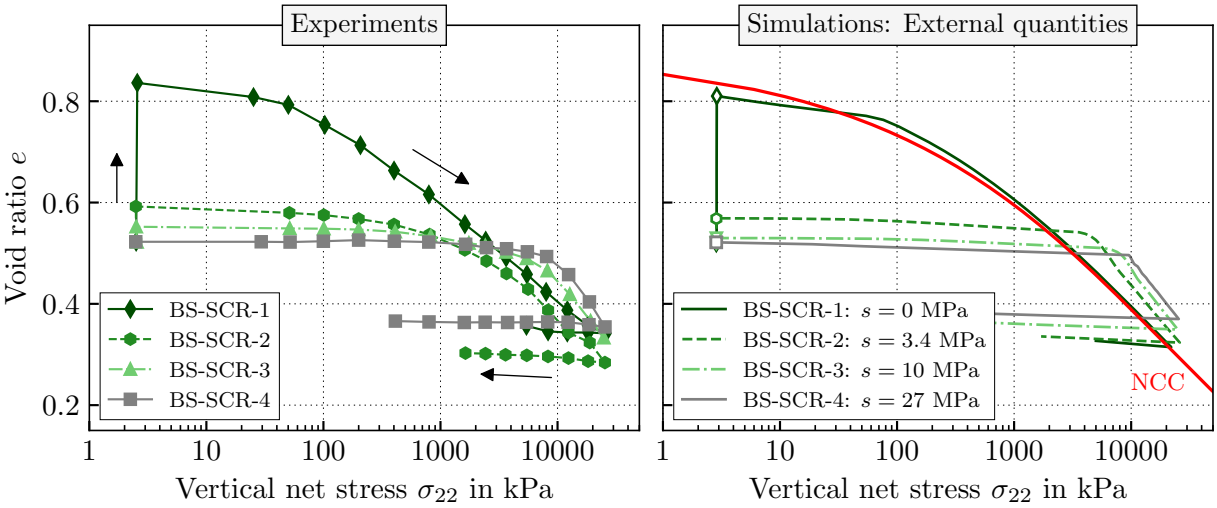

Figure 7.36.: Vertically unconfined swelling and oedometric compression and rebound tests on a bentonite-sand mixture at different suctions (Lang, 2019): experimental results (left) and simulation results in terms of external behaviour (right).

7.2. Large-scale example

The modelling framework developed in this work was applied to a large-scale BVP to demonstrate its capabilities beyond simulations on the centimetric scale of the presented laboratory tests. The geometry of an emplacement tunnel for high-level radioactive waste (HLW) disposal in a deep geological repository at several hundred meters depth was employed. Its longitudinal profile and cross sections are shown in Figure 7.37. It is based on the Swiss concept of high-level radioactive waste disposal, which is also currently investigated for the German concept in clay formations (Nagra, 2002; Jobmann et al., 2017). Within the multi-barrier system comprising the host rock (geological barrier), the buffer (geotechnical barrier) and the conditioned waste, the buffer primarily hinders the migration of pollutants or radionuclides. This is achieved through the hydration of the expansive buffer material by mountain water, which induces swelling therein. The HLW canisters are placed on pedestals made of highly compacted expansive material inside the tunnel (cross section B) and the remaining cavity within the tunnel is filled with compacted buffer material (cross section A). Bentonite and bentonite-sand mixtures are primary considered for use, however the reuse of the excavated clay shale is being examined either as-is or in mixtures as well (Zeng et al., 2022; Zhang and Kröhn, 2019; Souza and Pejon, 2020; GRS, 2023). The emplacement tunnel is supported by a tunnel lining.

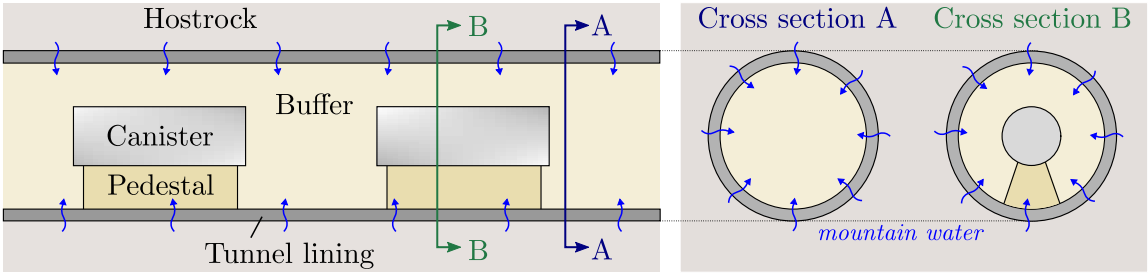

Figure 7.37.: Schematic longitudinal profile and cross sections of an emplacement tunnel for high-level radioactive waste disposal. Adapted from Nagra (2014) and Jobmann et al. (2017).

Two cross sections of the schematic emplacement tunnel were simulated in a two-dimensional half-plane assuming plane strain conditions, referred to as cross sections A and B. The geometry and meshes are displayed in Figure 7.38. The excavation diameter of the tunnel was chosen as $d = 3.0$ m. With a lining thickness of 0.25 m, the diameter of the open tunnel cross section was $d = 2.5$ m. In cross section B, the canister had a diameter of $d = 1.05$ m. The pedestal was modelled as a segment of the circular excavation cross section. The host rock was considered with boundaries at 10 m from the tunnel axis. The displacement of the outermost nodes was restricted orthogonally to the model boundary. The meshes consisted of quadrilateral elements, oriented centrally toward the centre of the tunnel. In the lining, buffer, and pedestal, the average element length was approximately $l_e = 0.05$ m, decreasing towards the tunnel centre. The rock was discretised coarser than the emplacement tunnel, with an element size increasing radially outward from the tunnel centre. Both cross sections were simulated under uniform radial infiltration along the tunnel lining (cross sections A.1 and B). An additional simulation considering an imperfection of the lining at the spring line (cross section A.2), resulting in a localized water ingress, was carried out.

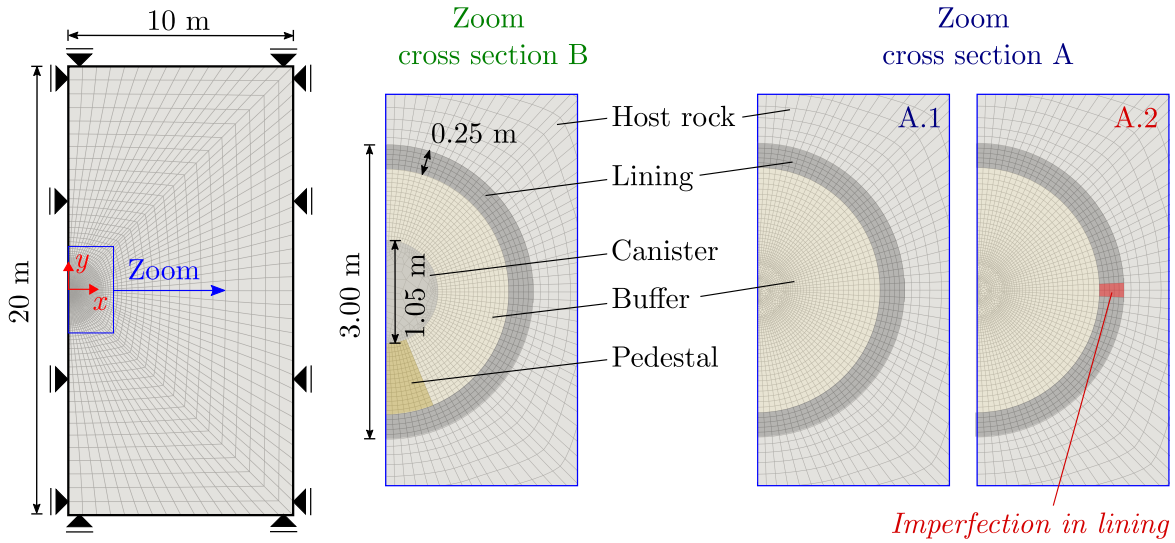

Figure 7.38.: 2D plane strain finite element model employed in simulations of the emplacement tunnel: dimensions and cross sections.

The backfilling and pedestal were modelled using „Hypoplasticity for expansive soils“ with the well-calibrated parameter set of reconstituted Opalinus clay shale (see Table 7.3). The saturation-driven strain rate was considered as isotropic ($m^w = 1$). As the focus of this study is on the behaviour inside the tunnel, the mechanical behaviour of the host rock and the tunnel lining were simplified as linear elastic. The mechanical and hydraulic material parameters for the host rock correspond to the in-situ Opalinus clay shale at Mont Terri underground rock laboratory (URL, Bossart (2012); Ferrari et al. (2014)). Representative values for the mechanical parameters were taken into account for the concrete lining. The hydraulic parameters were based on measurements of permeability in shotcrete samples from a full-scale emplacement experiment at the Mont Terri URL (Müller et al., 2017) and measurements of the SWRC of concrete by Pap et al. (2022). The canister in cross section B was modelled as a solid steel body, as well with linear elastic mechanical material behaviour. Representative material parameters ($E = 210$ GPa and $\nu = 0.25$) were used. The mechanical and hydraulic material parameters for the host rock and lining are gathered in Tables 7.9 and 7.10. For the host rock and tunnel lining, four node selectively reduced integrated elements with bilinear interpolation of both displacement and pore water pressure without consideration of swelling were used. The canister comprised of four node solid elements without pore water pressure as a degree of freedom and linear interpolation of the displacement. The solid displacement of the outer nodes of the canister were connected to the surrounding nodes of the buffer by multi point constraints. The buffer and pedestal comprised of four node selectively reduced integrated elements with bilinear interpolation functions for both displacement and pore water pressure and with consideration of swelling based on the extended TPM for expansive soils.

Table 7.9.: Material parameters for the mechanical and hydraulic model of the host rock.

Mechanical: Linear elasticity		Hydraulic: van Genuchten				
E in GPa	ν	α in kPa	n	S^{wr}	K^s in m^2	$k^w_{\min}$
7	0.28	0.00005	1.8	0.02	2×10^{-20}	1×10^{-3}

Table 7.10.: Material parameters for the mechanical and hydraulic model of the concrete lining.

Mechanical: Linear elasticity		Hydraulic: Fredlund & Xing							
E in GPa	ν	h_r in kPa	a_f in kPa	n_f	m_f	S^{wr}	K^s in m^2	s_i in kPa	$k^w_{\min}$
30	0.2	1600	1200	1	4	0	4×10^{-17}	0.1	1×10^{-1}

In all simulations, the host rock had an initial void ratio of $e_0 = 0.230$ and was initially fully saturated, which is in line with in-situ measurements of Opalinus clay shale at Mont Terri URL (Bossart, 2012; Bosch et al., 2023). The expansive material in the buffer and the pedestal was initially quasi-dry, which led to a pore water pressure gradient in the tunnel lining. The initial void ratio of the lining was $e_0 = 0.300$. For the imperfection of the tunnel lining in cross section A.2, the permeability and initial void ratio of the lining were increased to values of $K^s = 4 \times 10^{-13}$ m^2 and $e_0 = 1.0$, respectively. The stress state in the host rock corresponds to a depth of approximately 500 m and was initialized isotropically as $p = 11.5$ MPa. The net stress in the buffer and pedestal (only cross section B) were initialized isotropically with $p = 10$ kPa, corresponding to a small seating stress and assuming that the tunnel lining fully bears the mountain load. The initial state variables for „Hypoplasticity for expansive soils“ were determined in simulations of isotropic loading and unloading in the material preparation. The initial pore water pressure was defined hydrostatically with the bottom of the tunnel as the

reference level. The initial values were $p_0^w = -10$ kPa for the host rock and $p_0^w = -83$ MPa and $p_0^w = -101$ MPa for reconstituted Opalinus clay shale based on the SWRC shown in Figure 5.30 and parameters in Table 7.3, depending on the initial void ratio and assuming the same initial water content of $w_0 \approx 2$ %. The initial state for the pedestal and the buffer is given in Table 7.11 and the initial hydraulic conditions are shown in Figure 7.39 for both cross sections.

Table 7.11.: Initial state and reference permeability of reconstituted Opalinus clay shale as buffer and pedestal material for simulation of the emplacement tunnel.

Name	p_0 in kPa	e_0	n_{ref}	p_{d0} in kPa	e_{d0}	S_0^w	p_0^w in kPa	K_{ref}^s in m^2
Pedestal	-10	0.327	0.246	17944.8	0.294	0.151	-83000	6.2×10^{-16}
Buffer	-10	0.375	0.273	9941.9	0.343	0.131	-101000	9×10^{-16}

The simulations were carried out in two steps. The construction of the tunnel was not simulated, as the behaviour upon infiltration of mountain water into the emplacement tunnel was of interest in this study. In the geostatic step, the initial stress state, pore water pressure, void ratio and state variables were initialized. The step was performed as quasi-static with a step time of $t_{\text{step}} = 1$ s. In the subsequent infiltration step, the degree of freedom of pore water pressure was released in the buffer and the pedestal (only cross section B), which enabled flow from the fully saturated host rock through the tunnel lining and into the interior of the emplacement tunnel. The step was performed using the novel transient-critical analysis type with $f_{t_{\min}} = 0.80$ and $\Delta t_{\max} = 50000$ s and with a total step time of 10 years ($t_{\text{step}} = 315360000$ s).

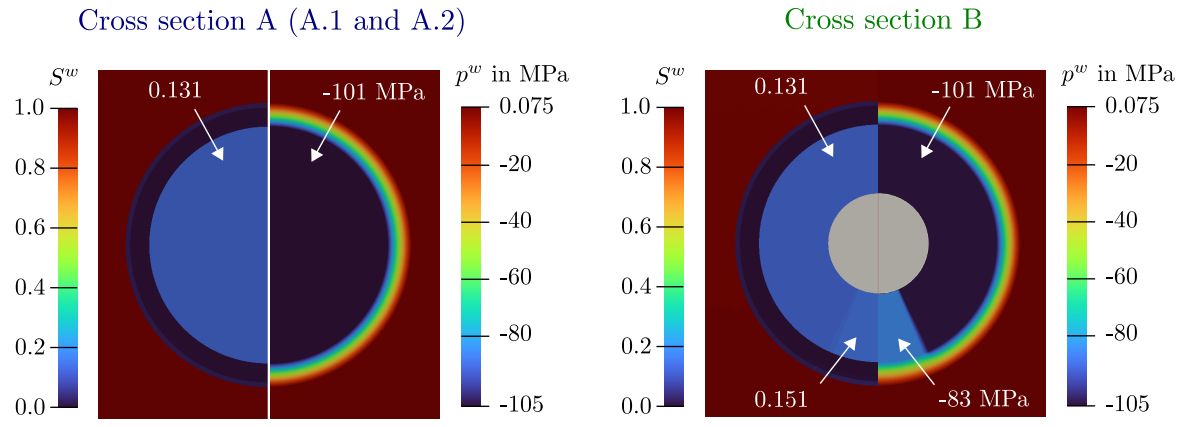

Figure 7.39.: Initial conditions of the degree of saturation and the pore water pressure for the simulations: cross section A (left, valid for A.1 and A.2) and cross section B (right).

7.2.1. Simulations with uniform, radially symmetric infiltration

7.2.1.1. Cross section A.1

Verification of the stress and deformation field after the geostatic step

Following the geostatic step, the plausibility of the computed stresses in the host rock and lining at the crown, invert and spring lines is first examined in comparison to the analytical solutions for isotropic in situ stress conditions. The simulation results showed a radial net stress of $\sigma_{rr}^{\text{rock}} \approx 6$ MPa in the host rock, corresponding to the x-component at the spring lines of the

tunnel and the y-component at crown and invert. The circumferential stress was $\sigma_{\theta\theta}^{\text{rock}} \approx 16.5$ MPa, corresponding to the y-component at the spring lines of the tunnel and the x-component at crown and invert, see left-hand side of Figure 7.40. According to the classical Kirsch solution for a cylindrical hole in an infinite elastic medium (Kirsch, 1898), which is based on the theory of a thick-walled pipe for isotropic stress in the far field ($\rightarrow \infty$), the corresponding circumferential stress $\sigma_{\theta\theta}$ in the rock at the excavation boundary computes from the isotropic initial stress state σ_0 and the inner pressure p_i. For $\sigma_0 = \sigma_{xx} = \sigma_{yy} = 11.5$ MPa and $p_i = \sigma_{rr}^{\text{rock}} \approx 6$ MPa it is:

$$\sigma_{\theta\theta}^{\text{rock}} = 2\sigma_0 - p_i = 23 - 6 = 17\,\text{MPa}, \tag{7.2}$$

and is thus consistent with the circumferential stress magnitude obtained numerically in the host rock. Furthermore, the simulation results gave a radial displacement of approximately $u_{rr} \approx 1.4$ mm, see right-hand side of Figure 7.40. The radial displacement at the tunnel boundary may be estimated from the Kirsch solution as well. For an initial stress of $\sigma_0 = 11.5\,\text{MPa}$, an inner pressure of $p_i \approx 6\,\text{MPa}$, an elastic modulus and Poisson's ratio of the rock of $E = 7$ GPa and $\nu = 0.28$, respectively, and a radius of $r = 1.5$ m, the expected radial displacement at the excavation boundary results in:

$$u_{rr} = \frac{r}{E}(1-\nu)(\sigma_0 - p_i) = \frac{1.5}{7 \times 10^6}\,(1 - 0.28)\,(11500 - 6000) \approx 0.85\,\text{mm}, \tag{7.3}$$

which is below the numerically obtained value. The difference is plausible, since the analytical estimate neglects the deformability of the buffer and lining as well as the load redistribution within the composite system of rock, buffer and lining.

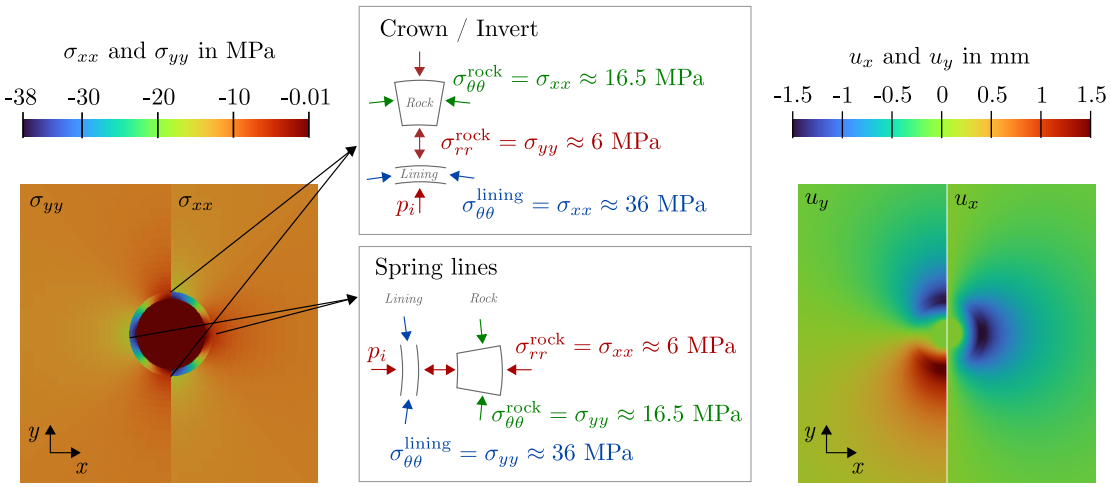

Figure 7.40.: Simulation of cross section A.1: Stress and displacement after the geostatic step in $x-$ and $y-$direction with discrete values for stresses at the excavation boundary in the lining and host rock.

The inner pressure of $p_i = 6$ MPa acted as well in the lining and allows to estimate the circumferential stress in the lining using Barlow's formula (german: Kesselformel) for a thin-walled pipe or pressure vessel. For a wall thickness of $t = 0.25$ m and radius of $r = 1.5$ m, it is:

$$\sigma_{\theta\theta} = p_i \frac{r}{t} \approx 6\,\frac{1.5}{0.25} \approx 36\,\text{MPa}, \tag{7.4}$$

and agrees satisfactorily with the value of $\sigma_{\theta\theta} \approx 32.5$ MPa, which was evident in the outer elements of the lining in the simulation results displayed on the left-hand side of Figure 7.40.

Note that Barlow's formula is strictly only valid for an empty pipe. Additional stiffness from the composite system of rock, buffer and lining accounts for the discrepancy between the analytical estimate and the numerically obtained value. Overall, the initial state before the onset of infiltration was found to be reasonable.

Behaviour upon infiltration

Figure 7.41 shows the evolution of the degree of saturation over time on the left-hand side and the evolution of the net stress and void ratio upon changes in the degree of saturation in the centre and on the right-hand side. The results from the simulation are presented for seven points in the buffer material distributed along the symmetry axis of the tunnel, as indicated in the centre of Figure 7.41. The degree of saturation increased evenly towards the centre of the buffer material, reaching full saturation after approximately 8 years. Its evolution shows some influence of gravity, as the lower part of the buffer (dashed lines) reached full saturation slightly before the upper part (solid lines) at equal distance from the tunnel lining.

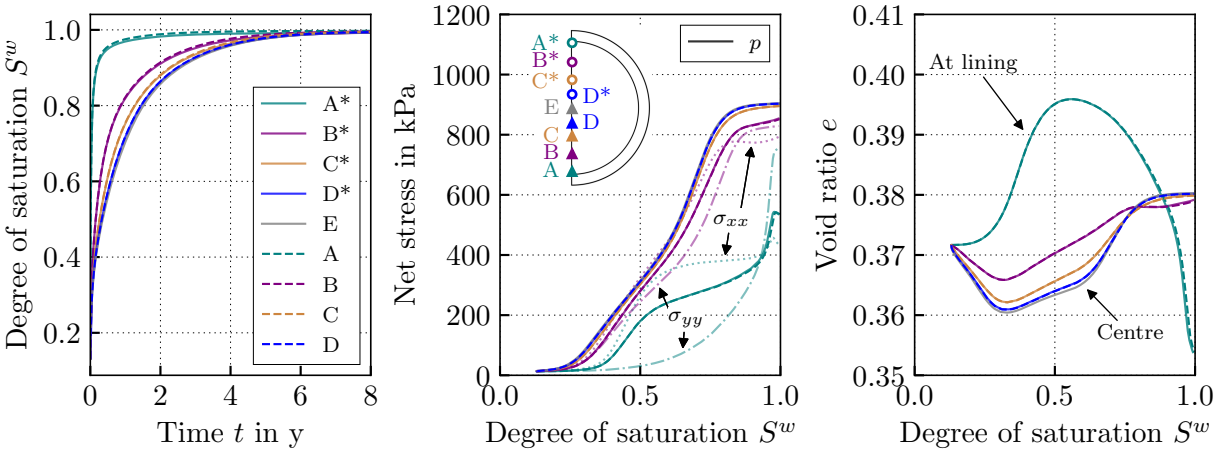

Figure 7.41.: Cross section A.1: Evolution of degree of saturation versus time and net stress and void ratio versus degree of saturation on the symmetry axis of the tunnel for radial infiltration.

The evolution of the mean net stress and the void ratio show an inhomogeneous material response of the expansive buffer material. The stiffness of the lining and host rock only allows for minor deformation and thus the mechanical conditions for the buffer material correspond approximately to those of constant volume. As was also evident for the simulation of swelling pressure tests as BVPs (see Section 7.1.1), the outer constant volume conditions did not apply to individual elements. The evolution of the void ratio on the right-hand side of Figure 7.41 exhibited a very similar behaviour to that of the centimetric simulation of swelling pressure. The outermost element at the tunnel lining first expanded upon infiltration, which compressed the inner elements of the buffer. With further increase of saturation, the swelling of the inner elements led to a delayed expansion, which resulted in renewed compression of the outer elements, whose compressibility had already been increased by saturation. In terms of stress evolution, however, the behaviour partly differs from the centimetric simulation of swelling pressure, in which the direction of infiltration clearly coincided with the constrained deformation direction. The mean net stress p was higher in the interior of the tunnel cross section than in the vicinity of the tunnel lining, as can be seen in the centre plot of Figure 7.41 (solid lines). This difference is mainly attributed to the contribution of the horizontal net stress component σ_{xx}, which is

shown exemplarily for points A and B (dotted lines), together with the vertical net stress component σ_{yy} (dash-dotted lines), in Figure 7.41. While the vertical net stress exhibited a similar magnitude at both points (approximately 800 kPa), the horizontal net stress was lower in the vicinity of the tunnel lining at point A (approximately 450 kPa) than at point B (approximately 800 kPa). This behaviour can be explained by the varying deformation constraints: in the inner part of the buffer, swelling-induced volumetric strains were more uniformly constrained, resulting in a nearly isotropic stress state, whereas near the lining, partial strain accommodation in the x-direction limited the build-up of the horizontal net stresses.

Figure 7.42 presents the distribution of the degree of saturation, the void ratio, the volume fraction of swelling water and the mean net stress at four different times (3 months, 6 months, 1 year and 3 years) upon infiltration. A radially symmetric material response along the entire circumference of the circular cross section becomes evident for all shown variables.

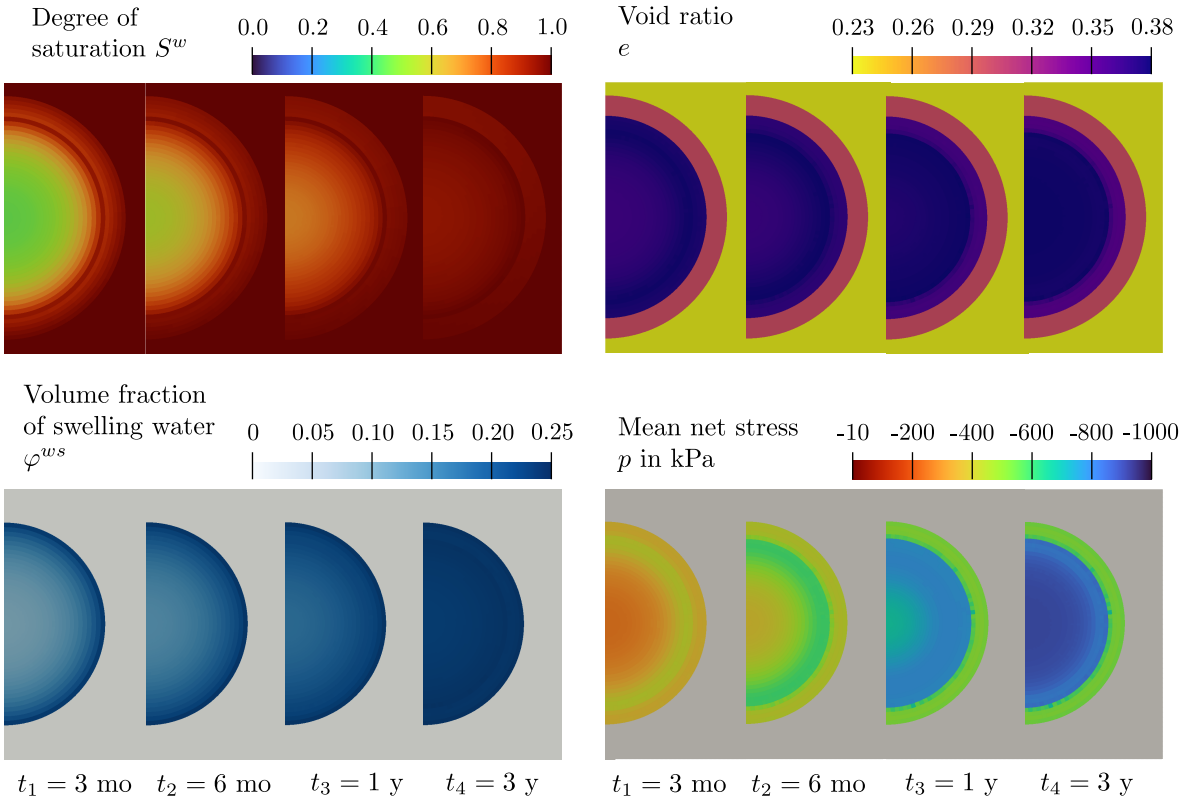

Figure 7.42.: Cross section A.1: Distribution of the degree of saturation, the void ratio, the volume fraction of swelling water and the mean net stress at different times upon radial infiltration.

The degree of saturation, shown in the upper left part of Figure 7.42, increased radially from the lining to the centre of the buffer with time, resulting in an equally distributed increase of the volume fraction of swelling water in the lower left part of Figure 7.42. The radial gradient in the distribution of the void ratio and the mean net stress, however, is clearly visible in the upper and lower right part of Figure 7.42, respectively. Both show the formation of two parts across the cross section, whose diverging behaviour became more pronounced with increasing time: an inner part, which was characterised by larger void ratios and higher mean net stress, and a more heavily compressed ring-shaped outer part with smaller mean net stress and smaller void ratios.

The time evolution of normal net stress in the soils which acts on the tunnel lining is shown in Figure 7.43 for three points at the crown (A*), invert (A) and spring line (F). It is evident that

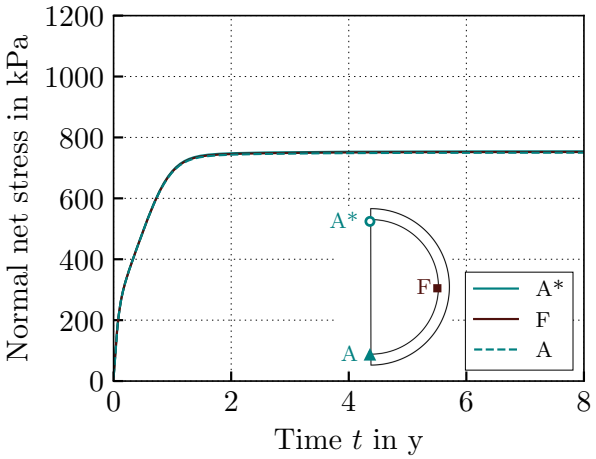

Figure 7.43.: Cross section A.1: Evolution of swelling pressure, expressed as the normal net stress in the soil acting on the tunnel lining, at the crown, invert and spring line for radial infiltration

the normal net stress near the lining reached a value of approximately 750 kPa after less than two years and no longer evolved thereafter. At this point in time, saturation of the outer buffer regions was already complete (see Figure 7.41). The stresses induced by the continued swelling of the inner buffer regions were redistributed within the circular cross section due to arching effects.

7.2.1.2. Cross section B

The material response of the buffer in the simulation of cross section B was characterised by different swelling behaviour of the pedestal and buffer due to their different initial void ratios (compaction state). Figure 7.44 shows the evolution of the degree of saturation over time on the left-hand side and the evolution of the mean net stress and void ratio upon changes in the degree of saturation in the centre and on the right-hand side. The results from the simulation are presented for six points distributed along the symmetry axis of the tunnel with points A*, B* and C* (solid lines) located in the less compacted buffer and points A, B and C (dashed lines) located in the pedestal. Similar to the simulation of cross section A.1, the degree of saturation increased evenly towards the centre, thus here towards the canister, reaching full saturation after a shorter duration of approximately 5 years due to the reduced infiltration length (radial thickness of the buffer). The evolution of the mean net stress and the void ratio exhibited distinctly different behaviour in the buffer and the pedestal. The material response of the buffer in cross section B is largely comparable to that of the homogeneous buffer simulated in cross section A.1, with only a minor influence from the canister. Owing to its high stiffness, the canister acted as a rigid structure in the centre of the emplacement tunnel, inducing additional compaction in the close, surrounding elements (point C*), when swelling took place in the outer elements near the lining. This effect was more pronounced in the pedestal located beneath the canister, where the load transfer led to an increased compression at the top of the pedestal (point C).

The overall trends of material behaviour along the symmetry axes in the pedestal were similar to those observed in the buffer. The lower initial void ratio in the pedestal resulted in higher

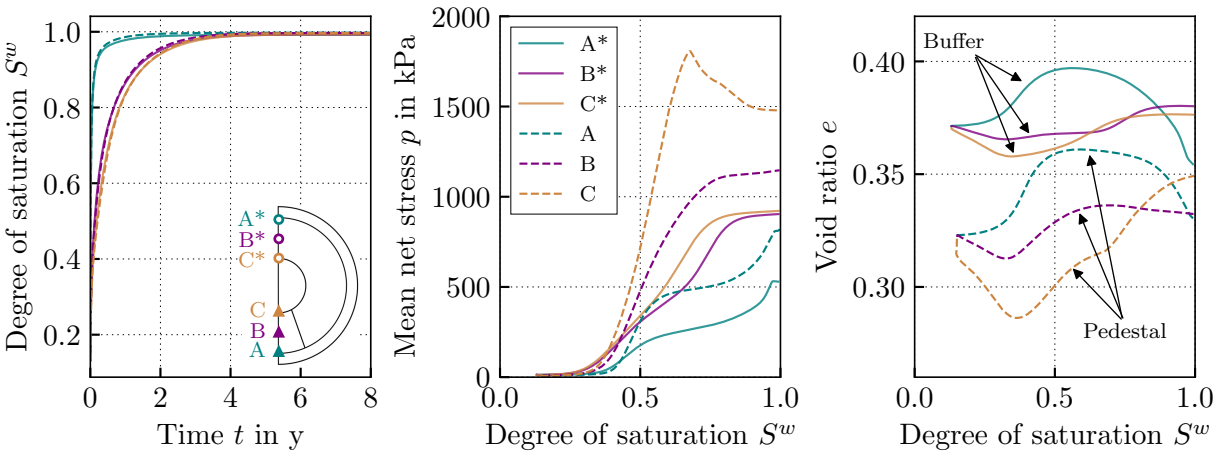

Figure 7.44.: Cross section B: Evolution of degree of saturation versus time and of void ratio and mean net stress versus degree of saturation on the symmetry axis of the tunnel for radial infiltration.

mean net stresses compared to the buffer at an identical distance from the infiltration boundary at the tunnel lining. Figure 7.45 provides a more detailed assessment of the spatially varying material response and the influence of the pedestal. It shows the distribution of the degree of saturation, the void ratio, the volume fraction of swelling water and the mean net stress at four different times (3 months, 6 months, 1 year and 3 years) upon infiltration.

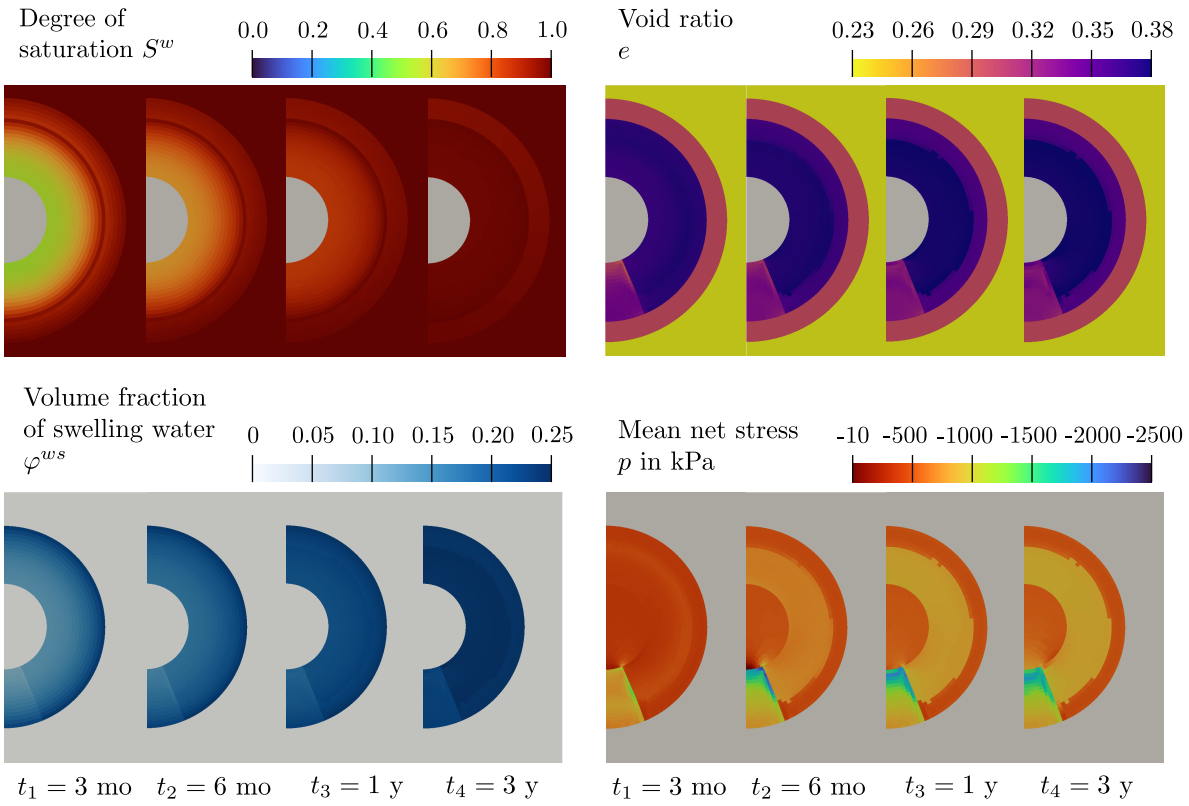

Figure 7.45.: Cross section B: Distribution of the degree of saturation, the void ratio, the volume fraction of swelling water and the mean net stress at different times upon radial infiltration.

In the distribution of the degree of saturation (upper left part of Figure 7.45) no pronounced difference between the pedestal and buffer existed, as the intrinsic permeability was only slightly smaller in the pedestal (see Table 7.11), while the initial degree of saturation was slightly larger. The distribution of the void ratio in the upper right part of Figure 7.45 highlights the effect of the rigid canister on the mutually influencing material behaviour of the pedestal and the buffer. In combination with the more pronounced swelling of the pedestal, compression initially developed along the boundary between the pedestal and the buffer. Over time, i.e. with progressing infiltration and swelling, the void ratio distribution became more homogeneous again. Different void ratios in the buffer and the pedestal remain, and the formation of an outer, more compressed element layer in the buffer, similar to that observed in cross section A.1, was evident. The differences in void ratio are also visible in the distribution of the volume fraction of swelling water (lower left part of Figure 7.45), which is overall smaller in the pedestal than in the buffer due to the smaller porosity. The constraints imposed by the pedestal, buffer, and canister are particularly noticeable in the distribution of the mean net stress in the lower right part of Figure 7.45. Stress concentrations arose from the coupled displacements at the interfaces between these components, initially increasing as saturation progressed and subsequently decreasing slightly as the system homogenized. Elevated stresses resulting from swelling in the pedestal are clearly visible, with decreasing tendency from the centre outwards.

Consequently, the normal net stress acting on the canister and lining differed significantly in the pedestal and in the remaining buffer, as can be seen on the left-hand side of Figure 7.46. Therein, the evolution of normal net stress acting on the canister and the lining at crown, invert and spring lines is presented. In the pedestal, the canister and the lining were subjected to a normal net stress of approximately 1200 kPa and 900 kPa, respectively. The normal net stress acting on the canister and the lining in the buffer is approximately 750 kPa, i.e. corresponding to the magnitude of the homogeneous cross section A.1. The right-hand side of Figure 7.46 presents the evolution of normal displacement at the same points. The results clearly show the movement of the rigid canister within the expansive material in the emplacement tunnel. First, the canister settled during infiltration and was subsequently lifted by the more pronounced swelling of the pedestal. Moreover, Figure 7.46 shows, that the lining experienced a tiny compression of $u = 0.14$ mm by the swelling of the expansive material within.

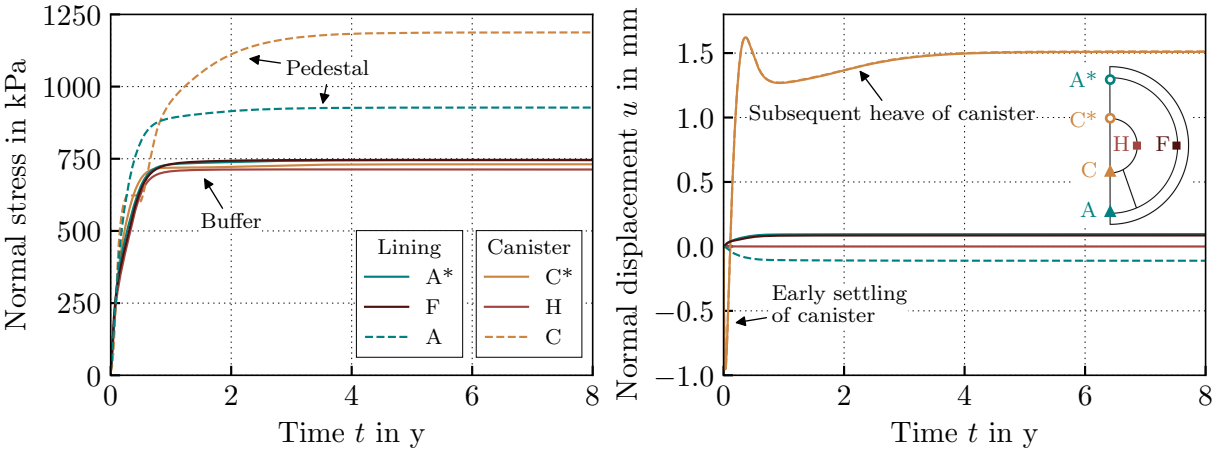

Figure 7.46.: Cross section B: Evolution of swelling pressure, expressed as the normal net stress in the soil acting on the tunnel lining at the crown, invert and spring line and acting on the canister and evolution of normal displacement at the same positions for radial infiltration.

7.2.2. Simulation with localized water ingress

The simulation results of cross section A.2, in which an imperfection of the tunnel lining at the spring line was considered, are presented in Figure 7.47. Therein, the evolution of the degree of saturation over time is shown on the left-hand side and the evolution of the mean net stress and void ratio upon changes in the degree of saturation in the centre and on the right-hand side. The evaluation was carried out for nine points, see in the centre plot of Figure 7.47. Five points (A*, B*, C*, D* and E) are located in the upper buffer material distributed along the symmetry axis of the tunnel and correspond to those of Sections 7.2.1.1 and 7.2.1.2. The additional four points (F, G, H and I) are located on the horizontal symmetry line at equal distance from the tunnel centre. The results demonstrate, that the localized water ingress did not result in a significantly faster evolution of the degree of saturation (left plot of Figure 7.47). Interestingly, the degree of saturation at point F, where the imperfection in the tunnel lining was located, was below that of point A* (at the crown) during most of the infiltration. However, a closer look at the initial phase of the infiltration, which is shown in the zoomed-in plot on the left-hand side of Figure 7.47, reveals that the degree of saturation close to the imperfection initially did increase more rapidly for a time period of approximately 22 days (0.06 y). The evolution of the mean net stress and the void ratio were more significantly affected by the imperfection of the tunnel lining. The centre plot of Figure 7.47 indicates an increased stress at full saturation in point F in comparison to point A*, which is also reflected in a larger final void ratio on the right-hand side plot. Apparently, the swelling of the inner elements did not result in the same recompression of the elements near the localized water ingress. A different material response is also evident between points G and B*, located second closest to the lining, whereas the remaining points present identical behaviour at an equal distance from the lining.

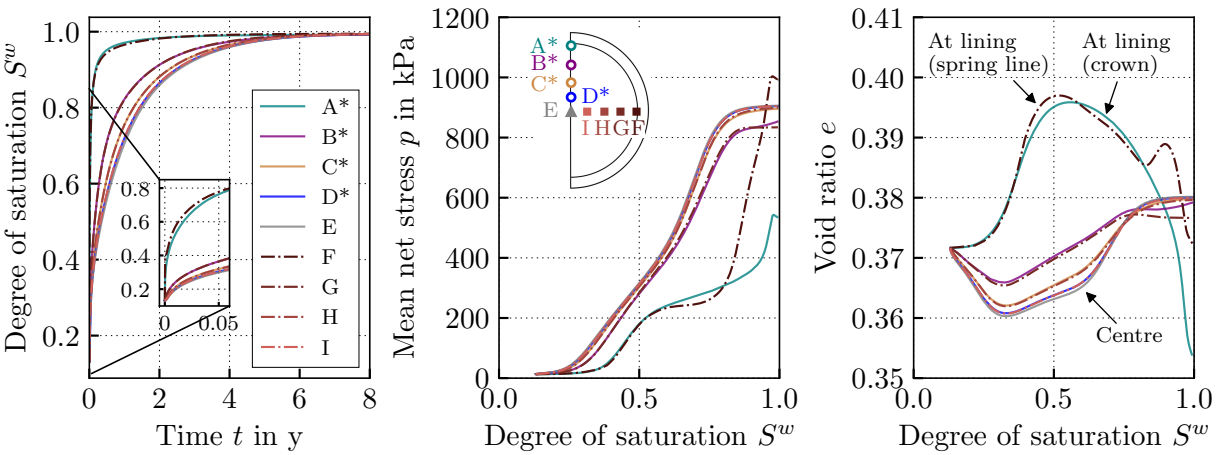

Figure 7.47.: Cross section A: Evolution of degree of saturation versus time and of void ratio and mean net stress versus degree of saturation on the symmetry axis of the tunnel for localized infiltration at the spring line.

The distribution of the degree of saturation, the void ratio, the volume fraction of swelling water and the mean net stress at four different times (3 months, 6 months, 1 year and 3 years) upon infiltration is shown in Figure 7.48. In contrast to the previous Sections, the distribution of the degree of saturation and the volume fraction of swelling water is additionally depicted after 0.5, 3 and 10 days, and 1 month. In the distribution of the degree of saturation in the upper part of Figure 7.48, the localized water ingress at the spring line is clearly evident in the lining itself. In the buffer, the existing differences are not visible for the displayed colour scale.

Due to the very low permeability of the buffer, the localized water ingress had only limited consequences on the infiltration behaviour. With progressing time, the degree of saturation in the lining homogenised and after 3 years, its distribution was radially symmetric. The impact of the localized water ingress is also visible in the distribution of the swelling water content for the first two depicted points in time in the second row in Figure 7.48, however, it homogenizes subsequently. For the void ratio in the lower left part of Figure 7.48, no pronounced influence of the imperfection in the tunnel lining is evident within the buffer and a homogenous, radially symmetric distribution was present. In contrast, the distribution of the mean net stress in the lower right part of Figure 7.48 demonstrates the influence of the localized water ingress on the development of locally higher swelling pressure at the spring line. Analogous to Figures 7.42 and 7.45, a more heavily compressed ring-shaped outer part with smaller mean net stress and smaller void ratios compared to the inner part developed.

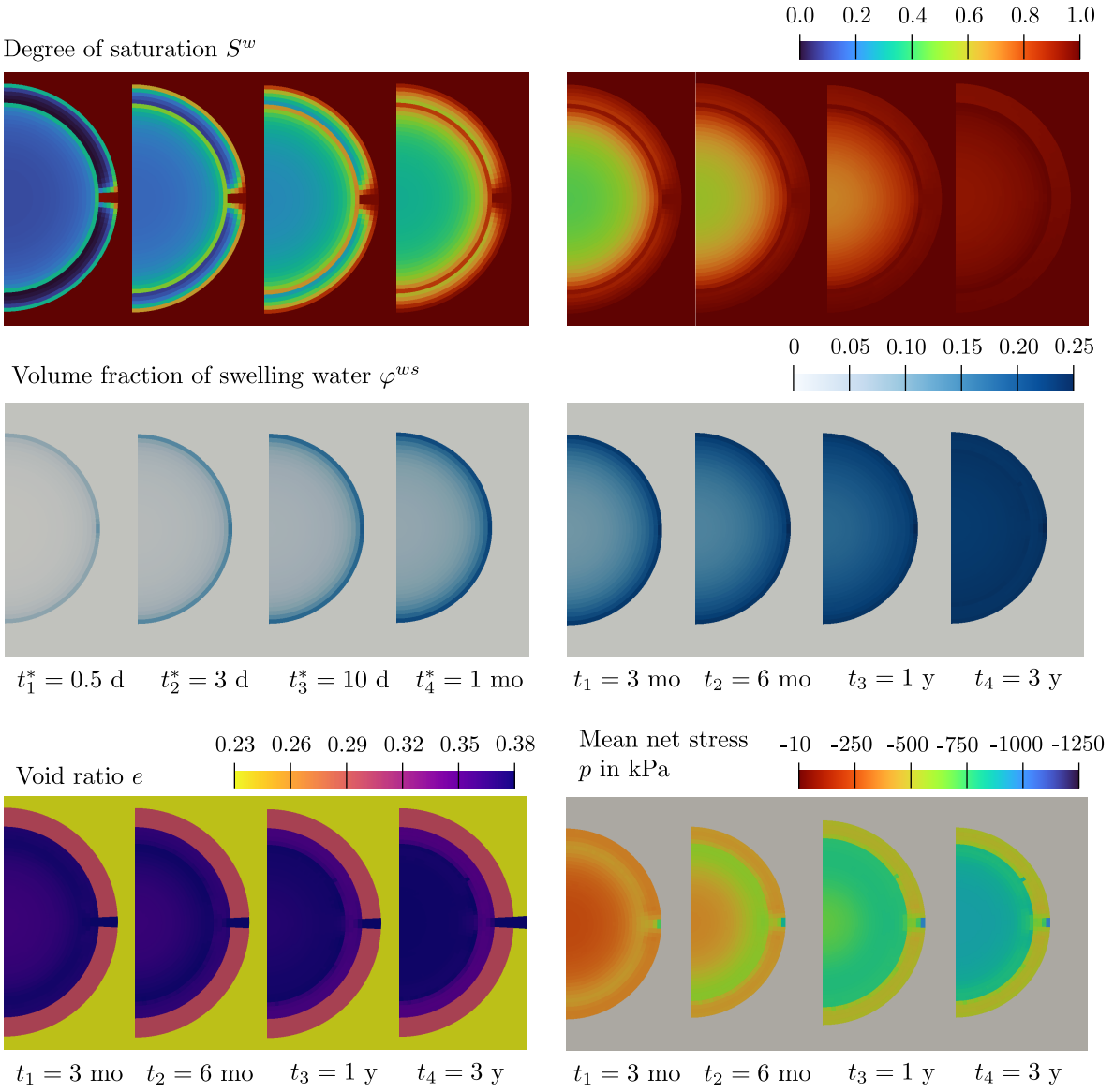

Figure 7.48.: Cross section A.2: Distribution of the degree of saturation, the void ratio, the volume fraction of swelling water and the mean net stress at different times upon localized infiltration at the spring line.

Finally, in Figure 7.49, the larger magnitude of normal net stress acting on the lining near the spring line, where the imperfection was located, is demonstrated. In comparison to the simulation results of radially symmetric infiltration in cross section A.1 (Figure 7.43), the normal net stress in point F was larger at approximately 1170 kPa, whereas it was identical in points A and A* with 750 kPa.

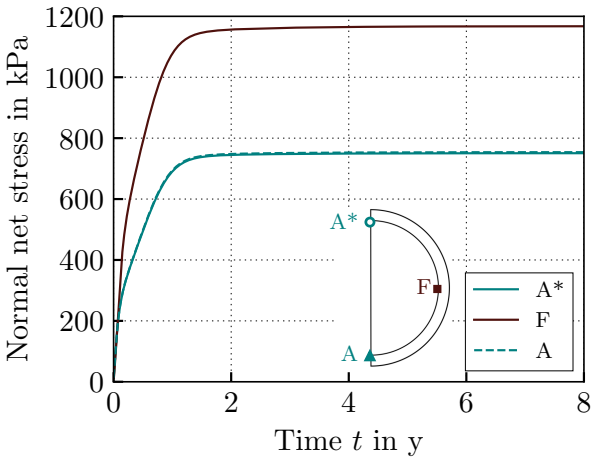

Figure 7.49.: Cross section A.2: Evolution of swelling pressure, expressed as the normal net stress in the soil acting on the tunnel lining at the crown, invert and spring line and acting on the canister and evolution of normal displacement at the same positions for localized infiltration at the spring line.

7.2.3. Overview of the simulations

All three simulations could be successfully carried out using the modelling framework of this work. In the simulations of cross section A.1 and B with uniform, radially symmetric infiltration, the buffer exhibited a radially symmetric swelling behaviour with only minor influence of the canister and pedestal on the response of the surrounding buffer material. The simulation of cross section A.2 with localized water ingress due to an imperfection in the tunnel lining exhibited larger normal net stresses in the buffer near the imperfection, however, an otherwise similar material response. The resulting swelling pressures were consistent with the magnitudes expected for the adopted parameter sets. More importantly, neither the different initial compaction states of the buffer and the pedestal, and the resulting differently pronounced tendencies of the material to swell, nor the local higher pore water pressure gradients resulting from the increased permeability in the imperfection, did pose a major difficulty for successful modelling with the novel framework. While the focus of this section was primarily on the applicability of the modelling framework to a large-scale BVP, the observed material response also allows for a qualitative assessment of the swelling behaviour of reconstituted Opalinus clay as a sealing material. The swelling pressure was comparatively lower than typically associated with more expansive materials such as bentonite or bentonite–sand mixtures, which are primarily investigated in the context of nuclear waste disposal. The use of excavated clay shale may therefore be more suitable in less critical regions of a deep geological repository.

7.3. Concluding remarks

The modelling framework of this work was applied to boundary value problems. Laboratory tests of expansive soils on the centimetric scale were simulated by discretising the sample with many finite elements. Furthermore, a large-scale problem representing an emplacement tunnel from a deep geological repository for nuclear waste disposal that is filled with an expansive buffer material and subjected to radial groundwater infiltration from the surrounding rock, was simulated.

The material behaviour of the presented experimental campaigns could be well simulated with the modelling framework, successfully predicting the time evolution and magnitude of expansion and swelling pressure. The simulation of laboratory tests, however, also revealed challenges for the simulation of constant volume swelling: The mechanical model relies on idealised swelling assumptions that are not strictly met in each element of a discretised boundary value problem. Adjacent elements caused load transfer, which changed the initial state before the onset of infiltration. As a result, the net stress and the void ratio were not homogeneous in the simulation of constant volume swelling. These inhomogeneities were more pronounced by certain combinations of hydraulic parameters and hydraulic conditions. Yet, overall the simulations captured the material behaviour with good accuracy.

The presented simulations of the large-scale example demonstrate that the modelling approach is applicable beyond idealised laboratory-scale boundary value problems, in which infiltration takes place orthogonally to element edges only. The framework was capable of resolving expansive material behaviour of a circular geometry with spatially varying initial void ratio and non-planar infiltration along the circular boundary. This highlights the suitability of the framework for analysing swelling-induced processes under real-scale geometric conditions, where more complex boundary interactions exist.

8. Summary, conclusions and outlook

This thesis comprises the development of a novel modelling approach for expansive soils using the Finite Element (FE) method. The modelling framework accounts for the attachment of swelling water to the solid phase in an extension of the governing equations of the theory of porous media (TPM). It predicts the hydro-mechanical material response with novel constitutive relationships for the mass transfer between free pore water and swelling water, for the swelling-induced relative permeability and for the stress-strain behaviour using a novel hypoplastic constitutive model for expansive soils. The main part of the thesis focused on the formulation, implementation, and application of the modelling framework.

First, an extension of the theory of porous media for expansive soils was derived by introducing the proportion of swelling water as an additional phase. This water is attached on negatively charged surfaces of the clay minerals upon swelling. Free pore water and swelling water were distinguished: While the free water could flow through the pore space, the swelling water was considered as bound to the solid by physio-chemical forces. A constitutive model for the bidirectional mass transfer between free water and swelling water was proposed to control the transition between both phases. This allowed the definition of an effective aggregate porosity which accounts for the reduction in total porosity caused by the presence of swelling water. The effective aggregate porosity and consistent mass balancing was used to define a swelling-induced relative permeability. Both the constitutive relations for mass transfer and the swelling-induced relative permeability were derived from experimental observations in permeability tests on reconstituted Opalinus clay conducted before and after swelling.

The second major contribution of this work was the formulation of a hypoplastic model for the simulation of the stress-strain response of expansive soils. The objective was to account for the most important swelling phenomena: expansion and swelling pressure, the oedometric compression and rebound behaviour and the evolution of mechanical material properties as a consequence of changes in saturation. The constitutive model was first proposed in a one-dimensional rate formulation and subsequently generalized as a full tensorial formulation by adopting a modified Cam Clay preconsolidation surface and flow rule. As core of the model, a saturation-driven swelling feature could predict expansion or swelling pressure with a single evolution equation without distinction of elastic and plastic strain rates. The model was formulated in terms of net stress and (effective) degree of saturation and with the preloading state as main internal variable. The capabilities of the mechanical constitutive model were presented for both, the one-dimensional and the three-dimensional formulation and its predictive performance was evaluated against several experimental campaigns. Recommendations for the determination of the material parameters were developed.

The modelling framework was implemented as a novel element library and mechanical material model into the FE software package `numgeo`. The implementation was discussed with regard to the extended TPM and the time integration of the mechanical model. Finally, the framework was applied in boundary value problems (BVP). In this way both the magnitude of swelling

phenomena and their temporal evolution could be predicted, which is controlled by the flow of water through the pore space. The aforementioned laboratory campaigns were simulated and the prediction qualities of the framework discussed. The applicability of the modelling framework within a large-scale BVP was demonstrated by simulating an emplacement tunnel of a deep geological storage facility backfilled with an expansive material.

8.1. Conclusions

The main outcome of this thesis is that the division of tasks between the continuum scale (finite element) and the constitutive level could effectively replicate the hydro-mechanical behaviour of expansive soils. The key aspects are as follows:

- The evolution equations of the volume fraction of swelling water and the aggregate porosity could be derived from mass balancing of the volume fractions within the extended TPM. A simple formulation of the mass transfer mechanism between free water and swelling water with the rate of the degree of saturation as the driving variable and two material parameters proved suitable for the loading paths in this work.
- In combination with a Kozeny-Carman proportionality between relative permeability, porosity and aggregate porosity, the swelling-induced reduction of permeability could be described without necessitating additional material parameters. Back calculations of permeability testing results on reconstituted Opalinus clay showed very good agreement.
- The novel hydro-mechanical constitutive model „Hypoplasticity for expansive soils“ could successfully capture the most prominent features of oedometric material behaviour with a single set of seven material parameters in the one-dimensional formulation: the development of wetting-induced expansion and swelling pressure, monotonic loading, reversible un- and reloading and the volumetric collapse, i.e. the reduction of the void ratio upon wetting, for different initial states.
- Describing the constitutive behaviour in terms of net stress and degree of saturation proved successful. The expansive soil behaviour could be captured without explicitly considering the double-porosity concept. Decoupling the material description from suction and avoiding a micro- and macrostructural distinction facilitates the calibration of the material parameters.
- Generalization of the one-dimensional (oedometric) formulation to a full tensorial formulation proved challenging due to the limited experimental results on the multi-dimensional material behaviour, especially on the evolution of radial stresses upon loading and saturation. However, the full formulation was successfully realized with adaption of the well-known preconsolidation surface of the modified Cam Clay (MCC) model and an associated flow rule. With only three additional material parameters in comparison to the one-dimensional formulation – the friction angles in dry and saturated state and the shape parameter for the preconsolidation surface – the full formulation was able to predict the aforementioned phenomena and reach critical state upon various loading paths.
- In `numgeo`, simulations of the experiments as discretised boundary value problems could predict the magnitude of swelling pressure, swelling strain, the mechanical material response, and the reduction in permeability associated with swelling, as well as the time

evolution of swelling. The comparison of experimental results and simulations showed very good agreement. The transient response is not fitted separately, but emerges from the adequate representation of the water attachement in the modelling framework.

- A range of expansive materials could be simulated with the framework. Its performance was demonstrated by back-calculation and simulations of experimental campaigns on reconstituted Opalinus clay shale under various saturation and loading conditions, as well as by comparison with additional experimental data on bentonite-based expansive materials from the literature, including partially saturated states.
- The modelling framework proved suitable for application in a large-scale boundary value problem, representing an emplacement tunnel of a deep geological repository for nuclear waste disposal. The material behaviour of expansive buffer material in two different exemplary cross sections subjected to radial symmetric ground water flow and localized higher water ingress was simulated.
- The consistent implementation of the hydro-mechanically coupled modelling framework was complex due to the pronounced dependencies between the mechanical and hydraulic domain. Full access to all parts of an FEM code was particularly valuable for realisation of this work. It enabled the straightforward implementation of the element library based on the extended TPM, including stabilised linear equal-order elements, the hydro-mechanical constitutive model and additional numerical tools as the enhanced time-stepping algorithm with consideration of the critical time increment necessary to ensure stable infiltration.

8.2. Recommendations for further investigations

During the development of the numerical framework, further questions were raised. The following recommendations are given for both, numerical and experimental work, to improve the capabilities and applicability of the modelling approach.

Hydro-mechanical constitutive model

- The magnitude and evolution of radial stress under oedometric conditions (at constrained radial deformation) significantly impacts the oedometric swelling behaviour. Experimental evidence has shown, that the remaining radial stress level after specimen preparation, thus compaction in the dry reference state, is much greater than the vertical stress. The resulting stress ratio K_0 is not constant during deformation and saturation. Investigation of dry sample preparation, oedometric compression tests in the dry and fully saturated state and oedometric swelling tests under constant volume and vertical constant stress conditions in a soft-oedometer device can provide the required information on radial stress evolution and indirectly indicate possible anisotropies of the swelling phenomena.
- In the current state of the modelling framework, a linear dependency of the angle of internal friction on the effective degree of saturation was employed to account for a saturation-induced decrease of shear strength. However, experimental results on expansive soils are still limited. Direct shear and triaxial tests in the dry, unsaturated and saturated states with variation of the mean stress are required to assess the relationship between the void ratio at critical state and pressure. These tests can deliver information on the nature

of the dependency of the angle of internal friction and the effective degreee of saturation. Similarly, the linear nature of the dependency of the elastic stiffness on the effective degree of saturation should be verified in further experiments.

- Further research is recommended on the geometry and evolution of the preconsolidation surface. Currently, the MCC surface is elliptical and always parallel to the isotropic stress axis. However, tests on non-swellable clay samples have shown that the preconsolidation surface is not best captured by an elliptic shape and that it expands while rotating around the origin of the $q - p$ space as a result of different, anisotropic preloading conditions (Mitchell, 1970). Both have a considerable influence on the material behaviour. For enhancement of the preconsolidation surface, triaxial tests in the dry and saturated state are required. For the determination of the shape of the preconsolidation surface, the triaxial tests should comprise identical preloading followed by different stress paths. To evaluate the influence of anisotropic preloading on the resulting strength and the stress/strain paths, different preloading paths must be studied.

- The generalisation of three characteristic lines from the one-dimensional oedometric space into the three-dimensional stress space for the mean net stress constituted an initial assumption in this work. The evolution of mean net stress and the preconsolidation pressure during (un)loading and swelling can be more reliably assessed through the previously recommended experimental investigations. Depending on the outcome, it may be appropriate to replace the mean net stress with a principal stress (specifically, the minimum principal stress) or to evaluate the three characteristic lines separately along their spatial directions. Preliminary simulations using the latter approach revealed difficulties, as unintentional collapse in individual spatial directions could not be excluded. Improved consideration of anisotropy in the saturation-driven strain rate, along with a refined representation of the three characteristic lines across space may help to overcome this issue. Currently, the ratio R is evaluated as a projection onto the isotropic axis of the yield surface. Better understanding of the three-dimensional material behaviour is required to evaluate an alternative projection, for example by transferring the three characteristic lines to surfaces. Moreover, the identical nature of the ratio R between the NCC and the w-line and the B-line, respectively, should be investigated. In particular for the simulation of swelling pressure, it is currently unclear whether the three-dimensional stress path must always remain within the preconsolidation surface (apart from the isotropic axis), or if intermediate states on or outside the preconsolidation surface are acceptable.

- The normal compression curve (NCC) defined by Bauer's equation (Bauer, 1996) provides a continuous representation of soil behaviour over wide stress ranges. Its three parameters offer a certain flexibility for reproducing key features of the material response of expansive soils under oedometric conditions. However, the parameters are strongly interdependent. For highly expansive materials, the calibration flexibility becomes limited, as a very large expansion upon wetting cannot be achieved without compromising the ability to represent the remaining aspects of the material behaviour accurately. Therefore, Bauer's equation may be replaced by an alternative equation that provides greater flexibility for modelling large expansions, e.g. in pure bentonite. This does not affect the general validity of the NCC concept in the model, only its shape.

- Possible correlations between the material parameters and mineralogical composition were already presented in the context of this work. Calibrations of many other materials and

simulations of the experimental results can reveal possible calibration equations based on the proportion of expansive clay minerals or possibly other index properties of the materials. This is of particular importance for the non-physically based parameters b and c of the current formulation. Both parameters may also become redundant or be replaced in an enhanced three-dimensional formulation. The above-mentioned further experimental investigations are essential for a more detailed assessment.

- The time integration of the hydro-mechanical constitutive model should be enhanced with an adaptive time stepping algorithm and suitable error control. Currently, only the error control based on the stress prediction is evaluated. Additional error quantities based on the evolution of other state variables or the governing hydraulic variable should be carefully investigated.

Extended theory of porous media

- In the implementation of the element based on the extended TPM, the mass transport was considered explicitly only. An implicit formulation including all time derivatives and additional contributions to the system of equations might enhance the prediction quality and simulation stability. Numerical differentiation using perturbation of the degrees of freedom might be suitable to derive the complex partial derivatives for the system of equations.

- Experimental evidence on the reference and the saturated permeability for a wide range of materials is required to support the formulation of the mass transfer mechanism and the swelling-induced relative permeability model, and to generalise the calibration procedure of the mass transfer mechanism. In this work, the swelling water content was initially set to zero for compacted samples, thereby defining the reference state in which the residual water content or degree of saturation was assumed not to induce swelling. For a broader application of the mass transfer model, the initialisation of the swelling water content should be admissible for all states. This requires improved understanding of the evolution of mass transfer processes under partially saturated conditions.

- Recent investigations by Babiy et al. (2025) proposed a novel methodology to quantify capillary and adsorbed water based on thermogravimetric analysis. In contrast to high swelling water ratios derived from permeability measurements, which were employed in this work, the study reported significantly smaller adsorbed water contents. Further investigations are required to confirm the broader applicability of the methodology and establish a reliable data base for the swelling water ratios. If the swelling water ratio is indeed lower than previously assumed, the formulation of the simple Kozeny-Carman relationship for the swelling-induced relative permeability requires improvement.

Overall framework and implementation

- The simulation of swelling pressure in boundary value problems revealed challenging numerical behaviour, which manifested itself in localised element response and mesh dependency. The results indicate that a regularisation technique might be necessary for selected equations of the mechanical model. The introduction of a non-local length scale can stabilise the evolution of swelling pressure over a physically meaningful range. Alternatively,

the onset of the mechanical material response during swelling, which is governed by the parameter b in the sigmoid relationship between volumetric deformation and water content, may require coupling to the hydraulic response, i.e. to changes in the degree of saturation, the permeability evolution or mass transfer.

- A higher order hydraulic model can be applied to consider the void ratio dependency of the water retention behaviour of unsaturated swelling clays. This is of particular importance for the simulation of cyclic drying and wetting, however it may also counteract the aforementioned hydraulic isolation and limitation of swelling evolution under constant volume conditions.
- In addition to advancing the modelling framework for expansive materials interacting with water, some engineering applications require consideration of the temperature and chemistry of the wetting fluid, e.g. as swelling phenomena are less pronounced for wetting with salt solutions than with water. The ionic concentration of the wetting fluid can serve as a dependency variable for the material parameters of the hydro-mechanical constitutive model and mass transfer mechanism.

Finally, the modelling framework should be investigated beyond the boundary conditions considered so far, covering a wider range of loading paths in the laboratory and a variety of expansive soils. Extending its application to geotechnical structures such as piles and retaining structures in expansive ground, as well as to varying and seasonally changing groundwater conditions, will strengthen the capabilities and applicability of the modelling framework.

A. Appendix: Experimental campaign on reconstituted Opalinus clay

The numerical modelling framework of this thesis was developed based on an experimental campaign carried out on reconstituted Opalinus clay. The most prominent results and constitutive assumptions were introduced in Chapter 2. The experimental campaign is published in Nitsch et al. (2021) and Nitsch et al. (2023a). As part of this work, the test campaign was extended to include selected tests, namely soft oedometer and direct shear tests. They were conducted on a different batch of Opalinus clay than the tests in Nitsch et al. (2023a) and both test devices, the soft oedometer and direct shear apparatus, had limitations in the measurement range for stress and deformation. Nevertheless the test results have provided important insights for the extension of the one-dimensional material model into three-dimensional space and are therefore included here. All tests were carried out under laboratory ambient conditions, where the pore air pressure corresponds to atmospheric pressure. As a results, total stress, which can be measured and controlled in the laboratory, equals net stress.

A.1. Swelling tests, oedometric compression and rebound tests and permeability measurement

This section is largely reproduced from the author's previous publication: Nitsch et al. (2023a). Here, the void ratio has been recomputed incrementally using the current strain increment to ensure consistency with evaluation within the FE simulations, whereas it was computed in reference to its initial state in the publication.

A.1.1. Material and specimen preparation

The material used in this study is Opalinus clay shale from the clayey facies in the Mont Terri Underground Rock Laboratory (URL) in Switzerland. The location of the blocks is not known so that no information about the sampling depth can be given. Opalinus clay shale is a fine-grained sedimentary rock that was deposited approximately 180 million years ago during the Aalenian stage of the Middle Jurassic. Subsequently, it was subjected to several burial stages with overburdening heights between 1000 m and 1350 m due to the lowering of the Rhine Graben. In the further course of its formation it experienced uplift and tilting during the Alpine orogeny (Bossart, 2012; Mazurek et al., 2006; Wetzel and Allia, 2003). Nowadays, the maximum 200 m thick layers of the clayey facies of Opalinus clay shale are found at a depth of about 300 m and are therefore considered as overconsolidated (Nagra, 2005). The mineralogical composition of the studied shale was determined in a x-ray-diffraction analysis and is reported in Table A.1. The clay content is 56 wt-% in total, which is in good agreement with the characteristics for Opalinus

clay shale from Mont Terri reported by Bossart (2012). From the clay fraction, approximately 59 wt-% were estimated as Smectite and Illite mineral phases, corresponding to a total amount of 33 wt-%, which is in good agreement with the result of the Rietveld calculation (37 wt-%). For the material, thus a highly expansive clay mineral content of 5 wt-% (pure smectite) and overall expansive mineral content of 35 wt-% is concluded.

In this study all experiments were carried out on reconstituted specimens. In order to attain repeatability of the experiments, a large number of tests on specimens with a small scattering in the material properties was performed. Another reason for the usage of reconstituted samples was to control the loading history of the samples to investigate the influence of mechanical preloading on the material behaviour. A procedure has been developed to prepare reconstituted specimens. In a first step, a powder from the intact rock material was produced. For that purpose, irregular formed hand pieces of the material were cut with a saw into smaller blocks and crushed with a jaw crusher. The material was then ground to a fine powder with a laboratory mortar grinder. The powder was not further processed or sieved, so that the mineralogical composition of the intact rock was preserved. A hydrometer analysis of two batches has been conducted afterwards as is shown in Figure A.1. The residual water content of the powder is $w = 1.82\%$. The grain density was determined as $\rho_s = 2.718$ g/cm^3.

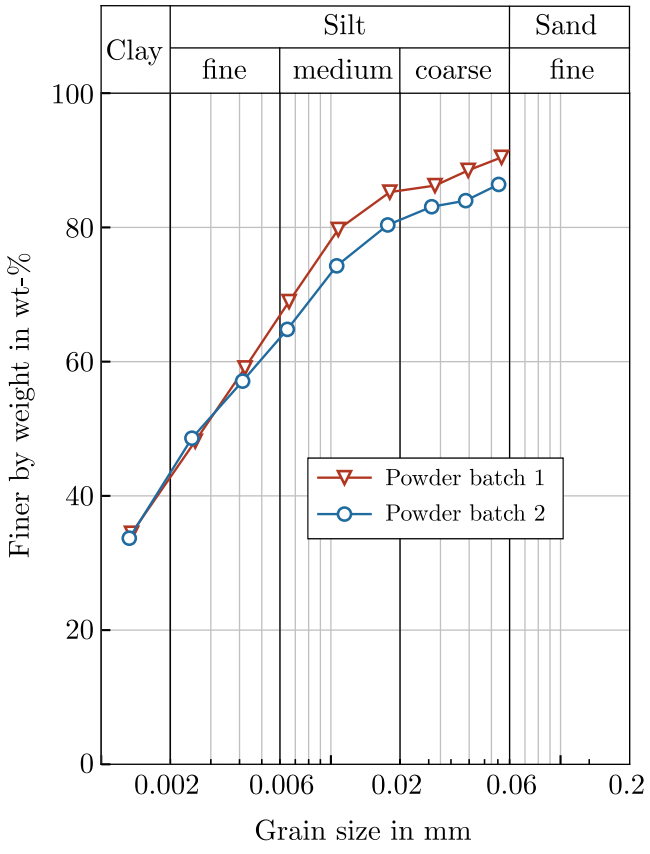

Figure A.1.: Grain size distribution curve of powdered Opalinus clay shale (Nitsch et al., 2023a).

Smectite	5
Illite	32
Chlorite	9
Kaolinite	10
Quartz	8
Feldspar-K	2
Feldspar-Na	2
Calcite	6
Dolomite	<0.1
Ankerite	<1.5
Siderite	1
Pyrite	<1.5
Apatite	1
Amorphous	≈ 20

Table A.1.: Mineralogical composition of the tested Opalinus clay shale (Rietveld calculation, in wt-%).

Specimens were prepared by compressing the powder in an oedometer ring up to the desired dry density ρ_d. This was realized by specifying the mass and the target height of the specimens. The required high pressures were applied by a servo-controlled uniaxial test set-up, see Figure A.2 a). A special preparation apparatus was mounted into the loading frame, see Figures A.2

b) and c). At the beginning of the preparation the powdered material was poured in a thick-walled hollow steel cylinder with the respective oedometer ring positioned at the bottom. The oedometer rings have an inner diameter of 60 mm, an outer diameter of 70 mm and a height of 20 mm. The loading piston was placed loosely on top of the material and the loading plate was lowered with a constant strain rate of $\dot{s} = 0.5$ mm/min until finally the piston was fully immersed in the cylinder and the loading plate was in contact with the upper surface of the cylinder. In this way, the compacted specimen was always level with the top of the oedometer ring and the sample height could be controlled by the use of specific spacers. Then the loading plate was fixed and the load on the specimen was held constant for 30 minutes. The axial load was measured by an external load cell below the bottom loading plate. Afterwards the samples were removed from the test set-up, measured, weighed and stored in a protected environment. A compacted sample inside an oedometer ring is shown in Figure A.3. During preparation of the reconstituted specimens it became evident that the very low void ratios of intact Opalinus clay shale could not be reached only by static compaction, as is also reported by e.g. Crisci et al. (2019).

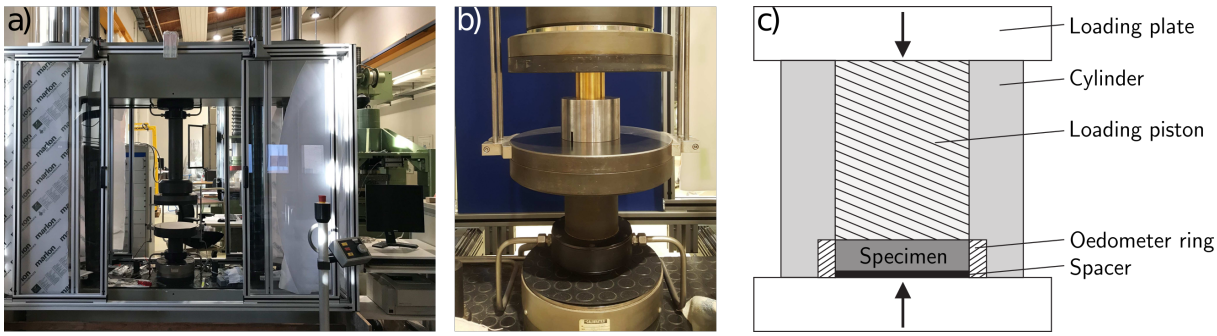

Figure A.2.: Experimental set-up for specimen preparation: a) Servo-controlled loading frame. b) and c) Preparation apparatus (Nitsch et al., 2023a).

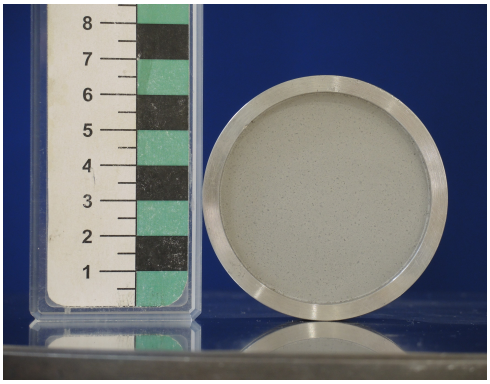

Figure A.3.: Specimen inside oedometer ring after compaction (Nitsch et al., 2023a).

To investigate the effect of the method of powder placement during the sample preparation procedure on the mechanical behaviour, different methods like pluviation and layer-wise tamping have been tested. The experimental results showed no influence on the mechanical behaviour and hence, pluviation was used in the specimen preparation. In Figure A.4 a) the temporal progression of the vertical net stress σ_{22} during the preparation procedure is shown. A unique relation between the target dry density ρ_d (or void ratio $e = \rho_s/\rho_d - 1$) and the required net stress can be identified with a slope of the virgin loading line of $C_C = 0.208$ (compression

index), see Figure A.4 b). Moreover, it is possible to approximate the unloading index of $C_S = 0.021$ (swelling index) by the measurements of the height of the compacted samples inside the oedometer ring after the preparation (faint lines). The indices were determined as followed:

$$C_S = -\frac{\Delta e}{\log_{10}\left(\frac{\sigma_{22,v}}{\sigma_{22,0}}\right)} \quad \text{and} \quad C_C = \frac{\Delta e}{\log_{10}\left(\frac{\sigma_{22,v}}{\sigma_{22,e}}\right)}, \tag{A.1}$$

with $\sigma_{22,0}$ and $\sigma_{22,e}$ being the vertical net stresses on the first compression and unloading line corresponding the the void ratio change Δe.

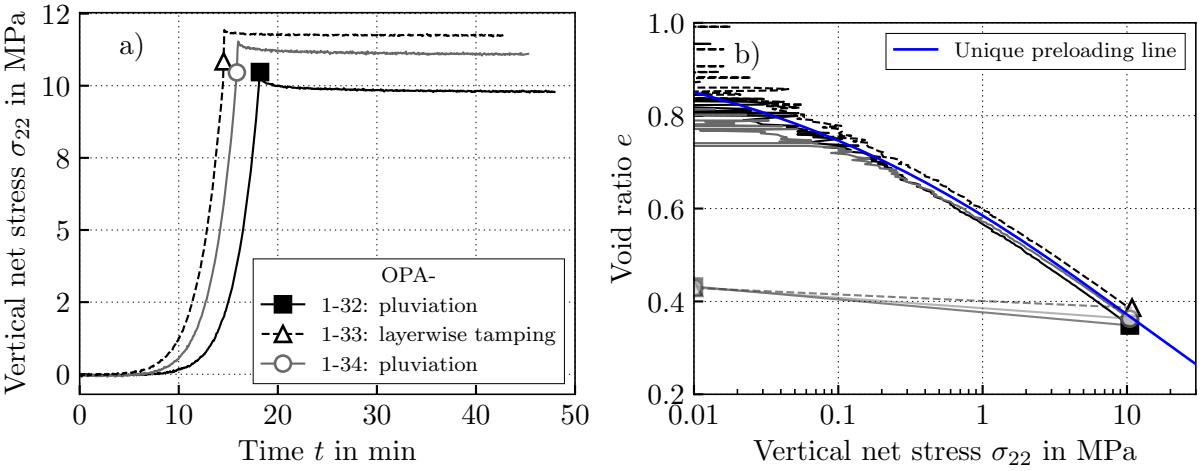

Figure A.4.: Specimen preparation: a) Vertical net stress vs. time during compaction. b) Void ratio vs. stress during compaction. Note that the oscillations are due to the resolution of the load cell in the range of small stresses. Modified from Nitsch et al. (2023a)

The required net stress for compaction is shown with markers in Figure A.4 b). As the loading plate was in contact with the hollow cylinder, any additional net stress did not act on the sample, but on the preparation apparatus instead. A stress relaxation during compaction becomes evident, see Figure A.4 a). Table A.2 summarizes the preparation characteristics of the tests as well as the initial water content w and degree of saturation S^w. Having a unique compression line during preloading, the vertical preconsolidation net stress for any dry density of the specimens can be approximated. Most specimens in this study had a target dry density of $\rho_{d,0} = 1.930 \pm 0.03$ g/cm^3, which corresponds to a vertical preparation net stress of $\sigma_{22,\text{prep}} = 10 - 11$ MPa. The vertical preloading net stress $\sigma_{22,\text{prep}}$ of the specimens was only varied in the oedometric swelling tests in order to investigate the influence of preloading on the swelling behaviour.

Table A.2.: Summary of the preparation characteristics of three representative tests

Specimen OPA-	Initial conditions after compaction			Vertical net preloading stress in MPa[1]
	e	ρ_d in g/cm^3	S^w	
1-32	0.432	1.899	0.126	10.74 (9.85)
1-33	0.429	1.902	0.127	10.84 (10.38)
1-34	0.430	1.901	0.126	10.46 (10.25)

[*] The initial water content of all specimens was $w = 1.82\%$
[1] Values shown within brackets correspond to the vertical net stress after relaxation

A.1.2. Testing equipment and test methods

The study includes oedometric swelling tests, oedometric compression tests and permeability measurements. Test set-ups and test methods used in this study are presented in the following.

The oedometric swelling tests and oedometric compression tests were carried out in an open watering cell (Figure A.5), which was mounted in three different loading frames for specific loading paths. The specimen inside the oedometer ring can easily be installed between a lower and upper porous stone. The bottom of the cell and the loading piston have special cutouts to secure a steady and continuous water supply through the porous stones to the sample. The watering cell allows water supply to the sample from the bottom and the top by filling the watering cell to the desired height.

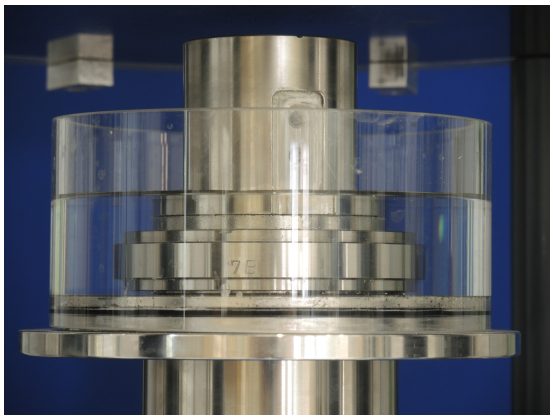

Figure A.5.: Specimen inside oedometer ring after compaction in open watering cell.

The majority of the tests was performed in a standard oedometric swelling cell, further referred to as *test set-up 1*. This test set-up was developed at the Institute of Soil Mechanics and Rock Mechanics (IBF) at the Karlsruhe Institute of Technology (KIT) and last modified by Vergara Quezada (2019). A detailed description and comparison to other simple cells can be found in Vergara et al. (2014). The test set-up is shown on the left-hand side of Figure A.6. The watering cell is mounted in a simple loading frame with a manually controlled load spindle on top of the specimen and a load cell located at the bottom of the cell. The vertical deformation is measured by two gauges with an accuracy of 0.001 mm at opposite sides of the specimen. To perform a test under constant volume and constant net stress conditions the vertical deformation has to be corrected manually.

To improve the precision of the test control and apply larger net stresses during oedometric compression tests, two servo-controlled test set-ups were used. In *test set-up 2* the open watering cell is mounted in the servo-controlled loading frame used for specimen preparation. As the acquisition system of the machine itself is outdated, the axial strain and the vertical net stress were measured with an external acquisition system, see right-hand side of Figure A.6. The axial displacement is measured with three displacement transducers against an aluminium ring that is fixed to the axial piston of the machine. The vertical net stress is measured with a load cell with a load capacity of 900 kN under the open watering cell. For *test set-up 3* a servo-controlled test machine type 815 from the company MTS is used. Similar to test set-up 2 the open watering cell is installed in the loading frame and the vertical net stress is measured with a load cell with a load capacity of 250 kN under the open watering cell. The vertical displacement is measured by

the axial displacement of the loading piston. A more detailed description of the machine itself is given in Leuthold et al. (2021). This test set-up is the best facility to get accurate results at small axial loads and with complex loading paths and was therefore used for the long lasting oedometric compression tests after swelling.

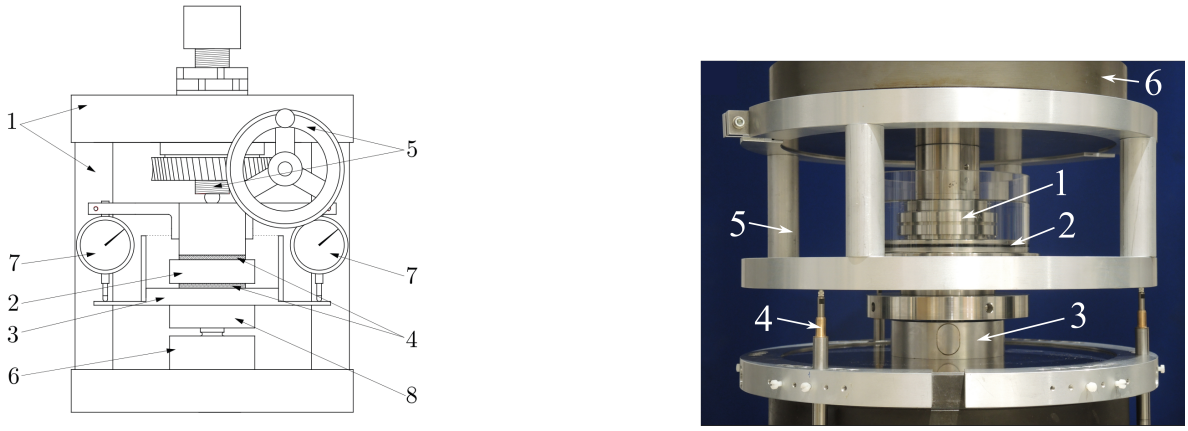

Figure A.6.: Left: *Test set-up 1* for oedometric swelling tests. Schematic drawing: (1) rigid frame, (2) oedometric ring with specimen, (3) watering cell, (4) porous metal plates, (5) spindle, (6) load cell and (7) dial gauges and (8) steel plate. Right: *Test set-up 2* for oedometric swelling tests and oedometric compression tests: (1) oedometric ring with specimen, (2) watering cell, (3) load cell, (4) displacement transducers, (5) aluminium ring and (6) loading piston. Modified from Vergara Quezada (2019) and Nitsch et al. (2023a).

The permeability testing is performed in *test set-up 4*, which consists of the same simple loading frame used in *test set-up 1*, but is modified by the usage of a fluid–tight pressure cell instead of an open watering cell. The axial deformation is measured with one strain gauge with an accuracy of 0.001 mm between the loading plate and the bottom of the watering cell. The vertical net stress is measured with a load cell located at the bottom. For water permeability testing the pressure cell is connected to an upstream and downstream stand pipe, in which the volume of water flowing through the sample in a certain time interval can be determined (see Figure A.7 b)). Pressure difference in the water is achieved using air pressure. A more detailed description is provided in Vergara Quezada (2019). For air permeability testing the pressure vessel is connected to a gas supply at the bottom and a soap bubble flow meter at the top drainage (see Figure A.7 c)). The volume of gas flow through the sample is evaluated by measuring the time of the outflowing gas passing a defined volume in the soap covered bubble flow meter.

Oedometric swelling tests

The material's ability to swell has a significant effect on the hydro-mechanical behaviour. To distinguish the different physical processes during saturation depending on the hydro-mechanical boundary conditions and to ensure reproducibility of the results, 30 oedometric swelling tests were performed (see Table A.3). The results of all tests were used in the analysis of this work, but for the sake of clarity, detailed discussion is limited to twelve representative tests only. The initial dry density was varied within the range $\rho_d = 1.693 - 2.013$ g/cm^3. Most of the swelling tests were carried out in *test set-up 1*. To investigate the effect of the manual adjustment of the axial displacement on the swelling process, swelling pressure tests were also performed in *test*

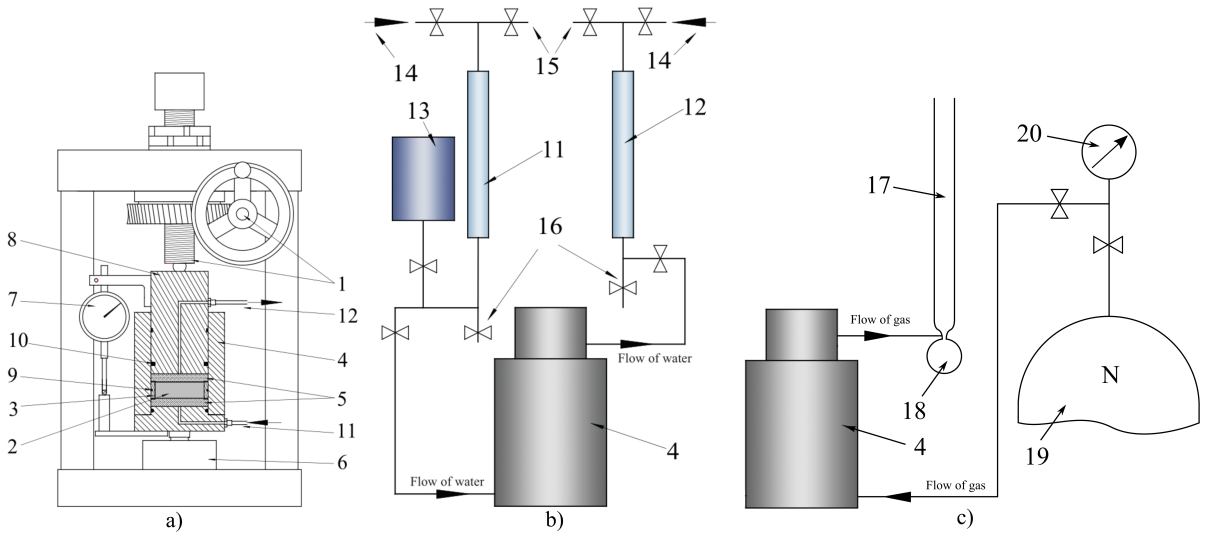

Figure A.7.: *Test set-up 4* for permeability testing. Schematic drawing of a) Swelling test apparatus b) Pressure cell and stand pipe system for water permeability testing and c) Soap bubble flow meter for air permeability testing. (1) manual spindle, (2) specimen, (3) oedometer ring, (4) pressure vessel, (5) porous discs, (6) load cell, (7) dial gauge, (8) loading piston, (9) O-ring, (10) piston seal, (11) upstream graduated stand pipe, (12) downstream graduated stand pipe, (13) water supply, (14) air pressure/vacuum, (15) air bleed, (16) water outlet, (17) flow meter, (18) soap bubble, (19) nitrogen reservoir and (20) pressure gauge. Modified from Vergara Quezada (2019) and Nitsch et al. (2023a).

set-up 2. The experimental results showed that the manual control of the axial displacement has no effect on the swelling behaviour so that all further swelling tests were performed in *test set-up 1*. Except one, all swelling tests in this study were performed with water supply from the top and the bottom.

Within this study swelling tests with different stress-strain paths have been investigated which are schematically shown in Figure A.8 and are as well summarized in Table A.3. In addition to single-step swelling pressure tests (confined conditions, Fig. A.8, A-B) and single-step swelling strain tests (unconfined conditions, Fig. A.8, A-D) a variety of multi-step tests has been carried out. The aim was to investigate the effect of the loading sequence on the axial deformation. Therefore, some specimens were unloaded from their swelling pressure (Fig. A.8, B) to half of the swelling pressure (Fig. A.8, C) and to the initial fixing net stress (Fig. A.8, D) (net stress-controlled). Additionally, the loading sequence was carried out in reverse direction: the specimens were loaded after unconfined swelling (Fig. A.8, D) to the estimated half of the swelling pressure (Fig. A.8, C) and estimated swelling pressure (Fig. A.8, B). In this context possible effects of the control variable were also studied by unloading one sample not to a specific net stress but estimated strain (strain-controlled, referred to as A-B-C'-C").

To investigate the relation between the degree of saturation and the swelling process, one single-step swelling strain test and one single-step swelling pressure test were performed in perspex oedometer rings in *test set-up 1*. The specimens were prepared as explained before. Afterwards they were pressed out of the steel oedometer ring and subsequently pressed in the perspex ring and the height of the specimens was measured. The subsequent pressing led to a small increase in density. In order to observe the propagation of the wetting front in the specimen through the

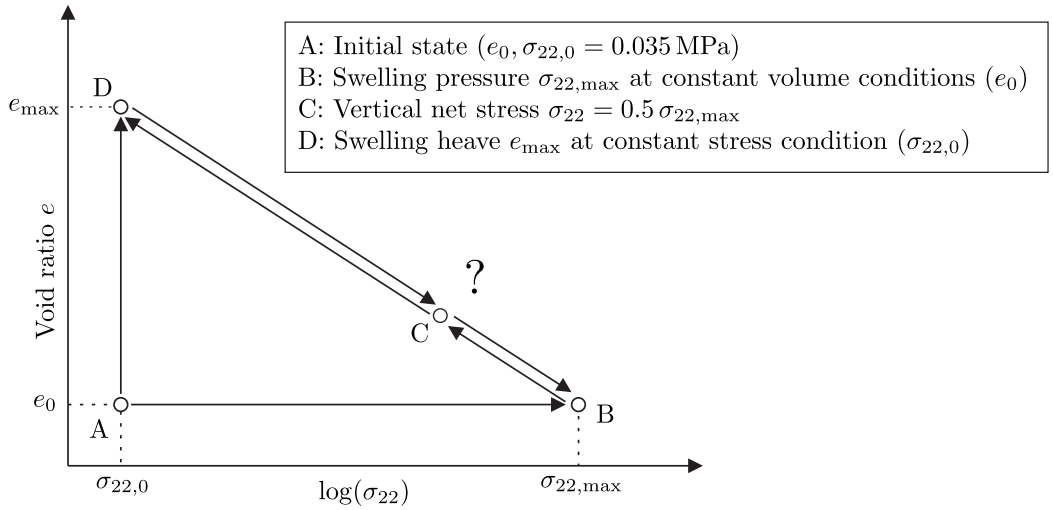

Figure A.8.: Test paths of the oedometric swelling tests.

ring, the water was only supplied to the sample from the bottom in these tests. A camera was permanently installed in front of the test set-up to record the progress of the wetting front in the specimen. The tests were stopped when the peak swelling pressure $\sigma_{22,\max,\mathrm{peak}}$ or the peak swelling strain $\epsilon_{22,\max}$ was reached or when the water front had reached the top of the specimen. The degree of saturation at the end of the test was determined by oven-drying at 105 °C. To gain further insight into the direct coupling of saturation and deformation two short single-step swelling strain tests (five minutes) were performed. One specimen was watered from both sides while the second specimen was only watered from the bottom.

Oedometric compression tests before and after swelling tests

To investigate the mechanical behaviour of the material before and after swelling, oedometric compression tests were performed on samples before and after saturation, respectively. The oedometric compression tests before saturation were performed in *test-set up 2*. The sample inside the oedometer ring is set in the open watering cell without supplying water (atmospheric conditions) and the vertical net stress is applied on the specimen with an axial piston with a diameter of 60 mm. The tests were strain-controlled and performed with an axial strain rate of $\dot{s} = 0.1$ mm/min. As the material is nearly dry the consolidation is not considered.

For the oedometric compression tests after saturation *test set-up 3* is used. To clarify whether the swelling process affects the net preloading stress and the stiffness, oedometric compression tests under drained conditions were performed on saturated samples, which experienced different net stress paths during swelling. In total three oedometric compression tests on saturated material have been performed:

1. After swelling under confined conditions (single-step swelling pressure test, OPA-0-34)
2. After swelling under unconfined conditions ($\sigma \approx 0$, single-step swelling strain test, OPA-0-24)
3. After a multi-step test (swelling pressure test with subsequent unloading, OPA-0-07).

For efficiency reasons the prior single-step swelling strain tests and multi-step test were performed in the standard cell (*test set-up 1*) and afterwards the specimen was transferred to *test*

Table A.3.: Summary of the performed oedometric swelling tests, sorted by loading paths and initial conditions.

Specimen OPA-	Path[a]	Initial Conditions [*]		
		e	ρ_d in g/cm^3	S^w
1-21	A-B	0.576	1.725	0.086
1-22	A-B	0.564	1.738	0.088
1-09	A-B	0.564	1.739	0.088
1-01	A-B	0.434	1.896	0.114
1-03	A-B	0.387	1.960	0.128
1-12	A-B	0.386	1.962	0.128
1-02	A-B	0.351	2.013	0.141
1-07	A-B-C	0.602	1.697	0.082
0-03	A-B-C	0.393	1.952	0.126
1-04	A-B-C	0.386	1.962	0.128
1-05	A-B-C	0.385	1.963	0.128
0-05	A-B-C	0.379	1.972	0.130
1-08	A-B-C-D	0.606	1.693	0.082
1-10	A-B-C-D	0.564	1.739	0.088
0-07	A-B-C-D	0.392	1.953	0.126
0-06	A-B-C-D	0.388	1.959	0.127
1-06	A-B-C-D	0.386	1.961	0.128
0-04	A-B-C-D	0.385	1.963	0.128
1-11	A-B-C-D[2]	0.384	1.964	0.129
0-02	A-B-C-D	0.382	1.967	0.129
0-29	A-B-C'-C"[3]	0.382	1.968	0.129
1-17	A-D	0.419	1.916	0.118
0-24	A-D	0.386	1.962	0.128
0-32	A-D	0.377	1.975	0.131
1-15	A-D-C[4]	0.386	1.962	0.128
1-16	A-D-C-B	0.386	1.962	0.128
0-15	A-D[P]	0.388	1.959	0.127
0-14	A-B[P]	0.380	1.970	0.130
1-30	A-D[6]	0.385	1.963	0.128
1-31	A-D[6**]	0.383	1.965	0.129

[*] The initial water content of all specimens was $w = 1.82\%$
[a] See Figure A.8
[1] In test set-up 2
[2] Unloading to $\sigma_{22} = 0.75\,\sigma_{22,\max}$
[3] Unloading to $\epsilon_{22} \approx 0.20\,\epsilon_{22,\max}$ and $\epsilon_{22} \approx 0.45\,\epsilon_{22,\max}$
[4] Loaded to an estimated net stress of $\sigma_{22} \approx 0.45\,\sigma_{22,\max}$ and $\sigma_{22} \approx 0.90\,\sigma_{22,\max}$
[P] Testing in perspex ring
[6] Test stopped after 5 minutes
[**] Watering only from the bottom

set-up 3. It is assumed that only a minimal elastic deformation is generated by the de- and reinstallation, so that it is not further considered. In contrast to the oedometric compression tests under dry conditions the vertical net stress is not applied continuously, but in steps. To guarantee drained conditions and assure consolidation during the loading steps, a preliminary consolidation test is performed on a saturated specimen. A duration of twelve hours for the initial loading and four hours for the un- and reloading paths has been established. All oedometric compression tests include unloading and reloading cycles. An overview of the oedometric

compression tests is given in Table A.4.

Table A.4.: Summary of the performed oedometric compression tests before and after saturation.

Specimen OPA-	Path[a]	Initial Conditions[*]		
		e	ρ_d in g/cm^3	S^w
1-34	dry	0.397	1.946	0.124
0-33	dry	0.376	1.977	0.131
0-28	dry	0.382	1.967	0.129
0-34	A-B	0.393 | 0.393[1]	1.953 | 1.953[1]	0.126 | 1.00[1]
0-24	A-D	0.386 | 0.516[1]	1.962 | 1.793[1]	0.128 | 1.00[1]
0-07	A-B-C-D	0.392 | 0.466[1]	1.953 | 1.854[1]	0.126 | 1.00[1]

[*] The initial water content of all specimens was $w = 1.82\%$
[a] See Figure A.8
[1] Values correspond to the start of the oedometric compression test (saturated state, $S = 1.0$ is assumed)

Permeability testing

The permeability K of the material might be affected by the swelling process depending on the current boundary conditions. Therefore, the permeability was measured before saturation on the nearly dry material and during different stages of oedometric swelling tests. Testing before saturation is done with steady state air-permeability testing in *test set-up 4b* on six samples. The permeability of saturated samples was measured with steady state water-permeability testing during two swelling tests in *test set-up 4a*. The stress paths during the swelling process were chosen identically to those of the oedometric compression tests. One swelling test was performed as a multi-step test consisting of a constant volume step and a complete unloading to the initial net stress $\sigma_{22,0}$ in the second step (A.8, A-B-D). The second swelling test was a single-step swelling strain test (A.8, A-D). At the end of each step, when the swelling pressure or the axial strain respectively reaches equilibrium, a water flow with a set pressure was applied from the bottom drainage. After the flow reached a steady-state the flow rate and thus, the permeability, were determined. The applied pressure was varied to investigate its effect on the water flow. A summary of the samples used for permeability testing is shown in Table A.5.

Table A.5.: Summary of the performed permeability tests.

Specimen OPA-	Path[a]	Pressure [kPa]	Initial Conditions[*]		
			e	ρ_d in g/cm^3	S^w
0-08	dry	25, 50, 70	0.388	1.959	0.127
0-09	dry		0.388	1.959	0.127
0-10	dry		0.391	1.955	0.126
0-11	dry		0.391	1.955	0.126
0-12	dry		0.385	1.963	0.128
0-13	dry		0.389	1.958	0.127
0-22	A-B-D	100, 200, 400	0.387[1]| 0.451[2]	1.960[1]| 1.873[2]	0.128 | 1.0[2]
0-35	A-D		0.387 | 0.512[2]	1.961 | 1.898[2]	0.128 | 1.0[2]

[*] The initial water content of all specimens was $w = 1.82\%$
[a] See Figure A.8
[1] Values correspond to the start of the steady-state water flow at $\epsilon_{22} = 0$ (saturated state, $S^w = 1.0$ is assumed)
[2] Values correspond to the start of the steady-state water flow at $\sigma_{22} = 0$ (saturated state, $S^w = 1.0$ is assumed)

A.1.3. Experimental results and discussion

Oedometric swelling behaviour

The results of the oedometric swelling tests are presented in the following. Specific values are given for discussion while the full results are given in Table A.6. Therein, the swelling pressure $\sigma_{22,\max}$ at Point B ($\epsilon_{22} = 0$, see Figure A.8), the strain ϵ_{22} at point C and $\epsilon_{22,\max}$ at point D for all tests and the swelling indices for the multi-step tests are summarized.

Table A.6.: Results of the oedometric swelling tests

Specimen OPA-	B: $\sigma_{22,\max}$ in MPa	C: ϵ_{22}	D: $\epsilon_{22,\max}$	C_S/C_C [-]
1-35	0.875	-	-	-
0-04	0.743	-0.00715	-0.05891	0.0527
0-07	0.663	-0.00953	-0.05144	0.0525
1-11	0.839	-0.00251 [1]	-0.04463 [1]	0.0381
0-29	0.958	-0.01514 (C')[2]	-0.02768 (C")[2]	0.0661
0-24	-	-	-0.09065	-
1-15	-	-0.03052 [3]	-0.09737	0.0806[5]
1-16	0.01291 ($\epsilon_{22,\max}$)[4]	-0.039	-0.11271	0.1133[5]

[1] Unloading to $\sigma = 0.75\,\sigma_{22,\max}$
[2] Unloading to $\epsilon \approx 0.20\,\epsilon_{22,\max}$ and $\epsilon \approx 0.45\,\epsilon_{22,\max}$
[3] Loaded to an estimated net stress of $\sigma \approx 0.45\,\sigma_{22,\max}$
[4] Loaded to an estimated net stress of $\sigma \approx 0.90\,\sigma_{22,\max}$
[5] Compression index

Path-dependency: influence of the loading sequence

The experimental results of all swelling tests are evaluated in terms of void ratio vs. net stress. The presented paths are depicted by arrows in a semi-logarithmic plot. Assuming that those paths follow the swelling law of Grob (1972)

$$\Delta\epsilon = -k \log_{10}\left(\frac{\sigma_{22,0}}{\sigma_{22,\max}}\right) \tag{A.2}$$

wherein $\sigma_{22,0}$ is the fixing net stress, $\sigma_{22,\max}$ the swelling pressure and k the corresponding swelling index, or its modification

$$\Delta e = \begin{cases} -C_S \log_{10}\left(\dfrac{\sigma_{22,0}}{\sigma_{22,\max}}\right) & \text{for unloading,} \\ -C_C \log_{10}\left(\dfrac{\sigma_{22,0}}{\sigma_{22,\max}}\right) & \text{for loading,} \end{cases} \tag{A.3}$$

the pairs of net stress and void ratio at each step of the multi-step tests can be characterised by a unique line whose slope can be determined similarly to Equation A.1 such as the swelling index C_S (unloading) and compression index C_C (loading). The swelling indices are evaluated over the overall net stress range of the respective tests (either unloading to point C ($\sigma = 0.5\,\sigma_{22,\max}$), or to point D ($\sigma = \sigma_{22,\max}$)). It has to be noted, that the results of the tests with full unloading may be more accurate as they include two steps.

As can be seen in Figure A.9 a), the variation of the control variable during unloading does not influence the magnitude of the swelling index. Both indices of the two representative multi-step tests with net stress-controlled unloading $C_{S,\text{OPA-0-04}} = 0.0515$ and $C_{S,\text{OPA-0-07}} = 0.0516$ are

in good agreement and only slightly smaller than the value $C_{S,\text{OPA-0-29}} = 0.0653$ of the test with strain-controlled unloading. Extrapolated to $\sigma = \sigma_0$ this results in very similar values for void ratio or strain, which are noticeably smaller than for the single- step swelling strain test on specimen OPA-0-24. A possible influence of the increment of the unloading steps can be assessed in Figure A.9 b) by evaluating the test on specimen OPA-1-11 with a first unloading step to $\sigma = 0.75\,\sigma_{22,\max}$. Taking possible scatter of the tests into account, the swelling index is determined to $C_{S,\text{OPA-1-11}} = 0.0376$. The loading of specimens OPA-1-15 and 1-16 after free axial swelling is presented in Figure A.10. The compression indices $C_{C,\text{OPA-1-15}} = 0.0801$ and $C_{C,\text{OPA-1-15}} = 0.1078$ are approximately twice as large as the swelling indices C_S of the unloaded specimens.

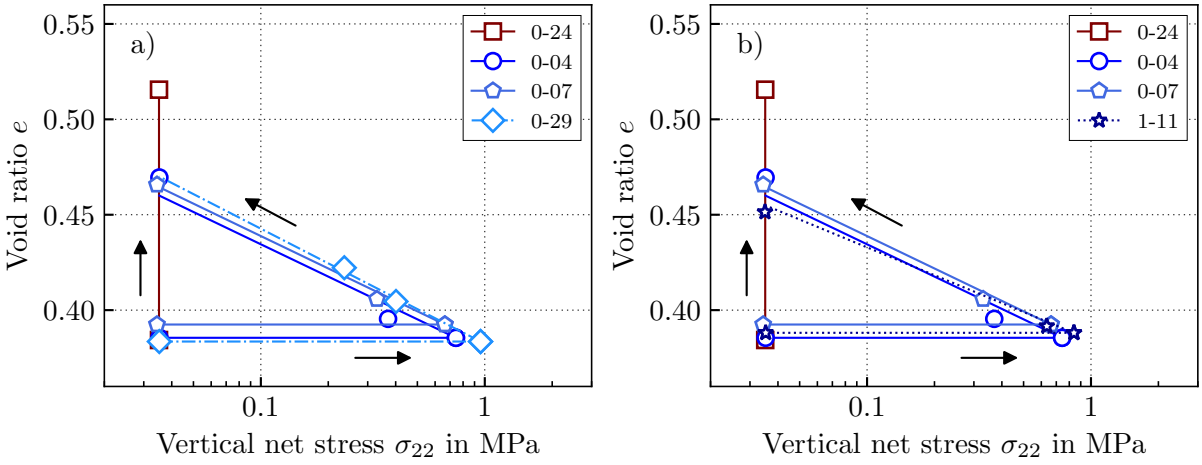

Figure A.9.: Void ratio vs. vertical net stress for multi-step swelling tests. Unloading after single-step swelling stress test: a) Stress vs. strain-controlled unloading and b) Stress controlled unloading with different magnitudes. Modified from Nitsch et al. (2023a).

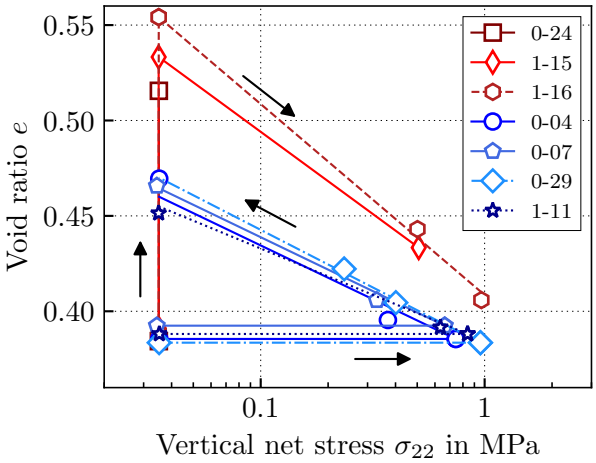

Figure A.10.: Void ratio vs. vertical net stress for multi-step swelling tests: loading after single-step swelling strain test. Modified from Nitsch et al. (2023a).

Overall, a significant path-dependency of deformation is identified. The deformation and resulting void ratio during unloading from the swelling pressure are significantly smaller than during free axial swelling, where the deformation takes place driven by the initial saturation.

An extrapolation of the loading path after vertically unconfined swelling to the initial void ratio results in a net stress larger than the swelling pressure, which corresponds to the generally known distinction of net stresses during swelling according to Sridharan et al. (1986).

The temporal evolution of net stress and strain in the tests is shown in Figures A.11-A.13. The tests that have already been discussed in detail are shown in saturated color, while the remaining tests are shown in unsaturated color. Swelling tests conducted in *test set-up 1* (manually controlled) are shown with markers while those conducted in *test set-up 2* (servo-controlled) are shown with solid lines. For similar dry densities, a relatively large scattering can be noted. The results of single-step tests demonstrate that the transient swelling behaviour can be divided into two phases with different progressions for swelling under confined and unconfined conditions (Fig. A.11). In multi-step testing it can be shown that the duration of each step can be significantly shorter when the sample is unloaded strain-controlled instead of stress-controlled. The temporal evolution of strain during unloading progresses more slowly than during the initial saturation.

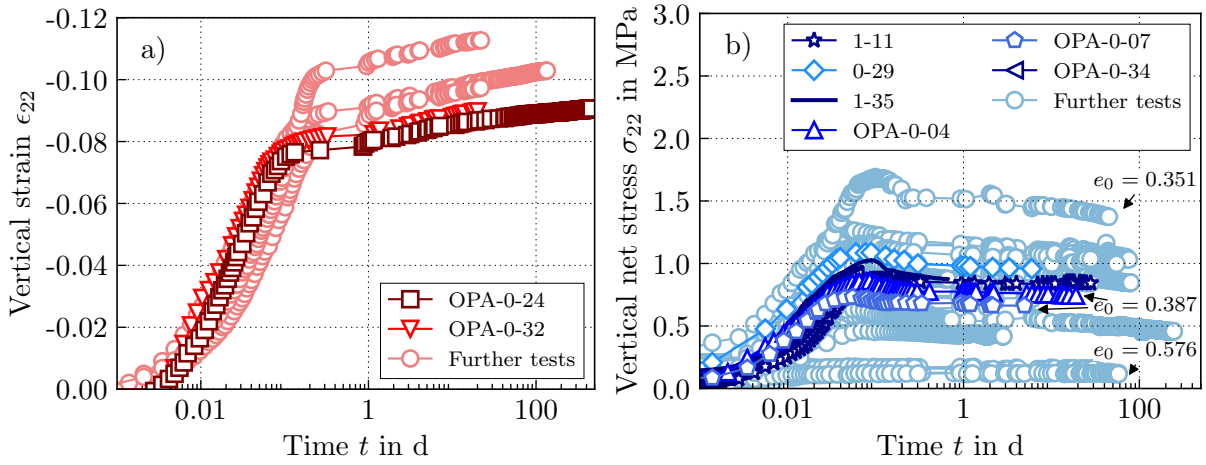

Figure A.11.: Evolution of strain and vertical net stress during saturation in single-step tests: a) Single-step swelling strain test (unconfined) and b) Single-step swelling pressure test (confined). Modified from Nitsch et al. (2023a).

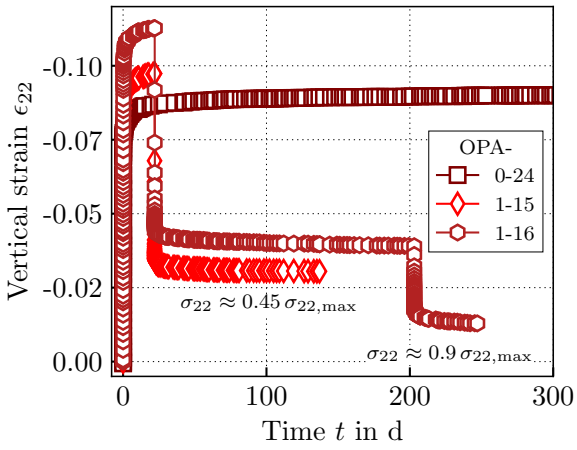

Figure A.12.: Evolution of strain during loading in multi-step swelling tests. Modified from Nitsch et al. (2023a).

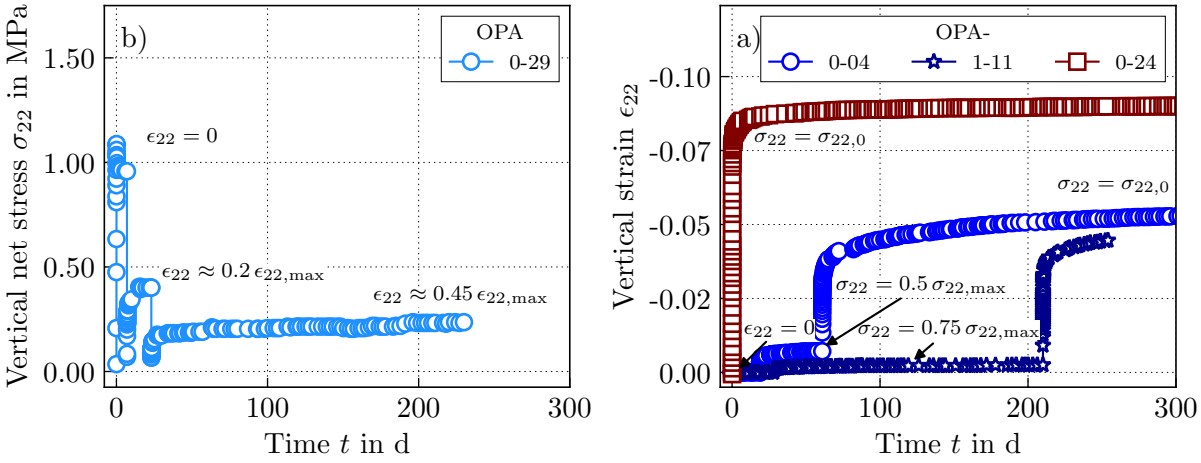

Figure A.13.: Evolution of strain and vertical net stress during unloading in multi-step swelling tests: a) Stress controlled and b) Strain controlled. Modified from Nitsch et al. (2023a).

Coupling between net preloading stress and swelling pressure

The swelling pressure increases with an increasing amount of expansive clay minerals per unit volume, hence with increasing dry density, cf. Villar and Lloret (2008), Schanz and Tripathy (2009), Middelhoff et al. (2019) and Zou et al. (2020), which also becomes evident in Figure A.11 b). However, it is more convenient to correlate the net compaction stress associated with the density, hence the net preolading stress with the swelling pressure. Figure A.14 shows the swelling pressure for different initial void ratios and the unique compression line from compaction. An affine trend line can be drawn for the results of all swelling pressure tests, which supports this approach.

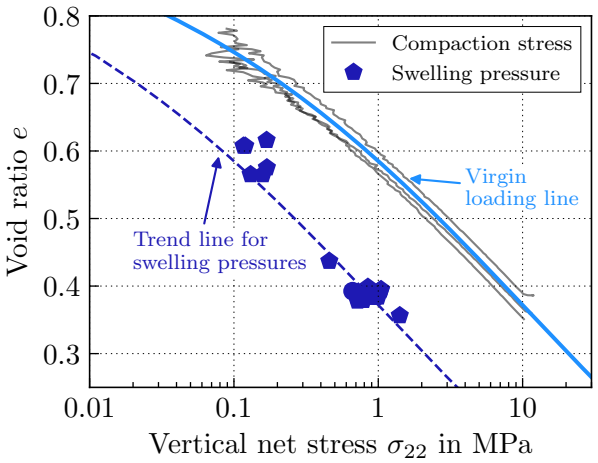

Figure A.14.: Results of swelling pressure tests with regard to the preloading state. Stress data from the load cell during compaction below its precision

Coupling between saturation and swelling behaviour

A first phase with a pronounced evolution of swelling strain was observed for swelling under unconfined conditions (see Figure A.11 a)) followed by a second phase with a slower increase in strain. The question arises at what time the saturation had fully progressed through the entire specimen and if a coupling between saturation and deformation could be established and

also be applied to swelling under confined conditions. These questions are addressed by testing two specimens in perspex rings. The progress of the saturation front was recorded during the measurement of strain/stress allowing a direct evaluation of the coupling between wetting and swelling. Pictures of a specimen in a perspex ring during saturation can be seen in Figure A.15. The results are displayed in Figures A.16 and summarised in Table A.7.

Table A.7.: Results of the oedometric swelling tests in perspex rings

Specimen OPA-	Path	σ_{22} in MPa	ϵ_{22}	S^w	t in h:mm
0-14	A-B	0.862	const.	0.94	2:48
0-15	A-D	const.	−0.066	0.98	2:36

The evolution of the axial strain and the saturation front of specimen OPA-0-15 under unconfined conditions proceeds parallel to each other and a linear coupling can be identified. The test has been stopped when the saturation front reached the top of the sample. The degree of saturation is determined to $S^w = 0.98$. The comparison of the maximum recorded strain $\epsilon_{22,\text{max,OPA-0-15}} = 0.0657$ to the strain of a single-step swelling strain test, e.g. OPA-0-24 (s. Figure A.11 a)), indicates that the saturation has approximately progressed through the entire specimen when the second phase is entered. The increase of strain in phase 1 is linear proportional to the degree of saturation or volumetric water content.

In the swelling pressure test on specimen OPA-0-14 the final degree of saturation was determined to $S^w = 0.94$. The net stress relaxation in the second phase thus begins before full saturation is reached (s. Figure A.11 b)). The saturation front progresses more slowly than under confined conditions.

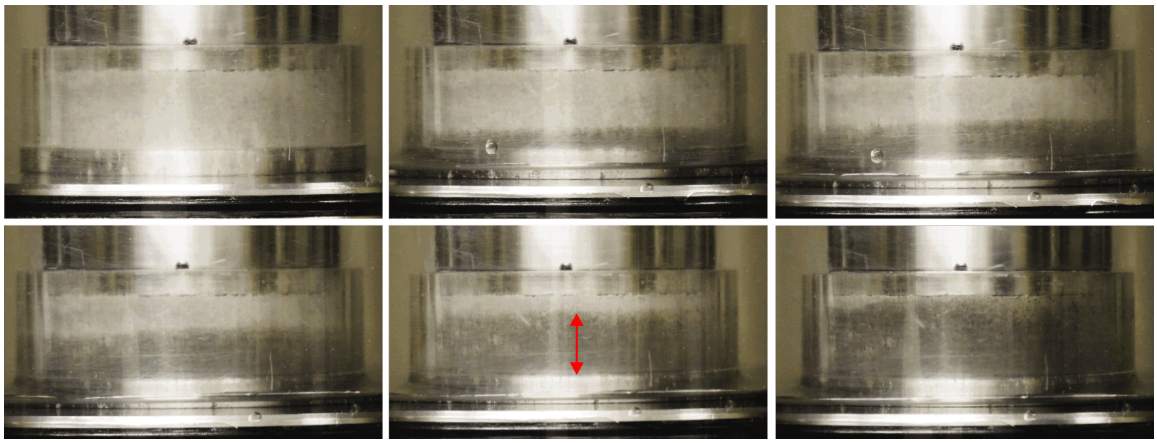

Figure A.15.: View of specimen OPA-0-15 during different stages of a single-step swelling strain test in a perspex oedometer ring (Nitsch et al., 2023a).

The linear coupling between saturation and deformation is confirmed by the results of the short swelling strain tests with variation of watering which are displayed in Figure A.17. Table A.8 summarises the values of strain and degree of saturation at the end of both tests. It becomes evident that for the identical time interval the watering from both sides results in a twice as large deformation and saturation of the specimen compared to the results from the test with watering from only one side. In agreement with the consolidation theory the same amount of deformation approximately takes four times as long for the twice as long drainage path.

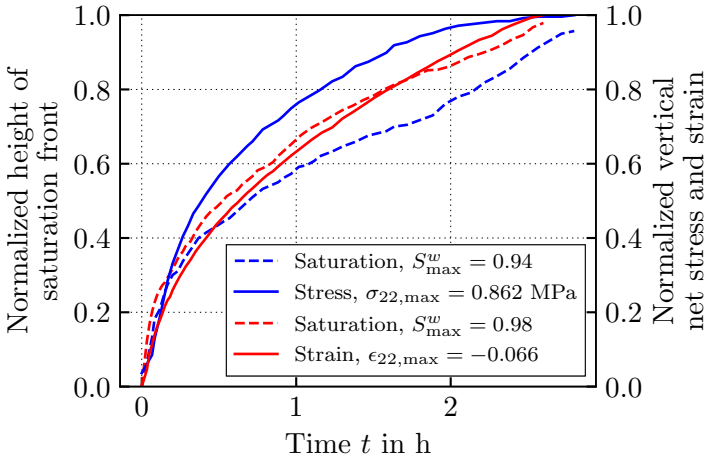

Figure A.16.: Testing in perspex rings: Evolution of the saturation fronts, strain and net stress. Strain and net stress are normalised to their maximum values. Modified from Nitsch et al. (2023a).

Table A.8.: Results of the short swelling strain tests with variation of watering

Specimen OPA-	Watering	ϵ_{22}	S^w
1-30	top, bottom	−0.0253	0.60
1-31	bottom	−0.0113	0.29

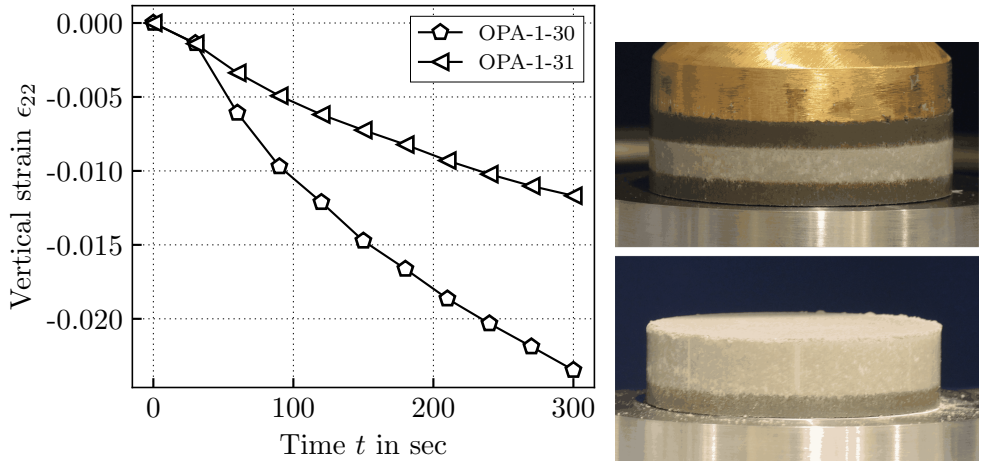

Figure A.17.: Initial phase of single-step swelling strain tests with variation of watering: Strain vs. time and view of the specimens after testing.

Oedometric compression behaviour before and after swelling tests

Stress and deformation measurements during specimen preparation indicate a unique virgin loading line with the compression index $C_{C,\text{prep}} = 0.208$, which gives the vertical preparation net stress for a specific targeted void ratio, e.g. $\sigma_{22,v,\text{prep}} = 10.16$ MPa for $e_0 = 0.430$ ($\rho_d = 1.901$ g/cm^3). The results of oedometric compression tests on nearly dry material before saturation support these findings. As it is shown in terms of void ratio vs. vertical net stress in Figure A.18 a) the magnitude of C_C, C_S as well as the relation between $\sigma_{22,\text{prep}}$ and ρ_d is confirmed. The mean value of the compression index obtained from oedometric testing $\bar{C}_{C,\text{dry}} = 0.220$ is only slightly higher than during preparation. The swelling index was overestimated before and can

now be determined more precisely to $\bar{C}_{S,\mathrm{dry}} = 0.015$. The net preloading stress, calculated from the intersection of the tangents of the virgin loading line and the elastic unloading/reloading line, confirms the magnitude registered during preparation. All test results are well reproducible, even for high net stress levels. A summary of the results is presented in Table A.9.

The results of swelling tests with subsequent oedometric compression tests are shown in Figure A.18 b) in terms of void ratio vs. vertical net stress. In contrast to the oedometric compression tests on dry material, these are not continuously measured values, but only the values at the end of each loading step.

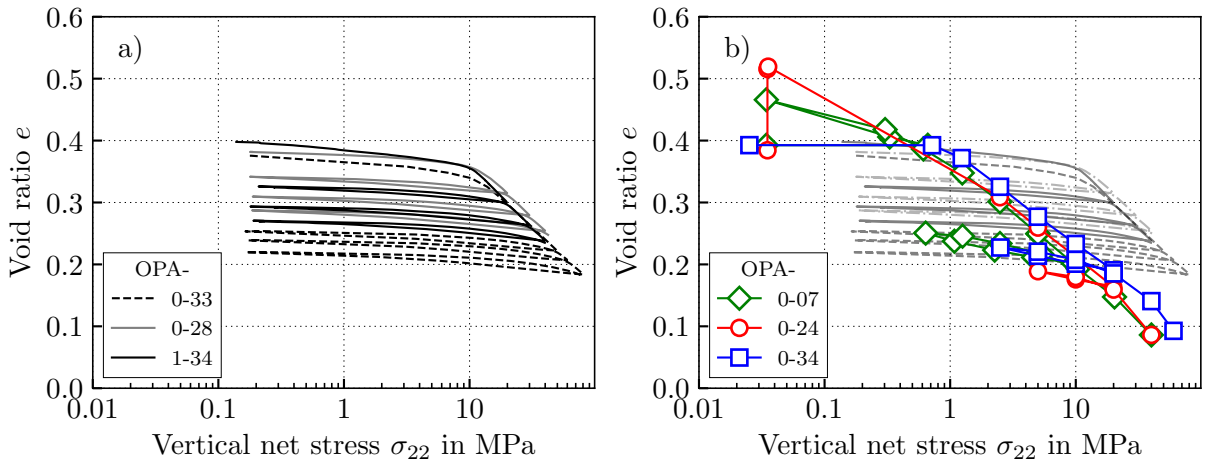

Figure A.18.: Void ratio vs. vertical net stress for all oedometric compression tests: a) Before saturation and b) After saturation. Modified from Nitsch et al. (2023a)

Several observations can be made from the net stress-void ratio plots: The first section of the loading path shows a similar slope as the un- and reloading paths, except for specimen OPA-0-24 (red plot in Figure A.18 b)) which is missing data in this section. The slope of the un- and reloading paths is significantly higher than in the oedometric compression tests on unsaturated specimens. A severe increase of the swelling index $\bar{C}_S = 0.055$ and hence reduction of the un- and reloading stiffness is observed (factor 3.7). The later section of the loading path exhibits a similar slope $\bar{C}_C = 0.174$ as the dry samples (factor 1.2), but is shifted to an area of a notably smaller net stress level, which indicates a noticeable reduction of net preloading stress. For all three specimens tested after swelling an approximately unique compression line is identified for net stresses larger than 1 MPa, independently of the type of the prior swelling test. A transitional area for smaller net stresses can be determined with the prior swelling test influencing the mechanical response only in this net stress range. For very large net stresses a further reduction of stiffness seems to occur in the area of extremely small void ratios. It is assumed that the grain size distribution and microstructure of the reconstituted specimens may be affected by these large net stresses - i.e. resulting in pore collapse - and an evaluation in terms of void ratio is not suitable. The existence of a normal compression line (NCL), which is approximated by all specimens in the saturated state, can be concluded.

The magnitude of the compression and swelling indices observed in oedometric compression tests are compared to the results of the oedometric swelling tests, see Section A.1.3. Figure A.19 shows the unloading paths of selected oedometric swelling tests (black) and the oedometric compression tests in the saturated state (in color). Overall, a reduced, but constant unloading and reloading stiffness can be derived in the saturated state, which is assumed to be independent

Table A.9.: Oedometric compression tests before and after swelling: mechanical properties

Specimen OPA-	C_C	C_S	$\sigma_{22,v}$ in MPa
1-34	0.226	0.018	9.6
0-33	0.215	0.014	11.6
0-28	0.218	0.012	12.1
0-07	0.179	0.058	-
0-24	0.163	0.053	-
0-34	0.180	0.054	-

of both, stress level and void ratio. The loading stiffness of the swelling tests can be evaluated as an elastic reloading stiffness in the transitional area before the NCL is reached.

The magnitude of the compression and swelling indices in the saturated state are in good accordance with those reported by Crisci et al. (2019) and Favero et al. (2016) for remoulded specimen. As expected, they differ from those of the intact shale, as the extremely small void ratios could not be achieved during compaction of the reconstituted specimens. For the behaviour in oedometric compression tests in the saturated state, the sample preparation method - remoulded as a slurry with a certain multiple of the liquid limit or dry compacted and then saturated - does not seem to have a significant influence. However, with remoulded specimens, the preloading history of the specimen is not known, so that the degradation of the material due to saturation and swelling cannot be assessed.

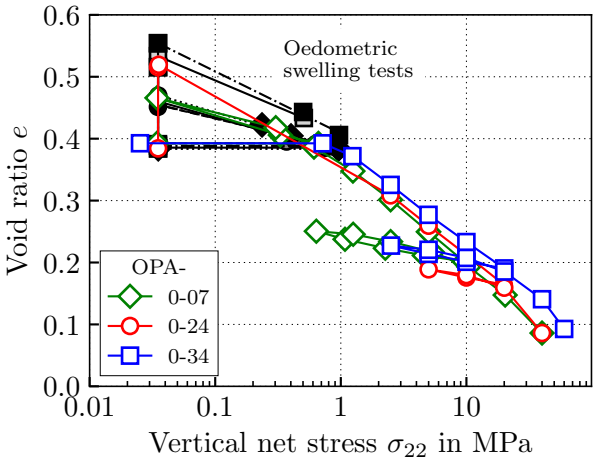

Figure A.19.: Void ratio vs. vertical net stress for oedometric compression tests after saturation and selected multi-step swelling tests. Modified from Nitsch et al. (2023a).

Permeability

The results of steady-state air permeability tests on the unsaturated specimens are presented in Table A.10. According to Klinkenberg (1941) the flow of gas through porous media is pressure-dependent. For smaller pressures the slip-effect along the walls of the pore channels is more pronounced and a higher gas flow rate, thus higher permeability, can be observed. The so-called

Klinkenberg effect can be neglected for very large pressures and the gas-phase permeability becomes the true permeability K_∞ according to

$$K_a = K_\infty \left(1 + \frac{b}{p}\right), \tag{A.4}$$

wherein K_a is the apparent permeability, b the Klinkenberg factor and p the applied air pressure. With an apparent unsaturated permeability $K_a = K_{\text{dry}} = 1.45 \times 10^{-15}$ m^2 at a mean pressure of $p = 50$ kPa and an estimation for the Klinkenberg factor of $b = 47.5$ kPa (Wu et al., 1998) the true unsaturated permeability results to $K_{\text{dry},\infty} = 7.44 \times 10^{-16}$ m^2 for the non-swollen material.

The evaluation of permeability from steady-state water permeability in the wet state is also presented in Table A.10. A reduction of the permeability by three orders of magnitude can be observed for both samples OPA-0-22 (multi-step test) and OPA-0-35 (single-step swelling strain test) from the dry to the wet state. Under constant volume conditions the contributing porosity has been significantly reduced by the swelling process whilst the global volume, hence the porosity, remained constant in sample OPA-0-22. The subsequent unloading of the sample and the vertical deformation led to a minor increase of the permeability. The same observation is made for the more increased permeability in the saturated sample OPA-0-35. Analogously to the results of the oedometric swelling tests, see Section A.1.3, the strain at the end of the single-step test is larger than after unloading.

In comparison to the magnitude of permeability in the dry reference state and taking into account the general uncertainties that occur during permeability testing (see i.e. Winhausen et al. (2021)), a mean value of saturated permeability of $K_{\text{sat}} = 1.78 \times 10^{-18}$ m^2 can be determined. Due to swelling the permeability of the material is thus reduced by a factor of approximately 300. For constant volume conditions the reduction of the permeability even amounts to a factor of approximately 600.

Table A.10.: Results of the performed permeability testing

Specimen OPA-	State	Fluid	e	K in m^2
0-08 − 0-13	Unsaturated	Nitrogen	0.389	5.38×10^{-16}
0-22	Saturated, A	Water	0.387	1.20×10^{-18}
	Saturated, D		0.387/0.451[1]	1.56×10^{-18}
0-35	Saturated, D	Water	0.387/0.512[2]	2.57×10^{-18}

[1] Multi-step test: after unloading from swelling pressure $\epsilon_{22} = -5.3\%$
[2] Single-step swelling strain test $\epsilon_{22} = -8.3\%$

The permeability K (in m^2) was further estimated during loading in the oedometric compression tests under saturated conditions. In Fig. A.20 it is shown as a function of the void ratio at the beginning of each loading step. Following Casagrande's log-time method the coefficient of consolidation c_v was evaluated from the time-settlement-curves and the permeability was derived. For the three oedometric compression tests an almost unique relation can be established. The mechanical compaction and associated reduction of porosity, hence void ratio, strongly decrease the permeability, which ranges between 2.37×10^{-19} and 1.01×10^{-17} m^2. This observation is in good agreement with the results from swelling tests in perspex rings (see Section A.1.3), where saturation was slower for smaller void ratios (constant volume swelling, lower permeability) than for larger void ratios (free axial swelling, higher permeability). The estimated permeability from oedometric compression tests agrees well with that from the permeability tests.

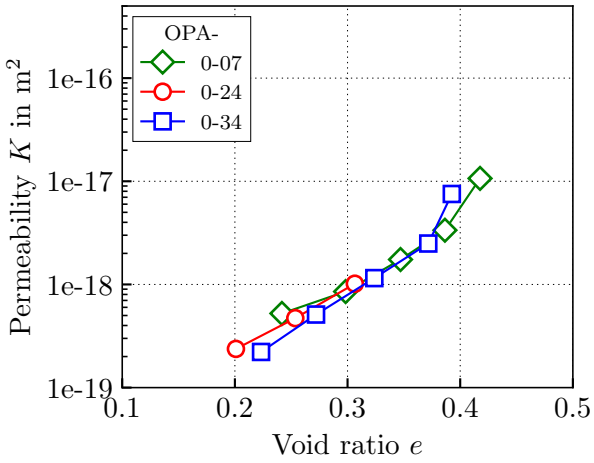

Figure A.20.: Evaluation of permeability [m^2] from loading paths of oedometric compression tests in the saturated state. Modified from Nitsch et al. (2023a).

A.2. Additional experiments: Direct shear tests

Three series of shear tests were carried out in an apparatus by Wykeham Farrance in a quadratic shearing box with dimensions $a = b = 6$ cm. Upon shearing with a steady shear rate under a dead load corresponding to a vertical stress σ_{22}, the vertical deformation u_v, the horizontal deformation u_h and shear force in the shear plane T are measured. From the latter, the shear stress $\tau = T/(a\,b)$ is determined.

Two series of tests were carried out on nearly dry samples, i.e. at ambient conditions, while in the third series the material was saturated prior to shearing. Each series includes tests on three or four samples. In the first series the samples were normally consolidated, in the second and third series overconsolidated. Initial conditions of the samples were limited by the technical specifications of the shear device. The maximum horizontal shearing deformation of the device was $u_h = 7$ mm and the maximum shear load corresponded to $\tau \approx 500$ kPa, which limited the maximal vertical load to $\sigma_{22} \approx 600$ kPa for the test series. The load was applied using a yoke and a suspended cantilever system. For normally consolidated tests, four vertical loads of $\sigma_{22,\text{shear}} = 104, 280, 442, 591$ kPa were chosen and the target void ratio and required mass were determined on the virgin loading line from soft-oedometer tests. For specimen preparation the material was poured in and slightly compacted by light tamping to the target height of $h \approx 2$ cm to ensure location of the shear plane in the centre of the sample height. For overconsolidated samples, the consolidation had to be carried out in the shear device itself and net consolidation stress was therefore also limited by the device to a maximum possible vertical load of $\sigma_{22,\text{cons}} = 1300$ kPa. With the known swelling index of the material $C_s = 0.015$ and application of same vertical loads upon shearing, the target net consolidation stress, void ratio and required mass were determined. OCR resulted in $2.12 - 2.54$. For saturated samples, the same conditions were chosen. After unloading from the net consolidation stress, the material was saturated by pouring water into the shear box and the vertical deformation was observed. The state of the samples prior to saturation was aimed to correspond to states on a theoretical w-line, hence resulting in as little deformation upon saturation as possible. However due to the overall low net stress regime, this was not fully achieved and all samples slightly collapsed upon saturation, but in an acceptable range for the location of the shear plane in the vertical centre of the sample, see Figure A.21.

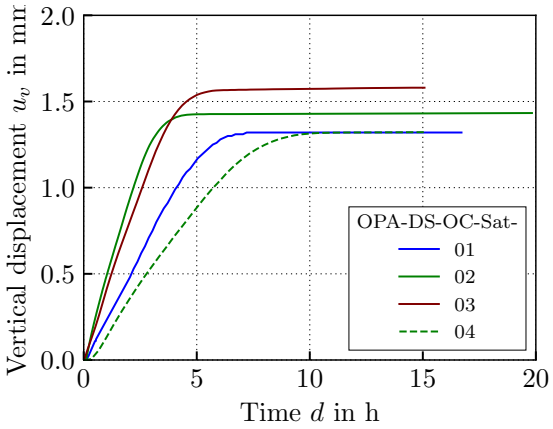

Figure A.21.: Vertical displacement upon saturation prior to shearing on overconsolidated, saturated samples of reconstituted Opalinus clay.

The loading paths of tests after specimen preparation were:

- Test series 1, normally consolidated, dry:
  Loading, consolidation, shearing.
- Test series 2, overconsolidated, dry:
  Loading, consolidation, unloading, consolidation, shearing.
- Test series 3, overconsolidated, saturated:
  Loading, consolidation, unloading, consolidation, saturation, shearing.

The shear rate was determined following DIN EN ISO 17892-10:2019-04 (2019) by evaluating the time-settlement curves of the oedometric compression tests. It is:

$$v_{\max} = \frac{s_f}{t_f} = \frac{s_f}{13\,t_c}, \tag{A.5}$$

wherein s_f is the expected horizontal deformation at failure and t_f the time required, which is estimated from the time t_c at which primary consolidation is finished at a similar load. As s_f is not known, it must be estimated from the width b of the shear box. Recommendation is $s_f = 10\%\,b$ for coarse-grained soils and $s_f = 2\%\,b$ for fine grained soils. As the reconstituted Opalinus clay in its nearly dry reference state shows characteristics of both, a middle value of $s_f = 6\%\,b = 6\%\,60$ mm $= 3.6$ mm was chosen. The completion of primary consolidation was determined from time-settlement curves in oedometric compression tests as at $t_c \approx 3$ min for the dry material and $t_c \approx 120$ min for the saturated material. Thus, in test series 1 and 2, a shear rate of $v_{\text{shear}} = 0.08128$ mm/min was chosen for the dry samples. The saturated samples were sheared with $v_{\text{shear}} = 0.0024384$ mm/min. To evaluate the drainage condition, one saturated test was repeated with the shear rate of the dry samples. All tests are summarized in Table A.11.

Test results

The results of all test series are first presented separately in terms of shear stress τ vs. horizontal deformation u_h and vertical deformation u_v vs. u_h in Figures A.22 - A.24. For test series 1 on normally consolidated, dry samples all tests have approximately reached a critical state, as the

Table A.11.: Overview of direct shear tests in three test series on Opalinus clay.

Specimen OPA-DS-	σ_{22} in kPa	e_0	$\rho_{d,0}$ in g/cm^3	$\sigma_{22,\text{shear}}$ in kPa	v_{shear} in mm/min
NC-01	104	0.854	1.476	104	0.08128
NC-02	279	0.737	1.574	279	0.08128
NC-03	441	0.645	1.662	441	0.08128
NC-04	590	0.541	1.776	590	0.08128
OC-01	712	0.427	1.916	279	0.08128
OC-02	1009	0.399	1.955	441	0.08128
OC-03	1250	0.415	1.933	590	0.08128
OC-sat-01	712	0.387	1.972	279	0.0024384
OC-sat-02	1009	0.358	2.014	441	0.0024384
OC-sat-03	1250	0.320	2.072	590	0.0024384
OC-sat-04	1009	0.253	2.183	441	0.08128

trend of the vertical displacement is flattened out (Figure A.22 right). The shear stress has asymptotically reached a maximum value (Figure A.22 left).

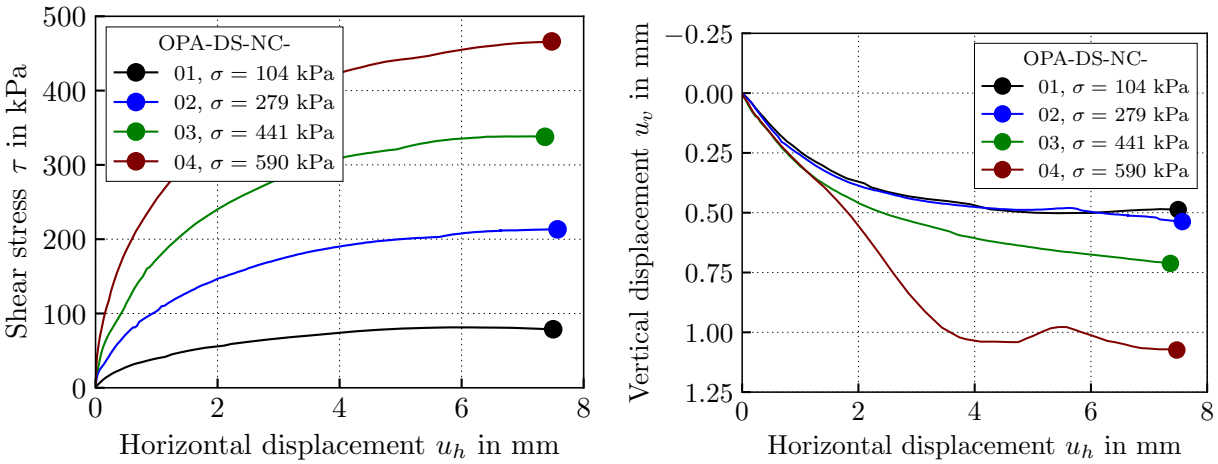

Figure A.22.: Shear stress (left) and vertical displacement (right) vs. horizontal displacement in direct shear tests on normally consolidated, dry samples of reconstituted Opalinus clay under different vertical loads.

For test series 2 on overconsolidated dry samples, the left-hand side of Figure A.23 displays slight peaks in the evolution of shear stress, but overall a steady value is reached. Due to the overconsolidated state, almost no vertical displacement occurred in the tests, see right-hand side of Figure A.23.

The results of test series 3 on overconsolidated, saturated samples show that a critical state was approximately reached in the evolution of vertical displacement, see Figure A.24 right. However, the shear stress evolution, see Figure A.24 left, has not reached a steady value, when the maximum horizontal displacement of the shear box was reached. After reaching a peak, the shear stress is still decreasing towards the residual state, more pronounced for the tests with higer loads and thus evaluation of the residual shear strength must be handled with caution. Test OPA-DS-OC-Sat-04, which was sheared faster and thus under partially drained conditions, shows a slightly different evolution of shear stress and vertical displacement than reference

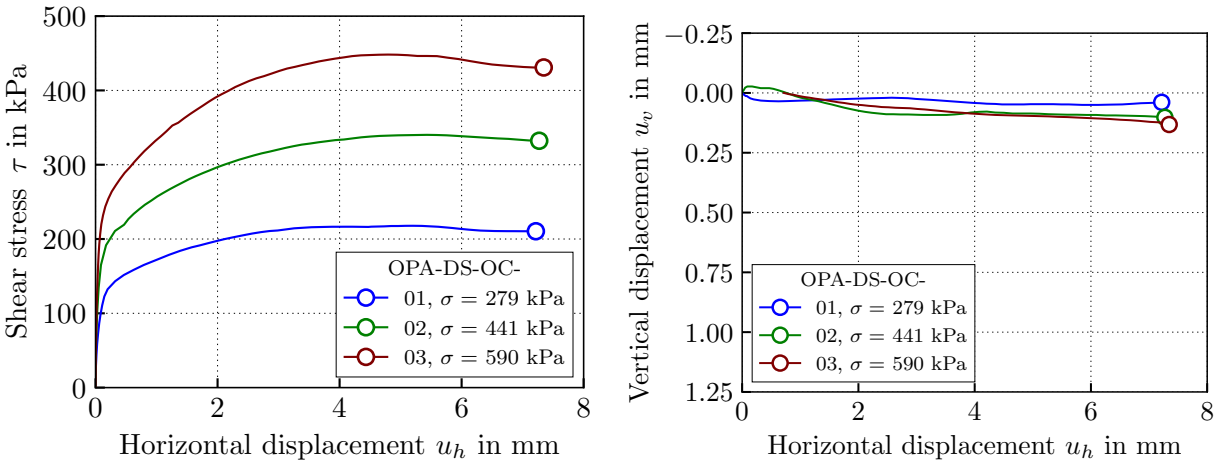

Figure A.23.: Shear stress (left) and vertical displacement (right) vs. horizontal displacement in direct shear tests on overconsolidated, dry samples of reconstituted Opalinus clay under different vertical loads.

test OPA-DS-OC-Sat-02 (Figure A.24). A final evaluation is not possible due to the limited horizontal deformation. Romero et al. (2014) amongst others showed, that shearing too quickly generally underestimates the shear strength. However, for clays with different plasticity, they showed that a shear rate of $v_{\text{shear}} = 0.089$ mm/min was sufficient to ensure drained conditions for (un)saturated samples.

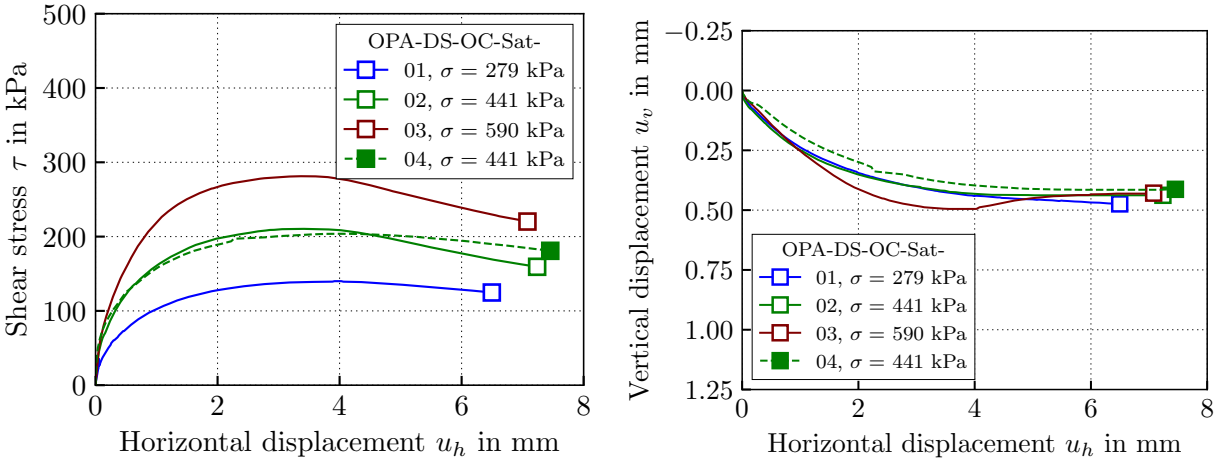

Figure A.24.: Shear stress (left) and vertical displacement (right) vs. horizontal displacement in direct shear tests on overconsolidated, saturated samples of reconstituted Opalinus clay under different vertical loads.

Evaluation of shear parameters

The left-hand side of Figure A.25 shows the evaluation of shear strength for all three test series in terms of shear stress τ vs. vertical net stress σ_{22}. For all tests, the last recorded value (markers in Figures A.22 - A.24) was used. For test series 1 and 2 these correspond to the residual state. For test series 3, the shear stress had not fully reduced to the residual value yet and the residual shear strength is overestimated by employing the last measured value of τ. The test results

were evaluated using the Mohr-Coulomb failure criterion without consideration of cohesion, see Equation (2.37).

For the normally consolidated dry and overconsolidated dry test series, the shear strength envelope is very similar, yielding a residual friction angle of $\varphi_{\text{ref}} = 37.9°$ or $\varphi_{\text{ref}} = 36.5°$, respectively. In the nearly dry reference state, no cohesion component is evident. For the saturated sample, the results in Figure A.25 show linear shear strength envelopes. In the saturated state, the linear shear strength envelope exhibits a significantly reduced slope, corresponding to a reduced friction angle φ_w. The results, however, do not clearly indicate whether cohesion is absent or present. Accordingly, two possible shear strength envelopes are established, corresponding either to $c = 0$ kPa with $\varphi_w = 21.1°$ or to $c = 25$ kPa with $\varphi_w = 20.1°$. The results may vary slightly under steady conditions. On the right-hand side of Figure A.25, the evaluated friction angles are displayed (without consideration of cohesion) vs. the effective degree of saturation (with $S_{\text{ref}} = 0.126$). A significant decrease of the friction angle upon saturation is apparent, which will be even more pronounced if a steady state is reached for the saturated samples. For modelling purpose $\varphi(S^e = 0) = 37°$ and $\varphi(S^e = 1) = 20°$ are derived.

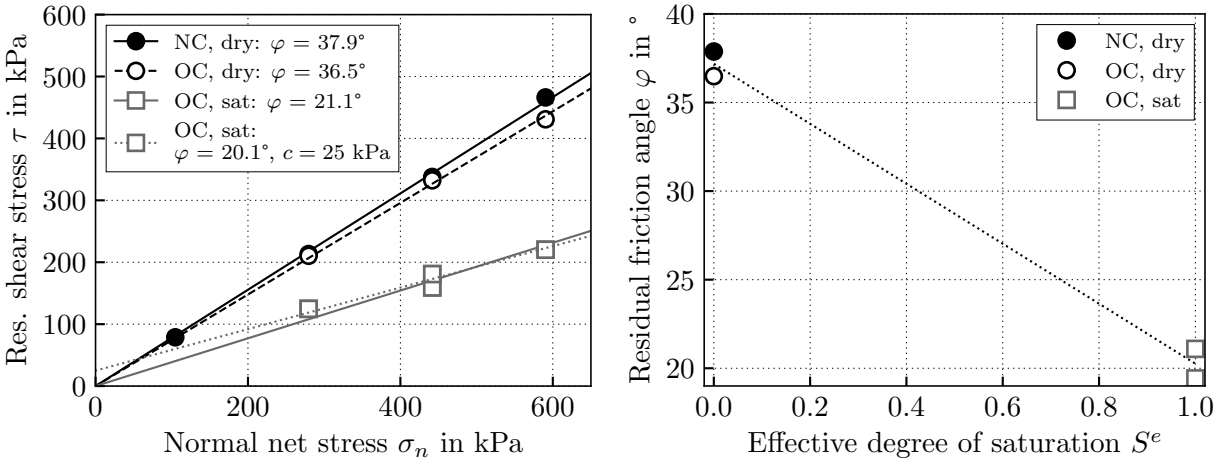

Figure A.25.: Residual shear strength vs. normal stress (left) and evaluated residual friction angle vs. effective degree of saturation (right) for three test series on Opalinus clay.

A.3. Additional experiments: Soft oedometer testing

Oedometric compression tests on dry OPA clay shale are carried out with the PERO oedometer cell in the laboratory of the Chair of Soil Mechanics and Foundation/ Goetechnical Engineering at Brandenburgische Technische Universität (BTU) Cottbus-Senftenberg, shown in Fig. A.26. The oedometer cell itself consists of a bottom part with a load cell and loading plate, the oedometric ring and a top part and load cap. The oedometer cell is mounted inside a simple oedometer loading frame. The load is applied using a cantilever system with an amplification factor of approximately 9.6. The deformation of the specimen is measured by a standard, non-integrated digital displacement transducer with an accuracy of 1μm. The oedometer ring is made of aluminium and has a height of $h = 51$ mm and a diameter of $d = 100$ mm, in which samples with arbitrary heights can be tested. The radial net stress is measured by strain gauges in the lower third of the oedometer ring with a maximum capacity of $\sigma_{11} = 2$ MPa. The normal force is measured by a load cell beneath the bottom loading cap, with a maximum capacity

of $F = 10$ kN, corresponding to a vertical net stress of $\sigma_{22} = 1.3$ MPa. The two measured quantities of radial net stress and normal force were calibrated with an air pressure cell. For evaluation of the results, the force calculated from the applied dead load is used.

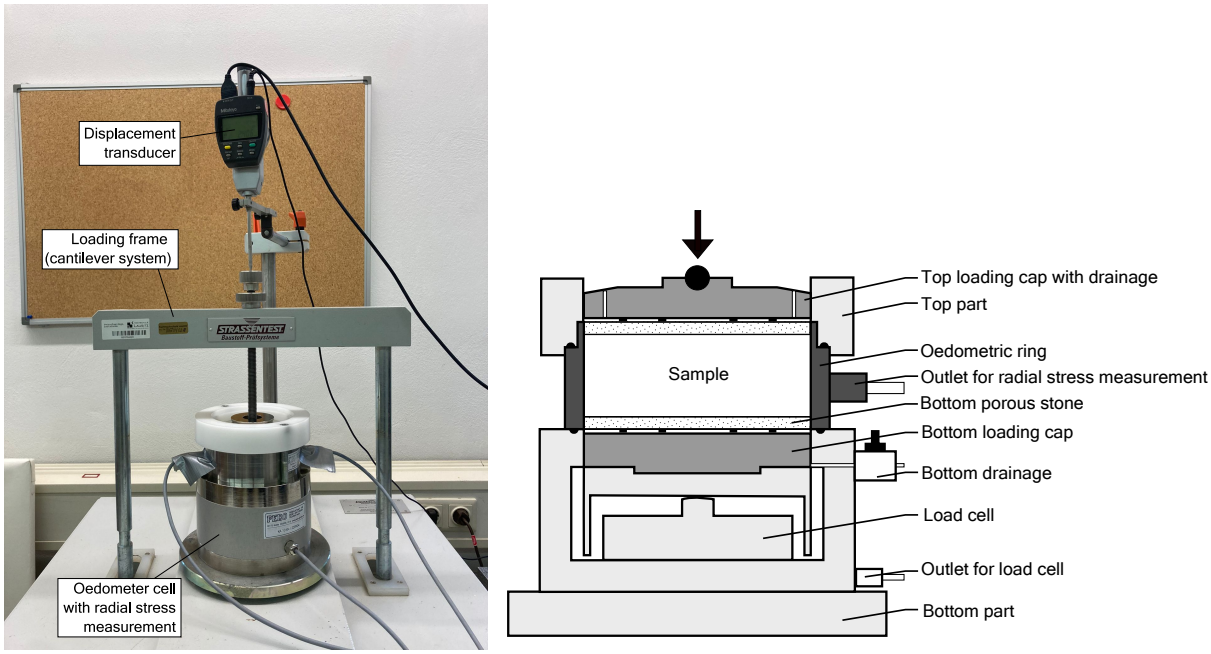

Figure A.26.: Soft oedometer cell with radial net stress measurement at BTU Cottbus-Senftenberg: photograph and technical drawing.

Note that a different material batch than in Nitsch et al. (2023a) was used. The material was poured into the oedometric ring and very lightly tamped to achieve an even surface. The required material mass was determined to achieve a predefined void ratio and a suitable sample height of $h \approx 31$ mm after loading to the maximum vertical load of approximately $\sigma_{22} = 1$ MPa, which would allow for enough vertical space for expansion upon wetting at constant net stress and precise guidance of the top cap. Afterwards the top loading cap was placed, exerting the first load step of 10 kPa under which the sample was allowed to consolidate. The material was then loaded up to $\sigma_{22} = 1000$ kPa and unloaded in the same sequence. Reloading took place for samples 01 and 02. During loading, the vertical deformation and radial net stress were measured.

Test results

The results of the soft oedometer tests are first displayed in semi-logarithmic vertical net stress vs. void ratio space in Fig. A.27. Very good agreement of the three soft oedometer loading and unloading paths can be observed, although specimen OPA-SO-01 starts from a slightly looser state, before all specimens approach the same virgin loading line with increasing load. The initial load steps should be interpreted with caution, as the top cap needed to settle evenly, making these steps less representative of the overall behaviour.

The evolution of vertical and radial net stress during loading, un- and reloading is displayed in Fig. A.28. The reloading branches are shown as dotted lines to differentiate them from unloading. In general, good agreement between the three tests is evident across all loading paths. During loading, the radial net stress increases with increasing vertical net stress up to

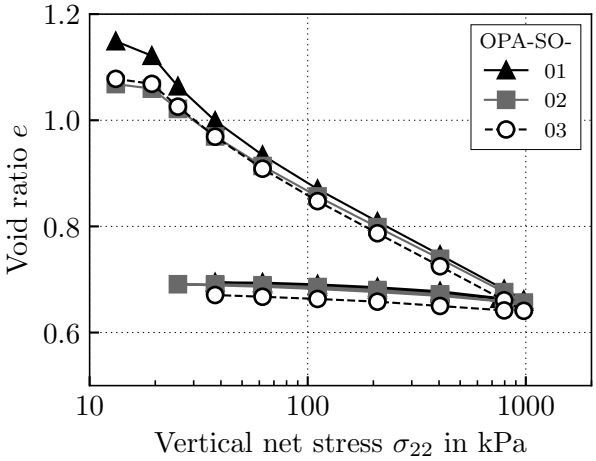

Figure A.27.: Void ratio vs. vertical net stress during loading, unloading and reloading or wetting for specimens OPA-SO-01 to -03.

.

a magnitude of $\sigma_{11} = 220$ kPa at a vertical net stress of $\sigma_{22} = 1$ MPa. The maximum stresses are referred to as radial and vertical preloading stress in the following. A linear evolution can be obseved except for very small loads in the beginning of the test, where rearrangement effects in the very loose sample may have occurred. During unloading, the radial net stress decreases alongside the vertical net stress, but this reduction is significantly less pronounced. For smaller loads, the lateral net stress exceeds the vertical net stress. A residual radial net stress remains, amounting approximately 25 % of the maximum radial net stress experienced. For reloading, the paths of specimens OPA-SO-01 and -02 show the reverse behaviour of unloading until the same stress state as after virgin loading is reached, although the trend of the reloading path on the left-hand side of Fig. A.28 is more linear than for unloading and thus similar as it was observed for first loading. Hence, in radial direction the un- and reloading does no behave purely reversible. For further loading beyond $\sigma_{22} = 1$ MPa the material is expected to move along the first loading path.

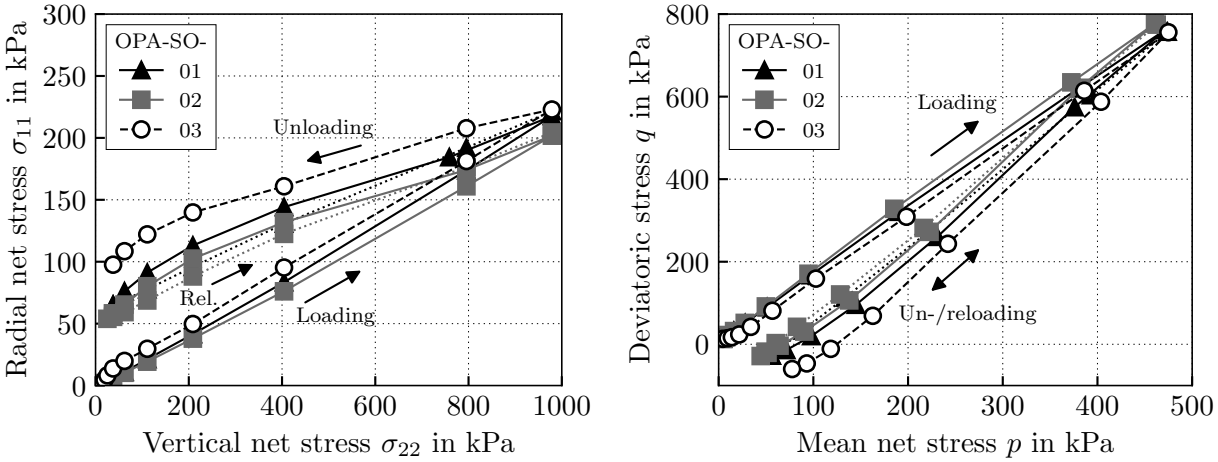

Figure A.28.: Radial net stress vs. vertical net stress (left) and Deviatoric stress vs. mean net stress (right) during loading, unloading and reloading for specimens OPA-SO-01 to -03.

There are thus two phenomena to note: (1) the radial preloading is smaller compared to the vertical preloading and (2) a residual radial net stress remains after unloading, indicating that

the material retains post-compaction net stress in the radial direction, consistent with the observations of Dyvik et al. (1985) and Tripathy et al. (2014).Additionally, the test results are also shown in terms of mean net stress $p = (\sigma_{22} + 2\sigma_{11})/3$ and deviatoric stress $q = \sigma_{22} - \sigma_{11}$ on the right-hand side of Fig. A.28. The anisotropy of the stress state after unloading becomes further apparent, as the mean net stress is significantly larger than the vertical net stress $p > \sigma_{22}$ and the deviatoric stress q is negative.

Evaluation of stress ratio

Typically, the evolution of radial net stress during compaction is unknown and the stress state after unloading can only be estimated. Several empirical approaches have been proposed to first approximate the ratio $K_0 = \sigma_{11}/\sigma_{22}$ and then compute σ_{11} for a known σ_{22}. It is common to use the mobilised angle of internal friction φ for an estimation of K_0, e.g. as done in Jaky's formula $K_0 = 1 - \sin\varphi$ (Jaky, 1944), which was originally introduced for granular soils and at-rest conditions with lateral constraint. For overconsolidated soils, Mayne and Kulhawy (1982) presented an extensive overview of relations between the overconsolidation ratio OCR$= \sigma_{22,d}/\sigma_{22}$ and stress ratio K_0, with $\sigma_{22,d}$ being the vertical preloading net stress. They proposed the following correlation:

$$K_0 = K_{0,NC}\,\mathrm{OCR}^{\sin\varphi} = (1 - \sin\varphi)\,\mathrm{OCR}^{\sin\varphi}, \tag{A.6}$$

wherein Jaky's formula is applied for the normally consolidated (NC) state. Eq. (A.6) thus represents an enhanced and yet simple way of estimating the ratio K_0 with knowledge of the friction angle (NC), current vertical net stress and vertical net preloading stress and is applied to the presented test results. The ratio K_0 computed from the vertical and radial net stresses from all three tests is shown in Fig. A.29.

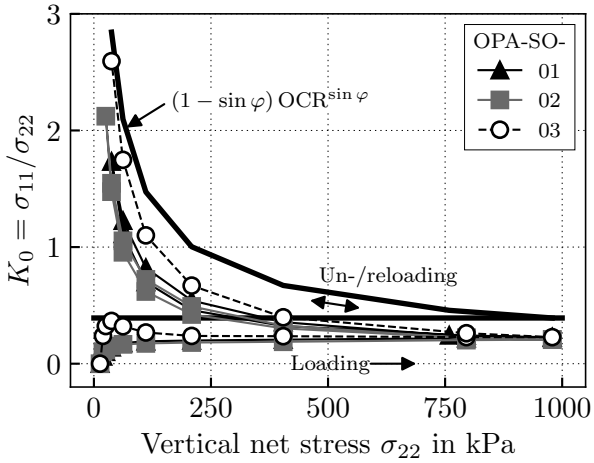

Figure A.29.: Stress ratio K_0 vs. vertical net stress during loading, unloading and reloading for specimens OPA-SO-01 to -03.

.

The prediction of K_0 by Eq. (A.6) with the friction angle $\varphi \approx 37°$ of the dry material is shown in a bold black line as well. As can be seen, during virgin loading the ratio in the experiments is constant at $K_0 \approx 0.22$ after some variations for smaller loads in all tests, but the prediction suggests almost the double value. During unloading, K_0 increases with decreasing vertical load in all tests. However, the final ratio after unloading somewhat scatters within the range $K_0 = 1.7 - 2.6$ whilst Eq. (A.6) yields $K_0 = 2.8$. It is concluded, that Eq. (A.6) can

be applied for estimating the radial state after unloading to approximate a sufficiently accurate three-dimensional stress state. Overall, Jaky's formula should not be applied for compacted specimens of swellable soils.

Bibliography

Abed, A. A. and Sołowski, W. T. (2017). A study on how to couple thermo-hydro-mechanical behaviour of unsaturated soils: Physical equations, numerical implementation and examples. *Computers and Geotechnics*, 92:132–155.

Agus, S. S. and Schanz, T. (2008). A method for predicting swelling pressure of compacted bentonites. *Acta Geotechnica*, 3(2):125–137.

Alexandersson, M., Askfelt, H., and Ristinmaa, M. (2016). Triphasic model of heat and moisture transport with internal mass exchange in paperboard. *Transport in Porous Media*, 112.

Alexandersson, M. and Ristinmaa, M. (2019). Multiphase transport model of swelling cellulose based materials with variable hydrophobicity. *International Journal of Engineering Science*, 141:112–140.

Alonso, E., Vaunat, J., and Gens, A. (1999). Modelling the mechanical behaviour of expansive clays. *Engineering Geology*, 54(1):173 – 183.

Alonso, E. E., Gens, A., and Josa, A. (1990). A constitutive model for partially saturated soils. *Géotechnique*, 40(3):405–430.

Alonso, E. E., Romero, E., Hoffmann, C., and García-Escudero, E. (2005). Expansive bentonite-sand mixtures in cyclic controlled-suction drying and wetting. *Engineering Geology*, 81(3):213–226.

Amstad, C. and Kovári, K. (2001). *Untertagbau in quellfähigem Fels*. Eidgenössisches Departement für Umwelt, Verkehr, Energie und Kommunikation (UVEK) und Bundesamt für Strassen (ASTRA), Zürich.

Anagnostou, G. (1992). *Untersuchungen zur Statik des Tunnelbaus in quellfähigem Gebirge*. PhD thesis, Eidgenössische Technische Hochschule (ETH) Zürich.

Anagnostou, G. (1993). A model for swelling rock in tunnelling. *Rock Mechanics and Rock Engineering*, 26(4):307–331.

Azizi, A., Jommi, C., and Musso, G. (2017). A water retention model accounting for the hysteresis induced by hydraulic and mechanical wetting-drying cycles. *Computers and Geotechnics*, 87:86–98.

Babiy, S., Tuttolomondo, A., and Laloui, L. (2025). Experimental quantification of capillary and adsorbed water in active clays for hydro-mechanical modelling. *Canadian Geotechnical Journal*, 62:1–18.

Babuška, I. (1973). The finite element method with lagrangian multipliers. *Numerische Mathematik*, 20(3):179–192.

Baille, W., Tripathy, S., and Schanz, T. (2010). Swelling pressures and one-dimensional compressibility behaviour of bentonite at large pressures. *Applied Clay Science*, 48(3):324–333.

Barrera, M. (2002). *Estudio experimental del comportamiento hidro-mecánico de suelos colapsables*. PhD thesis, Univ. Polytec. de Catalunya , Barcelona, Spain.

Bauer, E. (1996). Calibration of a comprehensive hypoplastic model for granular materials. *Soils and Foundations*, 36:13–26.

Bear, J. (2018). *Modeling phenomena of flow and transport in porous media*, volume 31. Springer.

Bentley Systems (2025). Plaxis 2d/3d – finite element software for geotechnical applications. https://www.plaxis.com.

Bergaya, F., Theng, B., and Lagaly, G. (2006). *Developments in Clay Science*. Elsevier Ltd.

BGR (2014). BGR–Faktenblatt: Ton- und Tonsteinforschung zur Endlagerung. https://www.bgr.bund.de/DE/Themen/Endlagerung/Downloads/Charakterisierung_Wirtsgesteine_geotech_Barrieren/1_Tongestein/2014-11-00_BGR_Faktenblatt_Ton_Tonsteinforschung_112014.pdf.

BGR (2020). Konzept Endlagerung 2020: Geowissenschaftliches Fundament für die Endlagerung radioaktiver Abfälle in Deutschland. https://www.bgr.bund.de/DE/Themen/Endlagerung/Downloads/Allgemein/2020-04-00_konzept_endlagerung_2020.pdf.

Bilke, L., Naumov, D., Wang, W., Fischer, T., Kiszkurno, F. K., Lehmann, C., Max, J., Zill, F., Buchwald, J., Grunwald, N., Kessler, K., Aubry, L., Dörnbrack, M., Nagel, T., Ahrendt, L., Kaiser, S., and Meisel, T. (2025). Opengeosys.

Bishop, A. W. (1959). The principle of effective stress. *Teknisk Ukeblad*, 39:859–863.

Bishop, A. W. and Blight, G. E. (1963). Some aspects of effective stress in saturated and partly saturated soils. *Géotechnique*, 13(3):177–197.

Blatz, J. and Graham, J. (2003). Elastic-plastic modeling of unsaturated soil using results from a new triaxial test with controlled suction. *Géotechnique*, 53:113–122.

Boffi, D., Brezzi, F., and Fortin, M. (2013). *Mixed Finite Element Methods and Applications*, volume 44 of *Springer Series in Computational Mathematics*. Springer Berlin Heidelberg.

Borja, R. I. (2006). On the mechanical energy and effective stress in saturated and unsaturated porous continua. *International Journal of Solids and Structures*, 43(6):1764 – 1786.

Bosch, J. A., Ferrari, A., and Laloui, L. (2021). Coupled hydro-mechanical analysis of compacted bentonite behaviour during hydration. *Computers and Geotechnics*, 140:104447.

Bosch, J. A., Qiao, Y., Ferrari, A., and Laloui, L. (2023). Thermo-hydro-mechanical analysis of the complete lifetime of the bentonite barrier in the febex in-situ test. *Geomechanics for Energy and the Environment*, 34:100472.

Bossart, P. (2012). Characteristics of the Opalinus Clay at Mont Terri. *Mont Terri Project, Wabern Switzerland*.

Bradbury, M. and Baeyens, B. (2001). Porewater chemistry in compacted re-saturated MX80 bentonite: Physicochemical characterisation and geochemical modelling. Bericht 02-10, Paul Scherrer Institut.

Brezzi, F. and Fortin, M. (1991). *Mixed and Hybrid Finite Element Method*.

Brezzi, F. and Pitkäranta, J. (1984). On the Stabilization of Finite Element Approximations of the Stokes Equations. In Hackbusch, W., editor, *Efficient Solutions of Elliptic Systems*, pages 11–19. Vieweg+Teubner Verlag.

Brooks, R. H. and Corey, A. T. (1964). Hydraulic properties of porous media and their relation to drainage design. *Transactions of the ASAE*, 7(1):26–0028.

Burdine, N. (1953). Relative Permeability Calculations From Pore Size Distribution Data. *Journal of Petroleum Technology*, 5(03):71–78.

Burke, T. d. S., Jacobsz, S., Elshafie, M., and Osman, A. (2022). Measurement of pile uplift forces due to soil heave in expansive clays. *Canadian Geotechnical Journal*, 59(12):2119–2134.

Burland, J. B. (1990). On the compressibility and shear strength of natural clays. *Géotechnique*, 40(3):329–378.

Butterfield, R. (1979). Natural compression law for soils (an advance on e-log p). *Géotechnique*, 29:469–480.

Byrne, H. and Preziosi, L. (2003). Modelling solid tumour growth using the theory of mixtures. *Mathematical Medicine and Biology*, 20(4):341–366.

Caicedo, B., Tristancho, J., Thorel, L., and Leroueil, S. (2014). Experimental and analytical framework for modelling soil compaction. *Engineering Geology*, 175:22–34.

Carman, P. C. (1939). Permeability of saturated sands, soils and clays. *The journal of Agricultural Science*, 29(2):262–273. Publisher: Cambridge University Press (CUP).

Chatzis, I. and Dullien, F. A. L. (1983). Dynamic immiscible displacement mechanisms in pore doublets: Theory versus experiment. *Journal of Colloid and Interface Science*, 91:199–222.

Chen, Y., Zhou, C., and Jing, L. (2009). Modeling coupled thm processes of geological porous media with multiphase flow: Theory and validation against laboratory and field scale experiments. *Computers and Geotechnics*, 36:1308–1329.

Childs, E. C., Collis-George, N., and Taylor, G. I. (1950). The permeability of porous materials. *Proceedings of the Royal Society of London. Series A. Mathematical and Physical Sciences*, 201(1066):392–405.

Chiu, C. F. and Ng, C. W. W. (2003). A state-dependent elasto-plastic model for saturated and unsaturated soils. *Géotechnique*, 53(9):809–829.

Cho, W.-J., Lee, J.-O., and Kang, C.-H. (2000). Influence of temperature elevation on the sealing performance of a potential buffer material for a high-level radioactive waste repository. *Annals of Nuclear Energy*, 27(14):1271–1284.

Christ, F. (2025). *Experimental investigations on the hydro-mechanical behaviour of clay shales for tunnelling relevant boundary conditions*. PhD thesis, Ruhr-Universität Bochum.

Collin, F. (2002). *Couplages thermo-hydro-mécaniques dans lessols et les roches tendres partiellement saturés*. PhD thesis, Université de Liège.

Collin, F., Chambon, R., and Charlier, R. (2006). A finite element method for poro mechanical modelling of geotechnical problems using local second gradient models. *Int. J. Numer. Meth. Engng.*, 65(11):1749–1772.

Crisci, E., Ferrari, A., Giger, S. B., and Laloui, L. (2019). Hydro-mechanical behaviour of shallow opalinus clay shale. *Engineering Geology*, 251:214–227.

Cui, W., Jing, H., Potts, D. M., Dong, L., Pedone, G., Zdravkovic, L., and Yao, Y. (2024). Time-step constraints in coupled hydro-mechanical finite element analysis of unsaturated soils. *Computers and Geotechnics*, 165:105914.

Cui, Y. and Delage, P. (1996). Yielding and plastic behaviour of an unsaturated compacted silt. *Géotechnique*, 46:291–311.

Cui, Y. J., Tang, A. M., Loiseau, C., and Delage, P. (2008). Determining the unsaturated hydraulic conductivity of a compacted sand-bentonite mixture under constant-volume and free-swell conditions. *Physics and Chemistry of the Earth, Parts A/B/C*, 33:S462–S471.

Daniel, D. E. (1982). Measurement of hydraulic conductivity of unsaturated soils with thermocouple psychrometers. *Soil Science Society of America Journal*, 46:1125–1129.

Dassault Systèmes (2024). *ABAQUS Documentation*. Version 2024, Dassault Systèmes Simulia Corp., Providence, RI, USA.

de Boer, R. (2000). *Theory of Porous Media - Highlights in Historical Development and Current State*.

Delage, P., Howat, M. D., and Cui, Y. J. (1998). The relationship between suction and swelling properties in a heavily compacted unsaturated clay. *Engineering Geology*, 50:31–48.

Delahaye, C. H. and Alonso, E. E. (2002). Soil heterogeneity and preferential paths for gas migration. *Engineering Geology*, 64(2):251–271.

Della Vecchia, G., Dieudonné, A.-C., Jommi, C., and Charlier, R. (2015). Accounting for evolving pore size distribution in water retention models for compacted clays. *International Journal for Numerical and Analytical Methods in Geomechanics*, 39(7):702–723.

Dieudonne, A.-C. (2016). *Hydromechanical behaviour of compacted bentonite:from micro-scale analysis to macro-scale modelling*. PhD thesis, Université de Liège.

Dieudonne, A.-C., Della Vecchia, G., and Charlier, R. (2017). Water retention model for compacted bentonites. *Can. Geotech. J.*, 54(7):915–925.

Dieudonné, A.-C. and Charlier, R. (2017). Evaluation of the instantaneous profile method for the determination of the relative permeability function.

DIN 4220:2020-11 (2020). *Pedologic site assessment - Designation, classification and deduction of soil parameters (normative and nominal scaling)*. Deutsches Institut für Normung: DIN, Beuth, Berlin.

DIN EN ISO 17892-10:2019-04 (2019). *Geotechnical investigation and testing - Laboratory testing of soil - Part 10: Direct shear tests (ISO 17892-10:2018); German version EN ISO 17892-10:2018*. Deutsches Institut für Normung: DIN, Beuth, Berlin.

Domitrovic, D. und Kovaevic Zelic, B. (2013). The relationship between swelling andshear strength properties of bentonites. In *Proceedings of the 18th International Con-ference on Soil Mechanics and Geotechnical Engineering, Paris 2013*.

Dubinin, M. M. (1947). The equation of the characteristic curve of activated charcoal. *Proceedings of the USSR Academy of Sciences*, 55:327–329.

Dyvik, R., Martin, R., and Lacasse, S. (1985). Coefficient of lateral stress from oedometer cell. In *11th International Conference on Soil Mechanics*, pages 1003–1006.

Ehlers, W. and Blome, P. (2003). A triphasic model for unsaturated soil based on the theory of porous media. *Mathematical and Computer Modelling*, 37(5):507–513.

Ehlers, W. and Bluhm, J. (2002). *Porous media. Theory, experiments and numerical applications*.

Emmerich, K., Madsen, F. T., and Kahr, G. (1999). Dehydroxylation behavior of heat-treated and steam-treated homoionic cis-vacant montmorillonites. *Clays and Clay Minerals*, 47(5):591–604.

Escario, V. and Sáez, J. (1986). The shear strength of partly saturated soils. *Géotechnique*, 36(3):453–456.

Estabragh, A. R., Moghadas, M., and Javadi, A. A. (2013). Effect of different types of wetting fluids on the behaviour of expansive soil during wetting and drying. *Soils and Foundations*, 53(5):617–627.

Estabragh, A. R., Parsaei, B., and Javadi, A. A. (2015). Laboratory investigation of the effect of cyclic wetting and drying on the behaviour of an expansive soil. *Soils and Foundations*, 55(2):304–314.

Favero, V., Ferrari, A., and Laloui, L. (2016). On the hydro-mechanical behaviour of remoulded and natural opalinus clay shale. *Engineering Geology*, 208.

Fellin, W. and Ostermann, A. (2002). Consistent tangent operators for constitutive rate equations. *International Journal for Numerical and Analytical Methods in Geomechanics*, 26(12):1213–1233.

Ferrari, A., Bosch, J., Tuttolomondo, A., and Laloui, L. (2021). Constitutive modelling of clays and bentonites in rad waste. GTC - Bentonite Training School - 9th September 2021.

Ferrari, A., Favero, V., and Laloui, L. (2016). One-dimensional compression and consolidation of shales. *International Journal of Rock Mechanics and Mining Sciences*, 88:15. 286–300.

Ferrari, A., Favero, V., Marschall, P., and Laloui, L. (2014). Experimental analysis of the retention behavior of shales. *International Journal of Rock Mechanics and Mining Sciences*, 72:61–70.

Flanagan, D. P. and Belytschko, T. (1981). A uniform strain hexahedron and quadrilateral with orthogonal hourglass control. *International Journal for Numerical Methods in Engineering*, 17(5):679–706.

Forsyth, P. A. (1988). Comparison of the single-phase and two-phase numerical model formulation for saturated-unsaturated groundwater flow. *Computer Methods in Applied Mechanics and Engineering*, 69(2):243–259.

François, B. and Laloui, L. (2008). Acmeg-ts: A constitutive model for unsaturated soils under non-isothermal conditions. *International Journal for Numerical and Analytical Methods in Geomechanics*, 32(16):1955–1988.

Fredlund, D., Rahardjo, H., and Fredlund, M. (2012). *Unsaturated Soil Mechanics in Engineering Practice*.

Fredlund, D. and Xing, A. (1994). Equations for the soil-water characteristic curve. *Canadian Geotechnical Journal*, 31:521–532.

Fredlund, D. G. and Morgenstern, N. R. (1977). Stress state variables for unsaturated soils. *Journal of the Geotechnical Engineering Division*, 103(5):447–466.

Fredlund, D. G., Morgenstern, N. R., and Widger, R. A. (1978). The shear strength of unsaturated soils. *Canadian Geotechnical Journal*, 15(3):313–321.

Fredlund, D. G., Xing, A., and Huang, S. (1994). Predicting the permeability function for unsaturated soils using the soil-water characteristic curve. *Canadian Geotechnical Journal*, 31(4):533–546.

Fredlund, D. G., Xing, A., and Huang, S. (1998). Predicting the permeability function for unsaturated soils using the soil-water characteristic curve. *Canadian Geotechnical Journal*, 31(4):533–546.

Fuentes, W. and Triantafyllidis, T. (2013). Hydro-mechanical hypoplastic models for unsaturated soils under isotropic stress conditions. *Computers and Geotechnics*, 51:72–82.

Fuentes Lacouture, W. M. (2014). *On the hydro-mechanical modelingof deposited materials*. PhD thesis, Karlsruher Institut für Technologie (KIT).

Gallipoli, D. and Bruno, A. W. (2017). A bounding surface compression model with a unified virgin line for saturated and unsaturated soils. *Géotechnique*, 67:703–712.

Gallipoli, D., Gens, A., Sharma, R., and Vaunat, J. (2003a). An elastoplastic model for unsaturated soil incorporating the effects of suction and degree of saturation on mechanical behavior. *Géotechnique*, 53:123–135.

Gallipoli, D., Wheeler, S. J., and Karstunen, M. (2003b). Modeling the variation of degree of saturation in a deformable unsaturated soil. *Géotechnique*, 53:105–112.

Gan, J., Fredlund, D., and Rahardjo, H. (2011). Determination of the shear strength parameters of an unsaturated soil using the direct shear test. *Canadian Geotechnical Journal*, 25:500–510.

Gao, Y., Li, Z., Sun, D., and Yu, H. (2021). A simple method for predicting the hydraulic properties of unsaturated soils with different void ratios. *Soil and Tillage Research*, 209:104913.

Gaspar, T. A. V., Jacobsz, S. W., Heymann, G., Toll, D. G., Gens, A., and Osman, A. S. (2022). The mechanical properties of a high plasticity expansive clay. *Engineering Geology*, 303:106647.

Gatabin, C., Talandier, J., Collin, F., Charlier, R., and Dieudonné, A.-C. (2016). Competing effects of volume change and water uptake on the water retention behaviour of a compacted mx-80 bentonite/sand mixture. *Applied Clay Science*, 121-122:57–62.

Gens, A. and Alonso, E. E. (1992). A framework for the behaviour of unsaturated expansive clays. *Canadian Geotechnical Journal*, 29(6):1013–1032.

Gens, A., Sánchez, M., and Sheng, D. (2006). On constitutive modelling of unsaturated soils. *Acta Geotechnica*, 1:137–147.

Gens, A., Valleján, B., Sánchez, M., Imbert, C., Villar, M. V., and Van Geet, M. (2011). Hydromechanical behaviour of a heterogeneous compacted soil: experimental observations and modelling. *Géotechnique*, 61(5):367–386.

Georgiadis, K., Potts, D., and Zdravkovic, L. (2005). Three-dimensional constitutive model for partially and fully saturated soils. *International Journal of Geomechanics*, 5:244–255.

Ghiadistri, G., Zdravkovic, L., Potts, D., and Tsiampousi, A. (2019). Calibration of a double structure constitutive model for unsaturated compacted soils. *E3S Web of Conferences*, 92:15002.

Grandas Tavera, C. E., Nitsch, A., and Machaček, J. (2022). A 1D Hypoplastic constitutive model for expansive soils. *Acta Geotechnica*, 17(10):4313–4331.

Grandas Tavera, C. E., Triantafyllidis, T., and Knittel, L. (2020). A Constitutive Model with a Historiotropic Yield Surface for Sands. In Triantafyllidis, T., editor, *Recent Developments of Soil Mechanics and Geotechnics in Theory and Practice*, pages 13–43, Cham. Springer International Publishing.

Grim, R. E. (1968). *Clay mineralogy. 2nd edition.* McGraw Hill.

Grob, H. (1972). Schwelldruck im Belchentunnel. In *Proc. Int. Symp. für Untertagebau, Luzern*, pages 99–119.

GRS (2020). In-situ research work of GRS at the mont terri rock laboratory and related modelling. Technical Report 556.

GRS (2023). Investigation of claystone / bentonite mixtures as barrier material for geological disposal of radioactive waste. Technical Report 703.

Gudehus, G. (1996). A comprehensive constitutive equation for granular materials. *Soils and Foundations*, 36(1):1–12.

Haines, W. B. (1930). Studies in the physical properties of soil. v. the hysteresis effect in capillary properties, and the modes of moisture distribution associated therewith. *The Journal of Agricultural Science*, 20(1):97–116.

Hanafy, E. A. D. E. (1991). Swelling/shrinkage characteristic curve of desiccated expansive clays. *Geotechnical Testing Journal*, 14(2):206–211.

Haque Mondol, N., Knut, B., and Jens, J. (2008). Experimental compaction of clays: relationship between permeability and petrophysical properties in mudstones. *Petroleum Geoscience*, 14(4):319–337.

Heidkamp, H. and Katz, C. (2002). Soils with swelling potential-Proposal of a final state formulation within an implicit integration scheme and illustrative FE-calculations. In *WCCMV Fifth World Congress on Computational Mechanics.*

Heidkamp, H. and Katz, C. (2004). The swelling phenomenon of soils - Proposal of an efficient continuum modelling approach. *EUROROCK 2004 and 53rd Geomechanics Colloquium.*

Herle, I. and Kolymbas, D. (2004). Hypoplasticity for soils with low friction angles. *Computers and Geotechnics*, 31(5):365–373.

Houlsby, G. T. (1997). The work input to an unsaturated granular material. *Géotechnique*, 47(1):193–196.

Hu, R., Chen, Y., Liu, H.-H., and Zhou, C. (2013). A water retention curve and unsaturated hydraulic conductivity model for deformable soils: Consideration of the change in pore-size distribution. *Géotechnique*, 63:1389–1405.

Huder, J. and Amberg, G. (1970). Quellung in Mergel, Opalinuston und Anhydrit. *Schweizerische Bauzeitung*, 88(43):975.

Humphrey, J. D. and Rajagopal, K. R. (2002). A constrained mixture model for growth and remodeling of soft tissues. *Mathematical Models and Methods in Applied Sciences*, 12(3):407–430.

IfG (2025). TALPA – Numerisches Simulationssystem zur Modellierung von Gesteinsverformungen. `https://www.ifg-leipzig.de`.

ISRM (1979). Suggested methods for determining water content, porosity, density, absorption and related properties and swelling and slake- durability index properties. *Int. Journal of Rock Mechanics and Mining Sciences*, 16:141–156.

Jadda, K. and Bag, R. (2020). Effect of initial compaction pressure and elevated temperature on swelling pressure of two indian bentonites. *Environmental Earth Sciences*, 79(197).

Jaky, J. (1944). The coefficient of earth pressure at rest (a nyugalmi nyomas tenyezoje). *Journal of the Society of Hungarian Architects and Engineering*, page 355–358.

Jobmann, M., Bebiolka, A., Burlaka, V., Herold, P., Jahn, S., Lommerzheim, A., Maßmann, J., Meleshyn, A., Mrugalla, S., Reinhold, K., Rübel, A., Stark, L., and Ziefle, G. (2017). Safety assessment methodology for a german high-level waste repository in clay formations. *Journal of Rock Mechanics and Geotechnical Engineering*, 9(5):856–876.

Karthikeyan, M., Tan, T.-S., and Phoon, K.-K. (2001). Numerical oscillation in seepage analysis of unsaturated soils. *Canadian Geotechnical Journal*, 38:639–651.

Keller, L. M., Seiphoori, A., Gasser, P., Lucas, F., Holzer, L., and Ferrari, A. (2014). The Pore Structure of Compacted and Partly Saturated MX-80 Bentonite at Different Dry Densities. *Clays and Clay Minerals*, 62(3):174–187.

Khoei, A. and Mohammadnejad, T. (2011). Numerical modeling of multiphase fluid flow in deforming porous media: A comparison between two- and three-phase models for seismic analysis of earth and rockfill dams. *Computers and Geotechnics*, 38(2):142–166.

Kiehl, J. (1990). Ein dreidimensionales quellgesetz und seine anwendung auf den felshohlraumbau. In *Sonderheft der Zeitschrift Geotechnik, Vorträge zum 9. Nationalen Felsmechanik Symposium.*

Kirsch, E. (1898). Die Theorie der Elastizität und die Bedürfnisse der Festigkeitslehre. *Zeitschrift des Vereines Deutscher Ingenieure*, 42:797–807.

Klinkenberg, L. J. (1941). The permeability of porous media to liquids and gases. *Drilling and Production Practice*, (API-41-200).

Kolymbas, D. (1977). A rate-dependent constitutive equation for soils. *Mechanics Research Communications*, 4(6):367–372.

Kolymbas, D. (1991). An outline of hypoplasticity. *Archive of Applied Mechanics*, 61(3):143–151.

Kolymbas, D. and Bauer, E. (1993). Soft oedometer–a new testing device and its application for the calibration of hypoplastic constitutive laws. *Geotechnical Testing Journal*, 16.

Komine, H. and Ogata, N. (1999). Experimental study on swelling characteristics of sand-bentonite mixture for nuclear waste disposal. *Soils and Foundations*, 39(2):83 – 97.

Komine, H. and Ogata, N. (2003). New equations for swelling characteristics of bentonite-based buffer materials. *Canadian Geotechnical Journal*, 40(2):460–475.

Kovári, K., Amstad, C., and Anagnostou, G. (1987). Tunnelbau im quellfähigen Gebirge. In *Frühjahrstagung der Schweizerische Gesellschaft für Boden- und Felsmechanik 1987*, volume 115, pages 19 – 26, Zürich. Schweizerische Gesellschaft für Boden- und Felsmechanik.

Kozeny, J. (1927). Über kapillare Leitung des Wassers im Boden. *Sitzber. Akad. Wiss. Wein, Math-naturw*, 136:Abt. II a, P. 277.

Kraehenbuehl, F., Stoeckli, H. F., Brunner, F., Kahr, G., and Mueller-Vonmoos, M. (1987). Study of the water-bentonite system by vapour adsorption, immersion calorimetry and X-ray techniques: I. Micropore volumes and internal surface areas, following Dubinin's theory. *Clay Minerals*, 22(1):1–9.

Lang, L. Z. (2019). *Hydro-Mechanical Behaviour of Bentonite-Based Materials Used for Disposal of Radioactive Wastes*. doctoralthesis, Ruhr-Universität Bochum.

Lee, J. O., Lim, J. G., Kang, I. M., and Kwon, S. (2012). Swelling pressures of compacted ca-bentonite. *Engineering Geology*, 129-130:20–26.

Leon Bal, A. R. (2023). *Numerical modeling and simulation of excavation processes of soft soils in mechanized tunneling*. PhD thesis, Ruhr-Universität Bochum.

Leong, E. and Rahardjo, H. (1997). Permeability functions for unsaturated soils. *Journal of Geotechnical and Geoenvironmental Engineering*, 123(12):1118–1126.

Leong, E.-C., Tripathy, S., and Rahardjo, H. (2003). Total suction measurement of unsaturated soils with a device using the chilled-mirror dew-point technique. *Géotechnique*, 53(2):173–182.

Leuthold, J., Gerolymatou, E., and Triantafyllidis, T. (2021). Effect of compaction banding on the hydraulic properties of porous rock - part ii: Constitutive description and numerical simulations. *Rock Mechanics and Rock Engineering*, 54(6):2685–2696.

Li, X., Li, X., Wu, Y., Wu, L., and Yue, Z. (2022). Selection criteria of mesh size and time step in fem analysis of highly nonlinear unsaturated seepage process. *Computers and Geotechnics*, 146:104712.

Likos, W. J. and Lu, N. (2004). *Unsaturated Soil Mechanics*. Wiley.

Liu, Y. and Vanapalli, S. K. (2019). Prediction of lateral swelling pressure behind retaining structure with expansive soil as backfill. *Soils and Foundations*, 59(1):176 – 195.

Lloret, A., Villar, M. V., Sánchez, M., Gens, A., Pintado, X., and Alonso, E. E. (2003). Mechanical behaviour of heavily compacted bentonite under high suction changes. *Géotechnique*, 53(1):27–40.

Machaček, J. (2020). *Contributions to the numerical modelling of saturated and unsaturated soils*. PhD thesis, Karlsruher Institut für Technologie (KIT).

Machaček, J., Fuentes, W., Staubach, P., Zachert, H., Wichtmann, T., and Triantafyllidis, T. (2023). A theory of porous media for unsaturated soils with immobile air. *Computers and Geotechnics*, 157:105324.

Machaček, J., Nitsch, A., and Grandas Tavera, C. E. (2022). An extended TPM for the coupled hydro-mechanical simulation of expansive soils. In *Workshop Numerische Methoden in der Geotechnik 2022*.

Machaček, J., Nitsch, A., Wichtmann, T., and Grandas Tavera, C. E. (2024). Numerical modelling of expansive geomaterials: Finite element formulation and constitutive models. *Computers and Geotechnics*, 176:106739.

Machaček, J. & Staubach, P. (2026). numgeo documentation. https://j-machacek.github.io/numgeo/.

Madsen, F. T. and Müller-Vonmoos, M. (1989). The swelling behaviour of clays. *Applied Clay Science*, 4(2):143 – 156.

Matsuoka, H. and Nakai, T. (1974). Stress-deformation and strength characteristics of soilunder three different principal stresses. In of Civil Engineers, J. S., editor, *Japan Society of Civil Engineers*, page 59–70.

Mayne, P. and Kulhawy, F. (1982). K0-OCR relationships in soil. *Journal of the Geotechnical Engineering Division*, 108:851–872.

Mazurek, M., Hurford, A. J., and Leu, W. (2006). Unravelling the multi-stage burial history of the swiss molasse basin: integration of apatite fission track, vitrinite reflectance and biomarker isomerisation analysis. *Basin Research*, 18(1):27–50.

Maßmann, J. (2008). *Modeling of Excavation Induced Coupled Hydraulic-Mechanical Processes in Claystone*. PhD thesis, Leibniz Universität Hannover.

Mašín, D. (2013). Double structure hydromechanical coupling formalism and a model for unsaturated expansive clays. *Engineering Geology*, 165:73–88.

Mašín, D. and Khalili, N. (2008). A hypoplastic model for mechanical response of unsaturated soils. *International Journal for Numerical and Analytical Methods in Geomechanics*, 32(15):1903–1926.

Merchan, V., Romero, E., and Vaunat, J. (2011). An adapted ring shear apparatus for testing partly saturated soils in the high suction range. *Geotechnical Testing Journal*, 34:103638.

Merchán, V., Vaunat, J., Romero, E., and Meca, T. (2008). Experimental study of the influence of suction on the residualfriction angle of clays. In *Proceedings of the 1st European Conference, E-UNSAT 2008*. Taylor and Francis.

Middelhoff, M., Cuisinier, O., Masrouri, F., and Talandier, J. (2021). Hydro-mechanical path dependency of claystone/bentonite mixture samples characterized by different initial dry densities. *Acta Geotechnica*, 16(10):3161–3176.

Middelhoff, M., Cuisinier, O., Masrouri, F., Talandier, J., and Conil, N. (2019). Combined impact of selected material properties and environmental condi- 1 tions on the swelling pressure of compacted claystone/ bentonite mixtures. *Applied Clay Science*, 184.

Miehe, C. (1996). Numerical computation of algorithmic (consistent) tangent moduli in large-strain computational inelasticity. *Computer Methods in Applied Mechanics and Engineering*, 134(3):223–240.

Mitchell, J. K. and Soga, K. (2005). *Fundamentals of Soil Behavior*. John Wiley & Sons, Inc, Hoboken, New Jersey, third edition edition.

Mitchell, R. J. (1970). On the yielding and mechanical strength of leda clays. *Canadian Geotechnical Journal*, 7(3):297–312.

Mohajerani, M., Delage, P., Monfared, M., Tang, A.-M., Sulem, J., and Gatmiri, B. (2011). Oedometric compression and swelling behaviour of the callovo-oxfordia, argillite. *International Journal of Rock Mechanics and Mining Sciences*, 48:606–615.

Mollins, L. H., Stewart, D. I., and Cousens, T. W. (1996). Predicting the properties of bentonite-sand mixtures. *Clay Minerals*, 31(2):243–252.

Monroy, R., Zdravkovic, L., and Ridley, A. (2010). Evolution of microstructure in compacted london clay during wetting and loading. *Géotechnique*, 60(2):105–119.

Monroy, R., Zdravkovic, L., and Ridley, A. M. (2015). Mechanical behaviour of unsaturated expansive clay under k0 conditions. *Engineering Geology*, 197:112–131.

Mualem, Y. (1976). A new model for predicting the hydraulic conductivity of unsaturated porous media. *Water resources research*, 12(3):513–522.

Mualem, Y. (1986). Hydraulic conductivity of unsaturated soils: prediction and formulas. In Klute, A., editor, *Methods of Soil Analysis. Part 1: Physical and Mineralogical Methods*, page 799–823., Madison, WI, USA. American Society of Agronomy (ASA) and Soil Science Society of America (SSSA).

Müller, H. R., Garitte, B., Vogt, T., Köhler, S., Sakaki, T., Weber, H., Spillmann, T., Hertrich, M., Becker, J. K., Giroud, N., Cloet, V., Diomidis, N., and Vietor, T. (2017). Implementation of the full-scale emplacement (fe) experiment at the mont terri rock laboratory. *Swiss Journal of Geosciences*, 110(1):287–306.

Nagra (2002). Projekt Opalinuston: Konzept für die Anlage und den Betrieb eines geologischen Tiefenlagers– Entsorgungsnachweis für abgebrannte Brennelemente, verglaste hochaktive sowie langlebige mittelaktive Abfälle. Technical report, Nagra, Wettingen, Switzerland.

Nagra (2005). Darstellung und Beurteilung der aus sicherheitstechnisch-geologischer Sicht möglichen Wirtgesteine und Gebiete. Technical report.

Nagra (2014). The long term geochemical evolution of the nearfield of the hlw repository. Technical report.

Nguyen, V. H., Sheppard, A. P., Knackstedt, M. A., and Val Pinczewski, W. (2006). The effect of displacement rate on imbibition relative permeability and residual saturation. *Journal of Petroleum Science and Engineering*, 52(1-4):54–70.

Niemunis, A. (2003). *Extended hypoplastic models for soils*. Number 34 in Schriftenreihe des Instituts für Grundbau und Bodenmechanik der Ruhr-Universität Bochum. Schriftenreihe des Instituts für Grundbau und Bodenmechanik der Ruhr-Universität Bochum. available from www.pg.gda.pl/∼aniem/anliter.html.

Niemunis, A., Grandas Tavera, C. E., and Prada Sarmiento, L. F. (2009). Anisotropic visco-hypoplasticity. *Acta Geotechnica*, 4(4):293.

Nitsch, A., Leuthold, J., Machaček, J., and Grandas Tavera, C. E. (2023a). Experimental investigations on hydro-mechanical processes in reconstituted clay shale and their significance for constitutive modelling. *Rock Mechanics and Rock Engineering*, 56(4):2457–2478.

Nitsch, A., Leuthold, J., Machaček, J., Wichtmann, T., and Grandas Tavera, C. E. (2021). Experimental investigations of the stress-dependent swelling behavior of reconstituted claystone. In *Fachsektionstage Geotechnik 2021*. Deutsche Gesellschaft für Geotechnik e.V.

Nitsch, A., Machaček, J., Grandas Tavera, C. E., and Wichtmann, T. (2023b). Zur numerischen Simulation expansiver Geomaterialien mit der Finite-Elemente- Methode. In *Fachsektionstage Geotechnik 2023*. Deutsche Gesellschaft für Geotechnik.

Nitsch, A., Machaček, J., Wichtmann, T., and Grandas Tavera, C. E. (2023c). An extended theory of porous media for expansive soils. In Zdravkovic, L., Kontoe, S., Taborda, D., and Tsiampousi, A., editors, *10th European Conference on Numerical Methods in Geotechnical Engineering*.

Nitsch, A., Machaček, J., Wichtmann, T., and Grandas Tavera, C. E. (2023d). Validierung und Kalibrierung eines hypoplastischen Stoffmodells für expansive Böden. *Bautechnik*, 100.

Norrish, K. and Rausell-Colom, J. A. (1962). Effect of freezing on the swelling of clay minerals. *Clay Minerals Bulletin*, 5(27):9–16.

Nowamooz, H. (2007). *Retrait/gonflement des sols argileux compactés et naturels*. PhD thesis, Institut national polytechnique de Lorraine.

Nowamooz, H. and Masrouri, F. (2008). Hydromechanical behaviour of an expansive bentonite/silt mixture in cyclic suction-controlled drying and wetting tests. *Engineering Geology*, 101:154–164.

Nuth, M. and Laloui, L. (2008). Advances in modelling hysteretic water retention curve in deformable soils. *Computers and Geotechnics*, 35(6):835–844.

Okrusch, M. and Matthes, S. (2013). *Mineralogie - Eine Einführung in die spezielle Mineralogie, Petrologie und Lagerstättenkunde*. Springer Spektrum Berlin, Heidelberg.

Olszak W., P. P. (1966). The constitutive equations of the flow theory for a nonstationary yield condition. In *Applied Mechanics, proceedings of the 11th International Congress*, page 545–553.

Pap, M., Mahler, A., and Nehme, S. (2022). Laboratory testing of water flow in building materials. In *Proceedings of the 20th International Conference on Soil Mechanics and Geotechnical Engineering*.

Papagiannakis, A. T., Bin-Shafique, S., and Lytton, R. L. (2014). Retaining structures in expansive clays. *Geotechnical and Geological Engineering*, 32(6):1405–1414.

Pereira, J.-M., Coussy, O., Alonso, E. E., Vaunat, J., and Olivella, S. (2010). Is the degree of saturation a good candidate for Bishop's parameter? In Alonso, E., E., Gens, and A., editors, *Unsaturated Soils - Proc. Fifth Int. Conf. on Unsaturated Soils*, volume 2, pages 913–919, Barcelona, Spain. CRC Press.

Pimentel, E. (2015). Existing methods for swelling tests – a critical review. *Energy Procedia*, 76:96–105.

Preisig, M. and Prévost, J. H. (2011). Stabilization procedures in coupled poromechanics problems: A critical assessment. *International Journal for Numerical and Analytical Methods in Geomechanics*, 35(11):1207–1225.

Pusch, R. (1977). Kbs:technical report 33: Required physical and mechanical properties of buffer masses. Technical report, Swedish Nuclear Fuel Supply Co, Stockholm.

Pusch, R., Karnland, O., and Hoekmark, H. (1990). GMM - a general microstructural model for qualitative and quantitative studies of smectite clays. Technical Report SKB-TR–90-43, Sweden.

Reed, M. B. (1984). An investigation of numerical errors in the analysis of consolidation by finite elements. *International Journal for Numerical and Analytical Methods in Geomechanics*, 8(3):243–257.

Romero, E. (1999). *Characterisation and thermo-hydro-mechanical beha-viour of unsaturated Boom clay: An experimental study*. PhD thesis, Univ. Polytec. de Catalunya , Barcelona, Spain.

Romero, E. (2013). A microstructural insight into compacted clayey soils and their hydraulic properties. *Engineering Geology*, 165:3–19.

Romero, E., Della Vecchia, G., and Jommi, C. (2011). An insight into the water retention properties of compacted clayey soils. *Géotechnique*, 61(4):313–328.

Romero, E., Gens, A., and Lloret, A. (1999). Water permeability, water retention and microstructure of unsaturated compacted boom clay. *Engineering Geology*, 54(1):117–127.

Romero, E., Vaunat, J., and Merchan, V. (2014). Suction effects on the residual shear strength of clays. *Journal of Geo-Engineering Sciences*, 2:17–37.

Roscoe, K. H. and Burland, J. (1968). On the generalized stress-strain behavior of wet clays. In Heyman, J. and Leckie, F., editors, *Engineering Plasticity*, Cambridge University Press, pages 535–609.

Rutqvist, J., Ijiri, Y., and Yamamoto, H. (2011). Implementation of the Barcelona Basic Model into TOUGH-FLAC for simulations of the geomechanical behavior of unsaturated soils. *Computers & Geosciences*, 37(6):751–762.

Saba, S., Barnichon, J.-D., Cui, Y.-J., Tang, A.-M., and Delage, P. (2014). Microstructure and anisotropic swelling behaviour of compacted bentonite/sand mixture. *Journal of Rock Mechanics and Geotechnical Engineering*, 6.

Sauerwein, M. (2021). *Simulation of Coupled Transfer and Transport Phenomenain Multi-Phase Materials with Application to Polymer Gels*. PhD thesis, Universität Stuttgart.

Sauerwein, M. and Steeb, H. (2018). A modified effective stress principle for chemical active multiphase materials with internal mass exchange. *Geomechanics for Energy and the Environment*, 15:19–34.

Schanz, T. and Tripathy, S. (2009). Swelling pressure of a divalent-rich bentonite: Diffuse double-layer theory revisited. *Water Resources Research*, 45(5).

Schoen, M. (2025). *Numerical analysis of tunnel excavation in swellable clay shales*. PhD thesis, Ruhr-Universität Bochum.

Schrefler, B., Simoni, L., Li, X., and Zienkiewicz, O. (1990). Mechanics of Partially Saturated Porous Media. In *Numerical Methods and Constitutive Modelling in Geomechanics*, pages 169–209.

Seiphoori, A., Ferrari, A., and Laloui, L. (2014). Water retention behaviour and microstructural evolution of mx-80 bentonite during wetting and drying cycles. *Géotechnique*, 64(9):721–734.

Seiphoori, A., Moradian, Z., Einstein, H. H., and Whittle, A. J. (2016). Microstructural characterization of opalinus shale. volume 4, pages 2742–2750.

Sheng, D., Gens, A., Fredlund, D., and Sloan, S. (2008). Unsaturated soils: From constitutive modelling to numerical algorithms. *Computers and Geotechnics*, 35:810–824.

SOFiSTiK AG (2025). Sofistik finite element software suite. `https://www.sofistik.com`.

Souza, R. F. C. and Pejon, O. J. (2020). Pore size distribution and swelling behavior of compacted bentonite/claystone and bentonite/sand mixtures. *Engineering Geology*, 275(105738).

Sridharan, A. (1968). *Some studies on the strength of partly saturated clays*. PhD thesis, Purdue University.

Sridharan, A. and Gurtug, Y. (2004). Swelling behaviour of compacted fine-grained soils. *Engineering Geology*, 72(1):9 – 18.

Sridharan, A., Rao, A., and Sivapullaiah, P. (1986). Swelling pressure of clays. *Geotechnical Testing Journal*, 9(1):24–33.

Srivastava, R. and Yeh, T.-C. J. (1991). Analytical solutions for one-dimensional, transient infiltration toward the water table in homogeneous and layered soils. *Water Resour. Res.*, 27(5):753–762.

Staubach, P. (2022). *Contributions to the numerical modelling of pile installation processes and high-cyclic loading of soils*. PhD thesis, Ruhr-Universität Bochum.

Staubach, P., Machaček, J., Skowronek, J., and Wichtmann, T. (2021). Vibratory pile driving in water-saturated sand: Back-analysis of model tests using a hydro-mechanically coupled cel method. *Soils and Foundations*, 61(1):144–159.

Steiner, W. (1993). Swelling rock in tunnels: Rock characterization, effect of horizontal stresses and construction procedures. *International Journal of Rock Mechanics and Mining Sciences & Geomechanics Abstracts*, 30(4):361 – 380.

Sánchez, M., Gens, A., Guimarães, L., and Olivella, S. (2005). A double structure generalized plasticity model for expansive materials. *International Journal for Numerical and Analytical Methods in Geomechanics*, 29:751–787.

Sánchez, M., Gens, A., and Olivella, S. (2012). THM analysis of a large-scale heating test incorporating material fabric changes. *International Journal for Numerical and Analytical Methods in Geomechanics*, 36(4):391–421.

Tafili, M. and Machaček, J. (2023). Generalized hydro-mechanically coupled hypoplastic constitutive model for unsaturated collapsible soils. *Canadian Geotechnical Journal*, 61(8):1622–1638.

Tang, A.-M., Cui, Y.-J., and Barnel, N. (2008). Thermo-mechanical behaviour of a compacted swelling clay. *Géotechnique*, 58(1):45–54.

Tarantino, A. (2009). A water retention model for deformable soils. *Géotechnique*, 59(9):751–762.

Taylor, R. K. and Smith, T. J. (1986). The engineering geology of clay minerals: swelling, shrinking and mudrock breakdown. *Clay Minerals*, 21(3):235–260.

Terzaghi, K. (1936). The shear resistance of saturated soil. In *First International Conference on Soil Mechanics at Harvard University*, volume 1, pages 54–56.

Thomas, H. R. and Zhou, Z. (1997). Minimum time-step size for diffusion problem in fem analysis. *International Journal for Numerical Methods in Engineering*, 40(20):3865–3880.

Tripathy, S., Bag, R., and Thomas, H. (2014). Effects of post-compaction residual lateral stress and electrolyte concentration on swelling pressures of a compacted bentonite. *Geotechnical and Geological Engineering*, 32:749–763.

Tripathy, S., Rao, K. S. S., and Fredlund, D. G. (2002). Water content - void ratio swell-shrink paths of compacted expansive soils. *Canadian Geotechnical Journal*, 39(4):938–959.

Truesdell, C. (1984). *Thermodynamics of Diffusion*, pages 219–236. Springer New York, New York, NY.

Truty, A. (2001). A galerkin/least-squares finite element formulation for consolidation. *International Journal for Numerical Methods in Engineering*, 52:763–786.

Truty, A. and Zimmermann, T. (2006). Stabilized mixed finite element formulations for materially nonlinear partially saturated two-phase media. *Computer Methods in Applied Mechanics and Engineering*, 195(13):1517–1546.

van Genuchten, M. T. (1980). A closed-form equation for predicting the hydraulic conductivity of unsaturated soils. *Soil Science Society of America Journal*, 44(5):892–898.

Vaunat, J. and Casini, F. (2017). A procedure for the direct determination of bishop's parameter from changes in pore size distribution. *Géotechnique*, 67.

Vaunat, J. and Gens, A. (2005). Analysis of the hydration of a bentonite seal in a deep radioactive waste repository. *Engineering Geology*, 81(3):317–328.

Vecchia, G. D. and Romero, E. (2013). A fully coupled elastic-plastic hydromechanical model for compacted soils accounting for clay activity. *International Journal for Numerical and Analytical Methods in Geomechanics*, 37(5):503–535.

Vergara, M., Balthasar, K., and Triantafyllidis, T. (2014). Comparison of experimental results in a testing device for swelling rocks. *International Journal of Rock Mechanics and Mining Sciences*, 66:177–180.

Vergara Quezada, M. (2019). *Experimental and numerical investigations on the swelling behavior of claystone and sulfate rock*. PhD thesis, Karlsruher Institut für Technologie (KIT).

Vermeer, P. A. and Verruijt, A. (1981). An accuracy condition for consolidation by finite elements. *International Journal for Numerical and Analytical Methods in Geomechanics*, 5(1):1–14.

Villar, M. (2004). Thermo-hydro-mechanical characteristics and processes in the claybarrier of a high level radioactive waste repository. Technical report, CIEMAT.

Villar, M. and Lloret, A. (2004). Temperature influence on the mechanical behaviour of a compacted bentonite. *Elsevier Geo-Engineering Book Series*, 2:305–310.

Villar, M. V. and Lloret, A. (2008). Influence of dry density and water content on the swelling of a compacted bentonite. *Applied Clay Science*, 39(1):38 – 49.

von Wolffersdorff, P.-A. (1996). A hypoplastic relation for granular materials with a predefined limit state surface. *Mechanics of Cohesive-frictional Materials*, 1(3):251–271.

Wang, Q., Cui, Y.-J., Tang, A.-M., Barnichon, J.-D., Saba, S., and Ye, W.-M. (2013a). Hydraulic conductivity and microstructure changes of compacted bentonite/sand mixture during hydration. *Engineering Geology*, 164:67–76.

Wang, Q., Tang, A. M., Cui, Y.-J., Barnichon, J.-D., and Ye, W.-M. (2013b). Investigation of the hydro-mechanical behaviour of compacted bentonite/sand mixture based on the BExM model. *Computers and Geotechnics*, 54:46–52.

Wetzel, A. and Allia, V. (2003). Der Opalinuston in der Nordschweiz: Lithologie und Ablagerungsgeschichte. *Ecologae Geologicae Helvetiae*, 96:451–469.

Wheeler, S. J., Gallipoli, D., and Karstunen, M. (2002). Comments on use of the Barcelona Basic Model for unsaturated soils. *International Journal for Numerical and Analytical Methods in Geomechanics*, 26(15):1561–1571.

Wheeler, S. J., Sharma, R. S., and Buisson, M. S. R. (2003). Coupling of hydraulic hysteresis and stress–strain behaviour in unsaturated soils. *Géotechnique*, 53(1):41–54.

White, J. A. and Borja, R. I. (2008). Stabilized low-order finite elements for coupled solid-deformation/fluid-diffusion and their application to fault zone transients. *Computer Methods in Applied Mechanics and Engineering*, 197(49):4353–4366.

Winhausen, L., Amann-Hildenbrand, A., Fink, R., Jalali, M., Khaledi, K., Hamdi, P., Urai, J. L., Schmatz, J., and Amann, F. (2021). A comparative study on methods for determining the hydraulic properties of a clay shale. *Geophysical Journal International*, 224(3):1523–1539.

Wittke-Gattermann, P. and Wittke, M. (2004). Computation of strains and pressures for tunnels in swelling rocks. *Tunnelling and Underground Space Technology*, 19(4-5):422–423.

Wu, Y.-S., Pruess, K., and Persoff, p. (1998). Gas flow in porous media with klinkenberg effects. *Transport in Porous Media*, 32(1):117–137.

Yang, C., Cui, Y. J., Pereira, J. M., and Huang, M. S. (2008). A constitutive model for unsaturated cemented soils under cyclic loading. *Computers and Geotechnics*, 35(6):853–859.

Ye, W. M., Cui, Y. J., Qian, L. X., and Chen, B. (2009). An experimental study of the water transfer through confined compacted gmz bentonite. *Engineering Geology*, 108(3):169–176.

Zeng, Z., Cui, Y.-J., and Talandier, J. (2022). Investigating the swelling pressure of highly compacted bentonite/sand mixtures under constant-volume conditions. *Acta Geotechnica*, 17(6):2573–2580.

Zhang, C.-L. and Kröhn, K.-P. (2019). Sealing behaviour of crushed claystone-bentonite mixtures. *Geomechanics for Energy and the Environment*, 17:90–105.

Zhang, F. and Fredlund, D. (2015). Examination of the estimation of relative permeability for unsaturated soils. *Canadian Geotechnical Journal*, 52.

Zhang, Z., Ye, W., Wang, Q., and Chen, Y. (2022). Investigation on healing behavior of unsaturated gmz bentonite pellet mixture based on compressibility. *Acta Geotechnica*, 17(10):4461–4471.

Zhou, A., Wu, S., Li, J., and Sheng, D. (2018). Including degree of capillary saturation into constitutive modelling of unsaturated soils. *Computers and Geotechnics*, 95:82–98.

Zhou, A.-N., Sheng, D., Sloan, S. W., and Gens, A. (2012a). Interpretation of unsaturated soil behaviour in the stress - saturation space, i: Volume change and water retention behaviour. *Computers and Geotechnics*, 43:178–187.

Zhou, A.-N., Sheng, D., Sloan, S. W., and Gens, A. (2012b). Interpretation of unsaturated soil behaviour in the stress-saturation space: Ii: Constitutive relationships and validations. *Computers and Geotechnics*, 43:111–123.

Ziefle, G. (2008). *Modeling aspects of coupled hydraulic–mechanical processes in clay material*. PhD thesis, Leibniz Universität Hannover.

Zienkiewicz, O. C., Taylor, R. L., and Zhu, J. Z. (2005). *The finite element method: its basis and fundamentals*. Elsevier.

Zienkiewicz, O. C., Xie, Y. M., Schrefler, B. A., Ledesma, A., and Bi̇canić, N. (1997). Static and dynamic behaviour of soils: a rational approach to quantitative solutions. II. Semi-saturated problems. *Proceedings of the Royal Society of London. A. Mathematical and Physical Sciences*, 429(1877):311–321.

Zou, W.-l., Han, Z., and Ye, J.-b. (2020). Influence of external stress and initial density on the volumetric behavior of an expansive clay during wetting. *Environmental Earth Sciences*, 79(10):211.

Åkesson, M., Jacinto, A. C., Gatabin, C., Sanchez, M., and Ledesma, A. (2009). Bentonite THM behaviour at high temperatures: Experimental and numerical analysis. *Géotechnique*, 59(4):307–318.

Schriftenreihe des Instituts für Grundbau, Wasserwesen und Verkehrswesen der Ruhr-Universität Bochum

Herausgeber: H.L. Jessberger

1 (1979) **Hans Ludwig Jessberger**
Grundbau und Bodenmechanik an der Ruhr-Universität Bochum

2 (1978) **Joachim Klein**
Nichtlineares Kriechen von künstlich gefrorenem Emschermergel

3 (1979) **Heinz-Joachim Gödecke**
Die Dynamische Intensivverdichtung wenig wasserdurchlässiger Böden

4 (1979) **Poul V. Lade**
Three Dimensional Stress-Strain Behaviour and Modeling of Soils

5 (1979) **Roland Pusch**
Creep of soils

6 (1979) **Norbert Diekmann**
Zeitabhängiges, nichtlineares Spannungs-Verformungsverhalten von gefrorenem Schluff unter triaxialer Belastung

7 (1979) **Rudolf Dörr**
Zeitabhängiges Setzungsverhalten von Gründungen in Schnee, Firn und Eis der Antarktis am Beispiel der deutschen Georg-von-Neumayer- und Filchner-Station

8 (1984) **Ulrich Güttler**
Beurteilung des Steifigkeits- und Nachverdichtungsverhaltens von ungebundenen Mineralstoffen

9 (1986) **Peter Jordan**
Einfluss der Belastungsfrequenz und der partiellen Entwässerungs-möglichkeiten auf die Verflüssigung von Feinsand

10 (1986) **Eugen Makowski**
Modellierung der künstlichen Bodenvereisung im grundwasserdurchströmten Untergrund mit der Methode der finiten Elemente

11 (1986) **Reinhard A. Beine**
Verdichtungswirkung der Fallmasse auf Lastausbreitung in nichtbindigem Boden bei der Dynamischen Intensivverdichtung

12 (1986) **Wolfgang Ebel**
Einfluss des Spannungspfades auf das Spannungs-Verformungsverhalten von gefrorenem Schluff im Hinblick auf die Berechnung von Gefrierschächten

13 (1987) **Uwe Stoffers**
Berechnungen und Zentrifugen-Modellversuche zur Verformungsabhängigkeit der Ausbaubeanspruchung von Tunnelausbauten in Lockergestein

14 (1988) **Gerhard Thiel**
Steifigkeit und Dämpfung von wassergesättigtem Feinsand unter Erdbebenbelastung

15 (1991) **Mahmud Thaher**
Tragverhalten von Pfahl-Platten-Gründungen im bindigen Baugrund, Berechnungsmodelle und Zentrifugen-Modellversuche

Schriftenreihe des Instituts für Grundbau der Ruhr-Universität Bochum

Herausgeber: H.L. Jessberger

16 (1992) **Rainer Scherbeck**
Geotechnisches Verhalten mineralischer Deponieabdichtungsschichten bei ungleichförmiger Verformungswirkung

17 (1992) **Martin M. Bizialiele**
Torsional Cyclic Loading Response of a Single Pile in Sand

18 (1993) **Michael Kotthaus**
Zum Tragverhalten von horizontal belasteten Pfahlreihen aus langen Pfählen in Sand

19 (1993) **Ulrich Mann**
Stofftransport durch mineralische Deponieabdichtungen:
Versuchsmethodik und Berechnungsverfahren

20 (1992) **Festschrift anlässlich des 60. Geburtstages von Prof. Dr.-Ing. H. L. Jessberger**
20 Jahre Grundbau und Bodenmechanik an der Ruhr-Universität Bochum

21 (1993) **Stephan Demmert**
Analyse des Emissionsverhaltens einer Kombinationsabdichtung im Rahmen der Risikobetrachtung von Abfalldeponien

22 (1994) **Diethard König**
Beanspruchung von Tunnel- und Schachtausbauten in kohäsionslosem Lockergestein unter Berücksichtigung der Verformung im Boden

23 (1995) **Thomas Neteler**
Bewertungsmodell für die nutzungsbezogene Auswahl von Verfahren zur Altlastensanierung

24 (1995) **Ralph Kockel**
Scherfestigkeit von Mischabfall im Hinblick auf die Standsicherheit von Deponien

25 (1996) **Jan Laue**
Zur Setzung von Flachfundamenten auf Sand unter wiederholten Lastereignissen

26 (1996) **Gunnar Heibrock**
Zur Rissbildung durch Austrocknung in mineralischen Abdichtungsschichten an der Basis von Deponien

27 (1996) **Thomas Siemer**
Zentrifugen-Modellversuche zur dynamischen Wechselwirkung zwischen Bauwerken und Baugrund infolge stoßartiger Belastung

28 (1996) **Viswanadham V. S. Bhamidipati**
Geosynthetic Reinforced Mineral Sealing Layers of Landfills

29 (1997) **Frank Trappmann**
Abschätzung von technischem Risiko und Energiebedarf bei Sanierungsmaßnahmen für Altlasten

30 (1997) **André Schürmann**
Zum Erddruck auf unverankerte flexible Verbauwände

31 (1997) **Jessberger, H. L. (Herausgeber)**
Environment Geotechnics, Report of ISSMGE Technical Committee TC 5 on Environmental Geotechnics

Schriftenreihe des Instituts für Grundbau und Bodenmechanik der Ruhr-Universität Bochum

Herausgeber: Th. Triantafyllidis

32 (2000) **Triantafyllidis, Th. (Herausgeber)**
Boden unter fast zyklischer Belastung: Erfahrung und Forschungsergebnisse (Workshop)

33 (2002) **Christof Gehle**
Bruch- und Scherverhalten von Gesteinstrennflächen mit dazwischenliegenden Materialbrücken

34 (2003) **Andrzej Niemunis**
Extended hypoplastic models for soils

35 (2004) **Christiane Hof**
Über das Verpressankertragverhalten unter kalklösendem Kohlensäureangriff

36 (2004) **René Schäfer**
Einfluss der Herstellungsmethode auf das Verformungsverhalten von Schlitzwänden in weichen bindigen Böden

37 (2005) **Henning Wolf**
Zur Scherfugenbänderung granularer Materialien unter Extensionsbeanspruchung

38 (2005) **Torsten Wichtmann**
Explicit accumulation model for non-cohesive soils under cyclic loading

39 (2008) **Christoph M. Loreck**
Die Entwicklung des Frischbetondruckes bei der Herstellung von Schlitzwänden

40 (2008) **Igor Arsic**
Über die Bettung von Rohrleitungen in Flüssigböden

41 (2009) **Anna Arwanitaki**
Über das Kontaktverhalten zwischen einer Zweiphasenschlitzwand und nichtbindigen Böden

Schriftenreihe des Lehrstuhls für Grundbau, Boden- und Felsmechanik der Ruhr-Universität Bochum

Herausgeber: T. Schanz

42 (2009) **Yvonne Lins**
Hydro-Mechanical Properties of Partially Saturated Sand

43 (2010) **Tom Schanz (Herausgeber)**
Geotechnische Herausforderungen beim Umbau des Emscher-Systems
Beiträge zum RuhrGeo Tag 2010

44 (2010) **Jamal Alabdullah**
Testing Unsaturated Soil for Plane Strain Conditions: A New Double-Wall Biaxial Device

45 (2011) **Lars Röchter**
Systeme paralleler Scherbänder unter Extension im ebenen Verformungszustand

46 (2011) **Yasir Al-Badran**
Volumetric Yielding Behavior of Unsaturated Fine-Grained Soils

47 (2011) **Usque ad finem**
Selected research papers

48 (2012) **Muhammad Ibrar Khan**
Hydraulic Conductivity of Moderate and Highly Dense Expansive Clays

49 (2014) **Long Nguyen-Tuan**
Coupled Thermo-Hydro-Mechanical Analysis: Experimental and Back Analysis

50 (2014) **Tom Schanz (Herausgeber)**
Ende des Steinkohlenbergbaus im Ruhrrevier: Realität und Perspektiven für die Geotechnik
Beiträge zum RuhrGeo Tag 2014

51 (2014) **Usque ad finem**
Selected research papers

52 (2014) **Houman Soleimani Fard**
Study on the Hydro-Mechanical Behavior of Fiber Reinforced Fine Grained Soils,
with Application to the Preservation of Historical Monuments

53 (2014) **Wiebke Baille**
Hydro-Mechanical Behaviour of Clays - Significance of Mineralogy

54 (2014) **Qasim Abdulkarem Jassim Al-Obaidi**
Hydro-Mechanical Behavior of Collapsible Soils

55 (2015) **Veselin Zarev**
Model Identification for the Adaption of Numerical Simulation Models -
Application to Mechanized Shield Tunneling

56 (2015) **Meisam Goudarzy**
Micro and Macro Mechanical Assessment of Small and Intermediate Strain
Properties of Granular Material

57 (2016) **Oliver Detert**
Analyse einer selbstregulierenden interaktiven Membrangründung für Schüttkörper
auf geringtragfähigen Böden

58 (2016) **Yang Yang**
Analyses of Heat Transfer and Temperature-induced Behaviour in Geotechnics

59 (2016) **Alborz Pourzargar**
Application of suction stress concept to partially saturated compacted soils

60 (2017) **Hanna Haase**
Multiscale Analysis of Clay-Polymer Composites for Geoenvironmental Applications

61 (2017) **Kavan Khaledi**
Constitutive modeling of rock salt with application to energy storage caverns

62 (2017) **Nina Silvia Müthing**
On the consolidation behaviour of fine-grained soils under cyclic loading

63 (2017) **Elham Mahmoudi**
Probabilistic analysis of a rock salt cavern with application to energy storage systems

64 (2017) **Negar Rahemi**
Evaluation of liquefaction behavior of sandy soils using critical state soil mechanics and instability concept

65 (2018) **Chenyang Zhao**
Numerical Modeling of Mechanized Tunnel Excavation:
Effects of Sub-systems and Advanced Process Simulation

66 (2018) **Tom Schanz (Herausgeber)**
Innovationen im Spezialtiefbau und in der Umweltgeotechnik
Beiträge zum RuhrGeo Tag 2018

67 (2019) **Linzhi Lang**
Hydro-Mechanical Behaviour of Bentonite-Based Materials Used for Disposal of Radioactive Wastes

68 (2019) **Usama Al-Anbaki**
Hydraulic Interaction of Soil and Nonwoven Geotextiles under Unsaturated Conditions

69 (2019) **Abhishek Rawat**
Coupled Hydro-mechanical Behavior of a Compacted Bentonite-Sand Mixture: Experimental and Numerical Investigations

Schriftenreihe des Lehrstuhls für Bodenmechanik, Grundbau und Umweltgeotechnik der Ruhr-Universität Bochum

Herausgeber: T. Wichtmann

70 (2019) **Mahmoud Qarmout**
Tunnel face stability using Kinematical Element Method (KEM)

71 (2021) **Raoul Hölter**
Optimal Experimental Design in Geotechnical Engineering

72 (2022) **Wolfgang Lieske**
Impact of polymer constitution on the hydro-mechanical behaviour of modified bentonite for the application in geotechnical and geoenvironmental engineering

73 (2022) **Patrick Staubach**
Contributions to the numerical modelling of pile installation processes and high-cyclic loading of soils

74 (2022) **Lingyun Li**
On the hydromechanical behaviour of loess and its effect on slope stability under rainfall infiltration

75 (2022) **Debdeep Sarkar**
Influence of particle characteristics on the behaviour of granular materials under static, cyclic and dynamic loading

76 (2023) **Torsten Wichtmann (Herausgeber)**
Umbau des Emscher-Systems - Geotechnische Erfahrungen
Beiträge zum RuhrGeo Tag 2023

77 (2023) **Abbas Farhat**
Fluidization and erosion of cemented granular materials - Experimental characterization and micromechanical simulation

78 (2023) **Andrea Geppetti**
Experimental and numerical investigations on the behaviour of tailing storage facilities under seismic loading

79 (2023) **Mohammad Hassan Sanayei**
Micromechanical modelling for the analysis of piping erosion in cemented soils for suction-assisted offshore foundations

80 (2024) **Christoph Schmütderich**
Contributions to the stability assessment of slopes subjected to seismic loading

81 (2024) **Thomas Barciaga**
Constitutive modeling of natural clay with application to mechanized tunneling

82 (2024) **Cristian Rodriguez**
Contributions to the modelling of large deformations of soils: A particle-based approach

83 (2025) **Florian Christ**
Experimental investigations on the hydro-mechanical behaviour of clay shales for tunnelling relevant boundary conditions

84 (2025) **Alireza Jebeli**
On the influence of a heterogeneous pore structure on collapse behavior of sandy soils

85 (2025) **Maximilian Schoen**
Numerical analysis of tunnel excavation in swellable clay shales

86 (2025) **Qian Gu**
On the effects of grain shape, gradation, fabric and stress state on the small-strain stiffness of granular soils

87 (2025) **Manh Cuong Le**
Experimental validation of the effective stress concept in unsaturated soils using the suction stress approach across multiple test types and a wide suction range

88 (2025) **Firas Hussain Ali Ghrairi**
Numerical simulation of flexible granular inclusions with special focus on the installation process

89 (2026) **Torsten Wichtmann (Herausgeber)**
Innovationen in der Geotechnik
Beiträge zum RuhrGeo Tag 2026

90 (2026) **Antonia Therese Nitsch**
A novel framework for the numerical modelling of the hydro-mechanical behaviour of expansive soils